Phase Multipath Modelling and Mitigation in Multiple Frequency GPS and Galileo Positioning

Thesis submitted for the degree of
Doctor of Philosophy (PhD)
of the University of London

Ki Yuen Lawrence Lau

Department of Geomatic Engineering
University College London

July 2005

ProQuest LLC
789 East Eisenhower Parkway
P.O. Box 1346
Ann Arbor, MI 48106-1346

ABSTRACT

Multipath is the main error source in short- to medium-baseline GNSS (Global Navigation Satellite System) relative positioning. So, in order to achieve the highest possible accuracy, multipath errors must be modelled and/or mitigated. A new era in GNSS positioning is on the horizon. GPS modernisation is being undertaken, which will provide an unencrypted civil signal (L2C) on the L2 frequency and the signal power of the L2 signal will be increased. Also an additional signal, the so-called L5, will be available on GPS Block IIF satellites scheduled for launch beginning in mid-2006. Furthermore, the European GNSS, named Galileo, is being developed to provide four carrier frequencies and its Full Operational Capability (FOC) is scheduled to be in 2008, but more likely in 2010. This study identifies and models the factors causing phase multipath errors and investigates some possible phase multipath mitigation techniques using the multiple frequency data that modernised GPS and Galileo will offer.

A GNSS data simulator has been developed to generate multipath contaminated data using a phase multipath model based on ray tracing. All known geometrical and physical factors have been taken into account and are described in detail. The model has been validated with real data collected in two experiments with reflectors of different materials. A GNSS data processor has been developed for this validation and for subsequent analyses. The results show good agreement (i.e. similar amplitude and frequency) with real multipath from a steel panel (planar reflector) and fairly good agreement (i.e. similar amplitude with slight different frequency) with real multipath from a lake (dynamic irregular reflector). They show that the multipath model has the potential to correct phase multipath errors in cases where the exact geometry of the reflection process and the nature of the reflector are known. Some of the characteristics of phase multipath and the sensitivities of simulated GNSS measurements to the factors causing multipath are investigated and described.

Multipath mitigation through averaging based on the least squares process and standard outlier detection technique using multiple frequency GPS, Galileo, and integrated GPS and Galileo data have been investigated. Since multiple frequency GPS and Galileo data are not yet available, all data has been generated by the GNSS data simulator described in the foregoing. It was found that standard outlier detection techniques were

not sufficiently robust to tackle the frequency-dependent multipath errors because they could not handle the worst case scenario when multiple frequency multipath errors from a particular satellite were all in-phase. Therefore a cocktail multiple outlier detection algorithm has been proposed and tested. Results show that a combination of more satellites, more frequencies and the cocktail multiple outlier algorithm can substantially mitigate multipath errors and so improve positioning accuracy.

TABLE OF CONTENTS

LIST OF FIGURES

LIST OF TABLES

ACRONYMS AND DEFINITIONS

Table 0-1: Acronyms

ACRONYM	MEANING
AC	Analysis Centre
AG	Automatic GIPSY
ARP	Antenna Reference Point
AR	Axial Ratio
BOC	Binary Offset Carrier
BPA	Bottom of PreAmplifier
BPSK	Biphase Shift Keying
C/A	Coarse Acquisition
CDDIS	Crustal Dynamics Data Information System
CDMA	Code Division Multiple Access
CMOD	Cocktail Multiple Outlier Detection
CODE	Centre for Orbit Determination in Europe
CS	Commercial Service
DCB	Differential Code Bias
DD	Double Difference
DF	Damping Factor
DLL	Delay Lock Loop
EC	European Commission
ESA	European Space Agency
ERP	Earth Rotation Parameter
FOC	Full Operational Capability
Galileo	The European Global Navigation Satellite System
GIPSY	GPS-Inferred Positioning System
GLONASS	The Russian Global Navigation Satellite System
GMT	Greenwich Mean Time
GNSS	Global Navigation Satellite System
GPS	The United States Global Positioning System
GR	Antenna Gain Ratio
GST	Galileo System Time

ACRONYM	MEANING
GTRF	Galileo Terrestrial Reference Frame
GUI	Graphical User Interface
IERS	International Earth Rotation Service
IFB	Inter-Frequency Bias
IGS	International GPS Service
ION	Institute of Navigation (US)
IONEX	IONospheric map Exchange format
LCPC	Laboratoire Central des Ponts et Chaussées
LCP	Left-handed Circular Polarisation
LS	Least Squares
JPL	Jet Propulsion Laboratory
MCAR	Multiple Carriers Ambiguity Resolution
MMW	Multipath Mitigation Window
MOD	Multiple Outlier Detection
NASA	National Aeronautics and Space Administration
NGS	National Geodetic Survey (U.S.)
OF	Obliquity Factor
OS	Open Service
PE	Polarisation Efficiency
PLL	Phase Lock Loop
PMMW	Phase Multipath Mitigation Window
PPP	Precise Point Positioning
PRN	Pseudorandom Noise
PRS	Public Regulated Service
QPSK	Quadrature Phase Shift Keying
RAIM	Receiver Autonomous Integrity Monitoring
RC	Reflection Coefficient
RCP	Right-handed Circular Polarisation
RINEX	Receiver Independent Exchange
RMS	Root Mean Square
RTK	Real-Time Kinematic
SD	Single Difference
SoL	Safety-of-Life Service
SV	Space Vehicle

ACRONYM	MEANING
TBC	To Be Confirmed
TBD	To Be Determined
TCAR	Three Carriers Ambiguity Resolution
TEC	Total Electron Content
TECU	Total Electron Content Unit
TVEC	Total Vertical Electron Content
UTC	Universal Time Coordinated
ZTD	Zenith Tropospheric Delay

ACKNOWLEDGMENTS

I would like to express my gratitude to my supervisor, Professor Paul Cross, for his constructive criticisms, help in problems I came across and providing material, his patience in supervising me, and for proof reading of this thesis. I want to extend my gratitude to the other departmental members, Mr. John Arthur (Departmental research student tutor) and Dr. Marek Ziebart, and to the faculty and staff at University College London for a fine education.

I am grateful to Dr. David Bétaille for providing raw GPS data collected in the Laboratoire Central des Ponts et Chaussées (LCPC) near Nantes in France. I want to thank Mr. Phillip Smith for his assistance in carrying out the GPS data collection in Hyde Park.

I appreciate very much the insights of the information in the RINEX Type C file and Auto-GIPSY (AG) given by Dr. Jim Ray in the US National Geodetic Survey. I want to thank Dr. Gerald Mader in the US National Geodetic Survey for his explanation on satellite antenna offset determination. I am grateful to Professor Ronald Marhefka in the Ohio State University for his help in polarisation matching factor computation. I am also grateful to Dr. Michael Heflin and Dr. Willy Bertiger in the Jet Propulsion Laboratory (JPL) of the US National Aeronautics and Space Administration (NASA) for their explanation in some IGS orbit determination issues.

I am grateful to Mr. Gordon Bentley for proof reading and corrections in English mistakes in this thesis, and to Trimble Navigation Limited and PIL Systems Limited for supplying GPS surveying instruments and support in 2000 to 2002 in Hong Kong.

I would like to thank my ex-colleagues at Nottingham Scientific Ltd., especially Dr. Kevin Sheridan and Professor Vidal Ashkenazi, for their support in my PhD study.

On a personal note I would like to thank my family and friends for their continued support. Especially, I want to thank my sweetheart, Josephine Lee, for her love, support and understanding.

Finally, I want to thank all those who have contributed in any way to the completion of this project.

1. INTRODUCTION

1.1 BACKGROUND

Global Positioning System (GPS) carrier phase-based precise positioning is widely used in attitude and orbit determination, geodesy, deformation monitoring, survey applications, Real-Time Kinematic (RTK) positioning for machine guidance, and other high-accuracy applications. Such relative positioning techniques and their associated, and often highly sophisticated, processing algorithms do, however, rely on the fact that they eliminate GPS biases and errors that are common to receivers over short to medium baselines. As a result it is possible to realise centimetre to millimetre- level positioning accuracies. However, multipath errors are not common to receivers, even over very short baselines. They may substantially degrade the quality of the positioning results if they are not properly taken into account. The maximum error of phase multipath is a quarter of the observing wavelength, for example, it is about five centimetres for GPS L1 carrier. Therefore, multipath mitigation is crucial to achieve centimetre and millimetre-level positioning accuracy.

Since a phase lock loop must be able to handle clock dynamics from user motion in order to prevent cycle slips, the state-of-the-art multipath mitigation techniques may not be applicable for short-delay multipath, for example, Bétaille at el. (2003) states that the effective path delay of multipath for Multipath Mitigation Window (MMW) is at least 7.5 m, short-delay multipath may remain undetectable and remain an error in phase measurement. Therefore, processing algorithm-based multipath mitigation techniques are still useful for further improvement of positioning accuracy, either integrated with other techniques or in a stand-alone mode. However, some algorithm-based multipath mitigation techniques may be limited by the degrees of freedom in currently available solutions, i.e. insufficient satellites and signals. This problem is similar to the un-robustness and unreliability of some outlier detection and rejection techniques used in RAIM and other integrity algorithms in the current GPS system.

GPS modernisation is being undertaken. The GPS Block IIR-M (modernised replenishment) satellites and Block IIF (follow-on generation) satellites will transmit an unencrypted civil signal (L2C) on L2 frequency. Moreover, the signal power of L2 will be increased. It will make tracking of L2 much easier and more reliable and will

increase the use of L2 in high precision kinematic applications. An additional signal, the so-called L5, will be available on GPS Block IIF satellites scheduled for launch beginning in mid-2006. Both the modernised L2 and the new L5 civil signals allow coherent tracking of code and phase and so avoid the losses that occur when tracking the current P(Y) code in L2. This had led to the extensive current interest, e.g. (Hatch et al., 2000) in investigating the potential of three-frequency data for a wide range of applications. On the other hand, the European GNSS, named Galileo, is being developed to provide four carrier frequencies and its Full Operational Capability (FOC) is scheduled to be in 2008, but more likely in 2010. Galileo signals will be available to users in four categories, they are Open Service (OS), Safety-of-Life (SoL) service, Commercial Service (CS), and Public Regulated Service (PRS).

1.2 Objective and Scope

The accuracy of precise positioning and attitude is limited by multipath error since GNSS measurements are often contaminated by an indirect signal reflected from the object carrying the GNSS antenna and/or nearby reflective objects. Multipath from nearby reflective objects is the major concern in this investigation. In high precision positioning, carrier phase data must be used. Therefore, only phase multipath error is considered in this research.

Understanding the physics and characteristics of phase multipath error may help us to find the techniques for phase multipath mitigation. Thus, this research investigates all possible geometric factors and physical factors of phase multipath, and tries to develop a phase multipath model to study the characteristics of phase multipath error.

In view of there being an unencrypted signal, and an increment in signal power, on L2, and there being a new L5 signal in GPS modernisation, the potential uses of L2 and L5 data for precise positioning can be identified. It will be possible to use the different frequencies (L1, L2, or L5 only) individually or different combinations of frequencies (L1 and L2, L1 and L5, L2 and L5, and L1, L2, and L5) for precise positioning in the near future. Regarding Galileo, since only the combination of L1, E5a and E5b is open to all users, this research considers only this combination as Galileo multiple-frequency data. Of course, the most significant improvement over the current GPS system will be the use of all available data from all frequencies. This has motivated this investigation of the potential of three-frequency and multiple-frequency data processing. The interoperation of Galileo and GPS will provide the maximum six open signals.

Therefore, the possible improvements of precise positioning accuracy in the presence of multipath on Galileo three-frequency data, GPS three-frequency data, and Galileo + GPS multiple-frequency data are investigated in this research. Actually the existing literature on multiple-frequency GNSS data processing has tended to concentrate on the use of more frequencies for improved ambiguity determination. Here this thesis addresses a different question. That is: to what extent can multiple frequencies GNSS phase data be used to reduce the impact of multipath in kinematic positioning? Two approaches to the problem are proposed. One is based on the averaging (through a rigorous least squares process) of data from combinations of the various frequencies and the other is based on multipath rejection through classical and advanced outlier detection techniques.

The overall objective of this research is to develop a phase multipath model and investigate the impact of multiple-frequency GNSS on multipath mitigation and detection and rejection of multipath contaminated measurements in single-epoch solution.

1.3 Research Limitations

The limitations of this research are:

- Multipath effect in carrier phase measurements is considered in this research.
- This research considers the GPS and Galileo systems only. The Russian GNSS, called GLONASS, isn't considered in this research because of the ambiguous status of the development/replenishment of satellites for its full operational capacity at the time of this research.
- As the GPS modernised signals and Galileo signals are not yet available, simulated multiple-frequency data are used for this investigation.
- The exact future positioning accuracy of Galileo and modified GPS can be verified when they are fully operational.
- The proposed techniques and algorithms for the modernised GPS and the new Galileo systems in this thesis cannot be validated with real data until Galileo in its FOC and after GPS modernisation.
- At the time of this research, the orbit and signal parameters of Galileo are still tentative. Therefore, the orbit and signal parameters used in simulation of Galileo data may be different to the parameters in Galileo's FOC.

- The performances of the proposed algorithms may vary in different satellite geometries.

1.4 THESIS OUTLINE

This thesis is structured as follows:

Chapter 1: Description of the background, objective and scope, limitations and contributions of this research.

Chapter 2: Necessary background knowledge for understanding this research is given in this chapter. It describes the related knowledge of GNSS, physics, electromagnetics, multipath, and GNSS data processing and snooping.

Chapter 3: Simulation of multiple-frequency GNSS data is very important in this research, so this chapter is devoted to describing the details of the GNSS data simulator, the GNSS biases and errors models, and its validation.

Chapter 4: This chapter describes phase multipath modelling and the validation of the proposed phase multipath model. Characteristics of phase multipath are studied and the sensitivities of factors in the proposed multipath model on multipath errors are investigated.

Chapter 5: The details of the simulated testing datasets for verification of the proposed multipath mitigation algorithms are described. Design of testing datasets is given and the methodology of testing is described.

Chapter 6: The impact of multiple-frequency data on multipath mitigation using the standard single-epoch least squares method is investigated in this chapter. Testing results and analyses are described.

Chapter 7: This chapter investigates the possibility of using the classical multiple outlier detection and rejection technique to detect and reject the multipath contaminated measurements. The detailed processing model is presented. Testing results and analyses are given.

Chapter 8: An advanced cocktail multiple outlier detection and rejection algorithm for detection and rejection of multipath contaminated measurements is proposed and described in this chapter. Testing results and analyses are given.

Chapter 9: The summary of the thesis is presented and the future possibilities and challenges are described.

1.5 RESEARCH CONTRIBUTIONS

The contributions of the research as conducted for this thesis can be summarised as follows:

- A realistic GNSS data simulator is developed to generate modernised three-frequency GPS data and Galileo three-frequency data for this research. It can be used to investigate the performance of the future modernised GPS system, Galileo system, and the inter-operational GPS and Galileo system in a wide range of areas such as the coverage, reliability, continuity, achievable positioning accuracy, RAIM algorithms, TCAR and MCAR, etc.
- A realistic phase multipath model is developed to study the characteristics of phase multipath error and impact of proposed multipath mitigation algorithms on positioning accuracy. The detailed model of ray tracing technique and physical models is presented. The model can simulate multipath from a single smooth planar reflector or multiple smooth planar reflectors. It can also simulate multipath from a carrying platform or the ground. The model can be used for investigation of the impact of multipath effect and multipath mitigation software techniques on positioning accuracy.
- The multipath mitigation capability of using the modernised GPS data and the new Galileo data, and the dual constellation data is investigated. It allows an early assessment of the multipath mitigation capability for the future GNSS.
- A classical multiple outlier detection and rejection technique is proposed to detect and reject multipath contaminated measurements in the three-frequency GPS and Galileo systems and the multiple-frequency GPS and Galileo system. The possibilities and weakness are analysed.

- An advanced cocktail multiple outlier detection and rejection algorithm is proposed to overcome the weakness of the classical technique in detection and rejection of multipath contaminated measurements using the three-frequency GPS and Galileo data and the multiple-frequency GPS and Galileo data. The possibility and limitations are analysed.
- A GNSS data processor is developed to process the three-frequency GPS and Galileo data and the integrated GPS and Galileo multiple-frequency data. The classical and advanced multiple outlier detection and rejection are implemented in the data processor for this research. The data processor can be used to process the current GPS data.

2. BACKGROUND OF RESEARCH

2.1 INTRODUCTION

No one can explain complex issues at this level without a clear understanding of the fundamentals. This chapter describes the background material of GNSS in the space and user segments. Section 2.2 describes the background knowledge of electromagnetics related to phase multipath, it involves GNSS signal structure and antenna. GPS signal structure, GPS modernisation and Galileo system design are described in Section 2.3. GNSS biases and errors related to GNSS data simulation to be described in Chapter 3 are given in Section 2.4. Section 2.5 presents the background of GNSS observables and data processing techniques related to Chapters 6 to 8. Impact and background of phase multipath effect on GNSS positioning, and importance of multipath mitigation are described in Section 2.6. Some state-of-the-art multipath mitigation techniques are presented in Section 2.7. Background of outlier detection related to Chapters 7 and 8 are briefly described in Section 2.8.

2.2 GNSS RELATED ELECTROMAGNETICS

This section presents the background of electromagnetics related to GNSS. It is necessary for multipath modelling described in Chapter 4.

2.2.1 Electromagnetics field and wave

The state of excitation which is established in space by the presence of electric charges is said to constitute an electromagnetic field. It is represented by two vectors. They are the electric vector **E** and the magnetic induction **B**. It is necessary to introduce a second set of vectors to describe the effect of the field on material objects. The vectors are the electric current density **j**, the electric displacement **D**, and the magnetic vector **H**. The space and time derivatives of the five vectors are related by Maxwell's equations, which hold at every point in whose neighbourhood the physical properties of the medium are continuous [Born and Wolf, 1999]:

$$\text{curl } \mathbf{H} - \frac{1}{c}\dot{\mathbf{D}} = \frac{4\pi}{c}\mathbf{j} \tag{2.1}$$

$$\text{curl } \mathbf{E} + \frac{1}{c}\dot{\mathbf{B}} = 0 \tag{2.2}$$

where c denotes the speed of light, the dot denotes the differentiation with respect to time and curl is explained in Appendix A. They are supplemented by two scalar relations:

$$\text{div } \mathbf{D} = 4\pi\rho \tag{2.3}$$

$$\text{div } \mathbf{B} = 0 \tag{2.4}$$

where div is the divergence and is explained in Appendix A. Equation (2.3) may be regarded as a defining equation for the electric charge density ρ and Equation (2.4) may be said to imply that no free magnetic poles exist. The Maxwell equations (2.1) to (2.4) relate the five basic quantities **E**, **H**, **B**, **D** and **j**. In order to allow a unique determination of the field vectors from a given distribution of currents and charges, these equations must be supplemented by relations which describe the behaviour of substances under the influence of the field. These relations are known as material equations (constitutive relations) [Born and Wolf, 1999]. Generally speaking, they are rather complicated. However, according to [Born and Wolf, 1999], if the field is time harmonic, and if the bodies are at rest, or in very slow motion relative to each other, and if the material is isotropic (i.e. when its physical properties at each point are independent of direction), they take usually the relatively simple form:

$$\mathbf{j} = \sigma\mathbf{E} \tag{2.5}$$

$$\mathbf{D} = \varepsilon\mathbf{E} \tag{2.6}$$

$$\mathbf{B} = \mu\mathbf{H} \tag{2.7}$$

where σ denotes the specific conductivity, ε denotes the dielectric constant (or permittivity) and μ denotes the magnetic permeability. Substituting Equation (2.5) into the Maxwell's curl equation (2.1) in differential form (Ampère's law):

$$\nabla \times \mathbf{H} = \mathbf{j} + \frac{\partial \mathbf{D}}{\partial t} \tag{2.8}$$

it is obtained:

$$\nabla \times \mathbf{H} = \sigma \mathbf{E} + \frac{\partial \mathbf{D}}{\partial t} \tag{2.9}$$

Considering a linearly polarised plane wave travelling in the x direction with $\mathbf{E}$ in the y direction, the vector equation (2.9) reduces to the scalar phasor equation [Kraus and Fleisch, 1999]:

$$-\frac{\partial H_z}{\partial x} = \sigma E_y + j\omega\varepsilon E_y \tag{2.10}$$

where j denotes the complex operation ($=\sqrt{-1}$, dimensionless) and ω denotes the radian frequency ($=2\pi f$, rad s^{-1}). The term σE_y represents the conduction-current density. While the term $j\omega\varepsilon E_y$ represents the displacement-current density. Therefore, according to (2.10) the space rate of change of H_z equals the sum of the conduction- and displacement-current densities. If σ is not equal to zero, it may arbitrarily define three conditions as follows:

1. $\omega\varepsilon >> \sigma$
2. $\omega\varepsilon \approx \sigma$
3. $\omega\varepsilon << \sigma$

If the displacement current is much greater than the conduction current, as in condition 1, the medium behaves like a dielectric. When $\sigma = 0$, the medium is perfect or lossless dielectric. For σ not equal to zero the medium is lossy or imperfect dielectric. However, if $\omega\varepsilon >> \sigma$, it behaves more like a dielectric than anything else and may, for practical purposes, be classified as a dielectric. On the other hand, when the conduction current is much greater than the displacement current, as in condition 3, the medium may be classified as a conductor. In between these two conditions, when the condition current is about the same order of magnitude as the displacement current, the medium

may be classified as a quasi-conductor (not to be confused with "semiconductor"). According to [Kraus and Fleisch, 1999], it can be even more specific and arbitrarily classify media as belonging to one of the three types using the value of the ratio $\sigma / \omega\varepsilon$ as follows:

Conductors: $$\frac{\sigma}{\omega\varepsilon} > 100 \tag{2.11}$$

Quasi-conductors: $$\frac{1}{100} < \frac{\sigma}{\omega\varepsilon} < 100 \tag{2.12}$$

Dielectrics: $$\frac{\sigma}{\omega\varepsilon} < \frac{1}{100} \tag{2.13}$$

where σ denotes the conductivity of medium in $\mho m^{-1}$, ε denotes the permittivity of medium in Fm^{-1}, and ω denotes the radian frequency ($=2\pi f$, where f is the frequency in Hz). However, Parton and Owen (1975) classifies $\sigma / \omega\varepsilon > 10$ as good conductor and poor dielectric, and $\sigma / \omega\varepsilon < 0.1$ as good dielectric and bad conductor. The ratio $\sigma / \omega\varepsilon$ is dimensionless. Frequency is an important factor in determining whether a medium acts like a dielectric or a conductor. For example, take the case of copper for which the relative permittivity $\varepsilon_r = 1$ and $\sigma = 5.8 \times 10^7$ $\mho m^{-1}$ and the frequency is the GPS L1 carrier (1575.42 MHz), the ratio $\sigma / \omega\varepsilon$ equals 6.62×10^7, which is the condition 1; it means that copper acts like a good conductor in L-band frequency.

In an electromagnetic wave, a changing electric field produces a changing magnetic field, which in turn generates an electric field, and so on, with a resulting propagation of energy. For a plane wave in space, the electric and magnetic field lines, **E** and **H**, are everywhere perpendicular to each other and perpendicular to the wave direction. **E** and **H** are also in phase. A wave of this type is called a Transverse ElectroMagnetic (TEM) wave [Kraus and Fleisch, 1999]. Therefore, the wave radiated by an antenna consists of an electric field component and a magnetic field component. The two components are orthogonal and perpendicular to the direction of propagation of the wave; they vary at the frequency of the wave. The direction of the electric field is not fixed, it is a function of time and position. In general, the electric field of a wave travelling in the z-direction may have both a y and x component. In this more general situation, with a phase difference between the components, the wave is said to be elliptically polarised (see Figure 2-1 (b)). At a fixed value of z the electric vector **E** rotates as a function of time,

the trip of the vector describing an ellipse called the polarisation ellipse (see Figure 2-1). Polarisation is characterised by the following parameters:

- Direction of rotation with respect to the direction of propagation: right-handed (clockwise) or left-handed (counter-clockwise).
- Axial ratio (AR): $AR = E_2/E_1$, that is the ratio of the major and minor axes of the polarisation ellipse. When the ellipse is a circle ($E_1 = E_2$, $AR = 1$), the polarisation is said to be circular (see Figure 2-1(c)). When the ellipse reduces to one axis ($AR = \infty$, the electric field maintains a fixed direction), the polarisation is said to be linear (see Figure 2-1(a)).

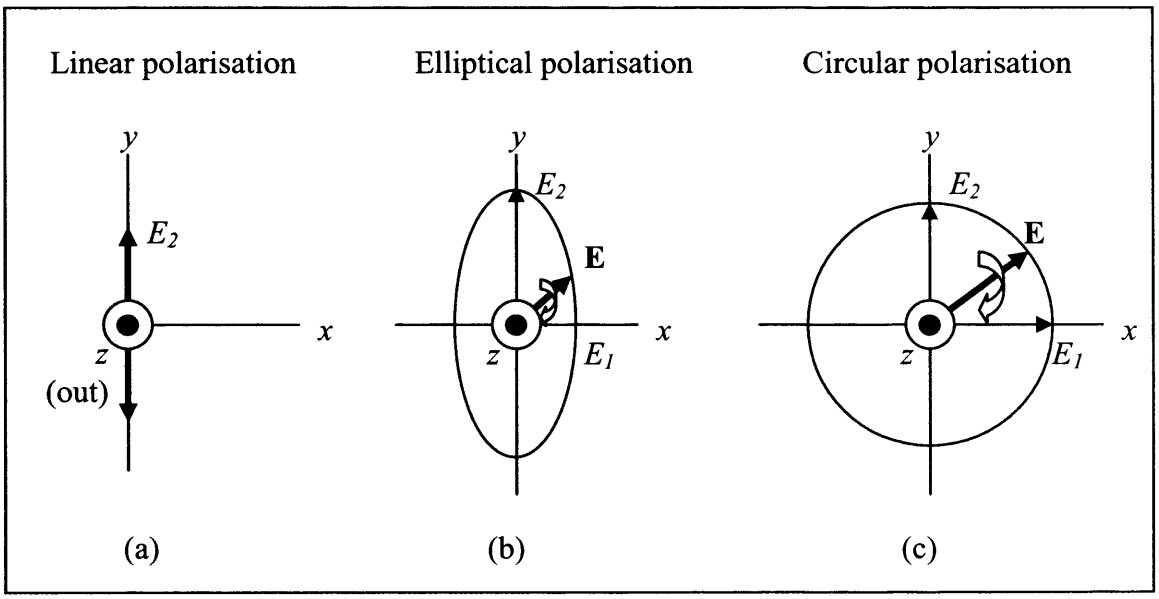

Figure 2-1: (a) Linear, (b) elliptical and (c) circular polarisation for left-handed circular polarised wave approaching. Note that the positive *z* direction points out of the page.

Two waves are in orthogonal polarisation if their electric fields describe identical ellipse in opposite directions. In particular, the following can be obtained:

- Two orthogonal circular polarisations described as right-handed circular and left-handed circular (the direction of rotation is for an observer looking in the direction of propagation).
- Two orthogonal linear polarisations described as horizontal and vertical (relative to a local reference).

An antenna designed to transmit or receive a wave of given polarisation can neither transmit nor receive in the orthogonal polarisation [Maral and Bousquet, 2002].

Now, the depth of penetration of an electromagnetic wave in a medium is considered. Kraus and Fleisch (1999) describes the depth of penetration δ (denoted as $1/e$) of a plane electromagnetic wave incident normally on a good conductor, such as copper, as:

$$\delta = \frac{1}{\sqrt{f\pi\mu\sigma}} = \frac{1}{e} \qquad \text{Depth of penetration} \qquad (2.14)$$

For copper $\mu_r = 1$, so that $\mu = 1.26\mu\,\mathrm{Hm}^{-1}$, and the conductivity $\sigma = 58$ MŬm^{-1}. Substituting these values in Equation (2.14), the depth of penetration for copper is obtained:

$$\delta = \frac{6.6\times10^{-2}}{\sqrt{f}} \qquad (2.15)$$

Evaluating Equation (2.15) at the GPS L1 carrier frequency (1575.42 MHz), the $1/e$ depth of penetration is 1.663×10^{-3} mm. This small penetration is often called the skin effect. Therefore, most reflection occurring in GPS (GNSS) L-band frequency may be considered as surface reflection.

2.2.2 Reflection with Oblique Incidence and Relative Permittivity (Dielectric Constant)

Changes of electromagnetic fields after reflections upon a perfect conductor and a dielectric half-space are described in [Ida and Bastos, 1992] and [Wolf, 2001]. This section concentrates on the reflection coefficients for oblique incidence. Kraus and Fleisch (1999) describes the reflection of oblique incidence for electromagnetic wave upon a perfect conductor and a dielectric half-space. They consider two cases: (1) the electric field perpendicular to the plane of incidence (the *xy* plane, see Figure 2-1) and (2) the electric field parallel to the plane of incidence. These waves are said to be perpendicularly polarised and parallel polarised, respectively. It is clear that any arbitrary plane wave can be resolved into perpendicular and parallel components. In the

case of an electromagnetic wave travelling in medium 1 to medium 2, they describe that the perpendicular component of the Fresnel reflection coefficient $\rho_{\perp}$ as:

$$\rho_{\perp} = \frac{Z_2 \cos\theta_i - Z_1 \cos\theta_t}{Z_2 \cos\theta_i + Z_1 \cos\theta_t} \tag{2.16}$$

where Z_1 and Z_2 are the impedances of medium 1 and medium 2, respectively, and θ_i and θ_t are the angle of incidence and angle of refraction, respectively. If medium 2 is a perfect conductor, Z_2 = 0 and $\rho_{\perp}$ = -1. If both media are lossless nonmagnetic dielectric, Equation (2.16) becomes:

$$\rho_{\perp} = \frac{\cos\theta_i - \sqrt{\varepsilon_2/\varepsilon_1 - \sin^2\theta_i}}{\cos\theta_i + \sqrt{\varepsilon_2/\varepsilon_1 - \sin^2\theta_i}} \qquad \text{(Reflection coefficient } \perp\text{)} \tag{2.17}$$

where ε_1 and ε_2 are the relative permittivities of medium 1 and medium 2 respectively. Provided medium 2 is a more dense dielectric than medium 1 ($\varepsilon_2 > \varepsilon_1$), the quantity under the square root will be positive and $\rho_{\perp}$ will be real. On the other hand, the parallel component of the Fresnel reflection coefficient ρ_{II} is found to be:

$$\rho_{\text{II}} = \frac{Z_2 \cos\theta_t - Z_1 \cos\theta_i}{Z_1 \cos\theta_i - Z_2 \cos\theta_t} \tag{2.18}$$

which for lossless nonmagnetic dielectrics becomes:

$$\rho_{\text{II}} = \frac{-\left(\varepsilon_2/\varepsilon_1\right)\cos\theta_i + \sqrt{\varepsilon_2/\varepsilon_1 - \sin^2\theta_i}}{\left(\varepsilon_2/\varepsilon_1\right)\cos\theta_i + \sqrt{\varepsilon_2/\varepsilon_1 - \sin^2\theta_i}} \qquad \text{(Reflection coefficient } \|\text{)} \tag{2.19}$$

and reduces to ρ_{II} = -1 if medium 2 is a perfect conductor. Relative permittivity (dielectric constant) is often used to determine reflection coefficient or reflectivity of material. For instance, Zavorotny and Voronovich (2000) and Masters et al. (2000) use

dielectric constant in the investigations of using GPS reflected signal from land to determine its moisture content, and Komjathy et al. (2000) use dielectric constant to identify features from reflected GPS signals in ocean science. This is because most natural and man-made structures are made of dielectric materials such as dry or wet urban ground (e.g. roads and pavements) and rural ground (e.g. soil), wood (e.g. trees, wooden structures), concrete buildings and bridges, glass (e.g. windows), and fresh and sea water. It may be that on engineering sites a lot of conductive materials such as steel and aluminum alloy, and construction machines and plants cause serious multipath problem. However, conductive materials may be considered as dielectric because their coatings are always dielectrics in L-band frequency such as silicon oxide ($Si0_2$) on the surface of some steel and aluminum oxide (Al_2O_3) on most aluminum products. Note that relative permittivity is preferred to dielectric constant in this thesis because it is frequency-dependent and not a constant.

Inan and Inan (2000) explains the change of polarisation of a circularly polarised incident wave at a dielectric interface after reflection. When the incident angle is less than the Brewster angle, whose definition is given in Section 4.3 and Equation (4.3), the reflected wave is elliptically polarised with the opposite sense of rotation to that of the incident wave. As the incident angle is equal to the Brewster angle, there is no reflection in the parallel component of Fresnel reflection coefficient, so the reflected wave would be linearly polarised with electric field perpendicular to the plane of incidence. This situation is explained in Section 4.3. When the incident angle is greater than the Brewster angle, the reflected wave is elliptically polarised with the same sense of rotation as that of the incident wave. When an RCP incident wave travels in air (medium 1) and arrives at a perfect conductor (medium 2), Kraus and Fleisch (1999) describe the reflected wave as LCP. However, perfect conductors are seldom found in most urban and rural environments.

In reflection with oblique incidence, the incident and reflected wavefronts may interfere with each other. In Figure 2-2, the dotted red lines representing the wavefronts of the reflected wave are interfered with by the dotted green lines representing the wavefronts of the incident wave before the reflected wave arrived at the antenna. On the other hand, the wavefronts of the incident wave are interfered with by the wavefronts of the reflected wave. It may lead to a complicated multipath problem.

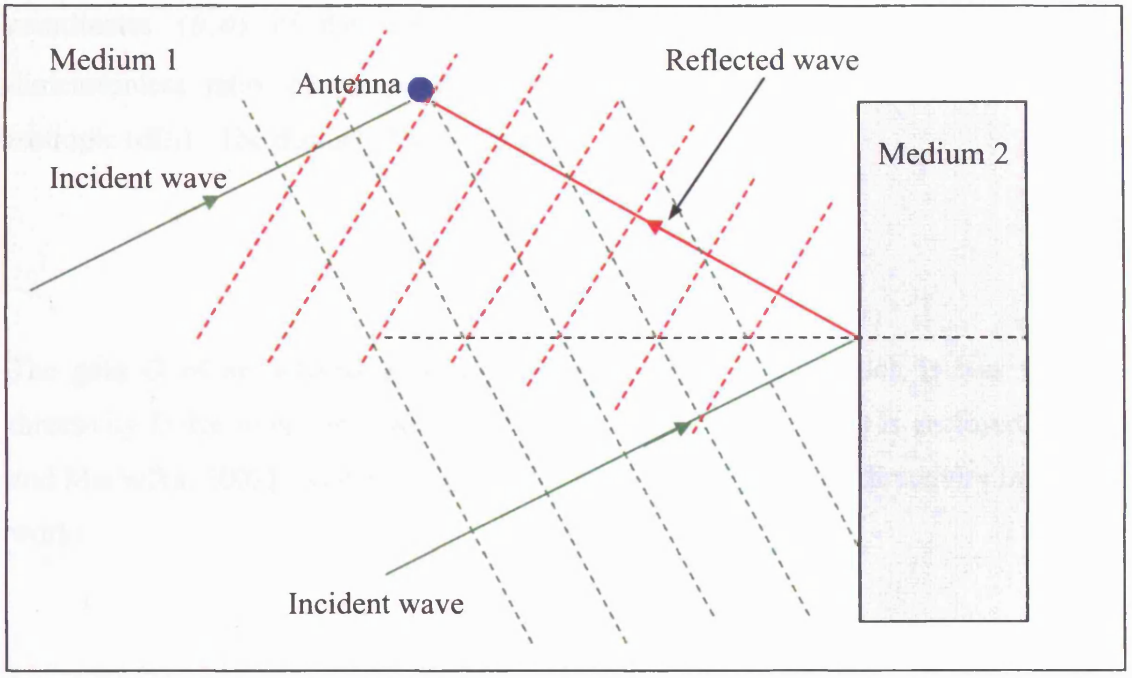

Figure 2-2: Interference of incident and reflected signals for oblique incidence.

2.2.3 Antennas

2.2.3.1 Directivity and gain

The directivity D and the gain G are probably the most important parameters of an antenna [Kraus and Marhefka, 2002]. The parameters describes the "focused-ness" of antennas.

The directivity of an antenna is equal to the ratio of power density in maximum direction to its average value over a sphere as observed in the far field of an antenna or to power density of an isotropic antenna (no preferred direction). Therefore, the directivity from pattern is defined as:

$$D = \frac{P(\theta,\phi)_{\max}}{P(\theta,\phi)_{av}} \text{ or } D = \frac{P(\theta,\phi)_{\max}}{P(\theta,\phi)_{iso}} \tag{2.20}$$

where $P(\theta,\phi)_{\max}$ denotes the maximum power density in the spherical coordinates (θ,ϕ) of the three-dimensional field pattern, $P(\theta,\phi)_{av}$ denotes the far field average power density in the spherical coordinates (θ,ϕ) of the three-dimensional field pattern, and $P(\theta,\phi)_{iso}$ denotes the power density of an isotropic antenna in the spherical

coordinates (θ,ϕ) of the three-dimensional field pattern. The directivity is a dimensionless ratio ≥ 1, however, directivity can be represented in decibels over isotropic (dBi). The decibel (dB) notation is:

$$X_{(dB)} = 10\log_{10}(X) \tag{2.21}$$

The gain G of an antenna is an actual or realised quantity which is less than the directivity D due to ohmic losses in the antenna or its radome (if it is enclosed) [Kraus and Marhefka, 2002]. Therefore, the gain can be described as the directivity in the real world:

$$G = kD \tag{2.22}$$

where k denotes the dimensionless antenna efficiency factor or radiation efficiency ($0 \leq k \leq 1$), which is the ratio of radiated power P_{rad} to input power P_{in}. Note that the gain takes into account the real power values, but it is still unitless (it can be also represented in dB).

2.3 GNSS SIGNALS

2.3.1 Global Positioning System

2.3.1.1 GPS signals

GPS multiplexes the civil (C/A) and precision (P) code on a signal carrier in phase quadrature and then employs CDMA so that the different signals can share the identical frequency band [Spilker, 1996]. Signals transmitted from GPS satellites are right-handed circular polarised (RCP). "Right-handed" means that when an observer looks in the direction from which the signal is coming, the end point of the electric vector appears to rotate in an anti-clockwise direction, as in Figure 2-3. The time-phase angle by which E_y leads E_x of RCP is -90° as shown in Figure 2-3(a). The ratio of the major to the minor axes of the polarisation is called the axial ratio (AR) and for circular polarisation E_1=E_2 and AR=1 as shown in Figure 2-3(b), where E_1 is the amplitude of

wave linearly polarised in x direction and E_2 is the amplitude of wave linearly polarised in y direction.

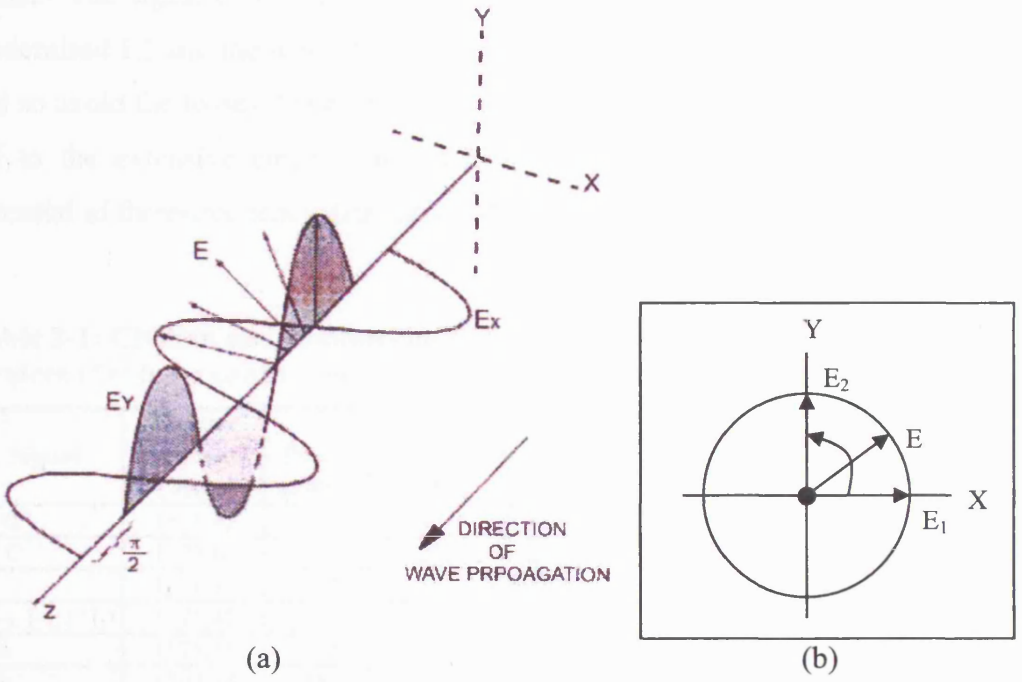

Figure 2-3: Right-handed circular polarised wave approaching. (a) The field vector E along the direction of propagation and its components in E_X and E_Y. (b) The rotational direction of the field vector and its amplitudes E_1 and E_2 in X and Y respectively.

The electromagnetic waves transmitted by GPS satellites are spherical, however, GPS satellites are far away from the Earth, and therefore it is possible to approximate the spherical wave as a plane wavefront. The signal parameters of GPS L1 frequency can be found in Table 2-1.

2.3.2 GPS Modernisation

GPS modernisation is being undertaken. The GPS Block IIR-M (modernised replenishment) satellites and Block IIF (follow-on generation) satellites will transmit an unencrypted civil signal (L2C) on L2 frequency. Moreover, the signal power of L2 will be increased. It will make tracking of L2 much easier and more reliable and will increase the use of L2 in high precision kinematic applications. The interface of the modernised L2C signal between the GPS space segment and the GPS navigation user segment are described in ICD-GPS-200C (2003). An additional signal, the so-called L5, will be available on GPS Block IIF satellites scheduled for launch beginning in mid-

2006. ICD-GPS-705 (2002) describes the requirements related to the interface between the space segment of the GPS and the navigation users of the GPS for the L5 navigation signal. The signal parameters for GPS L2C and L5 are listed in Table 2-1. Both the modernised L2 and the new L5 civil signals allow coherent tracking of code and phase and so avoid the losses that occur when tracking the current P(Y) code in L2. This has led to the extensive current interest, e.g. (Hatch et al., 2000) in investigating the potential of three-frequency data for a wide range of applications.

Table 2-1: Civilian and commercial GPS and Galileo signal parameters and services (* = to be confirmed, bps = bits per second, and sps = symbols per second).

Signal	Carrier Frequency (MHz)	Power (dBW)	Typical C/N0 (dBHz)	Modulation	Data rate	Chipping Rate	Services (Types of Data)
L1 C	1575.42	-160	45	BPSK(1)	50 bps	10.23 Mbps	OS
L2 C	1227.60	-160	51	BPSK(1)	25 bps	1.023 Mbps	OS
L5	1176.45	-154	50	QPSK(10)	50 bps	10.23 Mbps	OS
E1-L1-E2 (L1	1575.42	-155	50	BOC(2,2)	250 sps	1.023 Mbps	OS/CS/SOL
E5a	1176.45	-155	50	QPSK(10)	50 sps	10 Mbps*	OS/CS/SOL
E5b	1207.14	-155	50	QPSK(10)	250 sps	10 Mbps*	OS/CS/SOL
E6	1278.75	-155	50	BPSK(5)	1000 sps	5.115 Mbps	CS/PRS

2.3.3 Galileo

The European GNSS, named Galileo, is being developed to provide four carrier frequencies and its Full Operational Capability (FOC) is scheduled to be in 2008, but more likely in 2010. Galileo constellation consists of 30 satellites (27 operational plus 3 in-orbit spares) in 3 orbital planes with 120° apart. The inclination of the orbital planes is 56°, the orbital radius is 29,994 km, and the satellite orbiting period is about 14.4 hours. The illustration of Galileo constellation is shown in Figure 2-4. Table 2-2 shows the Galileo constellation parameters used in Galileo data simulation to be described in Chapter 3. Galileo signals will be available to users in four categories, they are Open Service (OS), Safety-of-Life (SoL) service, Commercial Service (CS), and Public Regulated Service (PRS). The definition of the services is described in [EC and ESA, 2001]. The signals for the services and signal parameters are listed in Table 2-1 [Eissfeller et al., 2002] [Hein et al., 2003] and the possible frequency combinations are given in Table 2-3. Since only the combination of L1, E5a and E5b is open to all users as shown in Table 2-1 and 2-3, this research considers only this combination as Galileo multiple-frequency data. Note that although all the Galileo frequencies will be available in space, only receivers designed to receive particular frequencies can collect the data

from these frequencies; this is because additional phase centre(s) and particular frequency bandwidth(s) is/are required in receivers in order to receive additional frequency(ies).

Table 2-2: Galileo constellation parameters (to be confirmed).

Semi-major axis	29,994 km
Inclination	56°
Eccentricity	0.0
Right ascension	-120°,0°,120°
Rate of right ascension	0.0°/day
Argument of perigee	0.0°
Mean anomaly (1st	-160, -120, …,
orbit plane)	120, 160
(2nd orbit plane)	-153.33, -113.33, …,
	133.33, 173.33
(3rd orbit plane)	-166.67, -126.67, …,
	106.67, 146.67

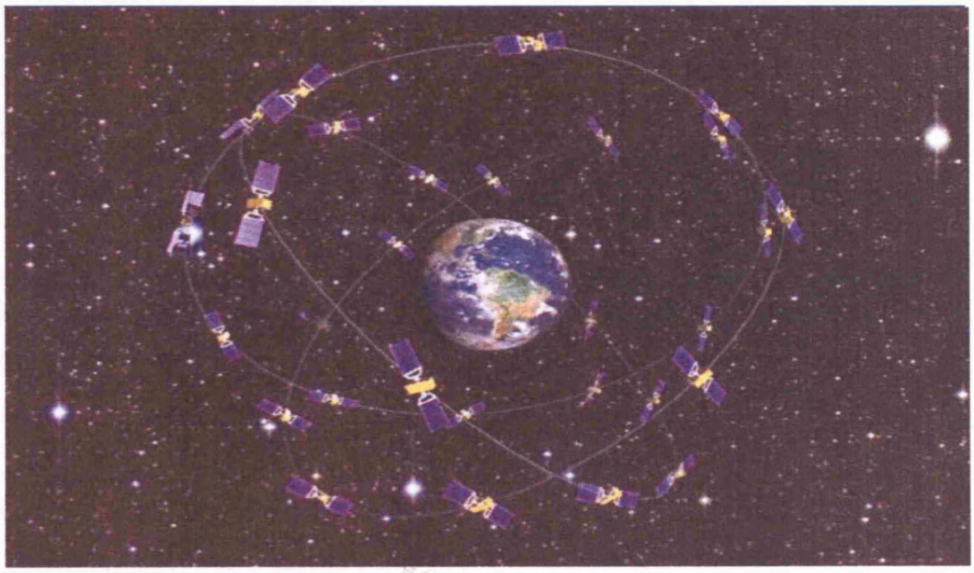

Figure 2-4: Illustration of Galileo constellation [Peckham, 2005].

Table 2-3: Galileo possible frequency combinations and services.

Frequency Comdinations	Services (Types of Data)
L1 E5a	OS/CS/SOL
L1 E5b	OS/CS/SOL
L1 E6	OS/CS/SOL + CS/PRS
L1 E5a E5b	OS/CS/SOL
L1 E5a E6	OS/CS/SOL + CS/PRS
L1 E5b E6	OS/CS/SOL + CS/PRS
L1 E5a E5b E6	OS/CS/SOL + CS/PRS

2.3.3.1 Galileo signals

Galileo will provide 10 navigation signals in right-handed circular polarisation (RCP) in the frequency ranges 1164–1215 MHz (E5a and E5b), 1260–1300 MHz (E6) and 1559–1592 MHz (E2-L1-E1), which are part of the Radio Navigation Satellite Service (RNSS) allocation [EC and ESA, 2001] [Hein et al., 2003]. The frequency band E2-L1-E1 is sometimes denoted as L1 for convenience. The signal parameters of L1, E5a, E5b, and E6 are listed in Table 2-1. These parameters may be different to the future Galileo's signals in FOC because the signal design has not been finalised at the time of this research. [Hein et al., 2003] points out the following criteria for the type of modulation in Galileo signal design:

- Minimization of the implementation losses in the Galileo satellites, making use of the current state-of-the-art related satellite components.
- Maximization of the power efficiency in the Galileo satellites.
- Minimization of the level of interference induced by the Galileo signals in GPS receivers.
- Optimization of the performance and associated complexity of future Galileo user receivers.

All the Galileo satellites will share the same nominal frequency and use of CDMA techniques as the GPS, which is therefore compatible with the GPS.

2.4 GNSS BIASES AND ERRORS

This section describes the GNSS biases and errors briefly. Multipath effect is the most important GNSS error in this research. It is described in Section 2.6. Table 2-4 lists the potential error size of the some major GPS biases and errors; it is obtained from [Misra and Enge, 2001]. Other relatively minor GPS biases and errors such as inter-frequency bias for single-frequency user, relativistic effect, integer carrier ambiguity, antenna phase centre offset and variation, and phase wind-up are not listed in the table but are considered in the GNSS data simulation and phase multipath modelling described in Chapters 3 and 4 respectively. The bias of integer ambiguity is the unknown cycles in phase measurement when the receiver locks on a satellite signal at the first epoch. The

determination of the integer phase ambiguity is always called ambiguity resolution. Ambiguity resolution is described in Section 2.5.

Table 2-4: A summary of the biases and errors in GPS measurement [Misra and Enge, 2001].

Bias or error	Source	Potential Error Size
Satellite clock bias	Clock modelling error	2 m (rms)
Satellite ephemeris error	Ephemeris prediction error	2 m (rms) along the line of sight
Ionospheric effect	Ionospheric delay in code and advancement in phase during signal travelling in the dispersive ionosphere; same size but opposite in code and phase	~2 - 10 m in zenith direction; this bias depends on satellite elevation and user latitude, time of the day, and solar activity
Tropospheric delay	Tropospheric delay during signal travelling in troposphere	~2.3 - 2.5 m; it depends on user altitude and satellite elevation
Multipath error	Indirect signal path(s) arriving antenna	Code: 0.5 - 1 m, carrier: 0.5 - 1 cm in a "clean" environment
Measurement noise	Random noise (receiver noise)	Code: 0.25 - 0.5 m, carrier: 1 - 2 mm

The potential error sizes, and the biases and errors described in this section are specific to GPS but they are similar to other GNSS including Galileo if the corresponding orbit and signal parameters are treated adequately because some biases and errors are frequency dependent and/or satellite elevation dependent.

- For more details about ionospheric effect, see [Klobuchar, 1996],
- Investigations on tropospheric effect can be found in [Davis et al., 1985] and [Ifadis, 1992],
- Ephemeris error and satellite clock bias can be found in [Zumberge and Bertiger, 1996],
- A description of the relativistic effect can be found in [Ashby and Spilker, 1996],
- Determination and details of inter-frequency bias can be found in [Wilson et al., 1999],
- Phase wind-up error is described in [Wu et al., 1993],
- Calibration of receiving antenna phase centre offset and variation can be found in [Akrour et al., 2005] and [Schupler and Clark, 2001], and

- The calibration of GPS Block IIA satellite antenna phase centre offset and variation can be found in [Mader and Czopek, 2002].

2.5 GNSS OBSERVABLES AND DATA PROCESSING

For high (centimetre or better) accuracy GNSS positioning, relative positioning technique and high precision carrier phase measurements must be used. Relative carrier phase-based GNSS precise positioning is being increasingly used in almost all disciplines of, or related to, geodesy, including attitude and orbit determination, engineering and geophysical deformation monitoring, land surveying and precise navigation. Such positioning is subject to a number of important error sources as described in Section 2.4. For different applications, and for relative positioning over different distances, particular error sources take on a special importance and effectively limit the performance of GNSS.

Remondi (1984) proposes some important differencing techniques using phase data in relative geodesy. The techniques are commonly used in most GNSS data processing algorithms. First of all, he introduces a single difference technique as shown in Figure 2-5, the single difference phase observable is obtained by differencing of measurements between two receivers b and r to a satellite i:

$$\varphi_{rb}^{i}(t) = \varphi_{r}^{i}(t) - \varphi_{b}^{i}(t) \tag{2.23}$$

where φ denotes the phase measurement and t denotes the measurement epoch.

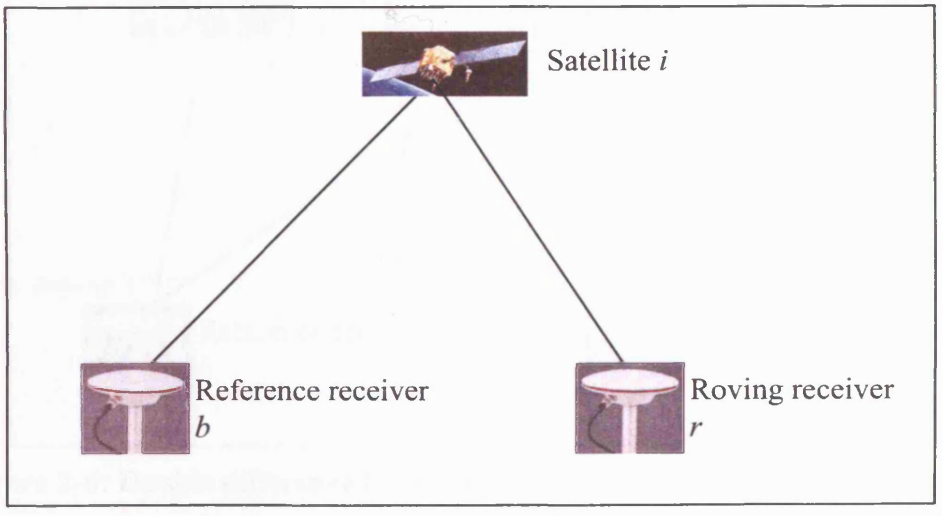

Figure 2-5: Single difference between receivers *b* and *r*.

This technique saves processing effort in modelling or estimation of satellite related biases and errors because these biases and errors are common to both phase measurements. The byproduct of this technique is a determination of the change in the time difference between two receiver clocks since the initial time difference. The actual integer ambiguity in each phase measurement can be determined in this single difference technique. However, this technique is susceptible to cycle slips, which are a sudden jump of integer ambiguity caused by, for example, ionospheric scintillation, receiver hardware failure, unknown loss of lock such as interference and jamming, or loss of lock in high dynamic applications.

The second differencing technique is the double differencing. It is two single differences between two satellites and two receivers as shown in Figure 2-6. The double difference (DD) observable is obtained by:

$$\varphi_{rb}^{ij}(t) = [\varphi_r^i(t) - \varphi_b^i(t)] - [\varphi_r^j(t) - \varphi_b^j(t)] \tag{2.24}$$

This technique further saves processing load in modelling or estimation of receiver related biases and errors, such as receiver clock biases of the two receivers, which are eliminated in double difference technique. Double difference integer phase ambiguities can be determined. However, the disadvantage is similar to that of the single difference technique; this technique is sensitive to cycle slips. Furthermore, it adds correlation of measurements in double difference cofactor matrix.

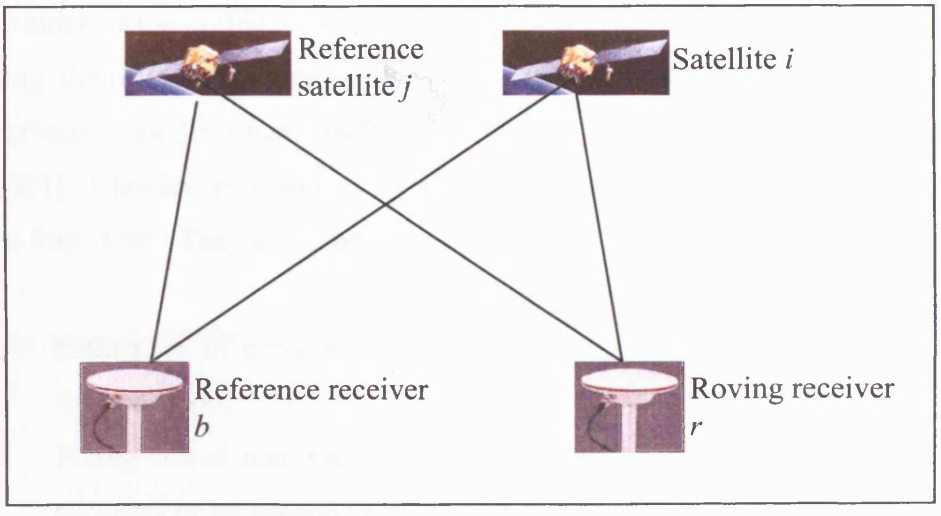

Figure 2-6: Double difference between receivers *b* and *r* and satellites *i* and *j*.

The final differencing technique is the triple differencing. It is the difference of two double differences between two consecutive epochs and the observable is obtained by:

$$\varphi_{rb}^{ij}(t \mid t-1) = \varphi_{rb}^{ij}(t) - \varphi_{rb}^{ij}(t-1) \tag{2.25}$$

The advantage of this technique is that it is insensitive to cycle slip. However, the phase ambiguity cannot be forced to integer because it is eliminated in differencing between two epochs. Therefore this technique is less accurate in short baseline applications when compared with single and double difference techniques.

Double difference observable is used in this research because it is more accurate than triple difference observable in short to medium baselines, which are the main concern of this research, and it requires less processing load when compared with single difference observable.

In order to achieve the high accuracy positioning solution, the integer phase ambiguity must be resolved. Therefore, most GNSS data processing algorithms involve ambiguity resolution. However, Counselman and Gourevitch (1981) propose a searching technique called Ambiguity Function Method (AFM) to determine position without actual fixing of ambiguities. It is achieved by searching the correct position among a set of trial positions within a defined search volume. This method is insensitive to the integer ambiguity because the cosine of phase residual is insensitive to the integer part of the phase residual. Remondi (1984), Mader (1992), Corbett and Cross (1995), Mok (1996), and Lau (2000) have further investigated this method. AFM can be used for ambiguity resolution sometimes. In this case the determined position is used to find the integer values of the ambiguities before the fixed solution. There are many GPS data processing algorithms presented by various authors, examples can be found in standard GPS textbooks like [Hofmann-Wellenhof et al. 2004], [Leick, 2003] and [Misra and Enge, 2001]. Classical processing procedure involving ambiguity resolution is typically based on four steps. They are summarised below:

i) Estimation of initial ambiguity parameters as real-values in a least squares float solution.

ii) Fixing initial real ambiguities to integer values based on their estimated accuracy or by general ordering search strategy.

iii) Introduction of ambiguity parameters as known quantities into the least squares observation equation to perform a fixed solution.

iv) Validation by evaluating the adjusted results and the a posteriori statistical quantities, such as residuals and variance-covariance matrix.

A variety of methods have been developed to fix real-valued estimates to integer quantities. The correctness and efficiency of these techniques based on ordering search strategy are mainly dependent on the number of fixed ambiguity sets evaluated to make the final choice. A full search over all possible combinations is optimal as far as reliability is concerned but it is definitely not efficient. Evaluation of only a few sets will take a risk that the correct set has not been selected. These classical approaches can be improved by using the statistical and geometrical information normally available during data processing. Examples include the algorithms proposed by [Beutler et al., 1984] and [Bock et al., 1986], the Fast Ambiguity Resolution Approach (FARA) [Frei, 1991] [Frei and Beutler, 1990], the Least Squares Ambiguity Search Technique (LSAST) [Hatch, 1991], and the Least squares AMBiguity Decorrelation Adjustment (LAMBDA) method [Teunissen, 1995].

2.6 MULTIPATH

2.6.1 Description of multipath effect

For different applications, and for relative positioning over different distances, particular error sources described in Section 2.4 take on a special importance and effectively limit the performance of GNSS. This research is concerned with one of these: phase multipath, and is therefore especially relevant to applications that require very high accuracy positioning over short distances (e.g. engineering surveying and attitude determination) when many of the other errors exhibit a high degree of spatial correlation and can be eliminated by differencing technique described in Section 2.5. In this case the only errors that remain are those that are primarily site dependent and include multipath, diffraction and receiver noise; and multipath is generally considered to be the most significant of these for the widest range of applications. It is also worth mentioning that as models for other error sources improve so multipath is increasingly becoming the limiting factor over longer distances (e.g. in network RTK applications).

Multipath errors are caused when direct signals from satellites are mixed with those reflected from objects in the vicinity of the antenna as shown in Figure 2-7. Phase

multipath errors typically display sinusoidal characteristics with the maximum amplitude of a quarter of the observing wavelength (see Section 2.6.2). For example, this maximum is about five centimetres for the GPS L1 carrier. The size of the multipath error in any particular GNSS phase measurement depends primarily on four factors: the reflecting environment, the satellite/antenna geometry, the type of antenna used and the receiver hardware and firmware. The reflecting environment is clearly the main driver: highly reflective surfaces lead to strong multipath signals (i.e. large amplitude), close objects cause multipath errors with long wavelengths and distant objects short wavelengths. The key geometrical factor is usually the satellite elevation angle with most reflected signals coming from nearby structures or the ground arriving at the receiving antenna at low-elevation angle. Multipath is also a function of the receiving antenna. For example, such antennas are usually designed to have lower gain for low-elevation incoming signals than for high-elevation incoming signals. Of course such a design can lead to problems when reflections are caused by objects significantly higher than the antenna and when a particular application requires direct signals from low elevation satellites. Receiver hardware design impacts multipath largely through the signal correlation process, although to date relatively little progress has been made with phase multipath mitigation in this way. For instance the narrow correlator can effectively prevent code multipath error that is larger than the half-correlator spacing passing the delay lock loop (DLL) filter. However, it cannot completely prevent phase multipath in the phase lock loop (PLL) because short code multipath from nearby objects can still pass the DLL filter and hence the much smaller phase multipath can pass to the PLL (see Section 2.6.2). Since the design of the PLL must be able to distinguish clock dynamics from user motion in order to prevent cycle slips, phase multipath at a certain level may always remain undetectable, leading to errors in phase measurement. Of course for a static receiver multipath can be significantly reduced during data processing by averaging the error over a period of time – but such an option is not available in dynamic applications.

Multipath is therefore likely to remain as a serious error in many GNSS carrier phase based positioning applications for the foreseeable future: users cannot usually alter the reflecting environment, receiver manufacturers cannot design antennas that fully mitigate multipath whilst still receiving the required signals, and the design of a receiver to mitigate fully phase multipath appears to be very difficult. Therefore multipath mitigation strategies based on phase data processing need to be developed. There has

been significant progress with this in recent years (e.g. Comp and Axelrad, 1996, and Wieser and Brunner, 2000) and there is much current work in this field.

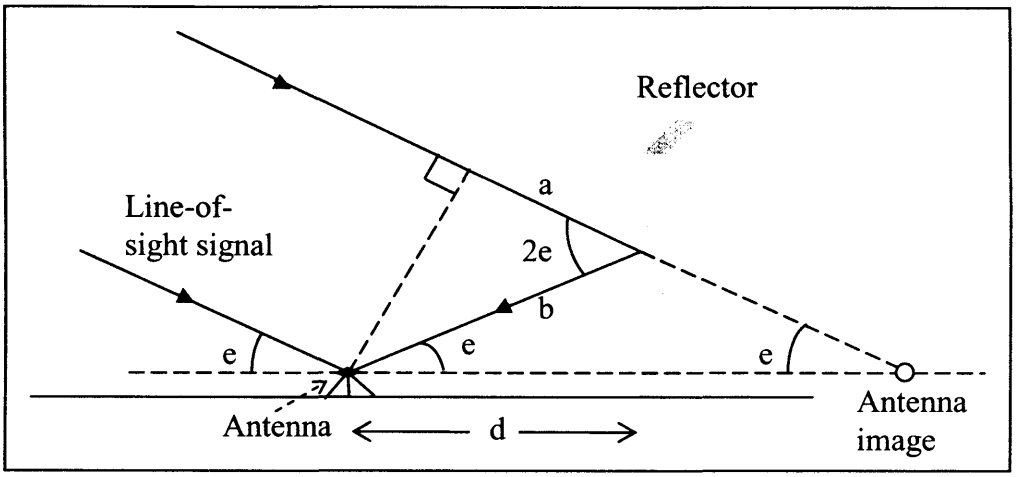

Figure 2-7: Multipath: Geometry of a signal, reflector, and an antenna.

2.6.2 Mathematical background of phase multipath

Differential path delay ∂ is defined as the extra path of reflected (multipath) signal traveled before it arrived at the antenna when compared with the line-of-sight signal. Therefore, the differential path delay ∂ in Figure 2-7 is $(a + b)$ or:

$$\partial = \cos(e) \times 2d \tag{2.26}$$

where e denotes the elevation angle from the receiving antenna to the satellite, d denotes the distance between the receiving antenna and reflector; $2d$ is the distance between the receiving antenna and its image behind the reflector. Thus, the phase shift θ_m of the reflected signal is:

$$\theta_m = \frac{2\pi\partial}{\lambda} \tag{2.27}$$

where λ denotes the wavelength of the signal. Braasch (1996) derives the phase multipath error ψ as:

$$\psi = \tan^{-1}\left[\frac{\alpha R(\tau-\delta)\sin(\theta_m)}{R(\tau)+\alpha R(\tau-\delta)\cos(\theta_m)}\right] \tag{2.28}$$

where α denotes the multipath signal damping or attenuation factor relative to the line-of-sight signal, τ denotes the DLL tracking error; the DLL tracks the peak of the correlation function by tracking the zero-crossing of the discriminator since both occur for τ=0, δ denotes the relative time delay of the reflected signal, and R denotes the PRN code correlation function without band limitation in code-tracking loop:

$$R(\tau) = 1 - \frac{|\tau|}{T_c}, \qquad |\tau| \le T_c \tag{2.29}$$

$$R(\tau) = 0, \qquad |\tau| > T_c \tag{2.30}$$

where T_c is the PRN code bit period. When taking correlator spacing (d_c) into account, Equations (2.29) and (2.30) become:

$$R(\tau) = 1 - \frac{2|\tau|}{d_c T_c}, \qquad |\tau| \le \frac{d_c T_c}{2} \tag{2.31}$$

$$R(\tau) = 0, \qquad |\tau| > \frac{d_c T_c}{2} \tag{2.32}$$

respectively. d_c has almost no impact on the correlation function $R(\tau)$ in Equation (2.31) if τ is very small. In this case, $R(\tau)$ is almost equal to one. It means that the correlator spacing and PRN code bit period have almost no effect on phase multipath error in Equation (2.28) if multipath time delay is very small. It occurs when multipath comes from a very close reflector because close reflectors always cause short differential path delays. In this case, Equation (2.28) becomes Equation (2.33). On the other hand, when tracking to the signal, assume the code voltage controlled oscillator (VCO) delay is continuously adjusted to keep a zero error voltage and negligible white noise in DLL and PLL, Equation (2.28) can be written approximately as:

$$\psi = \tan^{-1}\left[\frac{\alpha\sin(\varphi_m)}{1+\alpha\cos(\varphi_m)}\right] \tag{2.33}$$

By substituting some numerical values to Equation (2.33), the maximum phase multipath error in the carrier phase measurement can be found. Table 2-4 shows the numerical results with setting the damping factor α to one (the strongest possible reflected signal), it can be seen that the phase multipath error can be no more than 90°. At the GPS L1 frequency, this corresponds approximately to 4.8 cm.

Table 2-5: Phase multipath errors for some phase shift values

Phase shift φ_m (°)	Phase multipath error ψ (°)
0	0
45	22.5
90	45
135	67.5
180	90

2.7 STATE-OF-THE-ART MULTIPATH MITIGATION TECHNIQUES

Multipath mitigation techniques can be classified as site-dependent, hardware-dependent, and data processing algorithm-dependent techniques. Park et al. (2002) and Wanninger and May (2000) describe in-situ multipath calibrations for reference stations according to the spatial correlation of satellite-reflector-antenna geometry. Site-dependent techniques can mitigate multipath effectively since multipath error can be determined from the known satellite-reflector-antenna geometry. van Nee (1995) describes a receiver hardware-dependent technique called the Multipath Estimating Delay Lock Loop (MEDLL). With this technique it is possible to largely reduce both code and carrier multipath errors by a specific receiver structure which simultaneously estimates the parameters of line-of-sight plus multipath signals. Bétaille at el. (2003) describes another receiver hardware-dependent technique called the phase Multipath Mitigation Window (MMW), it relies on the gated correlator. Comparison of some receiver hardware-based multipath mitigation techniques can be found in [Weill, 2003]. Moreover, Cannon et al. (2000) describes an antenna array technique based on the geometric correlation of satellite-reflector-antenna array geometry. Rama Rao et al. (2000) describes the use of a GPS microstrip antenna with adaptive cross polarisation cancellation technique to mitigate left-handed polarised multipath and the left-handed polarised component of elliptically polarised multipath. Another special antenna design for multipath mitigation is the use of choke ring antenna, it can effectively prevent

multipath arriving at the antenna phase centres from below horizon but it cannot avoid multipath arriving at the phase centres from above horizon. The basic architecture of choke ring antenna is shown in Figure 2-8 and the performance of some choke ring antennas can be found in Novatel (n.d.). Antenna hardware based multipath mitigation techniques may not be practical for some kinematic applications because of their antenna sizes. Regarding processing algorithm-dependent techniques, Hartinger and Brunner (1999) and Lau and Mok (1999) describe the SIGMA-ϵ model and CALMS model respectively. The SIGMA-ϵ model is based on the correlation of carrier-to-noise power ratio and multipath, and the CALMS model is based on the correlation of signal-to-noise ratio and multipath.

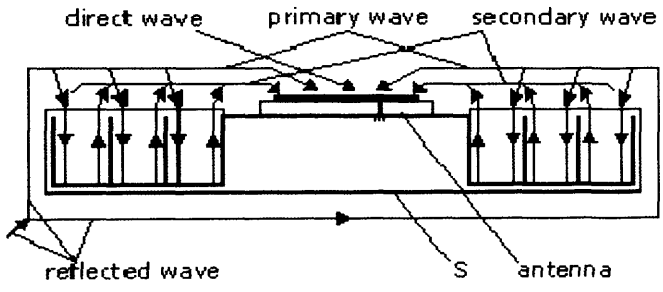

Figure 2-8: Architecture of coke ring antenna [Topcon, n.d.].

Stewart (2003) states that hardware improvements have, generally, failed to translate into improvements in positional accuracy. This is most probably due to difficulties in mitigating short-range phase multipath. As hardware design may not mitigate phase multipath effectively, especially multipath from close reflectors, algorithmic approaches for phase multipath mitigation are still important. Some algorithmic approaches (some of them involve hardware design or parameters from tracking loop) are described as follows:

2.7.1.1 Stochastic modelling

Stochastic model can be used to improve the positioning solution with the aid of extra information such as elevation angle dependent factors and the quality of the signal as obtained from receiver.

2.7.1.1.1 Elevation angle of satellite

Measurements collected from low elevation angle satellites are most likely to have multipath. Therefore, it is common for the elevation angle of satellites to be used in the stochastic model to reduce the influence of data collected from low elevation angle satellites on the positioning solution. This is the simplest way to mitigate multipath but potentially down weights measurements not affected by multipath.

2.7.1.1.2 Signal-to-noise ratio

Signal-to-noise ratio, S/N or SNR (or carrier-to-noise ratio, C/N) can be used to weight the measurement in a stochastic model, for example, SIGMA- Δ model [Brunner et al., 1999] and CALMS [Lau and Mok, 1999]. Bétaille (2004) has investigated the relationship of SNR and phase multipath error. He finds that the use of 1 dB SNR resolution or full SNR resolution makes almost no difference in his phase multipath reconstruction process, so he states 1 dB SNR resolution is sufficient to provide some information of multipath error in the measurement. However, the integer signal strength indicator in the current RINEX observation file format is in the range of 1 to 9 and it is not enough to represent the 1 dB SNR resolution. Therefore, if the relationship of SNR and phase multipath error is proved to be strong, the performance of using stochastic model with SNR on multipath mitigation will be further improved by having better signal strength resolution in RINEX observation file format or using the raw SNR obtained directly from GNSS receiver.

2.7.1.2 Sidereal day-to-day repeatability analysis

For static applications, the antenna-reflector geometry normally does not change with time and the GNSS satellite geometry repeats after a certain time such as one sidereal day for GPS. Therefore, the repeatability of satellite-antenna-reflector geometry can be used to identify the phase multipath error. After this analysis, the identified phase multipath error can be removed from measurement before data processing.

2.7.1.3 *Phase multipath reconstruction using the correlations of phase multipath with SNR*

Comp and Axelrad (1996) present a method to identify the amplitude and phase of multipath relative to the direct signal. The method uses SNR to reconstruct the multipath error. Bétaille (2004) has followed this up to investigate the correlation of phase multipath with code data, PWWM data and SNR for close range multipath, and tried to use the correlations to reconstruct the phase multipath error. He shows a 20% improvement in static mode but the initial result in kinematic mode is not consistent. Besides, Bilich et al. (2003) have investigated a similar method using SNR to reconstruct the geometry of the multipath environment and generate an expected error in the carrier phase observable at every measurement epoch. However, the detail of this method cannot be found because it was an oral presentation only.

2.7.1.4 *Antenna array*

Multipath can also be mitigated by using an antenna array (several closely spaced phase centres in one antenna and each centre has one channel for one satellite in receiver). When the antenna array simultaneously receives a signal from a satellite, the multipath geometry is different at each antenna phase centre in space. Therefore, each antenna centre will exhibit different characteristics of the multipath corrupted GNSS signal. By using spatial analysis technique and by simultaneously processing the multipath corrupted GNSS signal, the multipath signal may be identified and the multipath error may be computed. This method has been studied in [Ray et al., 1999], [Ray, 2000] and [Moore et al., 2002] and proved to be useful for multipath mitigation.

2.8 OUTLIER DETECTION (DATA SNOOPING)

Errors (outliers) in measurements cause unreliable positioning solutions. Therefore, a lot of tests for outliers have been developed in geodetic surveying in order to eliminate grossly falsified observations in network adjustment. Examples of the tests for outlier can be found in [Baarda, 1968], [Cross, 1994], [Koch, 1999], [Kok, 1984], and [Pope, 1976]. These tests basically test the residuals of measurements obtained in adjustment against various hypothesis tests with different statistical distributions such as the Studentized, *Tau* or the standardized normal distributions in various significant levels.

The measurement that fails the hypothesis testing will be rejected before re-adjustment, this process is sometimes called as data snooping. The success of the hypothesis tests depends on the actual error distribution and the redundancy of measurements. Outlier detection technique is applicable to detecting model errors [Cross, 1994].

In GNSS, outlier detection is widely used in the Receiver Autonomous Integrity Monitoring (RAIM) [Brown, 1996] and integrity monitoring in monitoring stations. However, some RAIM algorithms are not robust and reliable enough [EUROCONTROL, 2003]. It is probably due to the insufficient redundancy of measurements in the current GPS system.

3. MULTIPLE-FREQUENCY GNSS DATA SIMULATION

3.1 INTRODUCTION

As described in Section 2.3, the new GPS civil signal at L5 (1176.45MHz) will be incorporated into the GPS Block IIF satellites scheduled for launch beginning in mid-2006. It will take several years to complete the full constellation with L5 capability. On the other hand, the FOC of Galileo is scheduled to be in 2008, but more likely in 2010. In order to investigate the advantage of the additional GPS frequency and the new Galileo multiple frequency signals in this moment, a GNSS data simulator has to be developed for generation of the multiple-frequency GPS and Galileo data in the standard RINEX format. The GNSS simulator must model the GNSS biases and errors as realistically as possible.

This chapter describes the details of simulation of GNSS data. Section 3.2 describes the architecture of the GNSS data simulator and its computational procedure. Biases and errors models are given in Section 3.3. The assumptions of the GNSS data simulation are stated in Section 3.4. Verification procedure for the simulation, verification results, and analyses of results are discussed in Section 3.5. Finally, conclusion of the GNSS data simulation and its verification are given in Section 3.6.

3.2 GNSS DATA SIMULATOR

A GNSS data simulator, called GPS and Galileo Multiple-frequency Data Simulator (GGMDSim), has been developed in Microsoft Visual Basic 6.0. GPS data are simulated using an IGS final precise ephemeris file in the standard SP3 format and precise satellite clock bias in the SP3 file or the RINEX Type C file. Both files can be obtained from the IGS website. Regarding the simulation of Galileo data, since it has no real ephemeris file for Galileo satellites, a Galileo ephemeris simulator called SimGalileo has been developed to generate a SP3 file containing Galileo precise satellite position and precise satellite clock bias in SP3 format for data simulation and a RINEX navigation file containing broadcast ephemeris for data processing. The details of Galileo precise ephemeris simulation are described in Section 3.2.1.2. These precise ephemeris files must be specified before running the main engine of the simulator.

After that, the GUI main menu of the simulator will be displayed as shown in Figure 3-1.

Some information and a number of parameters have to input in the spaces provided. This information and the parameters are listed below.

Information required for simulating GNSS data in RINEX format:

- Measuring mode: static or kinematic.
- Measurement interval in second(s).
- Elevation angle: cut off measurements below 10°, 15° (default), or other.
- Time of first observation in yyyy mm dd hh:mm:ss, or in GPS week and GPS second (Galileo data are also referenced to GPS time, see Section 3.2.5 for details).
- Time of last observation in yyyy mm dd hh:mm:ss, or in GPS week and GPS second.
- Phase (and pseudorange) data to be simulated: GPS L1 only, L1 and L2, or L1, L2, and L5; Galileo L1 only, L1 and E5a, or L1, E5a, and E5b.
- Receiving antenna type.
- Antenna reference point in Cartesian coordinates.

It is important to note that all data to be simulated is referenced to phase centres but the input antenna reference point is referenced to a specific antenna reference point (ARP) not to phase centre, the station marker, the bottom of preamplifier (BPA) or other points at the selected station. This is because the available calibrated antenna data (antenna phase centre offset and variation) used for the simulation of the bias of antenna phase centre offset and variation in GNSS data are referenced to an antenna reference point of the selected antenna type. For the detail of this antenna phase centre offset and variation simulation, see Section 3.3.4.

Parameters required for simulating GPS/GNSS biases and errors:

- Total Vertical Electron Content (TVEC) in Total Electron Content Units (TECU) and elevation angle-dependent oblique factors are used to simulate ionospheric bias. TVEC can be obtained from IONEX file (Global Ionospheric Maps produced by CODE is used; not by other IGS AC), note that one TEC unit

is 10^{16} electrons/m^2. See Section 3.3.1 for details of the simulation of ionospheric effect.

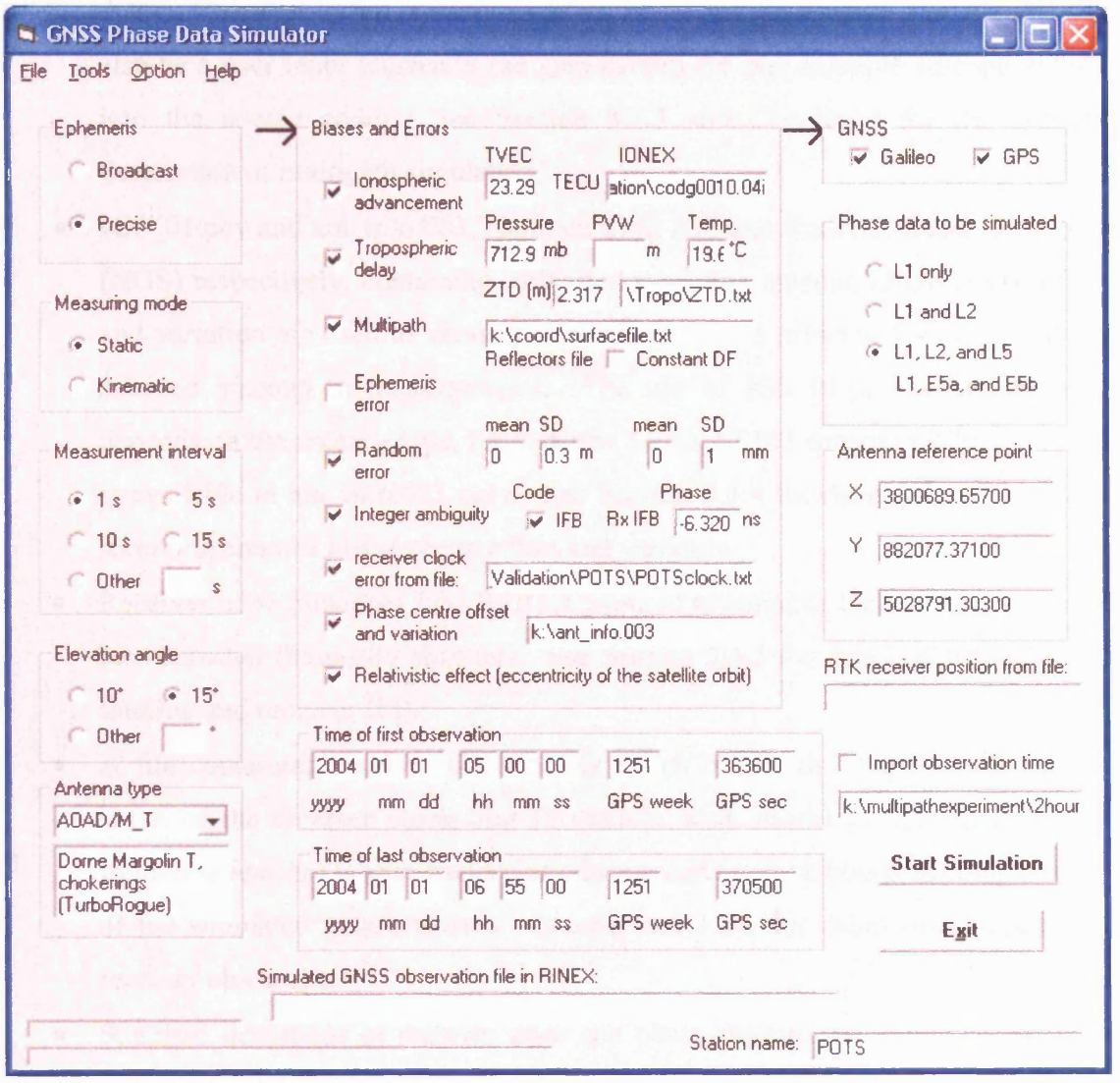

Figure 3-1: Main menu of the GNSS simulator.

- Zenith Tropospheric Delay (ZTD) and elevation angle-dependent mapping function are used to simulate tropospheric delay. If ZTD is not available, upper air pressure in millibars and temperature in degree Celsius (°C) are needed to simulate the dry component of tropospheric delay, otherwise, surface air and temperature are used. If Precipitable Water Vapor (PWV) in centimetres is available, the wet component of tropospheric delay can also be simulated. See Section 3.3.2 for details of the simulation of tropospheric delay.

- A file containing WGS-84 Cartesian coordinates of corners of planar structures around the selected station and permittivities (also called dielectric constants) or constant reflection coefficients of structures are required to simulate multipath delay. Note that in future versions of the simulator the antenna gain pattern will also be a user input (currently the gain pattern for one example antenna is built into the source code). See Section 3.3.3 and Chapter 4 for the detailed description of multipath simulation.
- IGS_01.pcv and ant_info.003, obtained from IGS and National Geodetic Survey (NGS) respectively, containing calibrated receiving antenna phase centre offset and variation are used to simulate the antenna phase offset and variation of the selected antenna in measurements. The use of IGS_01.pcv or ant_info.003 depends on the antenna type, for instance, Leica AT502 antenna calibrated result is available in ant_info.003 only. See Section 3.3.4 for detail of simulation of receiving antenna phase centre offset and variation.
- Receiver inter-frequency bias (IFB) is required to simulate the receiver hardware bias between frequency channels. See Section 3.3.5 for detail of simulation of satellite and receiver IFB.
- A file containing receiver clock biases epoch by epoch or an arbitrary initial value of the receiver clock bias (a random walk model is then used for the following epochs) is specified to introduce receiver clock biases in computations of the simulated measurements. See Section 3.3.6 for detail of simulation of receiver clock bias.
- Standard deviations of receiver code and phase random measurement errors in metres and millimetres respectively are used to generate normally distributed random noise with slightly coloured noise in measurements. See Section 3.3.8 for details of simulation of receiver clock bias.

No ephemeris error needs to be simulated because this is introduced to the measurements through using a precise ephemeris in the simulation but using the broadcast ephemeris in data processing; see Section 3.3.9. However, the relativistic effects on the satellite clock due to elliptical orbital motion are simulated using satellite position and velocity information; see Section 3.3.10. Finally, appropriate cycle-slip free integer ambiguities are generated to complete the phase measurements; see Section 3.3.7 for simulation of phase ambiguity.

Figure 3-2 shows the main steps in the simulator. The details and computations in each step are described in the following sub-sections.

3.2.1 Precise ephemeris

3.2.1.1 GPS precise ephemeris

GPS ephemeris, clock and earth orientation solutions are estimated in the International GPS Service (IGS). The final combinations are available with about 13 days latency. This minimally constrained 24-hour file is named as SP3. Precise satellite positions and clock biases in SP3 are given at 15-minute intervals for all healthy satellites. Details on SP3 format can be found in Spofford and Remondi (1994). The IGS GPS final precise ephemeris is the most accurate GPS ephemeris product, its orbital accuracy is less than 5 cm and its satellite clock accuracy is less than 0.1 ns (~0.3 m). Therefore, IGS final precise ephemeris is adopted in the simulator for computation of the "true" satellite position and clock bias.

The input precise ephemeris is used to interpolate satellite coordinates at specific epochs. A 17^{th}-order Lagrange interpolation is use for this purpose and is described in Section 3.2.5. A 3^{rd}-order Lagrange interpolation is used to interpolate the precise satellite clock biases at the required epochs. The interpolation accuracy is checked by comparing the interpolated clock biases one second before and after a session in SP3 file with the given clock bias in the session. This accuracy is found to be better than 10^{-11} second that is less than three millimetres in range. The precise satellite clock biases are used in the simulation of pseudorange and phase measurement in a later step described in Section 3.2.11.

3.2.1.2 Galileo precise ephemeris simulation

As described in the introductory section of Section 3.2, precise Galileo satellite position and clock are not available at the time of this research. In order to investigate the impact of the coming Galileo on GNSS data processing in this research, a Galileo ephemeris simulator has been developed in Microsoft Visual Basic 6.0. It is called SimGalileo. SimGalileo uses the proposed Galileo orbital parameters and signal parameters listed in Tables 2-1 and 2-3 (the latest parameters in the time of this research) respectively to generate precise Galileo satellite position and clock in the standard SP3 format for Galileo data generation.

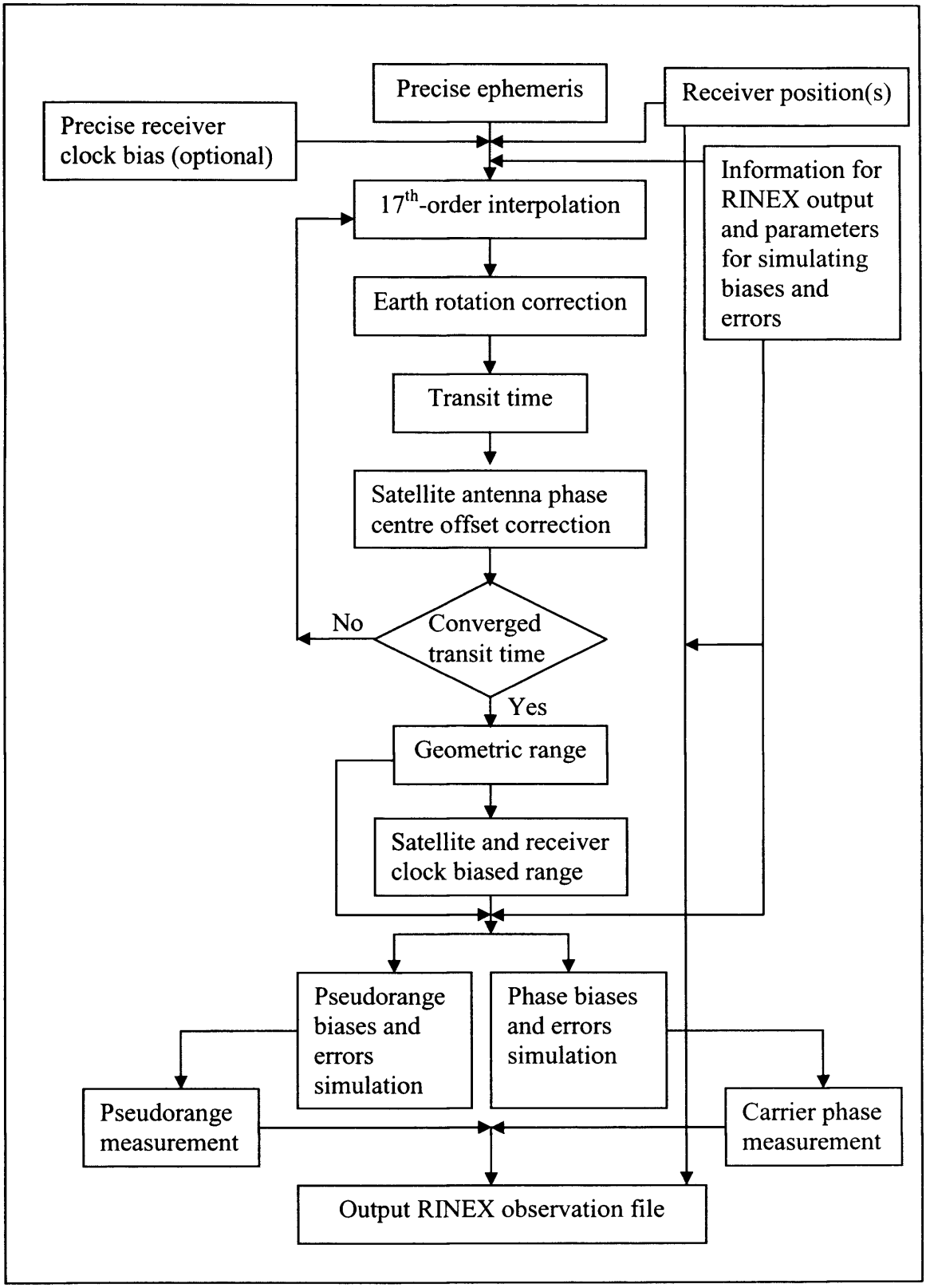

Figure 3-2: Flowchart showing the outline of the GNSS data simulation.

The Galileo reference time system called Galileo System Time (GST) and the reference frame called Galileo Terrestrial Reference Frame (GTRF) are also not well defined in the time of this research, the SimGalileo and GGMDSim use GPS reference time (GPS

week and GPS second) and reference frame (WGS-84) as the reference time system and reference frame for Galileo ephemeris simulation and data simulation. The impacts of the reference time system and reference frame between GPS and Galileo in data simulation and data processing are described in Section 3.3.6 and 6.2.

In the simulation of a Galileo precise ephemeris, SimGalileo also generates a less precise broadcast ephemeris in RINEX format for data processing. The purpose of this operation is to introduce ephemeris error in data processing; see Section 3.3.9 about this operation.

3.2.2 Information for RINEX output and parameters for simulating biases and errors

The information required for simulating GNSS data in RINEX and the parameters required simulating GNSS biases and errors are described in the introductory section of Section 3.2. The purpose of the information and parameters in simulation are described as follows.

3.2.2.1 Measuring mode

The simulator can generate GNSS data for a static or kinematic platform. If data to be simulated is in a static platform, "Static" must be selected and the Cartesian coordinates of the antenna reference point is required to enter in the X, Y, and Z spaces of antenna reference point as shown in Figure 3-1. If kinematic data is going to be generated by the simulator, "Kinematic" must be selected and the path (directory and filename) of the file containing kinematic positions of the antenna reference point is required to enter in the space of "RTK receiver position file from" in Figure 3-1.

3.2.2.2 Measurement interval

It is the sample rate of GNSS data to be generated. The measurement interval can be selected from the options provided which are 1, 5 10, or 15 second(s). The user can select "Other" and enter the interval of any positive integer number in the space provided, one epoch data will be generated when the entered interval is zero or greater than the interval between the time of first observation and the time of last observation defined in Section 3.2.2.4 and 3.2.2.5 respectively.

3.2.2.3 Elevation angle

It defines what satellite data is output to observation file. If the elevation angle of a satellite is lower than the input elevation mask angle, the satellite will be discarded and will not be considered in later stages of simulation. The simulator checks the satellite elevation angle at each epoch.

The elevation mask angle can be selected from the options of 10° and 15°. The user can select "Other" and enter any integer number in degree(s) from 0 to 90.

3.2.2.4 Time of first observation

It is the time for the first observation epoch in the RINEX observation file. It must be in the period covered by the precise ephemeris file(s).

3.2.2.5 Time of last observation

It is the time for the last observation epoch in RINEX observation file. It must be in the period covered by the precise ephemeris file(s).

3.2.2.6 Phase (and pseudorange) data to be simulated

As described in the introduction of Section 3.2, the user can select to generate data in different combinations of frequencies and GNSS (GPS, Galileo, or GPS and Galileo). Existing GPS frequencies are open to all users and the coming modernised signals will be open to the public as well. The simulator can generate data for all GPS existing and modernised signals. However, only three of the four Galileo frequencies will be open to the public as described in Section 2.3.3, the simulator can only generate L1, E5a, and E5b data for Galileo.

3.2.2.7 Receiving antenna type

It is used to simulate the effect of receiving antenna phase centre offset and variation in measurements; see Section 3.3.4 for the details of this simulation. The phase centre offset and variation are antenna dependent, therefore, the user should select the receiving antenna type to be used in the data simulation. The assumption of the receiving antenna type for Galileo is discussed in Section 3.3.4.

3.2.2.8 Antenna reference point

The input of antenna reference point in Cartesian coordinates is used to simulate GNSS data collected at a static point. Since no calibrated Galileo receiving antenna phase

centre offset and variation data is available at the time of this research, both GPS and Galileo data are referenced to the same antenna reference point. This assumption does not affect this research because the phase centre offset and variation are common in short- to medium-baseline relative positioning provided that the same antenna type is used at the base and rover.

3.2.2.9 TVEC

The IONEX file path is selected in Windows GUI before the simulator main menu in Figure 3-1, and the path is displayed in the space provided for "IONEX" as shown in Figure 3-1. TVEC values are obtained from the input IONEX file for simulation of ionospheric effect in GNSS data. See Section 3.3.1 for the details of the ionospheric effect simulation.

3.2.2.10 ZTD or MET data

A file containing ZTD values or MET data in the given GPS seconds at the receiver position is input to simulate tropospheric delay in GNSS measurements. Details for simulation of tropospheric delay are described in Section 3.3.2.

3.2.2.11 Reflectors file

The reflectors file is selected in Windows GUI before the simulator main menu. The file path is displayed in the space provided for "Reflectors file" as shown in Figure 3-1. It is used to simulate multipath error in measurement. Details of multipath simulation are described Chapter 4.

3.2.2.12 Receiving antenna phase centre offset and variation

User enters a file path of the file containing calibrated receiving antenna phase centre offset and variation in the space of "Antenna phase centre offset and variation" as shown in Figure 3-1. The simulator loads the antenna types contained in the file and the antenna types can then be selected in the drop down menu of "Antenna type". Simulation of receiving antenna phase centre offset and variation is given in Section 3.3.4.

3.2.2.13 Receiver inter-frequency bias

A value of receiver inter-frequency bias in nanoseconds is entered in the space of "Rx IFB" for the simulation of frequency dependent receiver hardware bias. Details of this simulation are provided in Section 3.3.5.

3.2.2.14 Standard deviation

The standard deviations for code and phase are used to simulate random code and phase measurement noise. The user should enter the appropriate noise level for the receiver hardware in the space provided as shown in Figure 3-1. Details of the measurement noise simulation are described in Section 3.3.8.

3.2.3 Receiver position(s)

Receiver position(s), as shown in Figure 3-2, in static or kinematic measuring mode and precise ephemeris are used to compute the geometric range between a satellite and receiver position at a specific epoch. See Sections 3.2.7 to 3.2.10 for the computation of signal transit time and hence geometric range.

3.2.4 Precise receiver clock biases

A file containing precise receiver clock biases at epochs to be simulated is entered for simulation of specific receiver clock bias values in measurements. Details of this simulation are described in Section 3.3.6.

The input of receiver clock biases from RINEX Type C file is very important in the validation of the GNSS simulator in measurement domain to be described in Section 3.5. The IGS derives precise receiver clock biases for the IGS global tracking stations by analysis of GPS phase/pseudorange data from the IGS tracking network. All clock biases are relative to a fixed clock adopted in the analysis. The clock biases can be re-aligned after estimation to remove the effect of the particular choice of reference clock. Re-alignment is most commonly done by using broadcast GPS time for the satellites as an underlying timescale, typically fitted to a low-order polynomial. Details on RINEX Type C can be found in Ray and Gurtner (1999).

Receiver clock biases are used in the computation of the time of transmission Equation (3.1) and hence satellite coordinates at time of transmission, and simulation of pseudorange and phase measurements in a later step in Section 3.2.11.

$$T_t = T_r - t_r - t_t \tag{3.1}$$

where T_t denotes the time of transmission from the satellite, T_r denotes receiver reception time, t_r denotes receiver clock bias, and t_t denotes transit time from satellite to receiver.

3.2.5 17th-Order Lagrange Interpolation for satellite position computation

Final precise orbit data product is used to calculate the precise satellite coordinates at time of transmission of each satellite of each epoch more precisely with 17th-order Lagrange interpolation:

$$f(x) = \sum_{k=0}^{n} L_k(x) f_k \tag{3.2}$$

where *f(x)* is the interpolated coordinates (x^s, y^s, or z^s), k is the n^{th} order of polynomial, n is the order of polynomial; it is set to seventeen, f_k is the precise coordinates (x_k, y_k, or z_k) at given epoch in precise ephemeris, and

$$L_0(x) = \frac{l_0(x)}{l_0(x_0)} = \frac{(x-x_1)(x-x_2)}{(x_0-x_1)(x_0-x_2)} \tag{3.3}$$

when k=0, and

$$L_1(x) = \frac{l_1(x)}{l_1(x_1)} = \frac{(x-x_0)(x-x_2)}{(x_1-x_0)(x_1-x_2)} \tag{3.4}$$

when k=1, etc.

Remondi (1991) demonstrates that accuracy at about the millimetre-level can be achieved based on 17th order interpolation of a precise ephemeris at 40-minute epoch intervals. However, since the time interval of the final precise orbit product from the

IGS is 15 minutes, the accuracy of interpolated satellite coordinates should be better than, or at least in, the millimetre-level.

In order to verify the interpolation accuracy of the simulator, a session orbit data in a SP3 file is deleted manually and then using the simulator to interpolate the session orbit data at exact time. It is found that the interpolation accuracy for satellite position is better than three millimetres.

3.2.6 Earth rotation correction

The interpolated satellite coordinates must be corrected for the earth rotation during the transit time of the signal from the satellite to the receiver:

$$R_E = t_t \dot{\Omega}_e \tag{3.5}$$

$$x_R^S = \cos(R_E)x^s + \sin(R_E)y^s \tag{3.6}$$

$$y_R^s = -\sin(R_E)x^s + \cos(R_E)y^s \tag{3.7}$$

$$z_R^s = z^s \tag{3.8}$$

where R_E denotes the earth's rotation angle during signal transmission, $\dot{\Omega}_e$ denotes WGS-84 value of earth's rotation rate, and (x_R^s, y_R^s, z_R^s) denote the satellite coordinates corrected to earth rotation during signal transmission.

3.2.7 Transit time

After applying the earth's rotation correction to the satellite coordinates, the transit time is obtained by:

$$\hat{t}_t = \frac{\sqrt{(x_R^s - X_r)^2 + (y_R^s - Y_r)^2 + (z_R^s - Z_r)^2}}{c} \tag{3.9}$$

where $\hat{t}_t$ denotes the initial transit time and c denotes the speed of light.

3.2.8 Satellite antenna phase centre offset correction

Satellite coordinates in SP3 precise ephemeris are referenced to the satellite centre of mass, however, the broadcast ephemeris is referenced to the satellite antenna phase centre. The difference between the centre of mass and the antenna phase centre is called the antenna phase centre offset or centre of mass correction. Therefore, the simulator checks each satellite PRN in simulation process with a database consisting PRN, type of satellite (i.e. Block II, Block IIA, or Block IIR; Block IIR-M or Block IIF in the future), and the antenna phase centre offset. Then, it applies the corresponding offset correction to the transit time of each satellite as:

$$t_t = \hat{t}_t - \frac{b_{APC}}{c} \tag{3.10}$$

where t_t denotes the corrected transit time, $\hat{t}_t$ denotes the initial transit time, b_{APC} denotes the antenna phase centre offset in metres, and c denotes the speed of light.

The antenna phase centre offsets are obtained from the header of SP3 file. IGS uses the antenna offset of 1.023 m in Z-axis (pointing to the centre of the Earth) for GPS Block II/IIA satellites and no offset for GPS Block IIR satellites. Before the application of the offset correction in Equation (3.10), geometrical correction to the Z-offset must be applied to get the correct b_{APC} according to the elevation angle of the satellite at the receiver position. Regarding the simulation of Galileo data, the satellite antenna phase centre coincides with the satellite centre of mass (i.e. the offset is zero).

3.2.9 Converged transit time

The updated transit time is compared with the transit time obtained in the last iteration. If they are the same in the double precision data type of Visual Basic, the iteration has converged and the final converged transit time is obtained. If the transit time has not converged, the iteration will carry on by using the updated transit time in the computation of time of transmission in Equation (3.1) and put it in the Lagrange interpolation again.

3.2.10 Geometric range

Geometric range (ρ_r^s) from satellite to receiver is determined by:

$$\rho_r^s = ct_t \tag{3.11}$$

where c denotes the speed of light and t_t denotes the transit time.

3.2.11 Satellite and receiver clock biased range

Satellite and receiver clock biases affect both pseudorange and phase data in the same extent. The simulator computes the satellite and receiver clock biased range as:

$$\hat{\rho}_r^s = \rho_r^s + (t_r - t^s)c \tag{3.12}$$

where $\hat{\rho}_r^s$ denotes the satellite and receiver clock biased range, ρ_r^s denotes the geometric range obtained from Equation (3.11), t_r denotes the receiver clock bias, t^s denotes the satellite clock bias, and c denotes the speed of light.

Note that the satellite clock bias in this step has "corrected" to the relativistic effect; the relativistic effect simulation is described in Section 3.3.10.

3.2.12 Pseudorange biases and errors simulation

This step simulates GNSS pseudorange biases and errors along the signal path from the satellite to the receiver in as realistic manner as possible. Details of the biases and errors used in the simulation are described in Section 3.3.

After bias and error simulation, delays are added to the clock biased range obtained in Equation (3.12). The complete biased range for code data R_e is obtained by:

$$R_e = \hat{\rho}_r^s + e_{code} \tag{3.13}$$

where e_{code} is the summation of simulated biases and errors such as ionospheric delay, tropospheric delay, code multipath error, and random error in pseudorange data.

3.2.13 Phase biases and errors simulation

This step simulates GNSS phase biases and errors along the signal path from the satellite to the receiver in as realistic manner as possible. Details of the biases and errors used in the simulation are described in Section 3.3.

After bias and error simulation, delays and advancement(s) are added to the clock biased range obtained in Equation (3.12). The biased range for phase data $\hat{\Phi}_e$ is obtained by:

$$\hat{\Phi}_e = \hat{\rho}_r^s + e_{phase} \tag{3.14}$$

where e_{phase} is the summation of simulated biases and errors such as ionospheric advancement, tropospheric delay, phase multipath error, and random error in phase data.

3.2.14 Pseudorange measurement

Pseudorange data for different frequencies of different GNSS are obtained as described in Section 3.2.12. The main differences of different pseudoranges in the same GNSS system are the frequency dependent biases or errors such as ionospheric delay and IFB. Simulation of ionospheric delay is described in Section 3.3.1 and that of IFB is given in Section 3.3.5.

3.2.15 Carrier phase measurement

Carrier phase measurements are obtained by scaling the biased ranges described in Section 3.2.13 with the corresponding carrier frequency for the different L-bands and including a cycle slip free arbitrary ambiguity as:

$$\phi_L = \frac{\hat{\Phi}_e}{\lambda_L} + N \tag{3.15}$$

where ϕ denotes the carrier phase measurement, $\hat{\Phi}_e$ denotes the biased range, λ_L denotes the wavelength of the carrier frequency, L denotes the carrier frequency (i.e.

GPS L1, L2, and L5; Galileo L1, E5a, and E5b), and N denotes the arbitrary integer ambiguity.

3.2.16 Output RINEX observation file

The header of the simulated RINEX file is generated according to the standard RINEX format described in Gurtner (2001) and the input information described in Section 3.2.2. Satellite measurements are output to a RINEX file only if the satellite's elevation angle is above the specified cut-off elevation angle. An example of a simulated RINEX observation file for few epochs is shown in Appendix B.

3.3 GNSS Biases and Errors Modelling

This section describes the detailed models of biases and errors to be simulated in GNSS data. The biases or errors are ionospheric effect, tropospheric delay, multipath effect, ephemeris error including satellite clock bias, integer ambiguity, receiving antenna phase centre offset and variation, inter-frequency bias, relativistic effect, receiver clock bias, and random error.

3.3.1 Simulation of ionospheric effect

The ionosphere causes delays in pseudorange measurements and advancements in phase measurements when a satellite signal passes through it. The ionosphere effect is mainly due to the refraction (the change in speed of propagation with negligible change in direction) of satellite signal path travelling through the total electron content (TEC). Usually, the total vertical electron content (TVEC) is modelled. The TVEC can be obtained, for instance, from the global ionosphere maps of the International GPS Service (IGS). Such global ionosphere maps are generated on a daily basis by the Centre for Orbit Determination in Europe (CODE), University of Berne, Switzerland. IONEX files produced by other IGS ACs are not used in the simulator because the mean heights of the ionosphere used in different ACs were different (same mean height is used now) when developing the simulator and different ACs use different methods to compute the obliquity factor and different models to determine TVEC and IFB. CODE's final IONEX files (named codgddd0.yyI) are made available with a delay of about eleven days in (ftp://cddisa.gsfc.nasa.gov/pub/gps/products/ionex/). The TEC is

modelled with a spherical harmonic expansion up to degree 12 and order 8 referring to a solar-geomagnetic reference frame. The ionosphere files are converted into IONEX files, IONEX is an internationally adopted format for the exchange of two- or three-dimensional ionosphere maps. TVEC of an observing station can be determined from the data in the IONEX files, using universal time and the coordinates of the station, by interpolating between consecutive rotated TEC maps [Schaer et al., 1998]:

$$E(\beta,\lambda,t)=\frac{T_{i+1}-t}{T_{i+1}-T_i}E_i(\beta,\lambda_i^{'})+\frac{t-T_i}{T_{i+1}-T_i}E_{i+1}(\beta,\lambda_{i+1}^{'}) \tag{3.16}$$

where E is the TEC, β is the geocentric latitude, λ is the geocentric longitude, t is the observing universal time, T is the record epoch in IONEX file in universal time, $T_i \le t < T_{i+1}$ and $\lambda_i^{'}=\lambda+(t-T_i)$.

3.3.1.1 Slant ionospheric effect modelling

The TVEC at a station at any particular time needs to be mapped to the elevation of the satellite for which the data is being simulated. The following assumptions are made in the model used for this purpose:

- Electron content is considered mainly in the ionosphere.
- Electron density is constant in the ionosphere (In reality electron density varies in the ionosphere but the TVEC is the integrated electron content along the signal path in the ionosphere).
- It is based on the so-called thin-shell or single-layer model (see Figure 3-3).

The approach of slant ionospheric effect simulation is as follows (refer to Figure 3-3):

i) The vertical total electron content (TVEC) in IONEX is determined by the electron density Ne and thickness of the ionosphere s_o (about 950 km) as:

$$TVEC=\int Ne\ ds_o \tag{3.17}$$

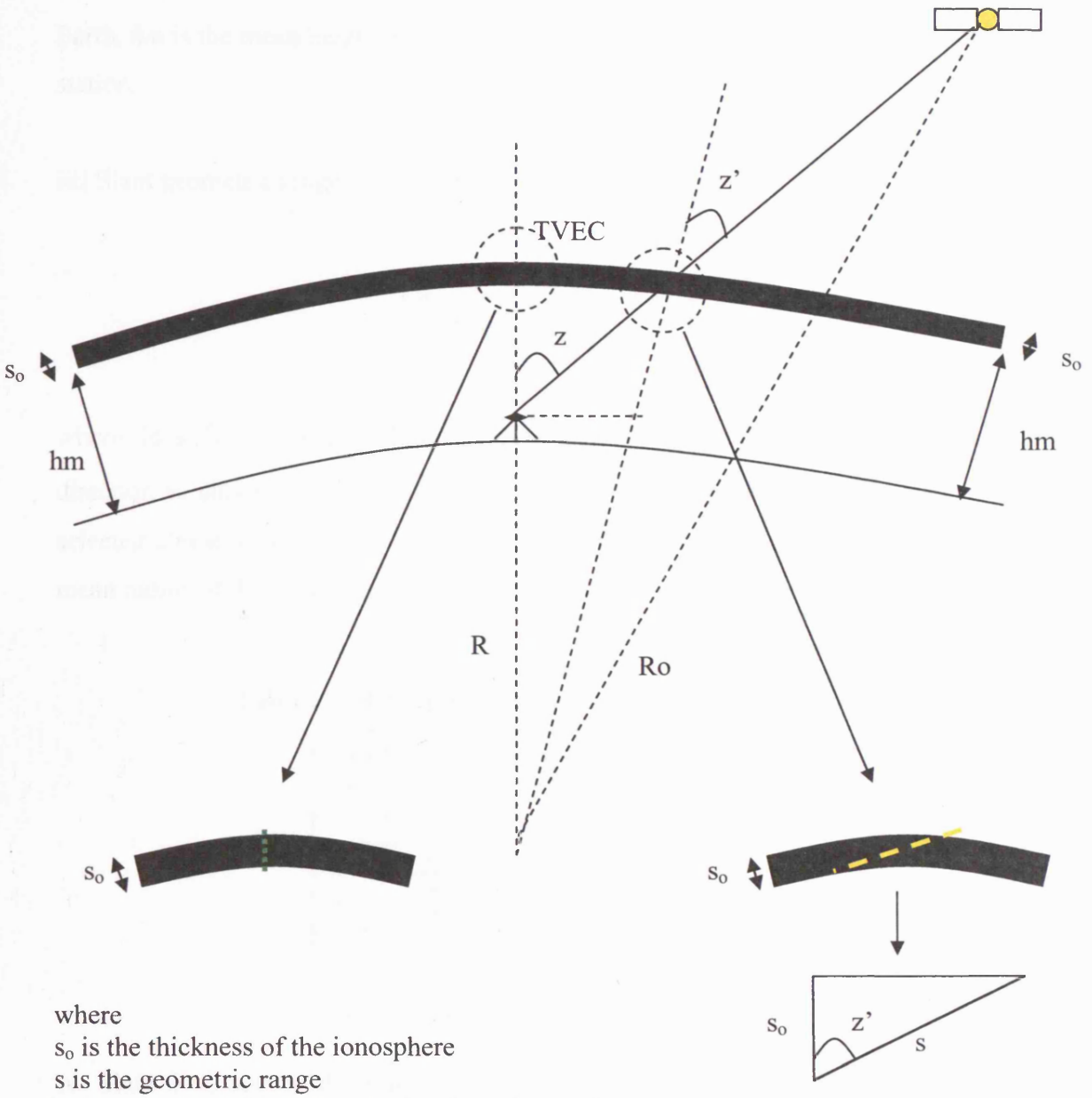

where
s_o is the thickness of the ionosphere
s is the geometric range
R is the radius with respect to the observing station
Ro is the mean radius of the Earth
hm is the mean height of the ionosphere
z is the zenith angle at the observing station
z' is the zenith angle at the ionospheric point

Figure 3-3: Thin-shell ionospheric model.

ii) Zenith angle at the ionospheric point z' is found by:

$$\sin z' = \frac{R}{Ro + hm} \sin z \tag{3.18}$$

where R is the radius with respect to the observing station, Ro is the mean radius of the Earth, hm is the mean height of the ionosphere, and z is the zenith angle at the observing station.

iii) Slant geometric range s is determined by z' and s_o:

$$s = \frac{s_o}{\cos z'} \tag{3.19}$$

where $(\cos z')^{-1}$ is called obliquity factor (OF). OF ranges from one for the zenith direction to about three for elevation angle of 5°. Table 3-1 shows the OFs of some selected elevation angles, the radius with respect to the observing station is taken as the mean radius of the Earth.

Table 3-1: Obliquity factors of some elevation angles.

Elevation angle (°)	Obliquity factor (OF)
10	2.7893
20	2.2003
30	1.7512
40	1.4545
50	1.2611
60	1.1357
70	1.0571
80	1.0138
90	1

iv) Slant TEC can be determined by integration of electron density Ne with the slant geometric range as Equation (3.17). Equivalently, it can be determined by using the TVEC and OF as:

$$STEC = TVEC \times OF \tag{3.20}$$

where $STEC$ denotes the slant TEC and OF denotes obliquity factor. The simulator uses Equation (3.20) to compute the slant TEC.

v) Finally, the first-order slant ionospheric delay of pseudorange measurement I_p is obtained by:

$$I_p = \frac{40.3}{f^2} STEC \tag{3.21}$$

and the first-order slant ionospheric advancement of phase measurement I_ϕ is obtained by:

$$I_\phi = -\frac{40.3}{f^2} STEC \tag{3.22}$$

where f is the frequency of the L-carrier. The ionospheric advancements of GPS L1, L2 and L5 for the minimum TEC of 10^{16} to the maximum TEC of 150×10^{16} at elevation angles 10°, 30°, 60°, and 90° are show in Table 3-2:

Table 3-2: Example of ionospheric advancement for GPS carrier frequencies.

Elevation angle (°)	Ionospheric advancement (m)					
	L1		L2		L5	
	TEC=10^{16}	TEC=1.5×10^{18}	TEC=10^{16}	TEC=1.5×10^{18}	TEC=10^{16}	TEC=1.5×10^{18}
10	0.453	67.935	0.746	111.885	0.812	121.826
30	0.284	42.652	0.468	70.246	0.510	76.487
60	0.184	27.660	0.304	45.554	0.331	49.602
90	0.162	24.356	0.267	40.113	0.291	43.677

3.3.2 Simulation of tropospheric delay

Tropospheric path delay (T) is defined by:

$$T = 10^{-6} \int N \, ds \tag{3.23}$$

where N is the tropospheric refractivity and s is the measured range. For radio frequencies up to about 30 GHz, the troposphere is non-dispersive and hence N is frequency independent.

Tropospheric delay can be separated into a dry and a wet component:

$$T = T_d + T_w \tag{3.24}$$

or, in terms of refractivity:

$$T = 10^{-6} \int N_d \, ds + 10^{-6} \int N_w \, ds \tag{3.25}$$

In radio meteorology, models for the dry ($N_{d,0}$) and wet ($N_{w,0}$) refractivity at the surface of the earth are:

$$N_{d,0} = c_1 \frac{p}{T} \tag{3.26}$$

$$N_{w,0} = c_2 \frac{e}{T} + c_3 \frac{e}{T^2} \tag{3.27}$$

where p is the atmospheric pressure in millibars (mb), T is the temperature in Kelvin (K), and e is the partial pressure of water vapor in mb. These parameters are specific to a geographical location.

In the simulator, Equation (3.26) is used and c_1 is set to 77.64 Kmb^{-1} as in [Hofmann-Wellenhof et al, 2004]. The dry portion of the tropospheric zenith delay has been empirically determined by Hopfield (1969) as:

$$T_{d,0} = \frac{10^{-6}}{5} N_{d,0} h_d \tag{3.28}$$

where h_d is the effective height for the dry layer of about 40 km (see Figure 3-4).

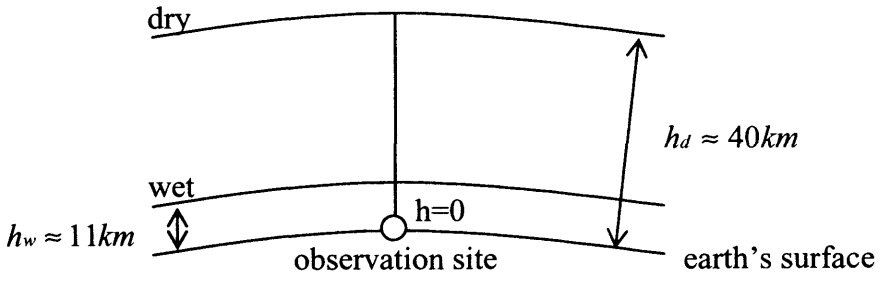

Figure 3-4. Thickness of the polytropic layers for the troposphere.

On the other hand, the wet portion is determined according to Hogg et al. (1981) as:

$$\text{zenith wet delay} = \frac{PWV}{\Pi} \tag{3.29}$$

where PWV is the precipitable water vapor in centimetres and Π is a dimensionless conversion factor approximately equal to 0.15. Values for *PWV* can be obtained from http://www.gst.ucar.edu/gpsrg/realtime.html. However, since *PWV* cannot be obtained in most observatories, the simulated tropospheric delay may ignore the wet component of tropospheric delay if this tropospheric delay simulation method is selected. Fortunately, the wet delay is estimated to be about 10% of the tropospheric delay.

Similar to the ionospheric effect, the tropospheric delay in zenith direction must be mapped to the slant delay according to the elevation angle (E) of the satellite at the receiver. Misra and Enge (2001) give the mapping functions (*MF*) for the dry delay as:

$$MF = \frac{1}{\sin E + \dfrac{0.00143}{\tan E + 0.0445}} \tag{3.30}$$

The dry component of slant tropospheric delay is therefore determined by:

$$T_d = T_{d,0} \cdot MF \tag{3.31}$$

Alternatively, the tropospheric delay can be simulated by using the zenith tropospheric delay (ZTD) at the receiver location. ZTD can be obtained from the IGS website. The IGS produces the final tropospheric zenith path delay data file for a week with the latency of less than four weeks. The ZTD is site-specific and its sampling interval and accuracy are two hours and about 4 mm respectively. The ZTD file is obtained by weighted mean of all IGS ACs. Mapping function used to simulate slant tropospheric delay from ZTD is obtained from Equation (3.30). If the data simulation location is not an IGS reference station, ZTD from the nearest IGS station or interpolation between stations may be used to simulate the tropospheric delay. However, tropospheric effect is highly location and altitude dependent.

Note that the simulation of tropospheric delay assumes that tropospheric effect is azimuth homogeneous.

3.3.3 Simulation of multipath effect

A realistic multipath model using ray tracing technique with a physical model is employed to simulate multipath error in phase data. The detail of the multipath model is described in Chapter 4.

3.3.4 Simulation of receiving antenna phase centre offset and variation

The antenna calibration file obtained from IGS or NGS contains L1 and L2 phase centre offsets from the reference marks of the antennas. For instance, the Leica mechanical reference plane (MRP) of the AT502 antenna is used as the reference mark for height offset in the antenna calibration file as shown in Figure 3-5. The offsets are given in a local coordinates system, i.e., offsets in easting, northing, and height.

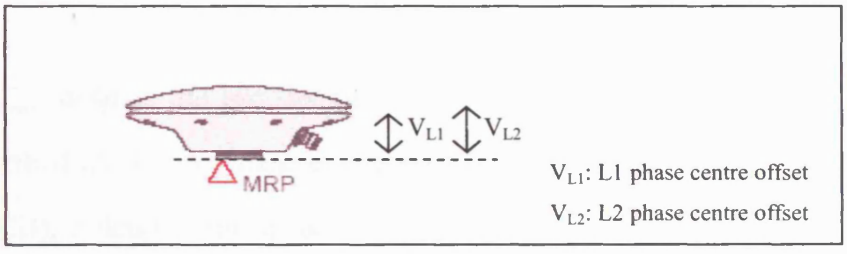

Figure 3-5: Reference mark for L1 and L2 phase centre offsets of the Leica AT502 antenna.

The simulator generates data, and biases and errors with each phase centre coordinates independently in order to take the phase centre offsets into account. Note that L5 phase centre is set to coincide with the L2 for GPS in data simulation, moreover, the receiving antenna phase centres for Galileo are set to coincide with the GPS phase centres in data simulation. Those settings do not affect the processing results and analyses of this research because the phase centre offset has no effect on relative positioning, which uses the same antenna model at the base and rover.

On the other hand, the antenna calibration file also contains the antenna phase centre variation data for most antennas. The phase centre variations in millimetres are given in the elevation angles (from 0° to 90° with 5° interval) of the incoming signal path. Interpolation is required for the elevation angle of the incoming signal path falling in the 5° interval. Simulation of phase centre variation uses the opposite sign of the phase centre variation correction. Similar to the phase centre offset described above in this

subsection, the same phase centre variation data are used for both GPS and Galileo simulated data.

3.3.5 Simulation of satellite and receiver IFB

The simulator uses the differential code biases (DCB; P1-P2) obtained from IONEX file to simulate the GPS satellite IFB in any circumstance and receiver IFB if the simulated data is for an IGS station, which is used in the verification of the simulator to be described in Section 3.5. The simulated pseudorange in L1 containing IFB ($P1_{IFB}$) can be written as:

$$P1_{IFB} = P1_{biases} + \kappa_2 c(b_{sat} + b_{rec}) \tag{3.32}$$

$$\kappa_2 = -f_2^2/(f_1^2 - f_2^2) \tag{3.33}$$

where $P1_{Biases}$ denotes the pseudorange in L1 containing the other GNSS biases and errors described above, b_{sat} denotes the satellite IFB (or DCB), b_{rec} denotes receiver IFB (or DCB), c denotes the speed of light, κ_2 is the second ionospheric-free linear combination factor; f_i denotes the frequency of the i-th carrier. IFB affects pseudorange and phase in the same way, Equation (3.32) is also used to simulate IFB in phase data by replacing the pseudorange with the phase measurement in metres. In the simulation of IFB in GPS L2, the numerator in Equation (3.33) is replaced by the L1 frequency f_1.

Since IFB is fairly constant in over week(s) or even a month, constant IFB is used in the simulation. However, according to [Schaer et al., 1998], satellite DCBs (b_{sat}) are related to the IFB (denoted τ_{GD} in [ICD-GPS-200C, 2003]), broadcast by the GPS system as:

$$\tau_{GD} = \kappa_2 b_{sat} + \tau_0 \tag{3.34}$$

There may be an arbitrary offset, denoted as τ_0. Estimated b_{sat} and b_{rec} are usually given in such a way that the zero-mean condition $\sum b_{sat} = 0$ is fulfilled. In this case, τ_0 should correspond to the mean $\sum \tau_{GD} / n_{sat}$.

Same set of IFB is used for both GPS and Galileo simulated data, it has no effect in the processing result and the reason is the same as the case of phase centre offset described in the previous subsection.

3.3.6 Simulation of receiver clock bias

Receiver clock biases (*Tr*) can be generated by a random walk model or obtained from a file (see Section 3.2.4). In case of no receiver clock biases input from file ("Receiver clock error from file" option is not checked in the main menu of the simulator as shown in Figure 3-1), a simple random walk model is used as follows:

$$Tr_i = Tr_{i-1} + RND \cdot k \tag{3.35}$$

where Tr denotes the receiver clock bias in seconds, $_i$ denotes the measurement epoch in GPS second; configurable receiver clock bias at the first epoch, RND denotes the normal distributed random number between zero and one, and k denotes the configurable magnitude of the random walk process in seconds according to the clock behaviour of the selected receiver type. An example of the simulated clock biases in one hour by the random walk process with the clock bias at the first epoch set to $6e^{-5}$s and the magnitude of the random walk process set to $1e^{-6}$s as shown in Figure 3-6.

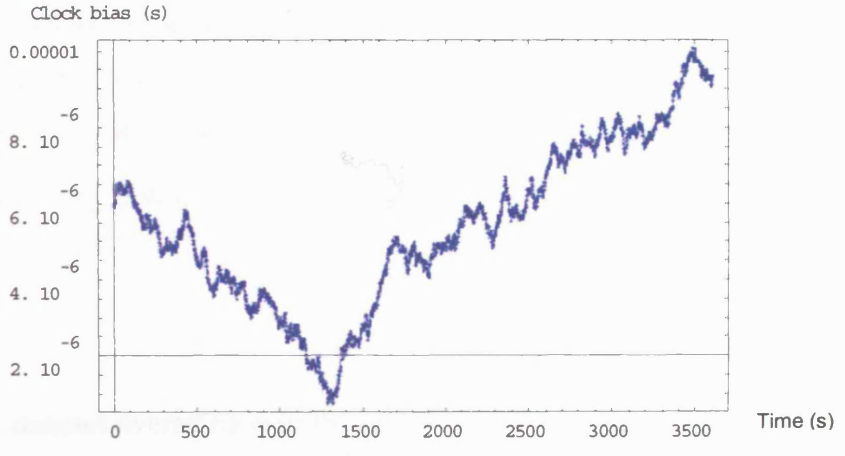

Figure 3-6: Simulated receiver clock bias for an hour.

In case of verification of the simulator to be described in Section 3.5 or specified receiver clock biases are required, the simulator can accept the input of receiver clock

biases from a file as shown in the main menu of the simulator in Figure 3-1. The simulator reads the receiver clock biases line by line in the input file to its corresponding epoch.

Regarding the simulation of GPS and Galileo data, two independent receiver clock bias files or random walk processes are used to simulate the receiver clock biases in measurements for each GNSS. The reference time offset between GPS time and GST is absorbed in the estimated receiver clock bias of either GPS or Galileo during data processing, it depends on which reference time system is used in data processing.

3.3.7 Simulation of integer ambiguity

An integer ambiguity (N) is arbitrarily generated to phase measurements depending on the measuring frequency and a multiplier (m):

$$N = -m \cdot L \tag{3.36}$$

where m is set to 10^8 and L is 1 for GPS and Galileo L1 carriers, 2 for GPS L2 carrier, 5 for GPS L5 and Galileo E5a carriers, 5.5 for Galileo E5b carrier.

3.3.8 Simulation of random error

A simple algorithm described in [Bartosch, 2001] is used to generate Gaussian coloured noise. Independent Gaussian random numbers Z_n with zero mean and unit variance are generated by the MatrixVB "randn" function. A recursive algorithm maps these onto real correlated Gaussian random number $X_n \equiv X(t_n)$ at the sample time $t_n (t_0 < t_1 < \cdots < t_{n-1})$ with:

$$\langle X_n \rangle = 0 \tag{3.37}$$

where $\langle ... \rangle$ denotes averaging over the probability distribution of $X(t)$, and

$$\langle X_m X_n \rangle = \sigma^2 e^{-|t_m - t_n|/\tau} \tag{3.38}$$

where σ denotes the input standard deviation of code or phase random noise, m and n denote the two consecutive epochs, and τ denotes the correlation time.

The recursive algorithm described in [Bartosch, 2001] is:

$$X_0 = \sigma Z_0 \tag{3.39}$$

$$X_n = \rho_n X_{n-1} + \sqrt{1-\rho_n^2}\,\sigma Z_n \tag{3.40}$$

where the correlation coefficients ρ_n are given by $e^{-|t_n - t_{n-1}|/\tau}$. Since the random numbers X_ns are given by a linear combination of the Gaussian random variables X_n and a linear combination can only turn one Gaussian distribution into another Gaussian distribution [Feller, 1971], the X_ns also have to be Gaussian random variables [Bartosch, 2001]. In the simulator, a small correlation time τ of 0.5s is used to generate the slightly coloured random noises. The simulated code and phase random noises are then added to code and phase measurements. An example of the simulated phase random noise with the input standard deviation of phase noise of one millimetre for a thousand samples is shown in Figure 3-7.

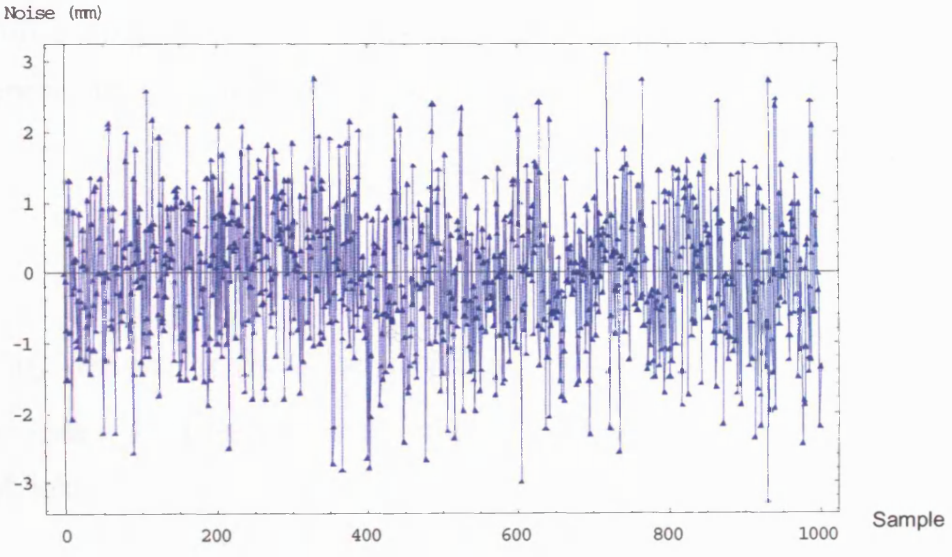

Figure 3-7: A thousand samples of phase random noise.

3.3.9 Simulation of ephemeris error

Actually, no ephemeris errors are introduced into measurements in the simulator. However, ephemeris errors are introduced to the computation of satellite positions when

the simulated measurements are generated using a precise ephemeris and then the simulated measurements are processed by any GNSS data processing software with a broadcast ephemeris. This way for the simulation of ephemeris error is illustrated in Figure 3-8.

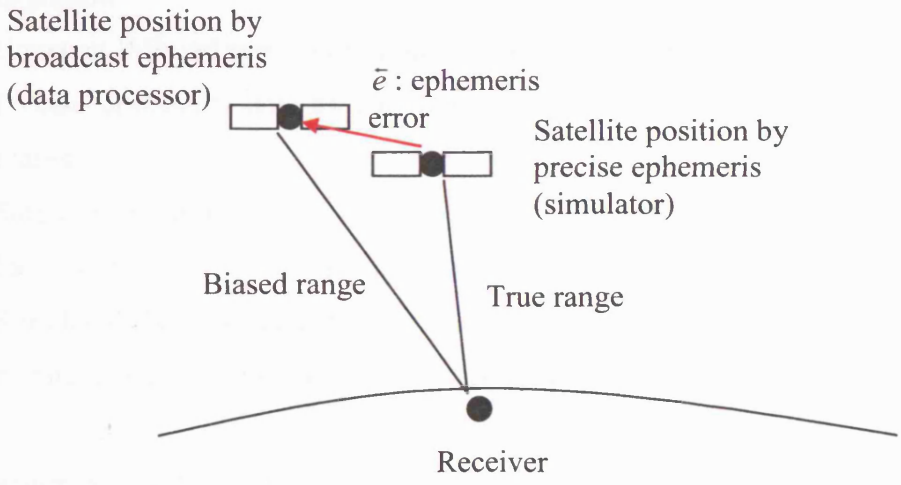

Figure 3-8: Ephemeris error introduced in simulation and data processing.

3.3.10 Simulation of relativistic effect

Relativistic effect due to eccentricity of satellite orbit is simulated using the instantaneous satellite position and velocity [ICD-GPS-200C, 2003] as:

$$\Delta t_r - \frac{2\vec{P}\cdot\vec{V}}{c^2} \tag{3.41}$$

where Δt_r denotes the relativistic correction, $\vec{P}$ denotes the instantaneous satellite position vector, $\vec{V}$ denotes the instantaneous satellite velocity vector, c denotes the speed of light.

3.4 Assumptions in the GNSS data simulation

This section lists the assumptions made in the GNSS data simulator. The assumptions are:

i) No bending of GNSS signal by refraction in ionosphere

ii) Tropospheric delay is azimuth homogeneous

iii) Assumed mapping functions for the elevation dependent ionospheric effect and tropospheric delay

iv) IFB is equivalent to the differential code bias (P1-P2) obtained from the IONEX file, modulation offset between C/A code and P-code in L1 are assumed to be negligible

v) Constant IFB and zero-mean in satellite IFBs as described in Section 3.3.5

vi) Precise ephemeris acts as the truth for satellite positions and satellite clock biases

vii) Satellite centre of mass to antenna phase centre offset is in Z direction (satellite local coordinates system, pointing towards the centre of the Earth) only

viii) Simulated data are referenced to the receiving antenna phase centre, therefore, no site displacements biases such as earth tides and ocean loading are generated

These assumptions affect the verification results of the simulator only but not affect the processing results and analyses in Chapters 6 to 8 and the conclusion in Chapter 9 because they have almost no effect on the short to medium baselines using double difference technique.

3.5 VERIFICATION OF THE GNSS DATA SIMULATOR

The GNSS data simulator generates some testing datasets for some IGS global tracking stations with the specific observation periods. The simulated data are compared with the real data, collected at the IGS stations, in measurement domain and their processing results are compared in position domain. It can verify the correctness of computational procedures in the simulator and the closeness of the simulated GNSS data to the real data. Section 3.5.1 describes the IGS stations used in the verification, inputs, settings, requirements, and methodology for the verification. Verification results of the simulated data in measurement domain are given in Section 3.5.2 and the results in position domain are presented in Section 3.5.3. The analyses of the results are described in Section 3.5.4. Finally, the conclusion of the verifications is presented in Section 3.5.5.

3.5.1 Description of the verification

3.5.1.1 Description of testing datasets

The IGS global tracking stations to be selected for the verification must fulfill the following requirements:

- ZTD data must be available in the IGS final tropospheric delay file
- The stations should have relatively stable ZTD data (less change in the selected observation periods and small standard deviations)
- The stations must have precise coordinates
- The station must have precise receiver clock bias data in RINEX Type C file, i.e. The station is used in precise clock analysis in the IGS network
- The stations' clock biases should be relatively stable
- The stations have P-code measurements in L1 obtained from good tracking loop (low noise) such as the Z-tracking technology of Ashtech Z-type receivers
- The stations must have IFB data from IONEX file

Three IGS global tracking stations (HRAO, POTS, and USNO) are selected for the verification test and their geographical locations are shown in Figure 3-9. The details of the three stations can be found in Appendix C.

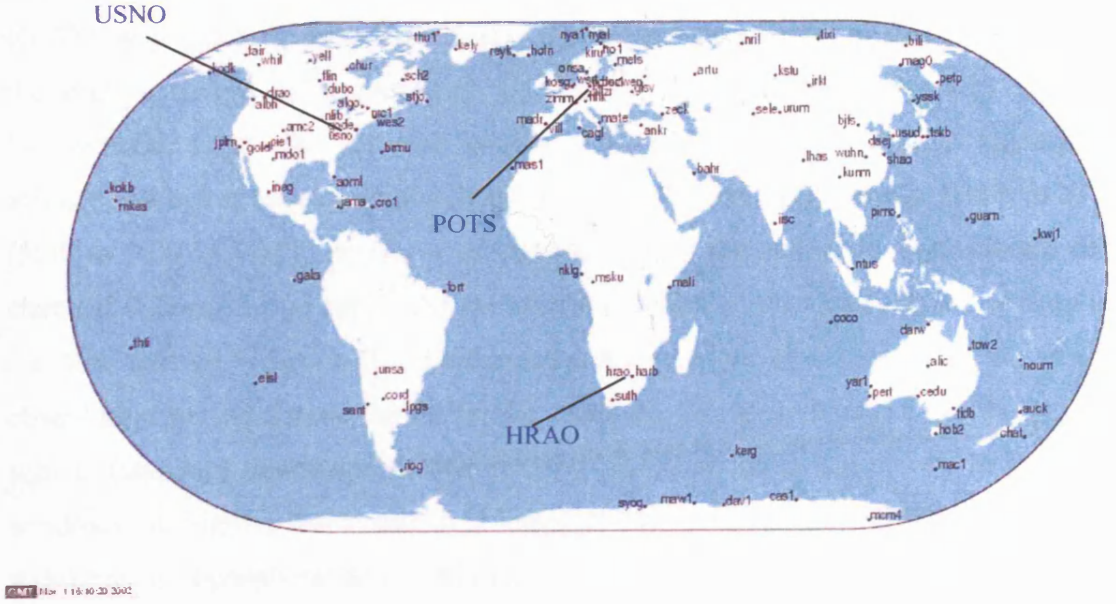

Figure 3-9: IGS global tracking stations (downloaded from IGS website).

In the rest of this section, site IDs are used to represent the sites.

The selected stations are distributed around the world. HRAO is located in the Southern hemisphere and to the east of the Greenwich meridian, POTS is located in the Northern hemisphere and to the east of the Greenwich meridian, and USNO is located in the Northern hemisphere and to the west of the Greenwich meridian. Therefore, WGS84 Cartesian coordinates of the stations have different signs in Y and Z-axis as shown in the above site descriptions. It can verify the correctness of the computation of the cut-off elevation angles of satellites.

The inputs for the simulation are described in Section 3.2. For the purpose of verification of the simulated data, precise station coordinates and precise receiver clock biases of the selected IGS global tracking stations are obtained from the RINEX Type C file. Moreover, the estimated receiver IFBs of the selected stations and TVEC values are obtained from the IONEX file. Precise ephemeris is used as the "true" satellite positions and clock biases to compute the "true" geometric range between the stations and the satellites.

In order to minimise the modelling error due to the interpolation of receiver clock biases in the given sampling interval of the RINEX Type C file, the measurement interval of the simulated observation data is set to the same interval as the RINEX Type C file, which is 300s (5 minutes). The observation period selected for the testing datasets is from GPS seconds 363600 to 370500 in the GPS week of 1251, which is 5:00 to 6:55 (GMT) on 1st January 2004. Moreover, in order to minimise the modelling error due to the high variation of tropospheric activity and the quality of the IGS estimated tropospheric delay, the selected period should have relatively stable tropospheric activity and better estimation quality. For instance, from GPS seconds 18000 to 25200 (5:00 to 7:00 in GMT) of day 1 of 2004 at POTS, the estimated tropospheric delay changed 0.2mm in two hours and the standard deviation was fairly small as shown in the blue text of Figure 3-10. Furthermore, the receiver clock biases in the selected observation period should be stable; for example, the receiver clock biases and their sigmas (standard deviations) in the selected period at POTS are shown in the dotted windows in Figures 3-11 and 3-12 respectively. HRAO and USNO have similar stabilities in tropospheric delay and receiver clock bias but they are not illustrated here.

```
+TROP/SOLUTION
*SITE ___EPOCH____ TROTOT _SIG #T #D DSTX DSTY DSTZ
*day 366
 POTS 04:001:03600 2325.4  1.3  6  0    0    0   -1
 POTS 04:001:10800 2321.8  0.9  6  1    0    0   -1
 POTS 04:001:18000 2317.0  0.9  6  0    0    0   -1
 POTS 04:001:25200 2317.2  1.5  6  0    0    0   -1
 POTS 04:001:32400 2321.7  2.0  6  0    0    0   -1
 POTS 04:001:39600 2321.0  1.7  6  0    0    0   -1
 POTS 04:001:46800 2318.3  0.9  6  0    0    0   -1
 POTS 04:001:54000 2317.7  0.8  6  0    0    0   -1
 POTS 04:001:61200 2320.1  1.5  6  0    0    0   -1
 POTS 04:001:68400 2318.8  2.3  6  0    0    0   -1
 POTS 04:001:75600 2322.1  1.6  6  0    0    0   -1
 POTS 04:001:82800 2320.4  1.9  5  0    0    0   -1
```

Figure 3-10: Example of the IGS tropospheric delay file at the station of POTS.

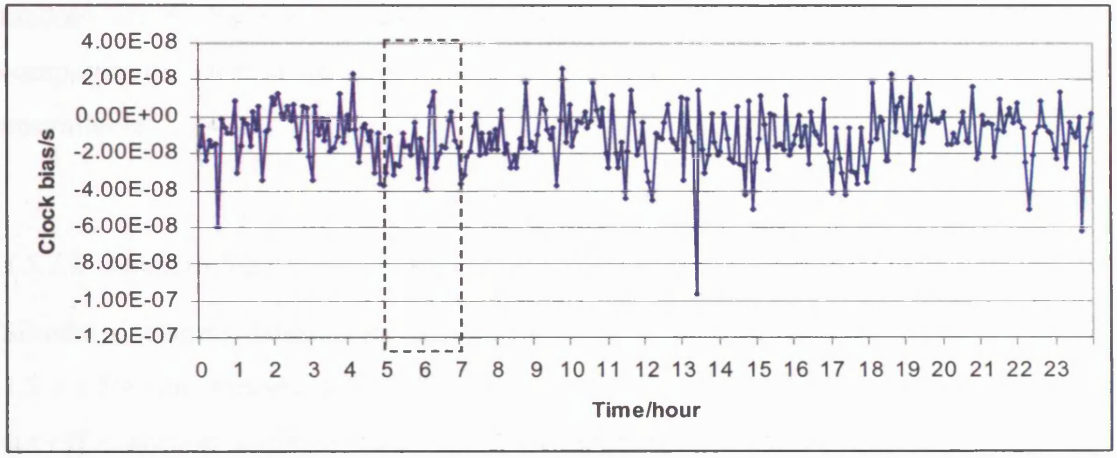

Figure 3-11: Receiver clock biases at POTS on 01/01/2004 (GMT); the selected observation period is shown in the dotted window.

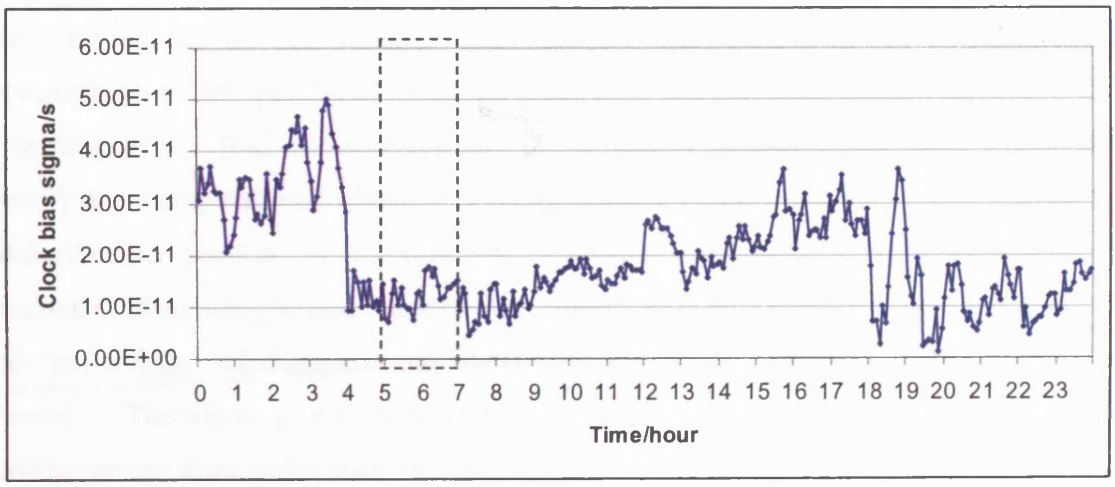

Figure 3-12: Receiver clock bias sigmas at POTS on 01/01/2004 (GMT); the selected observation period is shown in the dotted window.

Since the selected observation period of 5:00 to 6:55 in GMT is used to simulate the testing datasets for the three selected sites, the observation periods for the sites in local time are different. The observation period at HRAO and POTS is in the morning when the ionospheric effect is low to moderate, however, at USNO is at midnight when the ionospheric effect is low. Note that only two-hour data are used in this validation in order to prevent zero-mean and/or cancellation effects of some GNSS biases or errors over a long period of time (e.g. ionospheric and tropospheric effects) on the analyses of the statistical results.

Multipath errors have not been simulated in the verification testing datasets since unbiased multipath errors or environmental models of the sites are not available in this research; the verification of multipath modelling is described in Chapter 4. Moreover, random errors have not been simulated in order to avoid modelling error when comparing to real measurements since random error behaviour of receiver at each site is unavailable.

3.5.1.2 Methodology

Simulated testing datasets are generated using the information described in Section 3.5.1.1 for the selected three IGS stations in the selected observation period with the cut-off elevation angle as 15°. On the other hand, the real observation data of the stations for the selected observation period are downloaded from the IGS website. Two approaches for verification are carried out. They are verification in the measurement domain and the position domain.

In verification in the measurement domain, the simulated GPS pseudorange measurements are compared with the real GPS pseudorange measurements. This verification can find out how realistic the simulated measurements are. It can also verify the computations, biases and errors models in the simulator. The results are described in Section 3.5.2. Note that un-differenced measurements are compared because differencing would eliminate the common GNSS biases of a baseline and lead to "invisibility" of closeness and correctness for all the simulated GNSS biases and errors. Therefore, phase measurements are not suitable for verification in the measurement domain because ambiguities in the real data must be resolved before the comparison, however, ambiguity resolution in stand-alone positioning using un-differenced and un-linear combined (not ionospheric-free linear combined) phase measurements is difficult.

For verification in the position domain, the real and simulated datasets of the selected three IGS stations are processed by the Automatic GIPSY (AG) analyses service provided by JPL of NASA, details of whose service can be found in http://milhouse.jpl.nasa.gov/ag/. The position solutions of the simulated and real data are compared with the given coordinates in the RINEX Type C file and the results are given in Section 3.5.3. The processing technique used in AG is called Precise Point Positioning (PPP). PPP in AG uses pseudorange and phase measurements of all observation epochs and the final precise ephemeris to determine a stand-alone position. Most PPP algorithms use ionospheric-free pseudorange and phase observables in estimation in order to eliminate the first-order ionospheric effect. Moreover, precise correction models are applied to measurements such as site displacements corrections including earth tides, ocean loading and plate tectonic motion corrections, and corrections for systematic biases including phase wind-up bias, satellite phase centre to centre of mass offset, receiver antenna phase centre offset and variation and relativistic effect. However, the detailed processing model of the JPL's PPP cannot be found in the literature. Other PPP algorithms can be found in [Zumberge et al., 1997], [Zumberge, 1999], [Kouba and Héroux, 2001] and [Lau et al., 2003].

3.5.2 Measurement domain verification results

By comparing the simulated pseudorange measurements to the real pseudorange measurements, disagreements between the simulated and real measurements in terms of differences in decimetres are determined. Satellites with measurements in the two-hour observation period are selected for comparison. The differences at each epoch, their means, standard deviations, maxima (the greatest positive differences), and minima (the greatest negative differences) of pseudoranges P1 and P2 at HRAO, POTS, and USNO are tabulated in Tables 3-3, 3-4, and 3-5 respectively. Although, satellites PRN 10 and PRN 29 in Table 3-3 and satellite PRN 10 in Table 3-4 do not have measurements in all epochs, their differences are shown in the tables. This is because satellites PRN 10 and PRN 29 are observed at both HRAO and POTS and it aims to show any systematic bias in the differences.

The differences of the selected satellites at HRAO are plotted in Figures 3-13 to 3-16 and the satellites' elevation angles are plotted in Figure 3-17. The differences of the selected satellites at POTS are plotted in Figures D-1 to D-4 (in Appendix D) and the satellites' elevation angles are plotted in Figure D-5. Moreover, the differences of the

selected satellites at USNO are plotted in Figures D-6 to D-9 and the satellites' elevation angles are plotted in Figure D-10.

Table 3-3: Differences between simulated and measured P1 and P2 pseudoranges at HRAO in GMT 5:00 to 6:55 (local time: 7:00 to 8:55) on 01/01/2004.

	PRN 4		PRN 24		PRN 10		PRN 29	
Epoch	ΔP1 (m)	ΔP2 (m)	ΔP1 (m)	ΔP2 (m)	ΔP1 (m)	ΔP2 (m)	ΔP1 (m)	ΔP2 (m)
5:00	0.038	-0.133	0.385	0.528	-	-	-	-
5:05	0.193	-0.075	0.429	0.666	0.107	0.220	-	-
5:10	0.103	0.190	0.560	0.613	0.165	0.485	-	-
5:15	0.019	-0.060	0.395	0.512	0.366	0.259	-	-
5:20	0.215	0.085	0.449	0.362	0.125	0.356	-	-
5:25	0.109	-0.016	0.454	0.551	0.206	0.310	-	-
5:30	0.257	0.181	0.344	0.664	0.279	0.255	-	-
5:35	0.259	0.333	0.367	0.491	0.336	0.314	-	-
5:40	0.392	0.397	0.458	0.273	0.273	0.340	-	-
5:45	0.289	0.407	0.410	0.540	0.382	0.407	-	-
5:50	0.317	0.543	0.473	0.555	0.303	0.397	-	-
5:55	0.473	0.296	0.705	0.785	0.412	0.429	-	-
6:00	0.284	0.493	0.453	0.622	0.388	0.500	-	-
6:05	0.303	0.402	0.626	0.783	0.314	0.560	-	-
6:10	0.372	0.398	0.608	0.577	0.349	0.329	-	-
6:15	0.234	0.331	0.544	0.477	0.406	0.362	-	-
6:20	0.503	0.357	0.430	0.755	0.296	0.322	-	-
6:25	0.259	0.388	0.672	0.620	0.241	0.442	-	-
6:30	0.340	0.024	0.445	0.504	0.409	0.564	0.176	0.085
6:35	0.316	0.313	0.608	0.601	0.507	0.625	-0.087	-0.356
6:40	0.176	0.293	0.569	0.528	0.554	0.581	0.192	-0.120
6:45	-0.153	0.057	0.405	0.461	0.530	0.631	-0.040	-0.124
6:50	0.023	0.225	0.506	0.598	0.483	0.605	0.080	-0.222
6:55	0.186	0.024	0.509	0.657	0.648	0.698	0.260	-0.050
Mean	0.230	0.227	0.492	0.572	0.351	0.434	0.097	-0.131
SD	0.152	0.195	0.099	0.120	0.137	0.138	0.138	0.150
Max	0.503	0.543	0.705	0.785	0.648	0.698	0.260	0.085
Min	-0.153	-0.133	0.344	0.273	0.107	0.220	-0.087	-0.356

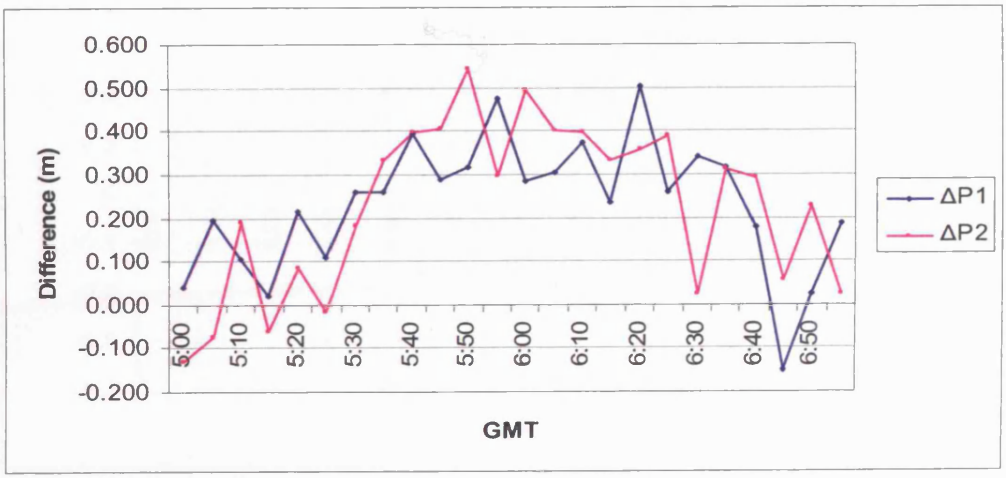

Figure 3-13: Differences between real and simulated pseudoranges P1 and P2 of satellite PRN 4 at HRAO in the selected observation period.

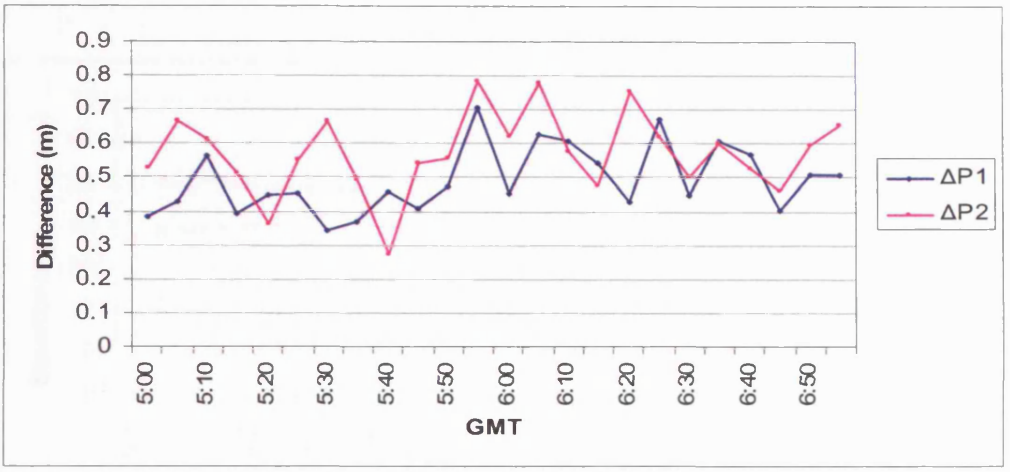

Figure 3-14: Differences between real and simulated pseudoranges P1 and P2 of satellite PRN 24 at HRAO in the selected observation period.

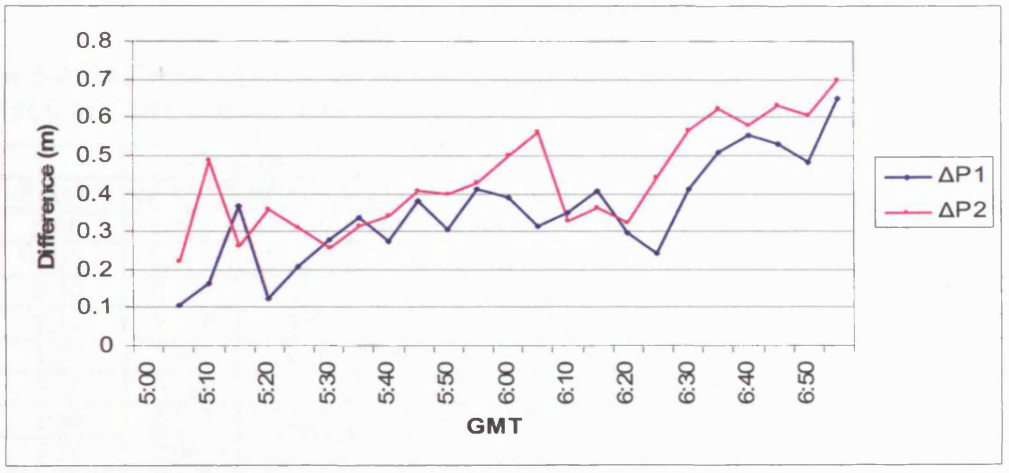

Figure 3-15: Differences between real and simulated pesudoranges P1 and P2 of satellite PRN 10 at HRAO in the selected observation period.

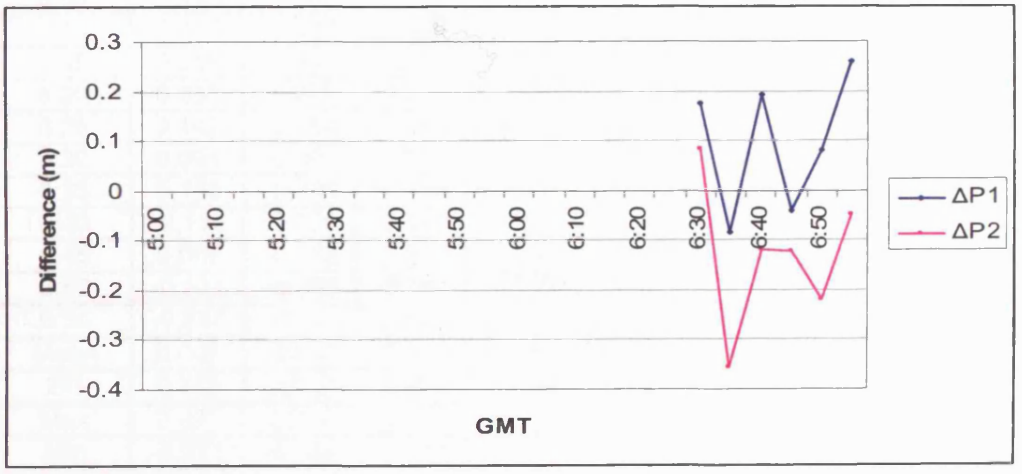

Figure 3-16: Differences between real and simulated pseudoranges P1 and P2 of satellite PRN 29 at HRAO in the selected observation period.

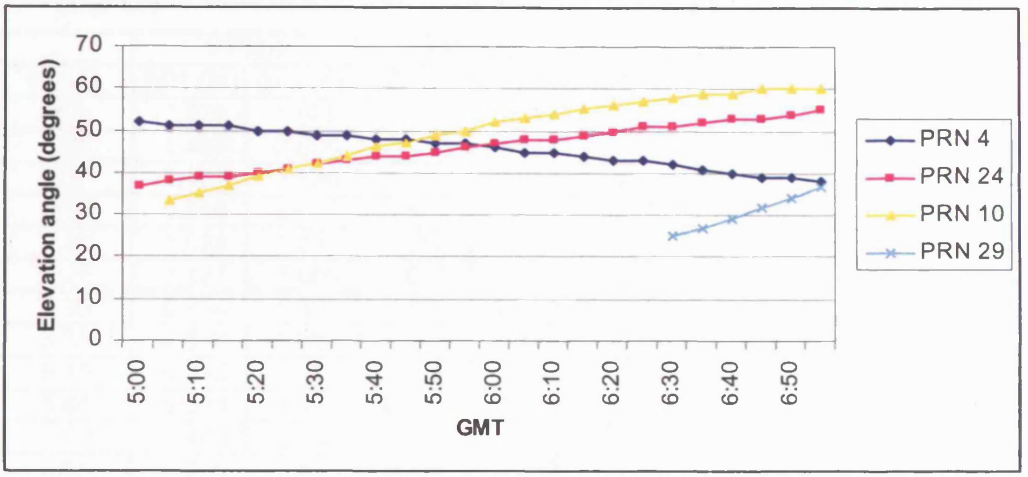

Figure 3-17: Elevation angles of the selected satellites at HRAO in the selected observation period.

Table 3-4: Differences between simulated and measured P1 and P2 pseudoranges at POTS in GMT 5:00 to 6:55 (local time: 6:00 to 7:55) on 01/01/2004.

	PRN 26		PRN 28		PRN 29		PRN 10	
Epoch	ΔP1 (m)	ΔP2 (m)	ΔP1 (m)	ΔP2 (m)	ΔP1 (m)	ΔP2 (m)	ΔP1 (m)	ΔP2 (m)
5:00	0.178	0.133	-0.071	-0.202	0.299	-0.045	-0.233	-0.879
5:05	0.040	0.157	0.345	-0.136	-0.014	-0.036	-0.268	-0.982
5:10	0.134	0.063	-0.105	0.022	0.197	0.027	-0.442	-0.784
5:15	0.106	0.132	-0.154	0.133	0.008	0.105	-0.032	-1.041
5:20	0.391	0.279	0.077	0.068	0.152	0.047	-0.481	-0.982
5:25	0.100	0.151	-0.218	-0.087	-0.039	-0.010	-0.655	-1.062
5:30	0.077	-0.031	-0.041	0.238	0.122	0.013	-0.520	-1.471
5:35	0.041	0.061	-0.120	-0.037	0.041	-0.050	-0.863	-1.261
5:40	0.217	-0.036	-0.326	0.220	-0.139	-0.127	-1.118	-1.311
5:45	-0.072	-0.034	-0.284	0.130	-0.110	0.127	-	-
5:50	0.069	0.018	-0.316	0.199	-0.126	-0.323	-	-
5:55	-0.130	-0.101	-0.251	0.249	-0.001	-0.122	-	-
6:00	-0.052	-0.081	-0.358	0.036	-0.167	-0.431	-	-
6:05	-0.049	-0.003	-0.064	0.094	-0.044	-0.225	-	-
6:10	0.158	-0.014	-0.103	0.287	-0.270	-0.118	-	-
6:15	0.015	0.050	0.103	0.079	-0.009	-0.396	-	-
6:20	0.035	0.079	0.172	0.143	-0.182	-0.350	-	-
6:25	0.142	-0.054	-0.054	0.253	-0.198	-0.475	-	-
6:30	0.094	-0.087	0.294	0.412	-0.313	-0.595	-	-
6:35	0.198	-0.169	-0.194	0.913	-0.064	-0.382	-	-
6:40	-0.127	-0.279	0.010	0.420	-0.450	-0.653	-	-
6:45	0.067	-0.285	0.050	0.883	-0.395	-0.784	-	-
6:50	-0.271	-0.294	-0.388	0.109	-0.621	-0.711	-	-
6:55	-0.241	-0.452	0.141	0.090	-0.715	-0.692	-	-
Mean	0.047	-0.033	-0.077	0.188	-0.127	-0.259	-0.512	-1.086
SD	0.148	0.169	0.200	0.266	0.244	0.283	0.333	0.220
Max	0.391	0.279	0.345	0.913	0.299	0.127	-0.032	-0.784
Min	-0.271	-0.452	-0.388	-0.202	-0.715	-0.784	-1.118	-1.471

Table 3-5: Differences between simulated and measured P1 and P2 pseudoranges at USNO in GMT 5:00 to 6:55 (local time: 0:00 to 1:55) on 01/01/2004.

	PRN 9		PRN 15		PRN 18		PRN 21	
Epoch	ΔP1 (m)	ΔP2 (m)	ΔP1 (m)	ΔP2 (m)	ΔP1 (m)	ΔP2 (m)	ΔP1 (m)	ΔP2 (m)
5:00	-1.276	-1.666	0.326	1.347	0.203	0.264	-0.096	-0.142
5:05	-1.468	-2.606	0.172	0.865	0.112	-0.001	0.171	-0.240
5:10	-1.133	-1.680	0.532	0.957	-0.029	0.338	-0.039	-0.335
5:15	-0.946	-2.078	0.509	0.934	0.439	-0.014	-0.282	-0.287
5:20	-1.039	-1.033	1.052	1.197	0.387	0.134	-0.213	-0.378
5:25	-1.121	-1.085	0.640	0.847	0.503	0.102	-0.228	-0.512
5:30	-0.854	-1.361	0.812	0.439	0.458	0.487	-0.553	-0.593
5:35	-0.583	-1.003	0.502	0.726	0.598	0.368	-0.477	-0.827
5:40	-0.693	-1.211	0.725	1.046	0.756	0.400	-0.292	-0.861
5:45	-0.534	-1.077	0.544	0.770	0.353	0.512	-0.588	-0.659
5:50	-0.348	-0.485	0.192	0.862	0.305	0.131	-0.544	-1.023
5:55	-0.240	-0.417	0.337	0.659	0.314	0.185	-0.763	-0.999
6:00	-0.766	-0.688	0.217	0.268	0.363	0.131	-0.675	-1.560
6:05	-0.258	-0.561	0.179	0.456	0.095	0.211	-0.739	-1.752
6:10	0.011	-0.314	0.664	0.631	-0.331	-0.099	-1.049	-2.179
6:15	0.091	-0.282	0.168	0.324	-0.113	0.349	-1.099	-2.631
6:20	-0.096	0.090	0.244	0.298	0.281	-0.075	-1.659	-2.645
6:25	-0.079	0.098	-0.132	0.366	-0.036	0.078	-1.325	-1.792
6:30	0.067	0.309	0.289	-0.058	0.125	0.195	-1.287	-1.860
6:35	0.242	0.308	0.195	0.387	0.229	0.146	-0.778	-2.201
6:40	0.495	0.422	0.318	0.299	-0.021	0.051	-1.615	-2.568
6:45	0.500	0.884	0.328	0.053	-0.097	-0.009	-1.634	-2.563
6:50	0.703	1.111	0.280	0.027	-0.067	-0.155	-1.894	-3.155
6:55	0.402	1.151	-0.311	-0.048	-0.058	-0.239	-1.968	-2.954
Mean	-0.372	-0.549	0.366	0.569	0.199	0.145	-0.818	-1.446
SD	0.622	0.985	0.294	0.394	0.263	0.198	0.620	0.983
Max	0.703	1.151	1.052	1.347	0.756	0.512	0.171	-0.142
Min	-1.468	-2.606	-0.311	-0.058	-0.331	-0.239	-1.968	-3.155

3.5.3 Position domain verification results

Since the simulated datasets do not contain site dependent multipath effect and site displacements effects such as earth tides, ocean loading and plate tectonic motion, 24-hour measurements are used in the real datasets to provide a better positioning accuracy and better averaging of multipath effect and some of the site displacements effects although PPP has modelled them. The AG positioning results of the simulated and real data are compared with the given station coordinates in RINEX Type C file and the differences in northing, easting and height are tabulated in Table 3-6. In addition, the differences in northing, easting and height between the simulated and real data are given in the table.

Table 3-6: Differences in northing (ΔN), easting (ΔE) and height (ΔH) among the AG processing results of simulated (Sim) and real (Real) data, and the given coordinates in RINEX Type C file (RINEX_C).

Stn	HRAO			POTS			USNO		
Column	(1)	(2)	(3)	(4)	(5)	(6)	(7)	(8)	(9)
Diff	Sim - RINEX_C	Real - RINEX_C	Sim - Real	Sim - RINEX_C	Real - RINEX_C	Sim - Real	Sim - RINEX_C	Real - RINEX_C	Sim - Real
ΔN (m)	0.130	0.002	0.128	0.032	0.002	0.030	0.286	0.005	0.281
ΔE (m)	0.112	-0.010	0.122	-0.072	0.001	-0.074	0.177	-0.005	0.182
ΔH (m)	-0.159	0.054	-0.212	-0.191	0.040	-0.231	0.246	-0.005	0.251

3.5.4 Analysis of results

3.5.4.1 Measurement domain verification

In most cases, the differences of P2 are larger that of P1. It may be due to the fact that the L2 frequency is weaker and noisier than the L1 frequency in the real datasets. Note that no random measurement noise is generated in the simulated datasets. The ranges of differences at HRAO are from -0.153 m to 0.705 m in P1 and from -0.365 m to 0.785 m in P2. The ranges of differences at POTS are from -1.118 m to 0.391 m in P1 and from -1.471 m to 0.913 m in P2. Moreover, the ranges of differences at USNO are from -1.968 m to 1.052 m in P1 and from -3.155 m to 1.347 m in P2. In most cases, the differences do not show the satellite elevation angle dependent characteristic. However, the differences of PRN 10 at HRAO (as shown in Figures 3-15 and 3-17) and POTS (as shown in Figures D-4 and D-5 in Appendix D), and PRN 21 at USNO (as shown in Figures D-9 and D-10) show the satellite elevation angle dependent characteristic. Therefore, it is not likely that the differences are due to the biases of the elevation angle dependent mapping functions of ionospheric and tropospheric delays. It is also impossible to conclude there are systematic errors because the common satellites PRN 10 and PRN 29 at HRAO and POTS do not have similar differences.

When looking at the HRAO dataset, almost all differences except those obtained from the low elevation satellite PRN 29 are positive, which mean that the simulated measurements are longer than the real measurements. It may be due to the fact that the mapping functions for atmospheric delays do not work very well in high altitude because the altitude of station HRAO is about 1414 m. Moreover, it may due to a bias in the estimated receiver clock biases obtained from RINEX Type C file. Although, the differences of PRN 29 show some negative values, they are within the range of the nominal pseudorange measurement noise (except the difference in P2 at epoch 6:35 is

slightly greater than the nominal noise level), which is about 0.25 m to 0.5 m in most receivers [Misra and Enge, 2001].

In the result of the dataset at POTS, almost all the differences except those obtained from the low elevation satellite PRN 10 are close to or within the nominal pseudorange noise. The differences of PRN 10 show a clear elevation angle dependent characteristic, it may be because the mapping functions of atmospheric delays do not work well in low elevation angles.

Regarding the result of the dataset at USNO, almost all the differences of the satellites PRN 9 and PRN 21 are negative, which mean that the simulated measurements are shorter than the real measurements. It may be because there are some short-range multipath errors although it may be rare at the IGS global stations.

Apart from the elevation angle dependent mapping functions of atmospheric delays, part of the differences may be due to a small azimuth dependent bias in atmospheric effect, which is the assumption (ii) in Section 3.4, and the arbitrary IFB offset obtained from the mean satellite IFBs, which is the assumption (v) in Section 3.4 and this offset can be up to few decimetres for individual satellite IFB. Besides, there are some residual errors in the GNSS biases and errors models in the simulator, which use the best available information from the IGS. The error budgets for the modelling errors in the simulator and in this verification are listed in Table 3-7.

Table 3-7: Error budgets for the verification of the simulator.

Biases or errors	Accuracy/potential error size	References
Satellite clocks	< 0.1 ns (< 0.3 m)	IGS website
Satellite orbits	< 5 cm	IGS website
Ionospheric TEC grid	2 - 8 TECU (0.3 - 1.3 m in L1, 0.5 - 2.1 m in L2)	IGS website
Final ZTD	4 mm	IGS website
Multipath	Code: 0.5 - 1 m in a "clean" environment	Misra and Enge (2001)
Receiver noise	Code: 0.25 - 0.5 m (rms)	Misra and Enge (2001)
IGS station position	Horizontal: 3 mm Vertical: 6 mm	IGS website
IFB (DCB)	Satellite: 3 mm (rms) Receiver: 14 mm (rms)	IONEX file used
Maximum possible range error (mapping functions are not considered)	~ 3.2 m for L1 ~4 m for L2	

The maximum absolute differences in L1 and L2 from Tables 3-3 to 3-5 are 1.968 m (in the low elevation angle satellite PRN 21 at USNO) and 3.155 m (in the low elevation angle satellite PRN 21 at USNO) respectively. If taking the multipath error budget (mainly from the ground) into account and ignoring the accuracies of the mapping

functions for ionospheric and tropospheric delays, the maximum differences of L1 and L2 in the verification datasets are smaller than the maximum possible range errors of L1 and L2 (see Table 3-7) respectively. Note that the maximum differences at USNO are negative therefore multipath errors are possible, and mapping functions can lead to larger error budgets for ionospheric and tropospheric delays in Table 3-7.

3.5.4.2 Position domain verification

From Table 3-6, the maximum positioning differences between the simulated datasets and the real datasets as well as the given coordinates in RINEX Type C file are about 0.29 m in horizontal and about 0.25 m in vertical. In columns (1), (3), (4) and (6) in Table 3-6, both HRAO and POTS have negative differences in height, which mean the estimated heights using the simulated datasets are lower than the estimated heights using the real datasets or the given coordinates in RINEX Type C file. In columns (7) and (9) in Table 3-6, USNO has positive differences in height, which mean the estimated height using the simulated dataset is higher than the estimated height using the real dataset or the given coordinates in RINEX Type C file. These results agree with the results in measurement domain validation to some extent.

In addition to the possible range errors in the measurement domain verification as described in Section 3.5.4.1, part of the differences in positioning solutions may be because there are some biases coming from the site displacements effects listed in Table 3-8.

Table 3-8: Error budgets for site displacements effects [Kouba and Héroux, 2001].

Effect	Magitude
Solid Earth tides	Periodic part: ~30 cm in radial, ~5 cm in horizontal
	Permanent part: <12.5 cm in radial, <5 cm in northing
Ocean loading (near coast)	<5 cm in radial, <2 cm in horizontal
Sub-daily Earth Rotation Parameters (Pole position, UT1-UTC)	<3 cm
Geocentre variation	few cm
Maximum possible position bias	~50 cm in radial, ~20 cm in horizontal

PPP solutions for the real datasets have corrected most of the site displacements effects, however, these effects contributed to position errors in this verification of the simulator, in which the simulated measurements are referenced to the antenna phase centre, because PPP applies corrections for site displacements effects to the simulated data. It

does not affect the investigation, results, and conclusions in the following chapters because medium- to short-baseline relative positioning is mainly considered in this research.

Note that some of the site displacements effects have to take a long time to average out therefore even using a longer observation time (even 24 hours) for the simulated datasets would be still biased to some long period site displacements effects.

3.5.5 Conclusion of verification

Many range differences in the measurement domain verification as shown in Tables 3-3 to 3-5 are within the nominal noise level. The large range differences always come from low elevation satellites. The maximum range differences in L1 and L2 are within the maximum possible range errors in L1 and L2 for the measurement domain verification as listed in Table 3-7, respectively.

In the position domain verification, the position differences agree with the "truths", which are determined by JPL AG (PPP solutions) or the given coordinates in RINEX Type C file, within three decimetres. These differences contain the site displacements effects, which can be up to 50 cm in radial and 20 cm in horizontal as shown in Table 3-8.

The verification shows that the simulator can generate reasonably realistic GPS data using the best available information from IGS since both the range differences and the position differences are within the maximum possible range error and position bias. It is expected that the better accuracy of the IGS information would improve the simulated range accuracy and hence reduce the position differences in the position domain verification.

3.6 Conclusion of the GNSS data simulation

The GNSS simulator has taken all possible GNSS biases and errors into account and has used the best models along with the best available information from IGS to generate GNSS data. The simulator has generated three testing datasets for the three selected IGS global tracking stations. The simulated datasets have been verified in measurement and position domains with real measurements and "true" positions respectively.

The reality of the simulated measurements is limited by the accuracies of the IGS products. Therefore, the range differences in measurement domain verification are

biased to the accuracies of the inputted data/information used in the GNSS biases and errors models of the simulator. The results in the measurement domain verification show that the range differences are within the maximum possible range error specific for the verification.

Verification in position domain shows that the simulated datasets agree with the real datasets and the given coordinates in RINEX Type C file in decimetres. The position differences are biased to the site displacements effects since the reference measurement point of the simulator is the receiving antenna phase centre. The reference point at the receiving antenna phase centre affects the verification of the simulator only because this research project considers single-epoch short- to medium-baseline relative positioning. Single-epoch solution (suitable for RTK applications) means that it will not be affected by the site displacements effects because the solution is referenced to the roving receiving antenna phase centre not at a specific position on the Earth. Moreover, relative positioning eliminates all common biases in short to medium baselines.

A test on relative positioning using the simulated data for a short baseline has been carried out. The result shows that the single-epoch relative positioning solutions agree with the inputted coordinates used in the simulation in one millimetre. It may suggest that there are some biases and/or GPS systematic errors in the simulator, which are eliminated in relative positioning. However, these common biases and/or systematic errors are masked by the possible range error (mixed error in range) and the possible positioning bias (mixed error in position) in Tables 3-6 and 3-7 and therefore they cannot be easily identified in the verification results. Even if there are some biases in the simulated data, it won't affect the results and conclusions of this thesis because relative positioning technique is employed in GNSS data processing, which common biases are eliminated in double difference technique described in Section 2.5. Note that the relative positioning testing results are not shown in this chapter because the results are straightforward and expected.

In conclusion, the assumptions for the simulator described in Section 3.4 have no effect on the investigations of this research to be described in the following chapters because single-epoch short- to medium-baseline relative positioning is concerned. With the verified reasonable realistic GPS data simulation, the GNSS data simulator can be used to extrapolate to the modernised GPS and Galileo for generation of multiple-frequency GNSS data.

4. MULTIPATH MODELLING AND SIMULATION

4.1 INTRODUCTION

This chapter describes the phase multipath modelling for multipath simulation in the GNSS data simulator. The multipath modelling takes all possible geometrical and physical factors into account. The geometrical factors are the satellite, reflector, and antenna positions; the physical factors are the relative permittivity (also called dielectric constant, however it is not constant, it is frequency-dependent) of material of the reflector, reflection coefficient, polarisation of multipath signal, antenna gain of multipath signal, signal frequency, PRN chipping rate, and correlation function of multipath signal in Delay Lock Loop (DLL) of receiver.

This chapter describes the multipath modelling in signal transmission order. Section 4.2 describes the signal transmitted from satellite antenna to the receiving antenna and reflector. The ways in which the signal changes during reflection and the properties of the reflected signal are discussed in Section 4.3. Section 4.4 describes the response of GNSS receiving antenna to line-of-sight and reflected signals and the resulting multipath errors in phase measurements are described in Section 4.5. Details of the multipath simulator are given in Section 4.6, and its verification with real multipathing data collected in two experiments is described in Section 4.7. Section 4.8 describes the characteristics of multipath in different scenarios and, finally, the conclusions of the multipath modelling and simulation are given in Section 4.9. Note that GPS signals are used as examples of GNSS signals throughout the chapter since it is the only full operational GNSS now – but the methods of the chapter are fully applicable to modernised GPS, GLONASS and GALILEO and the results should therefore be of special interest to those wishing to study the performance of these systems, and combinations of them, in the future.

4.2 TRANSMITTED SIGNAL FROM GNSS SATELLITES

As described in Section 2.3.1.1, signals transmitted from GPS satellites are right-handed circular polarised (RCP), which is $E_1=E_2$ and $AR=1$. Multipath occurs when an antenna not only receives a line-of-sight signal but also an indirect signal that has been reflected

by an object (see Figure 4-1). Long distance multipath (i.e. that due to reflectors far from the antenna) can often be filtered out by the receiver correlator, so most multipath errors in high precision GPS measurements are due to reflectors that are only short distances from the receiving antenna (or more strictly those that only introduce additional path lengths of a few metres). It is also relevant to note that the GPS signal transmitted from a satellite (i.e. before arrival at a receiving antenna or a reflector) has a phase wind-up error [Wu et al., 1993] as shown in Figure 4-2. Phase wind-up error is due to the change of satellite antenna reference orientation during its orbit as well as receiving antenna reference orientation in kinematic applications, but the magnitudes of phase wind-up errors in the direct and reflected signals are very similar as the distance between receiving antenna and reflector is rather small – so the effect can be ignored in this multipath modelling.

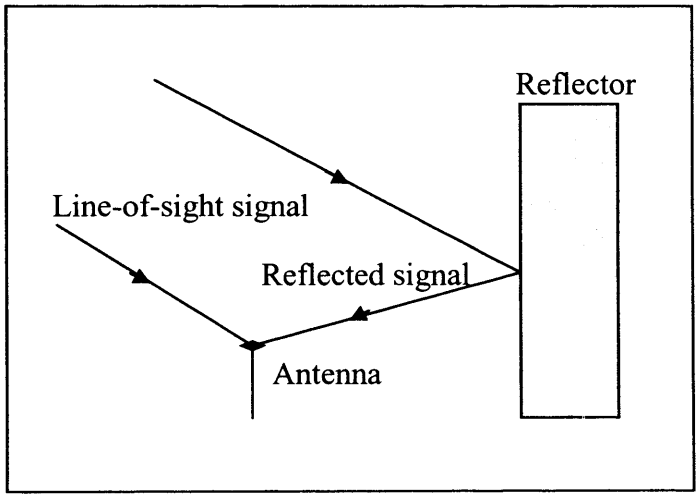

Figure 4-1: Line-of-sight and reflected signals arrive at antenna and causing multipath effect.

4.3 REFLECTED SIGNAL FROM REFLECTOR

When a GPS signal arrives at a reflector, it, or part of it, may be reflected from the reflector towards the antenna and part of it may be transmitted to the reflector as shown in Figure 4-2. The powers of the reflected and of the transmitted signals depend on the Fresnel reflection coefficient ρ and the relative permittivity $\varepsilon_2 / \varepsilon_1$ of the media. In the case of GPS multipath, the first medium is air and the second medium is the material of the reflector. The Fresnel reflection coefficient ρ is a function of incident angle θ_i and

the relative permittivity; and the relative permittivity of the material is a function of the signal frequency.

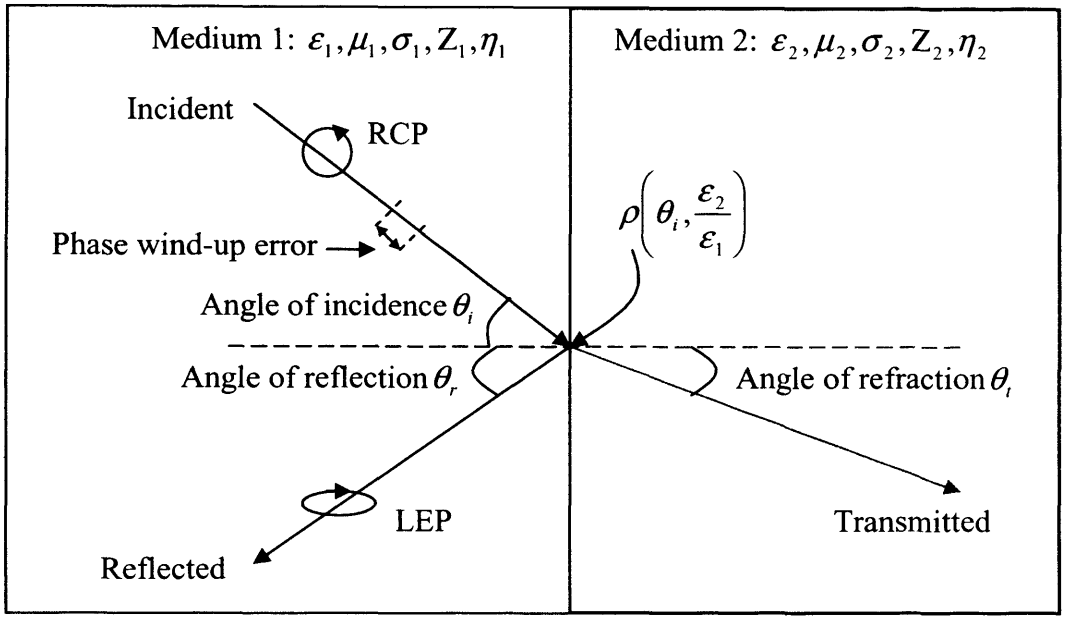

Figure 4-2: Reflection and transmission of signal between two media.

The electric field of an incident signal can be resolved into perpendicular and parallel components, therefore the Fresnel reflection coefficient can also be resolved into perpendicular $\rho_\perp$ and parallel ρ_{II} components. If both media are lossless nonmagnetic dielectrics [Kraus and Fleisch, 1999], the perpendicular Fresnel reflection coefficient $\rho_\perp$ is given by:

$$\rho_\perp = \frac{\cos\theta_i - \sqrt{\varepsilon_2/\varepsilon_1 - \sin^2\theta_i}}{\cos\theta_i + \sqrt{\varepsilon_2/\varepsilon_1 - \sin^2\theta_i}} \tag{4.1}$$

and the parallel Fresnel reflection coefficient ρ_{II} is given by:

$$\rho_{II} = \frac{-\left(\varepsilon_2/\varepsilon_1\right)\cos\theta_i + \sqrt{\varepsilon_2/\varepsilon_1 - \sin^2\theta_i}}{\left(\varepsilon_2/\varepsilon_1\right)\cos\theta_i + \sqrt{\varepsilon_2/\varepsilon_1 - \sin^2\theta_i}} \tag{4.2}$$

For parallel polarisation, it is possible to find an incident angle so that $\rho_{\text{II}} = 0$ and the signal is totally transmitted into medium 2. This angle is called Brewster angle θ_{iB} and is determined by:

$$\theta_{iB} = \tan^{-1}\sqrt{\frac{\varepsilon_2}{\varepsilon_1}} \tag{4.3}$$

The Brewster angle is also sometimes called the polarising angle since a signal composed of both perpendicular and parallel components and incident at the Brewster angle produces a reflected signal with only a perpendicular component. Thus, a circular polarised signal incident at the Brewster angle becomes linearly polarised on reflection. No matter the incident angle is equal to or is not equal to Brewster angle, the total reflection coefficient ρ is given by [Born and Wolf, 1999]:

$$\rho = \rho_{\text{II}} \cos^2\theta_i + \rho_{\perp} \sin^2\theta_i \tag{4.4}$$

If medium 2 is a more dense dielectric than medium 1, i.e., $\varepsilon_2 > \varepsilon_1$, the quantity under the square root in Equation (4.1) will be positive and $\rho_{\perp}$ will be real. If the incident signal travels from the more dense medium onto the less dense medium, i.e., $\varepsilon_1 > \varepsilon_2$, and if $\sin^2\theta_i \geq \varepsilon_1/\varepsilon_2$, then $\rho_{\perp}$ becomes complex and $|\rho_{\perp}| = 1$. Under these conditions, total internal reflection occurs that the incident signal is reflected back into the denser medium. This is true for both the parallel and perpendicular component. In this case, the incident angle is called critical angle. However, this case does not occur in GNSS applications because GNSS signals always travel from less dense air to the denser reflector.

When a signal is reflected, its polarisation state will be changed. Firstly definitions of the terms needed to describe polarisation state are given. At a fixed value of z (see Figure 2-3), the electric vector E rotates as a function of time, the tip of the vector describing an ellipse, called the polarisation ellipse as shown in Figures 4-3 and 4-5. Figure 4-3 also shows the relationship between the different angles describing polarisation (so-called parameters of polarisation): the tilt angle τ is the angle of the

major axis from X-axis, ε is an auxiliary angle defined in Equation (4.7) which characterises the ellipticity, and $\gamma = \tan^{-1}(E_2 / E_1)$.

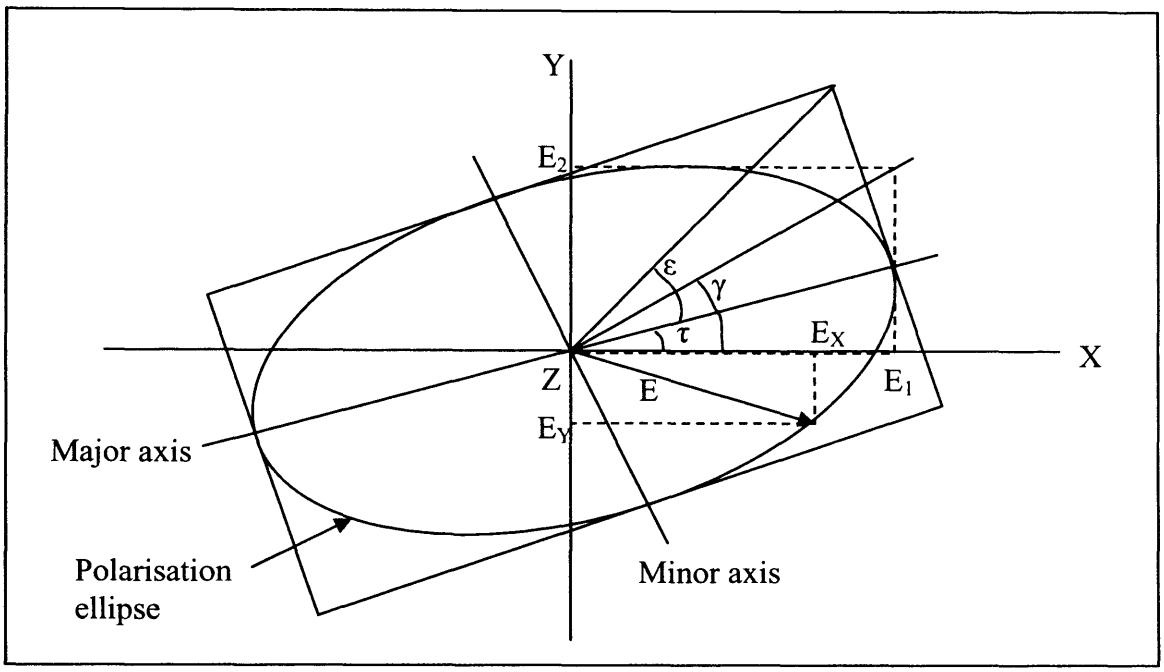

Figure 4-3: Polarisation ellipse at tilt angle τ showing instantaneous components of E_X and E_Y and amplitudes E_1 and E_2 and relation of angles ε, τ, and γ.

The polarisation state of a signal can be represented geometrically by a Poincaré sphere as shown in Figure 4-4. The definition of Poincaré sphere can be found in [Kraus and Fleisch, 1999] and its derivation can be found in [Born and Wolf, 1999]. A Poincaré sphere describes the polarisation state as a point on a sphere where the latitude and longitude of the point are related to parameters of the polarisation ellipse as follows:

$$\text{Latitude} = 2\varepsilon \tag{4.5}$$

$$\text{Longitude} = 2\tau \tag{4.6}$$

where τ denotes the tilt angle, $0° \le \tau \le 180°$ and

$$\varepsilon = \cot^{-1}(\mp AR) \tag{4.7}$$

where $-45° \le \varepsilon \le +45°$. The axial ratio ($AR$) and angle ε are negative for right-handed and positive for left-handed polarisation. The polarisation state can also be

expressed in terms of the angle subtended by the great circle drawn from a reference point on the equator and the angle between the great circle and the equator (see Figure 4-4) as follows:

$$\text{Great-circle angle} = 2\gamma \tag{4.8}$$

$$\text{Equator-to-great-circle angle} = \delta \tag{4.9}$$

The trigonometric relationships between the polarisation parameters ε, τ, γ, and δ are as follows (the derivation are based on spherical trigonometry and can be found in [Born and Wolf, 1999]):

$$\cos 2\gamma = \cos 2\varepsilon \cos 2\tau \tag{4.10}$$

$$\tan \delta = \frac{\tan 2\varepsilon}{\sin 2\tau} \tag{4.11}$$

$$\tan 2\tau = \tan 2\gamma \cos \delta \tag{4.12}$$

$$\sin 2\varepsilon = \sin 2\gamma \sin \delta \tag{4.13}$$

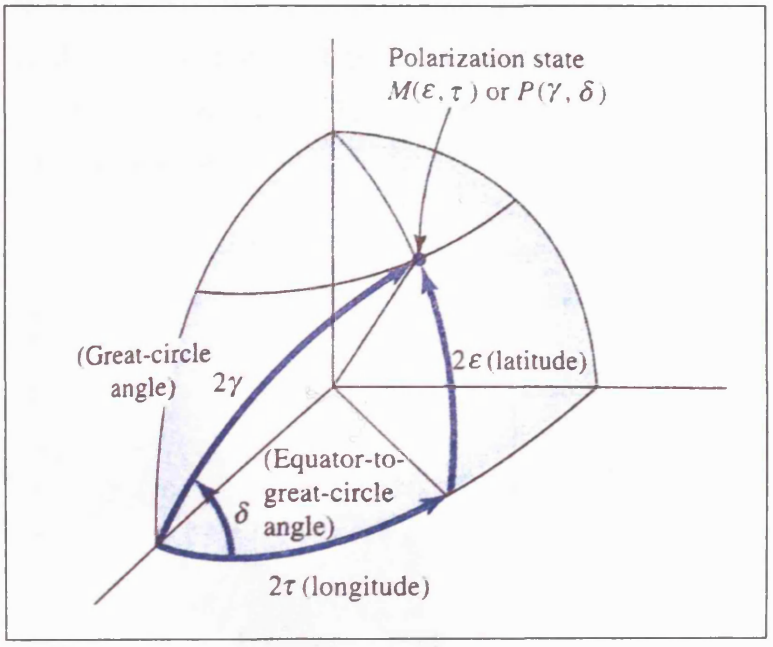

Figure 4-4: Poincaré sphere showing relation of angle ε, τ, δ, and γ [Kraus and Fleisch, 1999].

Using the above definition of polarisation parameters, the polarisation state of the reflected signal can be determined. For a RCP incident signal (GPS line-of-sight signal), $\gamma_i = 45°$, $\delta_i = -90°$, the phase angle of reflected signal δ_r by which electric field in parallel component leads the perpendicular component is given by [Kraus and Fleisch, 1999]:

$$\delta_r = \delta_i + \pi + (\phi_\perp - \phi_{\text{II}}) \tag{4.14}$$

where $\pi = 180°$, and ϕ_{II} and $\phi_\perp$ are the phase angles of the parallel and perpendicular reflection coefficients ρ_{II} and $\rho_\perp$, respectively. Moreover, the great circle component of reflected signal, γ_i, is given by:

$$\gamma_r = \tan^{-1}\left(\frac{\rho_{\text{II}}}{\rho_\perp}\tan\gamma_i\right) \tag{4.15}$$

Substituting δ_r and γ_r into Equations (4.12), (4.13), and (4.7), enables τ_r and AR_r of the reflected signal can be determined. If AR_r is positive and $AR_r \neq 1$, the reflected signal is left-handed ellipse polarised (LEP) as shown in Figure 4-5. A reflected (multipath) GPS signal is always LEP, however it can be LCP provided that the reflector is a perfect conductor.

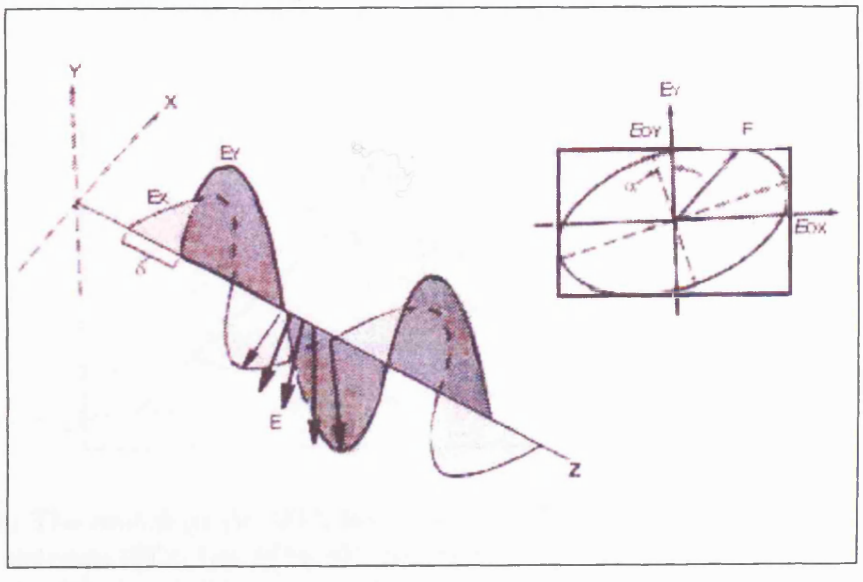

Figure 4-5: Elliptical polarisation.

4.4 Line-of-sight and Reflected Signals Reception at Receiving Antenna

When there is multipath, the receiving antenna receives both line-of-sight and reflected signals. GPS receivers usually use RCP antennas, as the received line of sight signal is RCP with a polarisation efficiency of almost 100% if the space loss is very small. As described in Section 4.3, the polarisation state of GPS signal will be changed after reflection and depends on the incident angle and the relative permittivity of the reflector. Therefore, the polarisation efficiency of a reflected signal at a GPS RCP antenna is always less than 100% since the reflected signal is no longer RCP. The polarisation efficiency (sometimes called the polarisation factor) F of a reflected signal at a RCP antenna can be determined, according to [Kraus and Marhefka, 2002], from

$$F = \cos^2 \frac{MM_a}{2} \tag{4.16}$$

where MM_a denotes the angle subtended by the great-circle from M to M_a, M is the polarisation state of the incident signal, and M_a is the polarisation state of receiving antenna (see Figure 4-7).

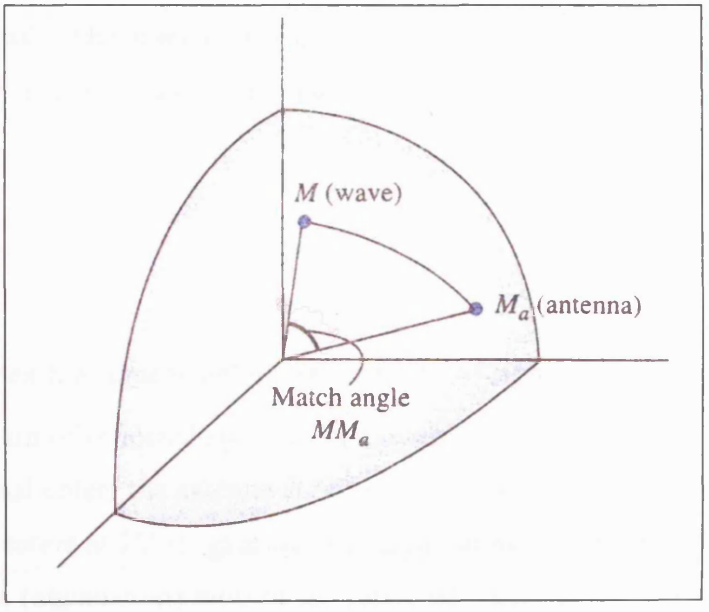

Figure 4-6: The match angle MM_a between the polarisation state of wave (M) and receiving antenna (M_a). For MM_a=0°, the match is perfect. For MM_a=180°, the match is zero [Kraus and Marhefka, 2002].

The polarisation efficiency can also be determined by using the axial ratio AR and the tilt angle τ [Mott, 1992] as:

$$F = \frac{(AR_1 AR_2 - 1)^2 + (AR_1 - AR_2)^2 + (AR_1^2 - 1)(AR_2^2 - 1)\cos 2(\tau_1 + \tau_2)}{2(AR_1^2 + 1)(AR_2^2 + 1)} \tag{4.17}$$

where AR_1 denotes the axial ratio of the incident signal (either line-of-sight or reflected), AR_2 denotes the axial ratio of the receiving antenna, and τ_1 and τ_2 denote the tilt angles of the incident reflected signal and the receiving antenna respectively. Using Equation (4.16) or (4.17), the polarisation efficiency of the reflected signal can be determined no matter whether the reflected signal is RCP, LCP, or LEP. Note that Equation (4.17) is used in the simulation described in Section 4.6 because it is easier to programme when comparing with the determination of MM_a in spherical coordinates in Equation (4.16). Additionally, because of the different incident angles of the line-of-sight and reflected signals at a receiving antenna, they have different antenna gains. How different they are depends of the type of antenna being used and the values of the two incident angles (as an example of this the antenna gain pattern for the Leica AT502 antenna is shown in Figure 4-7). In order to compute the receiving antenna response to a particular reflected signal, one of the things that must be computed is its power attenuation relative to the line-of-sight signal. The antenna gain (attenuation) ratio between the line-of-sight and reflected signals η_a can be determined by:

$$\eta_a = \frac{g_s}{g_m} \tag{4.18}$$

where g_s denotes the dimensionless gain of line-of-sight signal and g_m denotes the dimensionless gain of reflected signal. For example, for the Leica AT502 antenna, if a line of sight signal enters the antenna at 60° its gain will be 6.5 (dimensionless) and if a reflected signal enters at 20° its gain will be 12 (as shown in Figure 4-7), so in this case the antenna gain (attenuation) ratio of the reflected signal to the line of sight signal is 0.542, which means that the antenna gain of reflected signal is about 1.85 times less than that of line-of-sight signal.

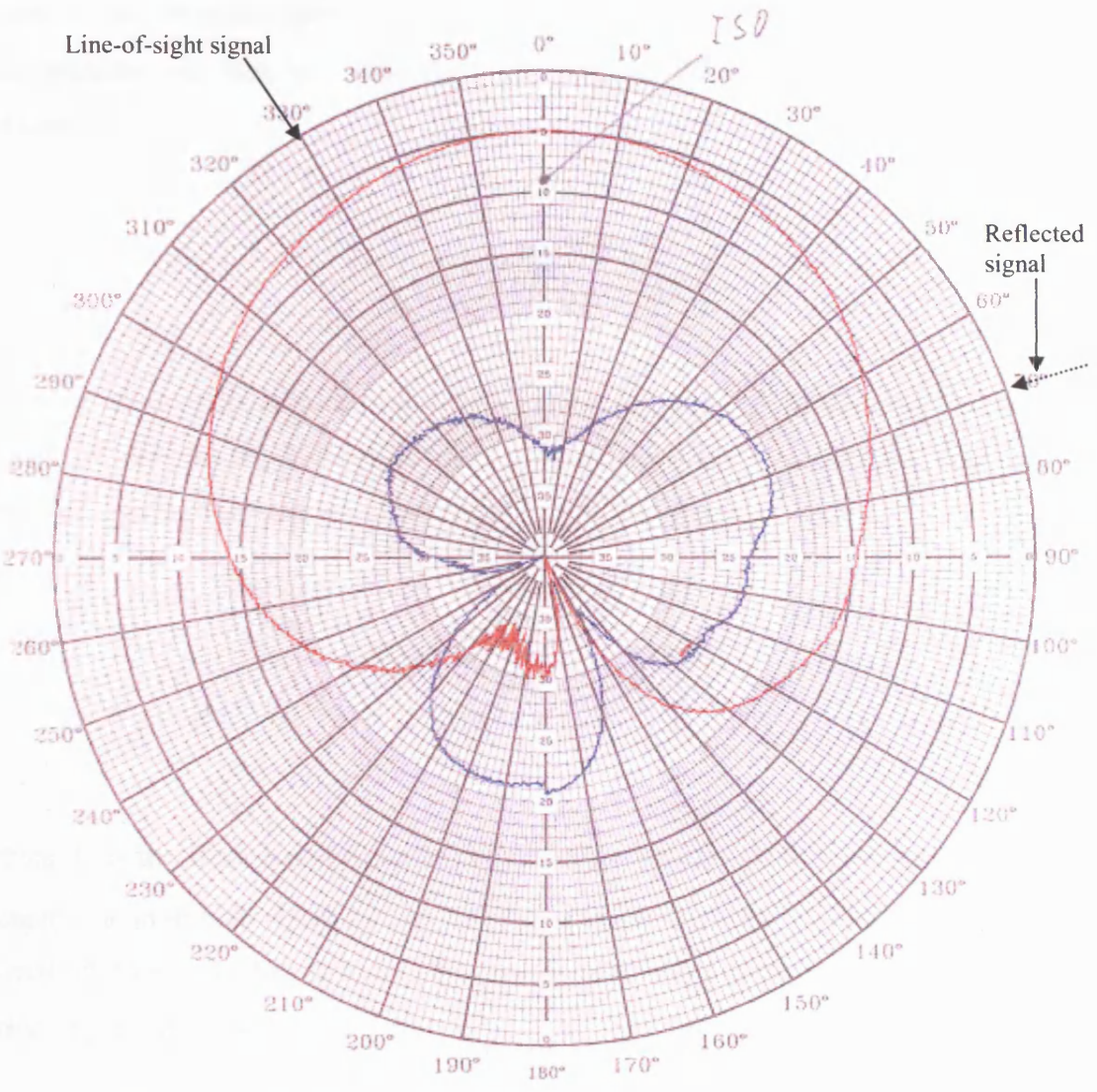

Figure 4-7: Antenna gain pattern of the Leica AT502 antenna; the red line represents the RCP gain pattern, the blue line represents the LCP gain pattern. [obtained from Leica Geosystems]

4.5 Multipath Error in Phase Measurement

It follows from the discussion in Sections 4.2, 4.3 and 4.4, that the damping factor α of the power of a reflected signal relative to that of a line-of-sight signal can be determined by:

$$\alpha = \rho F \eta_a \tag{4.19}$$

where ρ denotes the reflection coefficient, F denotes the polarisation efficiency or matching factor, and η_a denotes the antenna gain (attenuation) ratio of the multipath

signal to line-of-sight signal. The phase multipath error ψ in carrier lock loop phase discriminator can then be calculated using the formula given in [Braasch, 1996] as follows

$$\psi = \tan^{-1}\left[\frac{\alpha A(\tau)\sin\theta_m}{1+\alpha A(\tau)\cos\theta_m}\right] \tag{4.20}$$

where α denotes the damping factor of the multipath signal relative to the line-of-sight signal, A denotes the PRN code correlation function and τ is the time delay of the reflected signal relative to the direct signal. $A(\tau)$ is given by:

$$\begin{aligned} A(\tau) &= 1-\frac{|\tau|}{T}, & |\tau| \le T \\ &= 0, & |\tau| > T \end{aligned} \tag{4.21}$$

where T is the PRN code bit period, or correlator spacing, and θ_m in Equation (4.20) denotes the multipath relative phase due to the extra distance travelled by the multipath signal relative to the line-of-sight signal (as shown in Figure 4-8) plus a phase wind-up error. θ_m is given by

$$\theta_m = \frac{L_m - L_d}{\lambda} + \varphi_w \tag{4.22}$$

where L_m denotes the length of the multipath signal from the satellite antenna via the reflector to the receiving antenna, L_d denotes the length of the line-of-sight signal from the satellite antenna to the receiving antenna, λ denotes the wavelength of the signal, and φ_w denotes the phase wind-up error, which is insignificant for reasons explained in Section 4.2 (although it is included in Equation (4.22) for completeness). $(L_m - L_d)$ can be called the differential path delay of the reflected signal.

The foregoing can be summarised by stating that the characteristics of multipath error in phase measurements depend on the following factors.

i) The relative permittivity of the reflector – Equations (4.1)-(4.4), (4.14), and (4.15),

ii) The incident angles – Equations (4.1), (4.2), (4.4), and (4.18),

iii) The polarisation efficiency state – Equation (4.16) or (4.17),

iv) The correlator spacing – Equation (4.21),

v) The distance between the receiving antenna and the reflector – Equations (4.21) and (4.22), and

vi) The wavelength of carrier – Equation (4.22).

Note that factors (ii) and (v) are directly related to the satellite antenna, reflector, and receiving antenna geometry as shown in Figure 4-8.

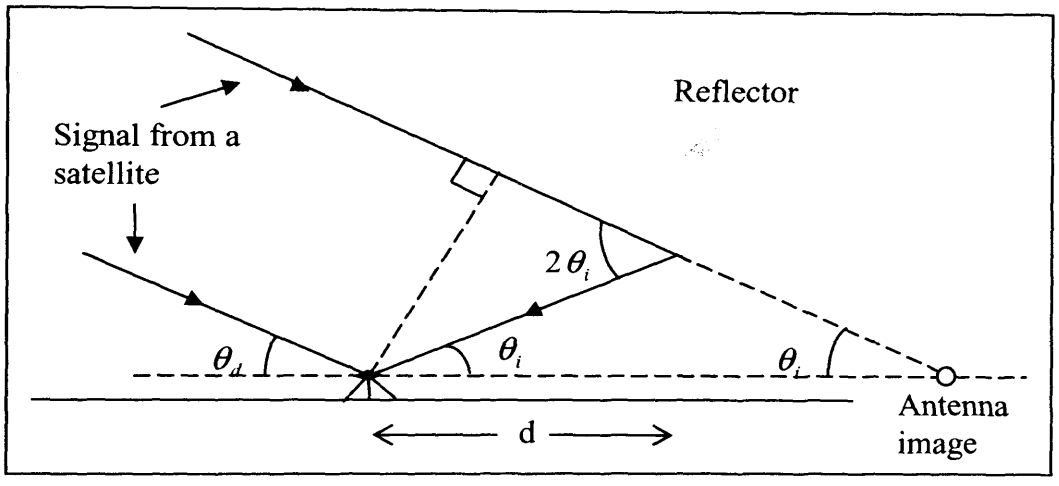

Figure 4-8: Geometry of a signal, reflector, and a receiving antenna for multipath effect; it shows a single specular reflection from a smooth surface only.

Additionally, multipath errors are affected by the fact that the position of the antenna phase centre varies with different signal incident angles. As an example, the phase centre variations of the Leica AT502 antenna for the GPS L1 frequency are shown in Table 1 (from the IGS). As explained in Section 4.4, the elevation angles of direct and reflected signals are always different therefore the phase centre for the direct and reflected signals will be different as shown in Figure 4-9. Note that the directions of the direct signal at both roving and reference antennas are very similar in short baseline and phase centre variations will have no impact on relative positions if the same antennas are used at both stations. The elevation angles of reflected signals are, however, usually not the same at nearby stations and, as a result, errors due to phase centre variations in reflected signals are completely absorbed in the form of sinusoidal phase multipath errors.

Table 4-1: Phase centre variation of the Leica AT502 antenna.

Elevation angle (°)	90	85	80	75	70	65	60	55	50	45
L1 phase (mm)	0.0	1.3	2.0	2.2	2.0	1.7	1.4	1.0	0.8	0.8
Elevation angle (°)	40	35	30	25	20	15	10	5	0	
L1 phase (mm)	1.0	1.4	2.0	2.5	3.3	4.1	5.1	0.0	0.0	

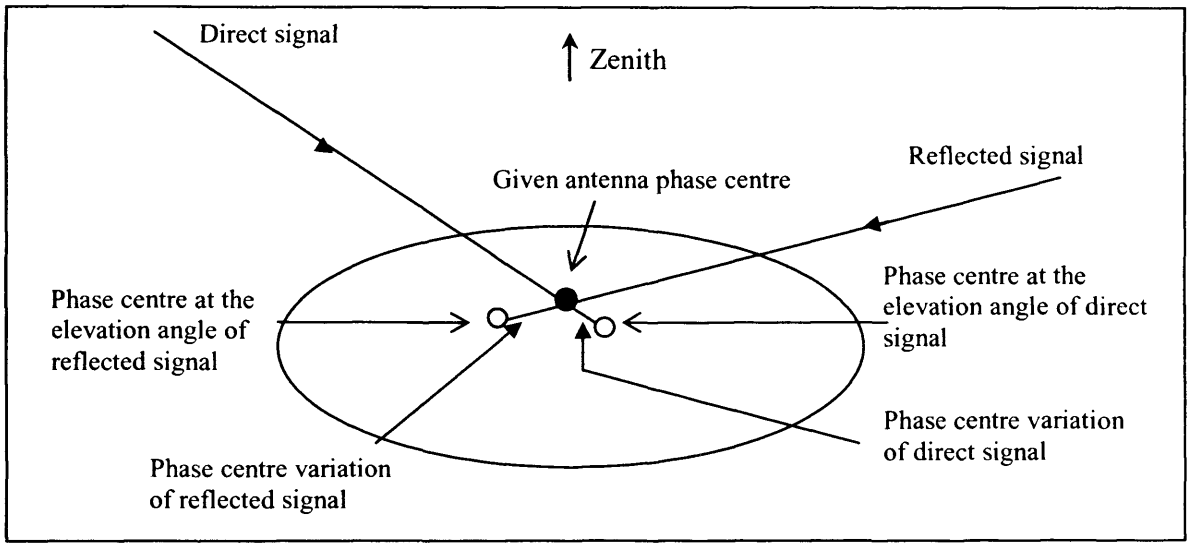

Figure 4-9: Phase centre variations in direct and reflected signals.

4.6 MULTIPATH SIMULATION

4.6.1 Ray Tracing of Multipath

In this section, the mathematical background of ray tracing is presented as the geometrical basis of multipath modelling (it is explained in Section 4.5 that four of the six factors affecting multipath are dependent on satellite antenna, reflector, and receiving antenna geometry). Section 4.6.1.1 describes the determination of the equation of a plane using a vector approach and Section 4.6.1.2 describes how to find the intersecting point of a line and a plane.

4.6.1.1 The vector equation of a plane

The dot product is used to find the equation of a plane in R^3 (three-dimensional space). A normal vector to a plane is any vector that starts at a point in the plane and has a direction that is orthogonal (perpendicular) to the surface of the plane. For example, **k** = (0,0,1) is a normal vector to the xy plane (the plane containing the x and y axes). Any

three distinct points define a plane, or alternatively, a single point in the plane and a given normal vector to the plane.

A way of checking whether a given point, with position vector **m** lies in the plane or not as shown in Figure 4-10, is as follows.

Let **a** be the position vector of the given point in the plane, and let **n** be the given normal vector to the plane. Then point **m** is in the plane only if

$$(\mathbf{m}-\mathbf{a})\cdot\mathbf{n}=0 \tag{4.23}$$

This is because **(m – a)** is the vector from point A to point M, and any vector that lies completely in the plane must be orthogonal to **n** which implies their dot product must equal zero.

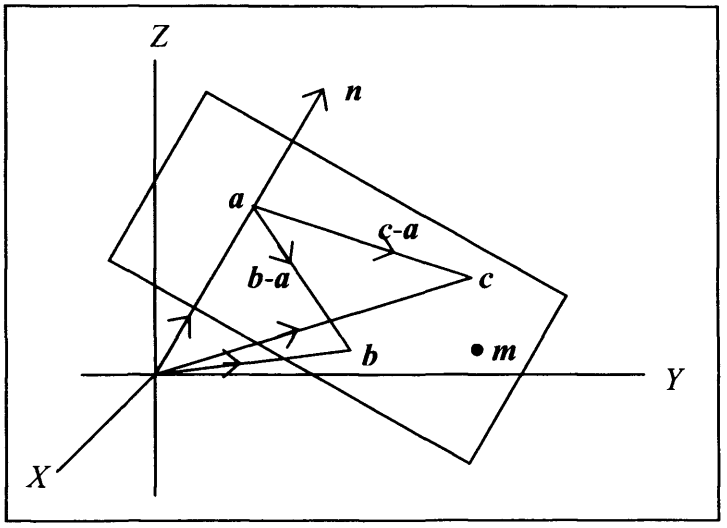

Figure 4-10: The vector equation of a plane.

The equation of plane may also be defined by using three points. Let **a**, **b**, and **c** be the position vectors of 3 points in the plane as shown in Figure 4-10. The two vectors,

$$\mathbf{b}-\mathbf{a} \quad \text{(point A to point B)} \tag{4.24}$$

$$\mathbf{c}-\mathbf{a} \quad \text{(point A to point C)} \tag{4.25}$$

must both lie in the plane, so their normal vector is found by taking their cross product:

$$\mathbf{n}=(\mathbf{b}-\mathbf{a})\times(\mathbf{c}-\mathbf{a}) \tag{4.26}$$

So as before our equation for the plane consists of all vectors, **m** satisfying

$$(\mathbf{m}-\mathbf{a})\cdot\mathbf{n}=0 \tag{4.27}$$

which is the same as Equation (4.23). Therefore

$$(\mathbf{m}-\mathbf{a})\cdot((\mathbf{b}-\mathbf{a})\times(\mathbf{c}-\mathbf{a}))=0 \tag{4.28}$$

Equation (4.26) is used with any three of the input four corners' coordinates of the reflector to determine the unique normal vector of the reflector.

4.6.1.2 The intersection of a line and a plane

In order to determine the possibility of multipath with a particular satellite-reflector-antenna geometry as shown in Figure 4-11, the following approach may be performed:

i) Find the closest point **r** on the planar reflector from the antenna **p** and hence to compute the position difference vector $(\mathbf{r}-\mathbf{p})$ from the antenna **p** to the closest point **r**,

ii) Find the antenna image position **q** (behind the reflector),

iii) Determine the point **s** on the reflector which is the intersection between the planar reflector and the line (the direct signal) joining satellite **g** and the antenna image **q**,

iv) Check whether or not the intersection point **s** is located in the definite size of the reflector using the known four corners' positions of the planar reflector; if it is located in the reflector, it is a multipath.

Regarding the problem (i), the closest point **r** is determined by using the equations for the closest point on a plane from a point:

$$t=((\mathbf{c}-\mathbf{p})\cdot\mathbf{n})/(\mathbf{n}\cdot\mathbf{n}) \tag{4.29}$$

where t is a real number parameter, **c** is any point on the plane; a corner position of the four input corners' positions of the reflector is used in our model, **p** is the antenna

position, and **n** is the determined normal vector of the planar reflector as described in Section 4.6.1.1;
and,

$$\mathbf{r} = \mathbf{p} + t\mathbf{n} \tag{4.30}$$

After obtaining **r**, the position difference vector (**r**-**p**) from antenna **p** to its closest point on the reflector **r** is computed. The image position **q** in problem (ii) is then determined by the parametric equation:

$$\mathbf{q} = \mathbf{p} + t(\mathbf{r} - \mathbf{p}) \tag{4.31}$$

where t is equal to two in this case because the distance between the closest point **r** and the antenna image position **q** equals to the distance between **p** and **r** in specular reflection.

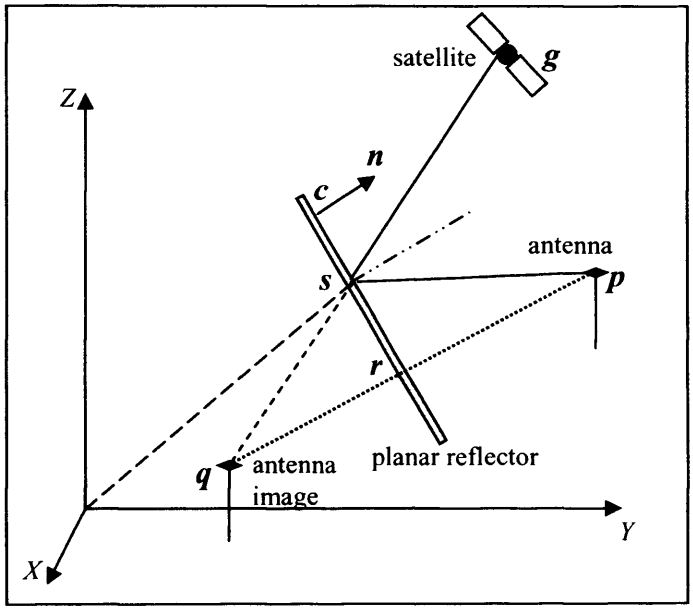

Figure 4-11: Geometry of the intersection of a line and a plane.

Regarding the problem (iii), it is needed to determine the intersection point **s** from the planar reflector and the line joining satellite **g** and image point **q** as shown in Figure 4.11. **s** can be determined from the parametric equation:

$$\mathbf{s} = \mathbf{g} + t(\mathbf{q} - \mathbf{g}) \tag{4.32}$$

where t is a real number parameter, it determines where is the intersection point in the line joining points **g** and **q**. Points **g** and **q** are known, therefore, it needs to find t as follows.

With the knowledge of any known point **c** on the planar reflector (any one of the four input corners) and the determined normal vector **n** of the reflector, **s** must satisfy:

$$(\mathbf{s}-\mathbf{c})\cdot\mathbf{n}=0 \tag{4.33}$$

because **s** lies in the planar reflector.

Putting Equations (4.32) and (4.33) together is enough to find the value of t:

$$(\mathbf{g}+t(\mathbf{q}-\mathbf{g})-\mathbf{c})\cdot\mathbf{n}=0 \tag{4.34}$$

By distributive property, therefore,

$$\mathbf{g}\cdot\mathbf{n}+t(\mathbf{q}-\mathbf{g})\cdot\mathbf{n}-\mathbf{c}\cdot\mathbf{n}=0 \tag{4.35}$$

$$t(\mathbf{q}-\mathbf{g})\cdot\mathbf{n}=\mathbf{c}\cdot\mathbf{n}-\mathbf{g}\cdot\mathbf{n} \tag{4.36}$$

$$t=((\mathbf{c}-\mathbf{g})\cdot\mathbf{n})/((\mathbf{q}-\mathbf{g})\cdot\mathbf{n}) \tag{4.37}$$

Putting t into Equation (4.32), **s** is determined.

If there is an intersection point **s** on the planar reflector, problem (iv) can be solved by carrying out a geometrical boundary test using the knowledge of the four input corners' positions of the reflector to check whether or not the intersection point lies on the definite size of the planar reflector. If the intersection point **s** lies on the reflector, the differential path delay is computed and used in Equation (4.22).

4.6.2 Multipath Simulation

This section concentrates on the multipath modelling aspects of the simulator. The following assumptions are currently made in the simulator.

i) Multipath(s) is/are from planar reflector(s).

ii) Specular reflection (smooth surface) – Law of reflection; in reality most surfaces are not smooth, the simulator can deal with a rough surface by considering it as many small reflectors, see scenario 3 in Section 4.8.

iii) No bending of signal path in the ionosphere.

iv) Space loss is negligible.

v) Reflection occurs on the surface of the reflector; the depth of penetration $1/e$ is negligible (skin effect; see Section 2.2.1).

vi) The reflectors are lossless (or negligible loss) nonmagnetic dielectrics (see Section 2.2.2).

vii) No interference occurs between the wavefronts of the reflected signal and the wavefronts of the direct signal in space (see Section 2.2.2).

The inputs are as follows.

i) Cartesian coordinates of the four corners of reflector(s).

ii) Relative permittivity(ies) of the reflector(s).

iii) Polarisation state of receiving antenna such as *AR* and RCP (in preparation for future GNSS that may not transmit RCP signal).

iv) Antenna gain pattern.

v) Correlator spacing of the receiver.

vi) Antenna phase centre offset and variation table such as IGS_01.pcv and ant_info.003, which can be obtained from the International GPS Service (IGS) and the U.S. National Geodetic Survey (NGS) respectively.

The steps in the phase multipath simulation procedure are as follows.

i) Determine the possibility of multipath based on the ray tracing method described in Section 4.6.1; Equations (4.26), (4.29)-(4.31), (4.37) and (4.32).

ii) Simulate the phase multipath error using the following equations: Equations (4.1)-(4.15) and Equations (4.17)-(4.22).

iii) Apply the phase centre offsets and variations using the appropriate input data.

iv) Add the simulated phase multipath error to the simulated phase of the direct signal as described in Section 3.2.

4.7 VALIDATION OF MULTIPATH SIMULATION

The multipath errors simulated by the methodology of Section 4.6 have been validated by comparing them with the errors in real GPS measurements collected in two experiments with known (and carefully controlled) reflector geometry. When processing real data, pre-determined integer ambiguities are applied to the measurements, which are then processed by the double difference (DD) method.

4.7.1 Experimental Data Set Collected in LCPC

In this experiment, two Leica System 530 receivers attached to lightweight AT502 antennas were used. The tests were carried out at the Laboratoire Central des Ponts et Chaussées (LCPC) near Nantes in France during May 2002. In order to create a sufficiently large multipath signal, a 5 m by 2.5 m steel panel was constructed and placed near to one of the receiving antennas as shown in Fig. 4-12. Full details of the experiment can be found in [Bétaille et al., 2003] and [Bétaille, 2004].

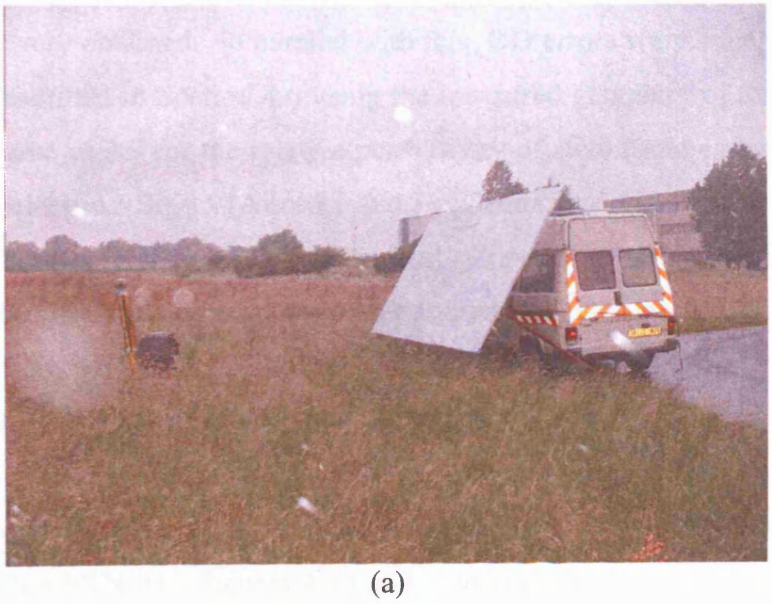

(a)

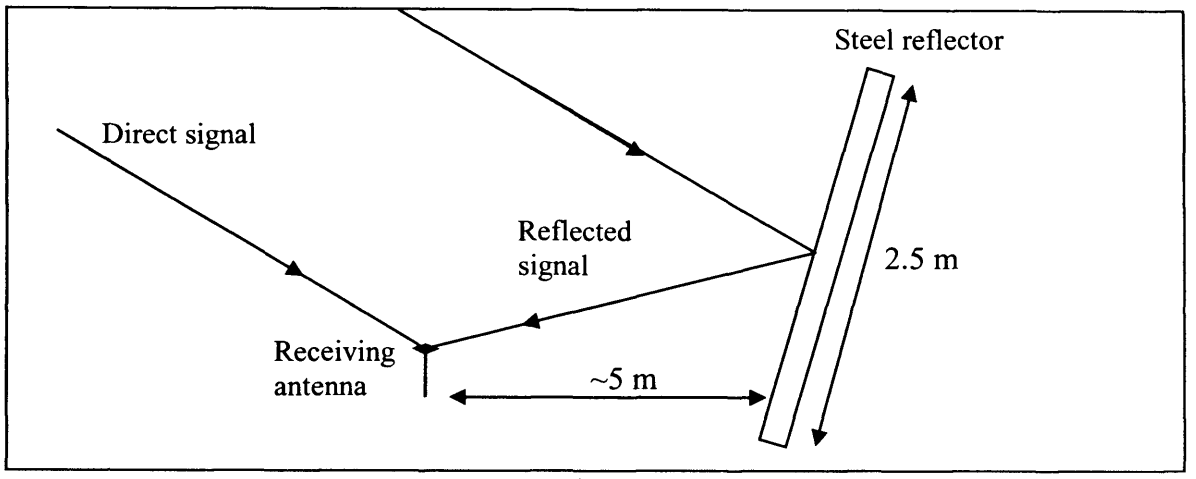

(b)

Figure 4-12: (a) Experimental setup for collection of multipath data in LCPC, (b) Diagram showing the geometry of experimental setup for collection of multipath data in LCPC.

4.7.1.1 Measurement domain validation

Double differenced (DD) phases computed from the known coordinates were subtracted from those computed from the observations in order to obtain DD residuals. Due to the shortness of the baseline (about 86 metres), these DD residuals comprised only multipath errors and measurement noise, and since the measurement noise was very small (and displayed largely white noise characteristics) time series of DD multipath errors is effectively obtained. In parallel with this, DD errors were simulated following the methods described in Section 4.6 using the measured geometry of the experimental set-up and a value of 3.9 for the relative permittivity of steel (sand casting carbon steel containing dielectric SiO_2 [AZoM, n.d.] [Cambridge University Engineering Department, 2003] [Nalwa, 1999] [Physical Constants, n.d.] [Samsonov, 1968] [Washburn, 2003]). The phase centre offset and variation table used in the simulation was obtained from the absolute antenna calibration results the in ant_info.003 file from (U.S. National Geodetic Survey).

Satellite PRN 02 was identified as a satellite with significant multipath and comparisons have been made between the real and simulated DD residuals for this satellite with the reference satellite PRN 03. Figures 4-13 and 4-14 show simulated DD residuals along with the observed DD residuals for of the GPS L1 and L2 data respectively. The simulated DD residuals for both GPS L1 and L2 are also plotted in Figure 4-15 so that the frequency dependency of multipath can be more clearly seen.

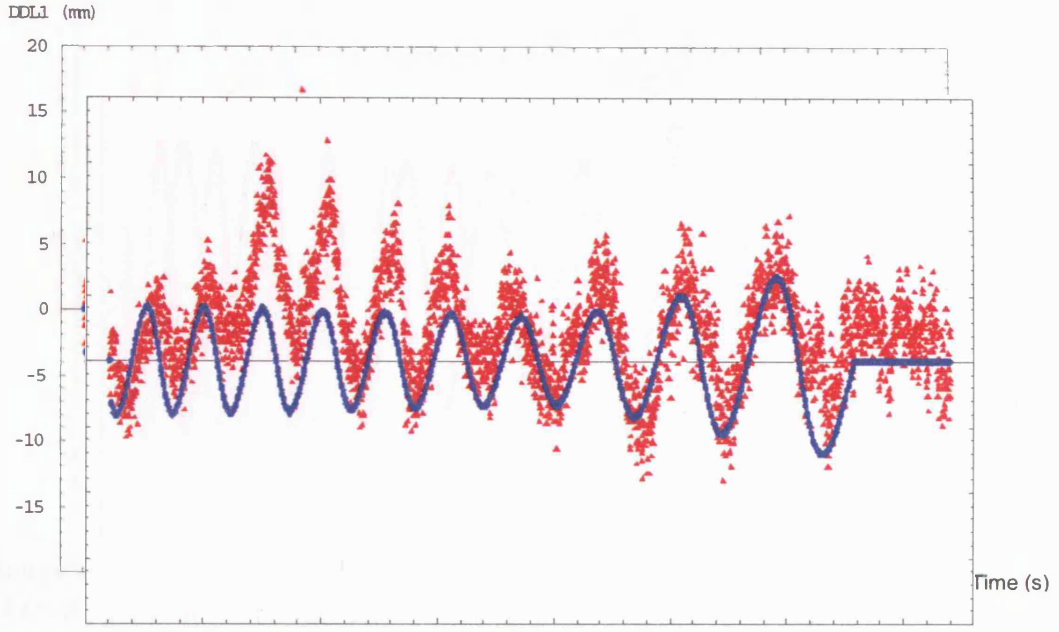

Figure 4-13: Double difference residual (observed minus computed) in L1 of raw (red) and simulated (blue) data. It shows multipath error in L1.

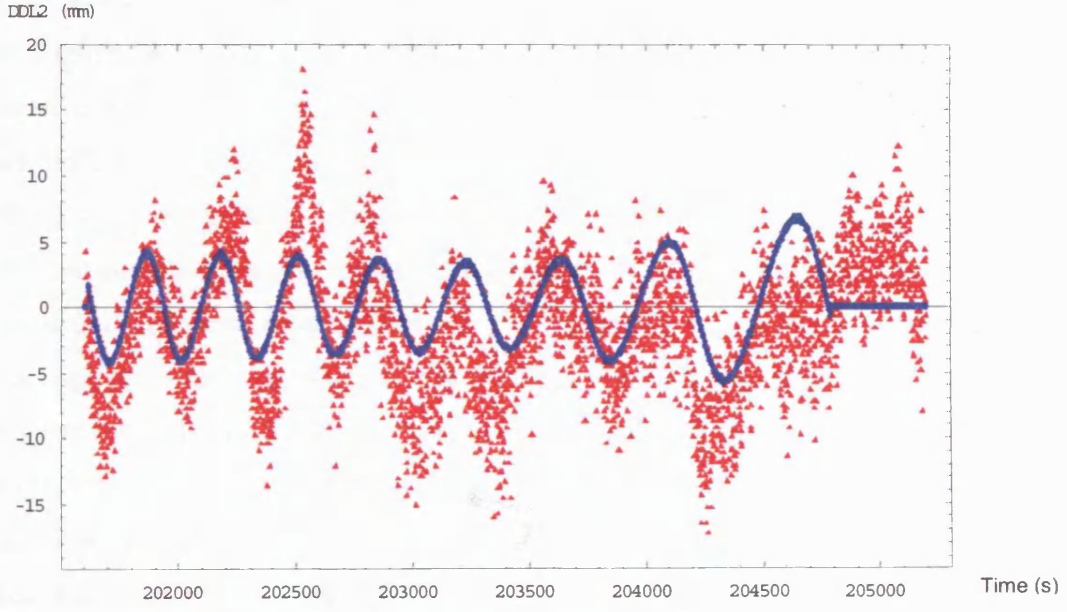

Figure 4-14: Double difference residual (observed minus computed) in L2 of raw (red) and simulated (blue) data. It shows multipath error in L2.

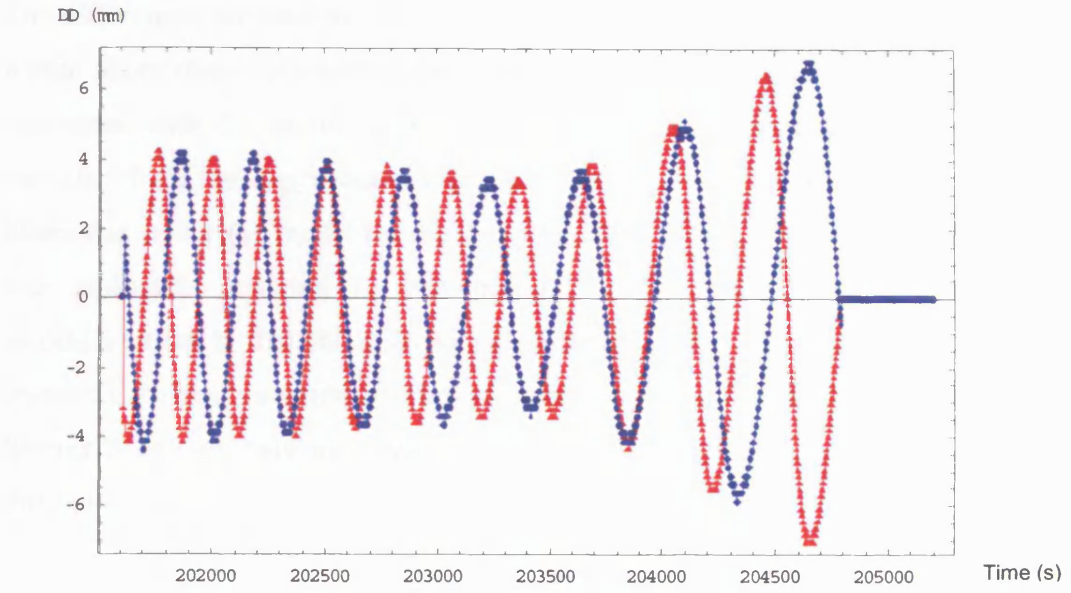

Figure 4-15: Double difference simulated multipath data minus DD true range in L1 (red) and L2 (blue).

The amplitudes of the multipath signal in the simulated DD data appear similar to those of the real DD data and the phases of both the simulated and real DD data are coherent, see Figures 4-13 and 4-14. The L1 multipath error, the damping factor, and its components (reflection coefficient, polarisation efficiency, antenna gain ratio of direct and reflected signals) are shown in Figure 4-16 as time series to enable their relationships to be seen. Figure 4-17 shows the elevation angles of the direct and reflected signals during the observation period. Theoretically multipath error should be a sinusoid with zero mean. However, the results in Figure 4-13 indicate a non-zero mean approximately between epochs 201830 and 203248. This may be due to there being more than one multipath source (reflections over the limited time period from nearby objects will lead to multipath errors with a non-zero mean). Therefore, a Time Fast Fourier Transform (TFFT), a sequence of 256-point Fast Fourier Transforms (FFT) executed on 21 overlapping signal segments in 167 steps, has been applied to trace the change of the multipath signal's frequency components through time and the result is shown in Figure 4-18. A relatively small peak frequency, close the maximum peak frequency can be seen, justifying the assertion that there is at least one other multipath source. Figure 4-18 has been rotated into Figure 4-19 for a better illustration of this fact. After removal of this bias, the L1 DD residuals are plotted in Figure 4-20. The results in Figures 4-20 and 4-14 show the agreements between real and simulated DD residuals using a variable damping factor for the L1 and L2 frequencies respectively.

The differences are now mainly due to measurement noise and for most of the time are within about three millimetres (the assumed nominal DD measurement noise), which is consistent with the normal level of noise for modern geodetic receivers. For those periods where the discrepancy is greater than three millimetres, it is considered most likely that either the model for the damping factor is still incomplete or that more than one multipath occurred in that period. A possible factor leading to model incompleteness is that the antenna gain pattern shown in Figure 4-7 might not truly represent the real variation in antenna gain. However, overall, the model described in Section 4-2 to 4-5 appears to lead to a good approximation of the real damping factor in this validation.

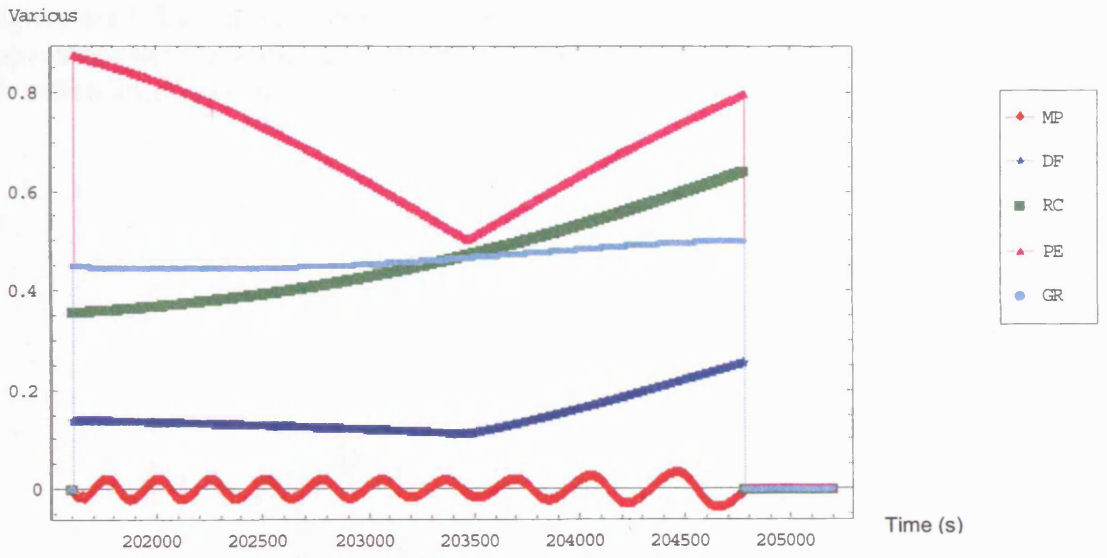

Figure 4-16: Relationships of the simulated multipath (MP), damping factor (DF), reflection coefficient (RC), polarisation efficiency (PE), and antenna gain ratio (GR) of the simulated multipath L1 data in the observation time series of PRN 02.

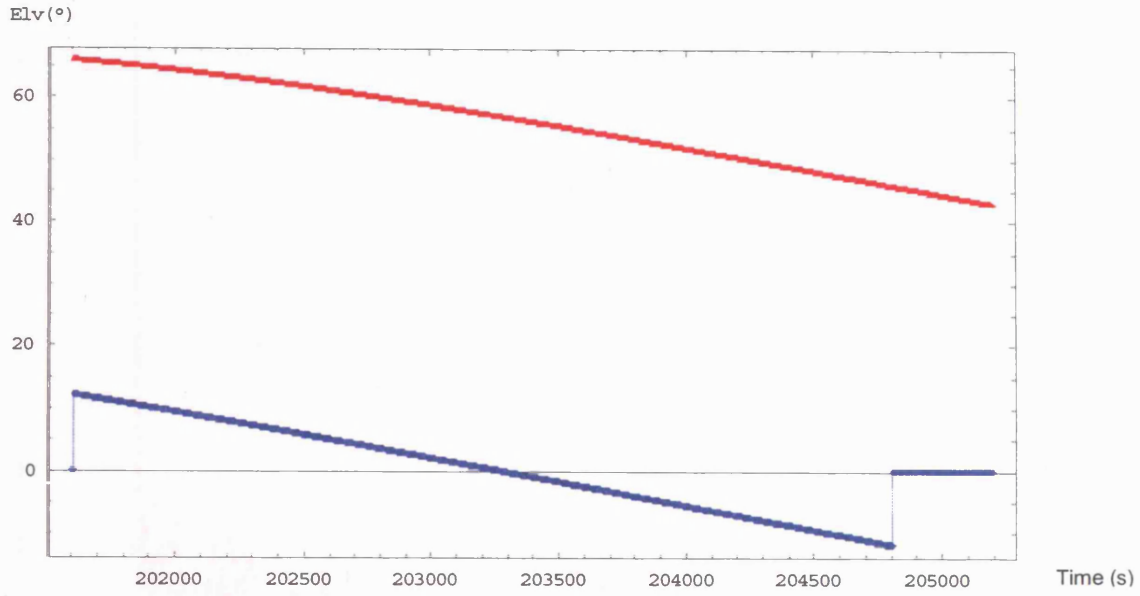

Figure 4-17: Elevation angle of the simulated multipath L1 data; Red line represents the elevation angle of direct signal and the blue line represents the elevation angle of reflected signal.

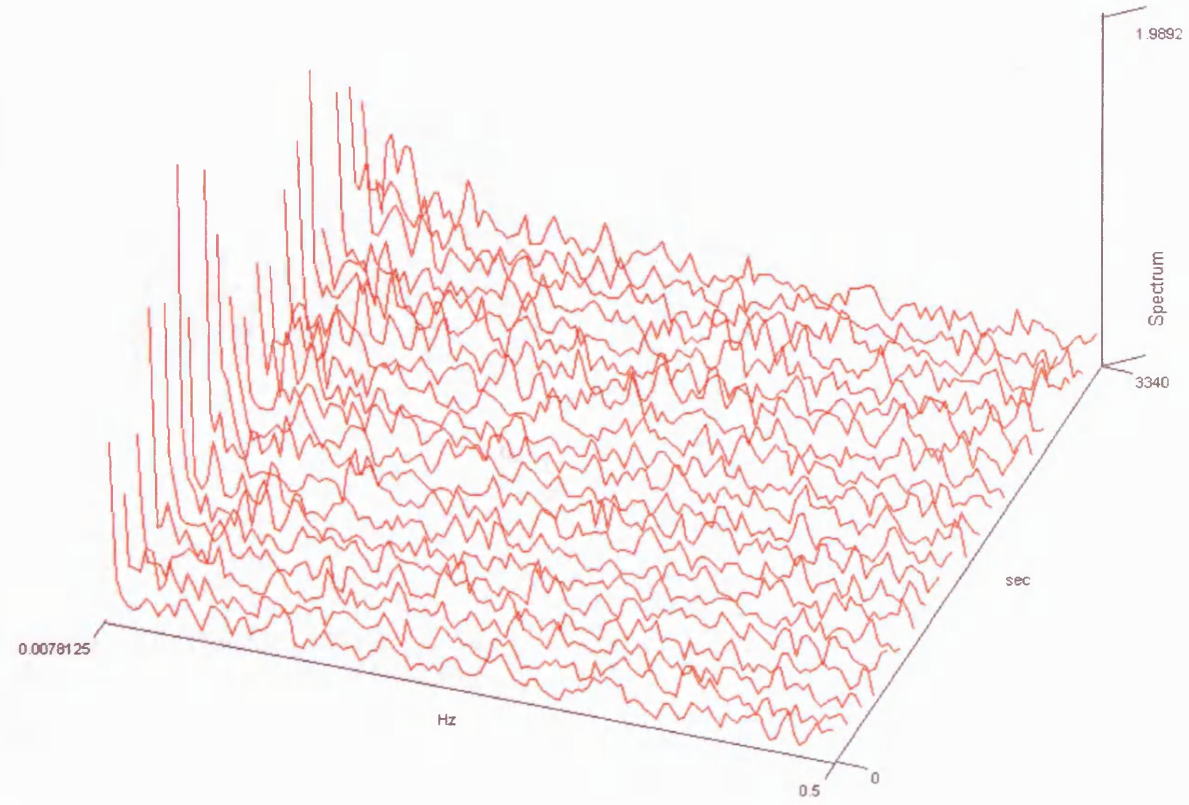

Figure 4-18: Time Fast Fourier Transform of L1 double difference residual to analyse change of signal's frequency components through time.

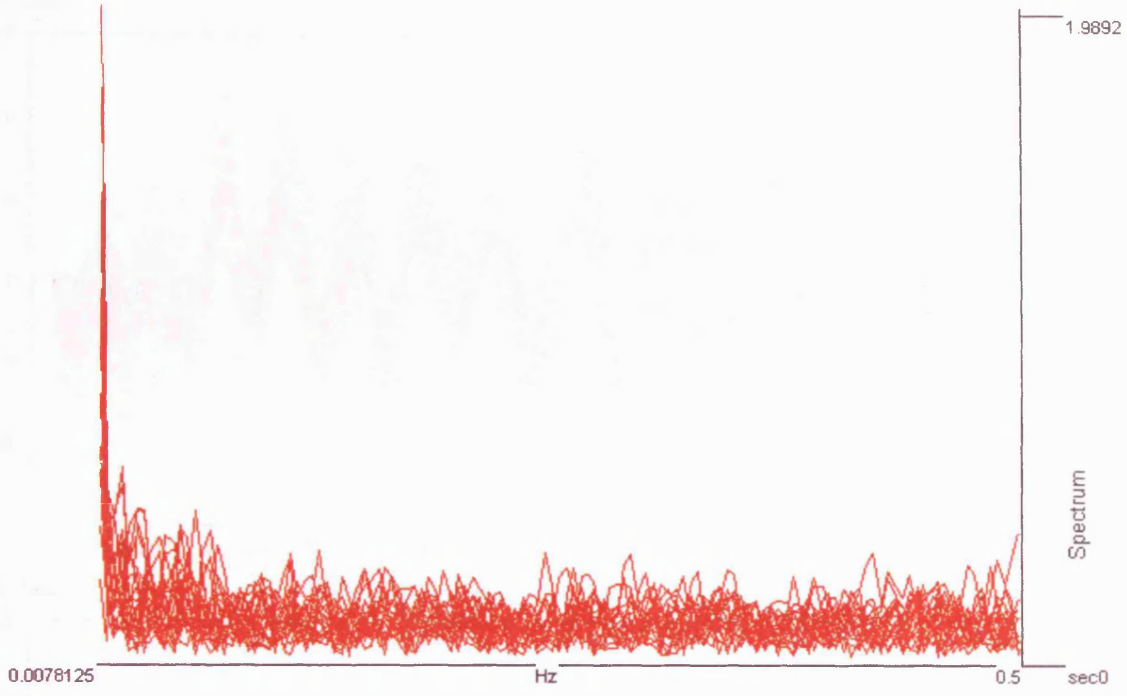

Figure 4-19: X-Z axes view of Figure 4-18.

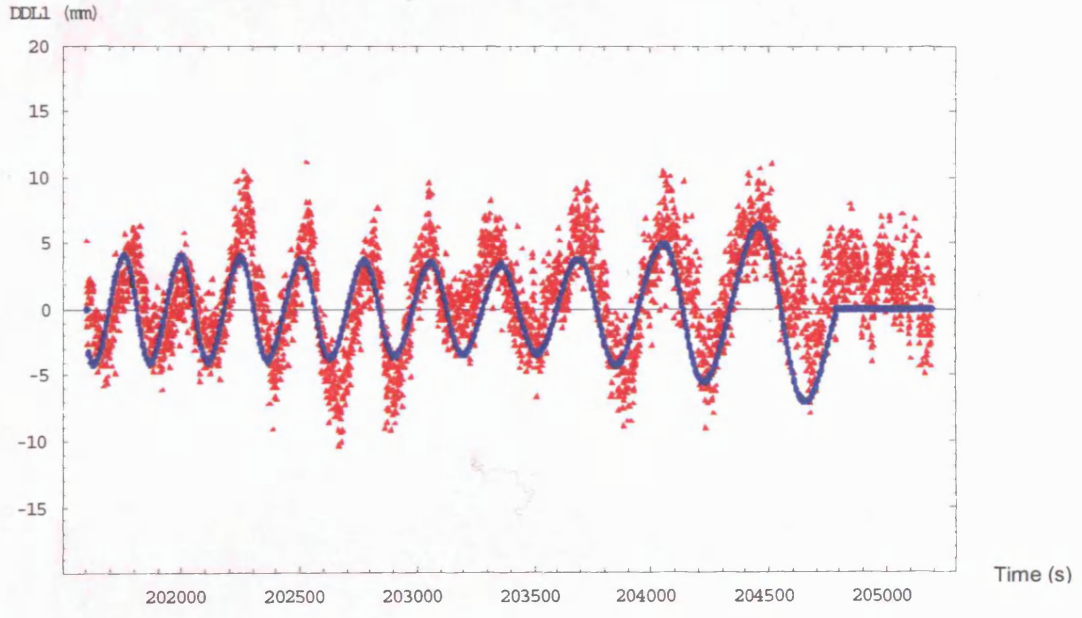

Figure 4-20: Double difference residual showing multipath error in L1 corrected to the bias from GPS second 201830 to 203248 in Figure 4-13.

4.7.1.2 Positioning domain validation

The positioning errors in local coordinates system for single-frequency real and simulated data are shown in Figure 4-21. They show good agreements – both in terms

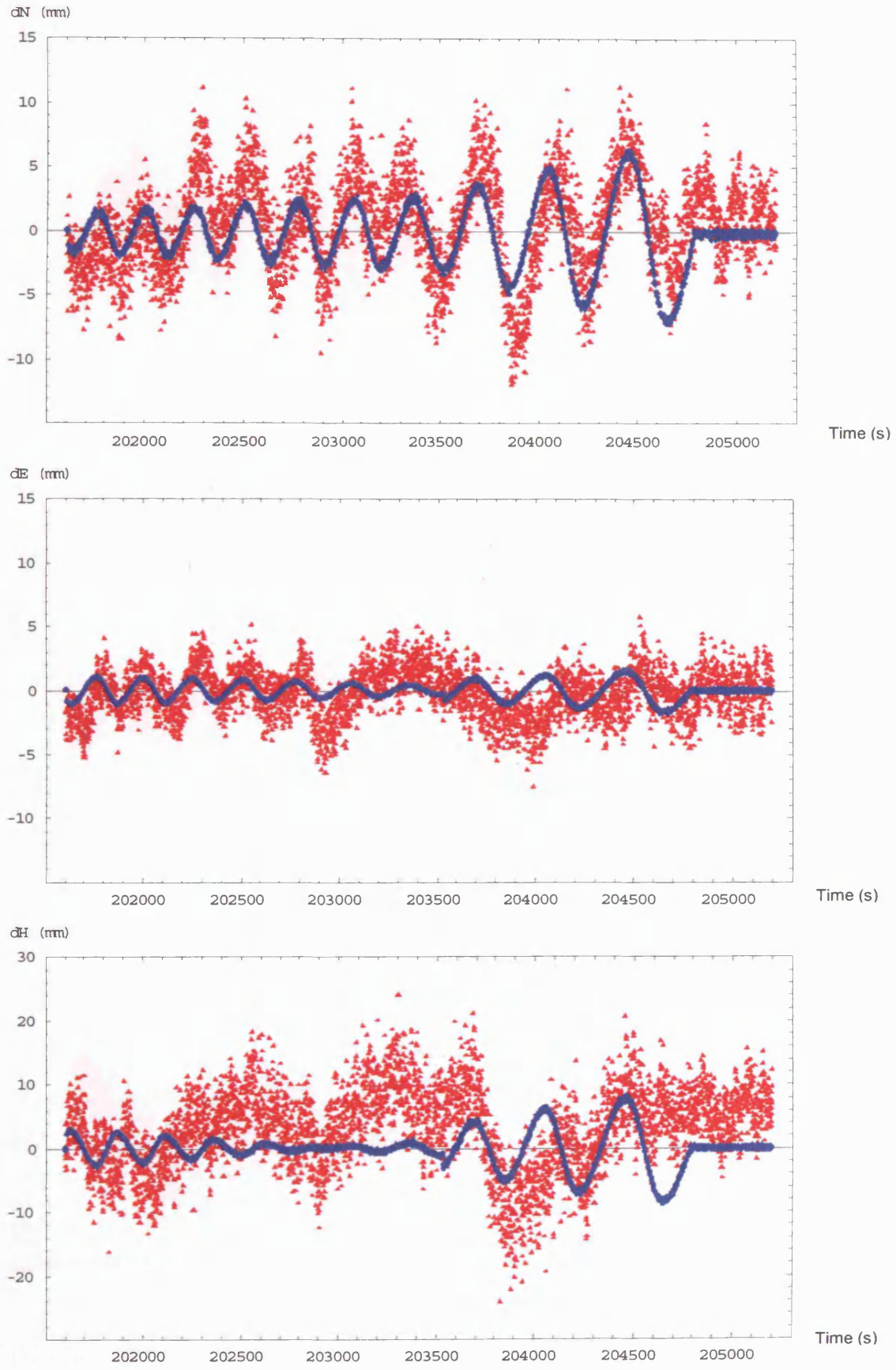

Figure 4-21: Differences in coordinates (Northing: top, Easting: middle, Height: bottom) between solutions using real (red) and simulated (blue) L1 data.

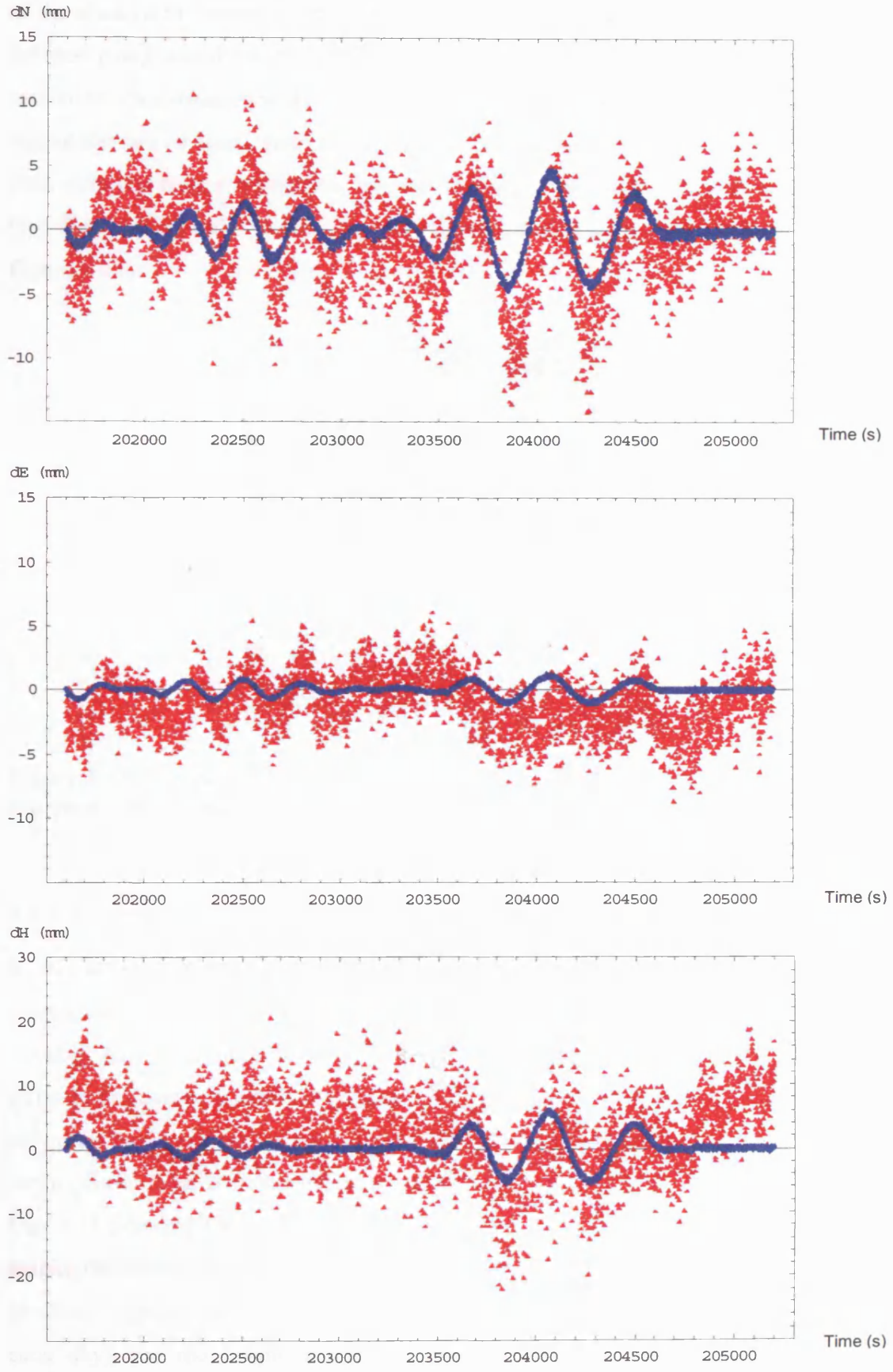

Figure 4-22: Differences in coordinates (Northing: top, Easting: middle, Height: bottom) between solutions using real (red) and simulated (blue) dual frequency data.

of the sizes of the errors and their frequency and phase especially in northing because the steel panel is to the north of the antenna, facing south, as shown in Figure 4-23. The results for dual-frequency data can be found in Figure 4-22, where similar levels of agreement can be seen. Note that the bias, as shown in Figures 4-13 and 4-20, has not been removed from the real data, so that the bias appears in the solution using L1 data (see Figure 4-21) but it is not noticeable in the solution using dual frequency data (see Figure 4-22).

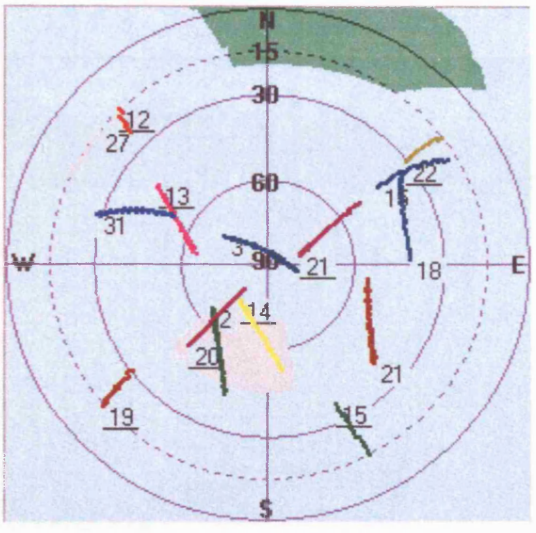

Figure 4-23: Sky plot of Galileo (underlined) and GPS satellites; the green area represents the reflector. This plot is produced by a tool developed by the author.

4.7.2 Experimental Data Set Collected in Hyde Park

In this experiment, two Leica System 530 receivers and lightweight AT502 antennas were used. The tests were carried out beside the Serpentine (a small lake in Hyde Park, London) on 4th and 5th March 2004 using the water surface about 850 m by 200 m as a reflector to generate a multipath signal, see Figures 4-24 and 4-25. A rover antenna was set up on the north side of the lake and the reference antenna was set up about 60 m further north. The experimental period in GPS seconds was from 384717 to 399146 for Day 1 (4 March 2004) and from 469609 to 483398 for Day 2 (5 March 2004). The height difference between the rover antenna and water surface was measured by levelling (repeated measurements were made before and after GPS observations for each day) and the height difference between the water surface and a temporary benchmark (TBM) was measured at least three times for each day during the data collection (also the rover station was tied to TBM as well). The mean height difference

between the rover station and water surface was then computed. Moreover, the reference antenna coordinates in Hyde Park were tied to the Ordnance Survey Continuous GPS station in London about three kilometres away using the Leica Geosystems Ski-Pro software. In this way it was ensured that the reference frame for the real GPS data was the same as that for the simulated data. GPS DD errors were then simulated following the methods described in Section 4.2 to 4.5 using the measured geometry of the experimental set-up and a value of 80 for the relative permittivity of water (see Table 4-2).

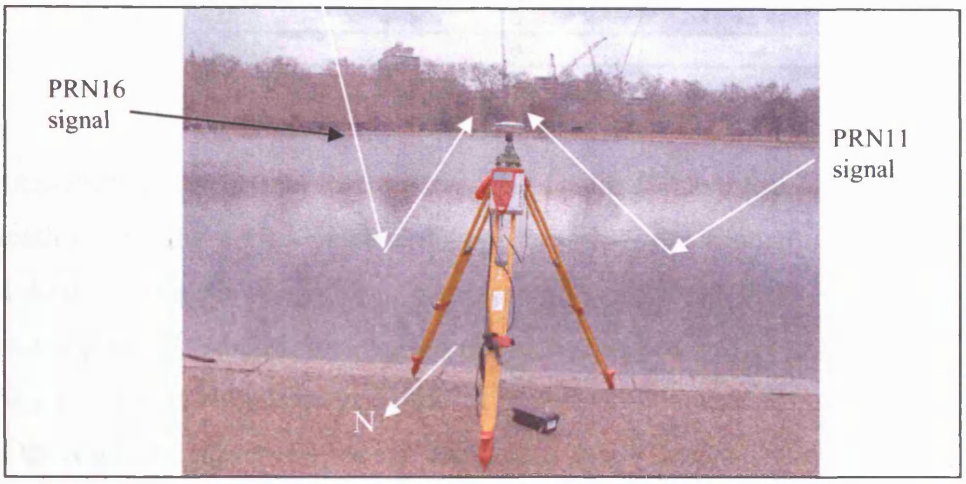

Figure 4-24: Experimental setup for collection of multipath data in Hyde Park. Approximate directions of multipathing signals from satellites PRN 11 and PRN 16 relative to the roving antenna are illustrated.

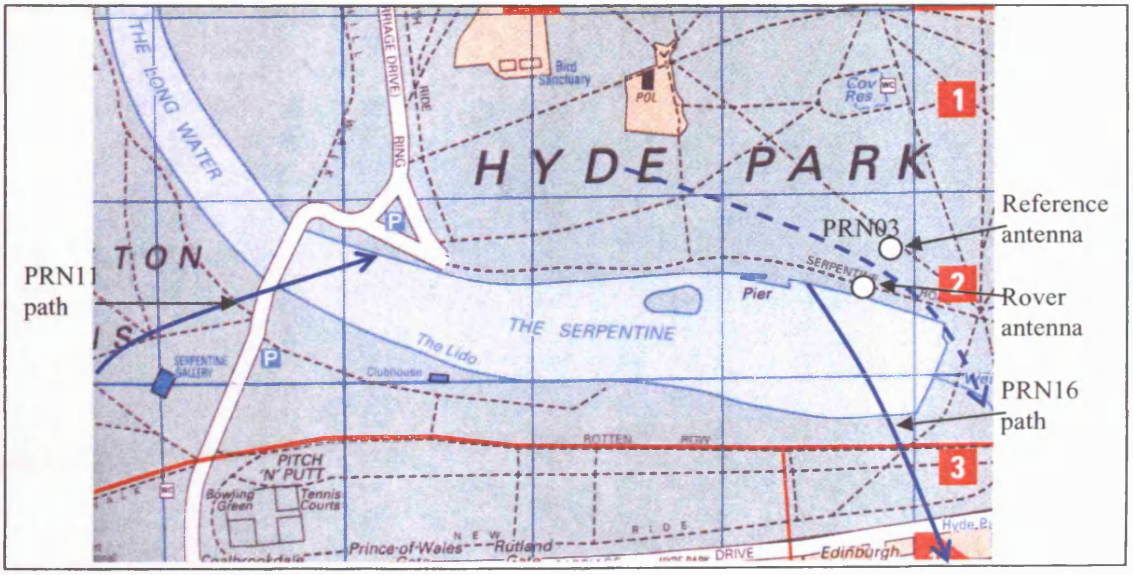

Figure 4-25: Map showing geometry of experimental setup for collection of multipath data in Hyde Park; it also shows approximate satellite paths in the sky

for satellites PRN 03 (reference satellite in double difference), PRN 11 and PRN 16 (having multipath) relative to the antennas.

Table 4-2: Table of constants for some common media (Kraus and Fleisch 1999).

Medium	Relative permittivity (dimensionless)	Conductivity ($\Omega^{-1}m^{-1}$)
Copper	1	5.80E+07
Sea water	80	4.00E+00
Rural ground	14	1.00E-02
Urban ground	3	1.00E-04
Fresh water	80	1.00E-03
Wood (dry)	2 - 4	-
Lead glass	6	-
Mica	6	-
Marble	8	-
Flint glass	10	-

Satellites PRN 11 and 16 (both are Block IIR satellites) have been identified as having multipath during the period of observation; therefore, the following investigations are based on the multipath occurring in measurements of the satellites PRN 11 and 16. In order to compute DDs a high elevation reference satellite has been chosen (one that is less likely to lead to signals being reflected from the reflector to the antenna).

The DD residuals (observed minus computed) from real and simulated L1 data for satellites PRN 11 and 16 are shown in Figures 4-26 and 4-27 respectively; validations for L2 data are not shown here because they show similar results as L1 data. Note that no measurement noise is generated in the simulated data served for the purpose of validation because the "true" measurement noise in raw data is unknown.

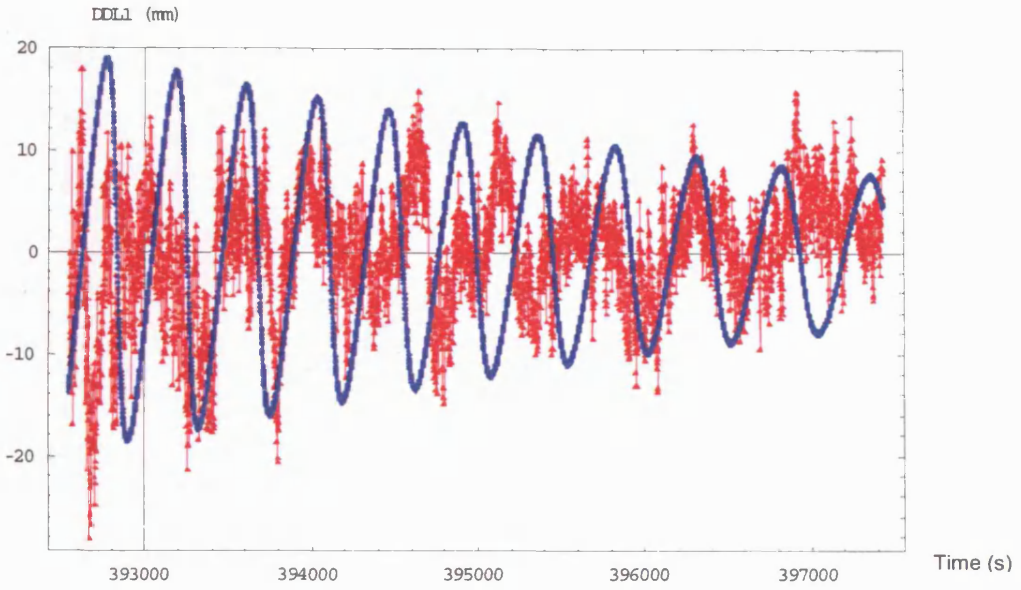

Figure 4-26: Double difference residuals in L1 of real (red) and simulated (blue) data for PRN11 in Day 1.

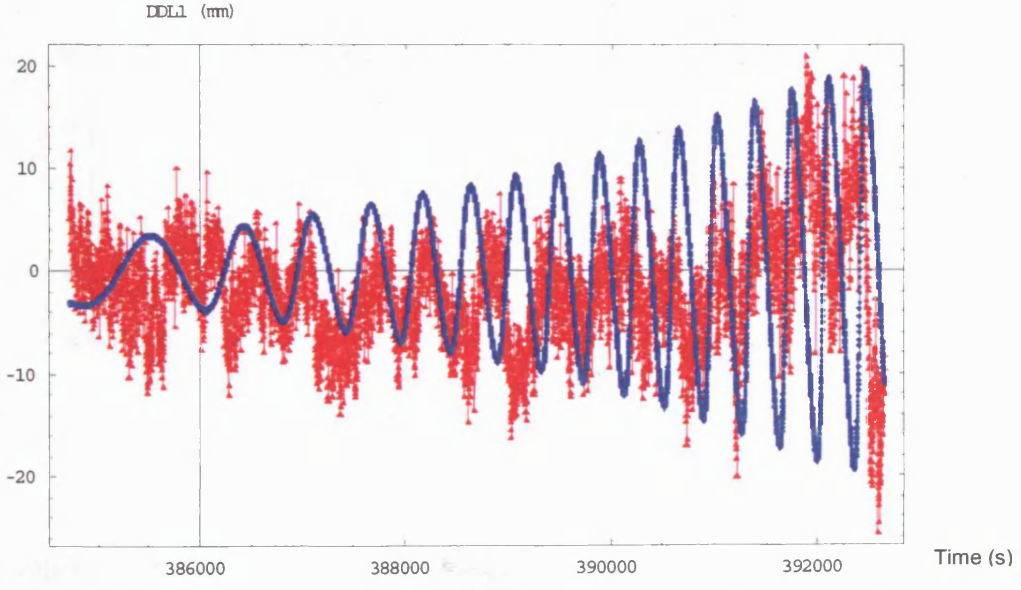

Figure 4-27: Double difference residuals in L1 of real (red) and simulated (blue) data for PRN16 in Day 1.

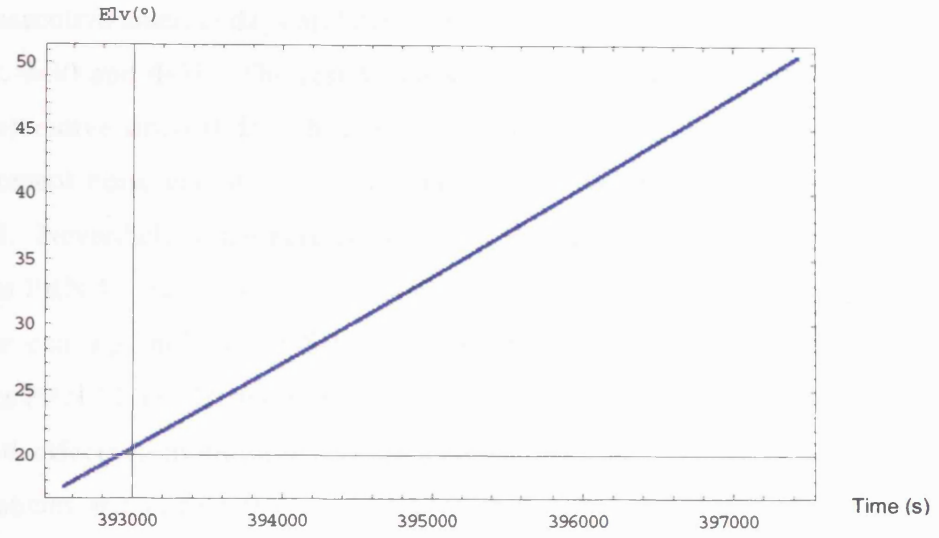

Figure 4-28: Elevation angles for PRN11 in Day 1.

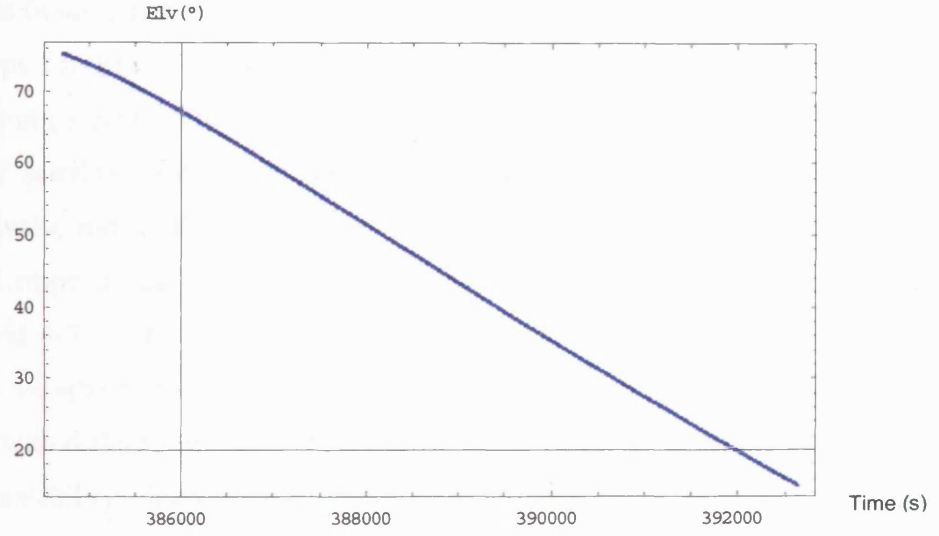

Figure 4-29: Elevation angles for PRN16 in Day 1.

The validation results in Figures 4-26 and 4-27 show good agreements of simulated multipath data with the real multipath data of both satellites PRN 11 and 16 in amplitudes of multipath signals (DD residuals) but rather poor agreements on frequencies especially when the elevation angle of direct signal is below about 50°, which can be found in Figures 4-26 to 4-29. In both satellites' data, the frequencies of simulated multipath signals increase with decrease in elevation angles, however, this trend is not very clear in the real data with low elevation angle of satellite. Moreover, the sinusoidal property of multipath signal is not very obvious in real data especially in low elevation angle of satellite. A day-to-day repeatability check was carried out to verify the presence of multipath by inspection of the similarity of multipath patterns in

two consecutive sidereal days and the results for satellites PRN 11 and 16 are shown in Figures. 4-30 and 4-31. The results show generally good agreements of multipath in two consecutive sidereal days, however, a lot of discrepancies greater than the nominal measurement noise can still be seen especially in low elevation angle of the satellite PRN 16. Nevertheless, the agreements prove the presence of multipath effects in both satellites PRN 11 and 16, the loss of sinusoidal properties may be due to more than one reflector causing multipath effects at other frequencies in the experimental site for satellites PRN 11 and 16 and/or the reference satellite may have multipath effect and/or multipath effects from multiple reflectors on water surface caused by wave motion. The discrepancies greater than the nominal measurement noise are probably due to multipath effects from multiple reflectors on water surface caused by wave motion. TFFT has therefore performed to analyse the frequencies of the multipath signals for both satellites (a sequence of 256-point FFTs executed on 28 overlapping signal segments in 171 steps for PRN 11 raw data and a sequence of 256-point FFTs executed on 46 overlapping signal segments in 170 steps for PRN 16 raw data) and the results in 3D-view of satellite PRN 11 are shown Figures 4-32(a) and 4-33(a) for Day 1 and 2 respectively, and results in X-Z-view are shown in Figures 4-32(b) and 4-33(b) for Day 1 and 2 respectively; the results in 3D-view of satellite PRN 16 are shown Figures 4-34(a) and 4-35(a) for Day 1 and 2 respectively, and results in X-Z-view are shown in Figures 4-34(b) and 4-35(b) for Day 1 and 2 respectively. It is obvious that a lot of signals with different frequencies are present in the raw data. Some peaks show day-to-day repeatability which suggests that a few multipath signals affected both satellites but many random peaks exist which are probably due to multiple reflectors on water surface caused by wave motion. By analysis of simulated data with TFFT using the same precisions, number of segments and steps as raw data, the TFFT results for satellites PRN 11 and PRN 16 are shown in Figures 4-36 and 4-37. Simulated multipath signals show good agreements with raw multipath data in dominant peak frequencies only and show agreements on spectrums sometimes. The most likely causes of spectrum discrepancies are the influences of occurrence of multipath from other reflectors in the area (ground and/or water surface) and unmodelled components in the damping factor. The sensitivity of modelled components of damping factor to multipath effect will be discussed in next section. The relationships of L1 multipath error, damping factor, and components (reflection coefficient, polarisation efficiency, antenna gain ratio of direct and reflected signals) of damping factor in time series for satellites PRN 11 and 16 of

this validation are shown in Figures 4-38(a) and 4-39(a) respectively, and the differential path delay of reflected signal of satellites PRN 11 and 16 are shown in Figures 4-38(b) and 4-39(b) respectively.

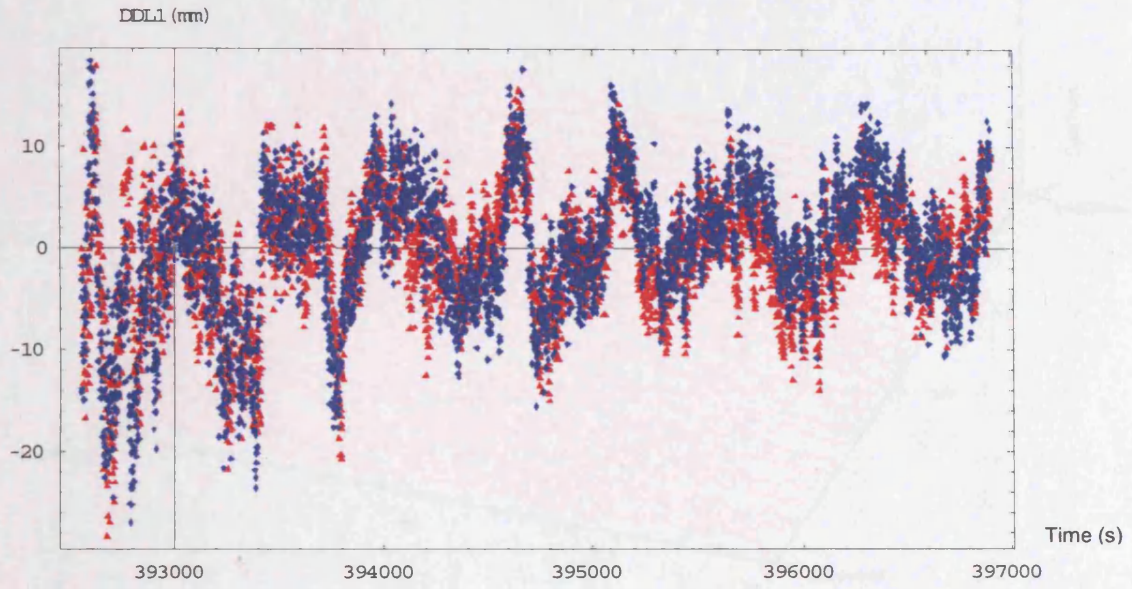

Figure 4-30: Day-to-day repeatability of double difference residuals in L1 of real data for PRN11 in Day 1 (red) and Day 2 (blue).

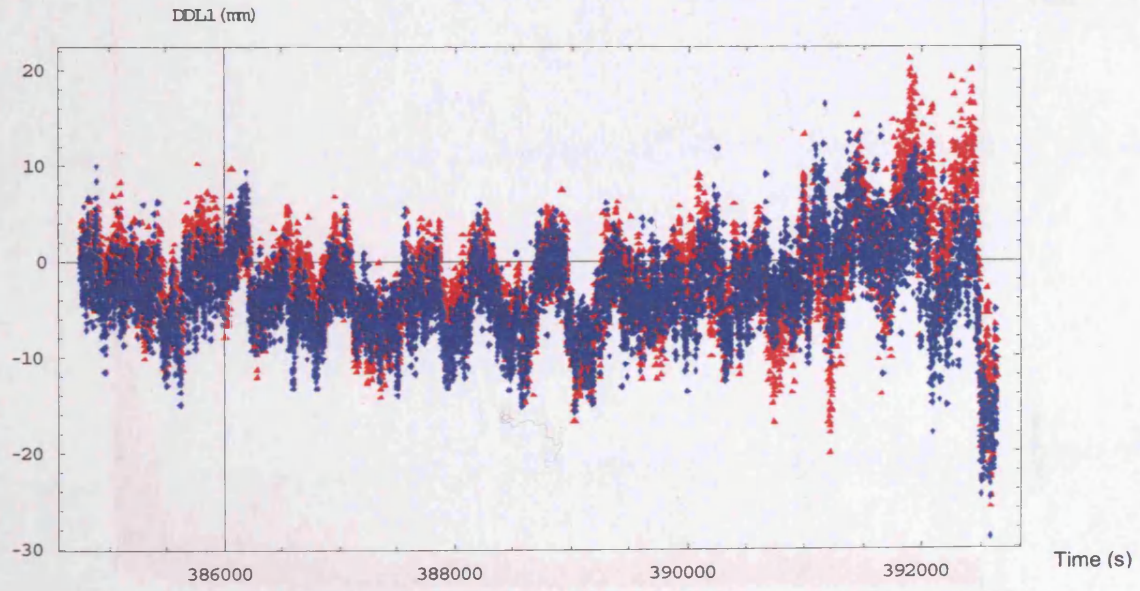

Figure 4-31: Day-to-day repeatability of double difference residuals in L1 of real data for PRN16 in Day 1 (red) and Day 2 (blue).

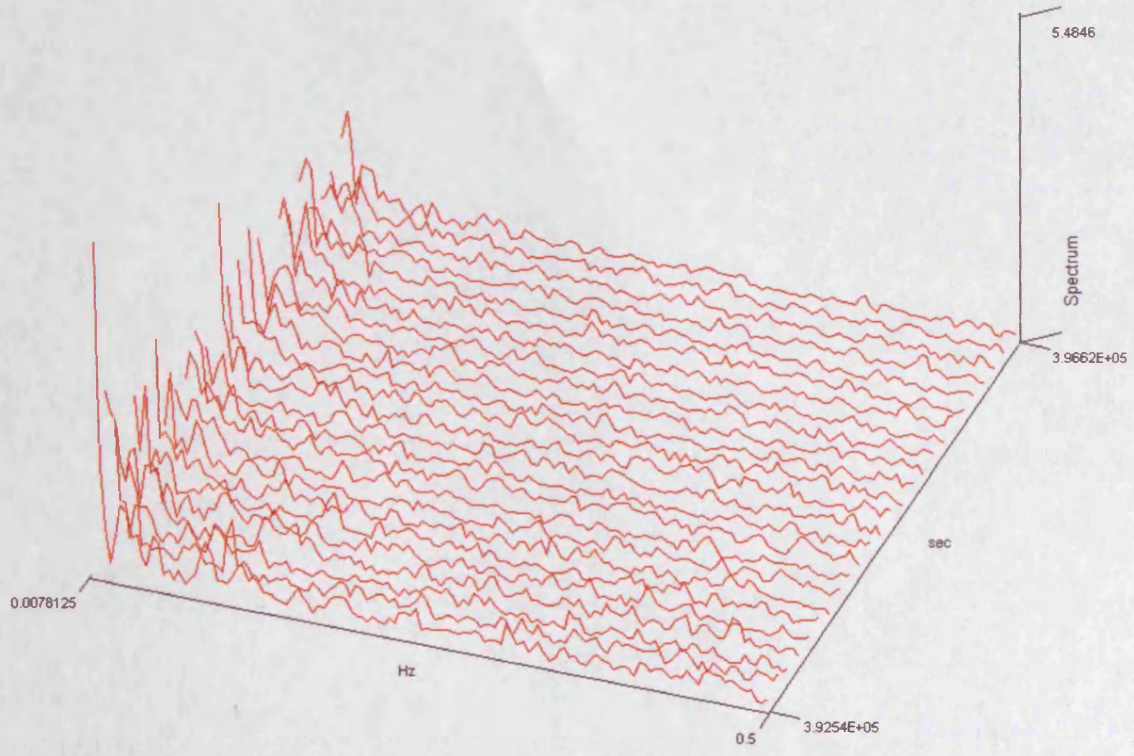

(a)

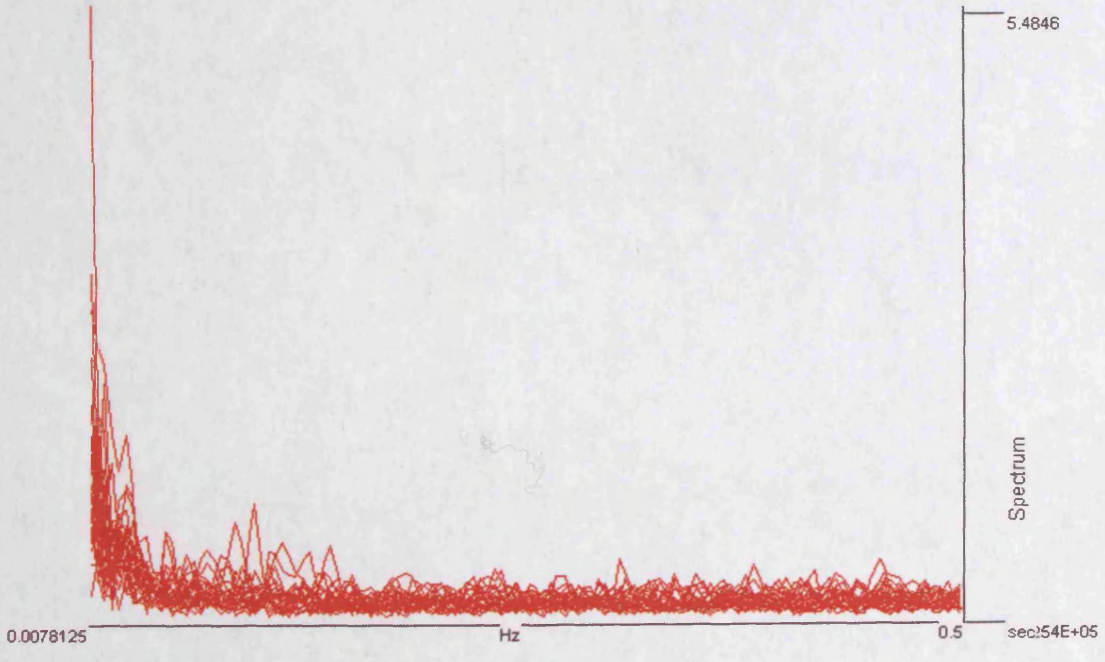

(b)

Figure 4-32: Time Fast Fourier Transform analysis of the frequencies of raw multipath signal of the satellite PRN 11 for Day 1. (a) 3D view; (b) X-Z view.

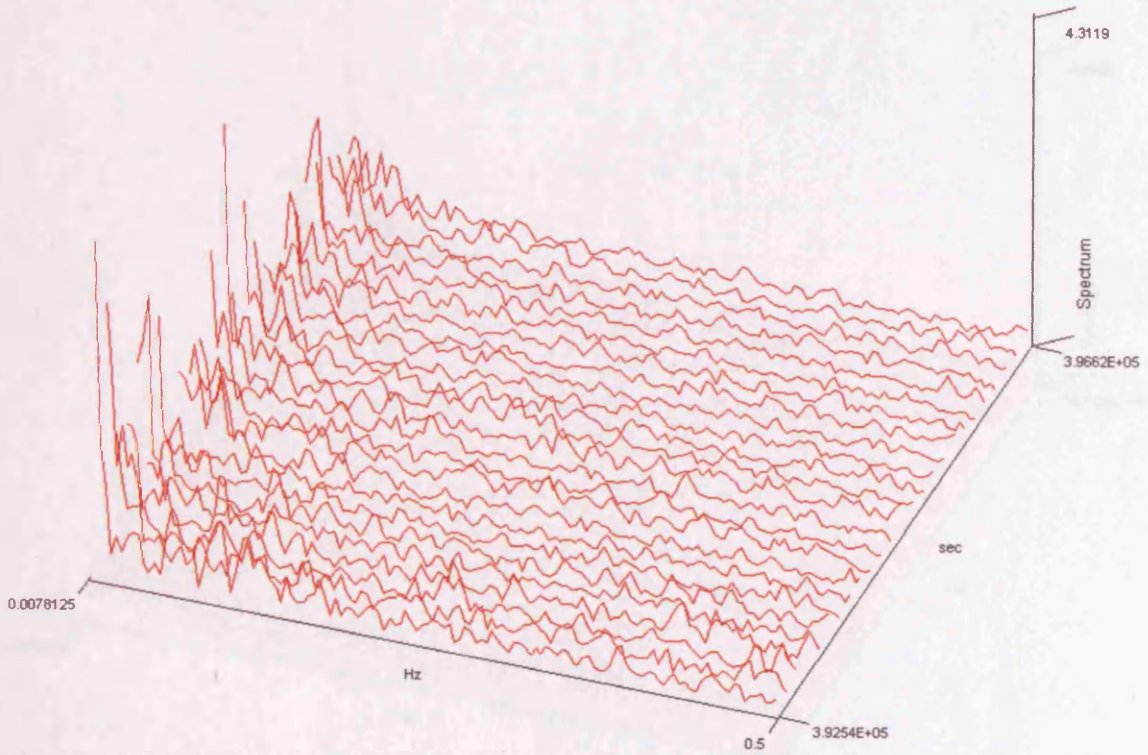

(a)

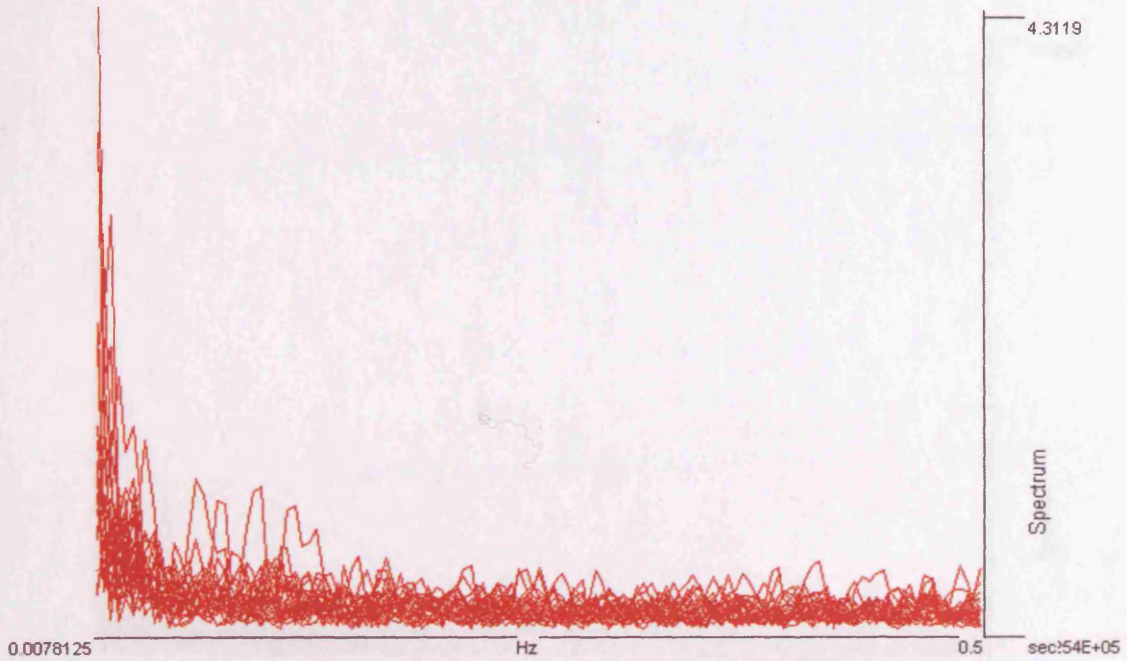

(b)

Figure 4-33: Time Fast Fourier Transform analysis of the frequencies of raw multipath signal of the satellite PRN 11 for Day 2. (a) 3D view; (b) X-Z view.

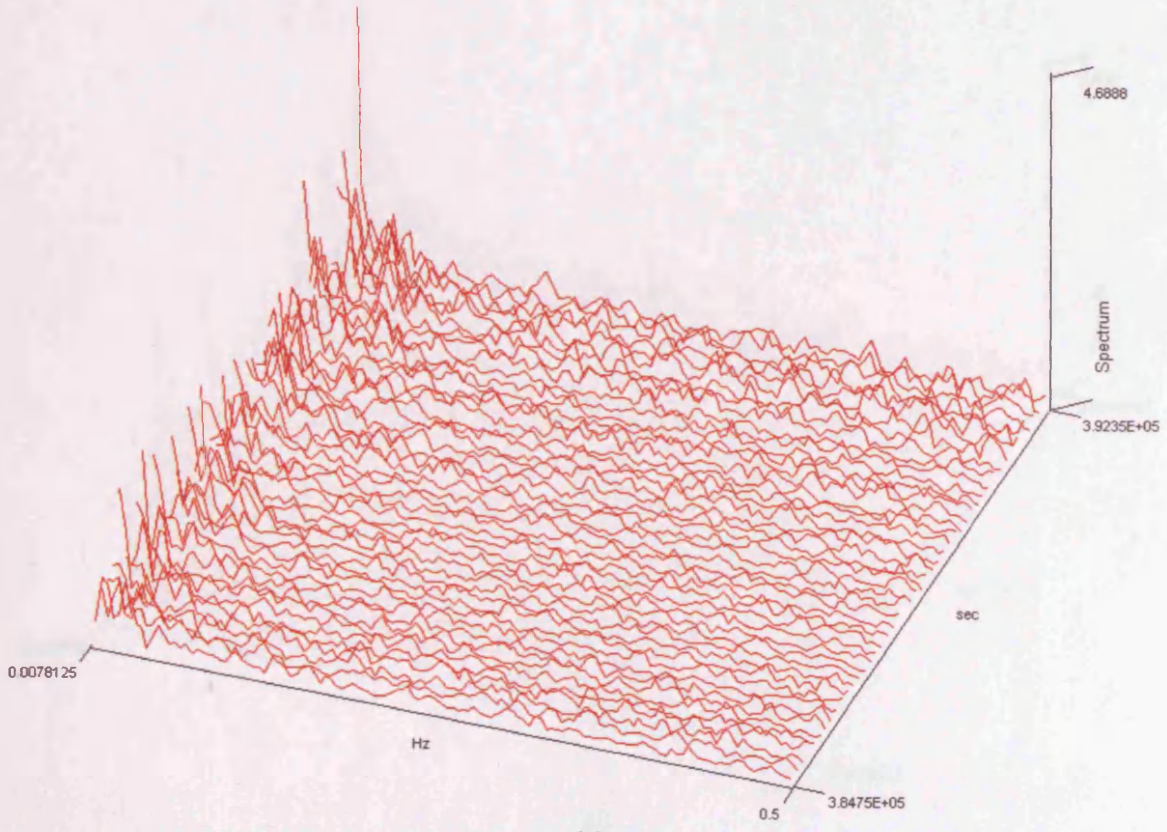

(a)

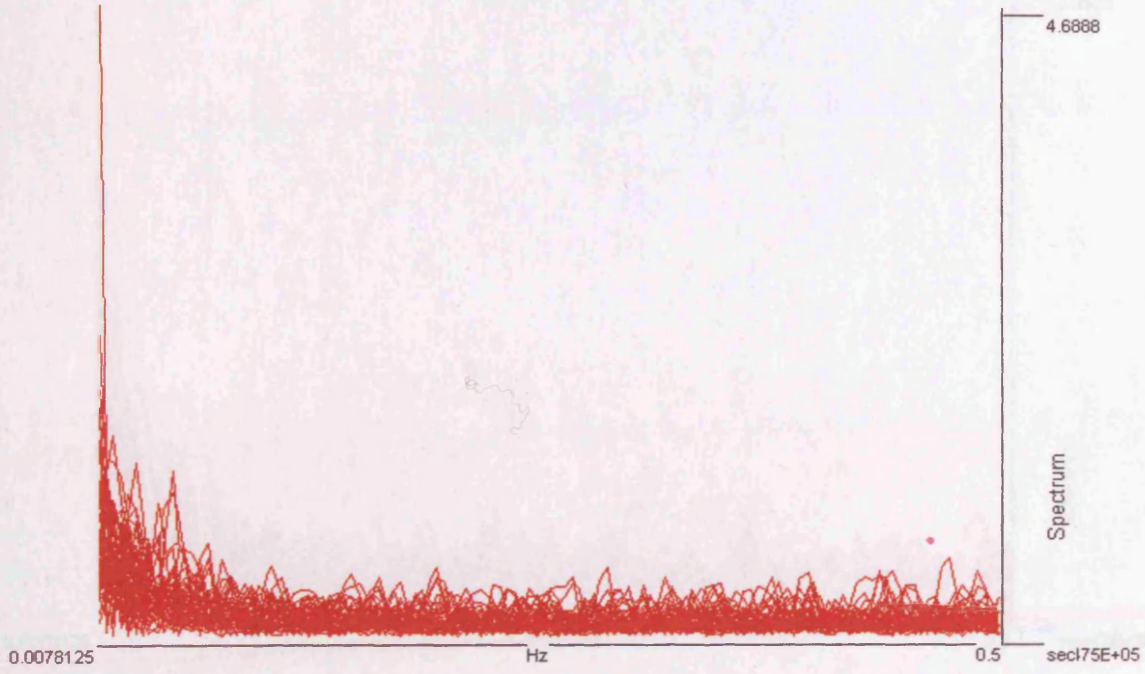

(b)

Figure 4-34: Time Fast Fourier Transform analysis of the frequencies of raw multipath signal of the satellite PRN 16 for Day 1. (a) 3D view; (b) X-Z view.

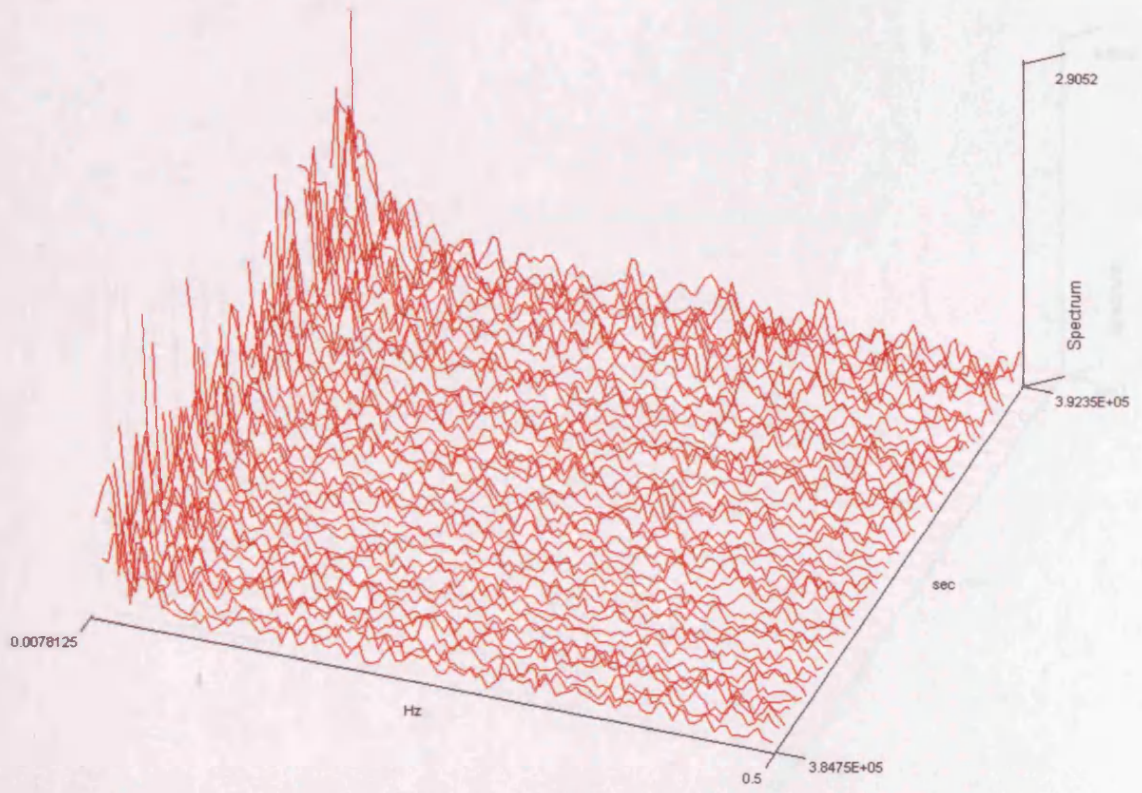

(a)

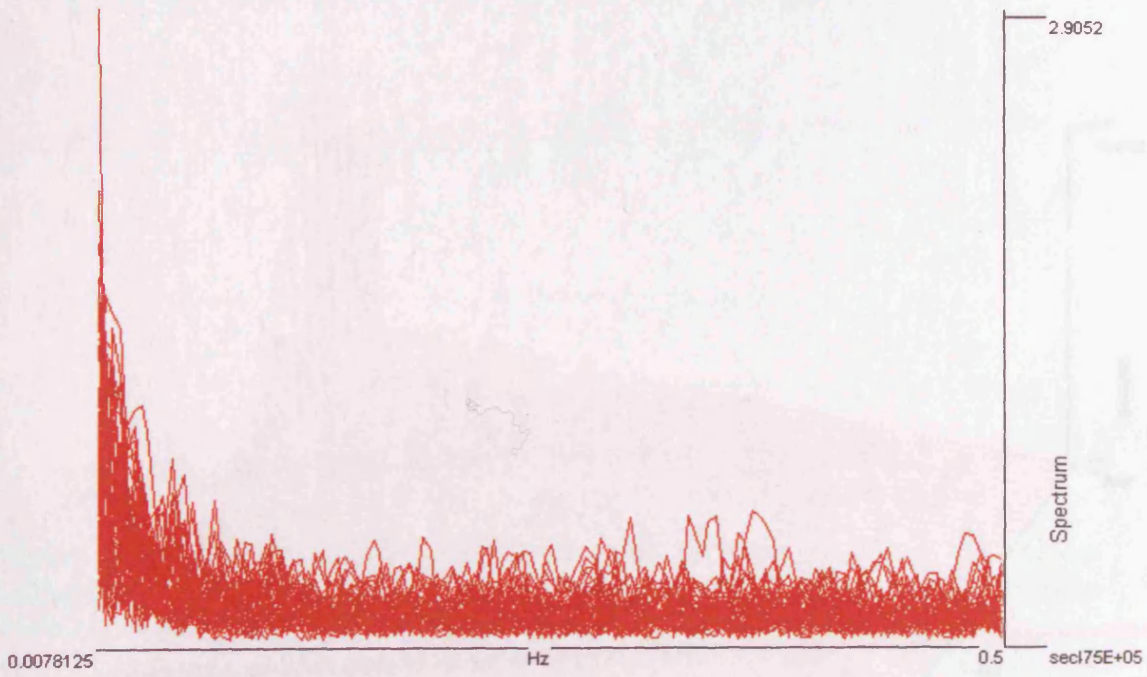

(b)

Figure 4-35: Time Fast Fourier Transform analysis of the frequencies of raw multipath signal of the satellite PRN 16 for Day 2. (a) 3D view; (b) X-Z view.

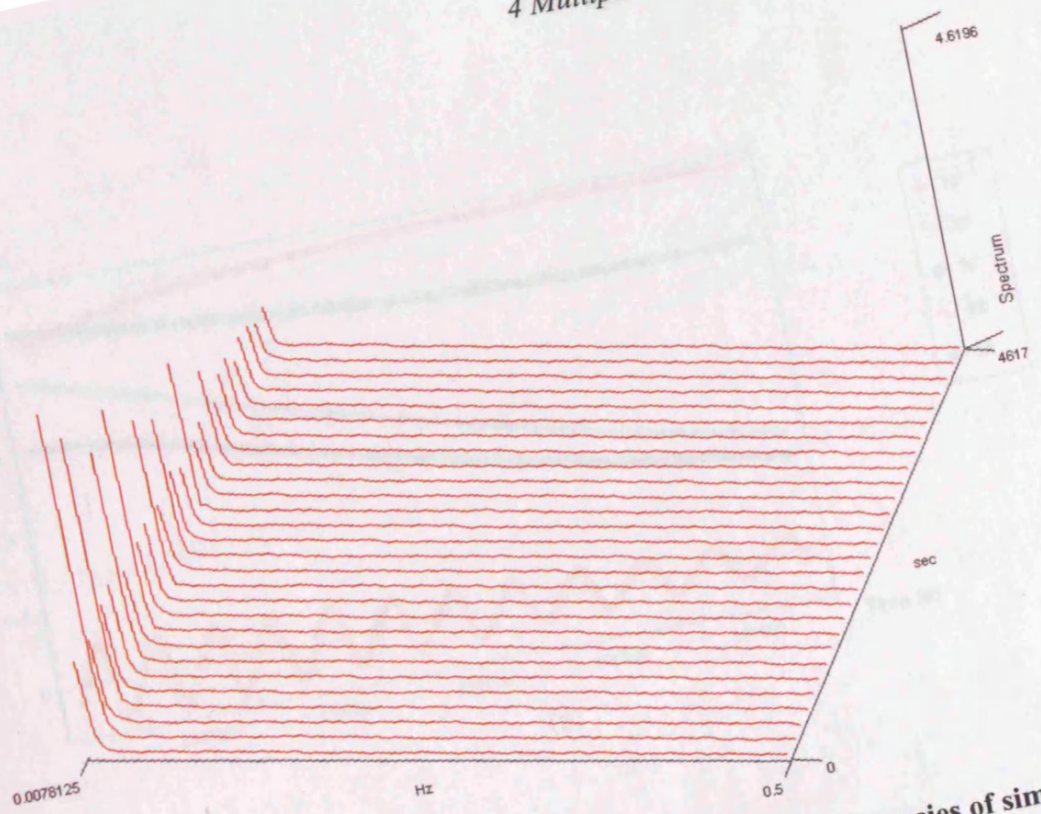

Figure 4-36: Time Fast Fourier Transform analysis of the frequencies of simulated multipath signal of the satellite PRN 11 for Day 1.

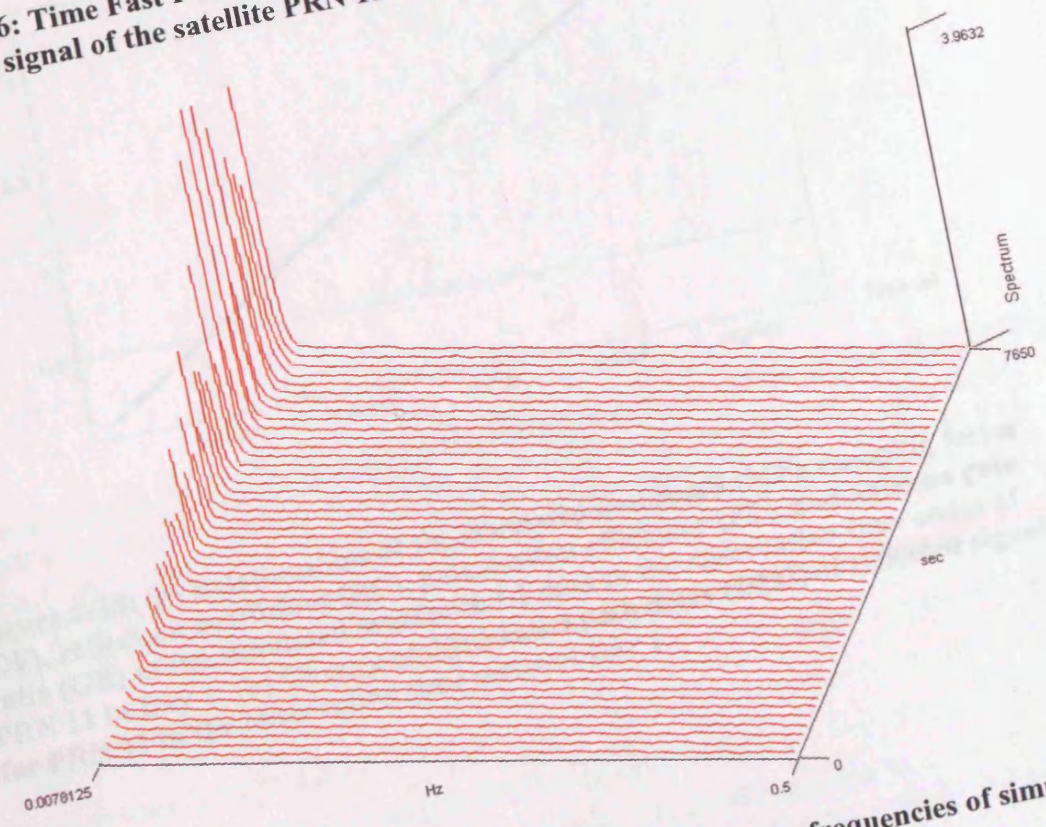

Figure 4-37: Time Fast Fourier Transform analysis of the frequencies of simulated multipath signal of the satellite PRN 16 for Day 1.

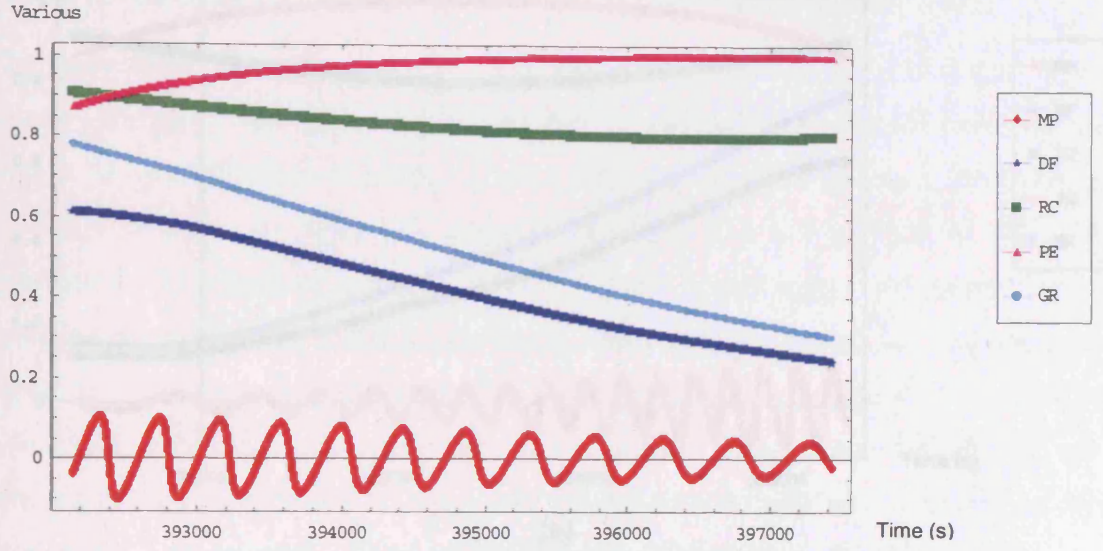

(a)

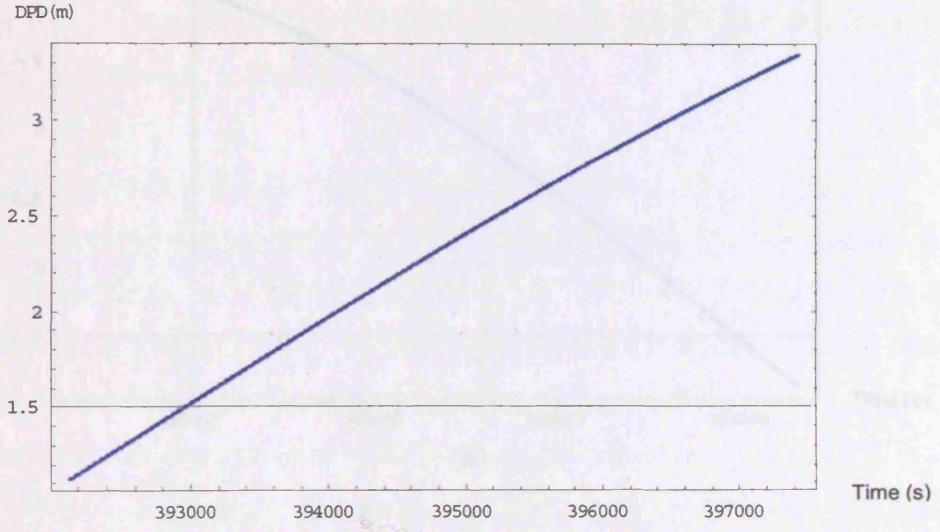

(b)

Figure 4-38: (a) Relationships of the simulated multipath (MP), damping factor (DF), reflection coefficient (RC), polarisation efficiency (PE), and antenna gain ratio (GR) of the simulated multipath L1 data in the observation time series of PRN 11 in Day 1; (b) Change of differential path delay (DPD) of reflected signal for PRN 11 in the observation time series of Day 1.

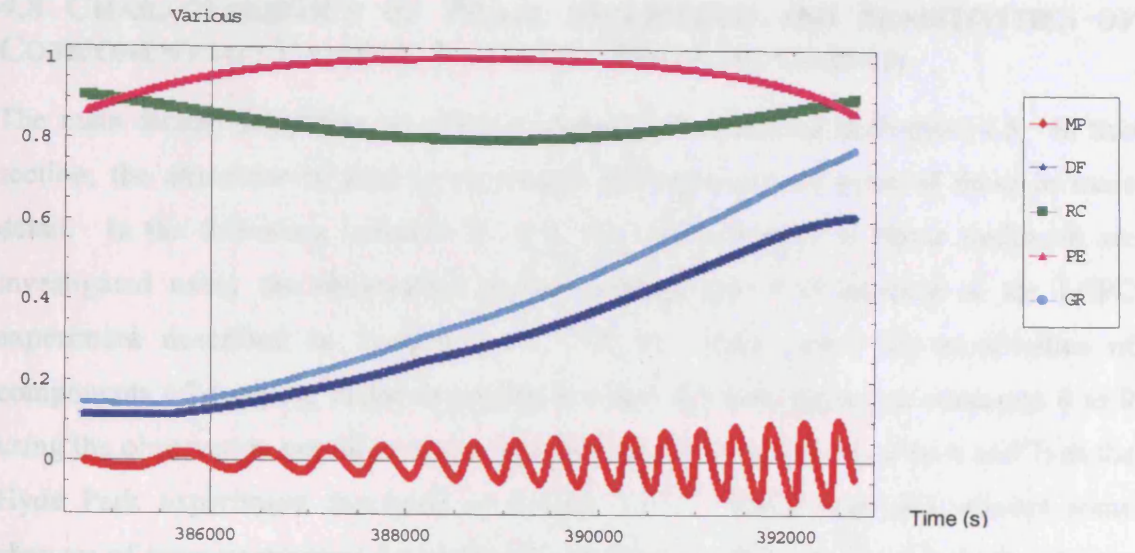

(a)

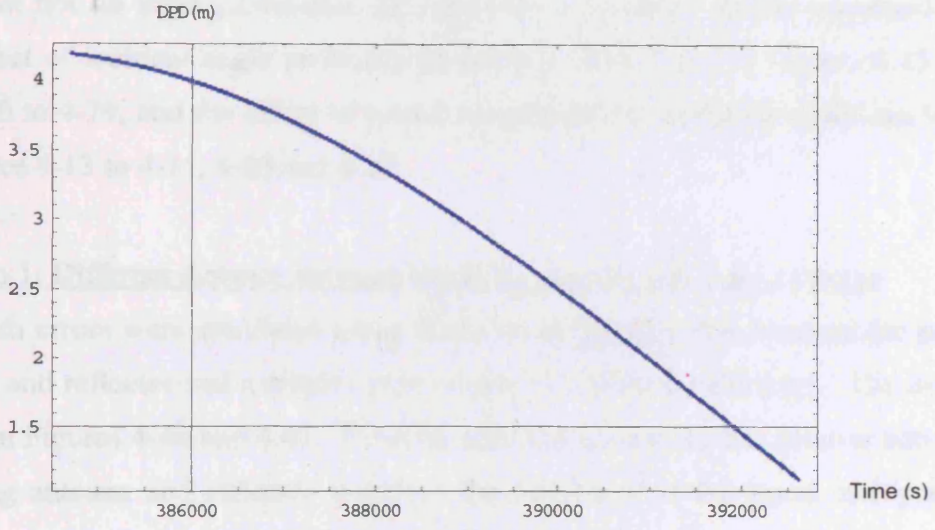

(b)

Figure 4-39: (a) Relationships of the simulated multipath (MP), damping factor (DF), reflection coefficient (RC), polarisation efficiency (PE), and antenna gain ratio (GR) of the simulated multipath L1 data in the observation time series of PRN 16 in Day1; (b) Change of differential path delay (DPD) of reflected signal for PRN 16 in the observation time series of Day 1.

In general, the assumption of specular reflection from water surface would never hold and it is impossible to measure the water wave motion in the observation period in order to input the real water wave motion for multipath simulation. It makes an uncertainty in this validation. The author proposes to carry out more experiments to verify it with different reflector materials and different geometries.

4.8 Characteristics of Phase Multipath and Sensitivities of Components of Damping Factor in Phase Multipath

The main factors impacting on phase multipath are described in Section 4.5. In this section, the simulator is used to investigate the influence of some of these in more detail. In the following scenarios 1 to 3, the characteristics of phase multipath are investigated using the observation period, antenna type and position as the LCPC experiment described in Section 4.7.1. On the other hand, the sensitivities of components of damping factor to multipath effect are investigated in scenarios 4 to 9 using the observation period, antenna type and position (except scenarios 6 and 7) as the Hyde Park experiment described in Section 4.7.2. These scenarios attempt some changes of input parameters for multipath simulation and check any measurement error causing the disagreements of raw multipath data with simulated multipath data.

Note that not all input parameters for multipath simulation will be investigated here. The effect of incident angle on multipath effect can be found in Figures 4-13 to 4-17 and 4-26 to 4-29, and the effect of carrier wavelength on multipath effect can be found in Figures 4-13 to 4-15, 4-26 and 4-27.

Scenario 1: Different distance between receiving antenna and close reflector

Multipath errors were simulated using distances of 5m and 10m between the receiving antenna and reflector and a relative permittivity of 3.9 for the reflector. The results are shown in Figures 4-40 and 4-41. It can be seen that increasing the distance between the receiving antenna and reflector increases the frequency of the phase multipath error. This is because the increase in distance leads to an increase in the rate of change of the satellite-reflector-antenna geometry (i.e. the rate of change of the differential path delay), which directly affects these characteristics, see Equations (4.20) to (4.22).

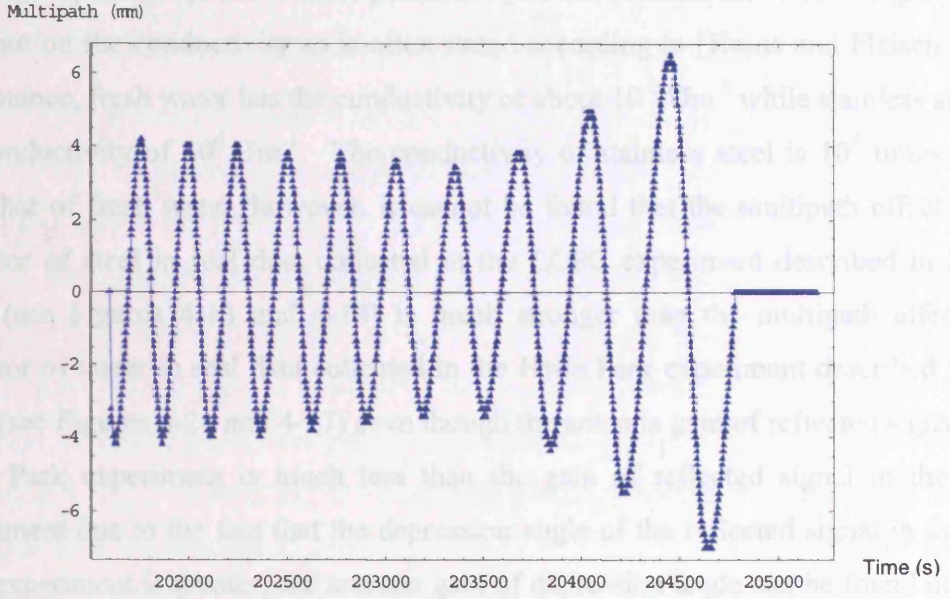

Figure 4-40: Simulated multipath error in L1 with the tilting reflector about 5 m away from the receiving antenna and a variable damping factor with a relative permittivity of 3.9.

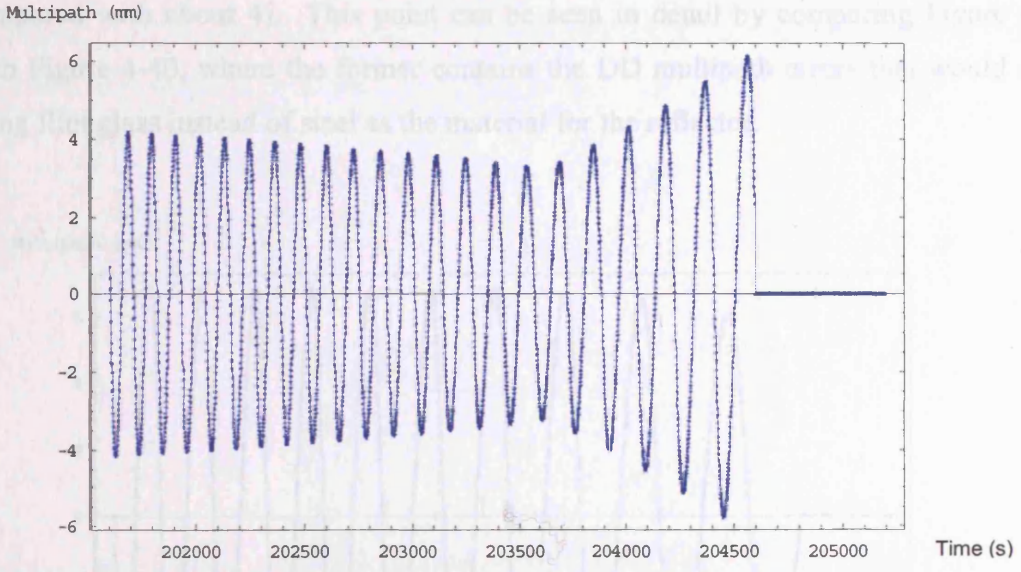

Figure 4-41: Simulated multipath error in L1 with the tilting reflector about 10 m away from the receiving antenna and a variable damping factor with a relative permittivity of 3.9.

Scenario 2: Different permittivities of reflector

Table 4-2 shows the relative permittivities of some common media that might cause reflections of GPS signals. As explained in Sections 4.3 and 4.5, and as is clear from Equations (4.1) and (4.2), the amplitude of multipath error arising from such reflections

is highly dependent on the relative permittivity of the medium for electromagnetic wave (and not on the conductivity as is often stated according to [Kraus and Fleisch, 1999], for instance, fresh water has the conductivity of about 10^{-2} $\mho m^{-1}$ while stainless steel has the conductivity of 10^{6} $\mho m^{-1}$. The conductivity of stainless steel is 10^{8} times greater than that of fresh water, however, it cannot be found that the multipath effect from a reflector of steel in real data collected in the LCPC experiment described in Section 4.7.1 (see Figures 4-13 and 4-14) is much stronger than the multipath effect from reflector of water in real data collected in the Hyde Park experiment described Section 4.7.2 (see Figures 4-26 and 4-27) even though the antenna gain of reflected signal in the Hyde Park experiment is much less than the gain of reflected signal in the LCPC experiment due to the fact that the depression angle of the reflected signal in the Hyde Park experiment is greater; the antenna gain of depression angle can be found in Figure 4-7). Therefore, for instance, and contrary to intuition, seawater (with a relative permittivity of 80) causes a larger multipath effect than that of copper (with a relative permittivity of 1). If flint glass had been used in the experiment described in Section 4.7.1, then the multipath effect would be more serious (relative permittivity of 10 compared with about 4). This point can be seen in detail by comparing Figure 4-42 with Figure 4-40, where the former contains the DD multipath errors that would arise using flint glass instead of steel as the material for the reflector.

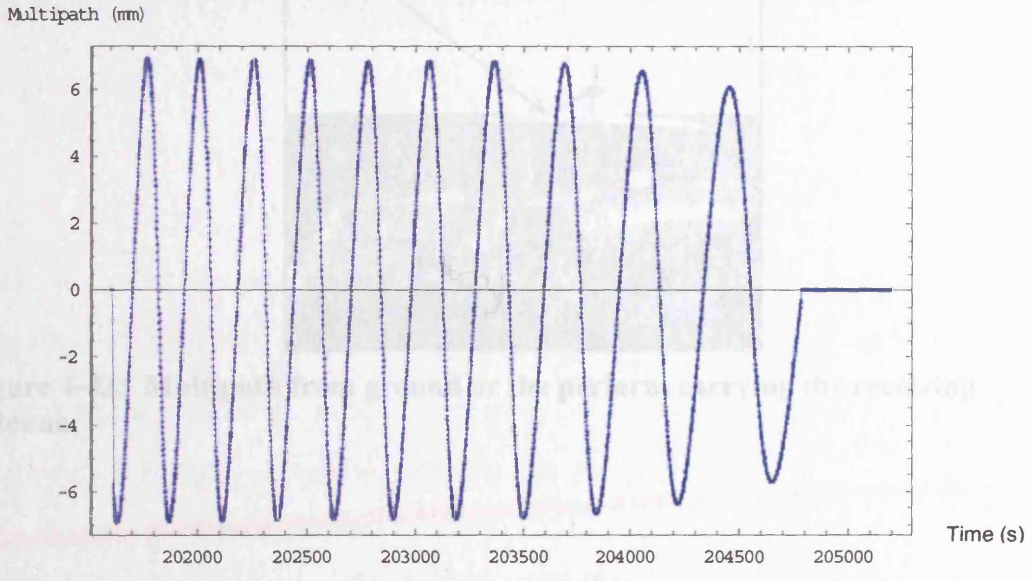

Figure 4-42: Simulated multipath error in L1 with the tilting reflector about 5 m away from the receiving antenna and a variable damping factor with a relative permittivity of 10.

Scenario 3: Reflection from antenna carrying platform and reflector below antenna

If a receiving antenna is set on a carrying platform (e.g. on top of a vehicle, as shown in Figure 4-43) or placed just above ground, multipath may come from very close reflections below the horizon. This is a very common situation in practice. In this scenario, multipath has been simulated from such reflections. The carrying platform is assumed to be horizontal, smooth (so causing specular reflection), static (compared with the antenna), and to be 29 cm below the L1 phase centre of the receiving antenna position. A relative permittivity of 3.9 is assumed, and all other factors are as described in Section 4.7.1. The resulting DD multipath errors are shown in Figure 4-44. It can be seen that both the amplitude and frequency of the errors are much smaller than those obtained in Scenario 1 (see Figures 4-40 and 4-41). The smaller amplitude is mainly due to the lower gain for the reflected signal coming from below the horizon of the antenna, and the lower frequency is because of the slow change in satellite-reflector-antenna geometry when the reflector is very close. This result shows that such errors, whilst small, are significant in dynamic environments where there is no opportunity for averaging. On the other hand, with a detailed knowledge of the materials and geometry, it should be possible to calibrate a particular antenna scenario for such errors.

Figure 4-43: Multipath from ground or the perform carrying the receiving antenna.

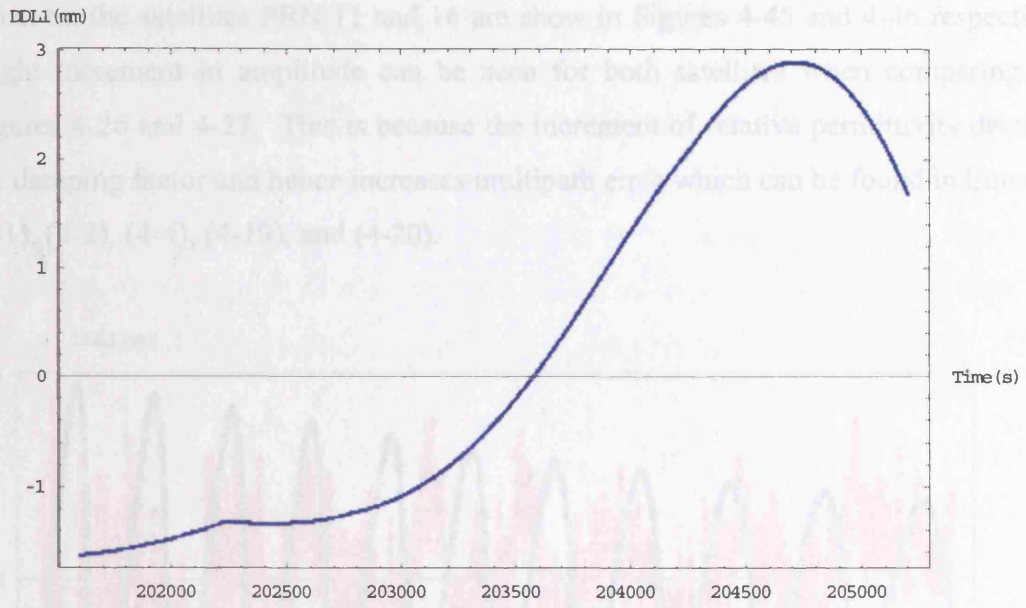

Figure 4-44: Simulated multipath error in L1 with the horizontal reflector about 29 cm below the receiving antenna and a variable damping factor with a relative permittivity of 3.9.

If the reflective surface is rough such as normal ground, it can be considered as causing many specular reflections from reflectors with different normal vectors. Lau and Mok (1999) describe that the resultant multipath error in positioning solution is the summation of the multipath errors from each satellite, each reflector, and each antenna. Regarding the resultant multipath error in each phase measurement, it would be the summation of the phase multipath errors from the reflectors as follows.

$$\psi = \tan^{-1}\left[\sum_{i=1}^{n}\left(\frac{\alpha_i A(\tau)_i \sin\theta_i}{1+\alpha_i A(\tau)_i \cos\theta_i}\right)\right] \tag{4.38}$$

where n denotes the number of reflectors causing multipath, α_i denotes the damping factor of the reflected signal coming from the reflector i, $A(\tau)_i$ denotes the code correlation function of the reflected signal coming from the reflector i, and θ_i denotes the phase shift of the reflected signal coming from the reflector i.

Scenario 4: Sensitivity of increasing the relative permittivity by 10%

Relative permittivity of 80 (see Table 4-2) for water is changed to 88 and it is input to multipath simulation but keeping the other input parameters unchanged. The multipath

effect on the satellites PRN 11 and 16 are show in Figures 4-45 and 4-46 respectively. Slight increment in amplitude can be seen for both satellites when comparing with Figures 4-26 and 4-27. This is because the increment of relative permittivity decreases the damping factor and hence increases multipath error which can be found in Equations (4-1), (4-2), (4-4), (4-19), and (4-20).

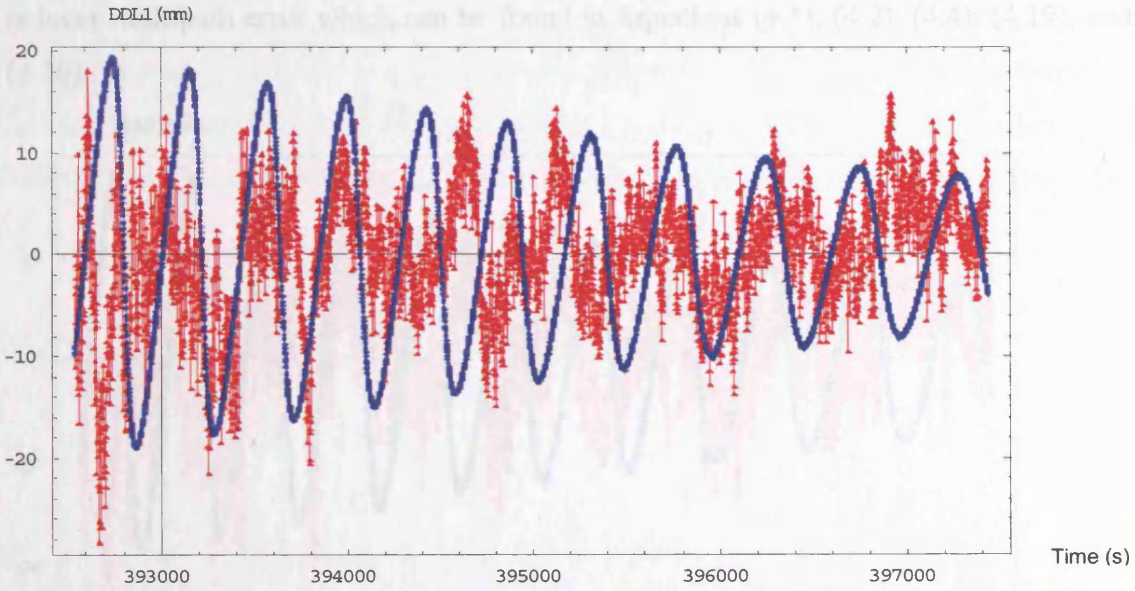

Figure 4-45: Sensitivity test of relative permittivity of 88 to multipath error in L1 for satellite PRN 11.

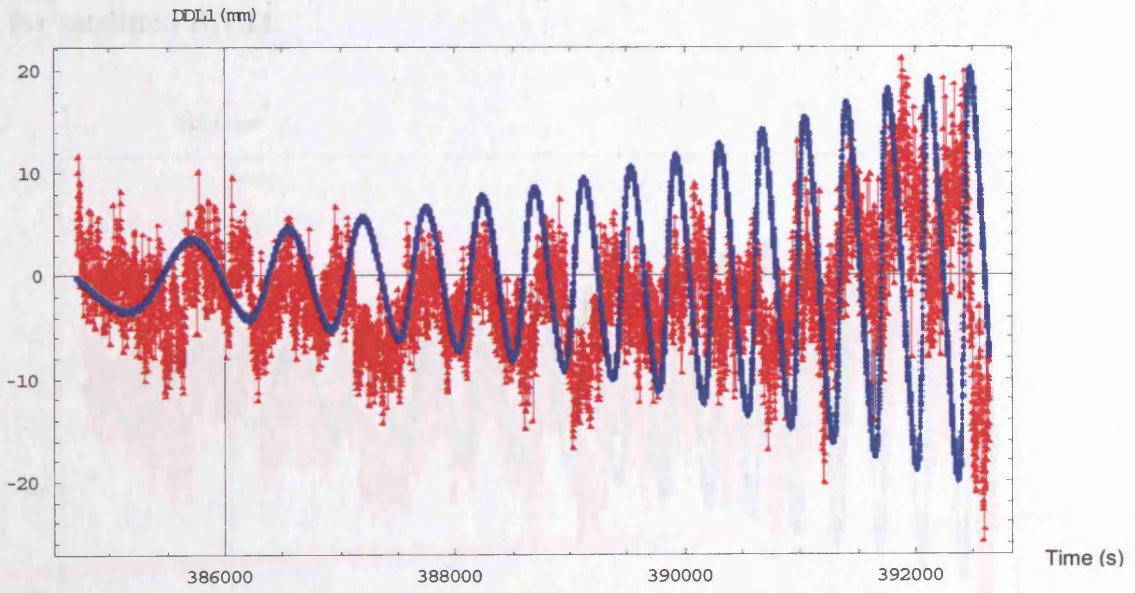

Figure 4-46: Sensitivity test of relative permittivity of 88 to multipath error in L1 for satellite PRN 16.

Scenario 5: Sensitivity of reducing the relative permittivity by 10%

Relative permittivity of 72 for water is used in multipath simulation but keeping the other input parameters unchanged. This effect on multipath for the satellites PRN 11 and 16 are shown in Figures 4-47 and 4-48 respectively. Slightly reduction in amplitude can be seen for both satellites when comparing with Figures 4-26 and 4-27. This is because the reduction of relative permittivity increases the damping factor and hence reduces multipath error which can be found in Equations (4.1), (4.2), (4.4), (4.19), and (4.20).

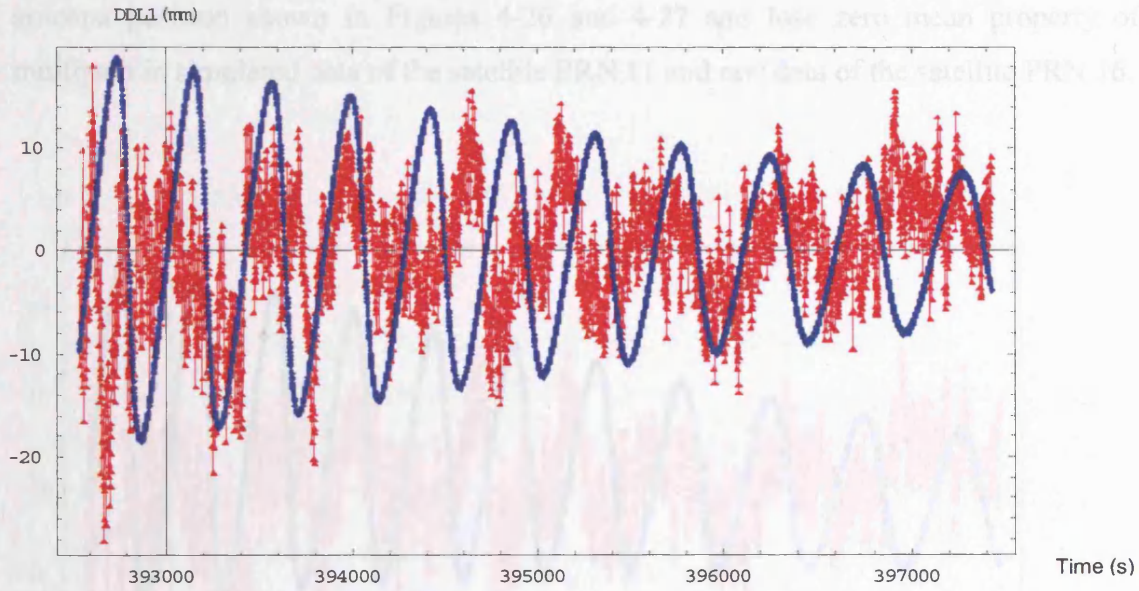

Figure 4-47: Sensitivity test of relative permittivity of 72 to multipath error in L1 for satellite PRN 11.

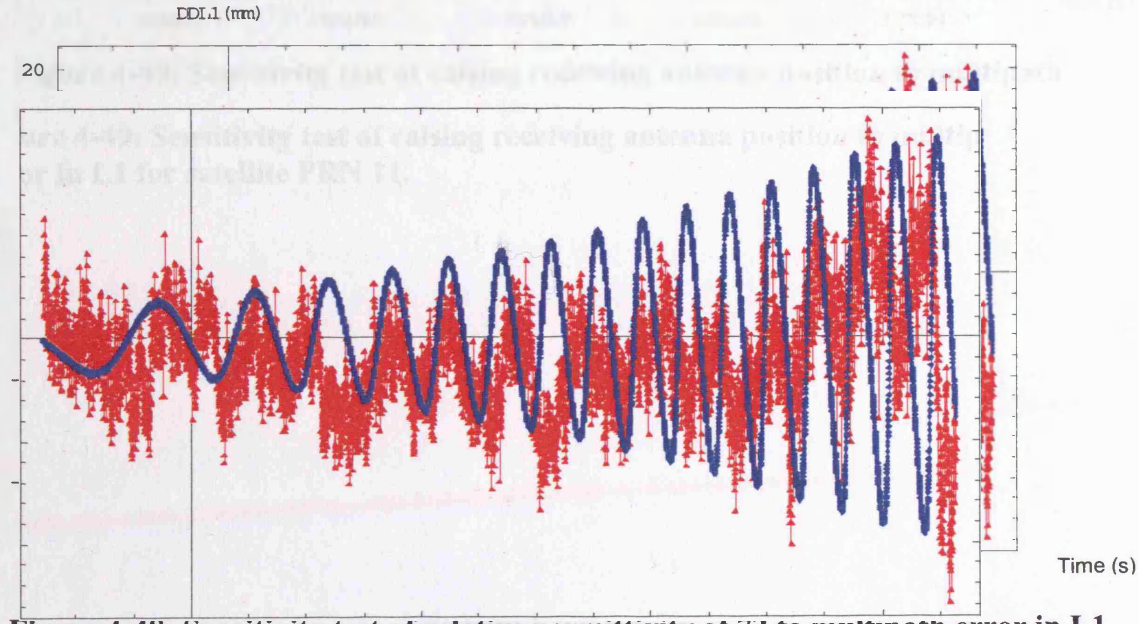

Figure 4-48: Sensitivity test of relative permittivity of 72 to multipath error in L1 for satellite PRN 16.

Scenario 6: Sensitivity of raising the receiving antenna position by 1 cm

The determined receiving antenna position described in Section 4.7.2 is raised by one centimetre and input to multipath simulation. Since this change affects the computation of DD residual, the true position for computation of true DD geometric range in both raw and simulated data must be changed accordingly. The DD residuals of raw and simulated data for the satellites PRN 11 and 16 are shown in Figures 4-49 and 4-50. They show worse agreements on amplitude than when using the determined receiving antenna position shown in Figures 4-26 and 4-27 and lose zero mean property of multipath in simulated data of the satellite PRN 11 and raw data of the satellite PRN 16.

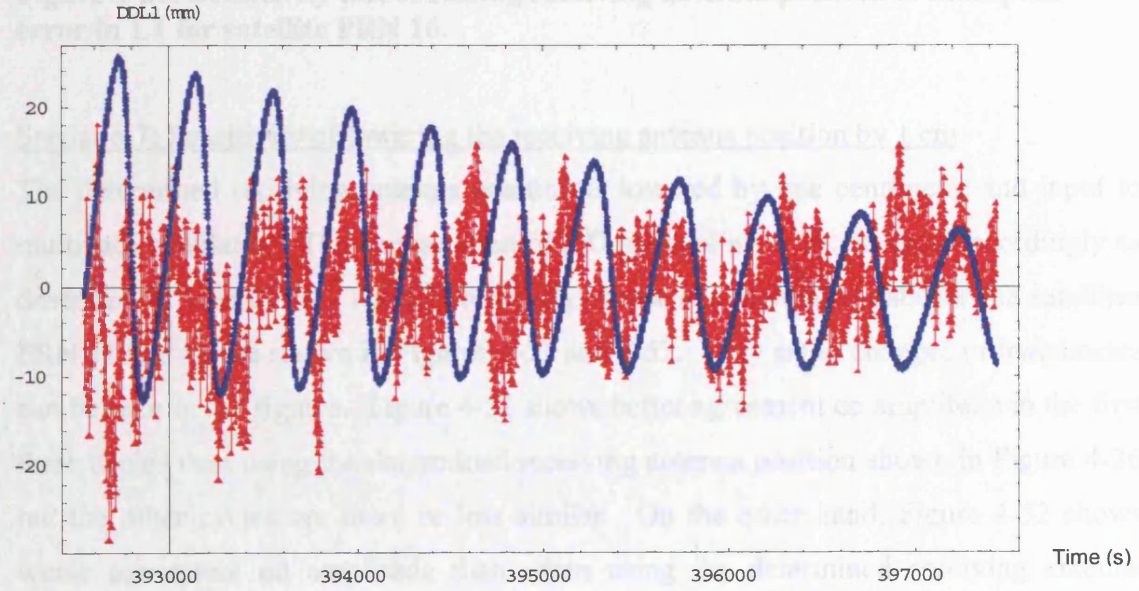

Figure 4-49: Sensitivity test of raising receiving antenna position to multipath error in L1 for satellite PRN 11.

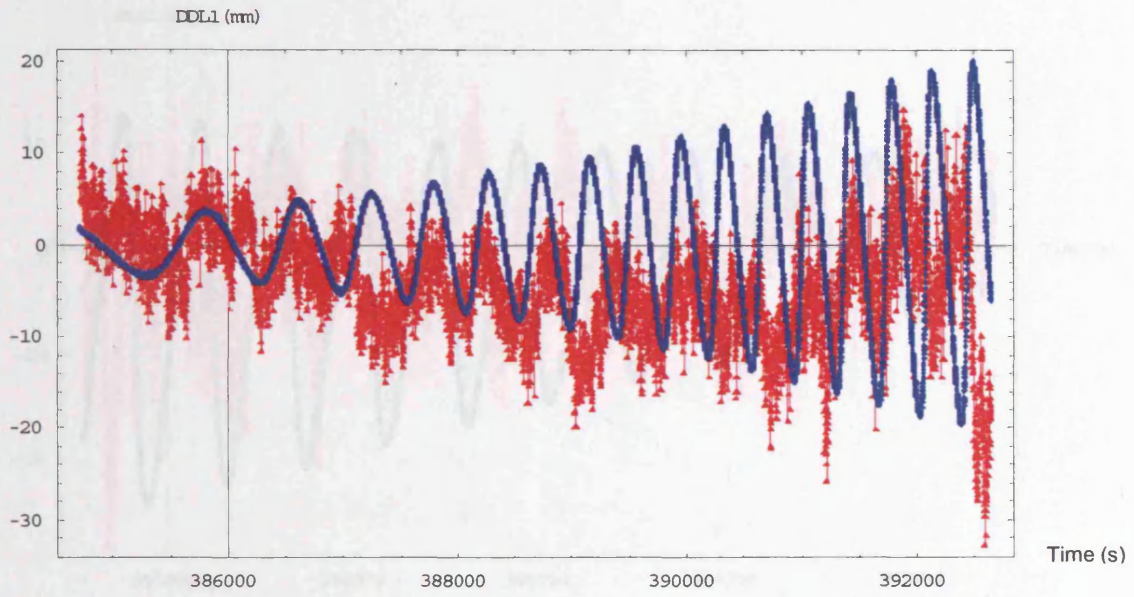

Figure 4-50: Sensitivity test of raising receiving antenna position to multipath error in L1 for satellite PRN 16.

Scenario 7: Sensitivity of lowering the receiving antenna position by 1 cm

The determined receiving antenna position is lowered by one centimetre and input to multipath simulation. The computation of DD residual must be changed accordingly as described in scenario 6. The DD residuals of raw and simulated data for the satellites PRN 11 and 16 are shown in Figures 4-51 and 4-52. Very small changes in frequencies can be seen in the figures. Figure 4-51 shows better agreement on amplitude in the first three cycles than using the determined receiving antenna position shown in Figure 4-26 but the other cycles are more or less similar. On the other hand, Figure 4-52 shows worse agreement on amplitude than when using the determined receiving antenna position shown in Figure 4-27 most of the time. However, it shows better zero mean property of multipath in the period approximately from 387500 to 389500 for raw data.

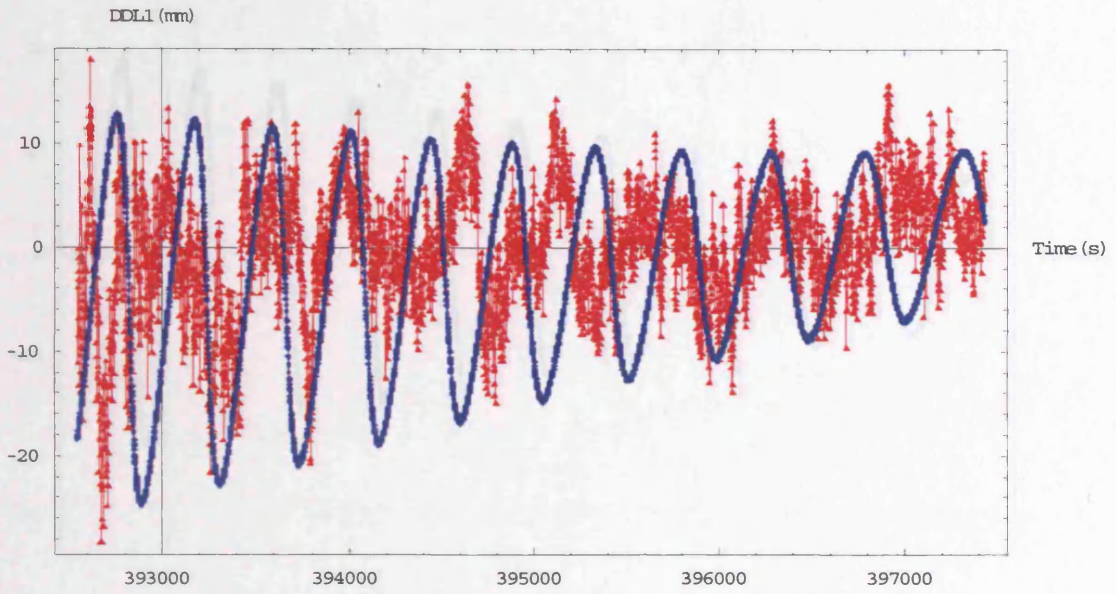

Figure 4-51: Sensitivity test of lowering receiving antenna position to multipath error in L1 for satellite PRN 11.

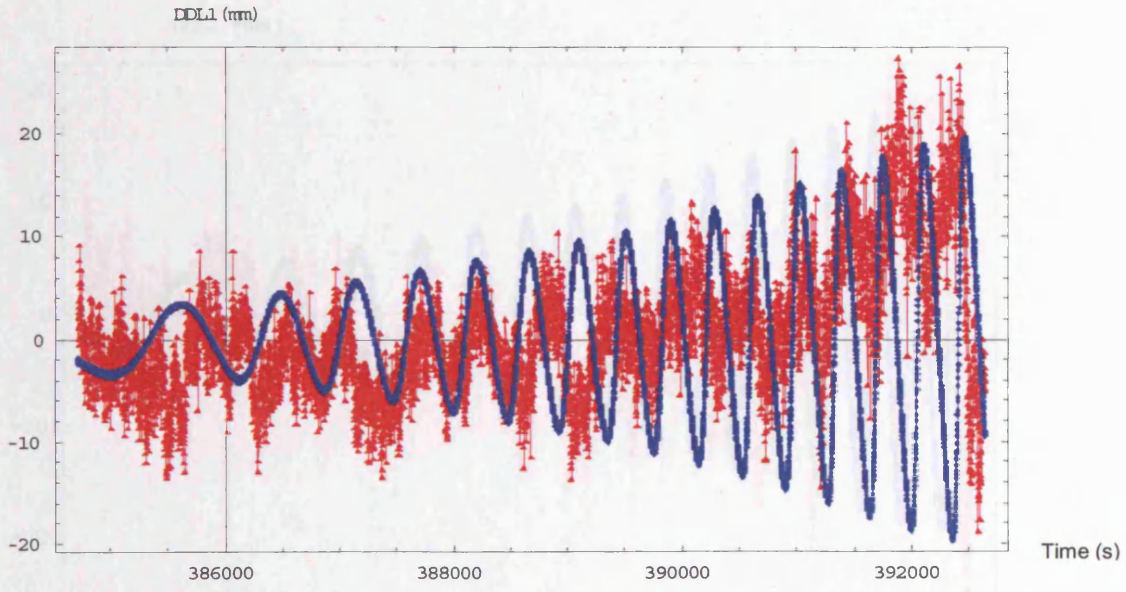

Figure 4-52: Sensitivity test of lowering receiving antenna position to multipath error in L1 for satellite PRN 16.

Scenario 8: Sensitivity of raising the water level by 1 cm

The measured water level is raised by one centimetre and input to multipath simulation while keeping other input parameters unchanged. The effect on DD residuals for the satellites PRN 11 and 16 are shown in Figures 4-53 and 4-54. Very small changes in both amplitudes and frequencies can be seen in the figures.

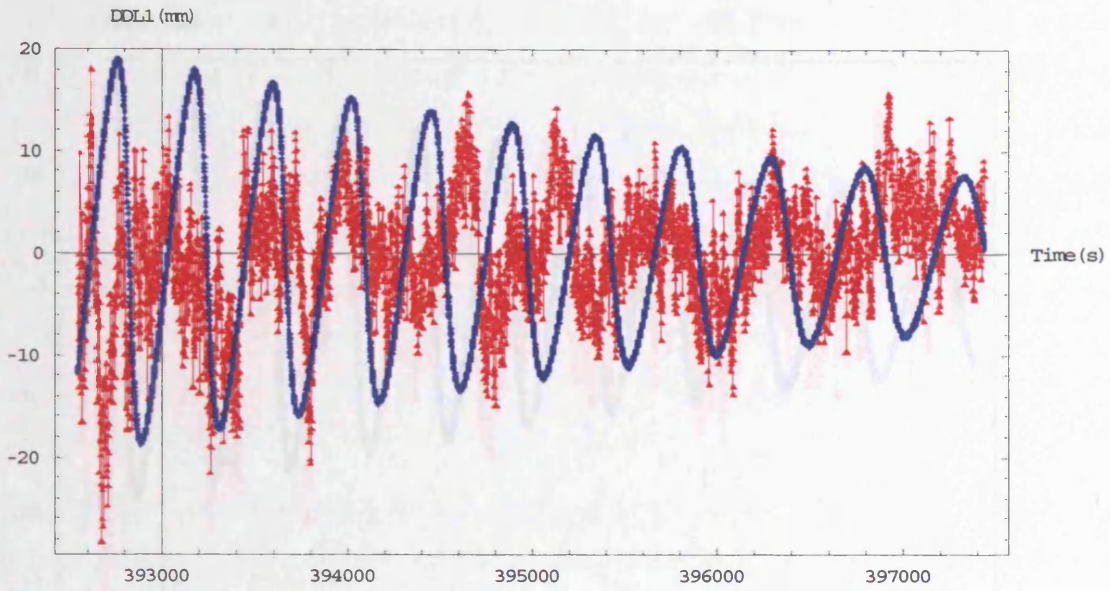

Figure 4-53: Sensitivity test of raising water surface level to multipath error in L1 for satellite PRN 11.

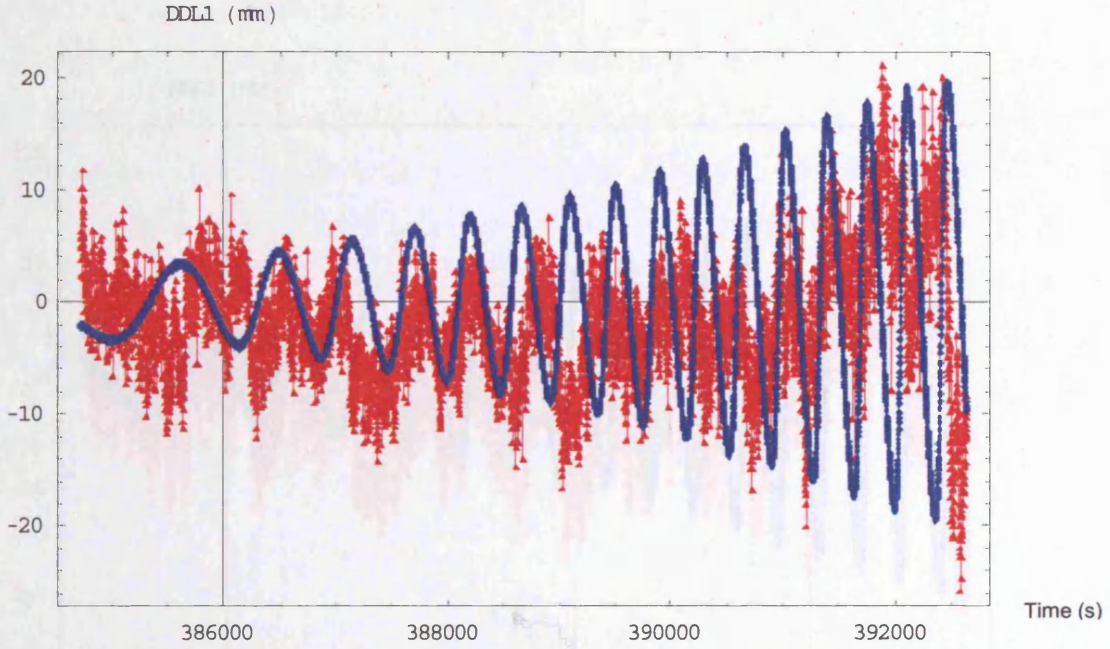

Figure 4-54: Sensitivity test of raising water surface level to multipath error in L1 for satellite PRN 16.

Scenario 9: Sensitivity of lowering the water level by 1 cm

The measured water level is lowered by one centimetre and input to multipath simulation while keeping other input parameters unchanged. The effect on DD residuals for the satellites PRN 11 and 16 are shown in Figures 4-55 and 4-56. Very small changes in both amplitudes and frequencies can be seen in the figures.

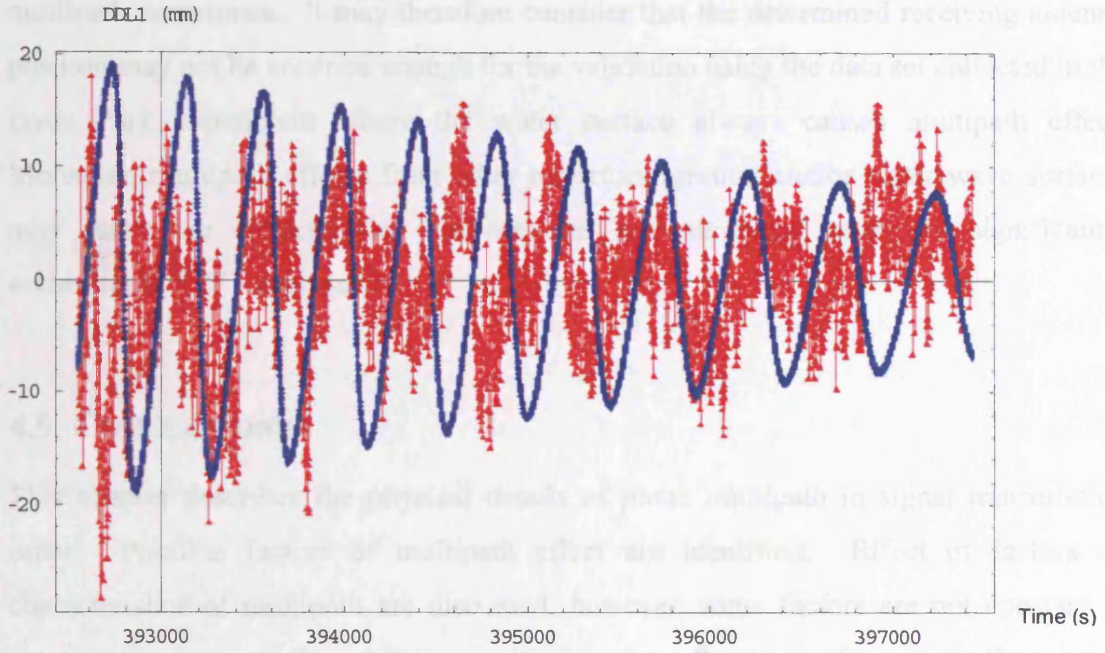

Figure 4-55: Sensitivity test of lowering water surface level to multipath error in L1 for satellite PRN 11.

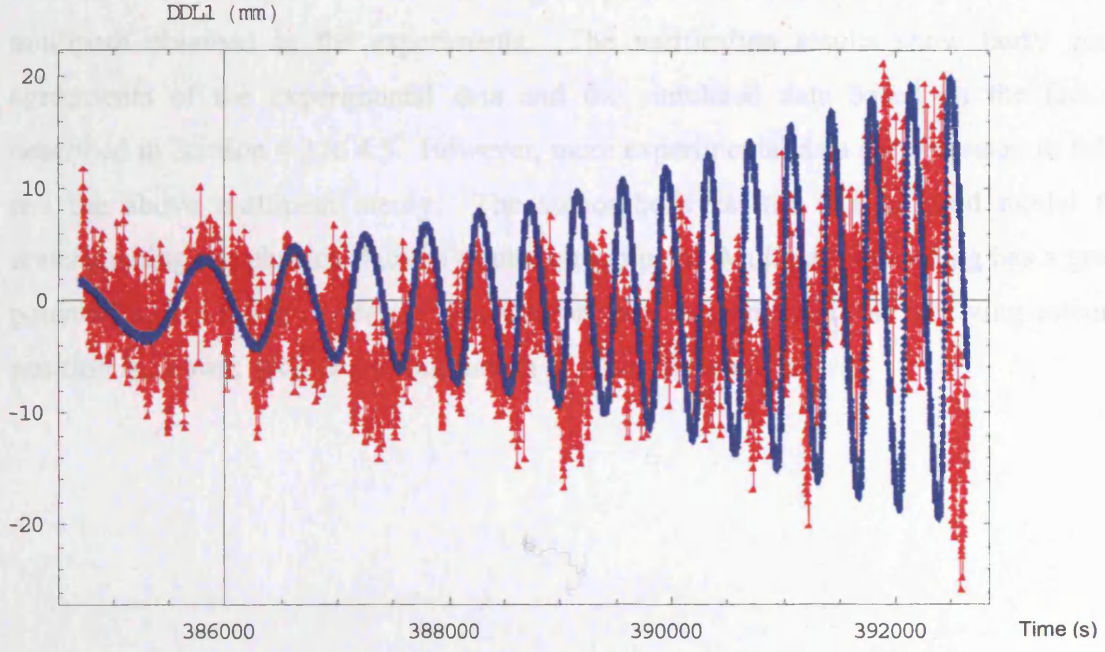

Figure 4-56: Sensitivity test of lowering water surface level to multipath error in L1 for satellite PRN 16.

From the tests for the sensitivity of the input parameters of multipath simulation on the agreement of raw and simulated multipath effects in scenarios 4 to 9, only the change of receiving antenna position in scenario 7 shows improvement on the agreement of raw multipath with simulated multipath in three cycles or better zero mean property of

multipath sometimes. It may therefore consider that the determined receiving antenna position may not be accurate enough for the validation using the data set collected in the Hyde Park experiment where the water surface always causes multipath effect. Moreover, multipath effects from other reflectors (ground and/or water wave surface) may cause the discrepancies between real and simulated multipath significantly according to TFFT analyses.

4.9 CONCLUSIONS

This chapter describes the physical details of phase multipath in signal transmission order. Possible factors of multipath effect are identified. Effect of factors on characteristics of multipath are discussed, however, some factors are not constant in practice: for instance the relative permittivity of a reflective surface is not the relative permittivity of the medium if it is wet, and the roughness of a surface relates the multipath possibility to the size of the surface.

Simulation of multipath error considering the possible factors tries to replicate the real multipath obtained in the experiments. The verification results show fairly good agreements of the experimental data and the simulated data based on the factors described in Section 4.2 to 4.5. However, more experimental data are necessary to fully test the above multipath theory. The author believes that it is a good model for understanding the physical factors of phase multipath. Multipath modelling has a great potential to be used to correct multipath errors in measurements if the receiving antenna position is known, such as site calibration in reference stations.

5. DESCRIPTION OF TESTING

5.1 INTRODUCTION

This chapter describes the design of testing for the multipath mitigation techniques using multiple-frequency GNSS data to be described in Chapters 6 to 8. Testing aims to assess the performances of the proposed multipath mitigation techniques. The testing results will be described in Chapters 6 to 8. This chapter focuses on the specifications and descriptions of the simulation of testing datasets to be used in Chapters 6 to 8.

5.2 TESTING SITES

Two testing sites were selected for the simulation of static testing datasets. One real testing site is at the Laboratoire Central des Ponts et Chaussées (LCPC) near Nantes in France as shown in Figure 5-1, where real data contaminated by multipath were collected and were used in the validation of multipath modelling described in Chapter 4. Another virtual testing site is at the IGS global tracking station LBCH in Long Beach, United States, as shown in Figures 5-2 and 5-3, where no real data contaminated by known multipath were collected.

Figure 5-1: Testing site in LCPC.

The two sites are far away from each other. It aims to provide testing datasets with different satellite geometries and locations. Note that some GNSS satellites can be "seen" in Europe but not in America or vice versa.

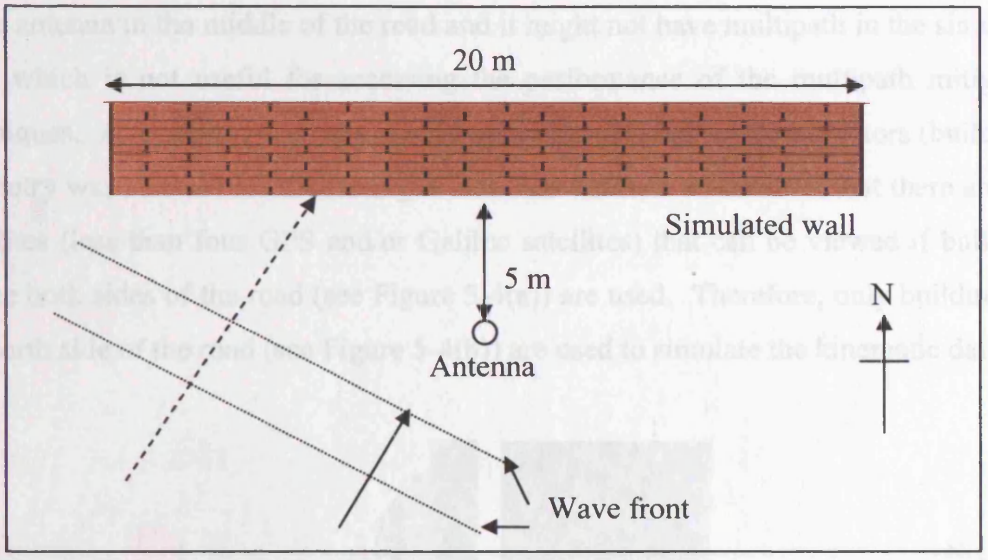

Figure 5-2: Virtual testing site at the IGS tracking station LBCH in Long Beach (Top view).

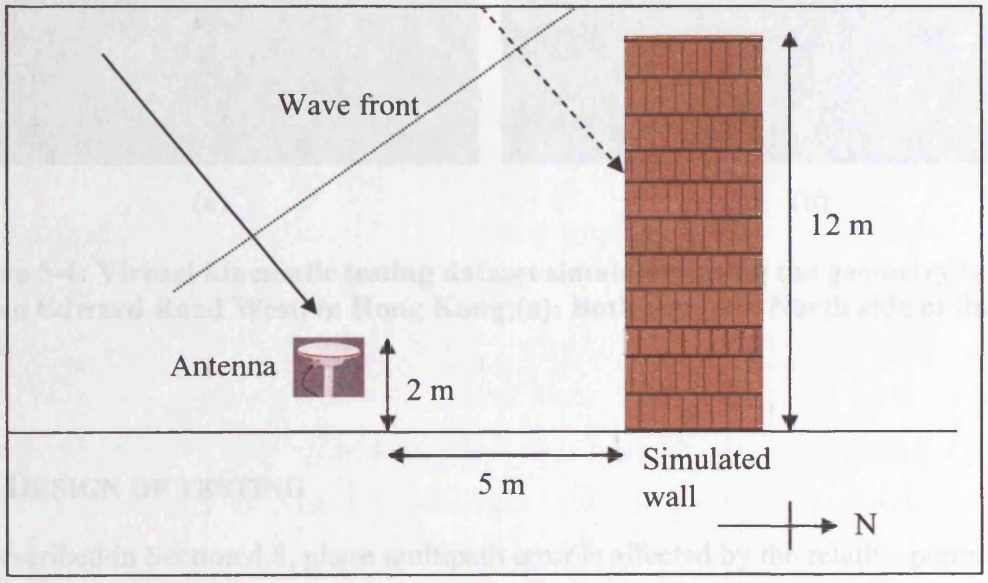

Figure 5-3: Virtual testing site at the IGS tracking station LBCH in Long Beach (Side view).

Furthermore, a road, which is the Prince Edward Road West, in Hong Kong is selected to simulate two kinematic testing datasets for testing the multipath mitigation capabilities of the proposed techniques in rapid change of satellite-reflector-antenna geometry and hence multipath errors. A section of the road is shown in Figure 5-4. As it can be seen in the Figure 5-4, the buildings in the road are not very high and the road is not very narrow when compared with the other areas in Hong Kong. If the buildings were high and the road was narrow, only signal from high elevation angle satellites

could have reflections from the buildings, however, the reflected signal might not arrive at the antenna in the middle of the road and it might not have multipath in the simulated data, which is not useful for accessing the performance of the multipath mitigation techniques. A feasibility test was carried out to check whether the reflectors (buildings) geometry was suitable for the testing or not. However, it was shown that there are few satellites (less than four GPS and/or Galileo satellites) that can be viewed if buildings on the both sides of the road (see Figure 5-4(a)) are used. Therefore, only buildings on the north side of the road (see Figure 5-4(b)) are used to simulate the kinematic datasets.

(a) (b)

Figure 5-4: Virtual kinematic testing dataset simulation using the geometry in the Prince Edward Road West, in Hong Kong;(a): Both side, (b): North side of the road.

5.3 DESIGN OF TESTING

As described in Section 4.8, phase multipath error is affected by the relative permittivity of the reflector and satellite-reflector-antenna geometry, reflectors with different relative permittivities should be considered in the testing datasets. Since the simulated multipath errors in LCPC described in Section 4.7.1 show the maximum magnitude of about +/- 5 mm, it may be too small to show the multipath mitigation capabilities of the proposed multipath detection and rejection techniques in Chapters 7 and 8. It is because the multipath errors are comparable with the double difference random phase measurement noise as shown in Figure 5-4, that multipath errors may be masked by the random noise. Therefore, in addition to the original relative permittivity, higher relative permittivities are used to simulate two additional testing datasets, which are described in Section 5.4. Relative permittivity is affected by the water content and the thickness of

the reflector, for instance, the relative permittivities of different concretes may be varied by the ratio of water, cement, sand and coarse aggregate during production and the thickness of the concrete block [Stavrou and Saunders, 2003]. In the simulation of multipath, standard values of relative permittivities obtained from literature are used.

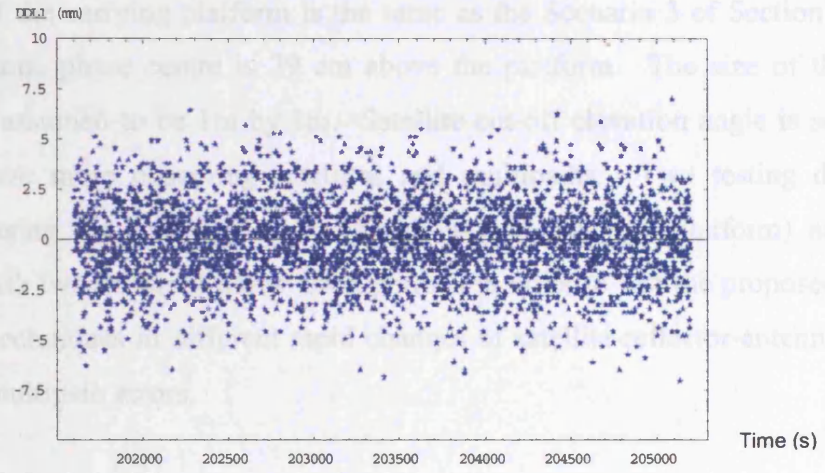

Figure 5-5: Example of double difference noise in simulated L1 phase data of PRN 02 in LCPC dataset.

The selection of static testing sites allows testing of the proposed multipath mitigation techniques in different satellite-reflector-antenna geometries. The distances between the antennas and the reflectors of the static datasets are about five metres because multipath errors from close reflectors are difficult to mitigate by receiver hardware design and hence still cause multipath errors in phase data. Although not a wide variety of reflector-antenna distances are tested in the case of static datasets with a single reflector, the author thinks that the different frequencies of phase multipath errors (low frequency for very close reflector, high frequency for distant reflector) would not affect the performances of the proposed multipath mitigation techniques described in Chapters 6 to 8. This is because the techniques should be able to average or detect different frequencies phase multipath errors without a priori information of antenna-reflector distance. Indeed, the magnitudes of multipath errors affect the performances of the techniques but the magnitudes are affected by the damping factor (relative permittivity is one of the components) as described in Chapter 4 not the reflector-antenna distance.

The satellite-reflector-antenna geometry of the LCPC testing datasets is based on the real setup in the experiment carried out in LCPC as described in Section 4.7.1.

The LBCH testing dataset is a worst case of serious multipath effect and bad geometry. A large wall made of concrete is near the antenna, it blocks almost all satellites in the

northern sky at the antenna position and many satellites from the southern sky at the antenna position have multipath as shown in Figures 5-2 and 5-3.

The kinematic testing datasets contain rapid changes in satellite-reflector-antenna geometry and hence rapid change in multipath errors from relatively distant reflectors. Moreover, multipath from the platform carrying the antenna is considered. The geometry of the carrying platform is the same as the Scenario 3 of Section 4.8, which the L1 antenna phase centre is 29 cm above the platform. The size of the carrying platform is assumed to be 1m by 1m. Satellite cut-off elevation angle is set to 10° in order to have more observing satellites and multipaths. Two testing datasets are simulated using the same reflectors (buildings and carrying platform) and antenna positions with two different observation periods in order to test the proposed multipath mitigation techniques in different rapid changes of satellite-reflector-antenna geometry and hence multipath errors.

5.4 DESCRIPTION OF TESTING DATASETS

Description of the LCPC testing datasets is the same as the description in the experiment in LCPC, which is described in Section 4.7.1, except the relative permittivity of the reflector in two of the three datasets. The antenna-reflector geometry is shown in Figure 5-6. As explained in Section 5.3, reflectors with the original relative permittivity of 3.9 (sand casting carbon steel) and the assumed higher relative permittivities of 10 (flint glass) and 20 (Hafnium oxides HfO_2) are used in multipath simulation. Therefore, the testing datasets are denoted as LCPC-3.9, LCPC-10 and LCPC-20 according to the relative permittivity used. The simulated observation period in GPS seconds is from 201600 to 205199 in the GPS week of 1168. The baseline length is about 86 m. The information used in multipath simulation is summarised in Table 5-1. The sky plot of the satellites-reflector-antenna geometry is shown in Figure 5-7. Moreover, the information about multipathing satellites is shown in Table 5-2 and the simulated multipath errors of the multipathing satellites of the LCPC-3.9, LCPC-10, and LCPC-20 datasets are plotted in Figures 5-8 to 5-11, 5-12 to 5-15, and E-1 to E-4 respectively. Note that the figures show the simulated multipath errors only, random measurement noises are generated in another module/step.

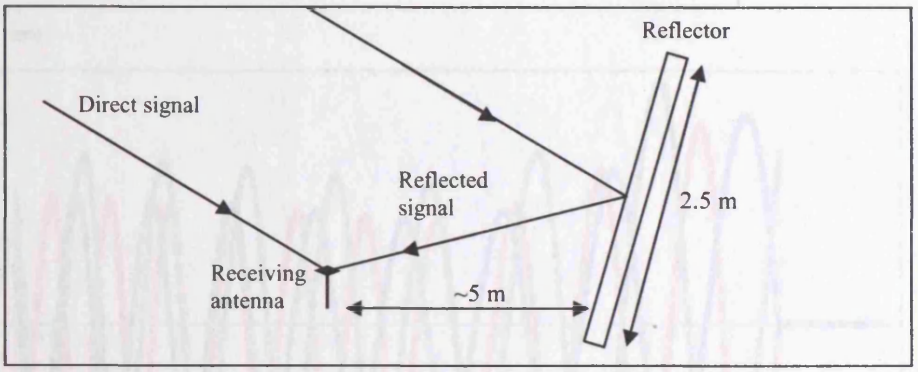

Figure 5-6: Diagram showing the geometry of the LCPC testing datasets.

Table 5-1: Information for multipath simulation in the static testing datasets.

Dataset	Distance	Reflector angle	Material	RP	Mask angle (°)
LCPC-3.9	~5m	Tilted	Sand casting carbon steel	3.9	15
LCPC-10	~ 5 m	Tilted	Flint glass	10	15
LCPC-20	~ 5m	Tilted	Hafnium oxides	20	15
LBCH-7	5 m	Vertical	Concrete	7	15

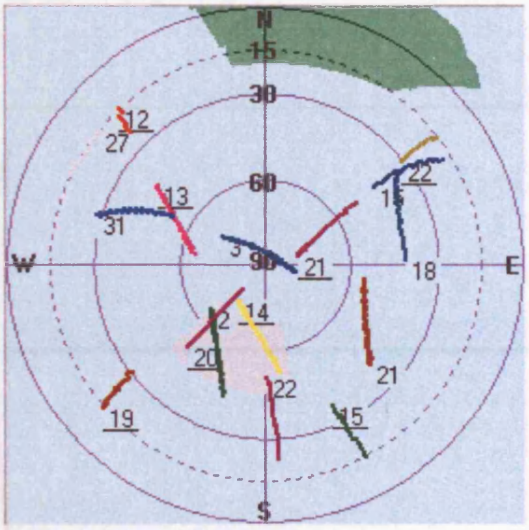

Figure 5-7: Sky plot of Galileo (underlined) and GPS satellites in the LCPC datasets; the green area represents the reflector; the grey area indicates that the data from the satellites in this area are contaminated by multipath in this antenna-reflector geometry.

Table 5-2: Multipathing satellite information in the static testing datasets.

	Multipathing satellites (PRN/SV ID)		Number of available satellites at epochs	Number of multipathing satellites
Dataset	GPS	Galileo		
LCPC-3.9	2, 22	14, 20	13 - 15	4
LCPC-10	2, 22	14, 20	13 - 15	4
LCPC-20	2, 22	14, 20	13 - 15	4
LBCH-7	7, 13, 31	17, 18, 22, 23	14 - 17	7

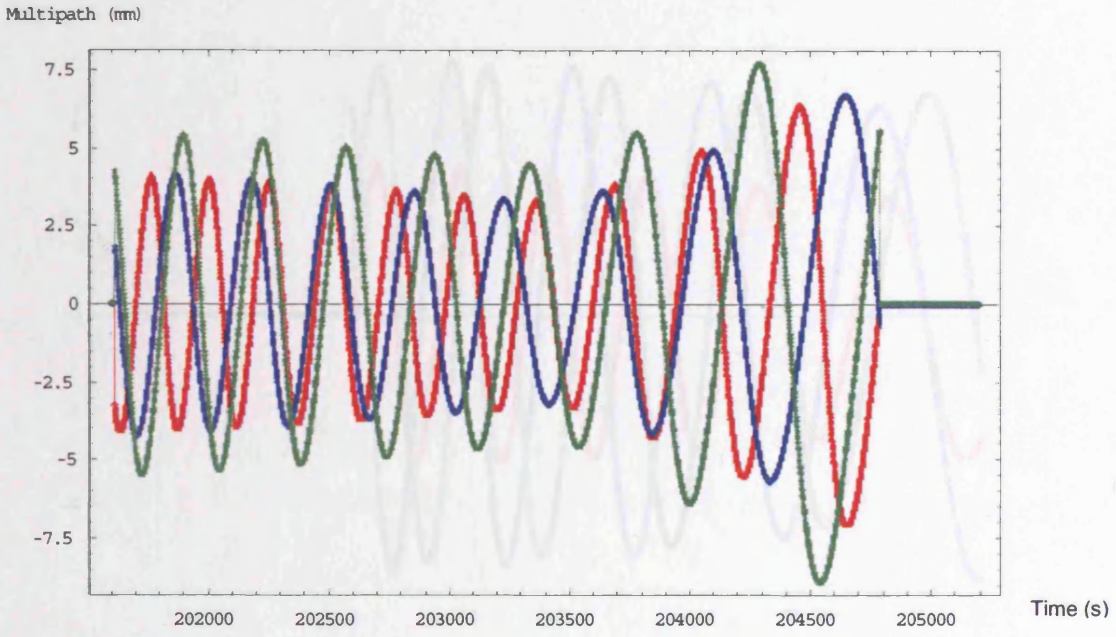

Figure 5-8: Simulated GPS three-frequency (red: L1, blue: L2, green: L5) multipath error in PRN02 of LCPC-3.9 dataset.

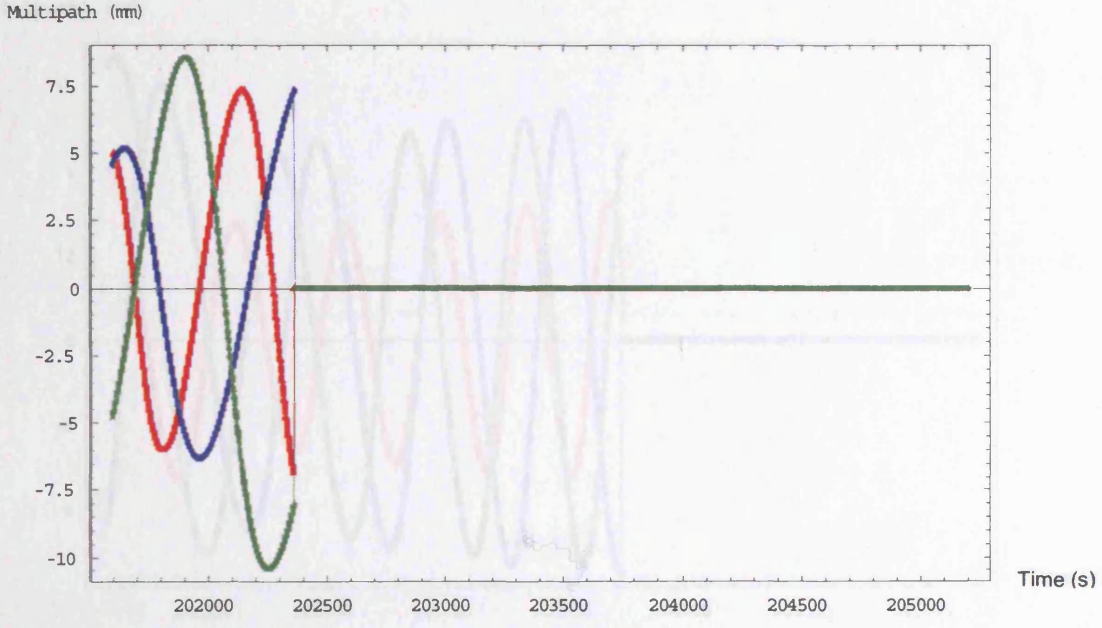

Figure 5-9: Simulated GPS three-frequency (red: L1, blue: L2, green: L5) multipath error in PRN22 of LCPC-3.9 dataset.

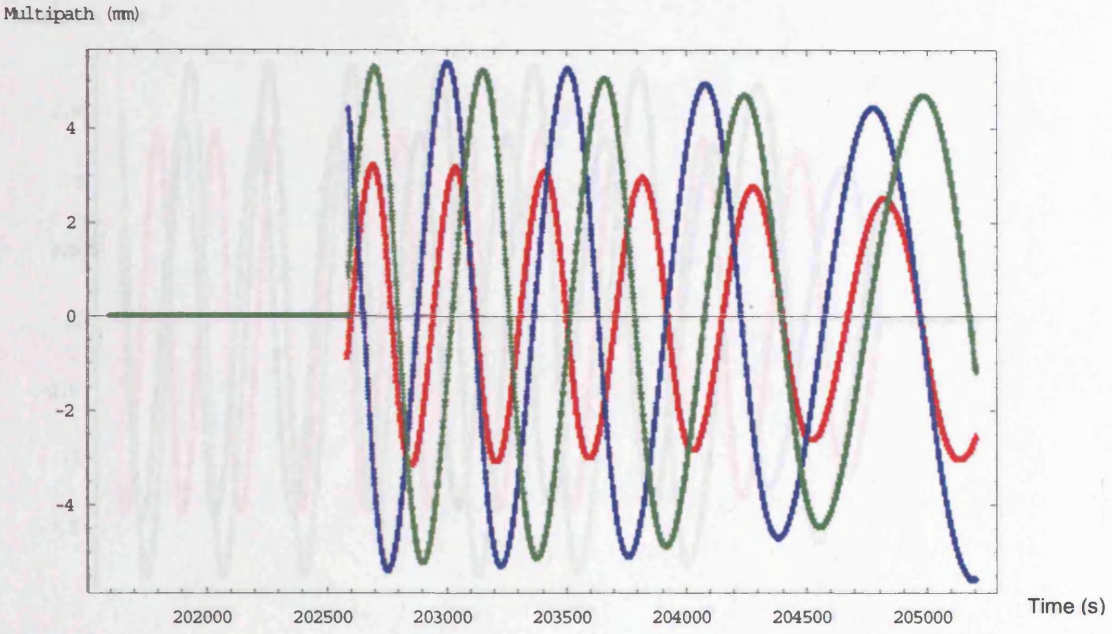

Figure 5-10: Simulated Galileo three-frequency (red: L1, blue: E5a, green: E5b) multipath error in SV14 of LCPC-3.9 dataset.

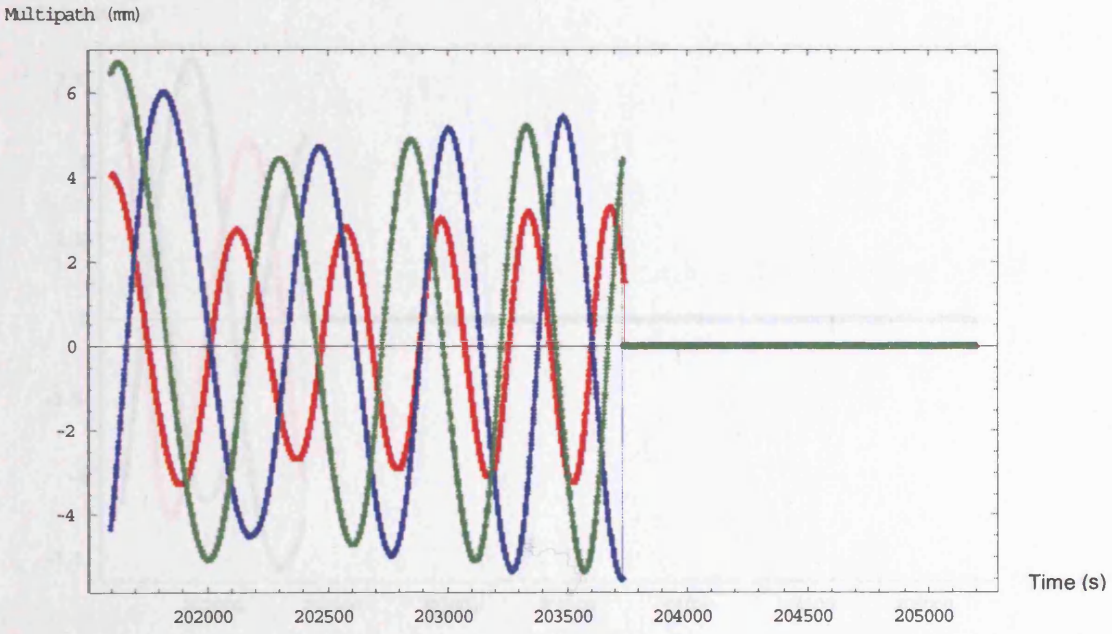

Figure 5-11: Simulated Galileo three-frequency (red: L1, blue: E5a, green: E5b) multipath error in SV20 of LCPC-3.9 dataset.

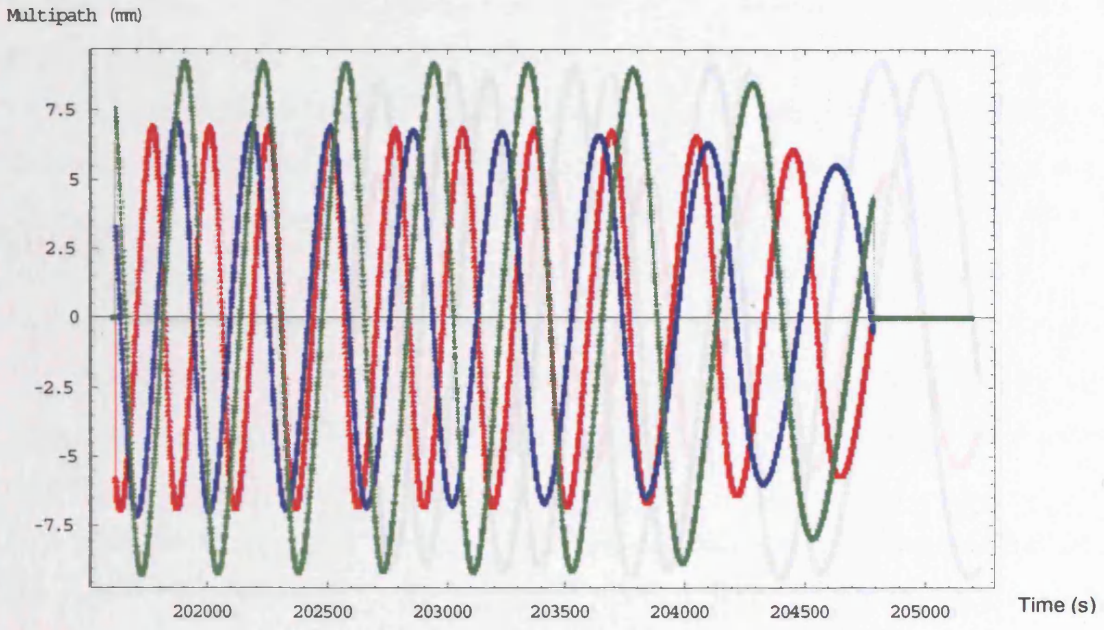

Figure 5-12: Simulated GPS three-frequency (red: L1, blue: L2, green: L5) multipath error in PRN02 of LCPC-10 dataset.

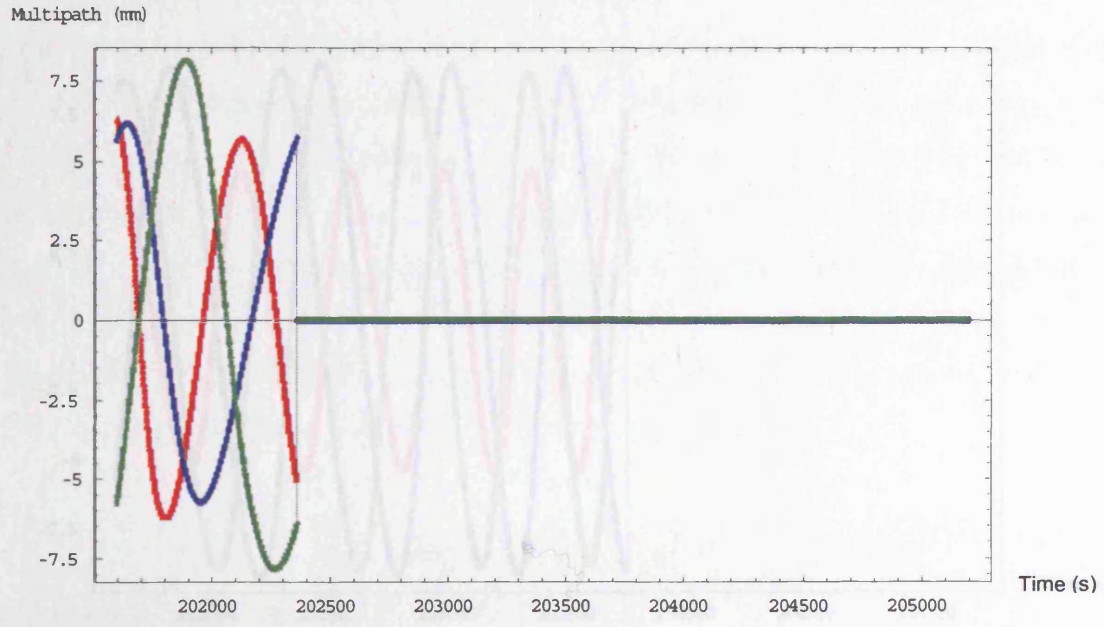

Figure 5-13: Simulated GPS three-frequency (red: L1, blue: L2, green: L5) multipath error in PRN22 of LCPC-10 dataset.

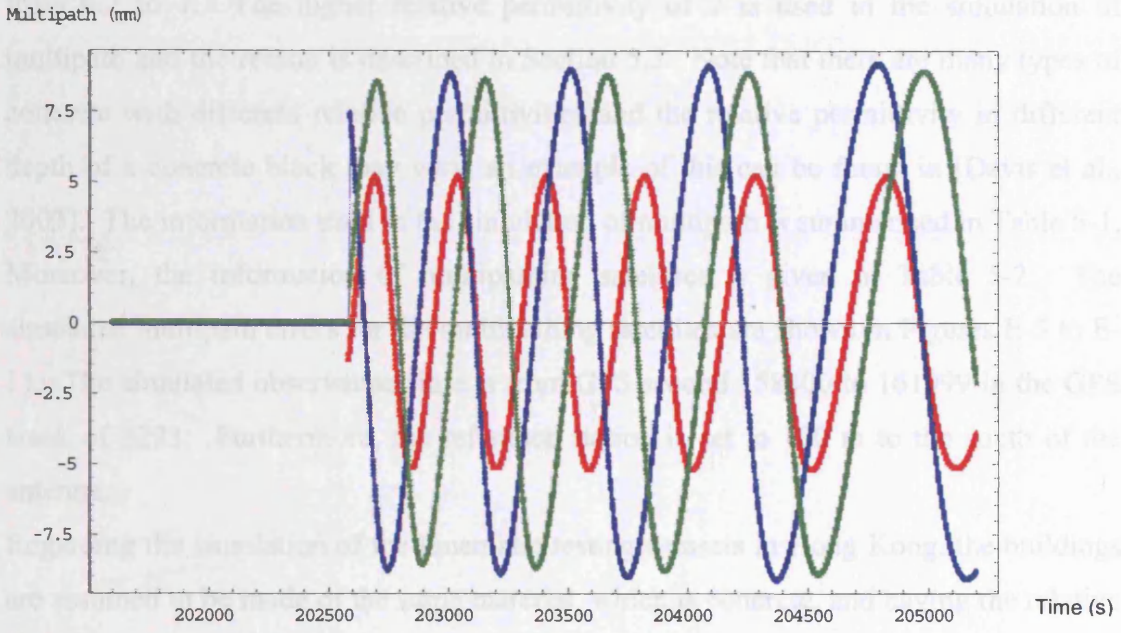

Figure 5-14: Simulated Galileo three-frequency (red: L1, blue: E5a, green: E5b) multipath error in SV14 of LCPC-10 dataset.

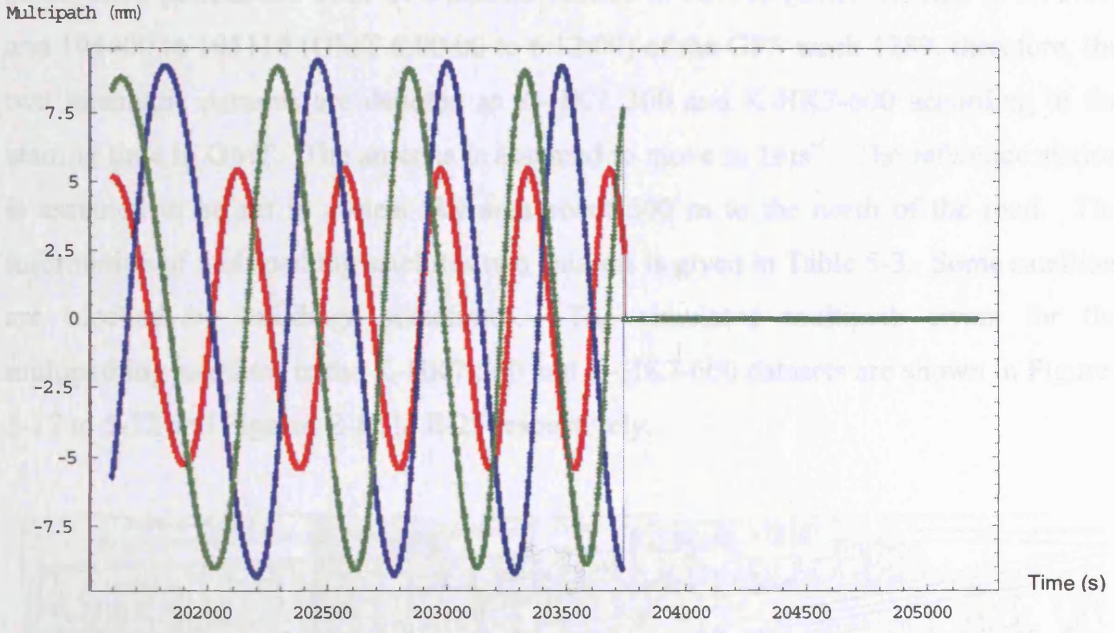

Figure 5-15: Simulated Galileo three-frequency (red: L1, blue: E5a, green: E5b) multipath error in SV20 of LCPC-10 dataset.

In the LBCH testing dataset, the wall (reflector) is set to the north of the antenna. The distance between the wall and antenna is 5 m as shown in Figures 5-2 and 5-3. It assumes that the wall is made of concrete. Stavrou and Saunders (2003) describes that the real part of the complex permittivity in the range of 1 to 95.9 GHz was found to vary

from 6.2 to 7. The higher relative permittivity of 7 is used in the simulation of multipath and the reason is described in Section 5.3. Note that there are many types of concrete with different relative permittivities and the relative permittivity in different depth of a concrete block may vary, an example of this can be found in [Davis et al., 2003]. The information used in the simulation of multipath is summarised in Table 5-1. Moreover, the information of multipathing satellites is given in Table 5-2. The simulated multipath errors for the multipathing satellites are shown in Figures E-5 to E-11. The simulated observation time is from GPS second 158400 to 161999 in the GPS week of 1293. Furthermore, the reference station is set to 100 m to the south of the antenna.

Regarding the simulation of the kinematic testing datasets in Hong Kong, the buildings are assumed to be made of the same material, which is concrete, and having the relative permittivity of 7. Therefore, these datasets are denoted as K-HK7. The trajectory is shown as the blue line in Figure 5-16, where the geometry of the buildings and trajectory are also shown. The length of the trajectory is 720 m. The simulated observation periods are from GPS second 183600 to 184319 (GMT 3:00:00 to 3:12:00) and 194400 to 195119 (GMT 6:00:00 to 6:12:00) of the GPS week 1289, therefore, the two kinematic datasets are denoted as K-HK7_300 and K-HK7-600 according to the starting time in GMT. The antenna is assumed to move in $1 ms^{-1}$. The reference station is assumed to be set in a clear sky area about 500 m to the north of the road. The information of multipathing satellites two datasets is given in Table 5-3. Some satellites are blocked by buildings sometimes. The simulated multipath errors for the multipathing satellites in the K-HK7-300 and K-HK7-600 datasets are shown in Figures 5-17 to 5-32 and Figures E-12 to E-25 respectively.

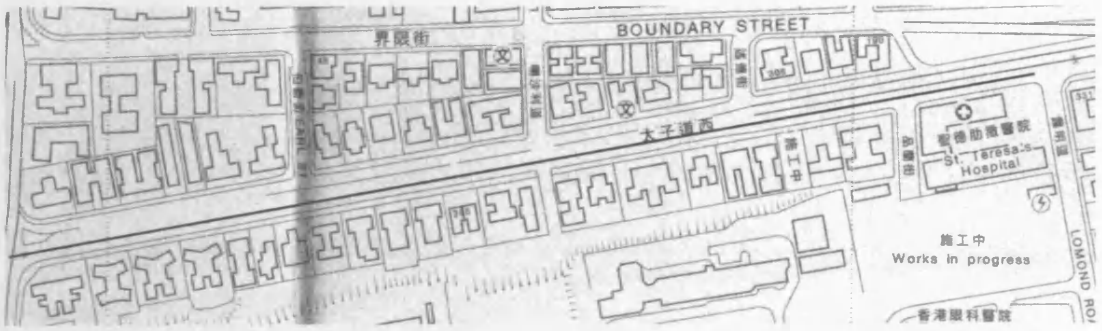

Figure 5-16: Diagram showing the known trajectory and reflector-antenna (kinematic) geometry for the kinematic testing dataset K-HK7.

Table 5-3: Multipathing satellite information in the kinematic testing datasets.

	Multipathing satellites (PRN/SV ID)		Number of available satellites	Number of multipathing satellites
Dataset	GPS	Galileo		
K-HK7-300	5, 6, 14, 15, 18, 22, 25, 30	4, 5, 6, 7, 24, 25, 26, 27	12 - 16	16
K-HK7-600	1, 3, 6, 14, 16, 20, 23, 25	3, 4, 5, 23, 24, 25	8 - 14	14

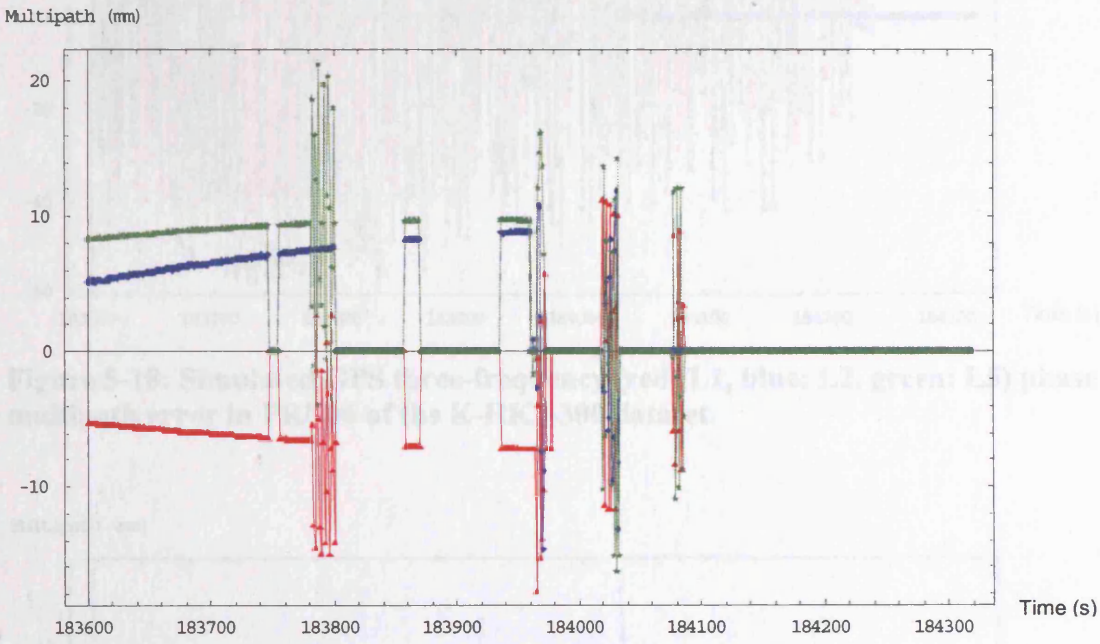

Figure 5-17: Simulated GPS three-frequency (red: L1, blue: L2, green: L5) phase multipath error in PRN05 of the K-HK7-300 dataset.

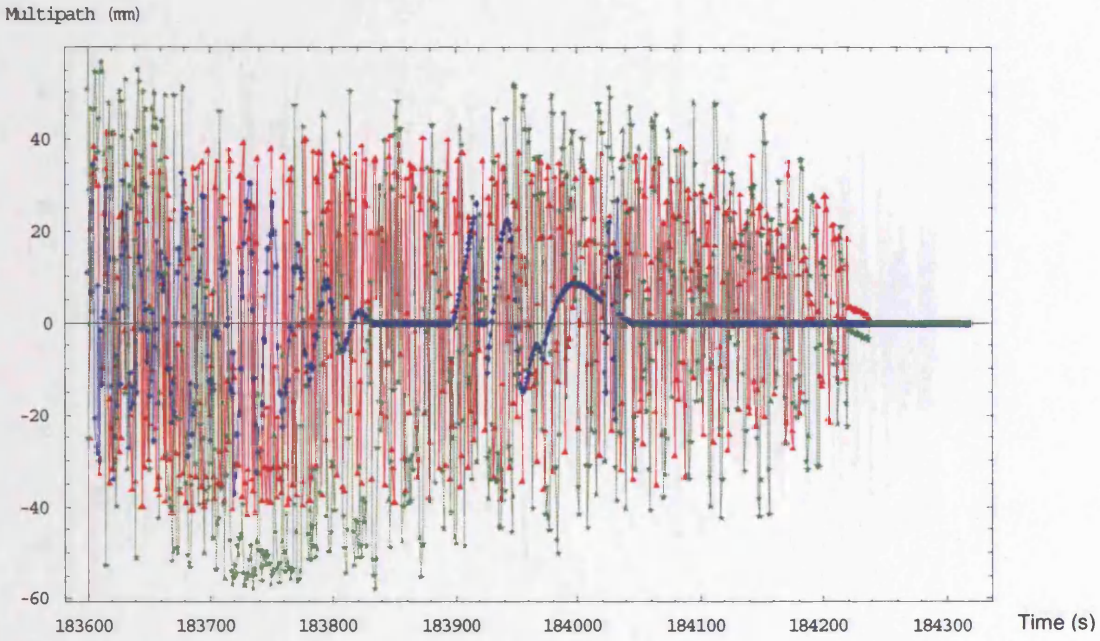

Figure 5-18: Simulated GPS three-frequency (red: L1, blue: L2, green: L5) phase multipath error in PRN06 of the K-HK7-300 dataset.

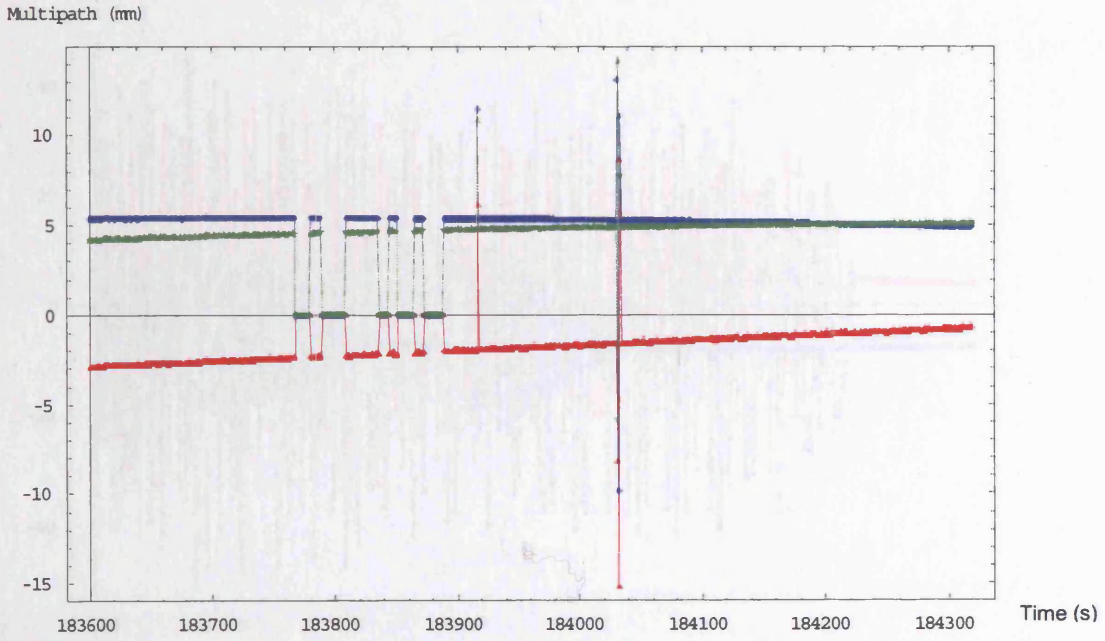

Figure 5-19: Simulated GPS three-frequency (red: L1, blue: L2, green: L5) phase multipath error in PRN14 of the K-HK7-300 dataset.

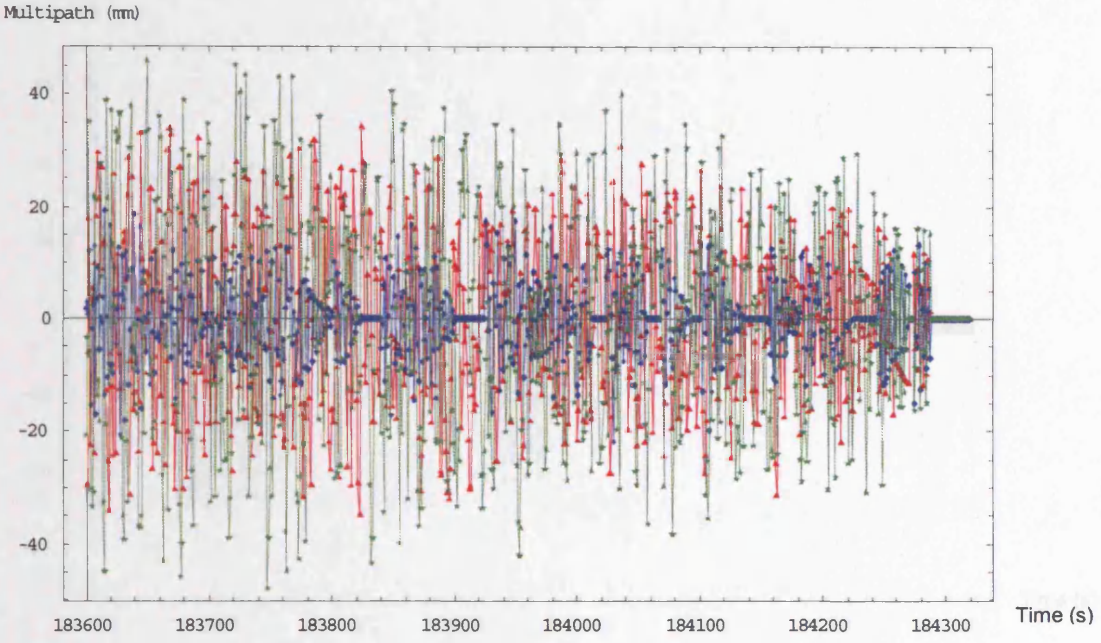

Figure 5-20: Simulated GPS three-frequency (red: L1, blue: L2, green: L5) phase multipath error in PRN15 of the K-HK7-300 dataset.

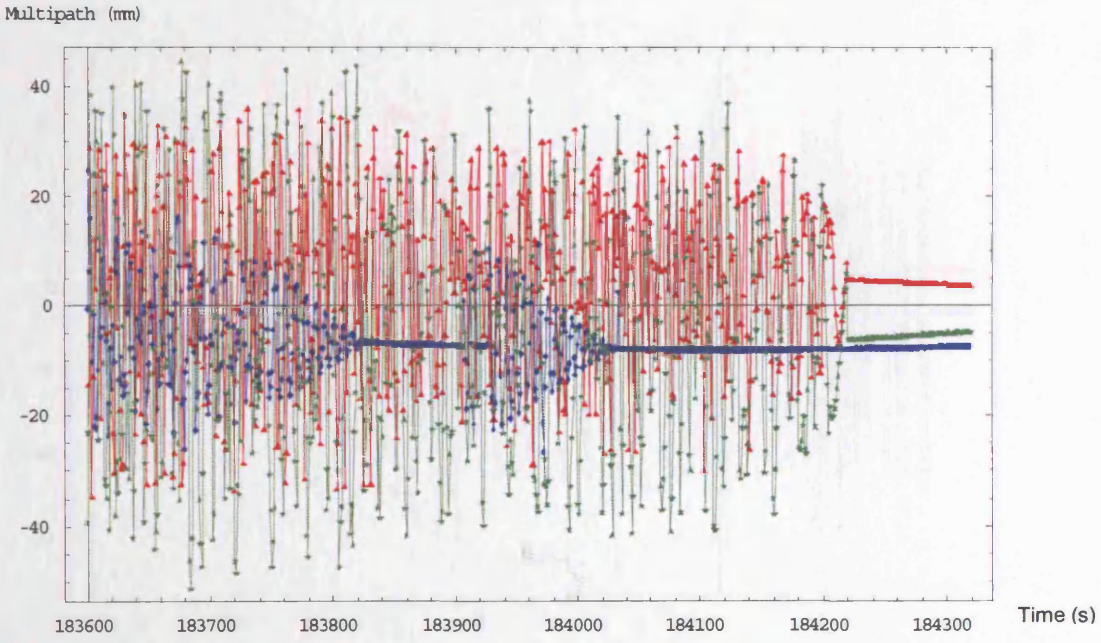

Figure 5-21: Simulated GPS three-frequency (red: L1, blue: L2, green: L5) phase multipath error in PRN18 of the K-HK7-300 dataset.

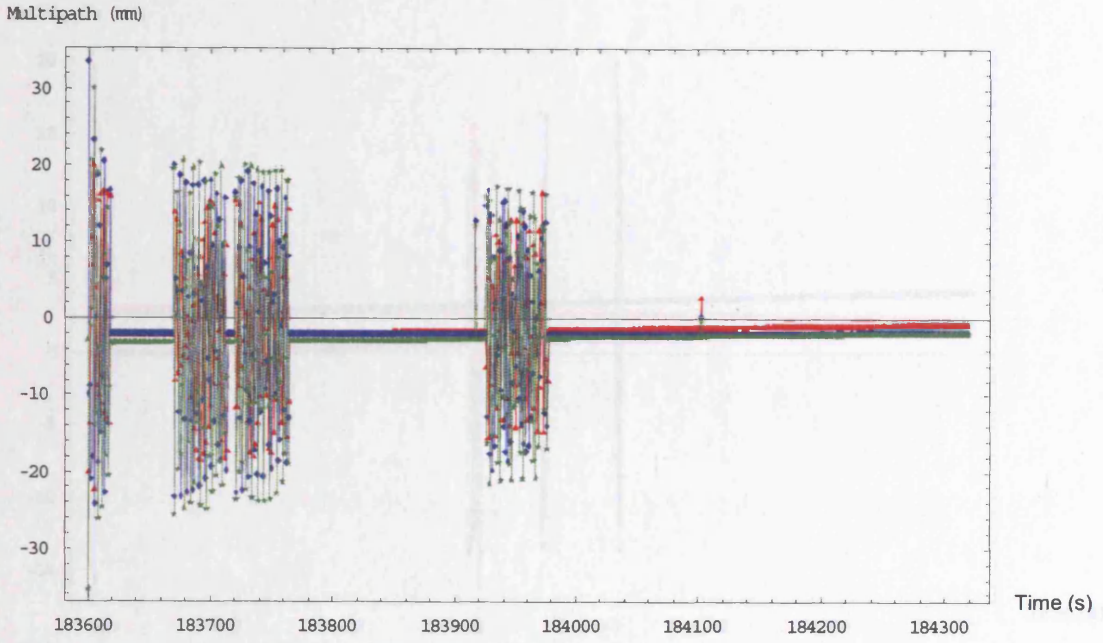

Figure 5-22: Simulated GPS three-frequency (red: L1, blue: L2, green: L5) phase multipath error in PRN22 of the K-HK7-300 dataset.

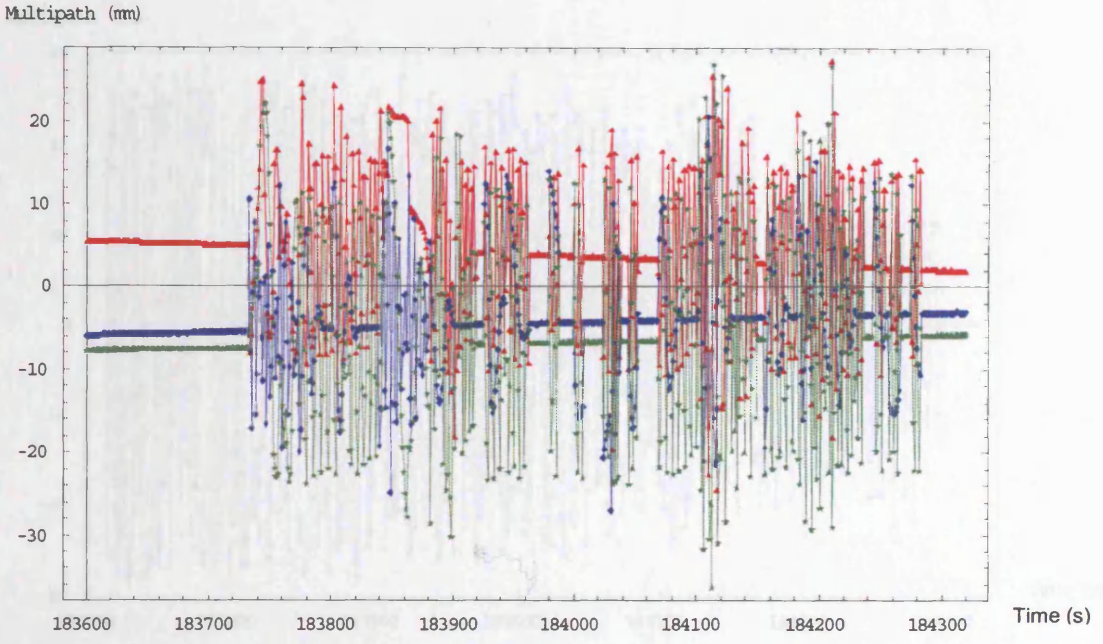

Figure 5-23: Simulated GPS three-frequency (red: L1, blue: L2, green: L5) phase multipath error in PRN25 of the K-HK7-300 dataset.

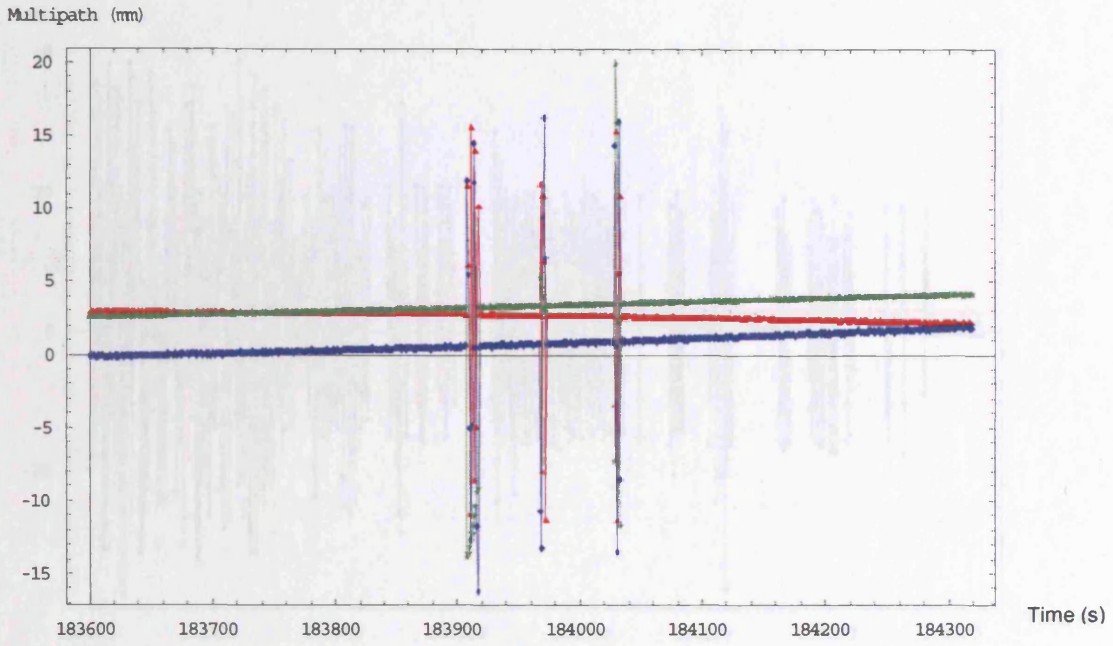

Figure 5-24: Simulated GPS three-frequency (red: L1, blue: L2, green: L5) phase multipath error in PRN30 of the K-HK7-300 dataset.

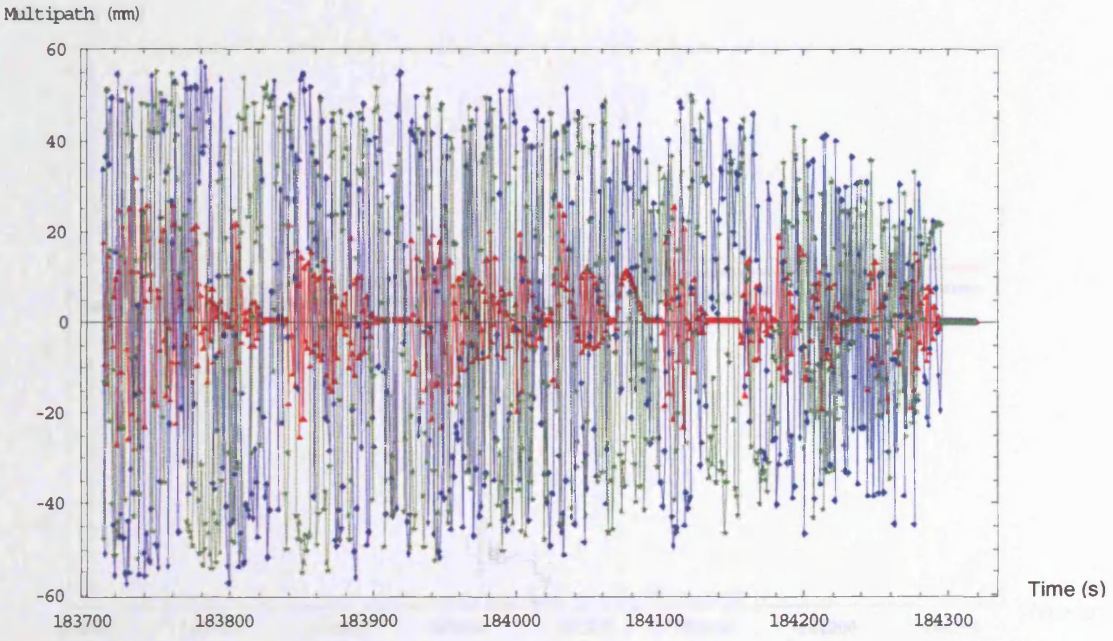

Figure 5-25: Simulated Galileo three-frequency (red: L1, blue: E5a, green: E5b) phase multipath error in SV04 of the K-HK7-300 dataset.

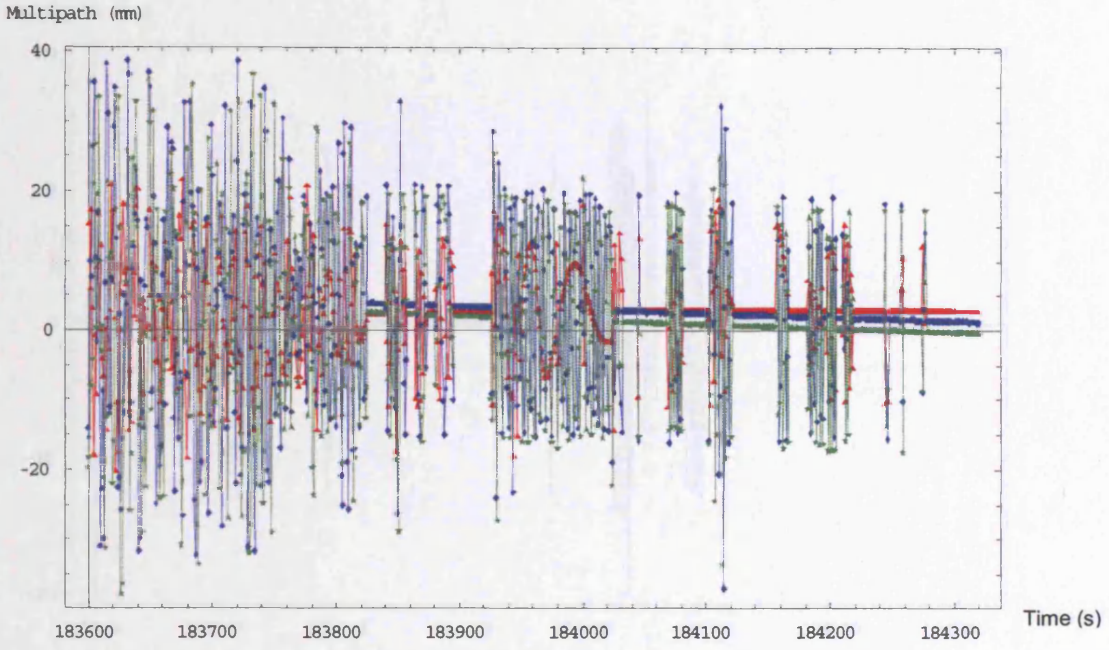

Figure 5-26: Simulated Galileo three-frequency (red: L1, blue: E5a, green: E5b) phase multipath error in SV05 of the K-HK7-300 dataset.

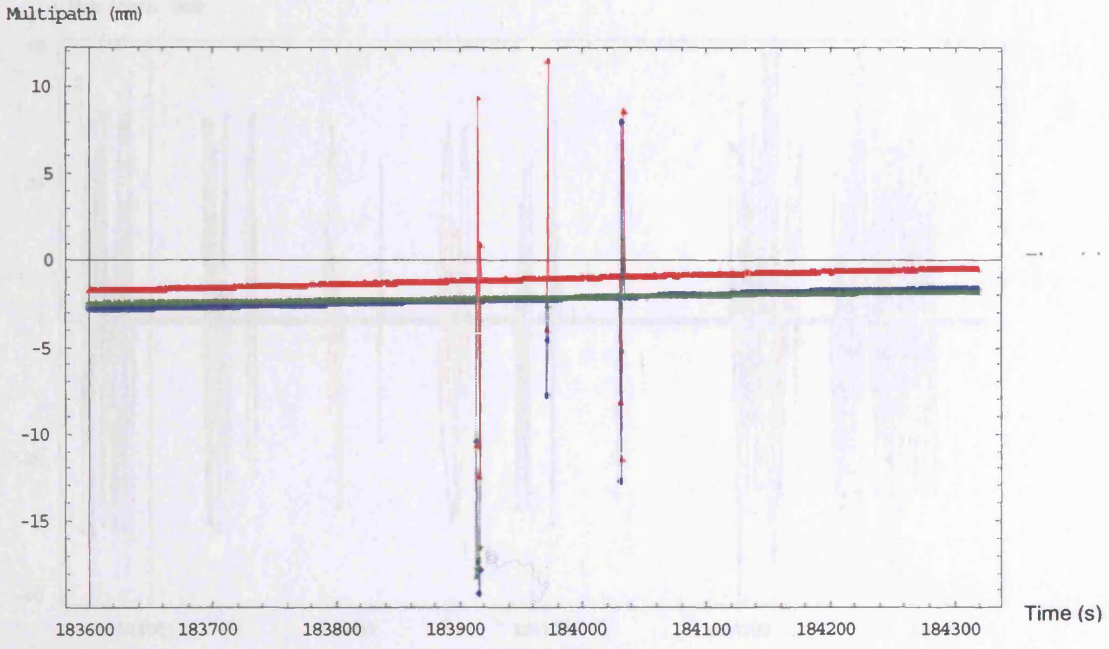

Figure 5-27: Simulated Galileo three-frequency (red: L1, blue: E5a, green: E5b) phase multipath error in SV06 of the K-HK7-300 dataset.

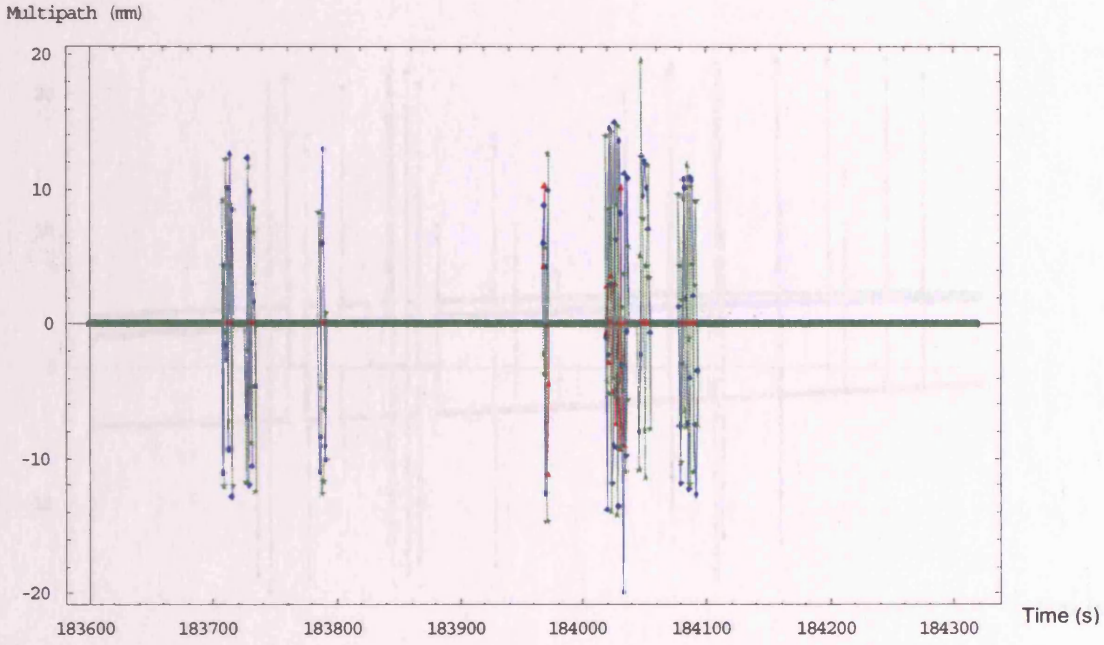

Figure 5-28: Simulated Galileo three-frequency (red: L1, blue: E5a, green: E5b) phase multipath error in SV07 of the K-HK7-300 dataset.

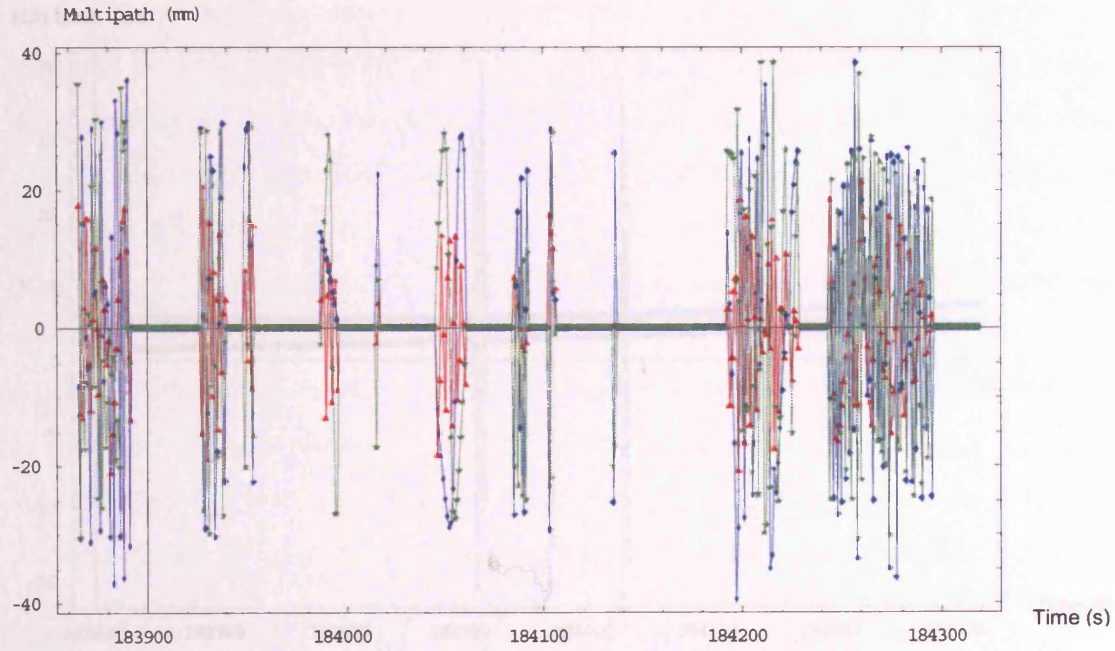

Figure 5-29: Simulated Galileo three-frequency (red: L1, blue: E5a, green: E5b) phase multipath error in SV24 of the K-HK7-300 dataset.

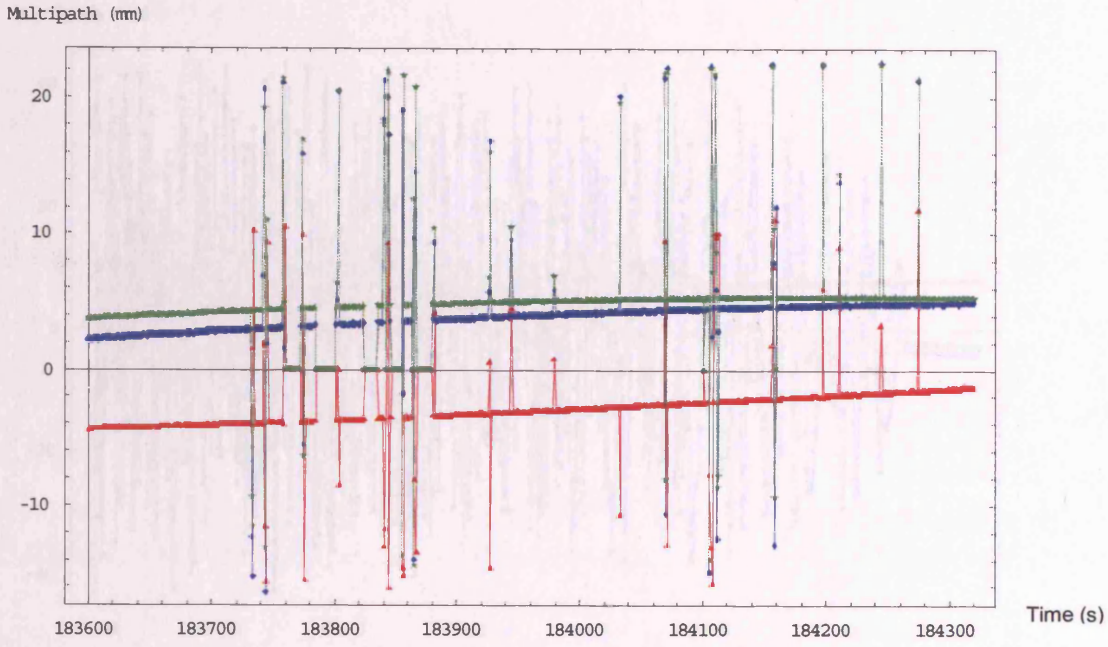

Figure 5-30: Simulated Galileo three-frequency (red: L1, blue: E5a, green: E5b) phase multipath error in SV25 of the K-HK7-300 dataset.

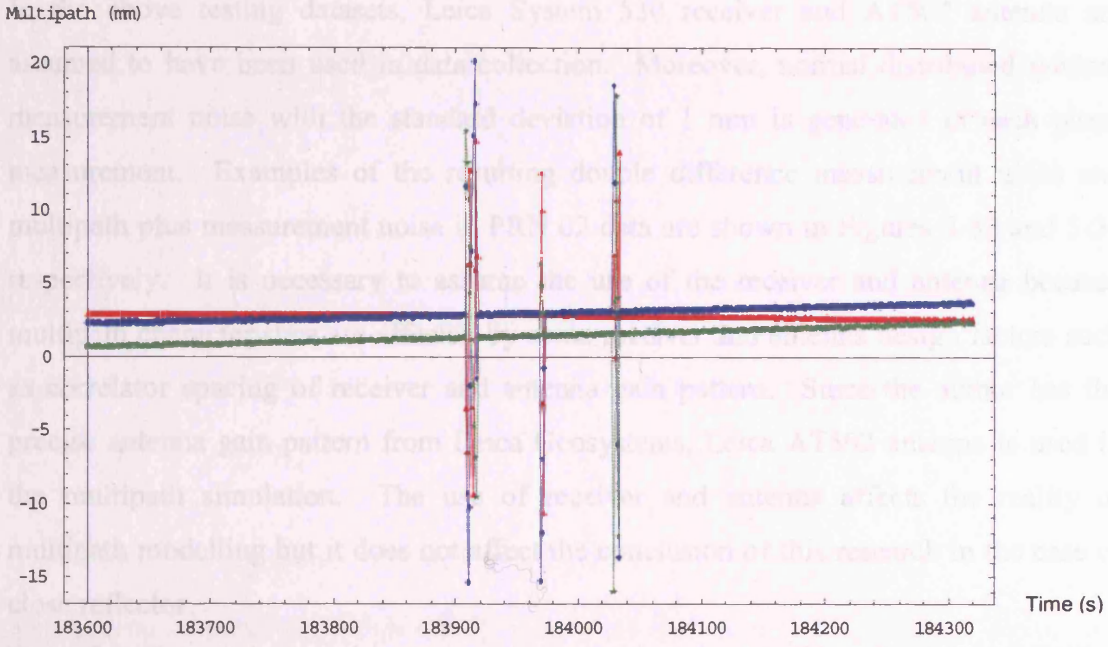

Figure 5-31: Simulated Galileo three-frequency (red: L1, blue: E5a, green: E5b) phase multipath error in SV26 of the K-HK7-300 dataset.

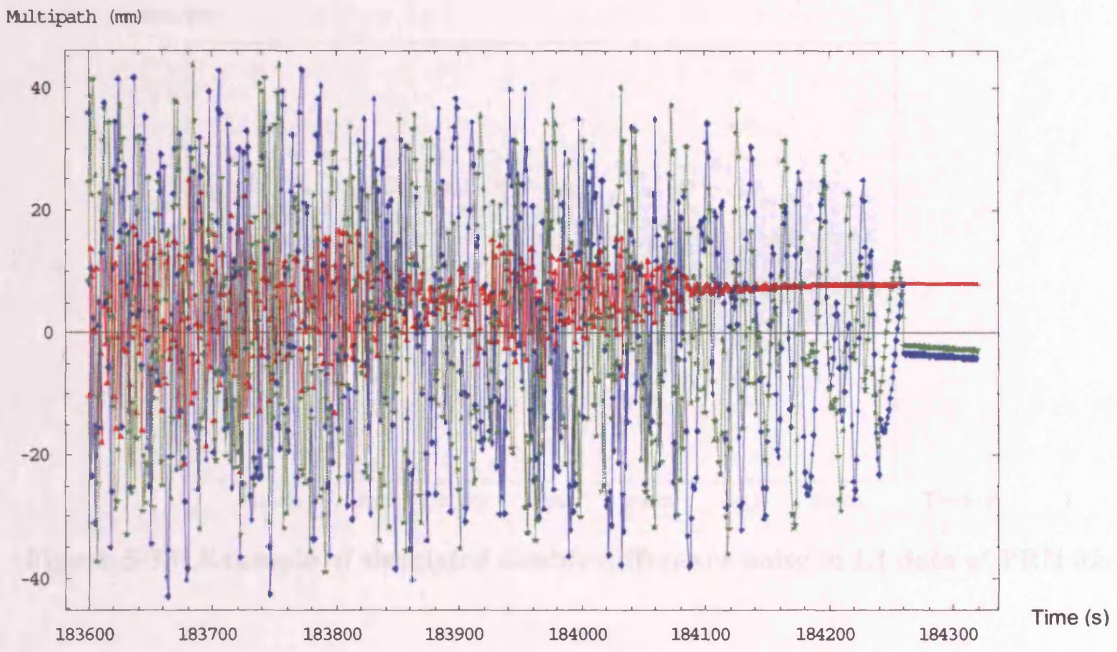

Figure 5-32: Simulated Galileo three-frequency (red: L1, blue: E5a, green: E5b) phase multipath error in SV27 of the K-HK7-300 dataset.

In the above testing datasets, Leica System 530 receiver and AT502 antenna are assumed to have been used in data collection. Moreover, normal distributed random measurement noise with the standard deviation of 1 mm is generated in each phase measurement. Examples of the resulting double difference measurement noise and multipath plus measurement noise in PRN 02 data are shown in Figures 5-33 and 5-34 respectively. It is necessary to assume the use of the receiver and antenna because multipath characteristics are affected by some receiver and antenna design factors such as correlator spacing of receiver and antenna gain pattern. Since the author has the precise antenna gain pattern from Leica Geosystems, Leica AT502 antenna is used in the multipath simulation. The use of receiver and antenna affects the reality of multipath modelling but it does not affect the conclusion of this research in the case of close reflector.

Note that the receiver and antenna are assumed to be capable of receiving Galileo signals, which assumption is described in Sections 3.2 and 3.3.

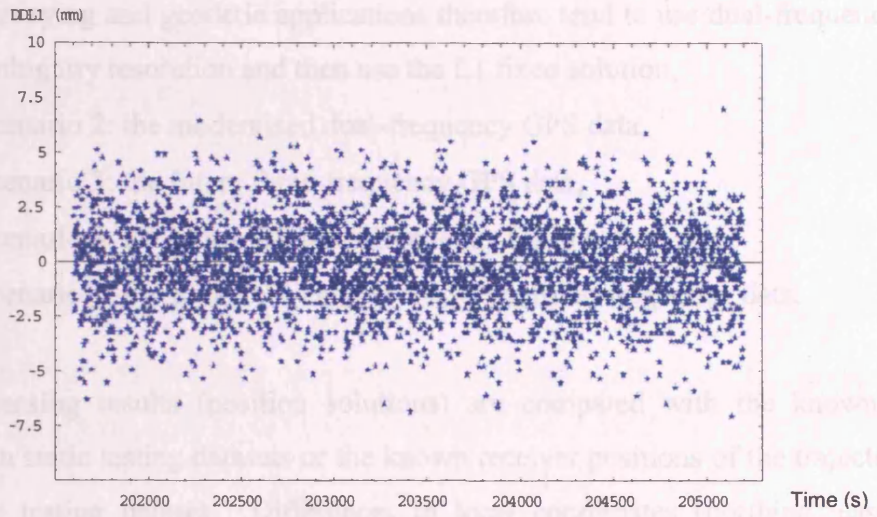

Figure 5-33: Example of simulated double difference noise in L1 data of PRN 02.

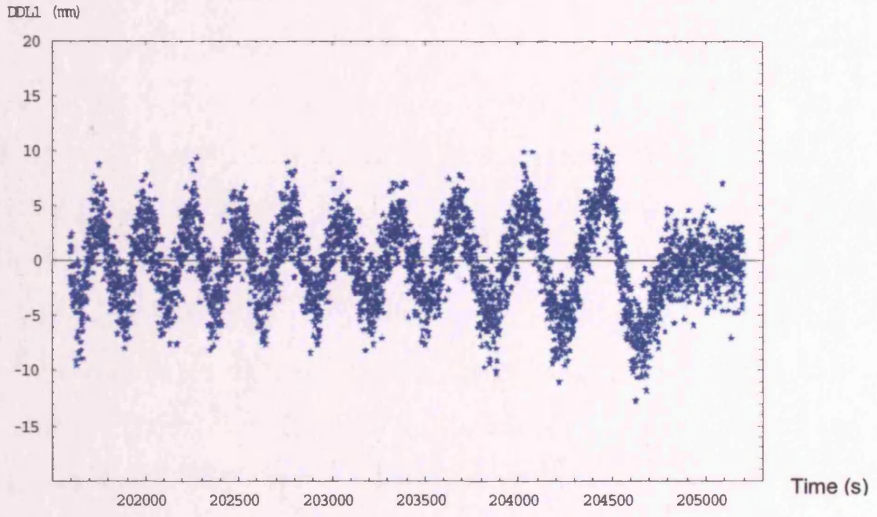

Figure 5-34: Example of double difference multipath and noise in L1 data of PRN 02.

5.5 TESTING METHODOLOGY

The testing datasets are processed by the proposed multipath mitigation techniques described in Chapters 6-8. In order to investigate the impact of multipath on GNSS multiple-frequency data, five scenarios with different GNSS or combinations of frequencies are tested:

- Scenario 1: the current single-frequency GPS data; although the current GPS provides dual-frequency data, L2 data are relatively weaker and noisier and most

surveying and geodetic applications therefore tend to use dual-frequency data in ambiguity resolution and then use the L1 fixed solution,

- Scenario 2: the modernised dual-frequency GPS data,
- Scenario 3: the future three-frequency GPS data,
- Scenario 4: the future OS three-frequency Galileo data, and
- Scenario 5: the future OS Galileo + GPS multiple-frequency data.

The processing results (position solutions) are compared with the known receiver position in static testing datasets or the known receiver positions of the trajectory in the kinematic testing dataset. Differences in local coordinates (northing, easting, and height) and their statistical results are then analysed.

6. MULTIPATH MITIGATION USING MULTIPLE FREQUENCY GNSS DATA

6.1 INTRODUCTION

This chapter investigates the impact of modernised GPS signals, European GNSS (named Galileo) multiple signals, and the combined Galileo and GPS multiple signals on precise carrier phase-based positioning in the presence of multipath.

As described in Chapter 2, GPS modernisation includes enhancements to the current L2 signal and a new L5 signal, and Galileo will provide L1, E5a, E5b, and E6 signals. It offers many different opportunities for the improvement of precise carrier phase GNSS. The most significant of these will arise from the use of all available data from all frequencies. This is the motivation of this chapter to investigate the potential of multiple-frequency data processing algorithm to mitigate multipath. Positioning accuracies using different GNSS and combined GNSS data in the presence of multipath are investigated. In order to do this a GNSS data processing program has been developed to treat the different GNSS data in this investigation. The program is based on the well-known double-difference single-epoch least squares approach.

Since multipath effects on different frequencies are different, improvement on the positioning accuracy for future multiple-frequency carrier phase-based precise positioning is tested. This is due to the fact that more redundancy leads to better averaging within the least squares process resulting in multiple-frequency GNSS having the potential for greater multipath mitigation than is the case with the current system [Lau and Cross, 2003]. This point has so far received very little attention in the literature, which has tended to concentrate on the use of the multiple-frequency for improved ambiguity determination.

Section 6.2 describes the details of the data processing using multiple-frequency GNSS data, the testing scenarios of different GNSS and frequencies are described. Results of the testing scenarios and their analyses are given in Section 6.3. Finally, some concluding remarks on the impact of multiple-frequency GNSS data on multipath mitigation are stated in Section 6.4.

6.2 PROCESSING OF GNSS MULTIPLE-FREQUENCY DATA

In order to carry out the investigation in this chapter, a GNSS data processing program has been developed to process the different combinations of GNSS data including single-, dual- and three-frequency Galileo or GPS data, and Galileo + GPS multiple-frequency data as described in Section 5.5. The program is based on the double-difference single-epoch least squares solution described, for instance in [Corbett and Cross, 1995].

The GNSS data processing program contains a pre-processing module to determine receiver position, receiver clock bias, and satellite coordinates at the time of signal transmission by using the standard single point positioning solution. When processing of Galileo + GPS data, two receiver clock biases are estimated, one for Galileo System Time (GST) and another for GPS time. This operation can compensate the time offset between the two GNSS reference time systems. In the future, GST offset parameters relating to another universal time system will be given in navigation data. It is similar to GPS in that the offset parameters relating GPS time (maintained by the master control station of the control segment) to Universal Coordinated Time (U.S. Naval Observatory) in 90 nanoseconds (one sigma) are given in navigation data. This relation can be found in [ICD-GPS-200C, 2003]. Therefore, synchronisation of GST and GPS time will be trivial in the user segment and GNSS data processing software because alignment of one GNSS reference time to another can be easily done by applying the time relation parameters in navigation data. Moreover, the current GPS reference frame (WGS-84) is tied the International Terrestrial Reference Frame (ITRF), and the future Galileo Terrestrial Reference Frame (GTRF) will be tied to the ITRF. The datum problem between Galileo and GPS will become insignificant in the user segment, Hein et al. (2003) describes that WGS-84 and GTRF will be practically identical within the accuracy available from both realisations of ITRF. Therefore, the author does not believe that the simulated Galileo data referenced to GPS time and WGS-84 datum have a significant impact on the overall conclusions of this investigation and investigations in this chapter and Chapters 7 and 8.

The double-difference technique in the main module of the data processing program eliminates almost all GNSS biases and errors in common to receivers over short to medium baselines. However, multipath errors are not common to receivers, even over very short baselines. In order to investigate the impact of multipath on GNSS multiple-frequency data, the five scenarios described in Section 5.5 with different GNSS or

combinations of frequencies are tested. Testing datasets described in Chapter 5 are used to test the scenarios. The processing results of these scenarios are given in next section.

6.3 Result of Multiple frequencies GNSS data processing and Analysis

6.3.1 LCPC-3.9 testing dataset

Positioning errors from single epoch solutions in nothing, easting, and height for scenarios 1 to 5 of LCPC-3.9 dataset are shown in Figures 6-1 to 6-5, respectively. RMS errors of the positioning errors in northing, easting, height, and 3D position are tabulated in Table 6-1. Note that Figures 6-1 and 6-2 are different to Figures 4-21 and 4-22 respectively apart from measurement noise because multipath effect from one satellite is investigated in the validation of the multipath modelling in Section 4.7.1. Therefore, only seven GPS satellites (PRN22 is ignored because its data was contaminated by multipath in the beginning 800 seconds of the observation window, see Figures 4-23 and 5-7) are processed in Section 4.7.1.2. However, simulated data from eight GPS satellites are processed in this section.

Table 6-1: RMS positioning errors in millimetres and percentage improvement of the testing scenarios in LCPC-3.9 dataset.

Scenario	N	E	H	3D	% improvement
1: Single-frequency GPS	1.490	1.238	3.306	3.832	-
2: Dual-frequency GPS	1.083	0.852	2.290	2.672	30
3: Three-frequency GPS	0.880	0.702	1.967	2.266	41
4: Three-frequency Galileo	0.888	0.928	1.750	2.171	43
5: Multiple-frequency GPS+Galileo	0.662	0.482	1.151	1.413	63

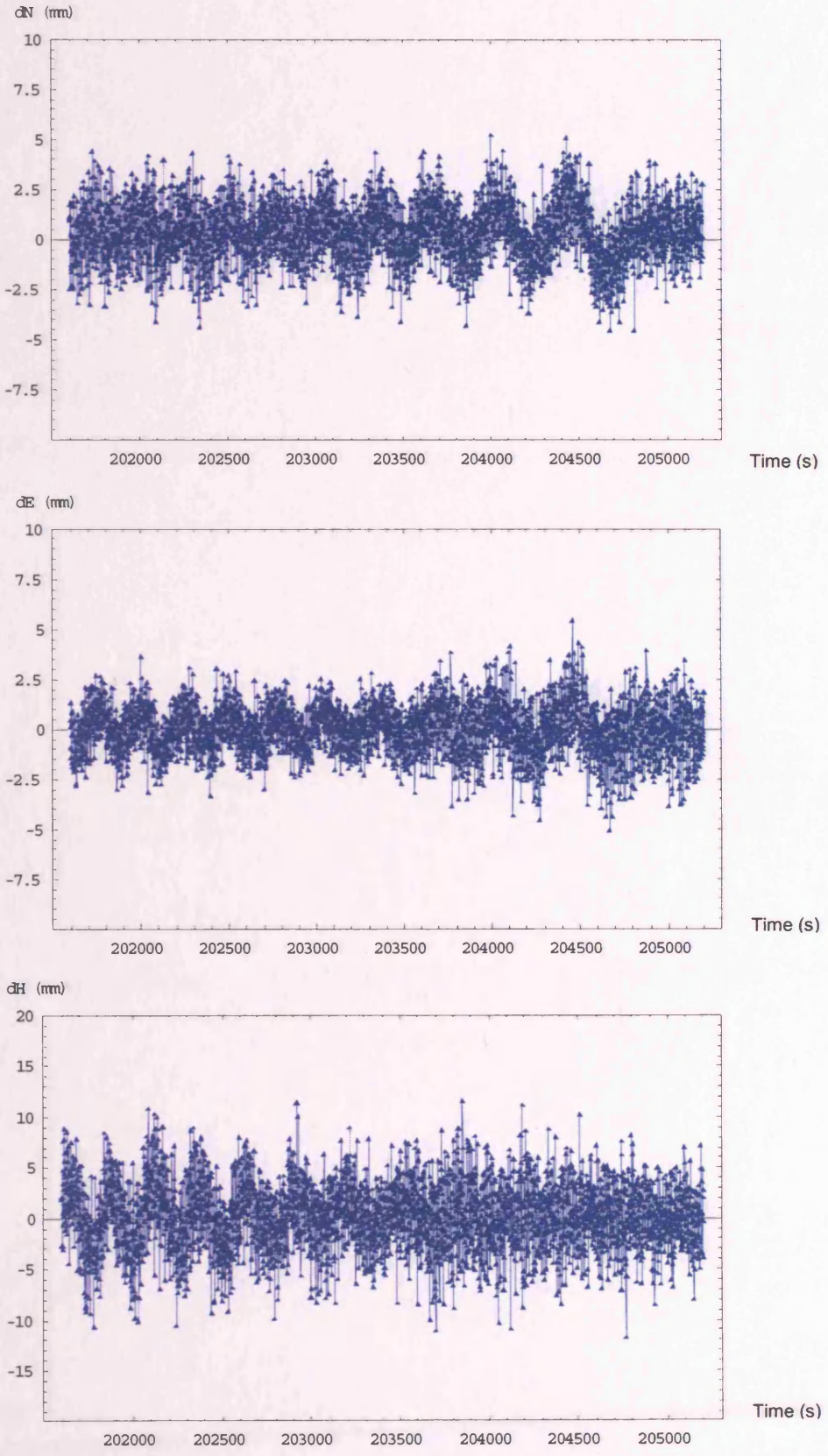

Figure 6-1: Positioning error in northing (top), easting (middle), and vertical (bottom) of single-epoch solution using GPS single-frequency data in the LCPC-3.9 dataset.

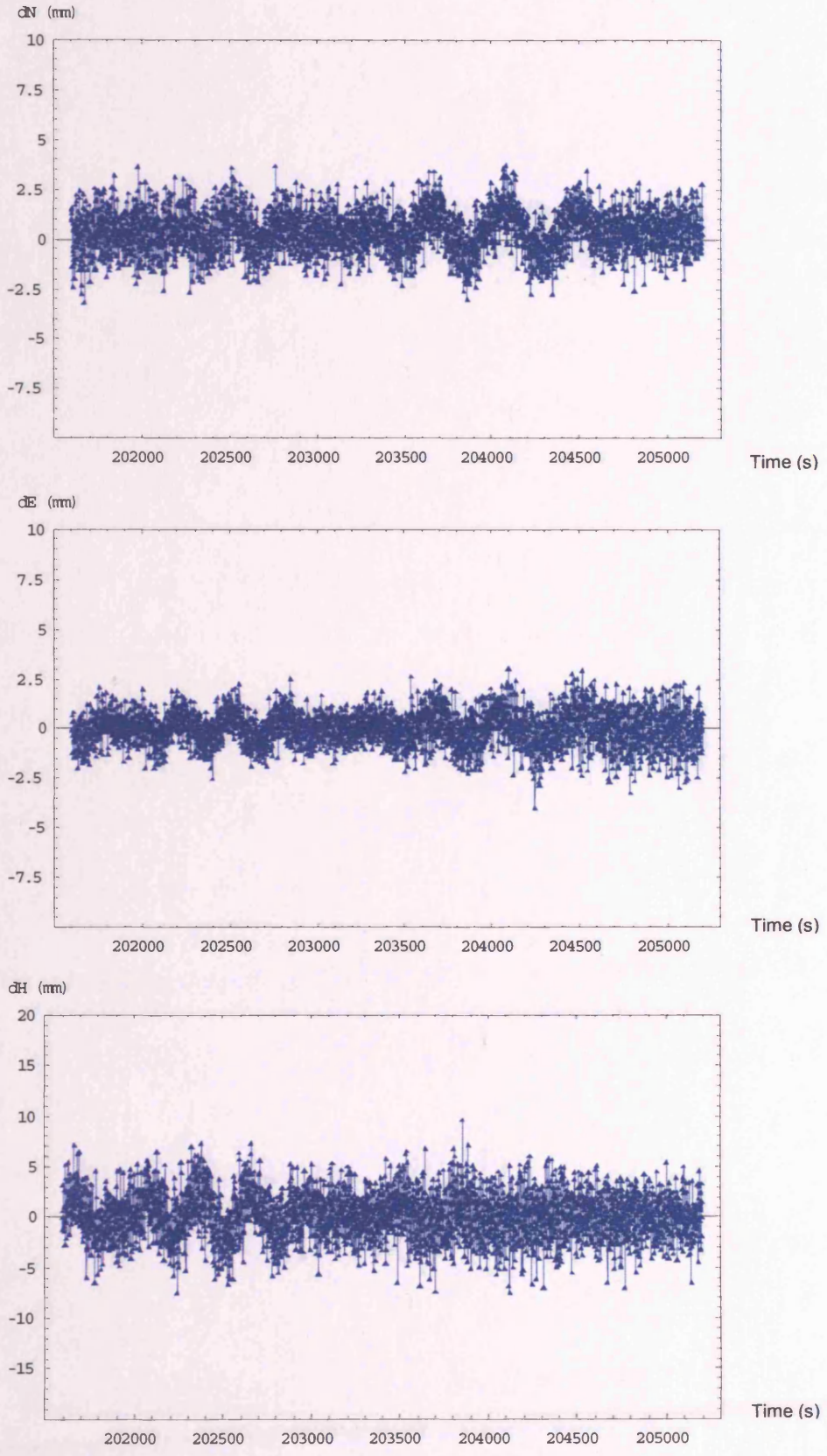

Figure 6-2: Positioning error in northing (top), easting (middle), and vertical (bottom) of single-epoch solution using GPS dual-frequency data in the LCPC-3.9 dataset.

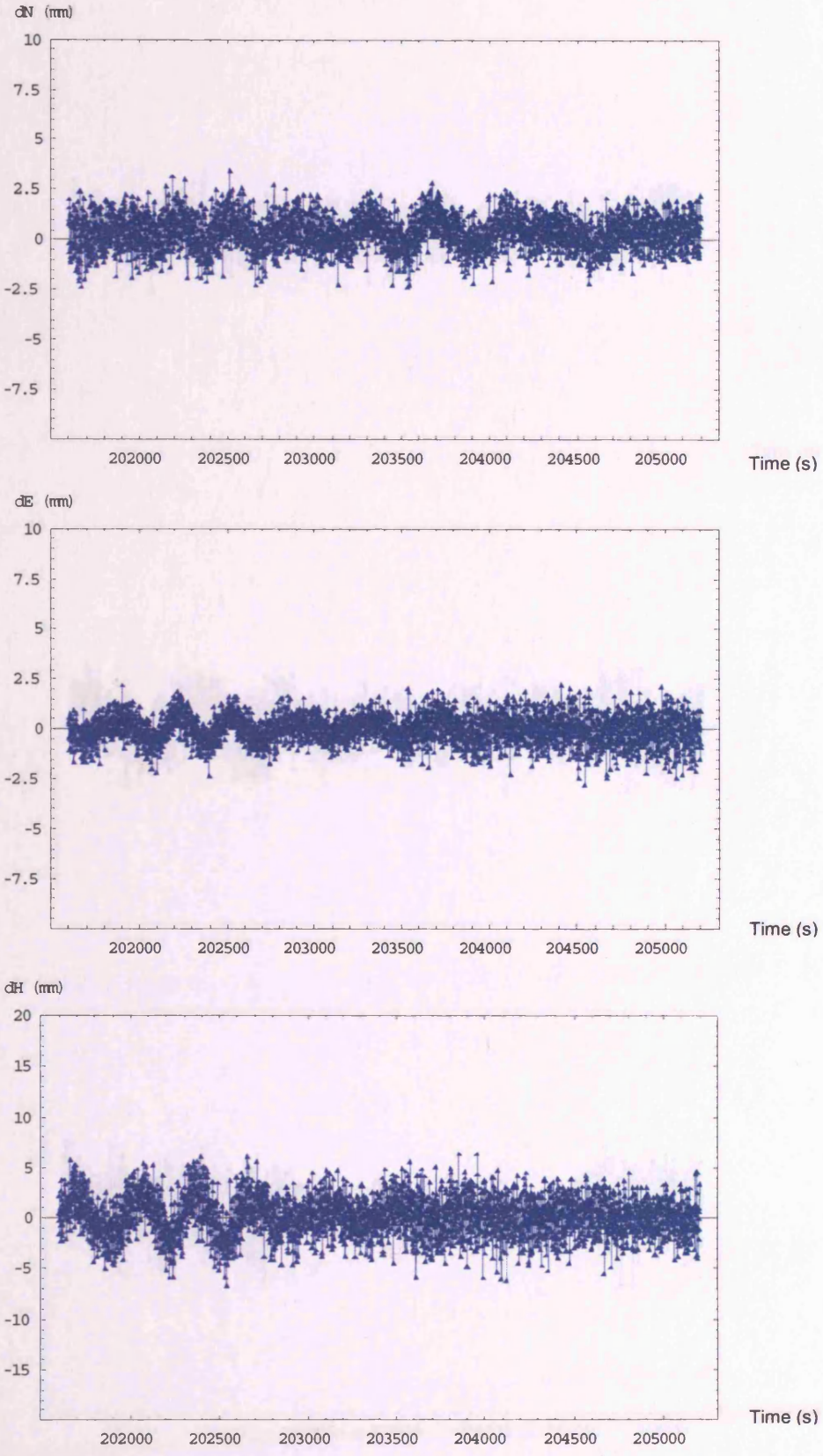

Figure 6-3: Positioning error in northing (top), easting (middle), and vertical (bottom) of single-epoch solution using GPS three-frequency data in the LCPC-3.9 dataset.

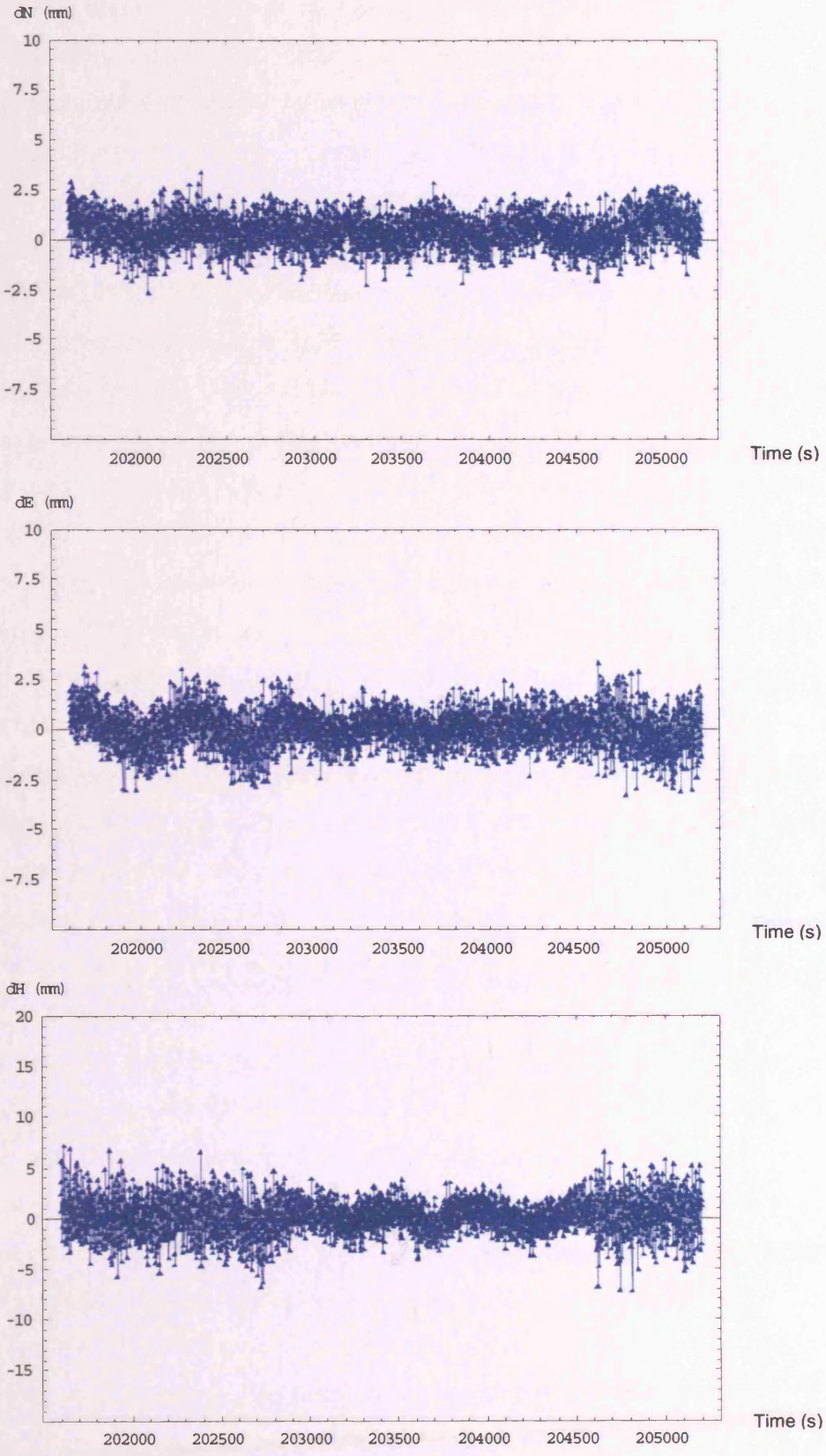

Figure 6-4: Positioning error in northing (top), easting (middle), and vertical (bottom) of single-epoch solution using Galileo three-frequency data in the LCPC-3.9 dataset.

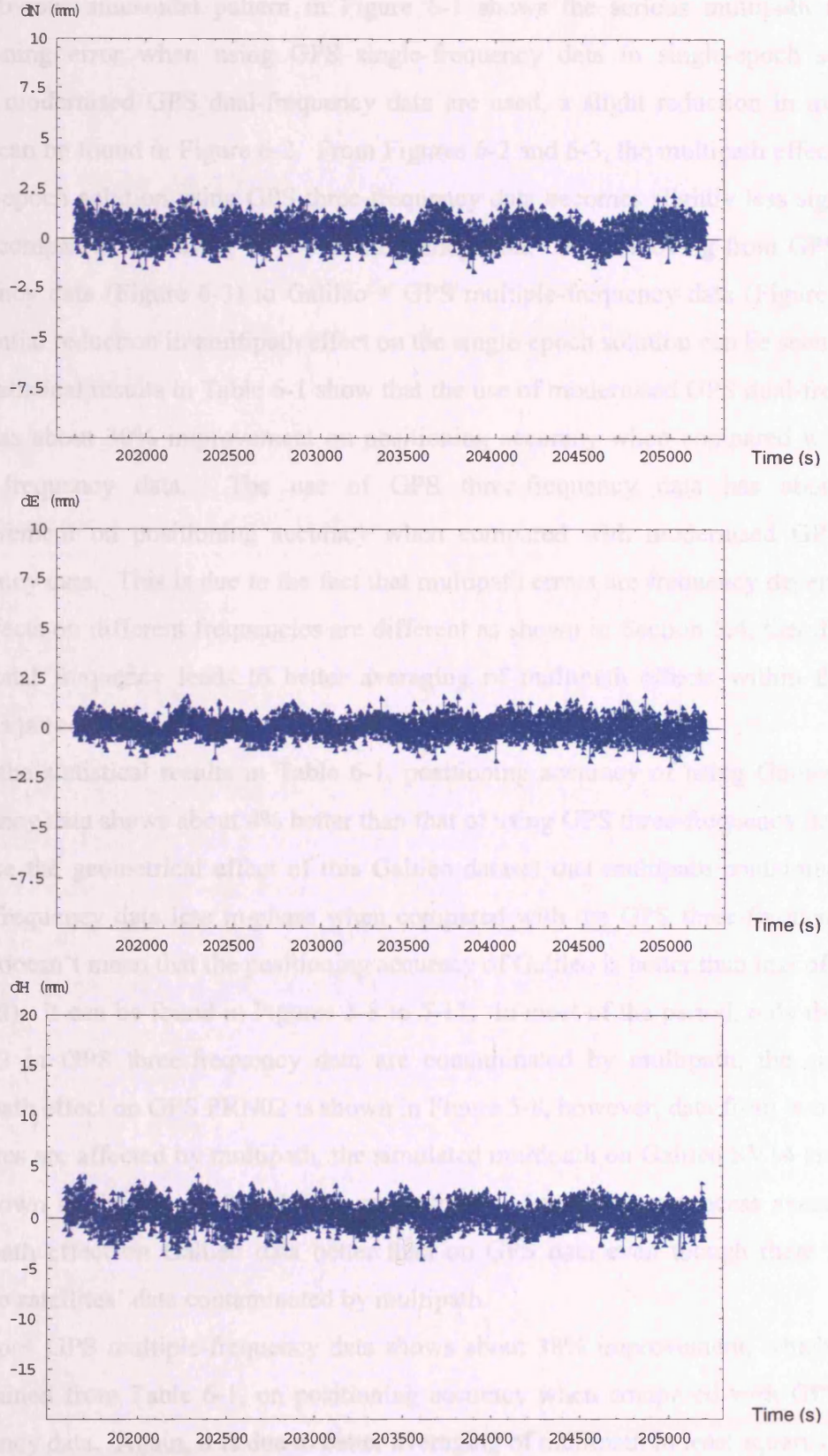

Figure 6-5: Positioning error in northing (top), easting (middle), and vertical (bottom) of single-epoch solution using Galileo + GPS multiple-frequency data in the LCPC-3.9 dataset.

The obvious sinusoidal pattern in Figure 6-1 shows the serious multipath induced positioning error when using GPS single-frequency data in single-epoch solution. When modernised GPS dual-frequency data are used, a slight reduction in multipath effect can be found in Figure 6-2. From Figures 6-2 and 6-3, the multipath effect on the single-epoch solution using GPS three-frequency data becomes slightly less significant when compared with using GPS dual-frequency data. When moving from GPS three-frequency data (Figure 6-3) to Galileo + GPS multiple-frequency data (Figure 6-5), a substantial reduction in multipath effect on the single-epoch solution can be seen.

The statistical results in Table 6-1 show that the use of modernised GPS dual-frequency data has about 30% improvement on positioning accuracy when compared with GPS single-frequency data. The use of GPS three-frequency data has about 15% improvement on positioning accuracy when compared with modernised GPS dual-frequency data. This is due to the fact that multipath errors are frequency dependent so the effects on different frequencies are different as shown in Section 5.4, therefore, the additional frequency leads to better averaging of multipath effects within the least squares process.

From the statistical results in Table 6-1, positioning accuracy of using Galileo three-frequency data shows about 4% better than that of using GPS three-frequency data. It is because the geometrical effect of this Galileo dataset that multipath contaminates the three-frequency data less in-phase when compared with the GPS three-frequency data set (it doesn't mean that the positioning accuracy of Galileo is better than that of GPS in general). It can be found in Figures 5-8 to 5-11. In most of the period, only data from PRN02 in GPS three-frequency data are contaminated by multipath, the simulated multipath effect on GPS PRN02 is shown in Figure 5-8, however, data from two Galileo satellites are affected by multipath, the simulated multipath on Galileo SV14 and SV20 are shown in Figures 5-10 and 5-11 respectively. Least square process averages the multipath effect on Galileo data better than on GPS data even though there are two Galileo satellites' data contaminated by multipath.

Galileo + GPS multiple-frequency data shows about 38% improvement, which can be determined from Table 6-1, on positioning accuracy when compared with GPS three-frequency data. Again, it is due to better averaging of multipath in least squares process with more redundant data from dual constellations. From the current GPS reliable single frequency to the coming maximum number of frequencies in OS - Galileo + GPS

multiple-frequency data, the statistical results in Table 6-1 show about 63% improvement on positioning accuracy.

6.3.2 LCPC-10 testing dataset

Positioning errors from single epoch solutions in northing, easting, and height for scenarios 1 to 5 of LCPC-10 dataset are shown in Figures 6-6 to 6-10, respectively. RMS errors of the positioning errors in northing, easting, height, and 3D position are tabulated in Table 6-2.

Table 6-2: RMS positioning errors in millimetres and percentage improvement of the testing scenarios in LCPC-10 dataset.

Scenario	N	E	H	3D	% improvement
1: Single-frequency GPS	1.611	1.410	3.879	4.431	-
2: Dual-frequency GPS	1.171	0.976	2.642	3.051	31
3: Three-frequency GPS	0.948	0.830	2.341	2.659	40
4: Three-frequency Galileo	0.985	1.059	1.940	2.420	45
5: Multiple-frequency GPS+Galileo	0.696	0.533	1.386	1.640	63

From Figures 6-1 to 6-5 and 6-6 to 6-10, more measurements can average multipath errors in the least squares process better even though the multipath amplitudes of the LCPC-10 dataset are greater than that of the LCPC-3.9 dataset (see Figures 5-8 to 5-10 and 5-11 to 5-13). Similar percentage improvements are obtained in the LCPC-10 dataset (Table 6-2) as the LCPC-3.9 dataset (Table 6-1). Therefore, a similar explanation can be found in Section 6.3.1. However, a relatively clear sinusoidal multipath pattern can still be seen in Figure 6-10 when compared with Figure 6-5. When inspecting Tables 6-1 and 6-2, RMS errors in Table 6-2 are greater than those in Table 6.1. It shows that more multipath errors remain in the positioning solutions when the amplitude of multipath error increases.

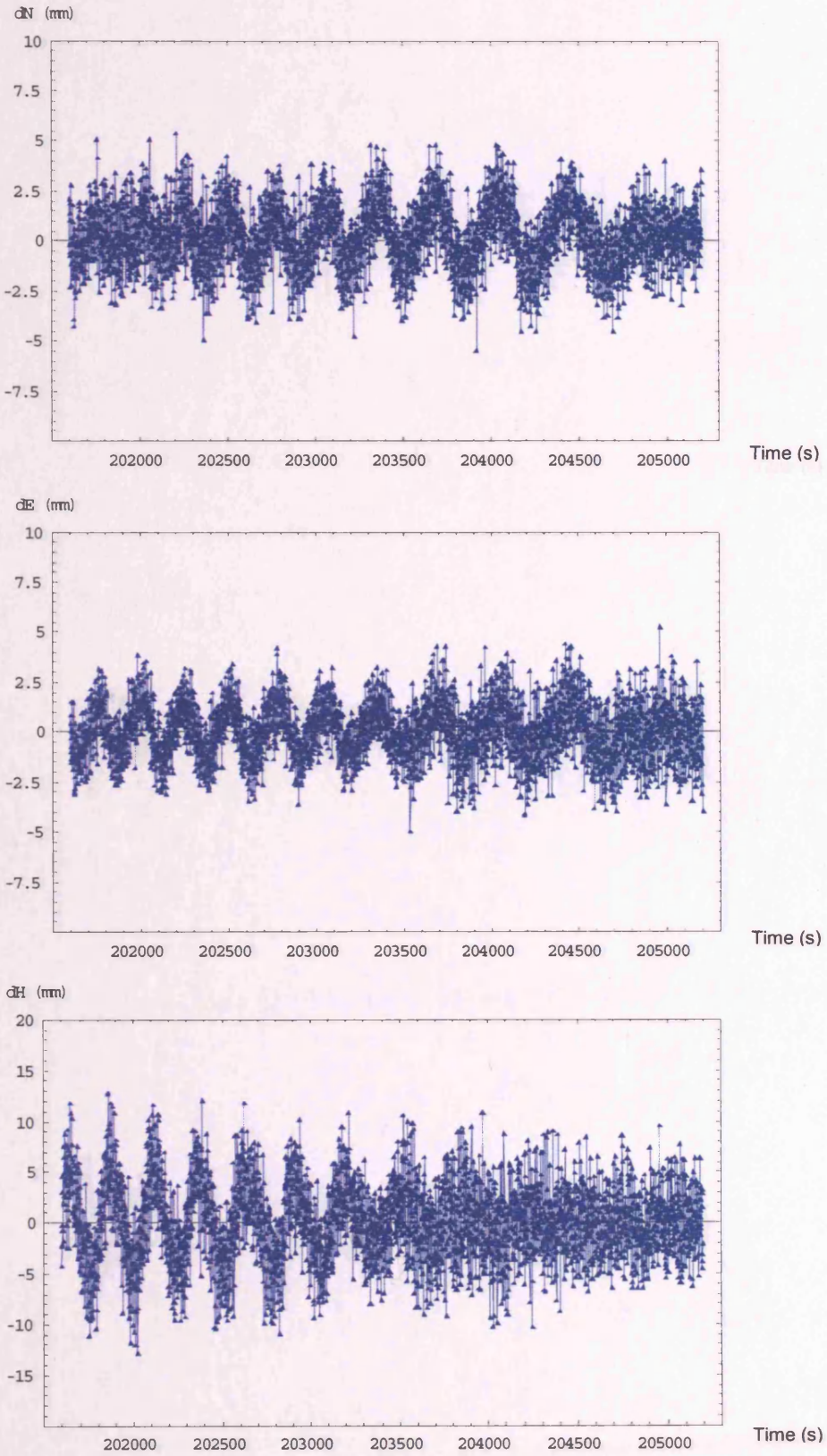

Figure 6-6: Positioning error in northing (top), easting (middle), and vertical (bottom) of single-epoch solution using GPS single-frequency data in the LCPC-10 dataset.

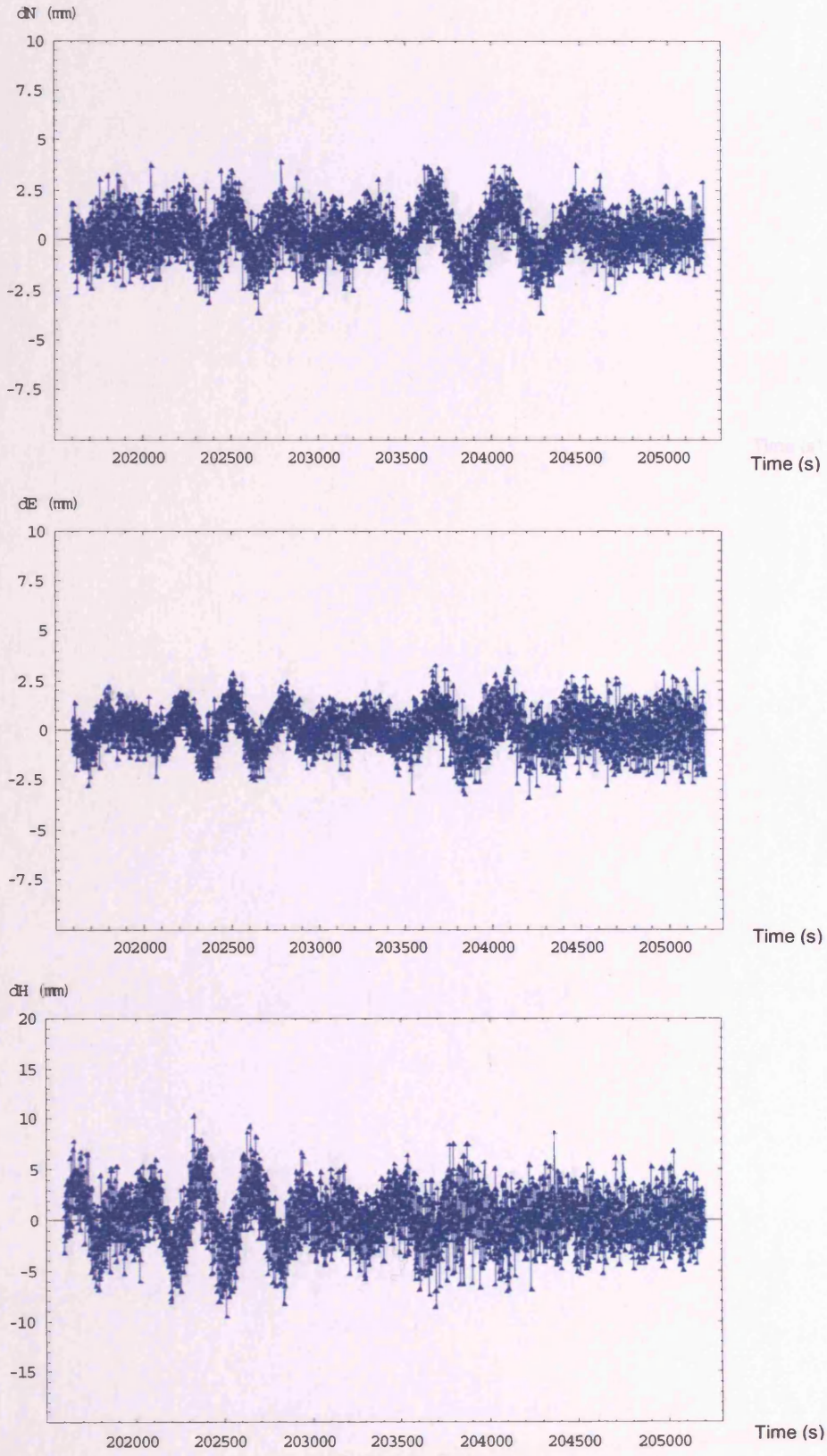

Figure 6-7: Positioning error in northing (top), easting (middle), and vertical (bottom) of single-epoch solution using GPS dual-frequency data in the LCPC-10 dataset.

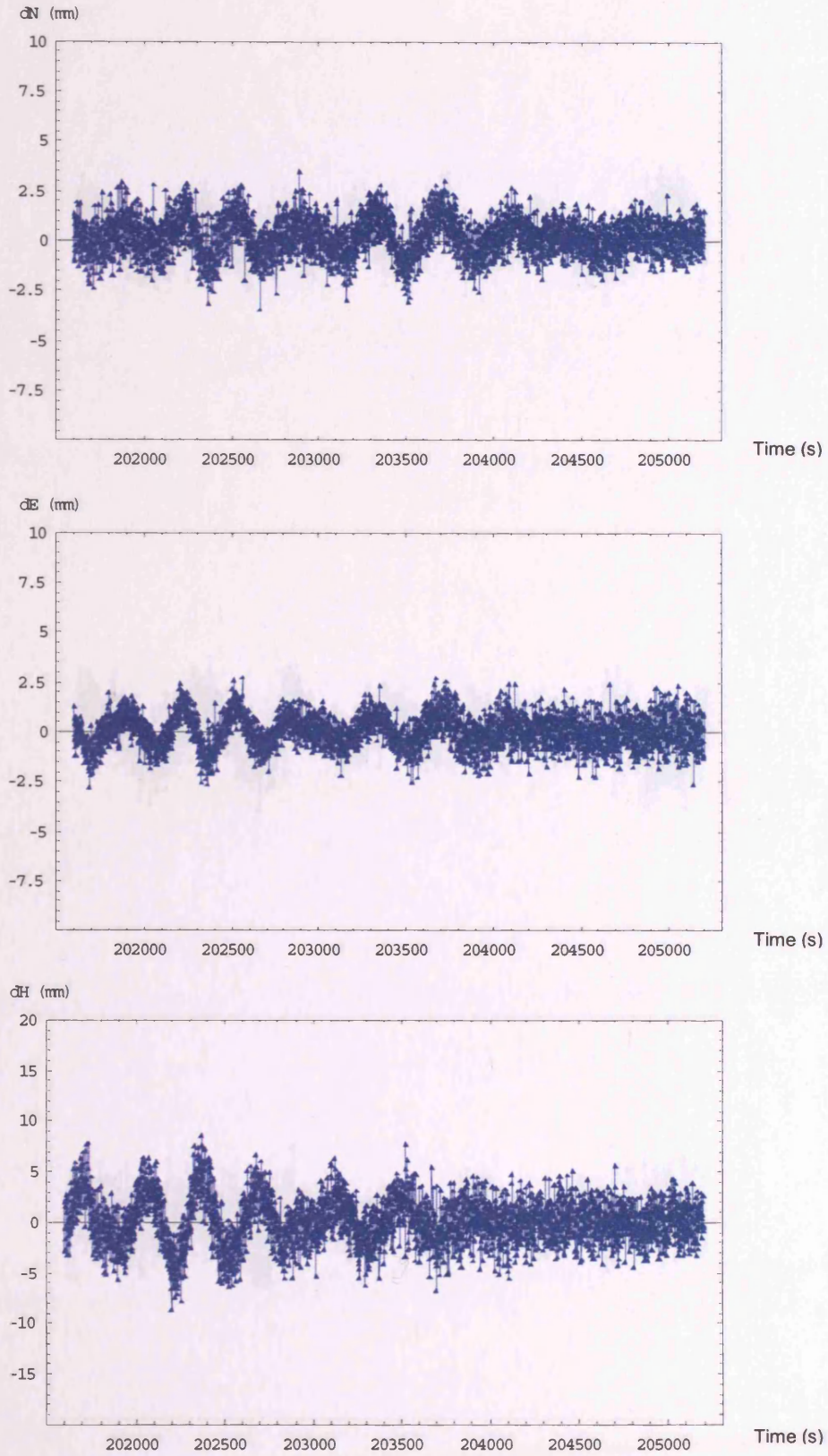

Figure 6-8: Positioning error in northing (top), easting (middle), and vertical (bottom) of single-epoch solution using GPS three-frequency data in the LCPC-10 dataset.

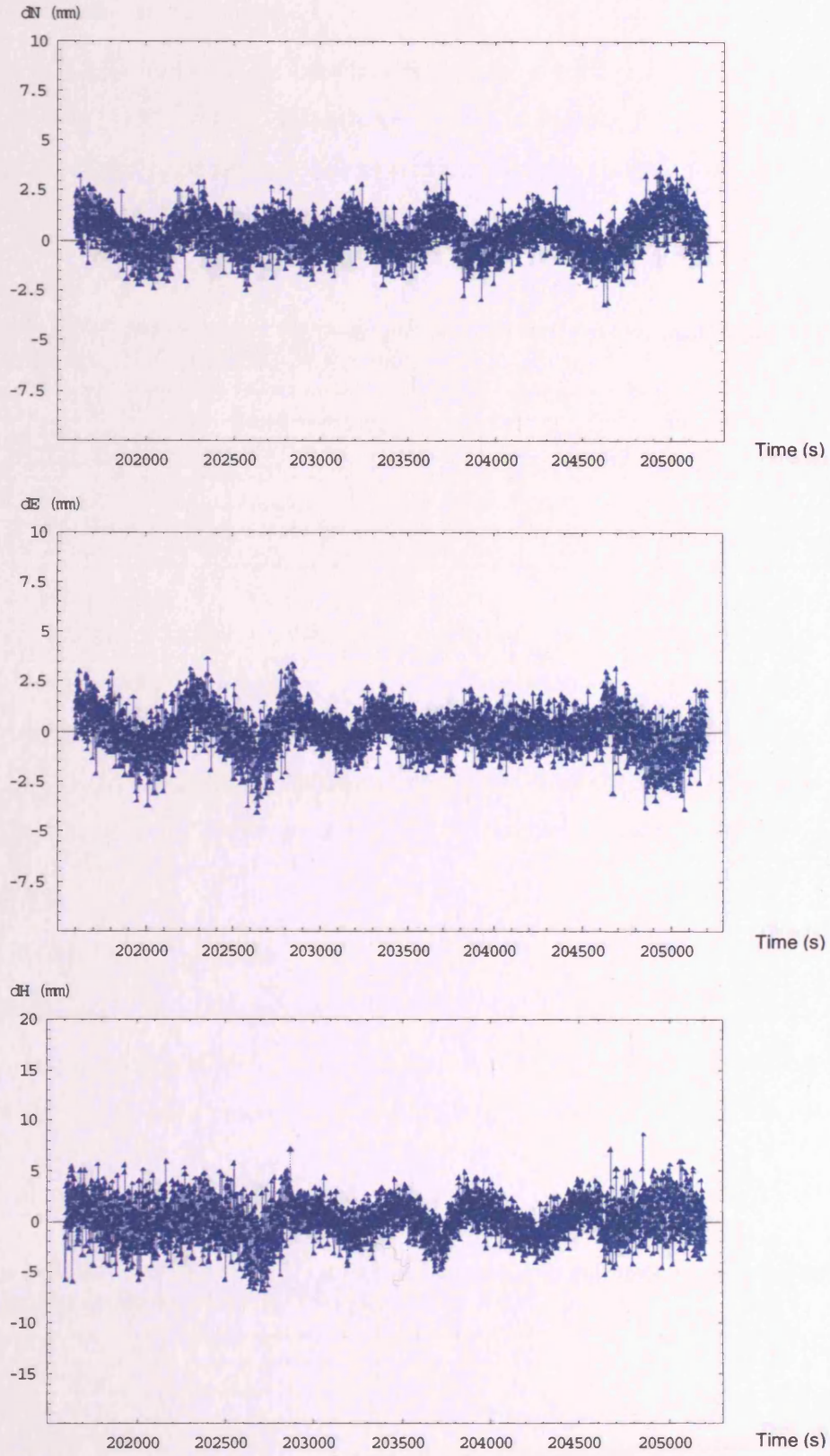

Figure 6-9: Positioning error in northing (top), easting (middle), and vertical (bottom) of single-epoch solution using Galileo three-frequency data in the LCPC-10 dataset.

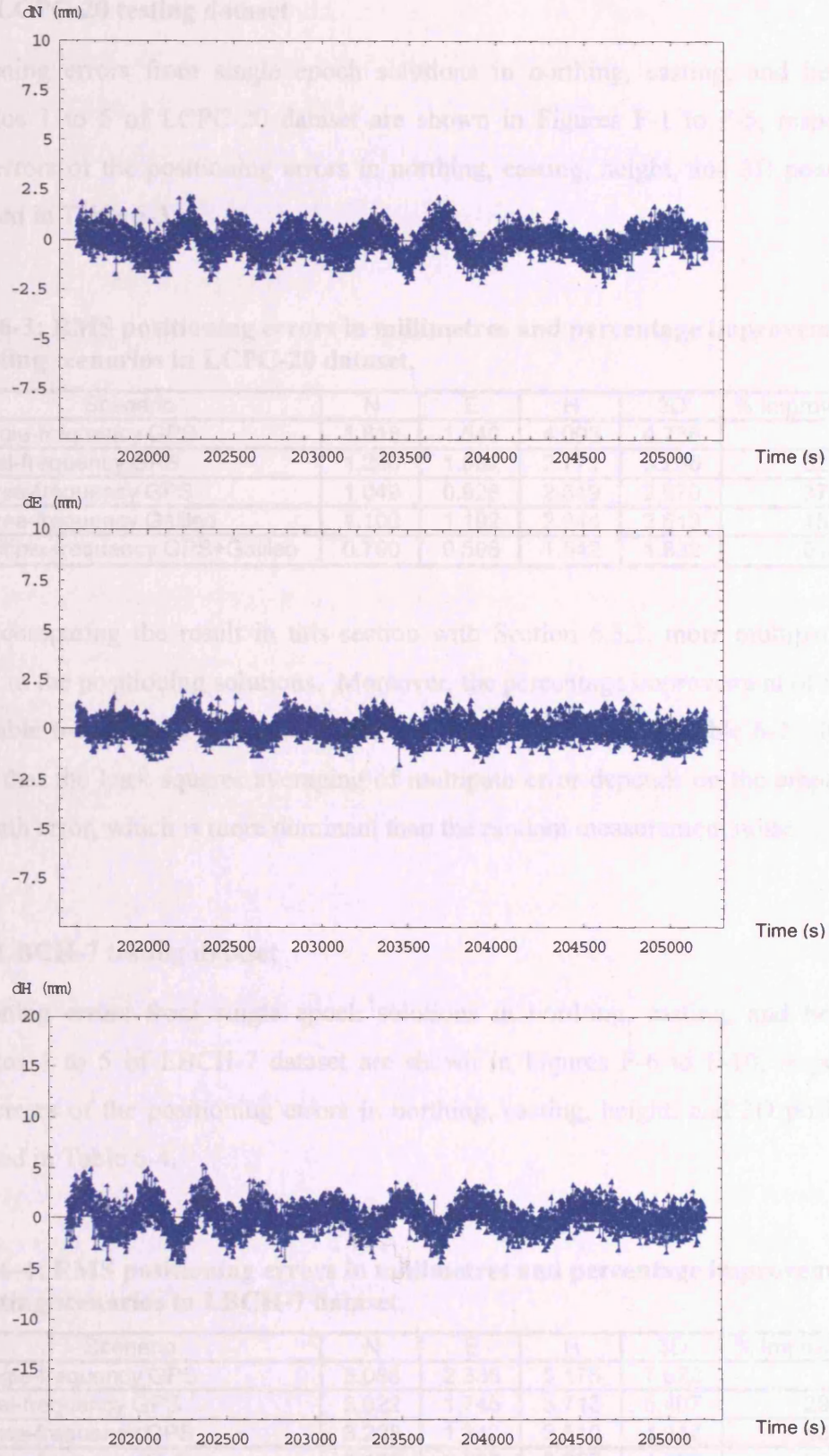

Figure 6-10: Positioning error in northing (top), easting (middle), and vertical (bottom) of single-epoch solution using Galileo + GPS multiple-frequency data in the LCPC-10 dataset.

6.3.3 LCPC-20 testing dataset

Positioning errors from single epoch solutions in northing, easting, and height for scenarios 1 to 5 of LCPC-20 dataset are shown in Figures F-1 to F-5, respectively. RMS errors of the positioning errors in northing, easting, height, and 3D position are tabulated in Table 6-3.

Table 6-3: RMS positioning errors in millimetres and percentage improvement of the testing scenarios in LCPC-20 dataset.

Scenario	N	E	H	3D	% improvement
1: Single-frequency GPS	1.818	1.540	4.093	4.736	-
2: Dual-frequency GPS	1.290	1.062	2.771	3.236	32
3: Three-frequency GPS	1.049	0.928	2.619	2.970	37
4: Three-frequency Galileo	1.109	1.192	2.044	2.613	45
5: Multiple-frequency GPS+Galileo	0.790	0.596	1.542	1.832	61

When comparing the result in this section with Section 6.3.2, more multipath errors remain in the positioning solutions. Moreover, the percentage improvement of Scenario 5 in Table 6-3 shows 2% reduction when compared with that in Table 6-2. It further shows that the least squares averaging of multipath error depends on the amplitude of multipath error, which is more dominant than the random measurement noise.

6.3.4 LBCH-7 testing dataset

Positioning errors from single epoch solutions in northing, easting, and height for scenarios 1 to 5 of LBCH-7 dataset are shown in Figures F-6 to F-10, respectively. RMS errors of the positioning errors in northing, easting, height, and 3D position are tabulated in Table 6-4.

Table 6-4: RMS positioning errors in millimetres and percentage improvement of the testing scenarios in LBCH-7 dataset.

Scenario	N	E	H	3D	% improvement
1: Single-frequency GPS	5.086	2.336	5.175	7.622	-
2: Dual-frequency GPS	3.522	1.745	3.713	5.407	29
3: Three-frequency GPS	3.208	1.340	2.610	4.347	43
4: Three-frequency Galileo	2.460	0.685	3.907	4.668	39
5: Multiple-frequency GPS+Galileo	1.997	0.667	2.279	3.103	59

In Figures F-6 to F-10, the reduced impact of multipath errors on positioning solutions from the single-frequency GPS to the multiple-frequency GPS + Galileo can be found.

The explanation to this is similar to Section 6.3.1. From Table 6-4, the RMS positioning errors of this dataset are greater than those of LCPC-3.9, LCPC-10, and LCPC-20 datasets. It is because there are more multipathing satellites (i.e. 7 satellites, whereas 3 multipathing satellites in LCPC datasets) in this dataset, and the amplitude of multipath error is greater (about 20 mm range error).

6.3.5 K-HK7-300 testing dataset

Positioning errors from single epoch solutions in northing, easting, and height for scenarios 1 to 5 of K-HK7-300 dataset are shown in Figures 6-11 to 6-15, respectively. RMS errors of the positioning errors in northing, easting, height, and 3D position are tabulated in Table 6-5.

Table 6-5: RMS positioning errors in millimetres and percentage improvement of the testing scenarios in K-HK7-300 dataset.

Scenario	N	E	H	3D	% improvement
1: Single-frequency GPS	0.558	0.466	1.103	1.321	-
2: Dual-frequency GPS	0.403	0.330	0.772	0.931	30
3: Three-frequency GPS	1.884	1.877	4.592	5.306	-302
4: Three-frequency Galileo	2.003	2.356	4.279	5.280	-300
5: Multiple-frequency GPS+Galileo	1.322	1.507	2.963	3.577	-171

From Figures 6-11 and 6-12, and Table 6-5, reduction in the impact of multipath on positioning solution can be seen when comparing the results of using dual-frequency GPS data with single-frequency GPS data and its percentage improvement (i.e. 30%) is similar to that in the LCPC and LBCH-7 datasets. However, moving from using dual-frequency GPS data to three-frequency GPS data, the positioning result becomes worse and the percentage improvement becomes negative, which means an approximately 300% deterioration. This is because more bad (multipath contaminated) measurements are introduced in data processing. Least squares should have a better averaging effect on the frequency-dependent phase multipath when more data are available, which is found in the results of the LCPC and LBCH-7 datasets. However, it is not found in this result. This is because the multipath errors on GPS L2 and L5 and/or Galileo E5a and E5b frequencies (they are in the quite close frequency band as shown in Table 2-1) are highly correlated when reflections occur at the very close carrying platform as shown in Figures 5-17 to 5-32 (the low frequency multipath errors indicated in the blue and green lines). Therefore, the introduction of another highly correlated multipath error will further drag the estimated position away from the true position. Table 6-6 shows the

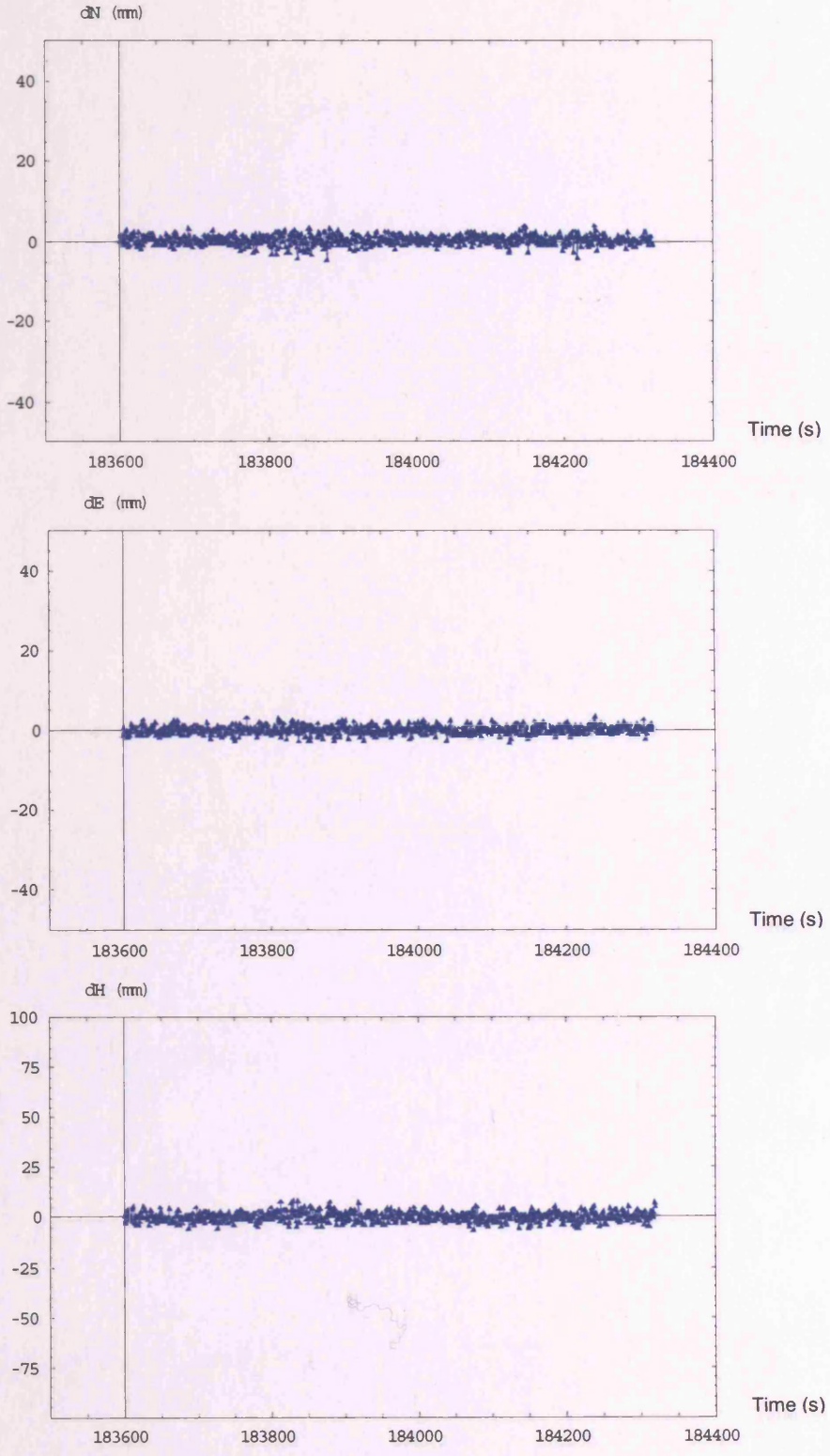

Figure 6-11: Positioning error in northing (top), easting (middle), and vertical (bottom) of single-epoch solution using GPS single-frequency data in the K-HK7-300 dataset.

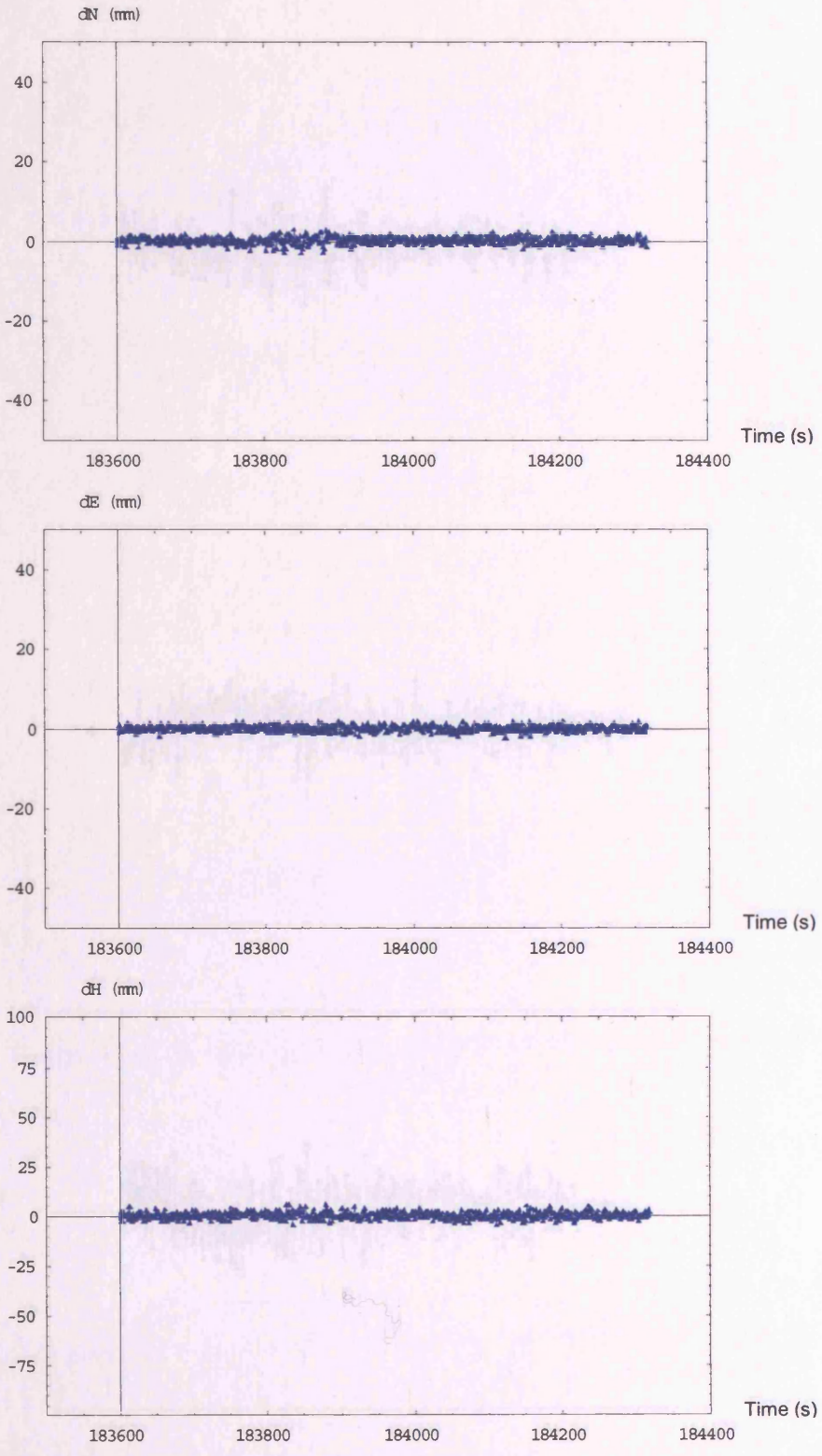

Figure 6-12: Positioning error in northing (top), easting (middle), and vertical (bottom) of single-epoch solution using GPS dual-frequency data in the K-HK7-300 dataset.

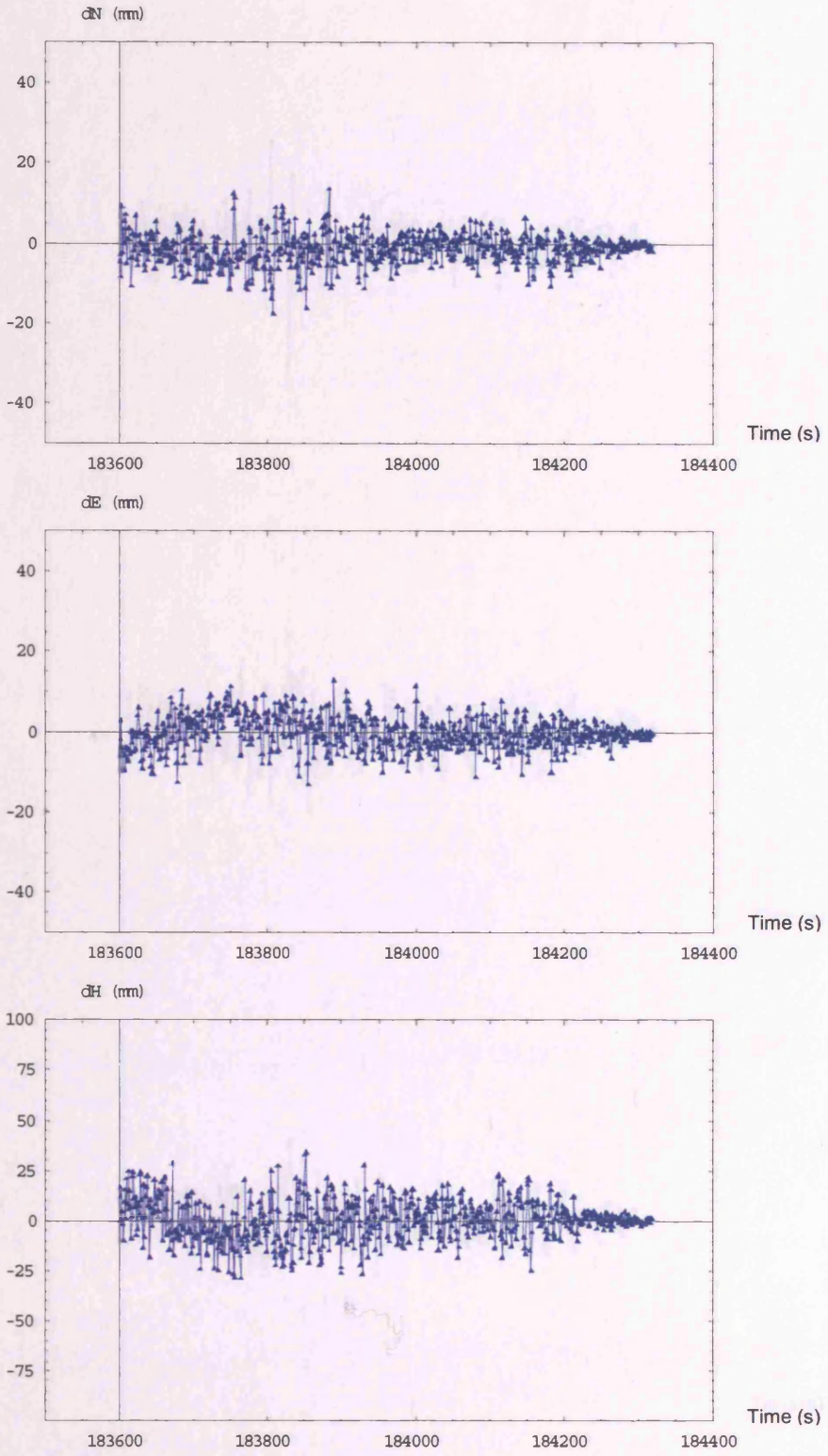

Figure 6-13: Fig.15. Positioning error in northing (top), easting (middle), and vertical (bottom) of single-epoch solution using GPS three-frequency data in the K-HK7-300 dataset.

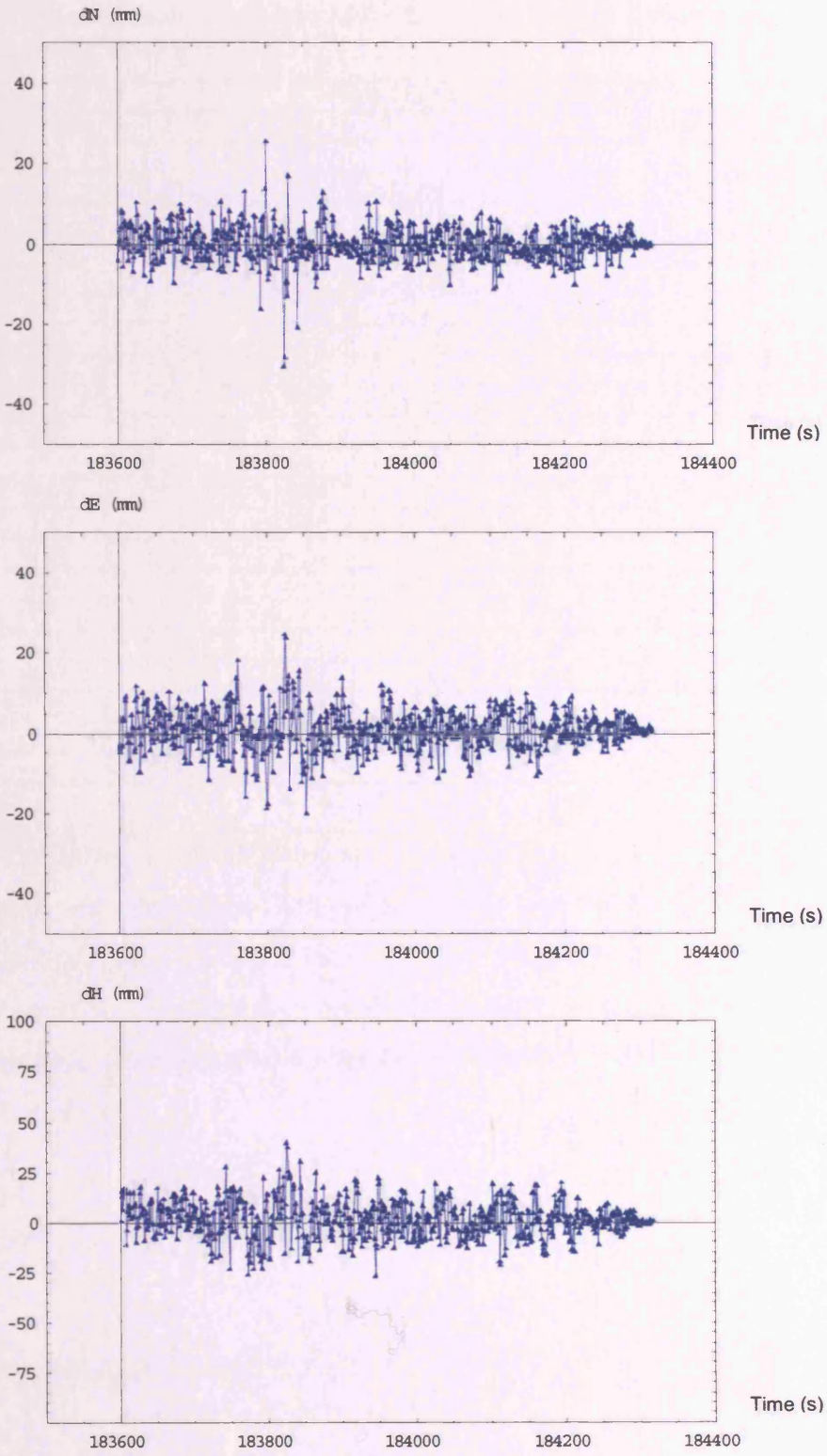

Figure 6-14: Positioning error in northing (top), easting (middle), and vertical (bottom) of single-epoch solution using Galileo three-frequency data in the K-HK7-300 dataset.

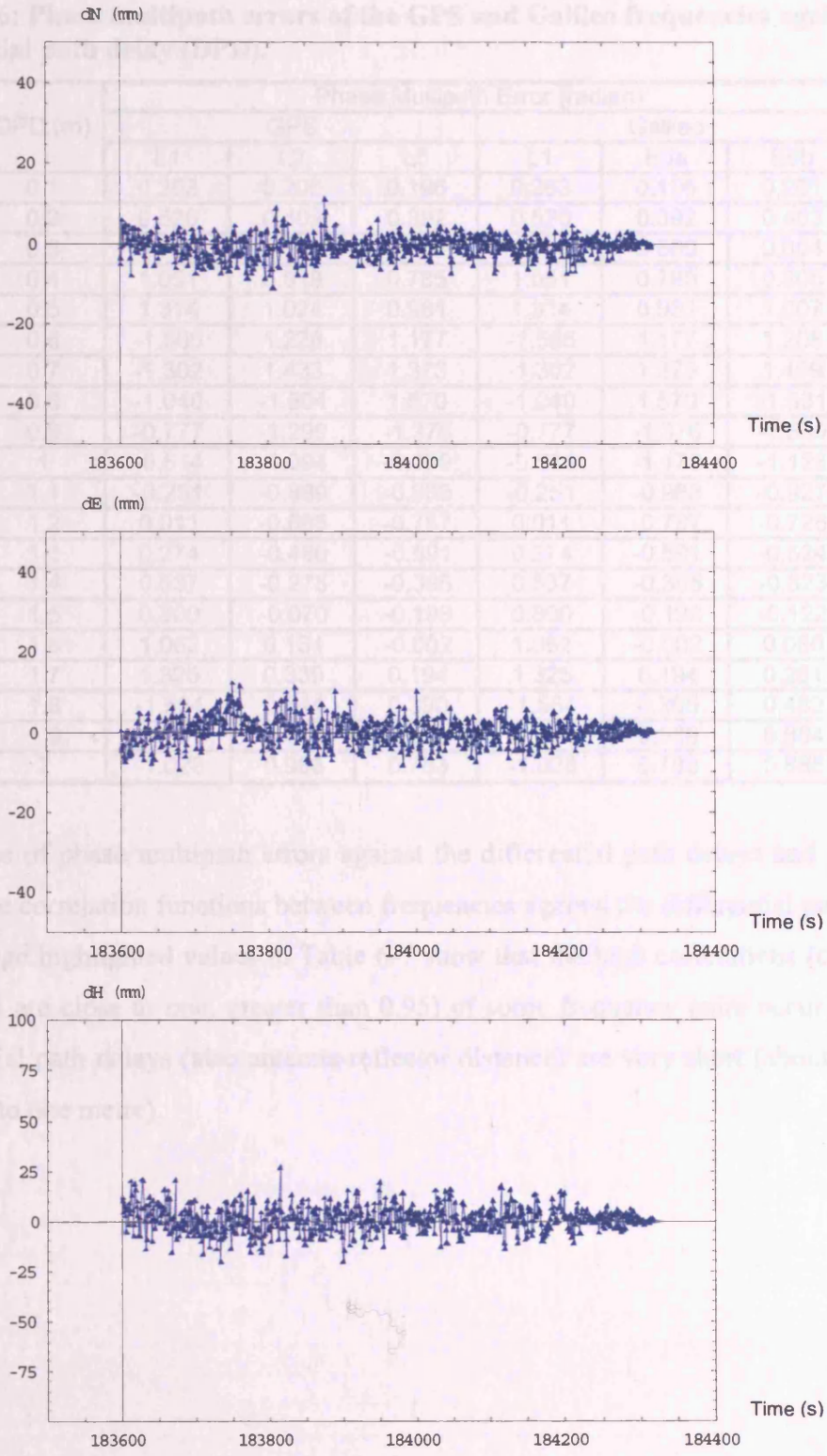

Figure 6-15: Positioning error in northing (top), easting (middle), and vertical (bottom) of single-epoch solution using Galileo + GPS multiple-frequency data in the K-HK7-300 dataset.

Table 6-6: Phase multipath errors of the GPS and Galileo frequencies against the differential path delay (DPD).

DPD (m)	Phase Multipath Error (radian)					
	GPS			Galileo		
	L1	L2	L5	L1	E5a	E5b
0.1	0.263	0.205	0.196	0.263	0.196	0.201
0.2	0.526	0.409	0.392	0.526	0.392	0.403
0.3	0.788	0.614	0.589	0.788	0.589	0.604
0.4	1.051	0.819	0.785	1.051	0.785	0.805
0.5	1.314	1.024	0.981	1.314	0.981	1.007
0.6	-1.565	1.228	1.177	-1.565	1.177	1.208
0.7	-1.302	1.433	1.373	-1.302	1.373	1.409
0.8	-1.040	-1.504	1.570	-1.040	1.570	-1.531
0.9	-0.777	-1.299	-1.376	-0.777	-1.376	-1.330
1	-0.514	-1.094	-1.179	-0.514	-1.179	-1.128
1.1	-0.251	-0.889	-0.983	-0.251	-0.983	-0.927
1.2	0.011	-0.685	-0.787	0.011	-0.787	-0.726
1.3	0.274	-0.480	-0.591	0.274	-0.591	-0.524
1.4	0.537	-0.275	-0.395	0.537	-0.395	-0.323
1.5	0.800	-0.070	-0.198	0.800	-0.198	-0.122
1.6	1.062	0.134	-0.002	1.062	-0.002	0.080
1.7	1.325	0.339	0.194	1.325	0.194	0.281
1.8	-1.554	0.544	0.390	-1.554	0.390	0.482
1.9	-1.291	0.748	0.586	-1.291	0.586	0.684
2	-1.028	0.953	0.783	-1.028	0.783	0.885

coherence of phase multipath errors against the differential path delays and Table 6-7 shows the correlation functions between frequencies against the differential path delays. The orange highlighted values in Table 6-7 show that the high correlations (correlation functions are close to one, greater than 0.95) of some frequency pairs occur when the differential path delays (also antenna-reflector distance) are very short (about less than or equal to one metre).

Table 6-7: Correlation functions of phase multipath errors among different GPS and Galileo frequencies in Table 6-7 against the differential path delay (DPD).

DPD (m)	Correlation Function						
	GPS L1 and Galileo L1 or GPS L5 and Galileo E5a	GPS/Galileo L1 and L2	GPS L1 and L5	GPS L2 and L5	GPS L2 and Galileo E5a	GPS L2 and Galileo E5a	Galileo E5a and E5b
0.1	1	0.78	0.75	0.96	0.96	0.98	0.97
0.2	1	0.78	0.75	0.96	0.96	0.98	0.97
0.3	1	0.78	0.75	0.96	0.96	0.98	0.97
0.4	1	0.78	0.75	0.96	0.96	0.98	0.97
0.5	1	0.78	0.75	0.96	0.96	0.98	0.97
0.6	1	0.78	0.75	0.96	0.96	0.98	0.97
0.7	1	0.91	0.95	0.96	0.96	0.98	0.97
0.8	1	0.69	0.66	0.96	0.96	0.98	0.98
0.9	1	0.60	0.56	0.94	0.94	0.98	0.97
1	1	0.47	0.44	0.93	0.93	0.97	0.96
1.1	1	0.28	0.26	0.90	0.90	0.96	0.94
1.2	1	0.02	0.01	0.87	0.87	0.94	0.92
1.3	1	0.57	0.46	0.81	0.81	0.92	0.89
1.4	1	0.51	0.73	0.70	0.70	0.85	0.82
1.5	1	0.09	0.25	0.36	0.36	0.58	0.61
1.6	1	0.13	0.00	0.02	0.02	0.59	0.03
1.7	1	0.26	0.15	0.57	0.57	0.83	0.69

6.3.6 K-HK7-600 testing dataset

Positioning errors from single epoch solutions in northing, easting, and height for scenarios 1 to 5 of K-HK7-600 dataset are shown in Figures F-11 to F-15, respectively. RMS errors of the positioning errors in northing, easting, height, and 3D position are tabulated in Table 6-8.

Table 6-8: RMS positioning errors in millimetres and percentage improvement of the testing scenarios in K-HK7-600 dataset.

Scenario	N	E	H	3D	% improvement
1: Single-frequency GPS	0.544	0.458	1.085	1.297	-
2: Dual-frequency GPS	0.390	0.326	0.764	0.917	29
3: Three-frequency GPS	1.897	2.338	3.825	4.868	-275
4: Three-frequency Galileo	2.483	2.312	3.765	5.068	-291
5: Multiple-frequency GPS+Galileo	1.314	1.370	2.007	2.763	-113

The results in Table 6-8 are similar to the results in the K-HK7-300 dataset shown in Table 6-5. Therefore, the explanation of this phenomenon is the same as in Section 6.3.5.

6.4 CONCLUDING REMARKS

The impact on single-epoch positioning accuracy in the presence of multipath using multiple-frequency data from the coming modernised GPS and Galileo in open service is investigated in this chapter. Galileo and modernised GPS multiple-frequency data are simulated in order to investigate the impact of using modernised GPS, Galileo and the dual constellations on positioning accuracy in the presence of multipath. Simulation results show substantial improvement on positioning accuracy when more frequencies and satellites are available in the LCPC-3.9, LCPC-10, LCPC-20, and LBCH-7 datasets, whose antenna-reflector distances are about 5 m. It shows about 62% improvement in average when comparing using Galileo + GPS multiple-frequency data with the present GPS reliable single-frequency system. However, the use of more frequencies from the modernised GPS and/or the new Galileo shows deterioration in the K-HK7-300 and K-HK7-600 datasets. This is because the additional measurements from closely allocated frequencies cause highly correlated phase multipath errors from a very close reflector (the antenna-reflector distance of the carrying platform in the K-HK7-300 and K-HK7-600 datasets is about 30 cm). It drags the estimated position further away from the true position.

Although the exact future positioning accuracy of Galileo and modified GPS can be verified when they are fully operational and the positioning accuracy depends on GNSS errors and satellite geometry, the performance of the coming GNSS would be expected to have a similar positioning accuracy because the simulation described in Chapters 3 and 4 is very realistic.

In conclusion, more measurements from the modernised GPS and/or the new Galileo would show substantial improvement on positioning accuracy if there is no reflector within about one metre (see Table 6-7) from the antenna.

7. MULTIPATH MITIGATION USING MULTIPLE-FREQUENCY GNSS DATA WITH MULTIPLE OUTLIER DETECTION

7.1 INTRODUCTION

Chapter 6 has investigated the impact of multiple-frequency GNSS data on multipath mitigation. It shows that the more redundant measurements can have better averaging of multipath errors in least squares process provided that no highly correlated multipath errors come from very close reflectors. How else can users benefit from the coming modernised GPS and the new Galileo systems?

Since multipath effects on different frequencies are different and more redundant measurements are available in multiple-frequency data, a multipath detection and rejection algorithm is proposed to improve the positioning accuracy for future multiple-frequency carrier phase-based precise positioning. This strategy, along with the fact that more redundancy leads to better averaging within the least squares process, leads to a modernised GPS and/or a new three-frequency Galileo having the potential for greater multipath mitigation than is the case with current GPS. The detailed processing model of this multipath detection and rejection algorithm is described in Section 7.2, the validation of the algorithm using the testing datasets described in Chapter 5 and its result with analysis is given in Section 7.3. Concluding remarks on the algorithm and the testing results are stated in Section 7.4.

7.2 MULTIPLE-FREQUENCY DATA PROCESSING ALGORITHM FOR MULTIPATH MITIGATION

As described in Chapter 6, a GNSS data processing program has been developed to process the different frequency data and the different combinations of data in this research. A module of multipath detection and rejection has been integrated into the GNSS data processor. The multipath detection and rejection algorithm is described in this section with the necessary background of least squares.

For high precision GPS positioning, the observation equations used in parameter estimation are usually linearized as:

$$E(y) = l + v = Ax \tag{7.1}$$

$$E(v) = 0,\ D(v) = D(l) = \sigma^2 C_l \tag{7.2}$$

where $E(\ )$ denotes the expectation operator, $D(\ )$ denotes the dispersion operator, l denotes the vector of double difference carrier phase observations, v denotes the vector of "true" residuals, A denotes the Jacobian matrix, x denotes the vector of unknown parameters, σ^2 denotes the a priori variance, and C_l denotes the cofactor matrix of observations. The GPS three-frequency phase observables are similar to the dual-frequency phase observables given in [Strang and Borre, 1997]:

$$\Phi_{1,ij}^{kl} = \rho_{ij}^{kl} - I_{ij}^{kl} + T_{ij}^{kl} + \lambda_1 N_{1,ij}^{kl} - \varepsilon_{1,ij}^{kl} \tag{7.3}$$

$$\Phi_{2,ij}^{kl} = \rho_{ij}^{kl} - (f_1 / f_2)^2 I_{ij}^{kl} + T_{ij}^{kl} + \lambda_2 N_{2,ij}^{kl} - \varepsilon_{2,ij}^{kl} \tag{7.4}$$

$$\Phi_{5,ij}^{kl} = \rho_{ij}^{kl} - (f_1 / f_5)^2 I_{ij}^{kl} + T_{ij}^{kl} + \lambda_5 N_{5,ij}^{kl} - \varepsilon_{5,ij}^{kl} \tag{7.5}$$

where $\Phi_{1,ij}^{kl}, \Phi_{2,ij}^{kl}$, and $\Phi_{5,ij}^{kl}$ are the double difference phase observations between satellites k and l, and stations i and j for GPS L1, L2, and L5 carriers respectively, ρ_{ij}^{kl} denotes the double difference geometric range, I_{ij}^{kl} denotes the double difference ionospheric effect, T_{ij}^{kl} denotes the double difference tropospheric delay, N_{ij}^{kl} denotes the double difference integer ambiguity, ε_{ij}^{kl} denotes the double difference measurement noise. The three-frequency observables in Equations (7.3) to (7.5) are similar to the Galileo three-frequency observables with the corresponding frequencies.

The unbiased estimate $\hat{x}$ of x is based on double-difference single-epoch least squares solutions. Such a solution has known statistical properties and an expectation of the residuals of zero. It is given by the following formula.

$$\hat{x} = (A^T W A)^{-1} A^T W l \text{ with } W = C_l^{-1} \tag{7.6}$$

or in simplified form:

$$\hat{x} = N^{-1} b \text{ with } N = (A^T W A), b = A^T W l \tag{7.7}$$

where W, the weight matrix, is the inverse of the covariance matrix of observations. Observations contaminated by unmodeled error are generally referred to as outliers and will have the following statistical characteristics:

$$E(v_i) \neq 0 \text{ and/or } D(v_i) > \sigma^2 C_{l,ii} \tag{7.8}$$

Since a multipath error is an unmodeled error in the observation model and since more observations will be available in the modernised GPS and/or the new Galileo, the hypothesis that is to be tested here is that the increased redundancy might make multipath detection and rejection possible. So the author proposes to consider multipath as an outlier and seek to detect it by statistical testing. Cross (1994) describes the test statistic $\hat{w}_i$ for the ith correlated observation (i.e. where the weight matrix W contains off-diagonal elements) as:

$$\hat{w}_i = \frac{-e_i^T W \hat{v}}{\sqrt{e_i^T W C_{\hat{v}} W e_i}} \tag{7.9}$$

where

$$C_{\hat{v}} = W^{-1} - A N^{-1} A^T \tag{7.10}$$

$$e_i = [0 \quad 0 \quad \cdots \quad 1 \quad \cdots \quad 0 \quad 0]^T \tag{7.11}$$

$$\hat{v} = A\hat{x} - l \tag{7.12}$$

The test statistic is then tested against a critical threshold c with l_i may contain a multipath error Δ_i whilst all other observations have only random and normally distributed errors ε_i:

$$H_0: l_i = \bar{l}_i + \varepsilon_i \tag{7.13}$$

$$H_1: l_i = \bar{l}_i + \varepsilon_i + \Delta_i \tag{7.14}$$

where $\bar{l}_i$ denotes the true value of the quantities that have been observed. The *Tau* rejection criterion c described in [Pope, 1976] is used as the critical threshold and the observation is rejected when:

$$\left|\frac{v_i}{\hat{\sigma}_{v_i}}\right| \geq c \tag{7.15}$$

with

$$c = f(NT, NU, \alpha) \tag{7.16}$$

where NT is the number of (non-outlying) observations, NU is the degree of freedom, and α is the desired probability of type I error. By changing the position of the unity in the vector e_i of Equation 7.11, this method can be used for multiple outlier detection. This multiple outlier detection method is called as MOD for future reference.

One impact of GPS modernisation and/or the new Galileo on multipath mitigation has already seen in Chapter 6. The next question is: could the increased redundancy help multipath detection and rejection and further improve positioning accuracy? In this investigation, the testing datasets described in Chapter 5 are processed using the described multipath detection and rejection technique MOD. The results and analyses are given in Section 7.3.

7.3 Result of Proposed Multipath Error Detection and Rejection Technique

7.3.1 LCPC-3.9 testing dataset

Positioning errors (in northing, easting, and height) after rejection of detected multipath using multiple-frequency data in the testing scenarios 3 to 5 are shown in Figures 7-1 to 7-3. Summary of the result is shown in Table 7-1, the results of scenarios 1 to 5 without using MOD are also shown in the table for comparison. Approximate percentages of right and wrong detections of simulated multipath errors are shown in Table 7-2, only approximate percentage can be shown because the simulated multipath errors may be zero or very small (smaller than measurement noise) sometimes, which can be found in Figures 5-8 to 5-11.

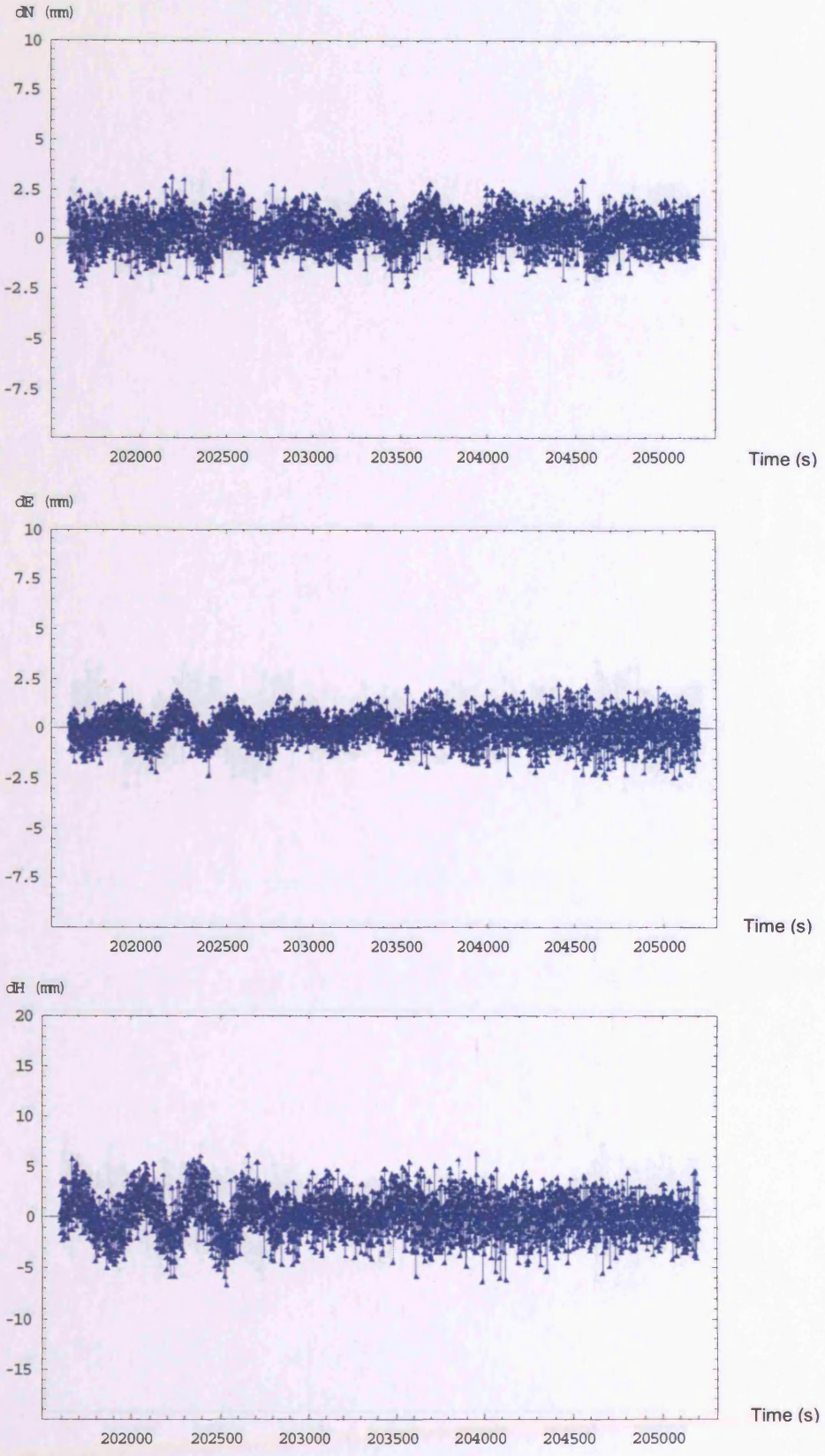

Figure 7-1: Positioning error in northing (top), easting (middle), and vertical (bottom) of single-epoch solution with MOD using GPS three-frequency data in the LCPC-3.9 dataset.

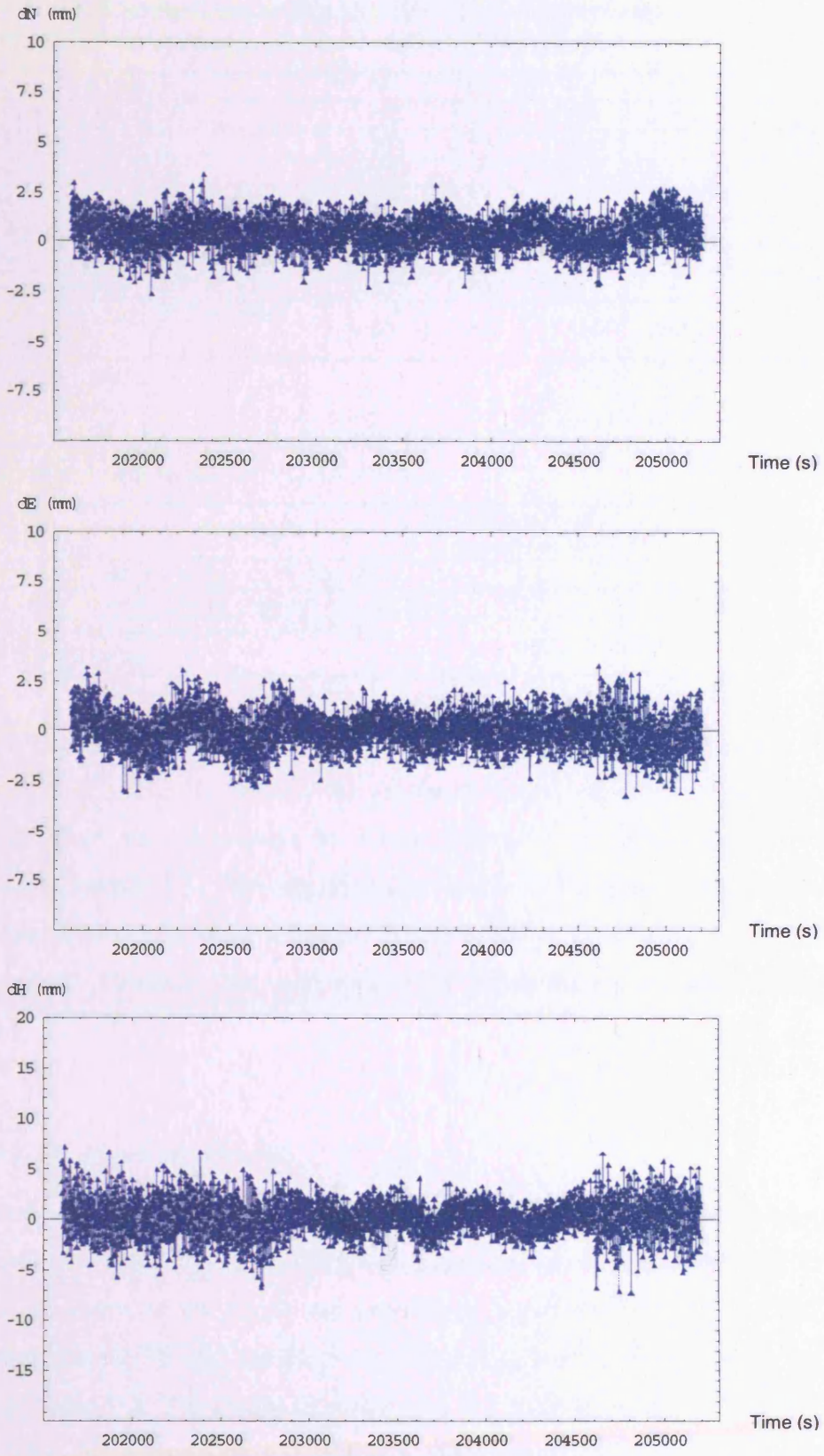

Figure 7-2: Positioning error in northing (top), easting (middle), and vertical (bottom) of single-epoch solution with MOD using Galileo three-frequency data in the LCPC-3.9 dataset.

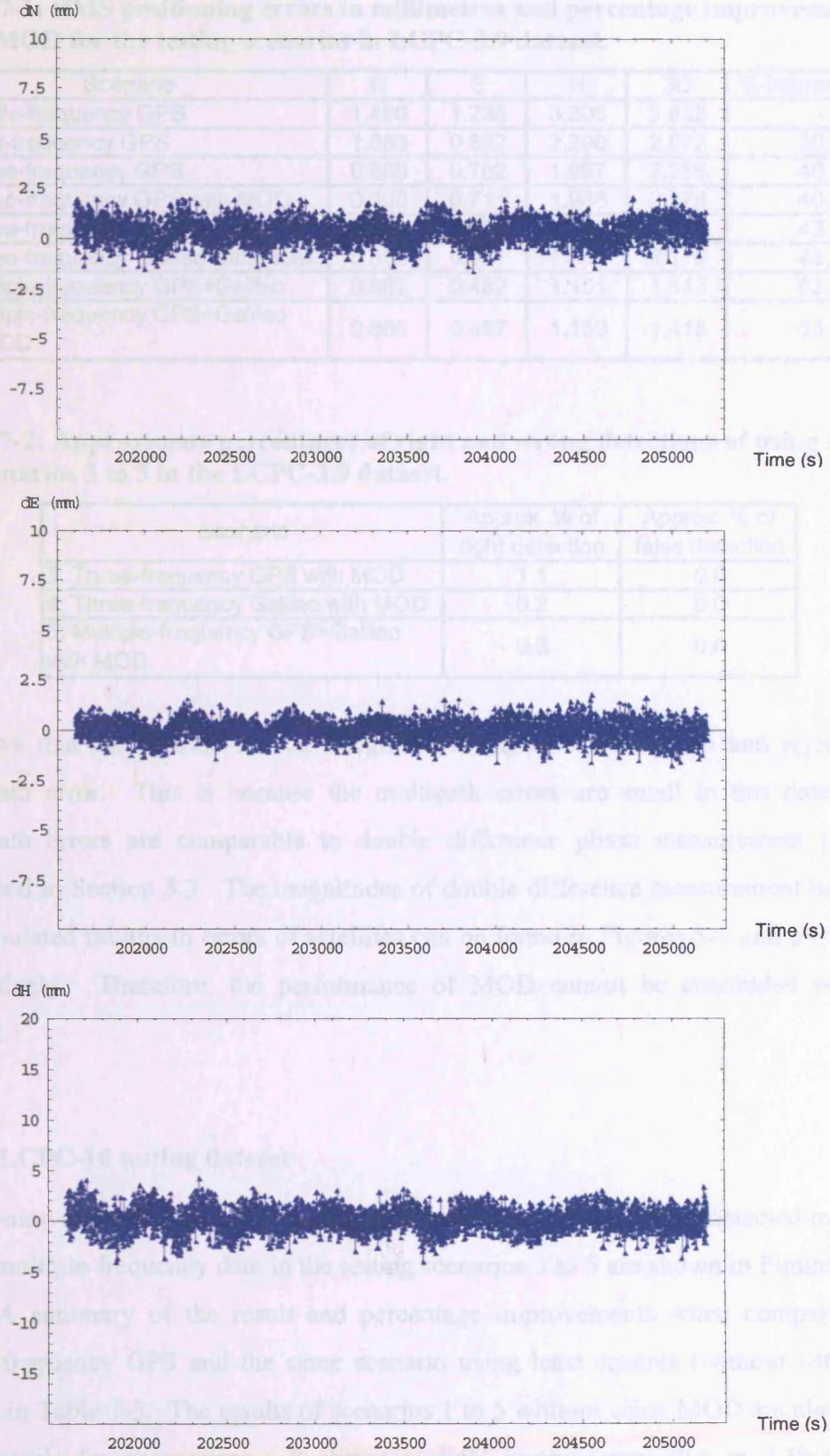

Figure 7-3: Positioning error in northing (top), easting (middle), and vertical (bottom) of single-epoch solution with MOD using Galileo + GPS multiple-frequency data in the LCPC-3.9 dataset.

Table 7-1: RMS positioning errors in millimetres and percentage improvement of using MOD for the testing scenarios in LCPC-3.9 dataset.

Scenario	N	E	H	3D	% improvement
1: Single-frequency GPS	1.490	1.238	3.306	3.832	-
2: Dual-frequency GPS	1.083	0.852	2.290	2.672	30.3
3: Three-frequency GPS	0.880	0.702	1.967	2.266	40.9
3: Three-frequency GPS with MOD	0.900	0.711	1.968	2.278	40.6
4: Three-frequency Galileo	0.888	0.928	1.750	2.171	43.3
4: Three-frequency Galileo with MOD	0.886	0.927	1.754	2.173	43.3
5: Multiple-frequency GPS+Galileo	0.662	0.482	1.151	1.413	63.1
5: Multiple-frequency GPS+Galileo with MOD	0.665	0.487	1.150	1.415	63.1

Table 7-2: Approximate percentages of right and wrong detections of using MOD for scenarios 3 to 5 in the LCPC-3.9 dataset.

Scenario	Approx. % of right detection	Approx. % of false detection
3: Three-frequency GPS with MOD	1.1	0.0
4: Three-frequency Galileo with MOD	0.2	0.0
5: Multiple-frequency GPS+Galileo with MOD	0.3	0.0

It shows that the method has an insignificant impact for detection and rejection of multipath error. This is because the multipath errors are small in this dataset; the multipath errors are comparable to double difference phase measurement noise as described in Section 5.3. The magnitudes of double difference measurement noise and the simulated multipath errors of satellites can be found in Figures 5-5 and 5-8 to 5-11 respectively. Therefore, the performance of MOD cannot be concluded with this dataset.

7.3.2 LCPC-10 testing dataset

Positioning errors (in northing, easting, and height) after rejection of detected multipath using multiple-frequency data in the testing scenarios 3 to 5 are shown in Figures 7-4 to 7-6. A summary of the result and percentage improvements when compared with single-frequency GPS and the same scenario using least squares (without MOD) are shown in Table 7-3. The results of scenarios 1 to 5 without using MOD are also shown in the table for comparison. It shows a slight improvement (0.6 to 2.3%) on 3D positioning accuracy. Table 7-4 shows that the method has an about 4 to 6% successful rate for detection and rejection of multipath error. In other words about 4 to 6% of the

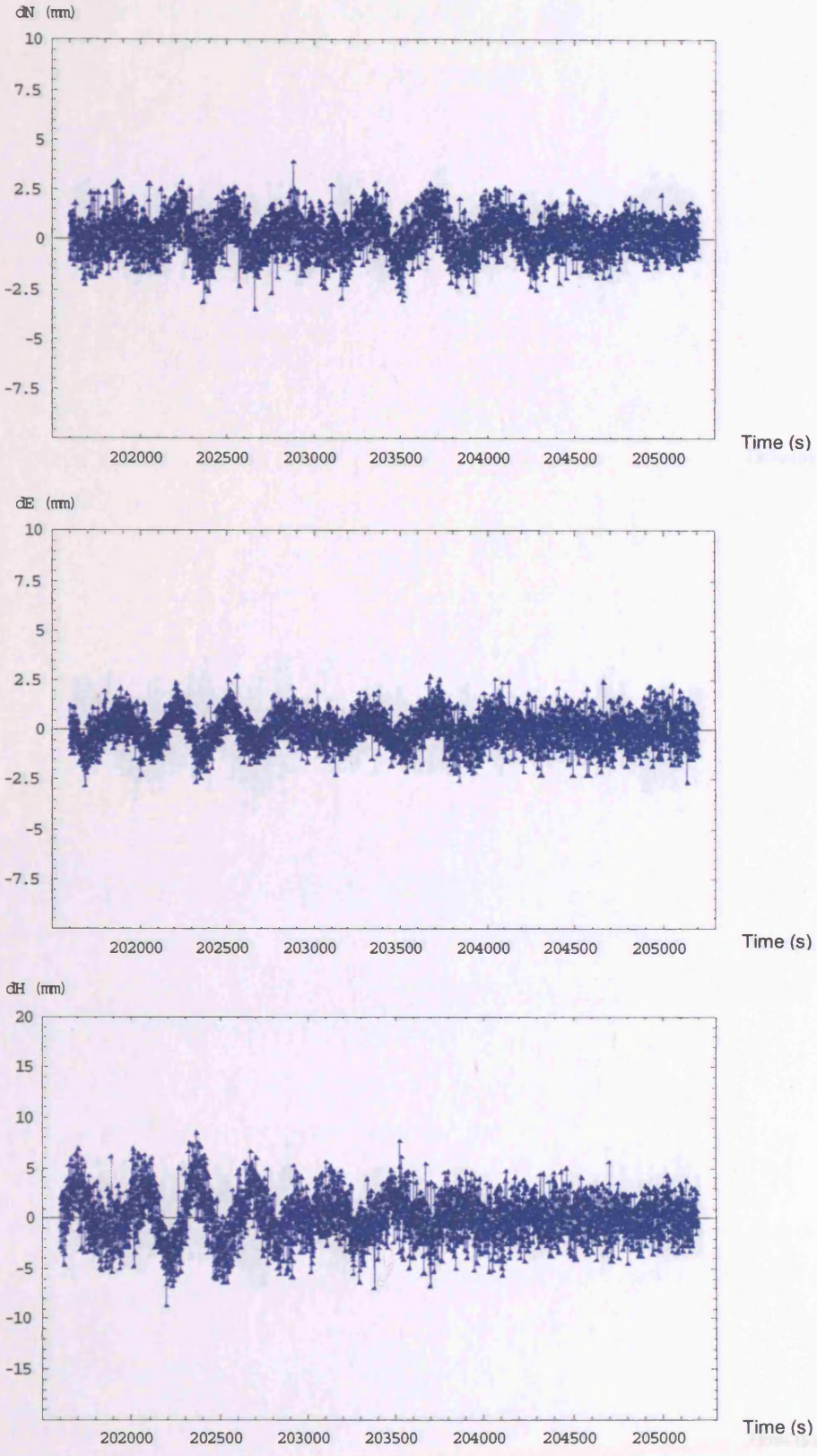

Figure 7-4: Positioning error in northing (top), easting (middle), and vertical (bottom) of single-epoch solution with MOD using GPS three-frequency data in the LCPC-10 dataset.

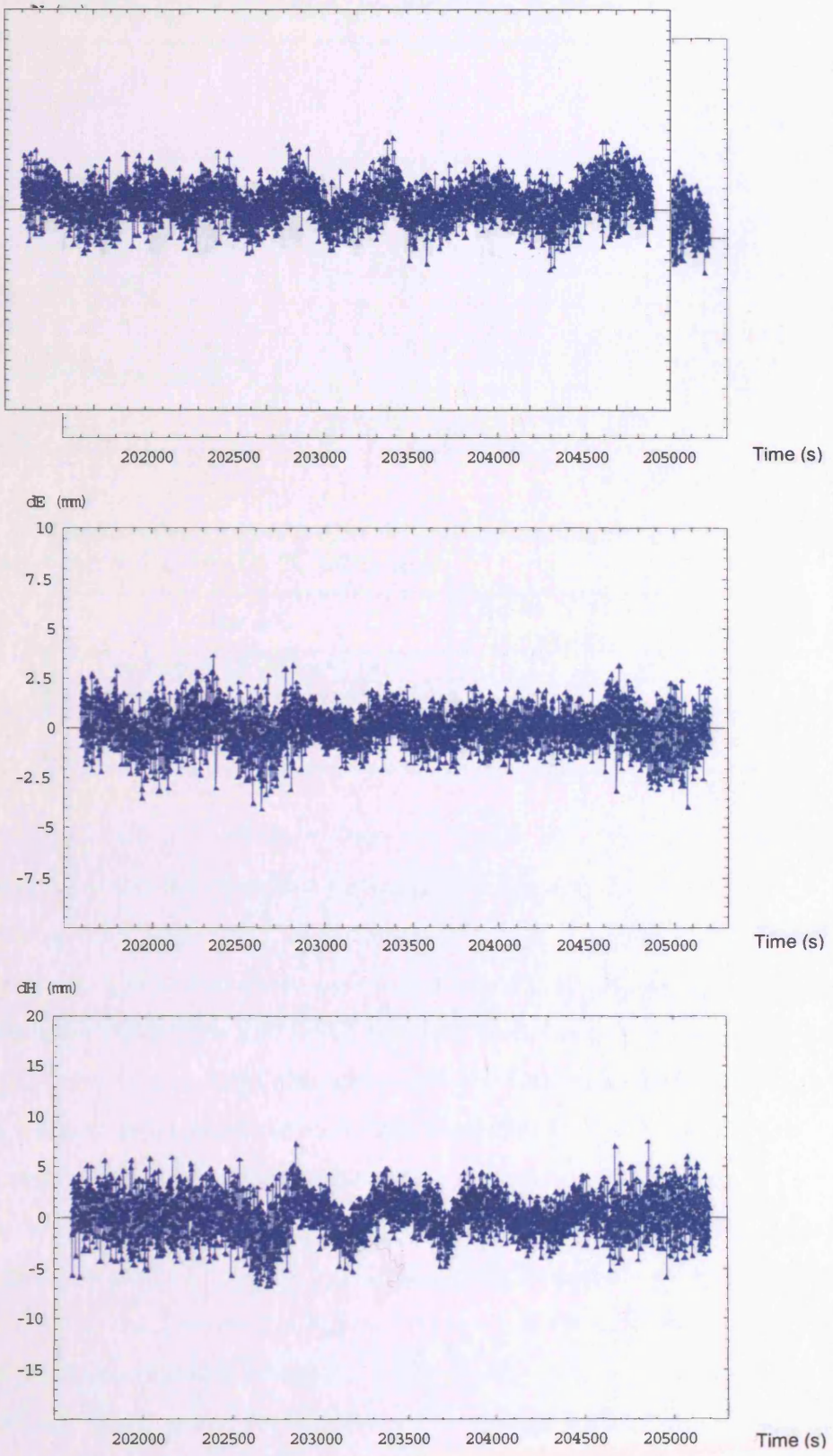

Figure 7-5: Positioning error in northing (top), easting (middle), and vertical (bottom) of single-epoch solution with MOD using Galileo three-frequency data in the LCPC-10 dataset.

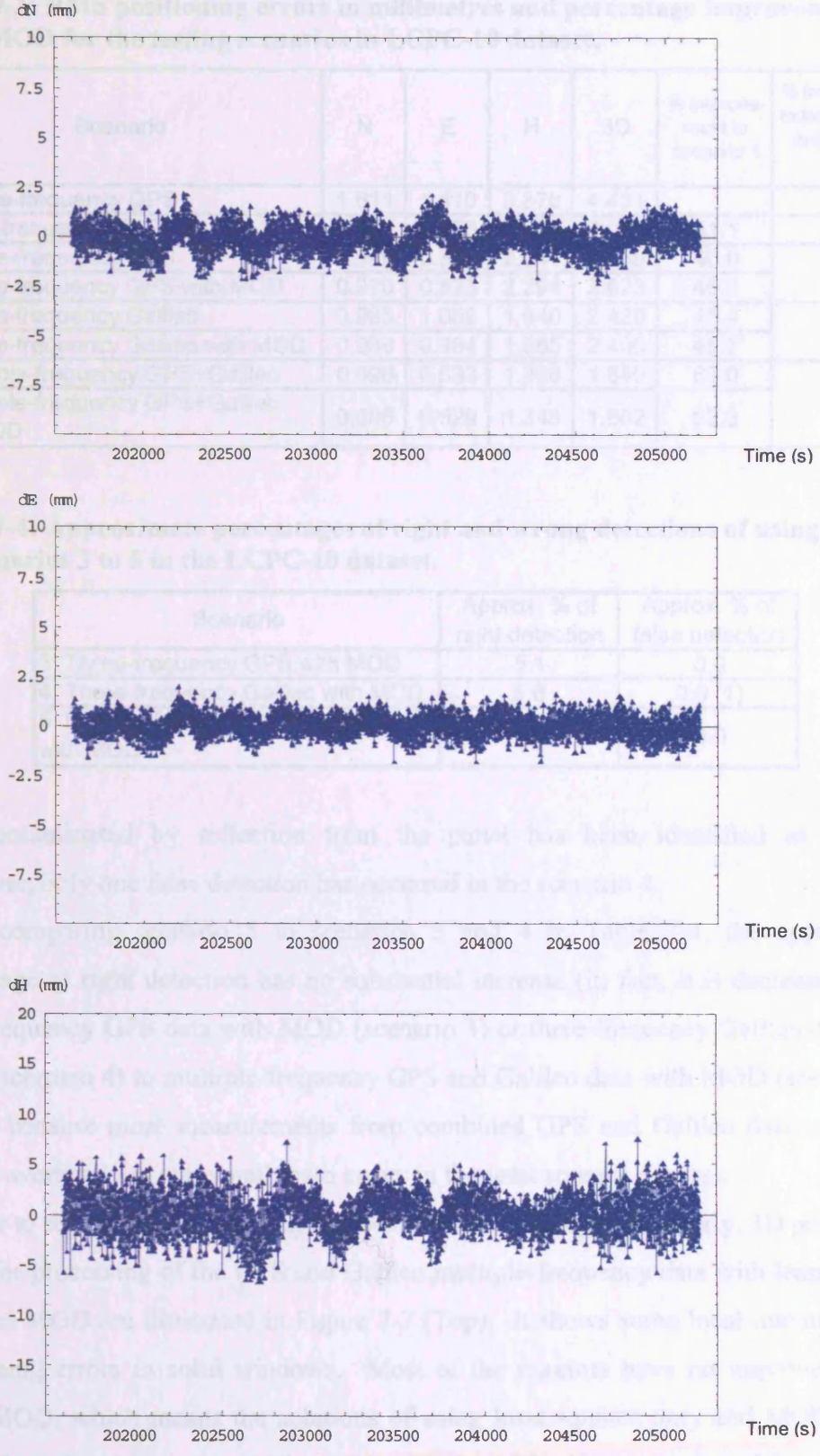

Figure 7-6: Positioning error in northing (top), easting (middle), and vertical (bottom) of single-epoch solution with MOD using Galileo + GPS multiple-frequency data in the LCPC-10 dataset.

Table 7-3: RMS positioning errors in millimetres and percentage improvement of using MOD for the testing scenarios in LCPC-10 dataset.

Scenario	N	E	H	3D	% improvement to scenario 1	% improvement to least squares only (without MOD)
1: Single-frequency GPS	1.611	1.410	3.879	4.431	-	-
2: Dual-frequency GPS	1.171	0.976	2.642	3.051	31.1	-
3: Three-frequency GPS	0.948	0.830	2.341	2.659	40.0	
3: Three-frequency GPS with MOD	0.970	0.823	2.294	2.623	40.8	1.4
4: Three-frequency Galileo	0.985	1.059	1.940	2.420	45.4	
4: Three-frequency Galileo with MOD	0.980	0.984	1.965	2.406	45.7	0.6
5: Multiple-frequency GPS+Galileo	0.696	0.533	1.386	1.640	63.0	
5: Multiple-frequency GPS+Galileo with MOD	0.686	0.529	1.348	1.602	63.8	2.3

Table 7-4: Approximate percentages of right and wrong detections of using MOD for scenarios 3 to 5 in the LCPC-10 dataset.

Scenario	Approx. % of right detection	Approx. % of false detection
3: Three-frequency GPS with MOD	5.1	0.0
4: Three-frequency Galileo with MOD	5.6	0.0 (1)
5: Multiple-frequency GPS+Galileo with MOD	3.6	0.0

data contaminated by reflection from the panel has been identified as outliers. Moreover, only one false detection has occurred in the scenario 4.

When comparing scenario 5 to scenarios 3 and 4 in Table 7-4, the approximate percentage of right detection has no substantial increase (in fact, it is decreased) from three-frequency GPS data with MOD (scenario 3) or three-frequency Galileo data with MOD (scenario 4) to multiple-frequency GPS and Galileo data with MOD (scenario 5). This is because more measurements from combined GPS and Galileo data may have already averaged out many multipath errors in the least squares process.

In order to see the impact of using MOD on multipath mitigation clearly, 3D positioning errors for processing of the GPS and Galileo multiple-frequency data with least squares only and MOD are illustrated in Figure 7-7 (Top). It shows some local maxima of 3D positioning errors in solid windows. Most of the maxima have no improvement by using MOD, which means the solutions of using least squares only and MOD are the same. In order to investigate this problem further, it had better look at 3D positioning errors caused by one satellite only. Therefore, 3D position errors for processing of the GPS three-frequency data with least squares and MOD are plotted in Figure 7-7 (Middle), and the corresponding simulated multipath errors in the GPS satellite PRN02

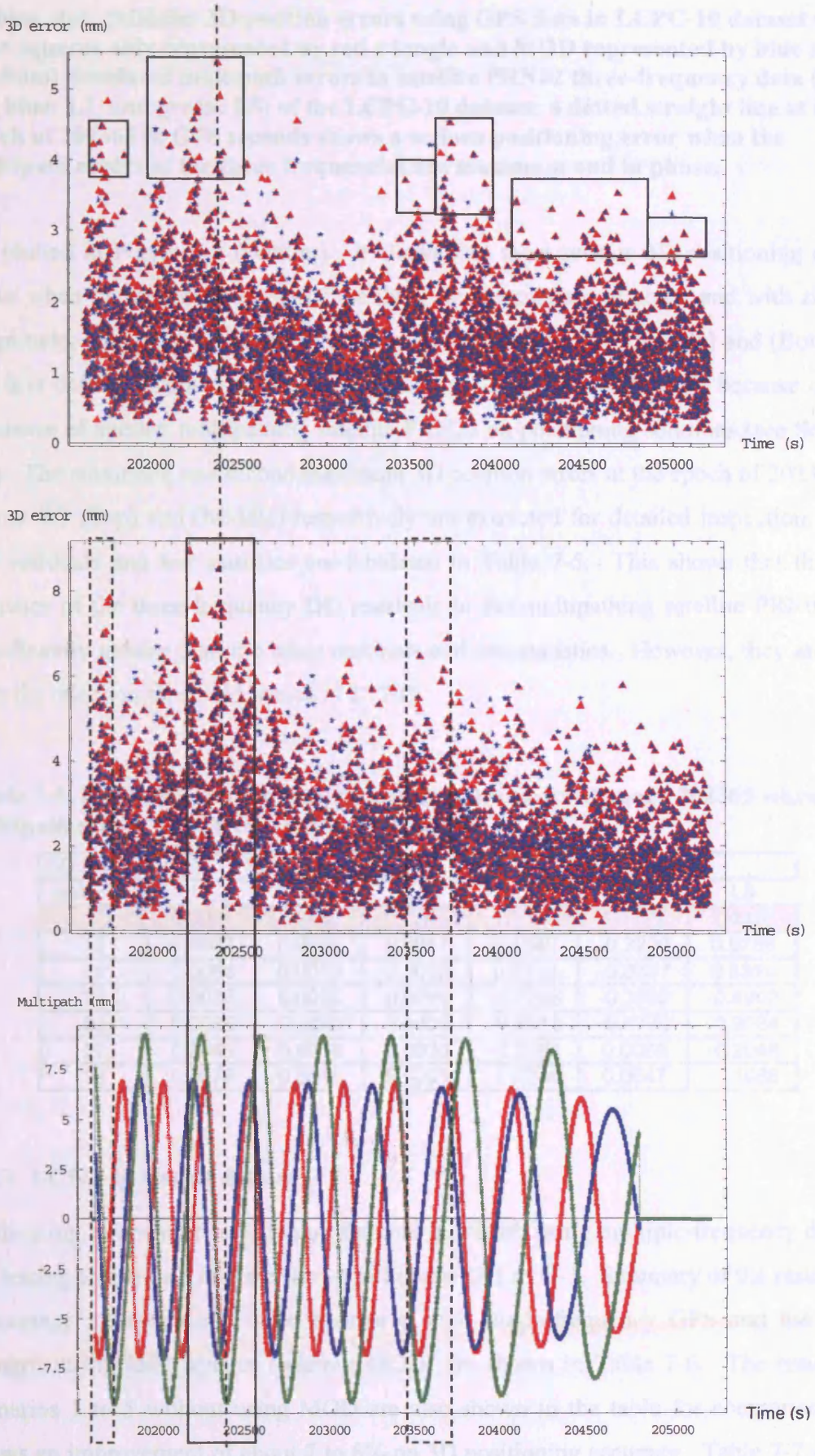

Figure 7-7: (Top) 3D position errors using GPS and Galileo data in LCPC-10 dataset with least squares only represented by red triangle and MOD represented

by blue star, (Middle) 3D position errors using GPS data in LCPC-10 dataset with least squares only represented by red triangle and MOD represented by blue star, (Bottom) simulated multipath errors in satellite PRN02 three-frequency data (red: L1, blue: L2, and green: L5) of the LCPC-10 dataset; a dotted straight line at the epoch of 202365 in GPS seconds shows a serious positioning error when the multipath errors of the three frequencies are maximum and in phase.

are plotted in Figure 7-7 (Bottom). It shows that most serious 3D positioning errors occur when the multipath errors of the three frequencies are in phase and with similar magnitude, which can be found in the windows in Figures 7-7 (Middle) and (Bottom); the first dotted window (on the far left) may not show it significantly because of the influence of another multipathing satellite PRN22 on positioning solutions (see Section 5.4). The maximum and second maximum 3D position errors at the epoch of 202365 in Figure 7.7 (Top) and (Middle) respectively are extracted for detailed inspection. The DD residuals and test statistics are tabulated in Table 7-5. This shows that the test statistics of the three-frequency DD residuals in the multipathing satellite PRN02 are significantly greater than the other residuals and test statistics. However, they are less than the rejection threshold, which is 2.7701.

Table 7-5: Residuals and test statistics of measurements at epoch 202365 when the multipath errors of all frequencies are in phase.

DD PRN 3	Residuals (m)			Test statistics		
and PRN	L1	L2	L5	L1	L2	L5
2	0.0085	0.0059	0.0092	1.3556	1.7729	2.4467
15	0.0062	0.0009	0.0047	0.4542	-0.2239	0.6786
18	0.0066	0.0013	0.0053	0.6138	-0.0337	0.8814
21	0.0033	0.0005	0.0019	-0.7056	-0.3692	-0.4902
22	0.0036	-0.0002	0.0009	-0.6013	-0.6770	-0.9084
27	0.0045	0.0014	0.0026	-0.2161	0.0080	-0.2048
31	0.0078	0.0016	0.0001	1.0794	0.0547	-1.1986

7.3.3 LCPC-20 testing dataset

Positioning errors after rejection of detected multipath using multiple-frequency data in the testing scenarios 3 to 5 are shown in Figures G-1 to G-3. Summary of the result and percentage improvements when compared with single-frequency GPS and the same scenario using least squares (without MOD) are shown in Table 7-6. The results of scenarios 1 to 5 without using MOD are also shown in the table for comparison. It shows an improvement of about 7 to 8% on 3D positioning accuracy. Table 7-7 shows that the method has an about 15, 10, and 12% successful rate for detection and rejection

of multipath error in scenarios 3, 4, and 5 respectively. Moreover, only one false detection has occurred in the scenario 4 and 5 and two in the scenario 3.

Table 7-6: RMS positioning errors in millimetres and percentage improvement of using MOD for the testing scenarios in LCPC-20 dataset.

Scenario	N	E	H	3D	% improve-ment to scenario 1	% improvement to least sqares only (without MOD)
1: Single-frequency GPS	1.818	1.540	4.093	4.736	-	
2: Dual-frequency GPS	1.290	1.062	2.771	3.236	31.7	
3: Three-frequency GPS	1.049	0.928	2.619	2.970	37.3	
3: Three-frequency GPS with MOD	1.020	0.865	2.410	2.757	41.8	7.2
4: Three-frequency Galileo	1.109	1.192	2.044	2.613	44.8	
4: Three-frequency Galileo with MOD	0.974	0.937	2.025	2.434	48.6	6.9
5: Multiple-frequency GPS+Galileo	0.790	0.596	1.542	1.832	61.3	
5: Multiple-frequency GPS+Galileo with MOD	0.715	0.563	1.416	1.683	64.5	8.1

Table 7-7: Approximate percentages of right and wrong detections of using MOD for scenarios 3 to 5 in the LCPC-20 dataset.

Scenario	Approx. % of right detection	Approx. % of false detection
3: Three-frequency GPS with MOD	15.4	0.0 (2)
4: Three-frequency Galileo with MOD	10.4	0.0 (1)
5: Multiple-frequency GPS+Galileo with MOD	11.6	0.0 (1)

According to the percentage improvements in Tables 7-3 and 7-6, a better multipath mitigation performance of using MOD can be seen in this dataset. This is because the only difference of this dataset from the LCPC-10 dataset is the greater relative permittivity, which leads to greater magnitude of multipath errors. Obviously, greater magnitude of multipath error is easier for MOD to detect and hence reject in data processing. This can be seen from the approximate percentage of right detection in Tables 7-7 and 7-4.

3D positioning errors for processing of the GPS and Galileo multiple-frequency data with least squares only and MOD are illustrated in Figure 7-8. It shows the similar local maxima of 3D positioning errors as in Figure 7-7 (Top). Epoch 203726 in GPS seconds shows no impact when using MOD when compared with using least squares only. The DD residuals and test statistics of this epoch are tabulated in Table 7-8. All multipath errors in the three-frequency GPS PRN02 data are maximum (L5 multipath error is almost maximum, see Figure E-1) and in phase. In this epoch, Galileo SV14 also have

multipath (see Figure E-2). Again, some test statistics highlighted in pink in Table 7-8 are significantly greater than the other test statistics, but they are not greater than the rejection threshold of 3.017 and so they cannot be detected and rejected. Therefore, it has a similar problem to the LCPC-10 dataset.

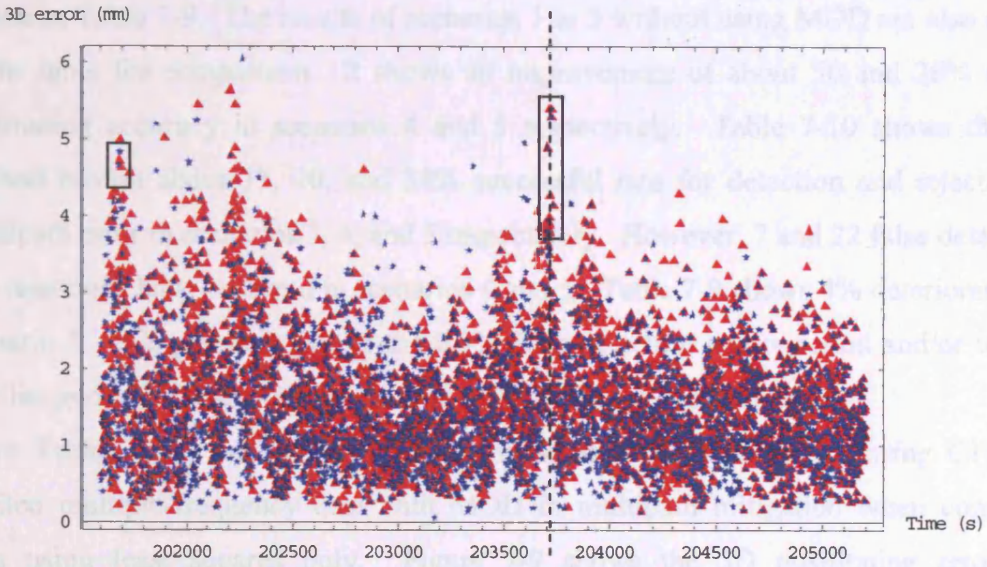

Figure 7-8: 3D position errors using GPS and Galileo data in LCPC-20 dataset with least squares only represented by red triangle and MOD represented by blue star; a dotted straight line at the epoch of 203726 in GPS seconds shows a serious positioning error when the multipath errors cannot be mitigated by using MOD.

Table 7-8: Residuals and test statistics of measurements at epoch 203726.

	DD PRN 3	Residuals (m)			Test statistics		
	and PRN	L1	L2	L5	L1	L2	L5
GPS	2	-0.0084	0.0014	-0.0075	-2.4528	0.7292	-2.2598
	15	-0.0030	-0.0011	-0.0013	-0.3560	-0.2706	0.1460
	18	-0.0017	-0.0007	-0.0003	0.1425	-0.1125	0.5354
	21	-0.0004	-0.0016	0.0006	0.6549	-0.4408	0.9029
	22	-0.0004	0.0012	-0.0019	0.6828	0.6558	-0.0999
	31	-0.0007	-0.0023	-0.0014	0.5613	-0.7706	0.1305
Galileo	DD SV20						
	and SV	L1	E5a	E5b	L1	E5a	E5b
	13	-0.0042	-0.0033	0.0096	-0.4301	-0.3574	1.9200
	14	-0.0031	-0.0021	-0.0011	0.0299	0.1316	-2.2763
	15	-0.0014	-0.0037	0.0064	0.7261	-0.5400	0.6913
	19	-0.0039	-0.0025	0.0078	-0.3038	-0.0269	1.2816
	21	-0.0053	-0.0020	0.0076	-0.8483	0.1754	1.1510
	22	-0.0042	-0.0033	0.0028	-0.4261	-0.3687	-0.8167

7.3.4 LBCH-7 testing dataset

Positioning errors (in northing, easting, and height) after rejection of detected multipath using multiple-frequency data in the testing scenarios 3 to 5 are shown in Figures G-4 to G-6. A summary of the result and percentage improvements when compared with single-frequency GPS and the same scenario using least squares (without MOD) is shown in Table 7-9. The results of scenarios 1 to 5 without using MOD are also shown in the table for comparison. It shows an improvement of about 50 and 26% on 3D positioning accuracy in scenarios 4 and 5 respectively. Table 7-10 shows that the method has an about 33, 20, and 38% successful rate for detection and rejection of multipath error in scenarios 3, 4, and 5 respectively. However, 7 and 22 false detections and rejections have occurred in scenarios 4 and 5. Table 7-9 shows 4% deterioration in scenario 3. It is probably due to the 0.8% false detection and rejection and/or weaker satellite geometry after correct rejection of multipathing measurements.

From Table 7-9, it can be found that a substantial improvement in using GPS and Galileo multiple-frequency data with MOD in multipath mitigation when compared with using least squares only. Figure 7-9 shows the 3D positioning errors for processing of the GPS and Galileo multiple-frequency data with least squares only and MOD. Reductions in 3D position errors in most epochs can be seen. Epoch 159045 shows a greater position error when using MOD than using least squares only. The DD residuals and test statistics of the epoch are tabulated in Table 7-11. Simulated multipath errors of the multipathing satellites at the epoch are shown in Figures E-6, E-7, and E-9. They are shown here in Figure 7-10 for better illustration of this problem. Table 7-11 shows the test statistics for the three-frequency data of the three multipathing satellites highlighted in pink are significantly greater than the other test statistics. However, they are not greater than the rejection threshold, which is 3.0505, and therefore they cannot be rejected from data processing. It is probably due to the correlated phases of multipath errors as described in Section 7.3.2. As it can be seen in Figure 7-10, multipath errors in any two of the three frequencies of the satellites at the epoch 159045 are in phase and almost maximum. Correct rejection of some multipath contaminated measurements leads to biased minimization of residuals in the least squares process and hence they may not be detected in the next detection cycle. In other words, the remaining (undetected) multipath errors are absorbed in the estimated position and lead to a large positioning error.

Table 7-9: RMS positioning errors in millimetres and percentage improvement of using MOD for the testing scenarios in LBCH-7 dataset.

Scenario	N	E	H	3D	% improvement to scenario 1	% improvement to least squares only (without MOD)
1: Single-frequency GPS	5.086	2.336	5.175	7.622	-	
2: Dual-frequency GPS	3.522	1.745	3.713	5.407	29.1	
3: Three-frequency GPS	3.208	1.340	2.610	4.347	43.0	
3: Three-frequency GPS with MOD	3.689	1.257	2.293	4.522	40.7	-4.0
4: Three-frequency Galileo	2.460	0.685	3.907	4.668	38.8	
4: Three-frequency Galileo with MOD	1.214	0.494	1.911	2.317	69.6	50.4
5: Multiple-frequency GPS+Galileo	1.997	0.667	2.279	3.103	59.3	
5: Multiple-frequency GPS+Galileo with MOD	1.734	0.477	1.449	2.309	69.7	25.6

Table 7-10: Approximate percentages of right and wrong detections of using MOD for scenarios 3 to 5 in the LBCH-7 dataset.

Scenario	Approx. % of right detection	Approx. % of false detection
3: Three-frequency GPS with MOD	32.9	0.8
4: Three-frequency Galileo with MOD	20.4	0.0 (7)
5: Multiple-frequency GPS+Galileo with MOD	38.4	0.0 (22)

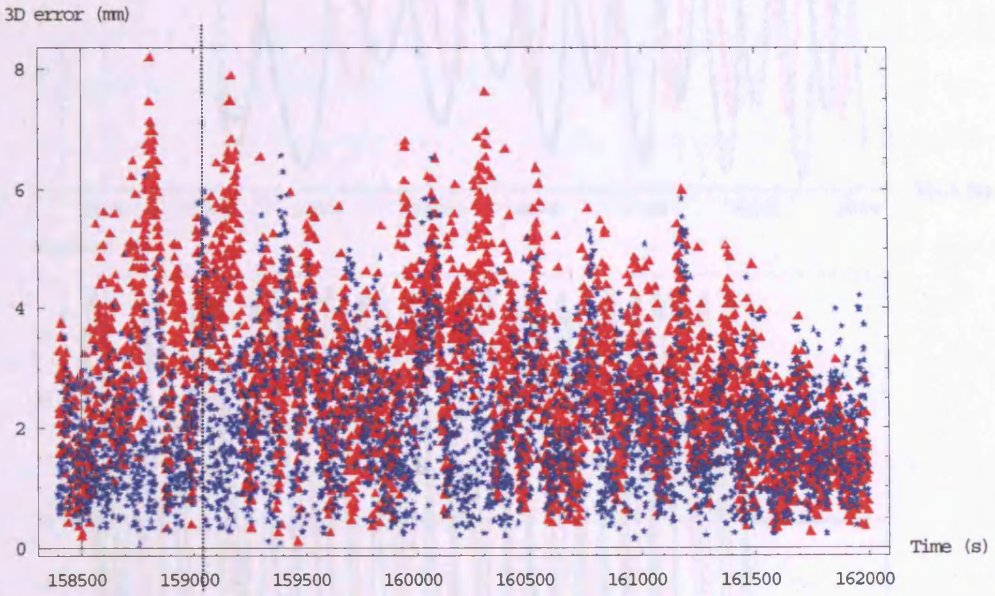

Figure 7-9: 3D position errors using GPS and Galileo data in LBCH-7 dataset with least squares only represented by red triangle and MOD represented by blue star; a dotted line at epoch 159045 in GPS seconds shows a greater positioning error when using MOD.

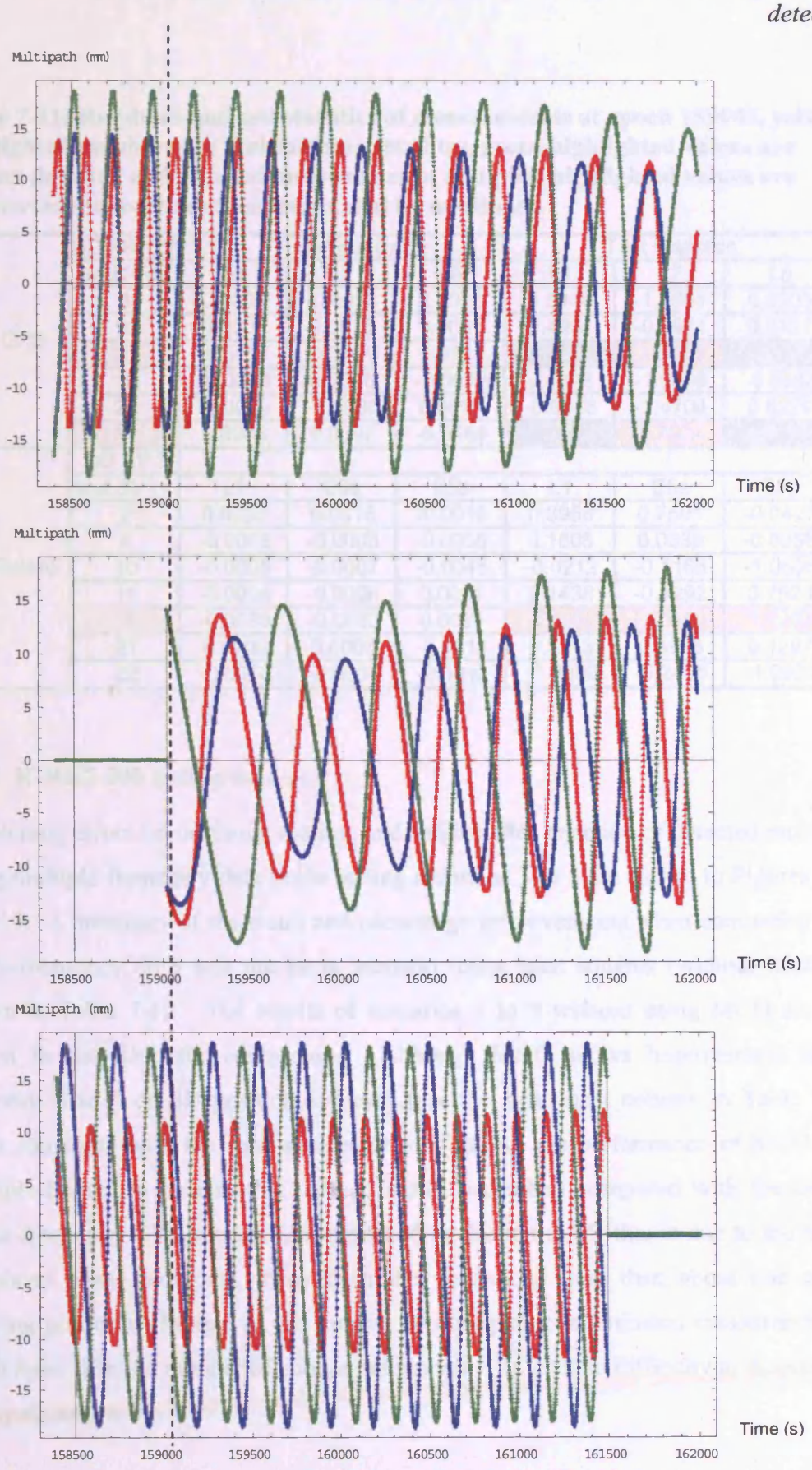

Figure 7-10: Simulated GPS and Galileo multiple-frequency (red: L1, blue: L2, green: L5) phase multipath error at epoch 159045 in the LBCH-7 dataset; (Top) GPS PRN13, (Middle) GPS PRN31, and (Bottom) Galileo SV18.

Table 7-11: Residuals and test statistics of measurements at epoch 159045, yellow highlighted numbers are multipathing satellites, green highlighted values are correct detected and rejected measurements, and pink highlighted values are undetected measurements contaminated by multipath.

	DD PRN27	Residuals (m)			Test statistics		
	and PRN	L1	L2	L5	L1	L2	L5
GPS	8	0.0007	-0.0003	0.0018	0.5446	-1.3691	0.5205
	10	0.0006	0.0025	0.0011	0.4954	-0.2971	0.2727
	13	-0.0111	0.0104	0.0161	-4.1025	2.8475	6.1297
	19	-0.0003	0.0006	-0.0009	0.1318	-1.0259	-0.5303
	28	-0.0029	-0.0006	0.0021	-0.8516	-1.4706	0.6229
	31	0.0083	0.0097	-0.0169	3.7395	2.7024	-7.2229
Galileo	DD SV 3						
	and SV	L1	E5a	E5b	L1	E5a	E5b
	2	0.0003	0.0015	-0.0018	0.3958	0.7501	-0.0427
	4	-0.0003	-0.0003	-0.0039	0.1605	0.0636	-0.8258
	10	-0.0008	-0.0007	-0.0045	-0.0212	-0.1166	-1.0508
	11	-0.0004	-0.0008	0.0001	0.1436	-0.1292	0.7523
	18	-0.0036	-0.0030	0.0021	-1.1352	-1.0163	1.5203
	21	0.0006	0.0008	-0.0014	0.5213	0.4986	0.1297
	22	-0.0016	-0.0011	-0.0045	-0.3609	-0.2435	-1.0923

7.3.5 K-HK7-300 testing dataset

Positioning errors (in northing, easting, and height) after rejection of detected multipath using multiple-frequency data in the testing scenarios 3 to 5 are shown in Figures 7-11 to 7-13. A summary of the result and percentage improvements when comparing with single-frequency GPS and the same scenario using least squares (without MOD) is shown in Table 7-12. The results of scenarios 1 to 5 without using MOD are also shown in the table for comparison. Although MOD shows improvement in the scenarios 3 to 5 on 3D position accuracy (see the right-most column in Table 7-12) when compared with the least squares only solutions, the performance of MOD with multiple-frequency data in this dataset is still bad when compared with the current single-frequency GPS system. As explained in Section 6.3.5, this is due to the highly correlated phase multipath errors from the very close (less than about one metre) carrying platform. Moreover, the number of multipath contaminated measurements is much more than the number of good measurements. It leads to difficulty in detection of multipath errors.

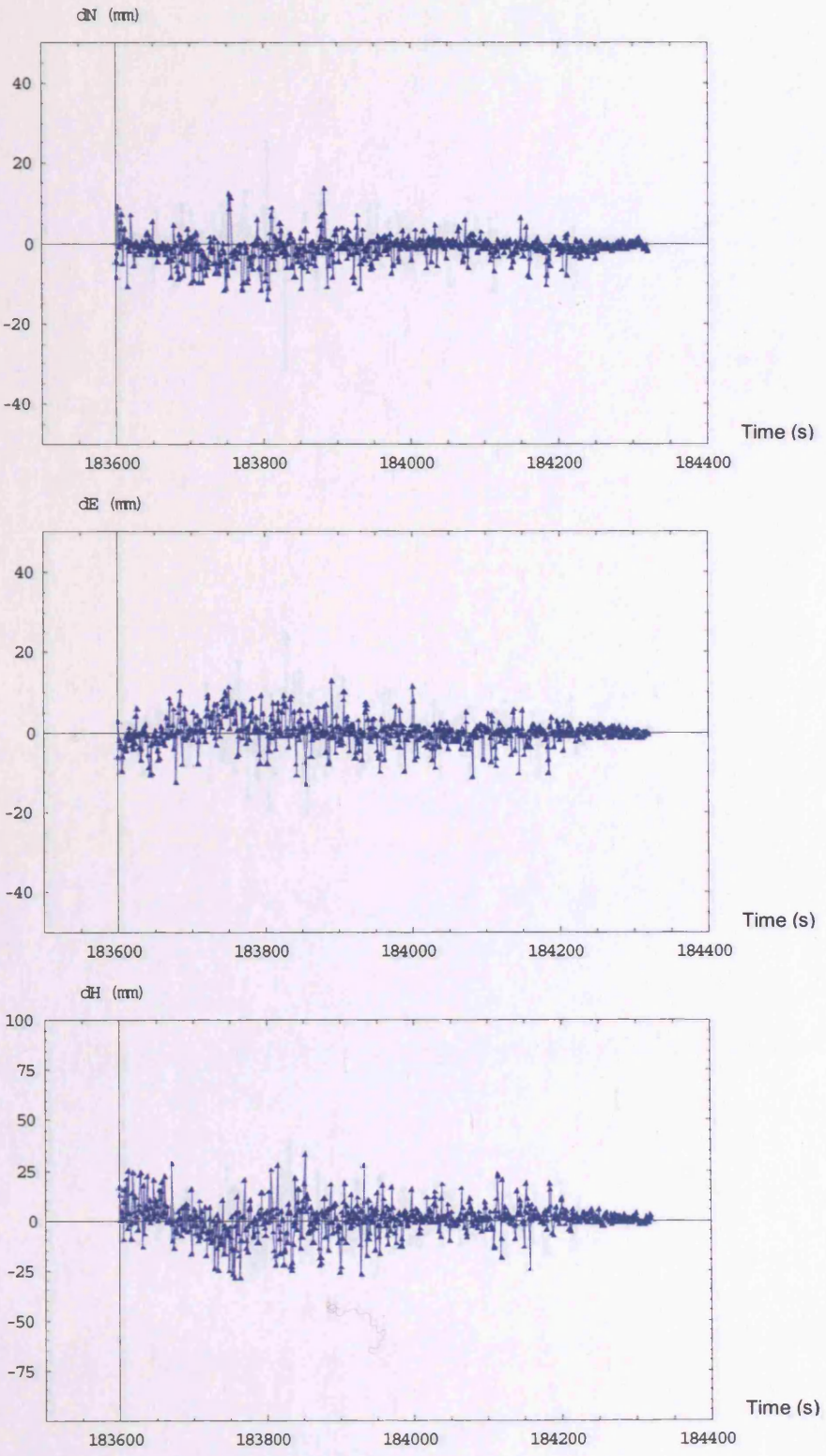

Figure 7-11: Positioning error in northing (top), easting (middle), and vertical (bottom) of single-epoch solution with MOD using GPS three-frequency data in the K-HK7-300 dataset.

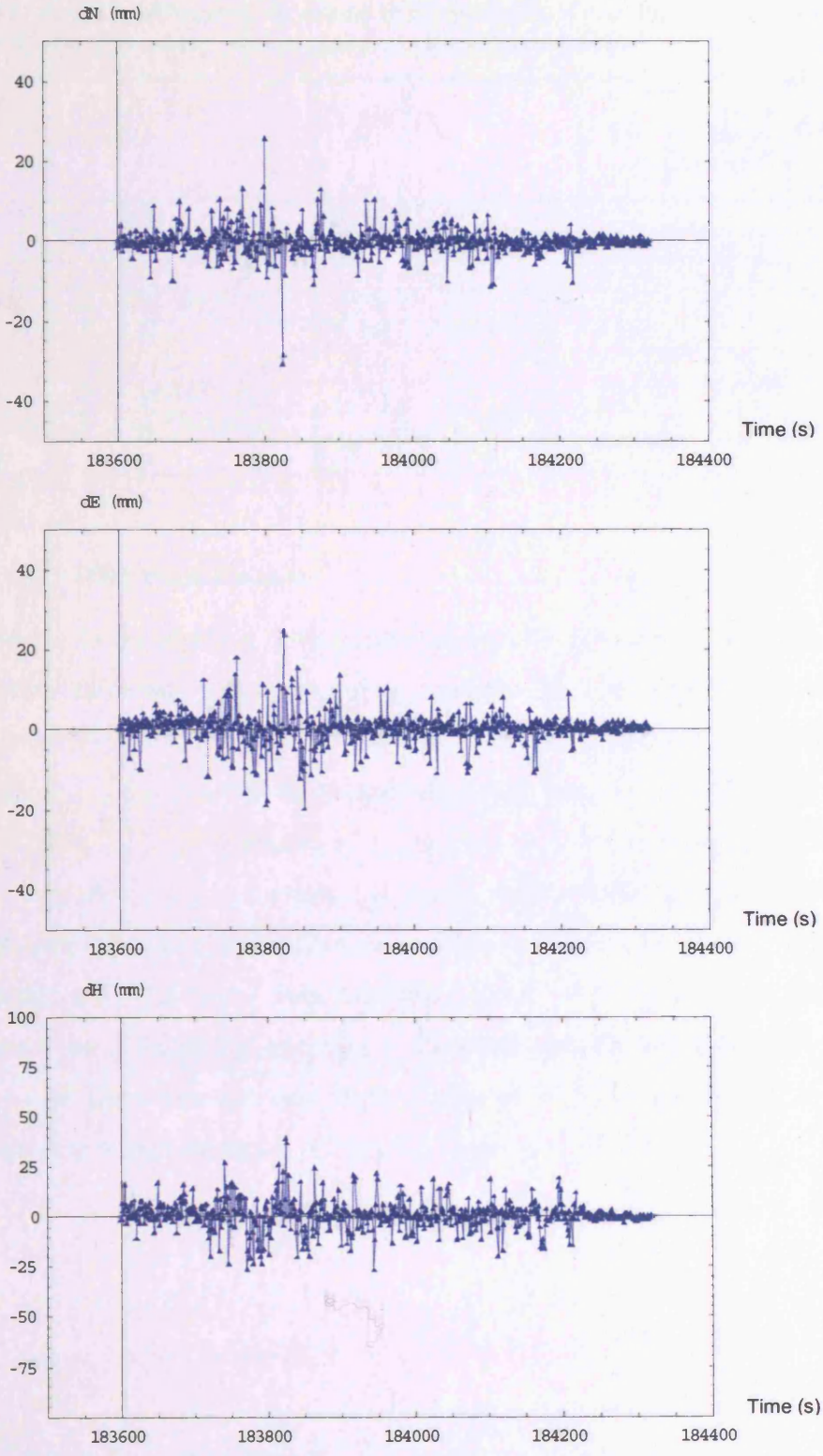

Figure 7-12: Positioning error in northing (top), easting (middle), and vertical (bottom) of single-epoch solution with MOD using Galileo three-frequency data in the K-HK7-300 dataset.

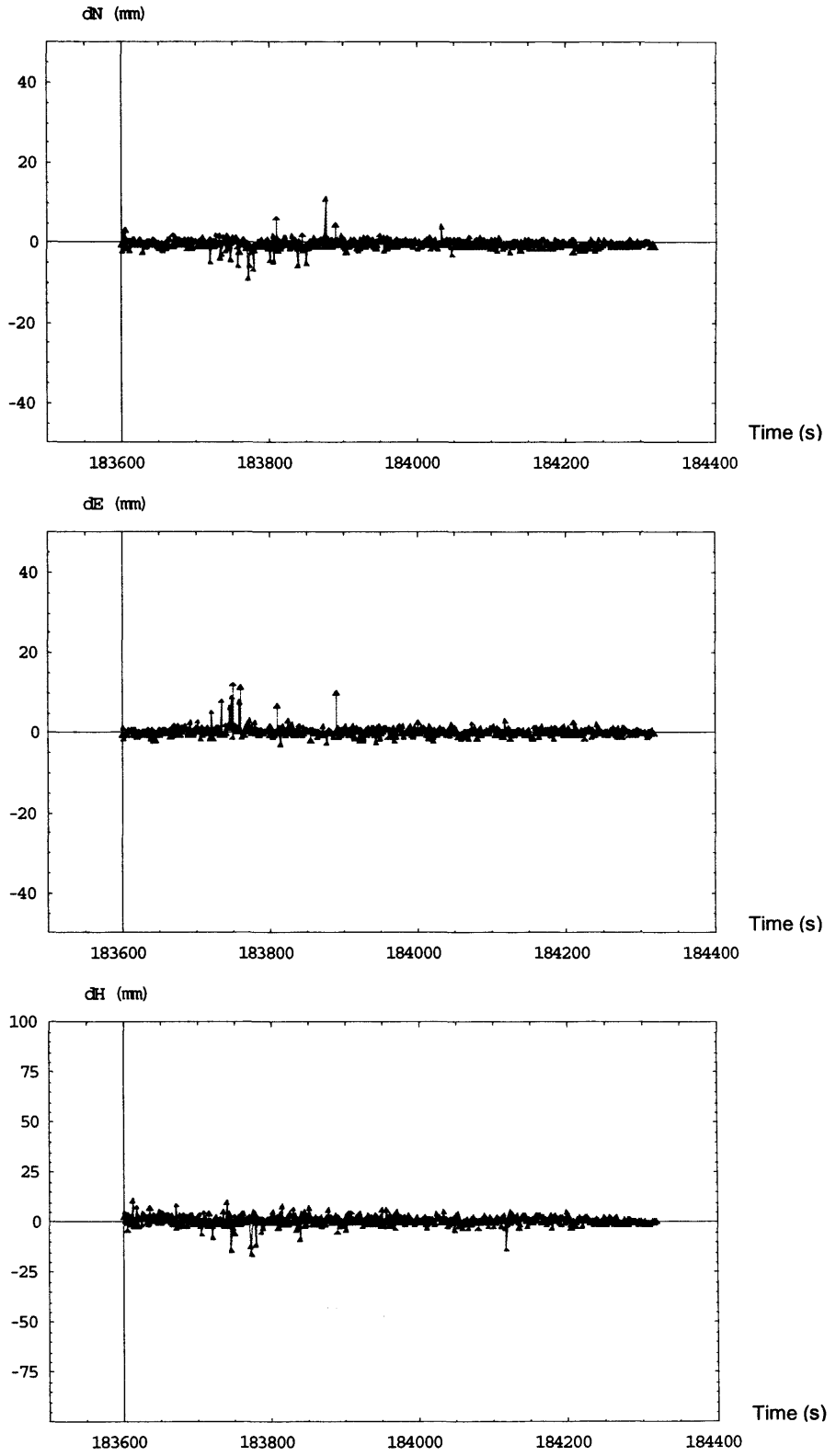

Figure 7-13: Positioning error in northing (top), easting (middle), and vertical (bottom) of single-epoch solution with MOD using Galileo + GPS multiple-frequency data in the K-HK7-300 dataset.

Table 7-12: RMS positioning errors in millimetres and percentage improvement of using MOD for the testing scenarios in K-HK7-300 dataset.

Scenario	N	E	H	3D	% improvement to scenario 1	% improvement to least squares only (without MOD)
1: Single-frequency GPS	0.558	0.466	1.103	1.321	-	
2: Dual-frequency GPS	0.403	0.330	0.772	0.931	29.5	
3: Three-frequency GPS	1.884	1.877	4.592	5.306	-301.6	
3: Three-frequency GPS with MOD	1.592	1.570	3.716	4.337	-228.2	18.3
4: Three-frequency Galileo	2.003	2.356	4.279	5.280	-299.5	
4: Three-frequency Galileo with MOD	1.536	1.801	3.350	4.102	-210.4	22.3
5: Multiple-frequency GPS+Galileo	1.322	1.507	2.963	3.577	-170.7	
5: Multiple-frequency GPS+Galileo with MOD	0.572	0.579	1.088	1.358	-2.8	62.0

7.3.6 K-HK7-600 testing dataset

Positioning errors (in northing, easting, and height) after rejection of detected multipath using multiple-frequency data in the testing scenarios 3 to 5 are shown in Figures G-7 to G-9. A summary of the result and percentage improvements when compared with single-frequency GPS and the same scenario using least squares (without MOD) is shown in Table 7-13. The results of scenarios 1 to 5 without using MOD are also shown in the table for comparison. It shows improvement by using MOD when compared with the least squares (see the right-most column in Table 7-13); MOD is able to detect and reject some measurements contaminated by multipath and leads to improvement on positioning accuracy. However, MOD solutions with multiple-frequency data show worse results when compared with the current single-frequency GPS system, the reason for this is discussed in Section 6.3.6.

Table 7-13: RMS positioning errors in millimetres and percentage improvement of using MOD for the testing scenarios in K-HK7-600 dataset.

Scenario	N	E	H	3D	% improvement to scenario 1	% improvement to least squares only (without MOD)
1: Single-frequency GPS	0.544	0.458	1.085	1.297	-	
2: Dual-frequency GPS	0.390	0.326	0.764	0.917	29.3	
3: Three-frequency GPS	1.897	2.338	3.825	4.868	-275.3	
3: Three-frequency GPS with MOD	1.356	1.743	2.767	3.541	-173.0	27.3
4: Three-frequency Galileo	2.483	2.312	3.765	5.068	-290.7	
4: Three-frequency Galileo with MOD	2.002	1.993	3.197	4.266	-228.9	15.8
5: Multiple-frequency GPS+Galileo	1.314	1.370	2.007	2.763	-113.0	
5: Multiple-frequency GPS+Galileo with MOD	0.442	0.483	0.975	1.175	9.5	57.5

7.4 CONCLUDING REMARKS

This study (in this chapter) investigates the possibility and impact of the use of multiple outlier detection and rejection technique (called MOD) with multiple-frequency data on multipath mitigation. From the RMS error analyses of simulated data of the LCPC and LBCH datasets (one reflector and no multipath from the carrying platform) in Tables 7-3, 7-6 and 7-9, multiple-frequency GPS and Galileo data with proposed MOD technique shows about 64-70% improvement on positioning accuracy when compared with the current single-frequency GPS data. The improvement depends on the phase and amplitude of phase multipath error. Moreover, multiple-frequency GPS and Galileo data processing with MOD can further improve the positioning accuracy of multiple-frequency GPS and Galileo data processing with only the least squares method by about 3-26%, which also depends on the phase and amplitude of phase multipath error. This is because more redundant frequency data can better average multipath errors and hence detect serious multipath errors.

In Tables 7-3, 7-6 and 7-9, it can be seen that using three-frequency GPS or Galileo data with MOD has significant improvement on positioning accuracy in most cases. However, from Table 7-9, deterioration can be seen when using three-frequency GPS with MOD instead of processing with least squares only. It shows that three-frequency data with MOD does not necessarily showing any improvement. It may be because the redundancy is not sufficient to detect and reject multipath contaminated measurement correctly, and/or there are too many measurements contaminated by multipath (see Table 5-2 and Figures E-5 to E-7).

From the RMS error analyses in Tables 7-12 and 7-13 for the K-HK7-300 and K-HK7-600 datasets, which have multipath from a very close carrying platform, significant improvement on positioning accuracy can be seen when compared with the use of using MOD with least squares only (far right columns of Tables 7-12 and 7-13) especially using multiple-frequency GPS and Galileo data. However, multiple-frequency GPS and/or Galileo data with MOD solution may still be worse than the current single-frequency GPS system because of suffering from the highly correlated GPS L2 and L5 multipath errors and/or Galileo E5a and E5b multipath errors as described in Sections 6.3.5 and 6.3.6.

The success rate of MOD, again, depends on the frequency and amplitude of multipath error. Sections 7.3.1 to 7.3.3 show how the amplitude of multipath error affects the success rate of this technique. Obviously, the greater amplitude of multipath error (greater than the measurement noise), the easier for MOD to detect and reject the measurement contaminated by multipath. On the other hand, two examples of the impact of the frequency and amplitude of multipath error on MOD performance are described in Sections 7.3.2 and 7.3.4. In the first example, when the multipath errors in all three frequencies are in phase as shown in Figures 7-7 (Bottom), the positioning error is serious as shown in Figures 7-7 (Top) and (Middle), and no multipath error can be detected at that epoch in the LCPC-10 dataset as shown in Table 7-8. In this case, MOD has no impact on the estimated position. In the second example, when the multipath errors in any two of the three frequencies are in phase and (almost) maximum as shown in Figure 7-10, the positioning error is larger than when using least squares only as shown in Figure 7-9, and partial detection and rejection occurred at that epoch in the LBCH-7 dataset as shown in Table 7-11. In this case, MOD makes the position solution worse than when using least squares only.

In conclusion, MOD can improve positioning accuracy if there is no very close (less than about one metre) reflector near the receiving antenna. The performance of MOD depends on the phase and amplitude of phase multipath errors in the carrier frequencies. A weakness of MOD has been identified in this investigation. When three-frequency multipath errors are in phase, rejection of one outlier (multipath) by one outlier in each least squares process leads to the redistribution of errors and makes the residuals of the rest two/one multipath contaminated measurement(s) in other frequency(ies) smaller and eventually they cannot be detected and rejected because their test statistics are not greater than the rejection threshold.

8. MULTIPATH MITIGATION USING MULTIPLE-FREQUENCY GNSS DATA WITH COCKTAIL MULTIPLE OUTLIER DETECTION

8.1 INTRODUCTION

As described in the previous chapter, the MOD method is not sufficiently robust to tackle the frequency-dependent multipath errors because it cannot handle the worst case scenario when multiple frequency multipath errors from a particular satellite are all (or any two of the three frequencies) in-phase. Therefore a cocktail multiple outlier detection algorithm is proposed and tested in this chapter.

8.2 COCKTAIL MULTIPLE OUTLIER DETECTION ALGORITHM

The basic principle of this algorithm is based on the MOD method described in Section 7.2. In the MOD method, the test statistic of each measurement is tested against a critical threshold. However, Cocktail Multiple Outlier Detection (CMOD) algorithm simultaneously tests all residuals of each satellite against a critical threshold and performs the test for all satellites in sequence. The test statistic (absolute value) of the three-frequency data φ_{f_1}, φ_{f_2} and φ_{f_3} of a particular satellite s from a GNSS system is obtained by:

$$\hat{w}_s = \frac{-e_s^T W \hat{v}}{\sqrt{e_s^T W C_{\hat{v}} W e_s}} \tag{8.1}$$

where

$$C_{\hat{v}} = W^{-1} - AN^{-1}A^T \tag{8.2}$$

$$e_i = [1 \quad 0 \quad \cdots \quad 1 \quad 0 \quad \cdots \quad 1 \quad 0 \quad \cdots]^T \tag{8.3}$$

which the measurements of n satellites are arranged as:

$$\left[\varphi_{f_1}^{s_1} \quad \cdots \quad \varphi_{f_1}^{s_n} \quad \varphi_{f_2}^{s_1} \quad \cdots \quad \varphi_{f_2}^{s_n} \quad \varphi_{f_3}^{s_1} \quad \cdots \quad \varphi_{f_3}^{s_n}\right]^T \tag{8.4}$$

and

$$\hat{v} = A\hat{x} - l \tag{8.5}$$

In order to tackle all possible cases when multipath errors of two or more frequencies from a satellite are in-phase as described in Sections 7.3.2 to 7.3.4 and shown in Figure 8.1, the CMOD algorithm carries out statistical tests for residuals from all possible combinations of frequencies of a satellite. This is done by using different combinations of frequencies in the vector e_i (the measurements are arranged as in Equation 8.4) as:

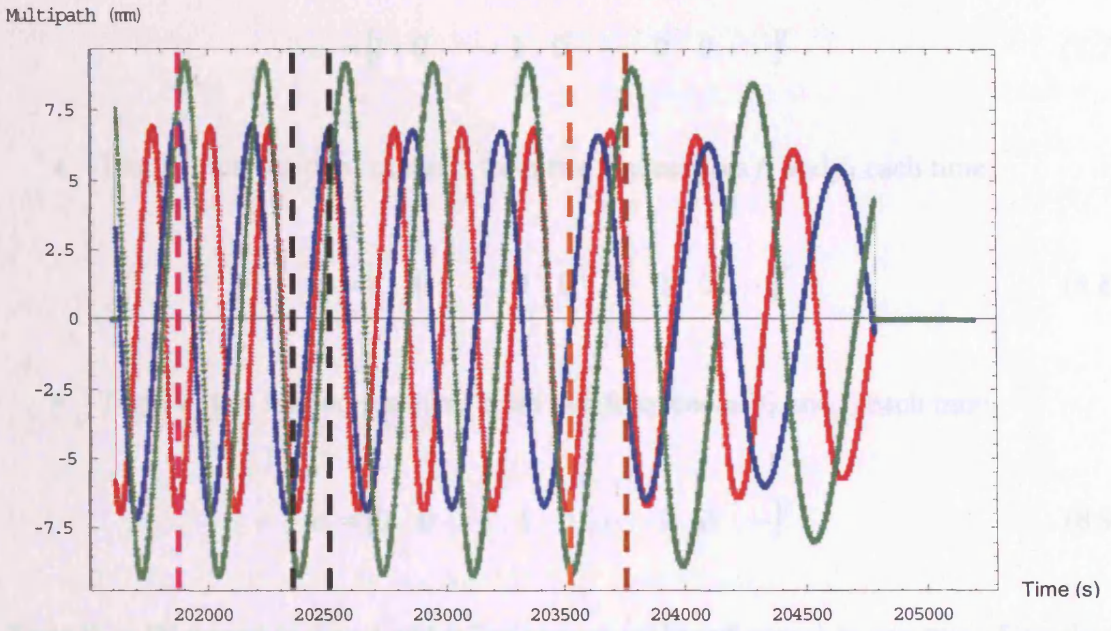

Figure 8-1: Simulated GPS three-frequency (red: L1, blue: L2, green: L5) multipath error in PRN02 in the LCPC-3.9 dataset.

- Test I: test for three residuals from the three frequencies (f_1, f_2, and f_3) each time. It aims at detection and rejection of the measurements of a satellite contaminated by significant multipath errors in all the three frequencies. It may have two cases. The first case is when any two frequencies have significant multipath errors and they are in phase whereas the other one has significant multipath error but it is out of phase when compared with the other two frequencies' multipath errors; this case in shown in the pink dotted line in Figure 8-1. Since absolute

values of the residuals are being used in the computation of the test statistics, the out of phase multipath error would not affect this test. Otherwise, the out of phase multipath error may have cancellation effect to certain extent on the other two in-phase multipath errors in least squares process, but it cannot completely cancel out the other two in-phase multipath errors if the three multipath errors have a similar amplitude. The second case is when all the multipath errors from the three-frequency data of a satellite are in phase as illustrated in the two black dotted lines of Figure 8-1.

$$e_i = [1 \quad 0 \quad \cdots \quad 1 \quad 0 \quad \cdots \quad 1 \quad 0 \quad \cdots]^T \tag{8.6}$$

- Test II: test for two residuals from two frequencies f_1 and f_2 each time.

$$e_i = [1 \quad 0 \quad \cdots \quad 1 \quad 0 \quad \cdots \quad 0 \quad 0 \quad \cdots]^T \tag{8.7}$$

- Test III: test for two residuals from two frequencies f_1 and f_3 each time.

$$e_i = [1 \quad 0 \quad \cdots \quad 0 \quad 0 \quad \cdots \quad 1 \quad 0 \quad \cdots]^T \tag{8.8}$$

- Test IV: test for two residuals from two frequencies f_2 and f_3 each time.

$$e_i = [0 \quad 0 \quad \cdots \quad 1 \quad 0 \quad \cdots \quad 1 \quad 0 \quad \cdots]^T \tag{8.9}$$

Tests II to IV intend to detect and reject serious multipath errors in any two of the three frequencies' data of a satellite whereas multipath error in another frequency is insignificant. An example is shown in the orange dotted line of Figure 8-1.

The final test is required to detect any multipath error from one frequency whereas the multipath errors from the other two frequencies are insignificant as indicated with the brown line in Figure 8-1. This vector e_i is the same as the one used in MOD:

- Test V: test for one residual from a frequency (f_1, f_2, or f_3) each time.

$$e_i = [1 \quad 0 \quad \cdots \quad 0 \quad 0 \quad \cdots \quad 0 \quad 0 \quad \cdots]^T \tag{8.10}$$

Tests I to V are performed for all residuals' combinations of all satellites at each epoch in order to detect any possible multipath error in each frequency of each satellite at each epoch. The author calls this algorithm the cocktail multiple outlier detection and rejection algorithm. It is named as CMOD in short for future reference. The testing results of using CMOD for the simulated testing datasets in scenarios 3 to 5 are described in Section 8.3.

8.3 RESULT OF PROPOSED COCKTAIL MULTIPLE OUTLIER DETECTION AND REJECTION ALGORITHM FOR MULTIPATH ERROR DETECTION AND REJECTION

8.3.1 LCPC-3.9 testing dataset

Positioning errors (in northing, easting, and height) after rejection of detected multipath by CMOD using multiple-frequency data in the testing scenarios 3 to 5 are shown in Figures 8-2 to 8-4. A summary of the result is shown in Table 8-1, the results of scenarios 1 to 5 without using CMOD are also shown in the table for comparison. Approximate percentages of right and wrong detections of simulated multipath errors are shown in Table 8-2, only approximate percentage can be shown because the simulated multipath errors may be zero or very small (smaller than measurement noise) sometimes, which can be found in Figures 5-8 to 5-11.

From the RMS error analyses and percentage improvement values of this dataset in Table 8-1, an insignificant impact of using CMOD on positioning accuracy can be seen. Table 8-2 shows that CMOD has detected and rejected some multipath errors correctly. It also shows there are some false detections and rejections when using GPS or Galileo three-frequency data. However, there is no false detection and rejection when using combined GPS and Galileo multiple-frequency data.

As described in Sections 5.3, 6.3.1 and 7.3.1, the simulated multipath errors in this dataset are comparable with the simulated double difference measurement noise. Therefore, the performance of CMOD in this dataset may not be used to conclude the usefulness of CMOD.

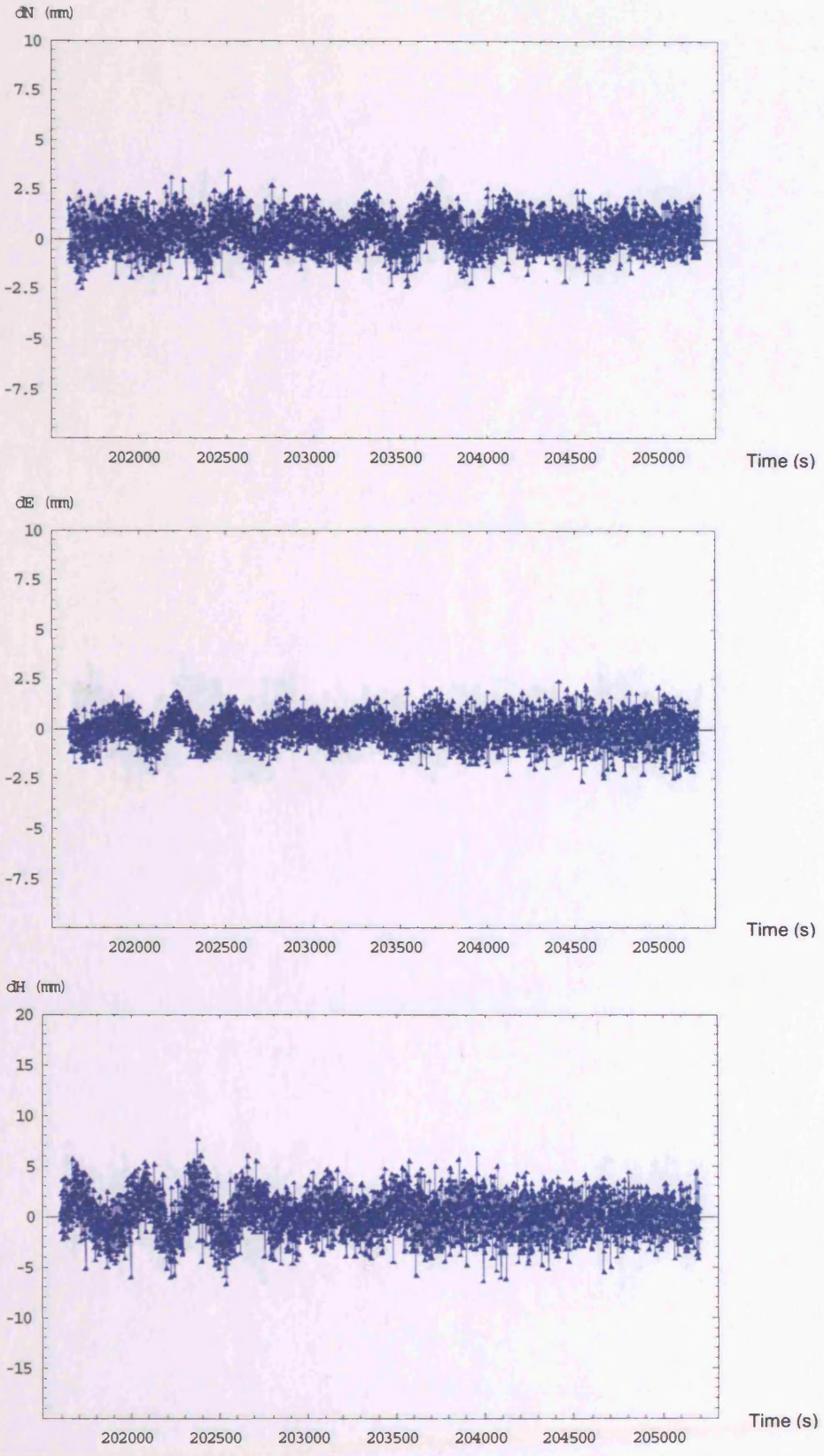

Figure 8-2: Positioning error in northing (top), easting (middle), and vertical (bottom) of single-epoch solution with CMOD using GPS three-frequency data in the LCPC-3.9 dataset.

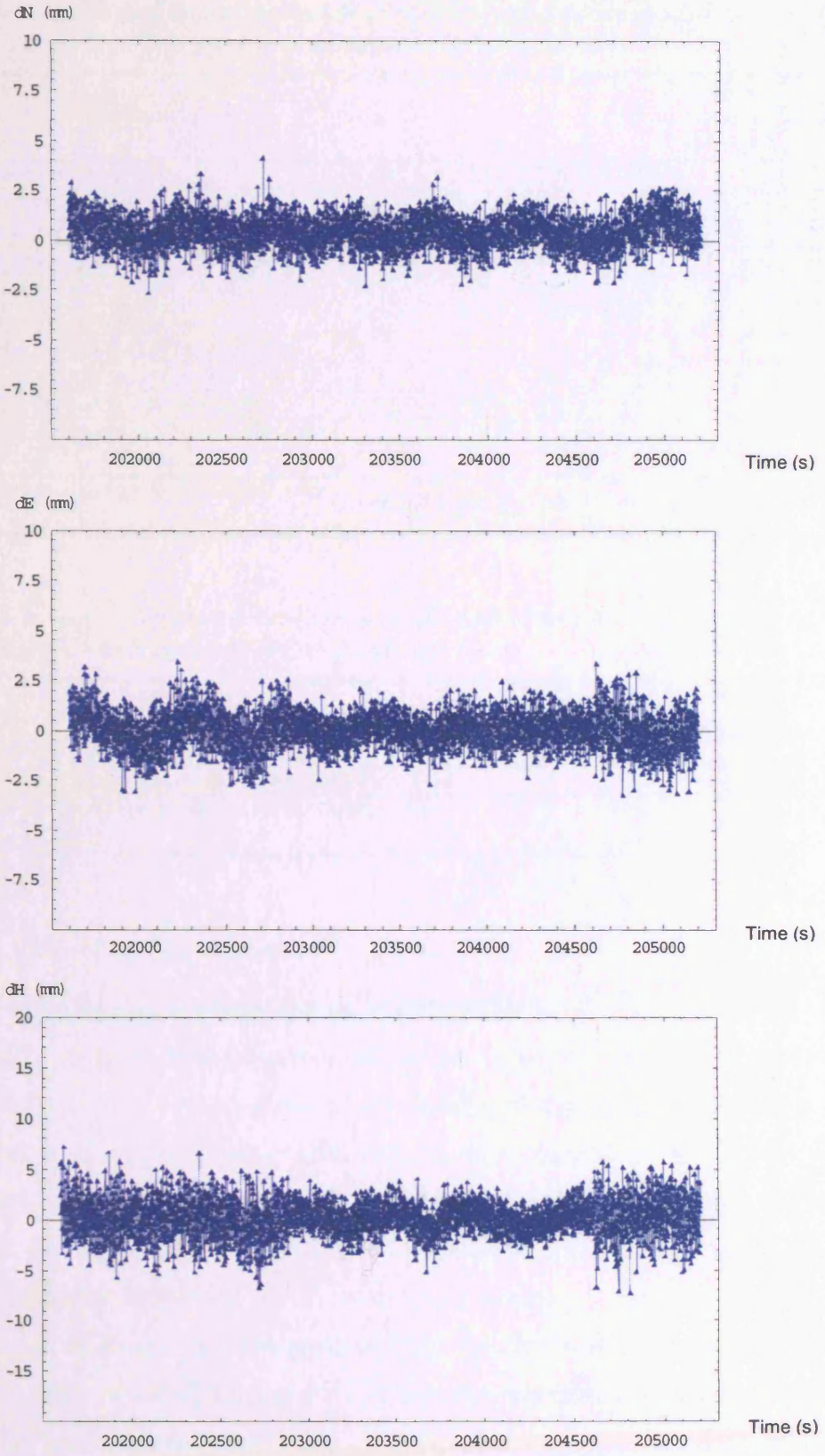

Figure 8-3: Positioning error in northing (top), easting (middle), and vertical (bottom) of single-epoch solution with CMOD using Galileo three-frequency data in the LCPC-3.9 dataset.

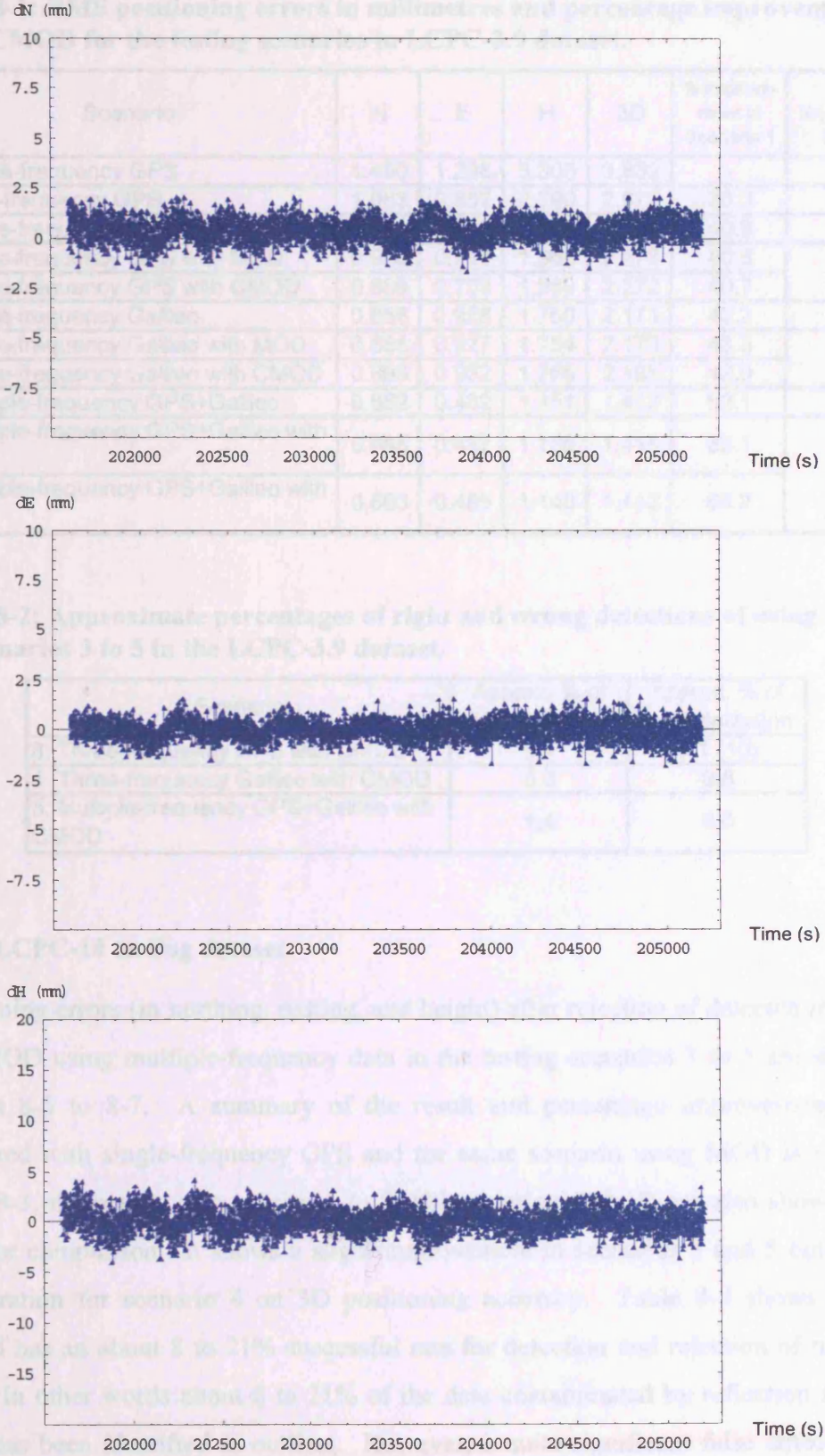

Figure 8-4: Positioning error in northing (top), easting (middle), and vertical (bottom) of single-epoch solution with CMOD using GPS + Galileo multiple-frequency data in the LCPC-3.9 dataset.

Table 8-1: RMS positioning errors in millimetres and percentage improvement of using CMOD for the testing scenarios in LCPC-3.9 dataset.

Scenario	N	E	H	3D	% improve-ment to Scenario 1	% improvement to MOD
1: Single-frequency GPS	1.490	1.238	3.306	3.832	-	
2: Dual-frequency GPS	1.083	0.852	2.290	2.672	30.3	
3: Three-frequency GPS	0.880	0.702	1.967	2.266	40.9	
3: Three-frequency GPS with MOD	0.900	0.711	1.968	2.278	40.6	
3: Three-frequency GPS with CMOD	0.889	0.703	1.969	2.272	40.7	0.28
4: Three-frequency Galileo	0.888	0.928	1.750	2.171	43.3	
4: Three-frequency Galileo with MOD	0.886	0.927	1.754	2.173	43.3	
4: Three-frequency Galileo with CMOD	0.893	0.932	1.765	2.187	42.9	-0.64
5: Multiple-frequency GPS+Galileo	0.662	0.482	1.151	1.413	63.1	
5: Multiple-frequency GPS+Galileo with MOD	0.665	0.487	1.150	1.415	63.1	
5: Multiple-frequency GPS+Galileo with CMOD	0.663	0.485	1.148	1.412	63.2	0.22

Table 8-2: Approximate percentages of right and wrong detections of using CMOD for scenarios 3 to 5 in the LCPC-3.9 dataset.

Scenario	Approx. % of right detection	Approx. % of false detection
3: Three-frequency GPS with CMOD	5.1	0.1 (10)
4: Three-frequency Galileo with CMOD	0.3	0.8
5: Multiple-frequency GPS+Galileo with CMOD	1.4	0.0

8.3.2 LCPC-10 testing dataset

Positioning errors (in northing, easting, and height) after rejection of detected multipath by CMOD using multiple-frequency data in the testing scenarios 3 to 5 are shown in Figures 8-5 to 8-7. A summary of the result and percentage improvements when compared with single-frequency GPS and the same scenario using MOD is shown in Table 8-3, the results of scenarios 1 to 5 without using CMOD are also shown in the table for comparison. It shows a slight improvement in scenarios 3 and 5 but a slight deterioration for scenario 4 on 3D positioning accuracy. Table 8-4 shows that the method has an about 8 to 21% successful rate for detection and rejection of multipath error. In other words about 8 to 21% of the data contaminated by reflection from the panel has been identified as outliers. However, a quite significant false detection and rejection rate has occurred in scenario 4. In scenario 5, there is no wrong detection and rejection when using GPS and Galileo data.

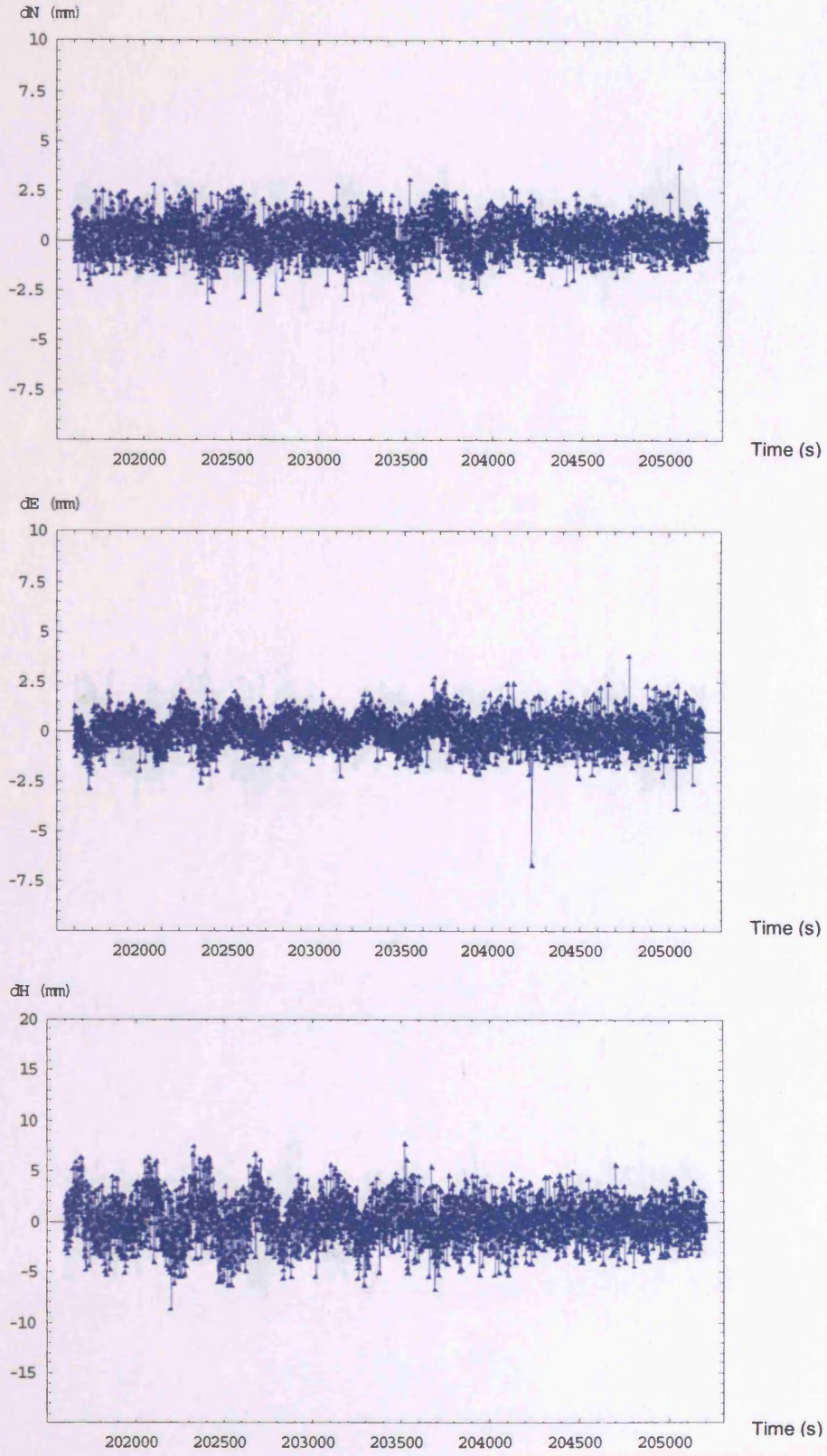

Figure 8-5: Positioning error in northing (top), easting (middle), and vertical (bottom) of single-epoch solution with CMOD using GPS three-frequency data in the LCPC-10 dataset.

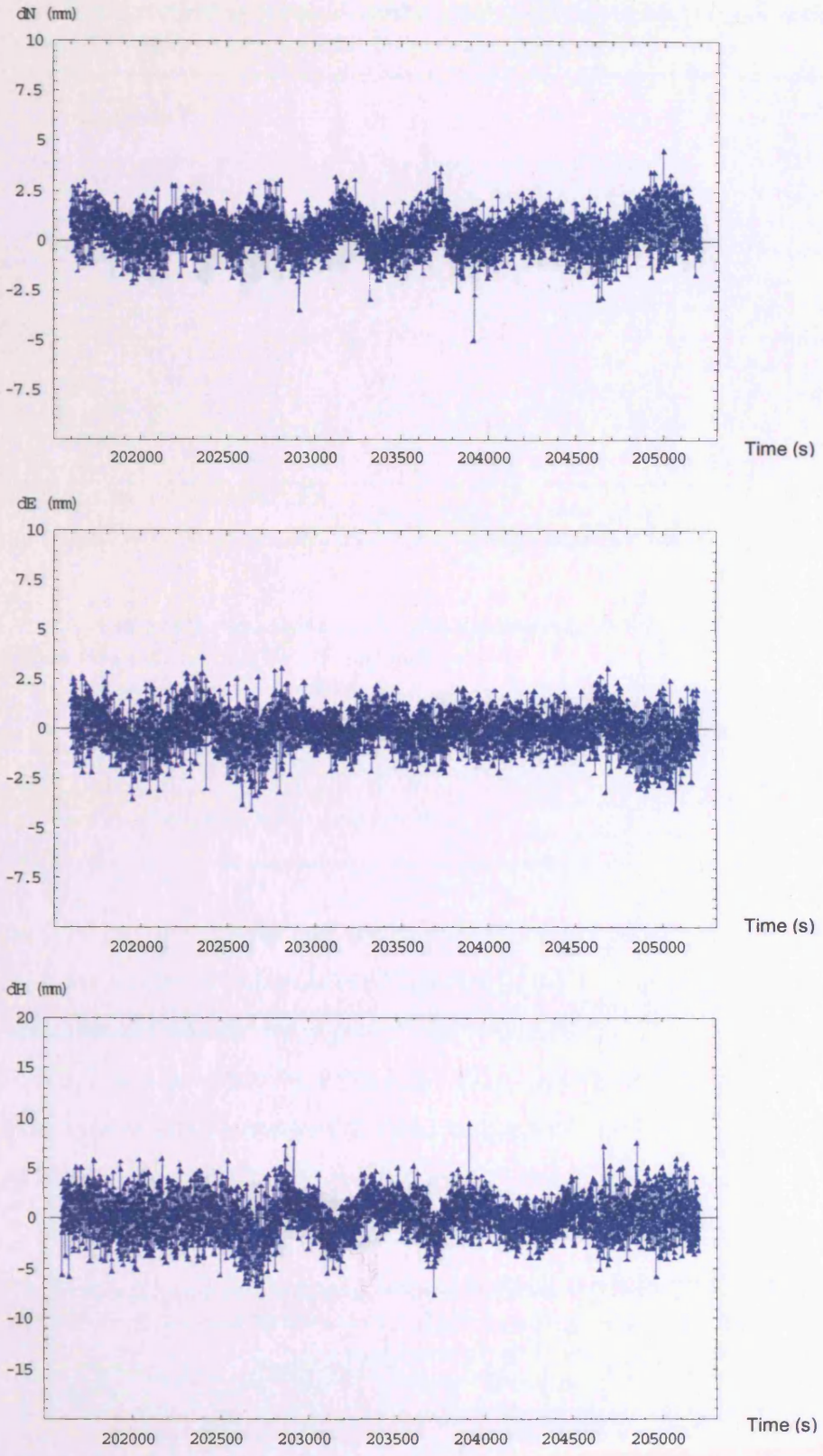

Figure 8-6: Positioning error in northing (top), easting (middle), and vertical (bottom) of single-epoch solution with CMOD using Galileo three-frequency data in the LCPC-10 dataset.

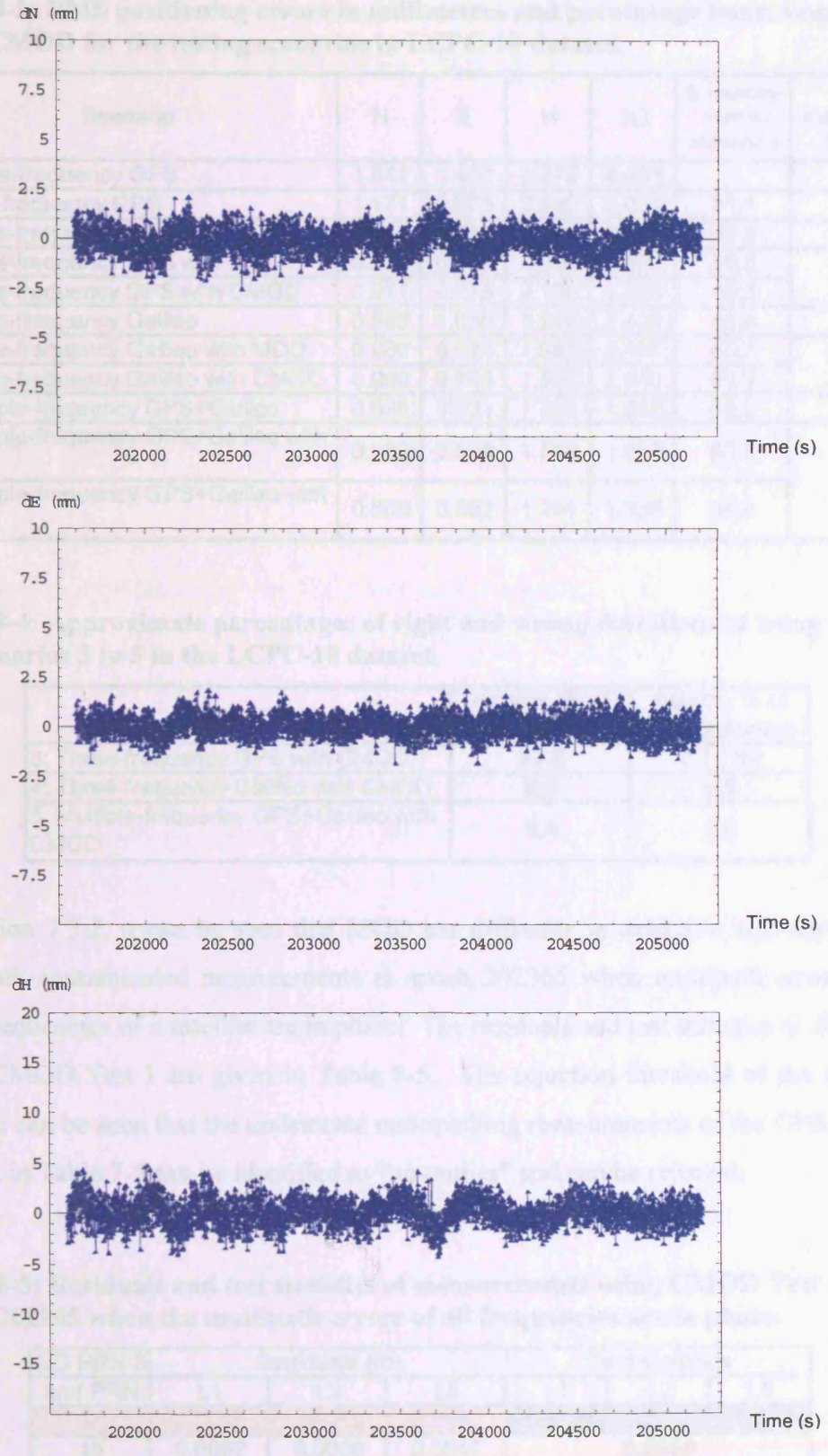

Figure 8-7: Positioning error in northing (top), easting (middle), and vertical (bottom) of single-epoch solution with CMOD using GPS + Galileo multiple-frequency data in the LCPC-10 dataset.

Table 8-3: RMS positioning errors in millimetres and percentage improvement of using CMOD for the testing scenarios in LCPC-10 dataset.

Scenario	N	E	H	3D	% improve-ment to scenario 1	% improvement to MOD
1: Single-frequency GPS	1.611	1.410	3.879	4.431	-	
2: Dual-frequency GPS	1.171	0.976	2.642	3.051	31.1	
3: Three-frequency GPS	0.948	0.830	2.341	2.659	40.0	
3: Three-frequency GPS with MOD	0.970	0.823	2.294	2.623	40.8	
3: Three-frequency GPS with CMOD	0.911	0.775	2.109	2.425	45.3	7.6
4: Three-frequency Galileo	0.985	1.059	1.940	2.420	45.4	
4: Three-frequency Galileo with MOD	0.980	0.984	1.965	2.406	45.7	
4: Three-frequency Galileo with CMOD	0.998	0.986	1.996	2.440	44.9	-1.4
5: Multiple-frequency GPS+Galileo	0.696	0.533	1.386	1.640	63.0	
5: Multiple-frequency GPS+Galileo with MOD	0.686	0.529	1.348	1.602	63.8	
5: Multiple-frequency GPS+Galileo with CMOD	0.668	0.522	1.309	1.559	64.8	2.7

Table 8-4: Approximate percentages of right and wrong detections of using CMOD for scenarios 3 to 5 in the LCPC-10 dataset.

Scenario	Approx. % of right detection	Approx. % of false detection
3: Three-frequency GPS with CMOD	20.8	0.1 (16)
4: Three-frequency Galileo with CMOD	8.3	0.9
5: Multiple-frequency GPS+Galileo with CMOD	9.8	0.0

In Section 7.3.2, it can be seen that MOD has difficulty in detection and rejection of multipath contaminated measurements at epoch 202365 when multipath errors in the three frequencies of a satellite are in phase. The residuals and test statistics of the epoch using CMOD Test I are given in Table 8-5. The rejection threshold of the epoch is 2.77. It can be seen that the undetected multipathing measurements of the GPS satellite PRN02 in Table 7-5 can be identified as "an outlier" and can be rejected.

Table 8-5: Residuals and test statistics of measurements using CMOD Test I at epoch 202365 when the multipath errors of all frequencies are in phase.

DD PRN 3	Residuals (m)			Test statistics		
and PRN	L1	L2	L5	L1	L2	L5
2	0.0085	0.0059	0.0092	3.6306		
15	0.0062	0.0009	0.0047	0.6358		
18	0.0066	0.0013	0.0053	0.9419		
21	0.0033	0.0005	0.0019	-1.0371		
22	0.0036	-0.0002	0.0009	-1.5146		
27	0.0045	0.0014	0.0026	-0.3917		
31	0.0078	0.0016	0.0001	-0.0556		

No more outliers have been detected by the next cycle CMOD Test I and the following CMOD Tests II to V at the epoch, which means no false detection and rejection. It shows that CMOD is working.

8.3.3 LCPC-20 testing dataset

Positioning errors after rejection of detected multipath by CMOD using multiple-frequency data in the testing scenarios 3 to 5 are shown in Figures H-1 to H-3. A summary of the result and percentage improvements when comparing with single-frequency GPS and the same scenario using MOD is shown in Table 8-6, the results of scenarios 1 to 5 without using CMOD are also shown in the table for comparison. It shows an improvement of about 16 to 7% for scenarios 3 and 5 but about 4% deterioration for scenario 4 on 3D positioning accuracy. Table 8-7 shows that the method has an about 39, 19, and 26% successful rate for detection and rejection of multipath error in scenarios 3, 4, and 5 respectively. However, it shows quite significant false detection and rejection in scenario 4. In scenario 5, there is only one false detection and rejection when combined GPS and Galileo multiple-frequency data are used. When comparing Table 8-7 with Table 8-4, a significant increase in correct detection and rejection in the LCPC-20 dataset can be seen. This is because the amplitude of multipath error in LCPC-20 dataset is larger than in LCPC-10 dataset.

In Section 7.3.3, it can be seen that MOD cannot detect and reject the measurements contaminated by multipath at epoch 203726. Table 8-8 shows the residuals and test statistics by MOD and CMOD at the epoch. The rejection threshold at the epoch is 3.017. It can be seen that the multipath contaminated measurements in the GPS satellite PRN02 cannot be detected and rejected by using MOD. The multipath errors in L1 and L5 can be detected and rejected by CMOD Test III. Actually, the multipath errors in the three frequencies at the epoch are serious and in phase as shown in Figure E-1. However, the multipath error in L2 carrier remains undetected by CMOD Tests I to V. On the other hand, the multipath contaminated measurements in Galileo satellite SV14 are also still undetected by CMOD Tests I to V. Nevertheless, no false detection and rejection has occurred at the epoch.

Table 8-6: RMS positioning errors in millimetres and percentage improvement of using CMOD for the testing scenarios in LCPC-20 dataset.

Scenario	N	E	H	3D	% improvement to scenario 1	% improvement to MOD
1: Single-frequency GPS	1.818	1.540	4.093	4.736	-	
2: Dual-frequency GPS	1.290	1.062	2.771	3.236	31.7	
3: Three-frequency GPS	1.049	0.928	2.619	2.970	37.3	
3: Three-frequency GPS with MOD	1.020	0.865	2.410	2.757	41.8	
3: Three-frequency GPS with CMOD	0.879	0.739	2.002	2.308	51.3	16.3
4: Three-frequency Galileo	1.109	1.192	2.044	2.613	44.8	
4: Three-frequency Galileo with MOD	0.974	0.937	2.025	2.434	48.6	
4: Three-frequency Galileo with CMOD	1.027	0.958	2.094	2.521	46.8	-3.6
5: Multiple-frequency GPS+Galileo	0.790	0.596	1.542	1.832	61.3	
5: Multiple-frequency GPS+Galileo with MOD	0.715	0.563	1.416	1.683	64.5	
5: Multiple-frequency GPS+Galileo with CMOD	0.661	0.532	1.315	1.565	67.0	7.0

Table 8-7: Approximate percentages of right and wrong detections of using CMOD for scenarios 3 to 5 in the LCPC-20 dataset.

Scenario	Approx. % of right detection	Approx. % of false detection
3: Three-frequency GPS with CMOD	37.8	0.1 (10)
4: Three-frequency Galileo with CMOD	18.9	1.0
5: Multiple-frequency GPS+Galileo with CMOD	25.6	0.0 (1)

Table 8-8: Residuals and test statistics of measurements by using MOD and CMOD at epoch 203726.

		Residuals (m)			Test statistics			
					MOD			CMOD Test III
	DD PRN 3 and PRN	L1	L2	L5	L1	L2	L5	L1 and L5
GPS	2	-0.0084	0.0014	-0.0075	-2.4528	0.7292	-2.2598	3.3531
	15	-0.0030	-0.0011	-0.0013	-0.3560	-0.2706	0.1460	0.1029
	18	-0.0017	-0.0007	-0.0003	0.1425	-0.1125	0.5354	-0.5399
	21	-0.0004	-0.0016	0.0006	0.6549	-0.4408	0.9029	-0.8260
	22	-0.0004	0.0012	-0.0019	0.6828	0.6558	-0.0999	-0.4851
	31	-0.0007	-0.0023	-0.0014	0.5613	-0.7706	0.1305	-0.5936
	DD SV20							
Galileo	and SV	L1	E5a	E5b	L1	E5a	E5b	L1 and E5b
	13	-0.0042	-0.0033	0.0096	-0.4301	-0.3574	1.9200	1.6451
	14	-0.0031	-0.0021	-0.0011	0.0299	0.1316	-2.2763	-1.1641
	15	-0.0014	-0.0037	0.0064	0.7261	-0.5400	0.6913	-0.1208
	19	-0.0039	-0.0025	0.0078	-0.3038	-0.0269	1.2816	1.1439
	21	-0.0053	-0.0020	0.0076	-0.8483	0.1754	1.1510	1.3854
	22	-0.0042	-0.0033	0.0028	-0.4261	-0.3687	-0.8167	-0.4033

8.3.4 LBCH-7 testing dataset

Positioning (in northing, easting, and height) errors after rejection of detected multipath by CMOD using multiple-frequency data in the testing scenarios 3 to 5 are shown in Figures H-4 to H-6. A summary of the result and percentage improvements when compared with single-frequency GPS and the same scenario using MOD is shown in Table 8-9, the results of scenarios 1 to 5 without using CMOD are also shown in the table for comparison. It shows deteriorations of about 19% and 29% on 3D positioning accuracy when comparing CMOD with MOD in scenarios 3 and 4 respectively. However, it shows an improvement of about 12% on 3D positioning accuracy when comparing CMOD with MOD in scenario 5, which is the use of combined GPS and Galileo multiple-frequency data. Table 8-10 shows that the method has an about 47, 37, and 55% successful rate for detection and rejection of multipath error in scenarios 3, 4, and 5 respectively. Moreover, some false detections and rejections have occurred in the scenarios 3 and 4 but there is no false detection and rejection in the scenario 5. The deteriorations when using CMOD in scenarios 3 (GPS only) and 4 (Galileo only) are probably due to the false detection and rejection of measurements and the weaker satellite geometry (reduced number of satellites/measurements) after correct rejection of multipathing measurements.

In section 7.3.4, it can be seen that MOD cannot detect and reject some multipath contaminated measurements with relatively large test statistics (but not greater than the rejection threshold) at the epoch 159045 as shown in Table 8-11. Table 8-11 shows that multipath contaminated measurements from the two GPS satellites PRN13 and PRN31 (yellow highlighted in the table) are detected and rejected by CMOD Test I. The rejection threshold of the epoch is 3.0505. However, the multipath contaminated measurements from the Galileo satellite SV18 with a relative large test statistic obtained by CMOD Test I remains undetected. It is because the test statistic is about 2.7 times less than the rejection threshold. The measurements also pass all CMOD tests (next cycle Test I and Tests II to V). Actually, the test statistic of 2.204 obtained by CMOD Test V for the multipath contaminated measurement in E5b frequency of the Galileo satellite SV18 is quite close to the rejection threshold, which is 2.9806; it is less than the original rejection threshold of 3.0505 because of the reduced number of observations in determination of the *Tau* rejection criterion c (see Equation (7.16)) after rejection of the six GPS measurements.

Table 8-9: RMS positioning errors in millimetres and percentage improvement of using CMOD for the testing scenarios in LBCH-7 dataset.

Scenario	N	E	H	3D	% improvement to scenario 1	% improvement to MOD
1: Single-frequency GPS	5.086	2.336	5.175	7.622	-	
2: Dual-frequency GPS	3.522	1.745	3.713	5.407	29.1	
3: Three-frequency GPS	3.208	1.340	2.610	4.347	43.0	
3: Three-frequency GPS with MOD	3.689	1.257	2.293	4.522	40.7	
3: Three-frequency GPS with CMOD	4.308	1.439	2.910	5.394	29.2	-19.3
4: Three-frequency Galileo	2.460	0.685	3.907	4.668	38.8	
4: Three-frequency Galileo with MOD	1.214	0.494	1.911	2.317	69.6	
4: Three-frequency Galileo with CMOD	1.755	0.582	2.355	2.995	60.7	-29.2
5: Multiple-frequency GPS+Galileo	1.997	0.667	2.279	3.103	59.3	
5: Multiple-frequency GPS+Galileo with MOD	1.734	0.477	1.449	2.309	69.7	
5: Multiple-frequency GPS+Galileo with CMOD	1.509	0.443	1.290	2.034	73.3	11.9

Table 8-10: Approximate percentages of right and wrong detections of using CMOD for scenarios 3 to 5 in the LBCH-7 dataset.

Scenario	Approx. % of right detection	Approx. % of false detection
3: Three-frequency GPS with CMOD	46.6	0.7
4: Three-frequency Galileo with CMOD	36.6	0.0 (7)
5: Multiple-frequency GPS+Galileo with CMOD	55.0	0.0

Table 8-11: Residuals and test statistics of measurements using MOD and CMOD at epoch 159045, yellow highlighted numbers are multipathing satellites, green highlighted values are correct detected and rejected measurements, and pink highlighted values are undetected measurements contaminated by multipath.

		Residuals (m)			Test statistics			
	DD PRN27				MOD			CMOD Test I
	and PRN	L1	L2	L5	L1	L2	L5	L1, L2, L5
GPS	8	0.0007	-0.0003	0.0018	0.5446	-1.3691	0.5205	-2.3330
	10	0.0006	0.0025	0.0011	0.4954	-0.2971	0.2727	-2.1830
	13	-0.0111	0.0104	0.0161	-4.1025	2.8475	6.1297	6.0984
	19	-0.0003	0.0006	-0.0009	0.1318	-1.0259	-0.5303	-2.6850
	28	-0.0029	-0.0006	0.0021	-0.8516	-1.4706	0.6229	-1.6297
	31	0.0083	0.0097	-0.0169	3.7395	2.7024	-7.2229	6.7977
Galileo	DD SV 3							
	and SV	L1	E5a	E5b	L1	E5a	E5b	L1, E5a, E5b
	2	0.0003	0.0015	-0.0018	0.3958	0.7501	-0.0427	-0.1493
	4	-0.0003	-0.0003	-0.0039	0.1605	0.0636	-0.8258	0.0455
	10	-0.0008	-0.0007	-0.0045	-0.0212	-0.1166	-1.0508	0.3998
	11	-0.0004	-0.0008	0.0001	0.1436	-0.1292	0.7523	-0.8577
	18	-0.0036	-0.0030	0.0021	-1.1352	-1.0163	1.5203	1.1379
	21	0.0006	0.0008	-0.0014	0.5213	0.4986	0.1297	-0.3624
	22	-0.0016	-0.0011	-0.0045	-0.3609	-0.2435	-1.0923	0.7368

8.3.5 K-HK7-300 testing dataset

Positioning errors (in northing, easting, and height) after rejection of detected multipath by CMOD using multiple-frequency data in the testing scenarios 3 to 5 are shown in Figures 8-8 to 8-10. A summary of the result and percentage improvements (or deteriorations) when compared with single-frequency GPS is shown in Table 8-12, the results of scenarios 1 to 5 without using CMOD are also shown in the table for comparison. CMOD shows deteriorations in the scenarios 3 to 5 on 3D position accuracy (see the right-most column in Table 8-12) when compared with the current single-frequency GPS system or the multiple-frequency least squares only solutions. As explained in Sections 6.3.5 and 7.3.5, it is due to the highly correlated phase multipath errors from the very close (less than about one metre) carrying platform. The performance of CMOD is worse than that of MOD in this dataset. There are two potential reasons after inspection of the processing log file. Firstly, the relative small multipath errors may not be detected and rejected by MOD but they may be detected and rejected by CMOD, which should be good. However, since there are many multipath contaminated measurements at each epoch in this dataset as shown in Table 5-3 and Figures 5-17 to 5-32, it may lead to rejection of many measurements/satellites, which then weakens the satellite geometry. Secondly, the highly correlated low-frequency multipath errors of some satellites from the very close reflector (the carrying platform) may lead to false detection and rejection of measurements without multipath error.

It is expected that the performance of CMOD should be better than that of MOD as found in Sections 8.3.1 to 8.3.4. Why do the results in this dataset not find this? The differences of this dataset from the LCPC and LBCH datasets are investigated here, the differences are:

i) the multipath errors come from a very close carrying platform,

ii) almost all measurements from satellites have multipath errors, that is the number of multipath contaminated measurements is much greater than the number of good measurements, and

iii) resultant phase multipath errors from multiple reflectors in moving antenna look like random noise (not a sinusoidal pattern, see Figures 5-17 to 5-32) with large standard deviation that may reach the maximum phase multipath error.

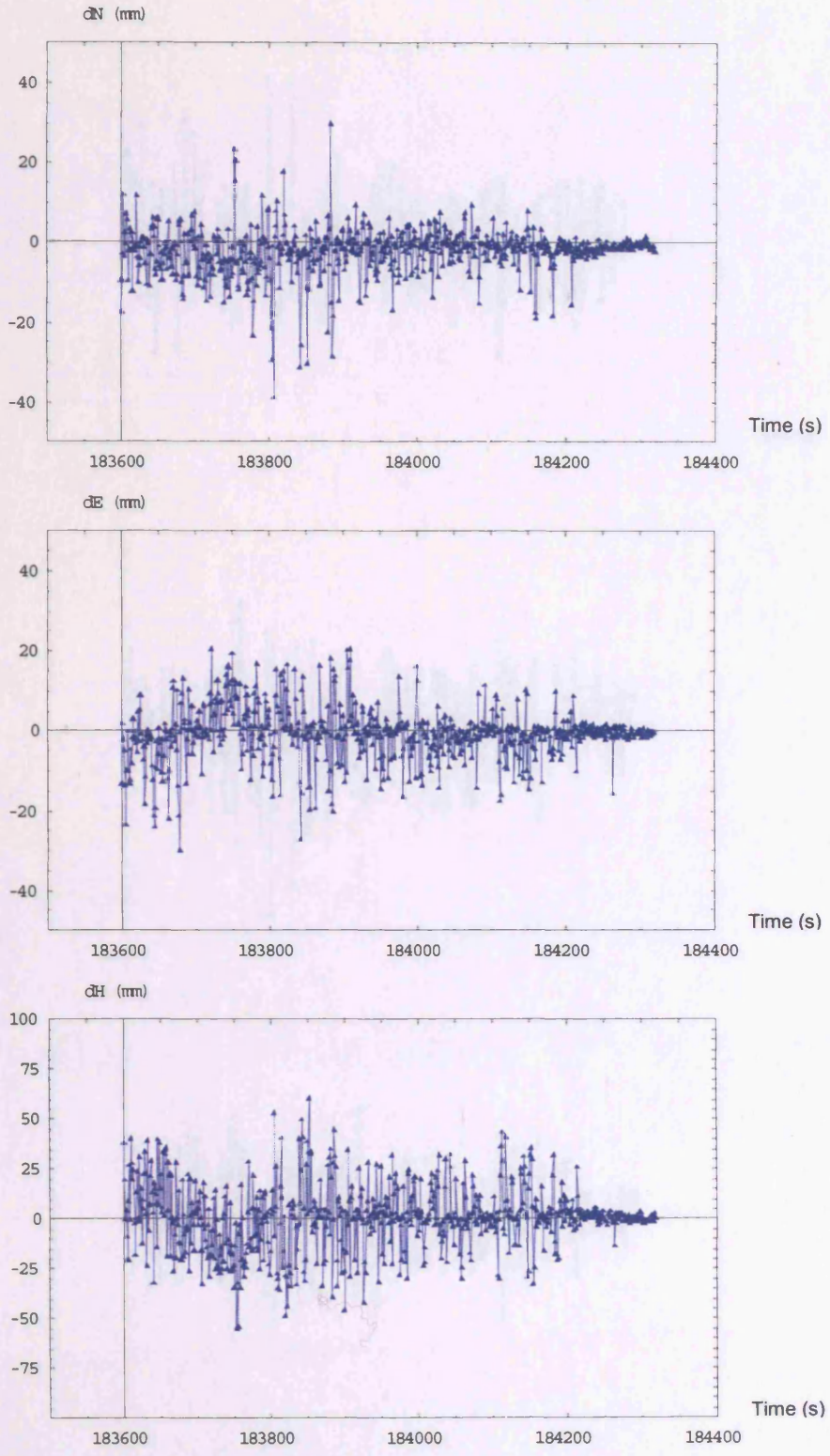

Figure 8-8: Positioning error in northing (top), easting (middle), and vertical (bottom) of single-epoch solution with CMOD using GPS three-frequency data in the K-HK7-300 dataset.

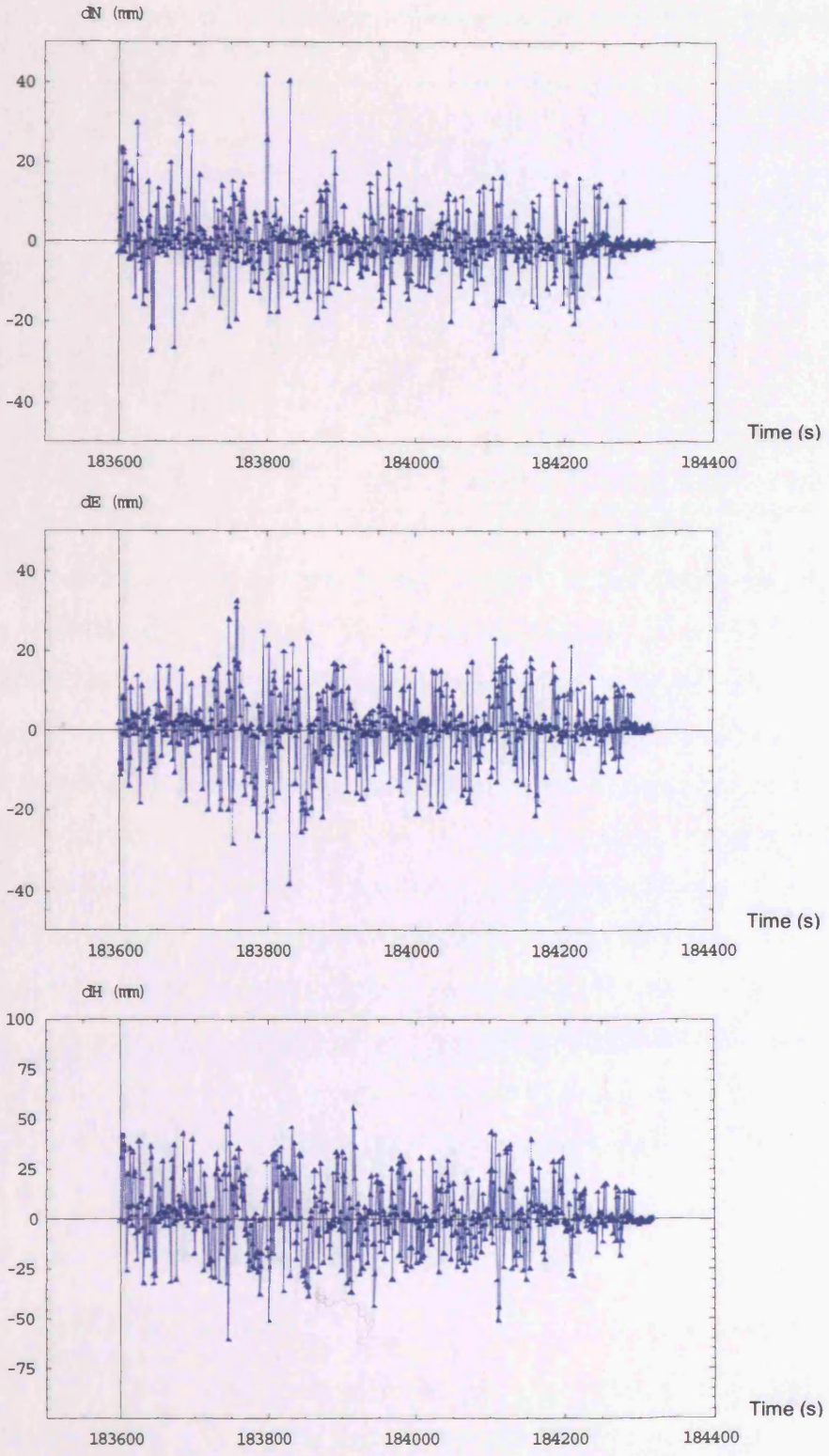

Figure 8-9: Positioning error in northing (top), easting (middle), and vertical (bottom) of single-epoch solution with CMOD using Galileo three-frequency data in the K-HK7-300 dataset.

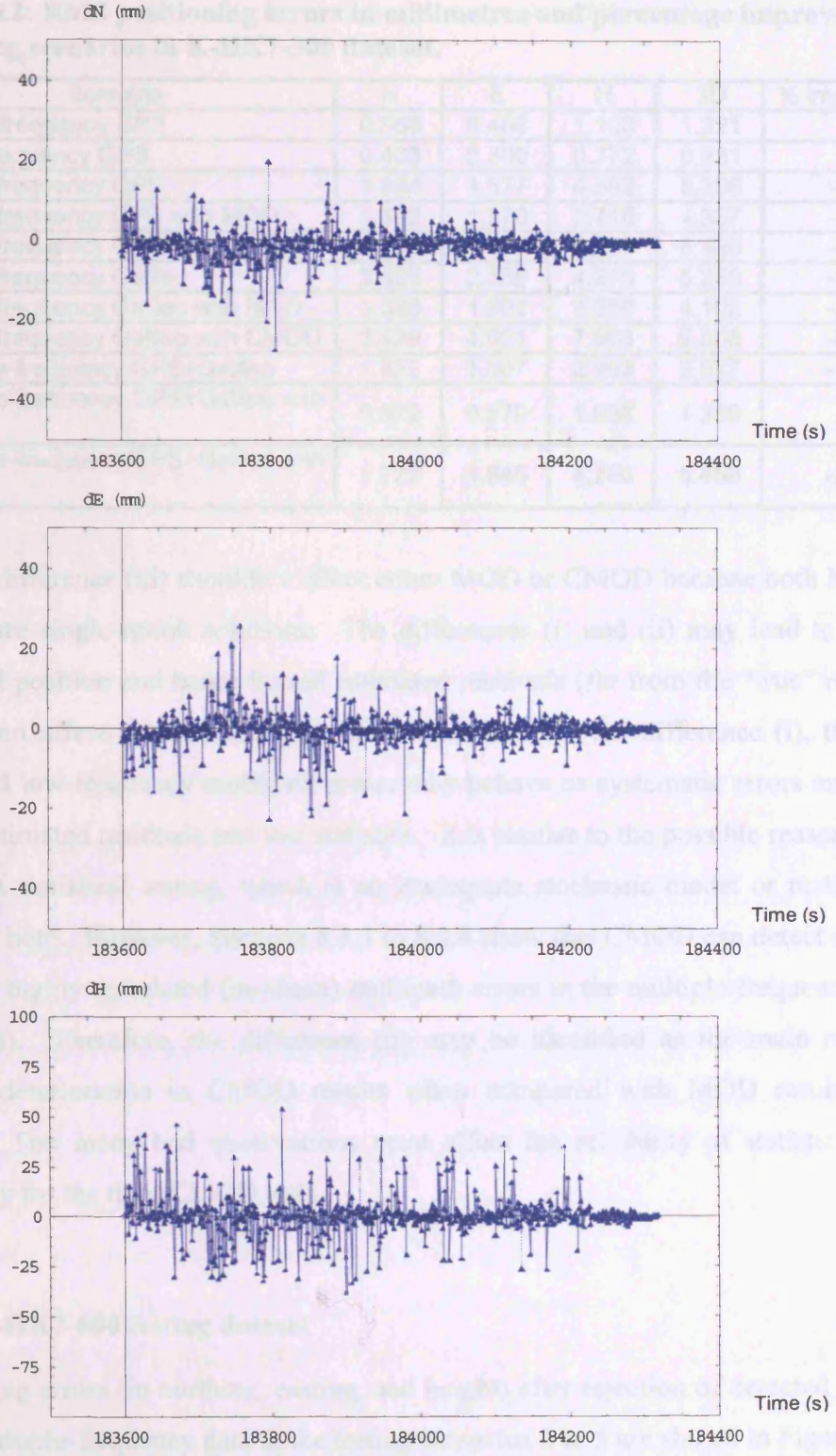

Figure 8-10: Positioning error in northing (top), easting (middle), and vertical (bottom) of single-epoch solution with CMOD using GPS + Galileo multiple-frequency data in the K-HK7-300 dataset.

Table 8-12: RMS positioning errors in millimetres and percentage improvement of the testing scenarios in K-HK7-300 dataset.

Scenario	N	E	H	3D	% improvement
1: Single-frequency GPS	0.558	0.466	1.103	1.321	-
2: Dual-frequency GPS	0.403	0.330	0.772	0.931	29.5
3: Three-frequency GPS	1.884	1.877	4.592	5.306	-301.6
3: Three-frequency GPS with MOD	1.592	1.570	3.716	4.337	-228.2
3: Three-frequency GPS with CMOD	2.795	3.027	7.350	8.426	-537.6
4: Three-frequency Galileo	2.003	2.356	4.279	5.280	-299.5
4: Three-frequency Galileo with MOD	1.536	1.801	3.350	4.102	-210.4
4: Three-frequency Galileo with CMOD	3.439	4.001	7.668	9.308	-604.3
5: Multiple-frequency GPS+Galileo	1.322	1.507	2.963	3.577	-170.7
5: Multiple-frequency GPS+Galileo with MOD	0.572	0.579	1.088	1.358	-2.8
5: Multiple-frequency GPS+Galileo with CMOD	1.779	1.945	4.780	5.458	-313.1

The last difference (iii) shouldn't affect either MOD or CMOD because both MOD and CMOD are single-epoch solutions. The differences (i) and (ii) may lead to a biased estimated position and hence biased estimated residuals (far from the "true" residuals), which then affect the computation of test statistics. In the difference (i), the highly correlated low-frequency multipath errors may behave as systematic errors and lead to biased estimated residuals and test statistics. It is similar to the possible reason of Type I error in statistical testing, which is an inadequate stochastic model or mathematical model or both. However, Sections 8.3.1 to 8.3.4 show that CMOD can detect and reject temporal highly correlated (in-phase) multipath errors in the multiple-frequency data of satellite(s). Therefore, the difference (ii) may be identified as the main reason for causing deterioration in CMOD results when compared with MOD results in this dataset. Too many bad observations must affect the reliability of statistical testing especially for the tight CMOD tests.

8.3.6 K-HK7-600 testing dataset

Positioning errors (in northing, easting, and height) after rejection of detected multipath using multiple-frequency data in the testing scenarios 3 to 5 are shown in Figures H-7 to H-9. A summary of the result and percentage improvements (or deteriorations) when comparing with single-frequency GPS is shown in Table 8-13, the results of scenarios 1 to 5 without using CMOD are also shown in the table for comparison. CMOD shows deteriorations in the scenarios 3 to 5 on 3D position accuracy (see the right-most column in Table 8-12) when compared with the current single-frequency GPS system,

the multiple-frequency least squares only solutions or MOD. The explanation to this is the same as in Section 8.3.5.

Table 8-13: RMS positioning errors in millimetres and percentage improvement of using CMOD for the testing scenarios in K-HK7-600 dataset.

Scenario	N	E	H	3D	% improvement
1: Single-frequency GPS	0.544	0.458	1.085	1.297	-
2: Dual-frequency GPS	0.390	0.326	0.764	0.917	29.3
3: Three-frequency GPS	1.897	2.338	3.825	4.868	-275.3
3: Three-frequency GPS with MOD	1.356	1.743	2.767	3.541	-173.0
3: Three-frequency GPS with CMOD	3.900	5.145	8.721	10.851	-736.6
4: Three-frequency Galileo	2.483	2.312	3.765	5.068	-290.7
4: Three-frequency Galileo with MOD	2.002	1.993	3.197	4.266	-228.9
4: Three-frequency Galileo with CMOD	3.835	4.117	6.914	8.914	-587.2
5: Multiple-frequency GPS+Galileo	1.314	1.370	2.007	2.763	-113.0
5: Multiple-frequency GPS+Galileo with MOD	0.442	0.483	0.975	1.175	9.5
5: Multiple-frequency GPS+Galileo with CMOD	1.764	1.445	2.452	3.349	-158.2

8.4 CONCLUDING REMARKS

A cocktail multiple outlier detection and rejection algorithm, called CMOD, is proposed and described to tackle the undetected outlier problem in MOD when phase multipath errors in two or more frequencies of a satellite are in-phase. CMOD has been tested with the testing datasets described in Chapter 5.

From the results of LCPC and LBCH datasets in Sections 8.3.1 to 8.3.4, it has been found that using CMOD with GPS or Galileo three-frequency data may not improve positioning accuracy when compared with MOD results. This is probably due to the fact that the redundancy of the three-frequency GNSS data is still insufficient for the tight multiple outlier detection in CMOD, which leads to the rejection of many measurements/satellites and weakens the satellite geometry. However, using CMOD with combined GPS and Galileo multiple-frequency data (scenario 5) shows a substantial increase in correct detection and rejection of multipath errors and significant reduction in false detection and rejection. Only one false detection and rejection has occurred in the LCPC-20 dataset. The results and analyses in Sections 8.3.1 to 8.3.4 show that the use of CMOD with combined GPS and Galileo multiple-frequency data shows a good performance in detecting and rejecting multipath errors, which cannot be detected and rejected by using MOD. CMOD also shows a very good reliability by

having a very low false detection and rejection rate, which has occurred only once in the tests with the LCPC and LBCH datasets.

From the results of the K-HK7-300 and K-HK7-600 datasets in Sections 8.3.5 and 8.3.6, CMOD shows deteriorations when compared with MOD and the current single-frequency GPS system. The reasons are identified. The primary reason is that the number of bad (multipath contaminated) observations is much greater than the number of good observations. The secondary reason is the existence of highly correlated multipath errors in multiple-frequency data of satellite(s) from a very close reflector. If the number of good observations is much or sufficiently greater than the number of multipath contaminated observations, the performance of CMOD would be better than that of MOD. If there was no multipath error from very close reflector(s), CMOD with combined GPS and Galileo multiple-frequency data would improve positioning accuracy when compared with the current single-frequency GPS system. Therefore, in the future, if users can avoid multipath from very close reflector(s) such as the carrying platform and if users can keep the number of multipath contaminated observations to a minimum (less than good observations), CMOD with combined GPS and Galileo multiple-frequency data would be able to detect and reject multipath errors correctly and hence improve positioning accuracy significantly with a very low false detection and rejection rate. How can users avoid too many multipath contaminated observations? Prediction of multipath severity using the multipath model described in Chapter 4 with a precise (or reasonably good product such as predicted ephemeris) satellite ephemeris and city model is a possible method to find a period with less multipath severity for carrying out GNSS observation.

9. SUMMARY AND CONCLUSIONS

9.1 SUMMARY AND CONCLUSIONS

This research has investigated phase multipath in GNSS positioning and the use of multiple-frequency GPS and Galileo data for its mitigation. Summary and conclusions of the thesis are presented as follows.

9.1.1 GNSS data simulator and processor

A GNSS data simulator has been developed to generate three-frequency GPS data for the coming modernised GPS and three-frequency Galileo data in the Open Service of the developing new European GNSS. The simulator has considered almost all GNSS biases and errors. The biases and errors are the ionospheric effect, tropospheric delay, ephemeris error including satellite clock bias, receiver clock bias, satellite and receiver inter-frequency bias, multipath error, receiving antenna phase centre offset and variation, integer ambiguity, relativistic effect, and random measurement noise. The simulated data has been verified in the measurement (L1 and L2 pseudoranges) domain by comparing simulated measurements with real measurements obtained from three IGS global tracking stations. Moreover, the simulated data has been verified in the position domain by comparing the solutions obtained from the Automatic Gipsy service provided by JPL with the known positions used in data simulation. Reasonably good agreements (the overall standard deviation in the measurement domain validation is about three decimetres; the difference in position domain validation is less than three decimetres) have been found. The realistic GNSS biases and errors models have been used to simulate modernised GPS data. A Galileo ephemeris simulator has been developed to generate a precise ephemeris for Galileo data simulation and a broadcast ephemeris for data processing using the latest orbit and signal parameters at the time of this research. The Galileo precise ephemeris and signal parameters with the realistic GNSS biases and errors models have been used to generate three-frequency Galileo data for this investigation. Also a GNSS data processor has been developed to process multiple-frequency GPS and Galileo data. The processing engine of the processor is the well-known single epoch least squares method. The processor can process different

combinations of data from GPS and Galileo multiple frequencies. The developed GNSS data simulator and processor are used as the platform for this research.

9.1.2 Phase multipath modelling

For the purpose of this investigation, the critical component of the data simulator is the phase multipath model. This model is based on ray tracing and electromagnetics. All known geometrical and physical factors have been taken into account and are described in detail. The model has been integrated into the GNSS data simulator. It has been validated with real data collected in two experiments with reflectors of different materials. The results show good agreement (i.e. similar amplitude and frequency between the real and simulated phase multipath errors) with real multipath from a steel panel (planar reflector) and fairly good agreement (i.e. similar amplitude with slight different frequency between the real and simulated phase multipath errors) with real multipath from a lake (dynamic irregular reflector). They show that the multipath model has the potential to correct phase multipath errors in cases where the exact geometry of the reflection process and the nature of the reflector are known. Some of the characteristics of phase multipath and the sensitivities of simulated GNSS measurements to the factors causing multipath are investigated and described. Furthermore, the model can be used to predict multipath severity if the city model of the area of interest is available.

9.1.3 Testing datasets

Six testing datasets have been generated for subsequent validations of multipath mitigation techniques and analyses of results. The datasets have been designed to test different multipath scenarios. Three datasets have been designed to test the impact of phase multipath amplitude (caused by the reflectors with different relative permittivities) on multipath mitigation. One dataset has been designed to investigate the impact of satellite geometry and the number of multipathing satellites on multipath mitigation. In these four datasets only one reflector is near to the antenna and the antenna-reflector distance is about five metres. Moreover, one dataset has been designed to study the impact and effect of multipath errors from a moving antenna with a very close reflective carrying platform on multipath mitigation. Another dataset has

been designed to test the impact of multipath errors from a moving antenna with a very close reflective carrying platform in different satellite geometry on multipath mitigation.

9.1.4 Multipath mitigation using multiple frequency GNSS data

The impact of the three-frequency GPS and Galileo data, and combined GPS and Galileo multiple-frequency data using the standard single-epoch least squares method on multipath mitigation has been investigated. It has been found that the use of three-frequency GPS, Galileo data, or multiple-frequency GPS and Galileo data can have better multipath mitigation capability in least squares averaging in the case of no very close reflector (less than about one metre from the antenna). The testing results using simulated data have found an about 62% improvement on positioning accuracy in average when compared using combined GPS and Galileo multiple-frequency data with the present GPS reliable single-frequency system. When using three-frequency GPS or Galileo data, it has shown an about 42% improvement on positioning accuracy in average when compared with the current single-frequency GPS system.

In the case of multipath errors from a very close reflective carrying platform, the use of an additional frequency (more than two frequencies, and the additional frequency close to one of the other two frequencies) from the modernised GPS or the new Galileo, or the combined GPS and Galileo multiple-frequency data has shown a deterioration in positioning accuracy when compared with the current single- or dual-frequency GPS system or the modernised dual-frequency GPS system. In other words, it has been found that using three-frequency and multiple-frequency GNSS data would cause more problems if there are multipath errors from very close reflector(s). Since the allocated GPS L2 and L5 frequencies, and Galileo E5a and E5b frequencies are very close and therefore the multipath errors from a very close reflector are very coherent it has been found that when the antenna-reflector distance is less than about one metre, phase multipath errors from GPS L2 and L5 or Galileo E5a and E5b frequencies have very high correlation functions, which means that the errors are very coherent (very similar phase and amplitude). This leads the positioning solution biased to the coherent multipath errors by dragging the estimated position further away from the true position. A very close reflector (less than about one metre from the receiving antenna) will destroy the advantage of using multiple-frequency GNSS data. Therefore, surveying and geodetic users always say that in order to reduce the multipath effect, the antenna

should be set as high as possible to prevent multipath from above horizon or from the ground. It is also true for reduction of the multipath effect from the very close carrying platform. Therefore, it is recommended to set the GNSS receiving antenna at least one metre away from any potential reflector and reduce the size of the carrying platform if possible. Setting the antenna far from any reflector increases the differential path delay and thus reduces the coherence of phase multipath errors of the closely allocated frequencies. It will help least squares averaging of multipath errors in the coming modernised GPS and Galileo systems. If the frequency allocation plan can separate the carrier frequencies far apart, it would help phase multipath mitigation in the multiple-frequency GNSS system.

9.1.5 Multipath mitigation using multiple frequency GNSS data with multiple outlier detection

A multiple outlier detection technique widely used in geodetic surveying has been proposed to detect and reject multipath contaminated measurements in the future multiple-frequency GNSS system. The author calls this technique MOD, which stands for multiple outlier detection. MOD has been integrated in the GNSS data processor and tested with the simulated testing datasets.

From RMS error analyses of the testing results of the datasets with only one reflector and no multipath from the carrying platform, combined GPS and Galileo multiple-frequency data with MOD has shown an about 64-70% improvement on positioning accuracy when compared with the current single-frequency GPS data. The improvement depends on the phase and amplitude of phase multipath error. Moreover, the multiple-frequency GPS and Galileo data processing with MOD has shown further improvement on the positioning accuracy by about 3-26% when compared with multiple-frequency GPS and Galileo data processing with only least squares method. It also depends on the phase and amplitude of phase multipath error. These results are due to the fact that more redundant frequency data can better average multipath errors and hence detect serious multipath errors.

Simulation results have found that MOD solution using three-frequency GPS or Galileo data is not always better than the least squares solution using three-frequency GPS or Galileo data. This is probably because the three-frequency GNSS system has insufficient redundancy to detect and reject outliers correctly and/or there are too many measurements contaminated by multipath.

From RMS error analyses in the datasets with multiple reflectors and a very close reflective carrying platform, a significant improvement on positioning accuracy has been found when compared the use of MOD with least squares only especially using combined GPS and Galileo multiple-frequency data. However, the multiple-frequency GPS and/or Galileo data with MOD solution may still be worse than the current single-frequency GPS system because of it suffering from the highly correlated GPS L2 and L5 multipath errors and/or Galileo E5a and E5b multipath errors.

A weakness of MOD has been identified. When multipath errors in two of three or all frequencies of a satellite are in-phase, MOD cannot detect and reject these multipath contaminated measurements. In this case, the test statistics of these multipath contaminated measurements are significantly greater than the other test statistics of good measurements but they are not greater than the rejection threshold and therefore they cannot be rejected. It may be because the multipath errors are absorbed in the estimated position and this leads to biased residuals. Consequently, the residuals of multipath contaminated measurements are less than the true residuals. Since the computation of test statistic is based on the estimated residual, biased residual affects the reliability of the computed test statistic.

9.1.6 Multipath mitigation using multiple frequency GNSS data with cocktail multiple outlier detection

A cocktail multiple outlier detection and rejection algorithm has been proposed to tackle the weakness of MOD in detection of in-phase multipath errors. This algorithm is called CMOD. CMOD has been integrated in the GNSS data processor and tested with the simulated testing datasets.

From the results of the datasets with only one reflector and no multipath from the carrying platform, CMOD solutions are always better than the MOD and least squares only solutions when using combined GPS and Galileo multiple-frequency data. It has been found that about 0.2 to 12% improvement on positioning accuracy can be achieved when comparing CMOD solutions to MOD solutions using combined GPS and Galileo multiple-frequency data. This percentage improvement depends on the amplitude of multipath errors and the occurrence of in-phase multipath errors in the measurements of each satellite. Moreover, it has been found that using combined GPS and Galileo

multiple-frequency data with CMOD has an about 65 to 73% improvement on positioning accuracy when compared with the least squares solutions using the current single-frequency GPS data.

The use of CMOD with combined GPS and Galileo multiple-frequency data performs well in detecting and rejecting multipath errors that cannot be detected and rejected by using MOD. CMOD also shows a very good reliability by having a very low false detection and rejection rate, something which has occurred only once in the tests with the datasets with only one reflector and without multipath from very close reflectors (less than about one metre from the antenna).

It has been found that the performance of CMOD using GPS or Galileo three-frequency data is not always better than that of MOD using the same data. This is probably because the redundancy of three-frequency GNSS system is still insufficient for the tight multiple outlier detection in CMOD, which leads to weakened satellite geometry by rejection of many measurements/satellites.

From the results of the datasets with multiple reflectors and with multipath from the carrying platform, CMOD performs less well than MOD and less well than the current single-frequency GPS system. The reasons are identified. The primary reason is that the number of bad (multipath contaminated) observations is much greater than the number of good observations. The secondary reason is the existence of highly correlated multipath errors in multiple-frequency data of satellite(s) from a very close reflector. If the number of good observations is sufficiently greater than the number of multipath contaminated observations, the performance of CMOD would be better than that of MOD. If there was no multipath error from very close reflector(s), CMOD with combined GPS and Galileo multiple-frequency data would improve positioning accuracy when compared with the current single-frequency GPS system. Therefore, in the future, if users can avoid multipath from very close reflector(s) such as the carrying platform and if users can keep the number of multipath contaminated observations to a minimum (less than good observations), CMOD with combined GPS and Galileo multiple-frequency data would be able to detect and reject multipath errors correctly and hence improve positioning accuracy significantly with a very low false detection and rejection rate. Prediction of multipath severity using the multipath model described in Chapter 4 with precise (or reasonably good product such as predicted ephemeris)

satellite ephemeris and city model is a possible method to find periods with less multipath severity for carrying out GNSS observations.

9.2 Overall Conclusions

In a serious multipath environment, the code multipath effect on navigation solution is affected by the number of multipath signals. However, phase multipath is not necessarily affected by the number of multipath signals. In kinematic applications, phase multipath has a random-noise-like characteristic which depends on satellite-reflector-antenna geometry as shown in Figures 5-17 to 5-32 and E-12 to E-25. Therefore, most multipath mitigation techniques applicable to static applications may not be suitable for kinematic applications. For instance, multipath mitigation techniques involving time-series analysis and filtering are not applicable to kinematic applications. Single-epoch based least squares averaging and outlier detection techniques for multipath mitigation work only when the number of good measurements is sufficiently greater than the number of multipath contaminated measurements.

In conclusion, the modernised GPS and the new Galileo three-frequency systems, and the integrated GPS and Galileo multiple-frequency system will have significantly better multipath mitigation capabilities than the current system if there is no multipath from reflectors less than about one metre from the antenna. This is in addition to the well-known improvement in the efficiency and reliability of ambiguity resolution. Moreover, using the proposed cocktail multiple outlier detection and rejection algorithm (CMOD) with combined GPS and Galileo multiple-frequency data will enable us to detect and reject multipath contaminated measurements reliably in case of no multipath from very close reflectors (less than one metre from the receiving antenna) and the number of good measurements is sufficiently greater than the bad (multipath contaminated) measurements.

9.3 Future possibilities and challenges

A very close reflector (less than one metre) will destroy the advantage of using multiple-frequency GNSS data because of the highly correlated multipath errors. At present, the geodetic community always set the antenna as high as possible in order to

reduce the chance of multipath effect from above the horizon. It will also reduce the coherence of phase multipath errors from the ground in the future multiple-frequency GNSS high precision positioning. Of course, users should avoid setting an antenna close to any reflector within about one metre from the antenna. However, since the multipath errors from very close reflectors change very slowly, and the phases and amplitudes of the errors for a satellite in the closely allocated frequencies (GPS L2 and L5; Galileo E5a and E5b) are very similar, these multipath errors may be able to be identified by time-series analysis and/or correlation analysis in static applications or even kinematic applications. The identified multipath errors (from a very close reflector) can then be applied to correct the phase measurements.

When there are too many multipath contaminated measurements, it is very hard for any algorithm to estimate positions accurately. A possible way to avoid too many multipath errors in data is to avoid the observation period with high possibility of multipath. Multipath prediction may let us know the severity of multipath in the given satellite geometry and city model in the specific observation time. Therefore, the development of a multipath severity information system will help multipath mitigation especially for real-time applications.

Multiple-frequency GNSS data may help detection and rejection of multipath contaminated measurements. However, rejection of multipath contaminated measurements may reduce the number of observations/satellites. It may lead to reduced redundancy and weakened satellite geometry. It may be better to correct multipath error rather than reject the measurement. Mitigation or correction of multipath error before data processing can keep the number of observations and redundancy and hence better positioning accuracy. Phase multipath error reconstruction technique or antenna array with spatial (geometrical) analysis technique described in Section 2.7 may be used to determine the multipath error and apply the correction to the measurement. Alternatively, a stochastic model may be used to down-weight the detected multipathing measurements rather than rejection of the measurements in data processing.

REFERENCES

Akrour, B., R. Santerre and A. Geiger (2005). Calibrating Antenna Phase Centers: A Tale of Two Methods. *GPS World*, February 1, 2005.

Ashby, N. and J. J. Spilker Jr. (1996). Introduction to Relativistic Effects on the Global Positioning System. *Global Positioning System: Theory and Applications*. Edited by Parkinson, B. W. and Spilker, J. J. Jr., Vol. 1. AIAA, pp. 623-697. ISBN 1-56347-106-X.

AZoM (n.d). The A to Z of Materials. http://www.azom.com/details.asp?ArticleID=1114, Retrieved at 14:00 19 February 2005.

Baarda, W. (1968). A Testing Procedure for Use in Geodetic Networks. Publication on Geodesy, New Series, 2(5), Netherlands Geodetic Commission.

Bartosch, L. (2001). Generation of Colored Noise. International Journal of Modern Physics C, Vol. 12, No. 6 (2001), pp. 851-855.

Bétaille, D. (2003). A Testing Methodology for GPS Phase Multipath Mitigation Techniques. *Proceedings of ION GPS GNSS 2003*, The Oregon Convention Center, Portland OR, September 9-12, 2003, 2151-2162.

Bétaille, D. (2004). Assessment and Improvement of the Capabilities of a Window Correlator to Model GPS Multipath Phase Errors. *PhD Thesis*, Department of Geomatic Engineering, University College London, University of London.

Bétaille, D, J. Maenpa, H. J. Euler and P. A. Cross (2003). New Approach to GPS Phase Multipath Mitigation. *Proceedings of ION National Technical Meeting 2003.*

Beutler, G., D. A. Davidson, R. B. Langley, R. Santerre, P. Vanicek and D.E. Wells (1984). Some theoretical and practical aspects of geodetic positioning using carrier

phase difference observations of GPS satellites. University of New Brunswick, Canada, *Technical Report*, Vol. 109.

Bilich, A., K. Larson and P. Axelrad (2003). Observing and correcting the effects of multipathed signals using the signal-to-noise ratio (SNR). *Geophysical Research Abstract*, Vol. 5, 07835, European Geophysical Society. (presented at EGS-AGU-EUG Joint Assembly, Nice, 6-11 April).

Bock, Y., S. A. Gourevitch, C. C. Counselman, R. W. King and R. I. Abbot (1986). Interferometric analysis of GPS phase observations. *Manuscripta Geodaetica*, Vol.11, Number 4, pp.282-288.

Born, M. and E. Wolf (1999). Principles of Optics. 7th (Expanded) Edition, Cambridge University Press. ISBN 0-521-78449-2.

Braasch, M. S. (1996). Multipath Effects. *Global Positioning System: Theory and Applications*. Edited by Parkinson, B. W. and Spilker, J. J. Jr., Vol. 1. AIAA, pp. 547-568. ISBN 1-56347-106-X.

Brown, R. G. (1996). Receiver Autonomous Integrity Monitoring. *Global Positioning System: Theory and Applications*. Edited by Parkinson, B. W. and Spilker, J. J. Jr., Vol. 2. AIAA, pp. 143-165. ISBN 1-56347-106-X.

Brunner, F.K., Hartinger, H. and Troyer, L. (1999) GPS signal diffraction modelling: the stochastic SIGMA-Δ model, *Journal of Geodesy*, Vol. 73, pp. 259-267.

Cambridge University Engineering Department (2003). Materials Data Book, Cambridge University Engineering Department, 2003 Edition.

Cannon, M. E., J. K. Ray and J. Deschamps (2000). Attitude Determination Using Multipath Mitigation on Multiple Closely-Spaced Antennas. *Proceedings of ION GPS 2000*, Salt Lake City UT, September 19-22, 2000, 2201-2208.

Comp, C. J. and P. Axelrad (1996). An adaptive SNR-based carrier phase multipath mitigation technique. *Proceedings of ION GPS-96*, The Institute of Navigation, Kansas City, Missouri, 1996, pp. 683-697.

Corbett, S. J. and P. A. Cross (1995). GPS Single Epoch Ambiguity Resolution. *Survey Review*, Vol. 33, No. 257, pp. 149-160.

Counselman, C. C. and S. A. Gourevitch (1981). Miniature interferometer terminals for earth surveying: Ambiguity and multipath with Global Positioning System. *IEEE Transactions on Geoscience and Remote Sensing*, Vol. GE-19(4), pp.244-252.

Cross, P. A. (1994). Advanced Least Squares Applied to Position-Fixing. *Working Paper No. 6*, Department of Land Surveying, University of East London. ISSN 0260-9142.

Davis, J., Y. Huang, S. G. Millard and J. H. Bungey (2003). Determination of dielectric properties of insitu concrete at radar frequencies. *Proceedings of International Symposium of Non-Destructive Testing in Civil Engineering NDT-CE 2003*, Berlin, Germany, September 16-19, 2003.

Davis, J. L., T. A. Herring, I. I. Shapiro, A. E. E. Rogers and G. Elgered (1985). Geodesy by Radio Interferometry: Effects of Atmospheric Modeling Errors on Estimates of Baseline Length. *Radio Science*, Vol. 20, No. 6, pp. 1593-1607.

EC and ESA (2001). GALILEO: Mission High Level Definition, European Commission and European Space Agency, 3rd April 2001.

Eissfeller, B., C. Tiberius, T. Pany and G. Heinrichs (2002). Real-Time Kinematic in the Light of GPS Modernisation and Galileo. *Galileo World*, Autumn, 2002, 28-34.

EUROCONTROL (2003). GNSS Sole Service Feasibility Study. EEC Note No. 04/03, Project GNS-Z-SBAS, EUROCONTROL Experimental Centre, European Organisation for the Safety of Air Navigation, EUROCONTROL Agency, May, 2003.

Feller, W. (1971). An Introduction to Probability Theory and its Applications. Vol. II, 2nd edition, Wiley, New York. ISBN 0471257095.

Frei, E. (1991). GPS-Fast Ambiguity Resolution Approach "FARA": theory and application. Presented paper at XX General assembly of IUGG, *IAG-Symposium GM ¼*, Vienna, August 11-24.

Frei, E. and G. Beutler (1990). "Rapid static positioning based on the fast ambiguity resolution approach 'FARA': Theory and first results." *Manuscripta Geodaetica*, 15 (6), pp.325-356.

Gurtner, W. (2001). RINEX: The Receiver Independent Exchange Format Version 2.10. 8 June 2001. http://www.ngs.noaa.gov/CORS/rinex210.txt.

Hartinger, H. and F. K. Brunner (1999). Variances of GPS Phase Observations: The SIGMA-ϵ Model. *GPS Solutions* 2(4), 35-43.

Hatch, R. (1991). Instantaneous Ambiguity Resolution. *Proceedings: Kinematic System in Geodesy, Surveying and Remote Sensing*, IAG Symposium No. 107, Springer, New York, pp. 299-308.

Hatch, R., J. Jung, P. Enge and B. Pervan (2000). Civilian GPS: The benefits of three frequencies. *GPS Solutions*, 3(4), 1-9.

Hein, G. W., J. Godet, J. Issler, J. Martin, P. Erhard, R. Lucas-Rodriguez and T. Pratt (2003). Galileo Frequency and Signal Design. *GPS World*, Vol. 14, No. 6, 30-37.

Hofmann-Wellenhof, B., H. Lichtenegger and J. Collins (2004). Global Positioning System: Theory and Practice. 5th ed., Springer-Verlag – Wien New York. ISBN 3211835342

Hogg, D. C., F. Guiraud and M. Decker (1981). Measurements of Excess Transmission Length on Earth-Space path. *Astron. Astrophys.*, 95, pp. 304-307.

Hopfield, H. S. (1969). Two-Quadratic Tropospheric Refractivity Profile for Correcting Satellite Data. *Journal of Geophysical Research*, Vol. 74, No. 18, pp. 4487-4499.

ICD-GPS-200C (2003). Navstar GPS Space Segment/Navigation User Interfaces, Revision C, U.S. Air Force.

ICD-GPS-705 (2002). Navstar GPS Space Segment/User Segment L5 Interfaces, GPS NAVSTAR JPO and SMC/CZ (AFMC), Revision Two.

Ida, N. and J. P. A. Bastos (1992). Electromagnetics and Calculation of Fields, Springer-Verlag. ISBN 0-387-97852-6.

Ifadis, I. (1992). The Excess Propagation Path of Radio Waves. Study of the Influence of the Atmospheric Parameters on its Elevation Dependence. *Survey Review*, Vol. 31, No. 243, January 1992, pp. 289-298.

Inan, U. S. and A. S. Inan (2000). Electromagnetic Waves. Prentice Hall. ISBN 0-201-36179-5

International GPS Service (IGS). http://igscb.jpl.nasa.gov.

Klobuchar, J. A. (1996). Ionospheric Effects on GPS. *Global Positioning System: Theory and Applications*. Edited by Parkinson, B. W. and Spilker, J. J. Jr., Vol. 1. AIAA, pp. 485-515. ISBN 1-56347-106-X.

Koch, K. R. (1999). Parameter Estimation and Hypothesis Testing in Linear Models. Second Edition, Springer. ISBN 3540652574

Kok, J. J. (1984). On Data Snooping and Multiple Outlier Testing. *NOAA Technical Report NOS NGS 30*, U.S. Department of Commerce, National Oceanic and Atmospheric Administration, and National Ocean Service.

Komjathy, A., J. Maslanik, V. U. Zavorotny, P. Axelrad and S. J. Katzberg (2000). Sea Ice Remote Sensing Using Surface Reflected GPS Signals. *Proceedings of the IEEE International Geoscience and Remote Sensing Symposium (IGARSS): Taking the Pulse*

of the Planet: The Role of Remote Sensing in Managing the Environment, IEEE, Piscataway, N. J., pp. 2855-2857.

Kouba, J. and P. Héroux (2001). Precise Point Positioning using IGS Orbit and Clock Products. *GPS Solutions*, Vol. 5 No. 2, pp. 12-28.

Kraus, J. D. and D. A. Fleisch (1999). Electromagnetics with Applications, Fifth Edition, McGraw-Hill. ISBN 0-07-116429-4.

Kraus, J. D. and R. J. Marhefka (2002). Antennas for All Applications, Third Edition, McGraw-Hill. ISBN 0-07-112240-0.

Lau, L. (2000). Improved Ambiguity Function Method Applied to GPS Static Deformation Monitoring. *MPhil Thesis*, Department of Land Surveying and Geo-Informatics, The Hong Kong Polytechnic University.

Lau, L. and P. Cross (2003). Impact of GPS Modernization on Precise Carrier Phase-Based Positioning in the Presence of Multipath. *Proceedings of ION GPS/GNSS 2003*. Portland, Oregon, 9-12 September 2003.

Lau, L. and E. Mok (1999). Improvement of GPS Relative Positioning Accuracy By Using SNR. *Journal of Surveying Engineering*, November, 1999, Vol. 125, No. 4.

Lau, L., M. Pattinson and K. Sheridan (2003). Adapted Precise Point Positioning within Galileo Development and Validation Activities. *Proceedings of GNSS 2003 The European Navigation Conference*, 22-25 April 2003, Graz, Austria.

Leick, A. (2003). GPS Satellite Surveying. 3rd ed., Wiley-Interscience. ISBN 0471059307.

Mader, G. L. (1992). Rapid Static and Kinematic Global Positioning System Solutions using the Ambiguity Function Technique. *Journal of Geophysical Research* 97(B3), pp.3271-3283.

Mader, G. L. and F. M. Czopek (2002). Calibrating Antenna Phase Centers: The Block IIA Satellite. *GPS World*, May 2002, pp. 40-46.

Maral, G. and M. Bousquet (2002). Satellite Communications System: Systems, Techniques and Technology. Fourth Edition, John Wiley & Sons, Ltd. ISBN 0471496545.

Masters, D., V. Zavorotny, S. Katzberg, W. Emery (2000). GPS Signal Scattering from Land for Moisture Content Determination. *Proceedings of the IEEE International Geoscience and Remote Sensing Symposium (IGARSS): Taking the Pulse of the Planet: The Role of Remote Sensing in Managing the Environment*, IEEE, Piscataway, N. J., pp. 3090-3092.

Misra, P. and P. Enge (2001). Global Positioning System: Signals, Measurements, and Performance. Ganga-Jamuna Press. ISBN 0970954409.

Mok, E. (1996). A New Ambiguity Function Algorithm for Short Baseline Engineering Surveying Applications. *PhD Thesis*, Department of Geomatics, University of Newcastle upon Tyne, U.K.

Moore, M., C. Rizos, and J. Wang (2002). Quality control issues relating to an attitude determination system using a multi-antenna GPS array. *Geomatics Research Australasia*, 77, 27-48.

Mott, H. (1992). Antennas For Radar and Communications: A Polarimetric Approach. Wiley-Interscience. ISBN 0471575380.

Nalwa, H. S. (1999). Handbook of Low and High Dielectric Constant Materials and Their Applications: Materials and Processing. Vol. 1, Academic Press. ISBN 0125139055.

NGS. U.S. National Geodetic Survey (NGS). http://www.ngs.noaa.gov.

Novatel (n.d.). http://www.novatel.com/Documents/Papers/3D_choke_ring.pdf, Retrieved at 15:05 10 April 2005.

Park, K., J. L. Davis, P. O. J. Jarlemark, P. Elosegui, J. E. Normandeau, B. E. Corey, A. E. Niell, C. M. Meertens and V. Andreatta (2002). Multipath Characteristics of GPS signals as determined from the Antenna and Multipath Calibration System (AMCS). *Proceedings of ION GPS Meeting*, Portland OR, September 24-27, 2002, 2103-2110.

Parton, J. E. and S. J. T. Owen (1975). Applied Electromagnetics. The Macmillan Press Ltd. SBN 333-17993-5.

Peckham, R. (2005). Galileo Status. In CD-ROM of the Galileo Masters Competition UK Challenge 2005/6, 14 April 2005, London, Hertfordshire Business Incubation Centre.

Physical Constants (n.d.). http://www.mogami-wire.co.jp/paper/physical-constants.html, Retrieved at 23:00 16 April 2005.

Pope, A. J. (1976). The Statistics of Residuals and The Detection of Outliers. *NOAA Technical Report NOS 65 NGS 1.*

Rama Rao, B., J. H. Williams, E. N. Rosario and R. J. Davis (2000). GPS Microstrip Antenna Array on a Resistivity Tapered Ground Plane for Multipath Mitigation. *Proceedings of ION GPS 2000*, 19-22 September 2000, Salt Lake City, UT, USA, pp. 2468-2476.

Ray, J. K. (2000). Mitigation of GPS Code and Carrier Phase Multipath Effects Using a Multi-Antenna System. *PhD Thesis*, Department of Geomatics Engineering, University of Calgary.

Ray, J., M. E. Cannon and P. Fenton (1999). Mitigation of Static Carrier-Phase Multipath Effects Using Multiple Closely Spaced Antennas. *Navigation*, Vol. 46, No. 3, pp. 193-202.

Ray, J. and W. Gurtner (1999). RINEX Extensions to Handle Clock Information. http://www.aiub.unibe.ch/download/wwwpubs/rinex_clock.txt.

Remondi, B. W. (1984). Using The Global Positioning System (GPS) Phase Observable for Relative Geodesy: Modeling, Processing, and Results. *PhD Thesis*, The University of Texas at Austin, May 1984.

Remondi, B. W. (1991). NGS Second Generation ASCII and Binary Orbit Formats and Associated Interpolated Studies. *Proceedings of the Twentieth General Assembly, International Union of Geodesy and Geophysics*. Vienna, Austria, August 11-24, 1991, 28 pp.

Samsonov, G. V. (1968). Handbook of The Physicochemical Properties of The Elements, IFI/Plenum.

Schaer, S., W. Gurtner and J. Feltens (1998). IONEX: The IONosphere Map Exchange Format Version 1. *Proceedings of the IGS AC Workshop*, Darmstadt, Germany, February 9 – 11, 1998.

Schupler, B. R. and T. A. Clark (2001). Characterizing the Behavior of Geodetic GPS Antennas. *GPS World*, February 2001, pp. 48-55.

Spilker, J. J. Jr. (1996). GPS Signal Structure and Theoretical Performance. *Global Positioning System: Theory and Applications*. Edited by Parkinson, B. W. and Spilker, J. J. Jr., Vol. 1. AIAA, pp. 57-119. ISBN 1-56347-106-X.

Spofford, P. R. and B.W. Remondi (1994). The National Geodetic Survey Standard GPS Format SP3. http://gibs.leipzig.ifag.de/cgi-bin/sp3_doc.cgi?en or http://www.ngs.noaa.gov/GPS/SP3_format.html.

Stavrou, S. and S. Saunders (2003). Review of Constitutive Parameters of Building Materials. *12th International Conference on Antennas and Propagation*, Exeter, 31st March – 3rd April 2003.

Strang, G. and K. Borre (1997). Linear Algebra, Geodesy, and GPS. Wellesley-Cambridge Press. ISBN 0961408863.

Stewart, M. (2003). Report of Special Study Group 1.182 "Multipath Mitigation". International Association of Geodesy, http://www.cage.curtin.edu.au/~mike/ssg1.182/.

Teunissen, P. J. G. (1995). The Least-squares Ambiguity Decorrelation Adjustment: A Method for Fast GPS Integer Ambiguity Estimation. *Journal of Geodesy*, 70, pp. 65-82.

Topcon (n.d.). http://www.topcongps.com/support/ChokeRingTheory.html, Retrieved at 15:00 10 April 2005.

van Nee R. D. J. (1995). Multipath and Multi-Transmitter Interference in Spread-Spectrum Communication and Navigation Systems. Delft University Press. ISBN 90-407-1120-8.

Wanninger, L. and M. May. (2000). Carrier Phase Multipath Calibration of GPS Reference Stations. *Proceedings of ION GPS 2000*, Salt Lake City UT, September 19-22, 2000, 132-144.

Washburn, E. W. (2003). International Critical Tables of Numerical Data, Physics, Chemistry and Technology (1st Electronic Edition). Knovel.

Weill, L. R. (2003). How Good Can It Get with New Signals? Multipath Mitigation. *GPS World*, June 2003, Vol. 14, No. 6, pp. 106-113.

Wieser, A. and F. K. Brunner (2000). An Extended Weight model for GPS Phase Observations. *Earth, Planets and Space*, 52, pp. 777-782.

Wilson, B. D., C. H. Yinger, W. A. Feess and C. Shank (1999). New and improved: The broadcast interfrequency biases. *GPS World*, September 1999, Vol. 10, No. 9, pp. 56-66.

Wolf, D. de (2001). Essentials of Electromagnetics for Engineering. Cambridge University Press. ISBN 0-521-66281-8.

Wu, J. T., S. C. Wu, G. A. Hajj, W. I. Bertiger and S. M. Lichten (1993). Effect of Antenna Orientation on GPS Carrier Phase. *Man. Geodetica*, 18, pp. 91-98.

Zavorotny, V. U. and A. G. Voronovich (2000). Bistatic GPS Signal Reflections at Various Polarizations from Rough Land Surface with Moisture Content, *Proceedings of the IEEE International Geoscience and Remote Sensing Symposium (IGARSS): Taking the Pulse of the Planet: The Role of Remote Sensing in Managing the Environment*, IEEE, Piscataway, N.J., pp. 2852-2854.

Zumberge, J. F. and W. I. Bertiger (1996). Ephemeris and Clock Navigation Message Accuracy. *Global Positioning System: Theory and Applications*. Edited by Parkinson, B. W. and Spilker, J. J. Jr., Vol. 1. AIAA, pp. 585-599. ISBN 1-56347-106-X.

Zumberge, J. F, M. B. Heflin, D. C. Jefferson, M. M. Watkins and F. H. Webb (1997). Precise point positioning for the efficient and robust analysis of GPS data from large networks. *Journal of Geophysical Research (JGR)*. Vol. 102, No. B3, pp. 5005-5017.

Zumberge, J. F. (1999). Automated GPS Data Analysis Service. *GPS Solutions*. Vol. 2, No. 3, pp.76-78.

APPENDIX A. MEANING OF THE DIVERGENCE AND CURL

'Del', ∇ - A defined operator.

$$\text{'del'} = \nabla = \frac{\partial}{\partial x}\hat{i} + \frac{\partial}{\partial y}\hat{j} + \frac{\partial}{\partial z}\hat{k} \tag{A.1}$$

Gradient - A vector where each dimensional component is the rate of change of a scalar value for that dimension in space. The direction of greatest change for the scalar is the gradient vector itself.

$$\text{grad } \rho = \nabla\rho = \frac{\partial \rho}{\partial x}\hat{i} + \frac{\partial \rho}{\partial y}\hat{j} + \frac{\partial \rho}{\partial z}\hat{k} \tag{A.2}$$

Divergence - The total variation or 'divergence' of a vector field at a point in space.

$$\text{div F} = \nabla \cdot F = \frac{\partial F_x}{\partial x} + \frac{\partial F_y}{\partial y} + \frac{\partial F_z}{\partial z} \tag{A.3}$$

Curl - A vector whose components are the circulation of the vector field perpendicular to the component direction at a point in the vector field. Circulation around a normal is the sums of the variations of the each field component in the direction perpendicular to that field component and the normal direction. The curl vector itself is the normal around which the greatest circulation exists for that point in the vector field.

$$\text{curl F} = \nabla \times F = \left(\frac{\partial F_z}{\partial y} - \frac{\partial F_y}{\partial z}\right)\hat{i} + \left(\frac{\partial F_x}{\partial z} - \frac{\partial F_z}{\partial x}\right)\hat{j} + \left(\frac{\partial F_y}{\partial x} - \frac{\partial F_x}{\partial y}\right)\hat{k} \tag{A.4}$$

APPENDIX B. SIMULATED DATA SAMPLES

```
     2                    OBSERVATION DATA                        RINEX VERSION / TYPE
Simulator V1.0            UCL                 20Feb 2005 00:17:36 PGM / RUN BY / DATE
1                                                                 MARKER NAME
Lawrence Lau              UCL                                     OBSERVER / AGENCY
111111111                 SIMULA              1.0                 REC # / TYPE / VERS
Phase Multipath Simulated                                         COMMENT
Measurement Noise Simulated                                       COMMENT
Phase Centre Offset and Variation Simulated                       COMMENT
LEIAT502                  Aero element L1/L2, External            ANT # / TYPE
   4343445.7856 -124877.3983 4653445.9401                         APPROX POSITION XYZ
         0.0000       0.0000       0.0000                       ANTENNA: DELTA H/E/N
         1   1                                                    WAVELENGTHFACT L1/2/3
         6   L1   C1   L2   P2   L5   C5                        # / TYPES OF OBSERV
         1                                                        INTERVAL
      2002   5   28   8    0   0.000000                         TIME OF FIRST OBS
      2002   5   28   8    59  59.000000                        TIME OF LAST OBS
                                                                  END OF HEADER
02 05 28 08 00  0.0000000  0 14  2  3 15 18 21 22 27 31A13A14A15A20A21A22
109810701.30505  20896281.66205  85566780.20005  20896281.66505  82001497.69305
 20896281.45705
107067097.74205  20374191.26105  83428907.30105  20374191.14305  79952702.83105
 20374191.29805
113413949.50605  21581957.01605  88374506.08305  21581956.92905  84692235.00305
 21581956.93505
115725244.69305  22021781.75305  90175515.31405  22021781.90505  86418202.16805
 22021782.00005
117927050.98705  22440771.64605  91891208.51705  22440771.62005  88062408.16705
 22440771.64205
112324637.30705  21374667.74505  87525691.37105  21374667.64505  83878787.56105
 21374667.78105
127204779.44105  24206264.68405  99120607.32805  24206264.70605  94990582.03105
 24206264.65605
118155020.13005  22484152.66805  92068846.81905  22484152.51605  88232644.86305
 22484152.39205
133085145.49505  25325260.99605  99381764.46505  25325261.35105 101974332.22705
 25325261.03305
125072002.68205  23800410.89105  93397924.04705  23800410.76905  95834391.62305
 23800410.76105
135658323.50905  25814920.61005 101303293.49105  25814920.86105 103945988.10705
 25814920.51705
130112966.18405  24759674.33805  97162279.89705  24759673.98305  99696948.09905
 24759674.18705
124761852.51705  23741391.00205  93166318.39805  23741391.05705  95596744.09305
 23741391.41105
138082336.55105  26276194.79105 103113433.11205  26276195.02405 105803348.75705
 26276194.92105
02 05 28 08 00  1.0000000  0 14  2  3 15 18 21 22 27 31A13A14A15A20A21A22
109810813.57705  20896302.99805  85566867.68705  20896303.00205  82001581.53405
 20896302.99405
107066060.92605  20373994.09105  83428099.38605  20373993.63705  79951928.58405
 20373993.94905
113416415.36105  21582426.29805  88376427.52505  21582426.20705  84694076.37905
 21582426.23705
```

115724613.41105 22021661.70805 90175023.40105 22021661.65205 86417730.76005
22021661.68805
117924722.61605 22440328.61205 91889394.21305 22440328.43405 88060669.45005
22440328.63105
112327159.70205 21375147.86905 87527656.86905 21375147.78005 83880671.16305
21375147.78605
127203997.01705 24206115.78605 99119997.64305 24206115.73705 94989997.74505
24206115.83405
118151970.72105 22483572.36405 92066470.65305 22483572.30705 88230367.71205
22483572.48305
133082510.89505 25324759.47305 99379797.06705 25324759.60705 101972313.51205
25324759.84805
125072222.87505 23800452.68005 93398088.47405 23800452.84105 95834560.34305
23800452.89005
135661146.40905 25815457.88005 101305401.50005 25815457.80105 103948151.11005
25815457.72505
130110558.70405 24759216.22405 97160482.10905 24759216.13605 99695103.41105
24759215.68605
124762422.78405 23741499.78405 93166744.25005 23741499.51305 95597181.06305
23741499.59305
138085323.09805 26276763.30705 103115663.31705 26276763.32705 105805637.14605
26276763.68805
02 05 28 08 00 2.0000000 0 14 2 3 15 18 21 22 27 31A13A14A15A20A21A22
109811078.94805 20896353.39205 85567074.46405 20896353.20505 82001779.69205
20896353.37905
107065177.00105 20373825.82405 83427410.60105 20373825.72705 79951268.50005
20373825.81605
113419034.08705 21582924.52105 88378468.08305 21582924.53005 84696031.91305
21582924.55205
115724135.27905 22021570.85205 90174650.83305 22021571.01205 86417373.71705
22021570.67305
117922547.16805 22439914.57905 91887699.05105 22439914.55605 88059044.92805
22439914.60905
112329835.02605 21375657.03305 87529741.54005 21375656.94005 83882668.97405
21375657.00305
127203367.66305 24205996.02105 99119507.24905 24205996.32805 94989527.77805
24205995.75505
118149073.98905 22483021.04005 92064213.46205 22483021.33305 88228204.57905
22483021.04605
133080029.15705 25324287.29105 99377943.81405 25324287.51305 101970411.91305
25324287.42605
125072596.07205 23800523.58405 93398367.16505 23800523.77605 95834846.30305
23800523.56305
135664122.08105 25816024.04405 101307623.59405 25816024.13405 103950431.17005
25816024.13905
130108304.10305 24758787.04605 97158798.47905 24758787.06405 99693375.85705
24758787.17305
124763146.03605 23741637.14005 93167284.35205 23741637.24805 95597735.24505
23741637.34105
138088462.34905 26277360.61905 103118007.56405 26277360.47105 105808042.55705
26277360.83705

APPENDIX C. DETAILS OF THE THREE IGS STATIONS USED IN THE GNSS DATA SIMULATOR VALIDATION

i)
Site name : Hartebeesthoek RAO
Four character ID : HRAO
Agency : HRAO-JPL
City : Krugersdorp
Country : South Africa
Tectonic Plate : Africa plate, Kaapvaal Craton
Receiver Type : ASHTECH Z-XII3
Antenna Type : AOAD/M_T (ASH701945C_M, after 19/11/2004)
Approximate Position (ITRF)
X coordinate (m) : 5085352.447
Y coordinate (m) : 2668395.795
Z coordinate (m) : -2768731.573
Latitude (deg) : 25.89010634 S
Longitude (deg) : 27.68697900 E
Elevation (m) : 1414.1877

ii)
Site Name : Potsdam, GeoForschungsZentrum
Four Character ID : POTS
Agency : GeoForschungsZentrum Potsdam
City or Town : Potsdam
State or Province : Brandenburg
Country : Germany
Tectonic Plate : Eurasian
Receiver Type : AOA SNR-8000 ACT
Antenna Type : AOAD/M_T
Approximate Position (ITRF)
X coordinate (m) : 3800725.3
Y coordinate (m) : 882088.5
Z coordinate (m) : 5028799.8
Latitude (deg) : 52.38 N
Longitude (deg) : 13.07 E
Elevation (m) : 174

iii)
Site Name : U.S. Naval Observatory
Four Character ID : USNO
Agency : U.S. Naval Observatory
City or Town : Washington
State or Province : District of Columbia (DC)
Country : U.S.A.
Tectonic Plate : North American
Receiver Type : ASHTECH Z-XII3T
Antenna Type : AOAD/M_T
Approximate Position (ITRF)

X coordinate (m)	: 1112189.9031
Y coordinate (m)	: -4842955.0319
Z coordinate (m)	: 3985352.2376
Latitude (deg)	: 38.9190 N
Longitude (deg)	: 77.0662 W
Elevation (m)	: 48.878

APPENDIX D. FIGURES OF THE MEASUREMENT DOMAIN VALIDATION OF THE GNSS DATA SIMULATOR

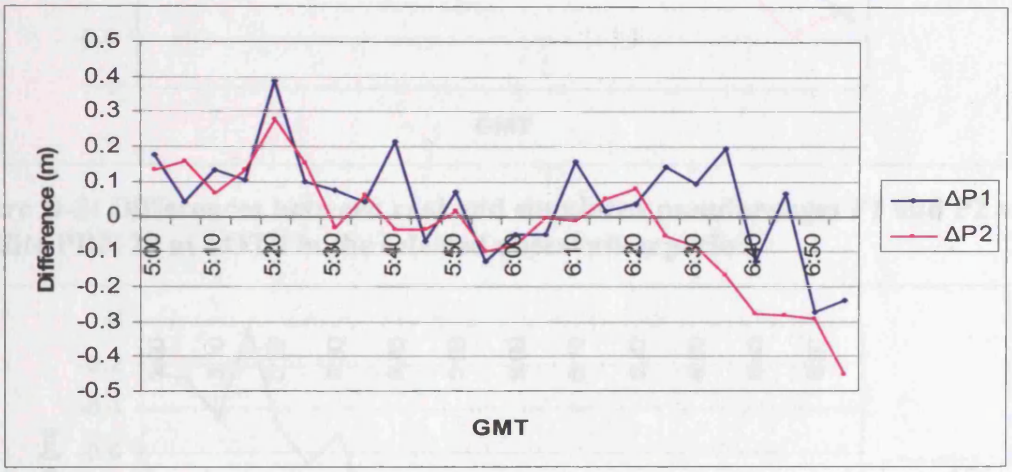

Figure D-1: Differences between real and simulated pseudoranges P1 and P2 of satellite PRN 26 at POTS in the selected observation period.

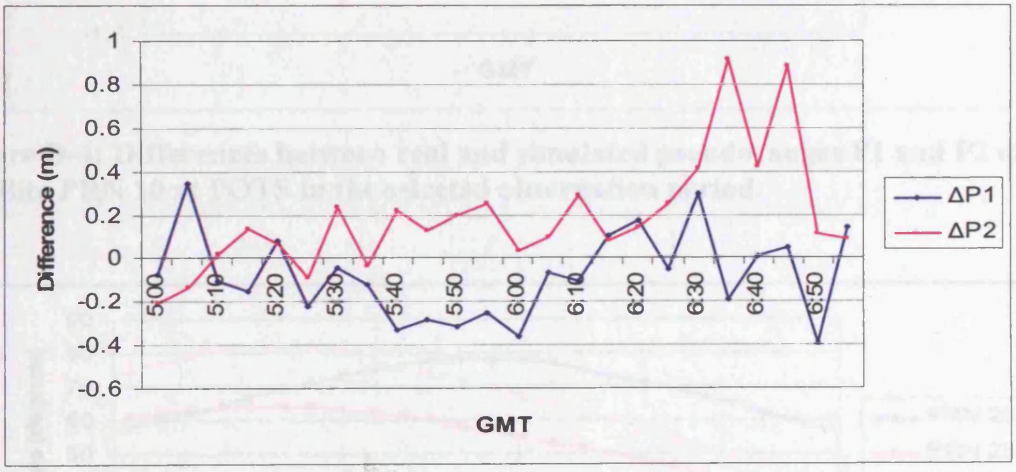

Figure D-2: Differences between real and simulated pseudoranges P1 and P2 of satellite PRN 28 at POTS in the selected observation period.

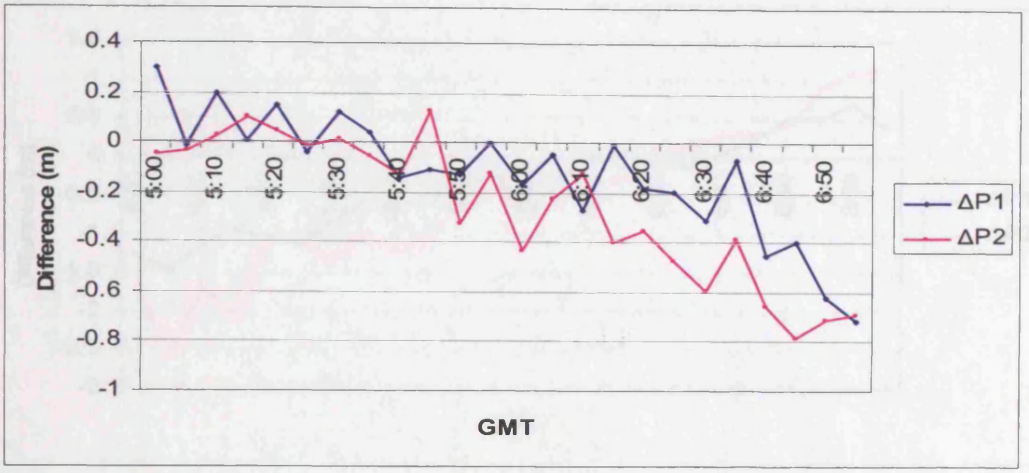

Figure D-3: Differences between real and simulated pseudoranges P1 and P2 of satellite PRN 29 at POTS in the selected observation period.

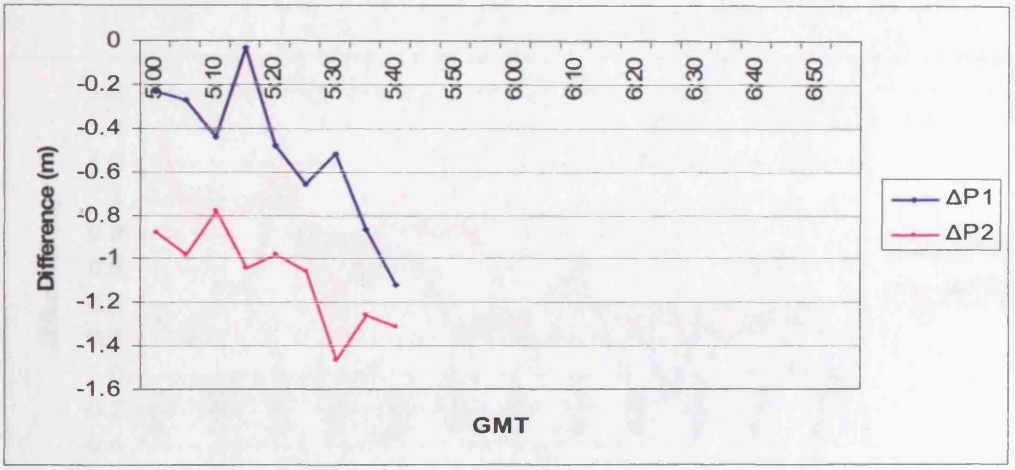

Figure D-4: Differences between real and simulated pseudoranges P1 and P2 of satellite PRN 10 at POTS in the selected observation period.

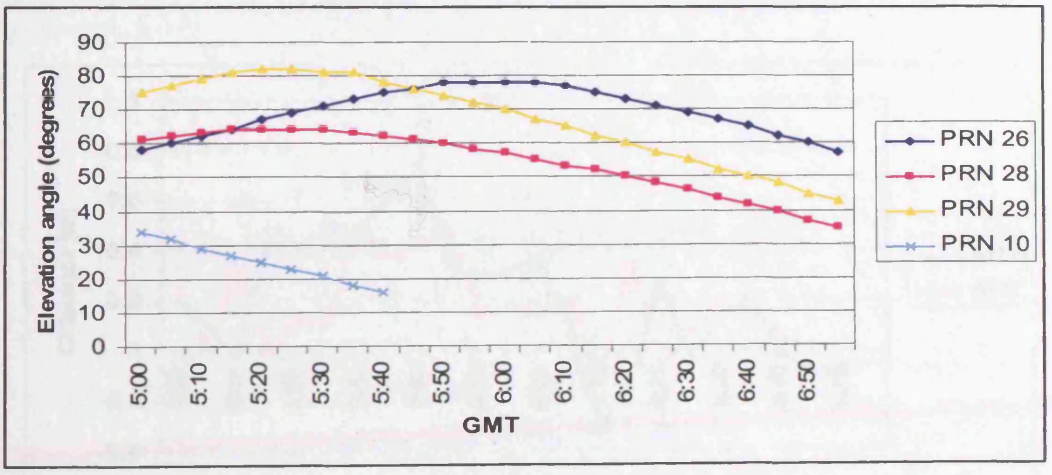

Figure D-5: Elevation angles of the selected satellites at POTS in the selected observation period.

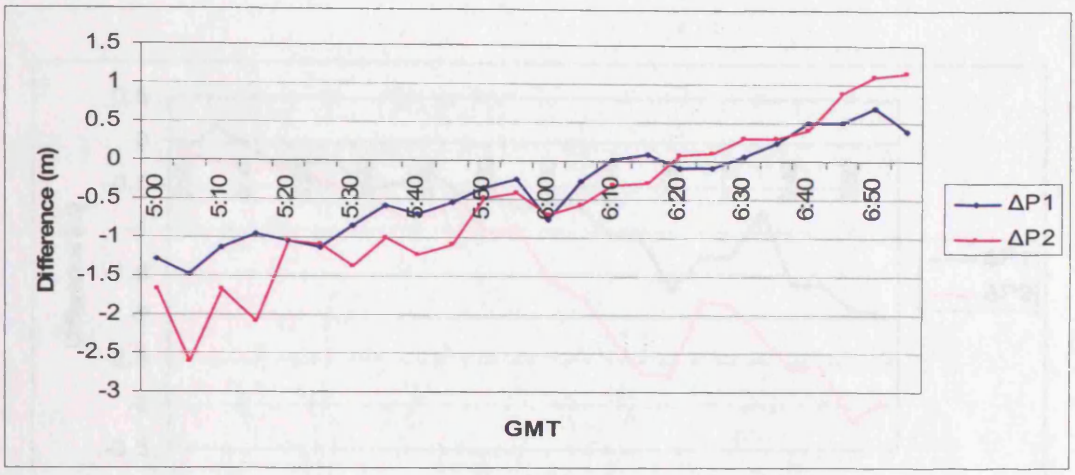

Figure D-6: Differences between real and simulated pseudoranges P1 and P2 of satellite PRN 9 at USNO in the selected observation period.

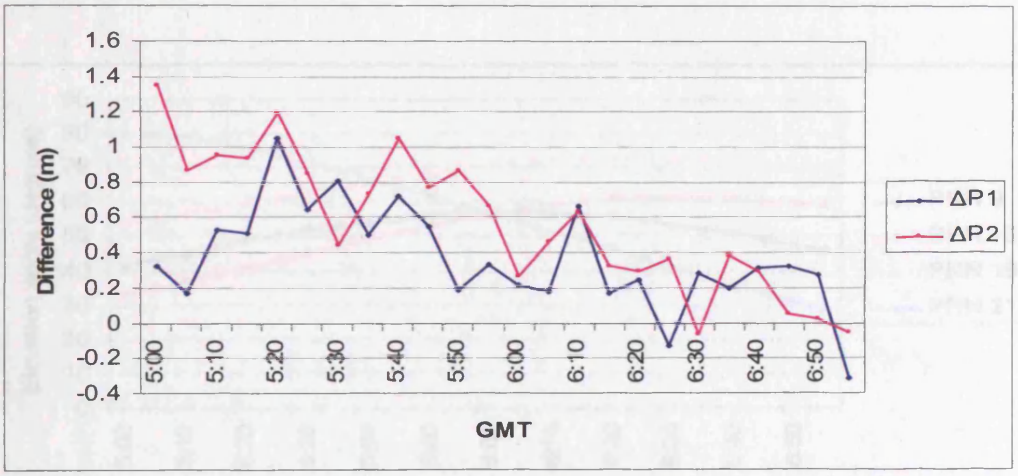

Figure D-7: Differences between real and simulated pseudoranges P1 and P2 of satellite PRN 15 at USNO in the selected observation period.

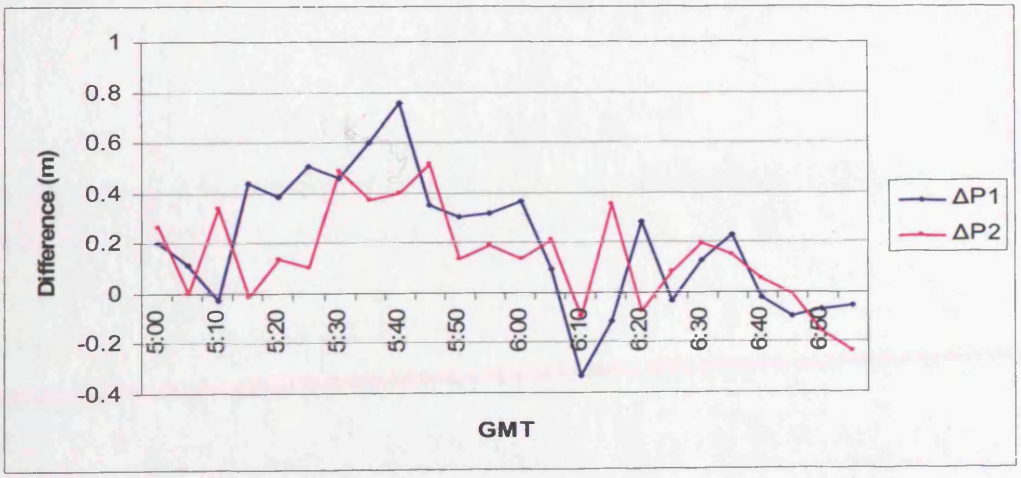

Figure D-8: Differences between real and simulated pseudoranges P1 and P2 of satellite PRN 18 at USNO in the selected observation period.

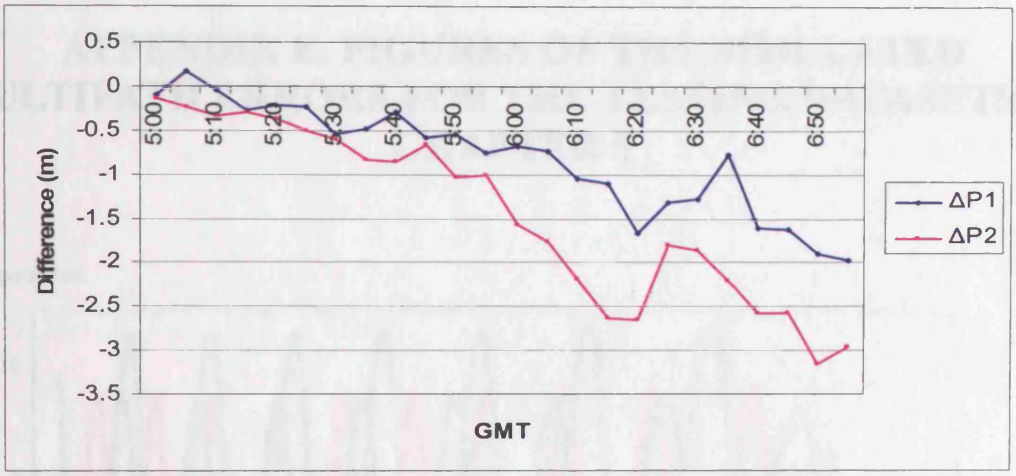

Figure D-9: Differences between real and simulated pseudoranges P1 and P2 of satellite PRN 21 at USNO in the selected observation period.

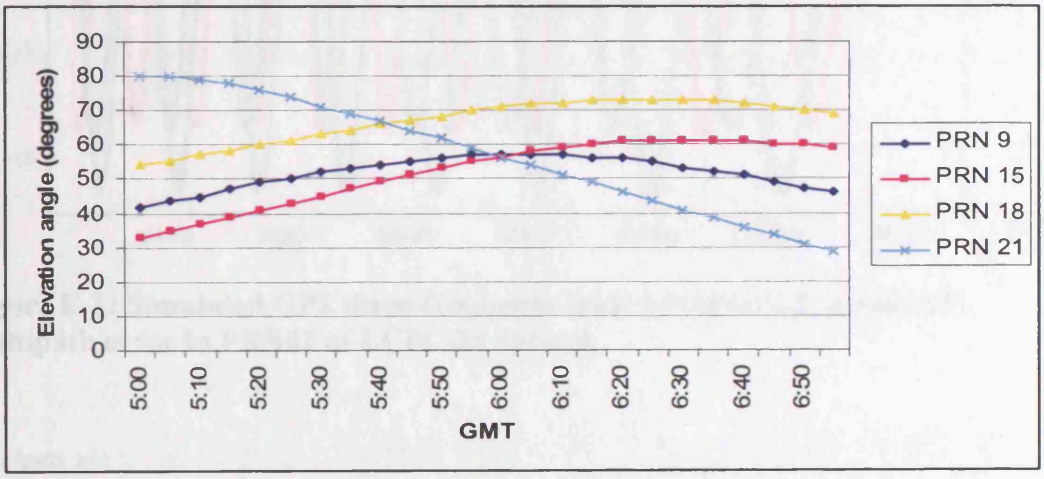

Figure D-10: Elevation angles of the selected satellites at USNO in the selected observation period.

APPENDIX E. FIGURES OF THE SIMULATED MULTIPATH ERRORS FOR THE TESTING DATASETS IN CHAPTER 5

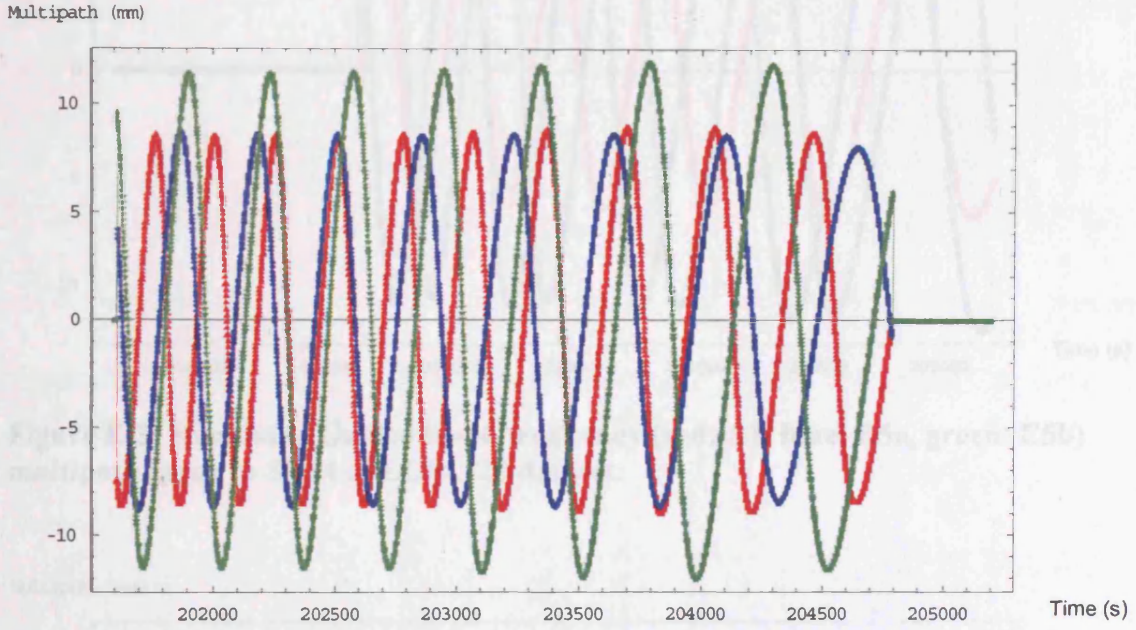

Figure E-1: Simulated GPS three-frequency (red: L1, blue: L2, green: L5) multipath error in PRN02 of LCPC-20 dataset.

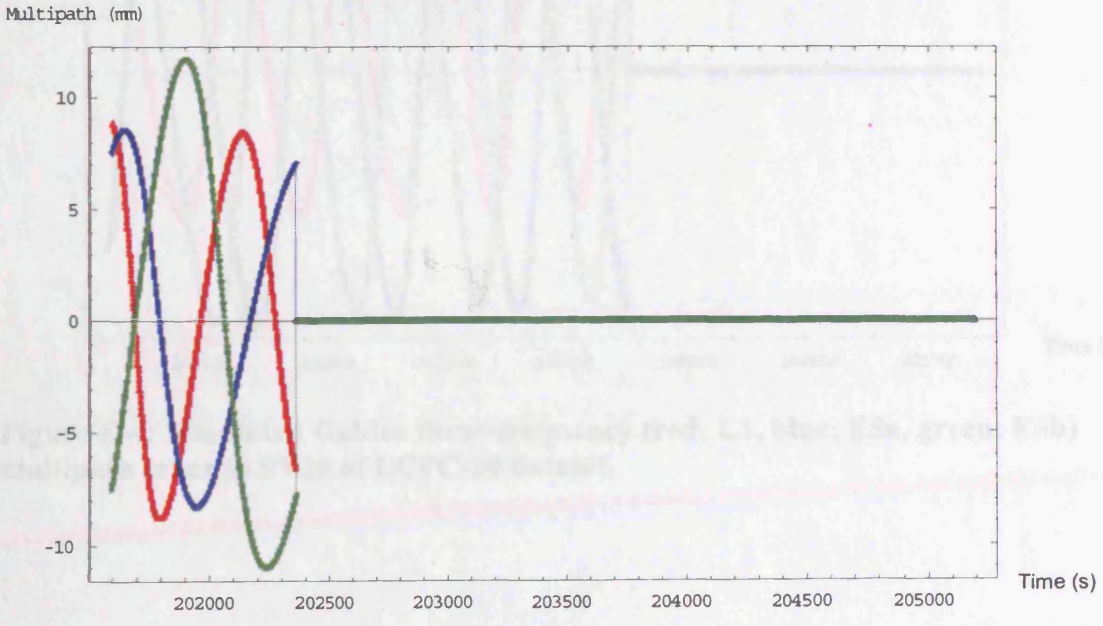

Figure E-2: Simulated GPS three-frequency (red: L1, blue: L2, green: L5) multipath error in PRN22 of LCPC-20 dataset.

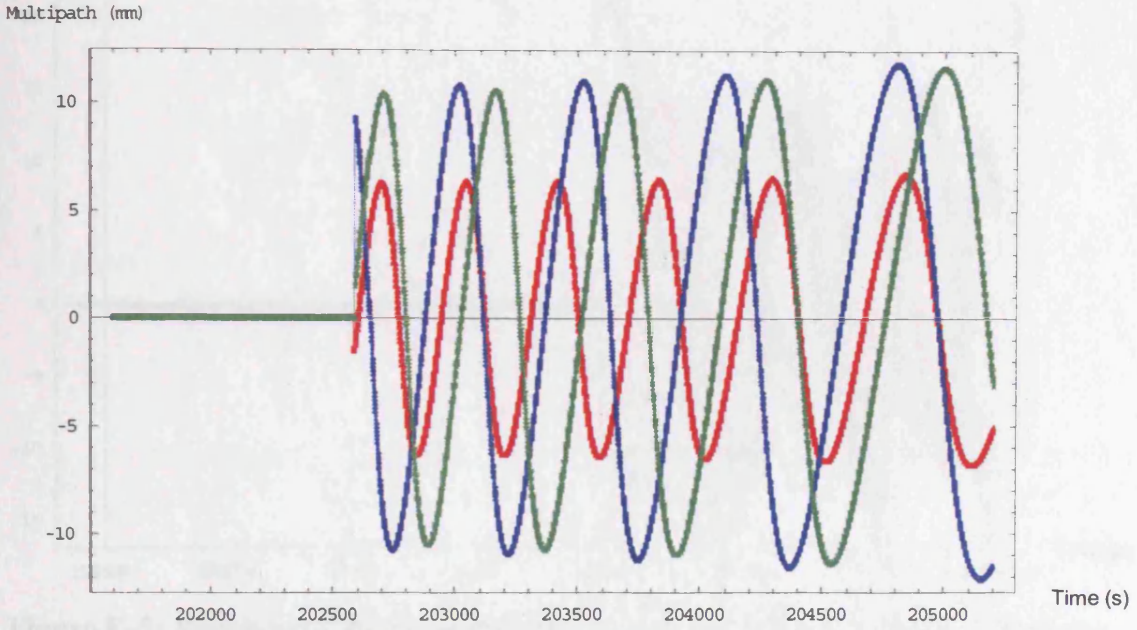

Figure E-3: Simulated Galileo three-frequency (red: L1, blue: E5a, green: E5b) multipath error in SV14 of LCPC-20 dataset.

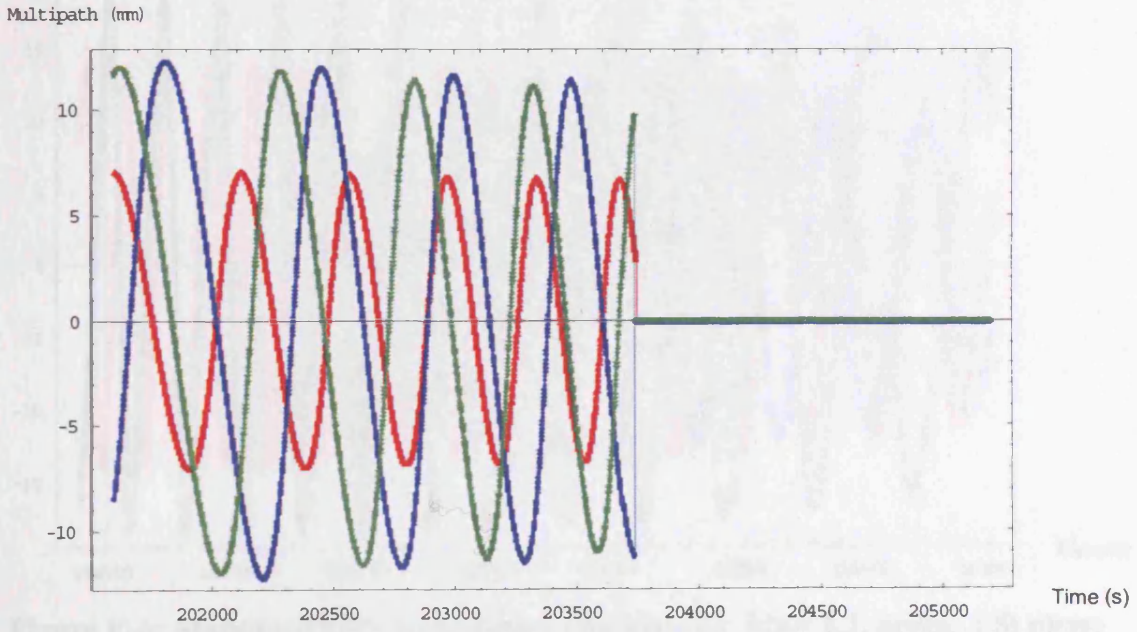

Figure E-4: Simulated Galileo three-frequency (red: L1, blue: E5a, green: E5b) multipath error in SV20 of LCPC-20 dataset.

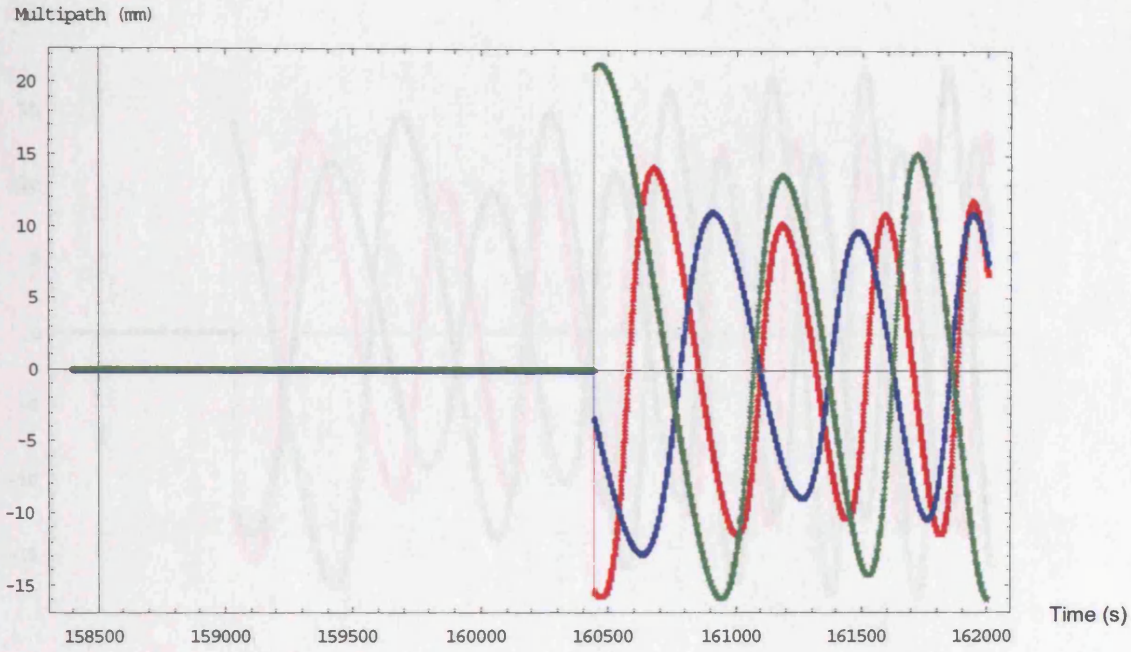

Figure E-5: Simulated GPS three-frequency (red: L1, blue: L2, green: L5) phase multipath error in PRN07 of the LBCH-7 dataset.

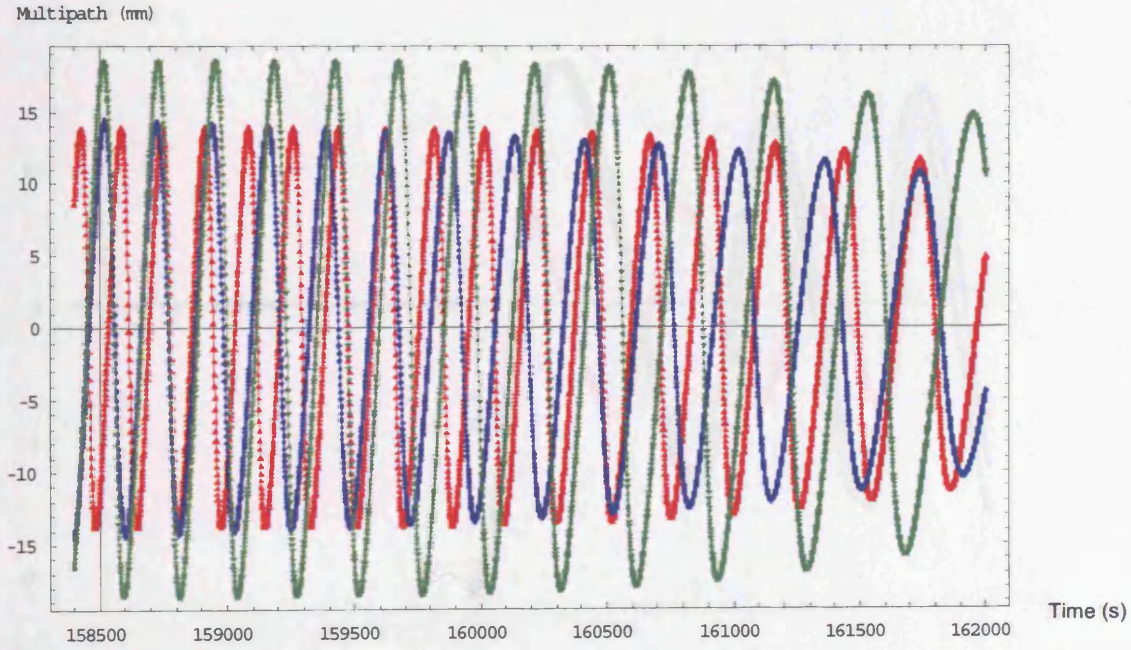

Figure E-6: Simulated GPS three-frequency (red: L1, blue: L2, green: L5) phase multipath error in PRN13 of the LBCH-7 dataset.

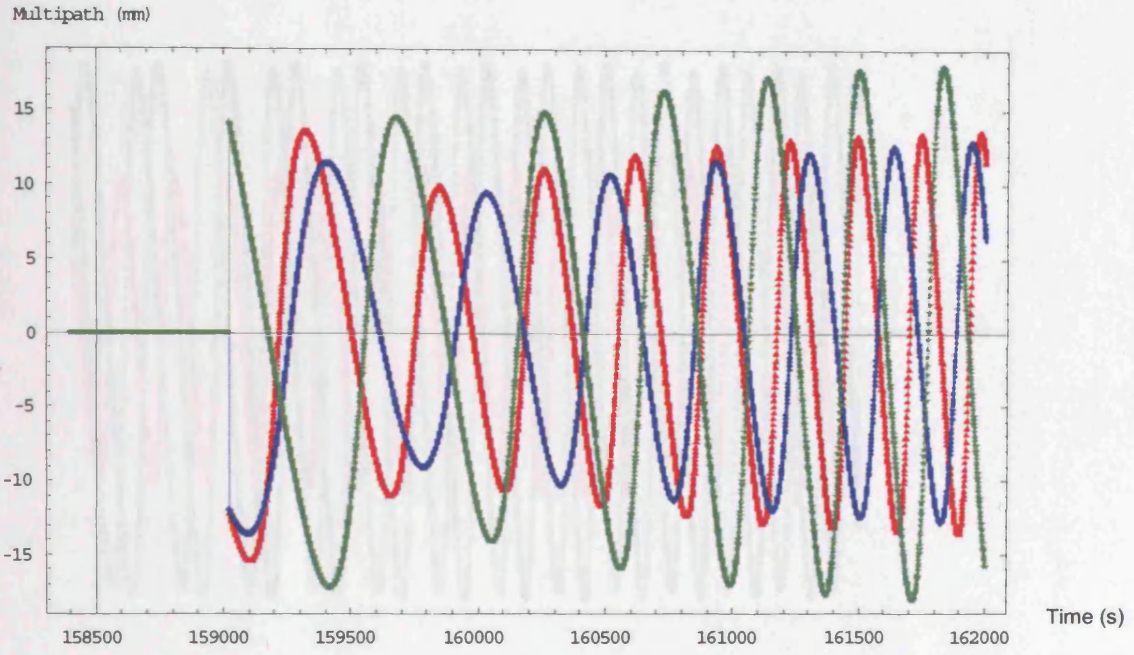

Figure E-7: Simulated GPS three-frequency (red: L1, blue: L2, green: L5) phase multipath error in PRN31 of the LBCH-7 dataset.

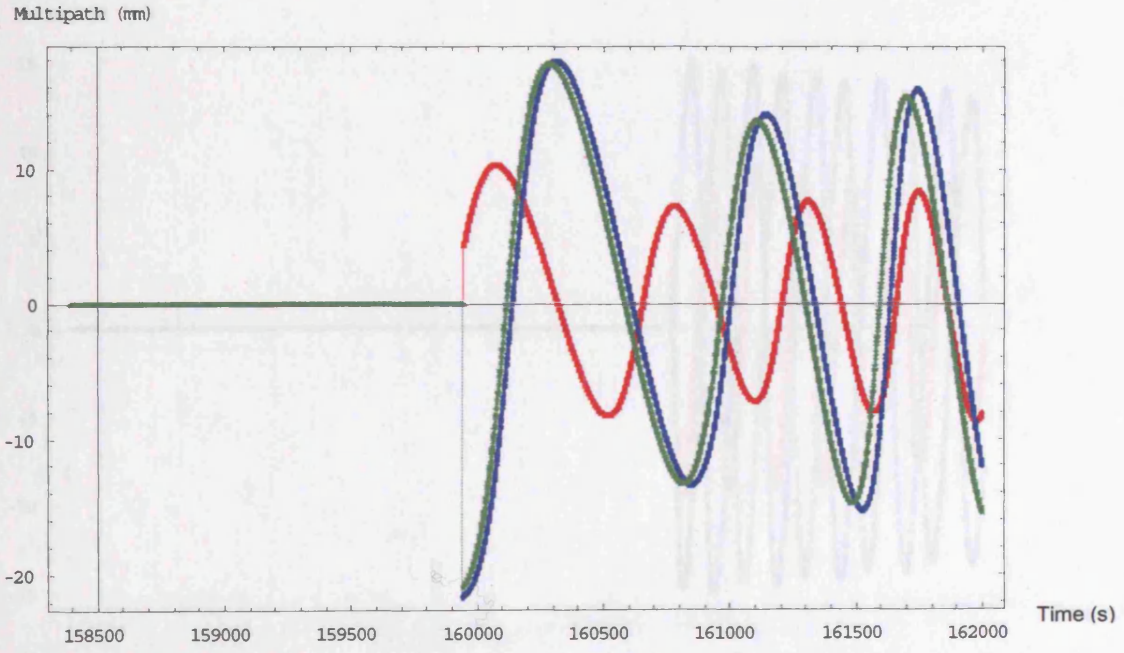

Figure E-8: Simulated Galileo three-frequency (red: L1, blue: E5a, green: E5b) phase multipath error in SV17 of the LBCH-7 dataset.

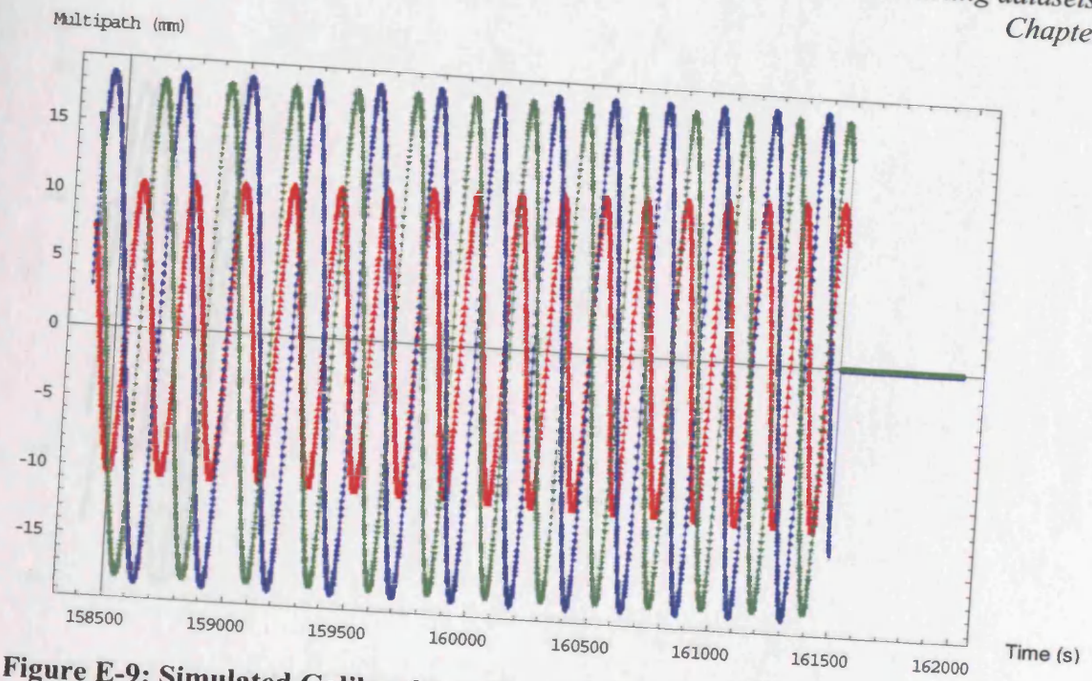

Figure E-9: Simulated Galileo three-frequency (red: L1, blue: E5a, green: E5b) phase multipath error in SV18 of the LBCH-7 dataset.

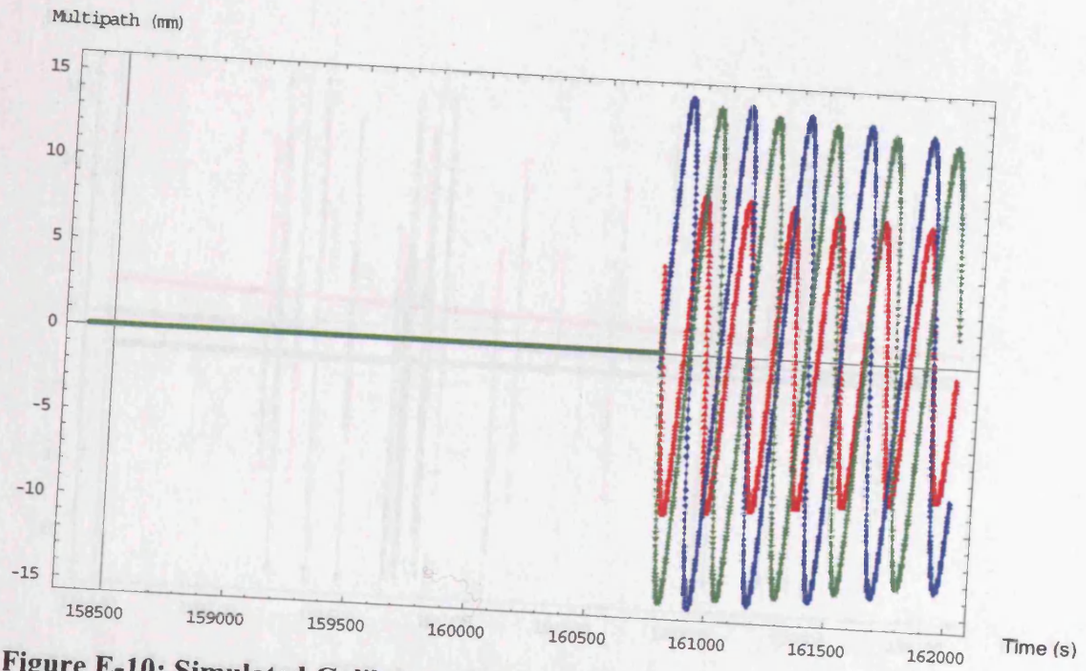

Figure E-10: Simulated Galileo three-frequency (red: L1, blue: E5a, green: E5b) phase multipath error in SV22 of the LBCH-7 dataset.

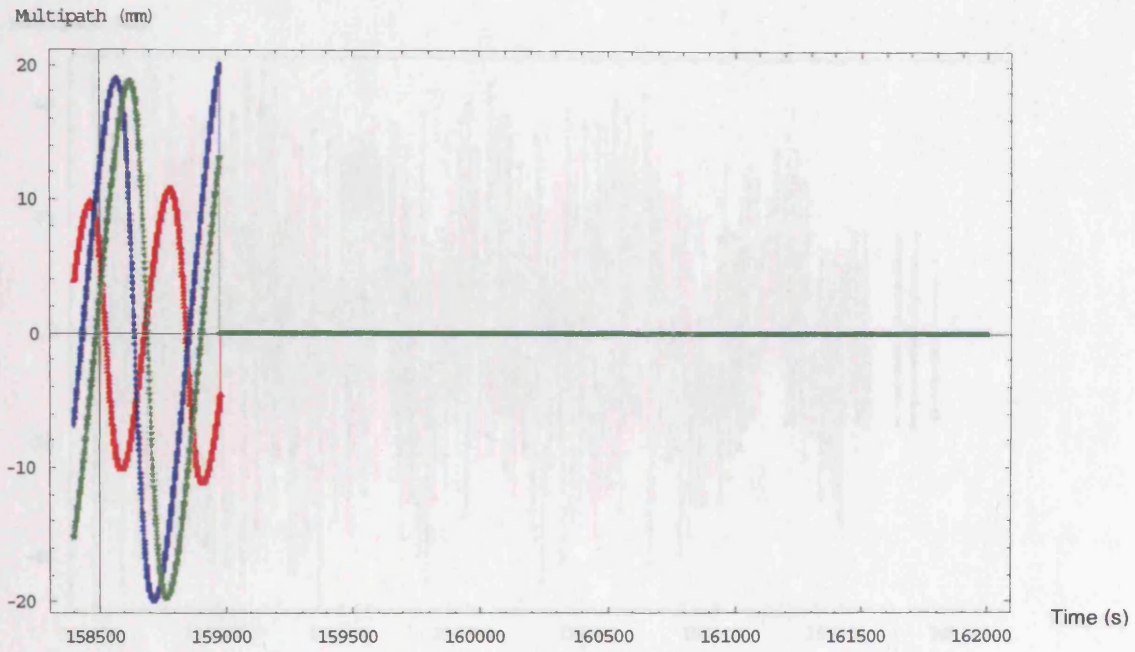

Figure E-11: Simulated Galileo three-frequency (red: L1, blue: E5a, green: E5b) phase multipath error in SV23 of the LBCH-7 dataset.

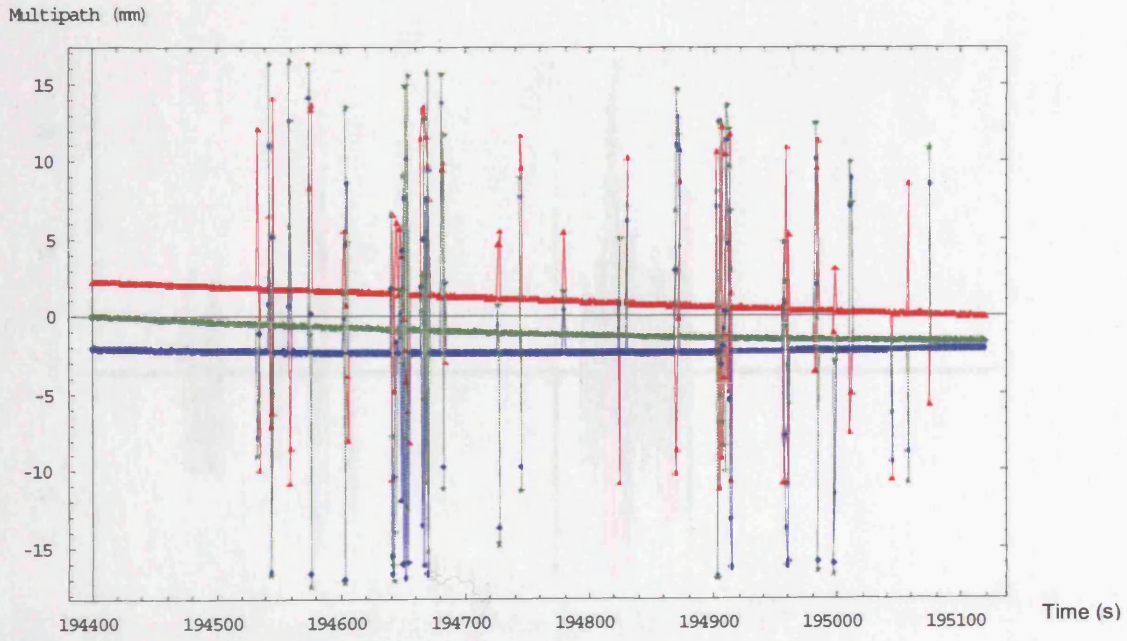

Figure E-12: Simulated GPS three-frequency (red: L1, blue: L2, green: L5) phase multipath error in PRN01 of the K-HK7-600 dataset.

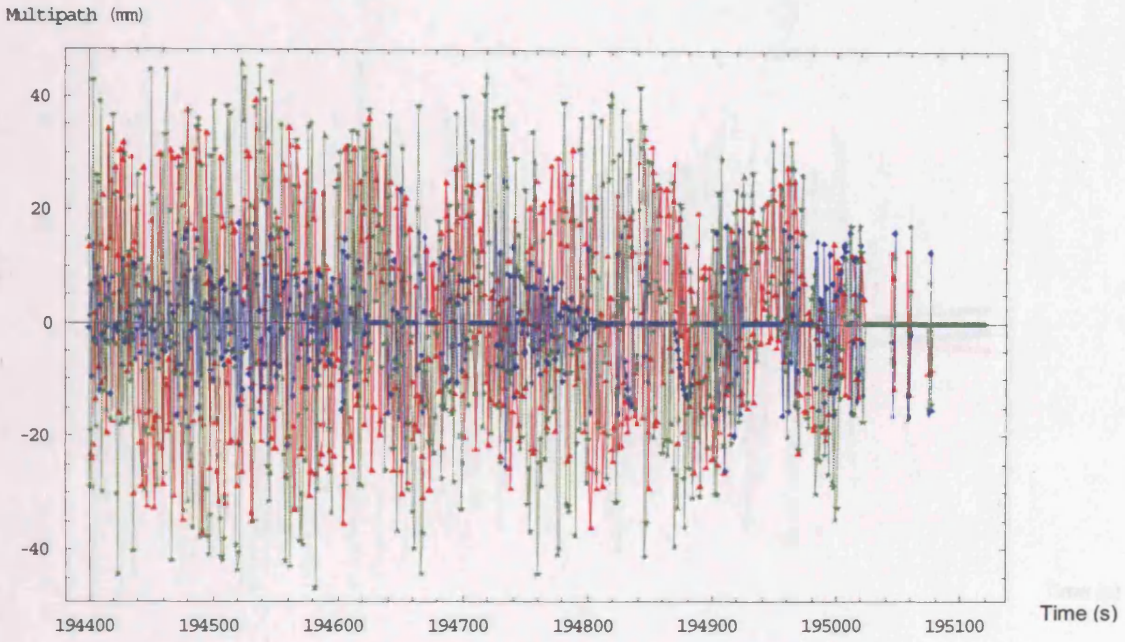

Figure E-13: Simulated GPS three-frequency (red: L1, blue: L2, green: L5) phase multipath error in PRN03 of the K-HK7-600 dataset.

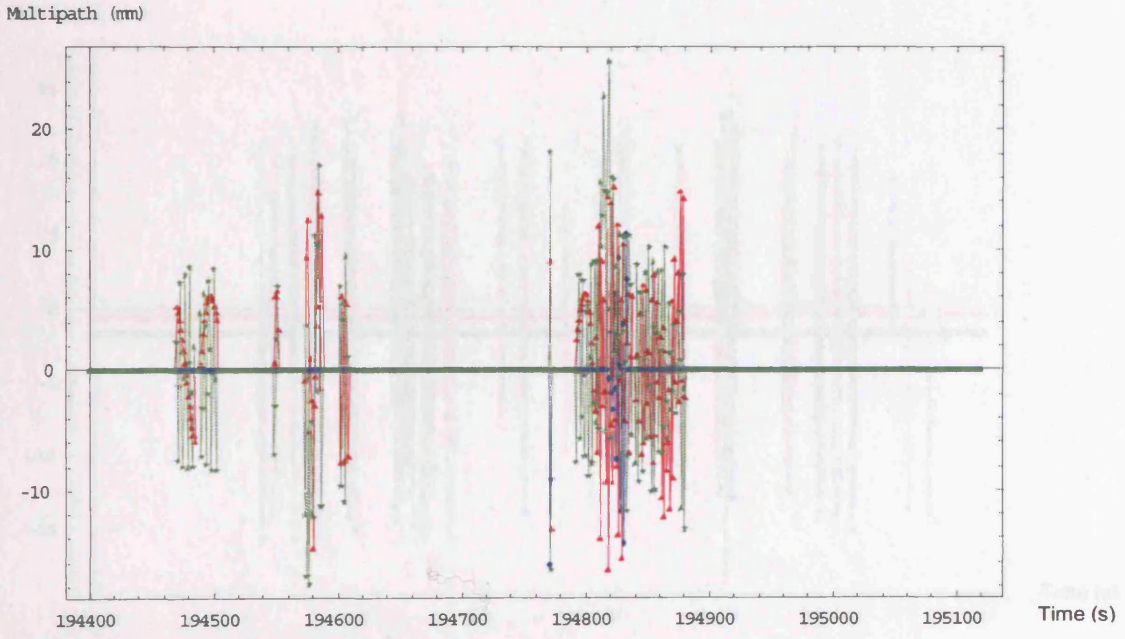

Figure E-14: Simulated GPS three-frequency (red: L1, blue: L2, green: L5) phase multipath error in PRN06 of the K-HK7-600 dataset.

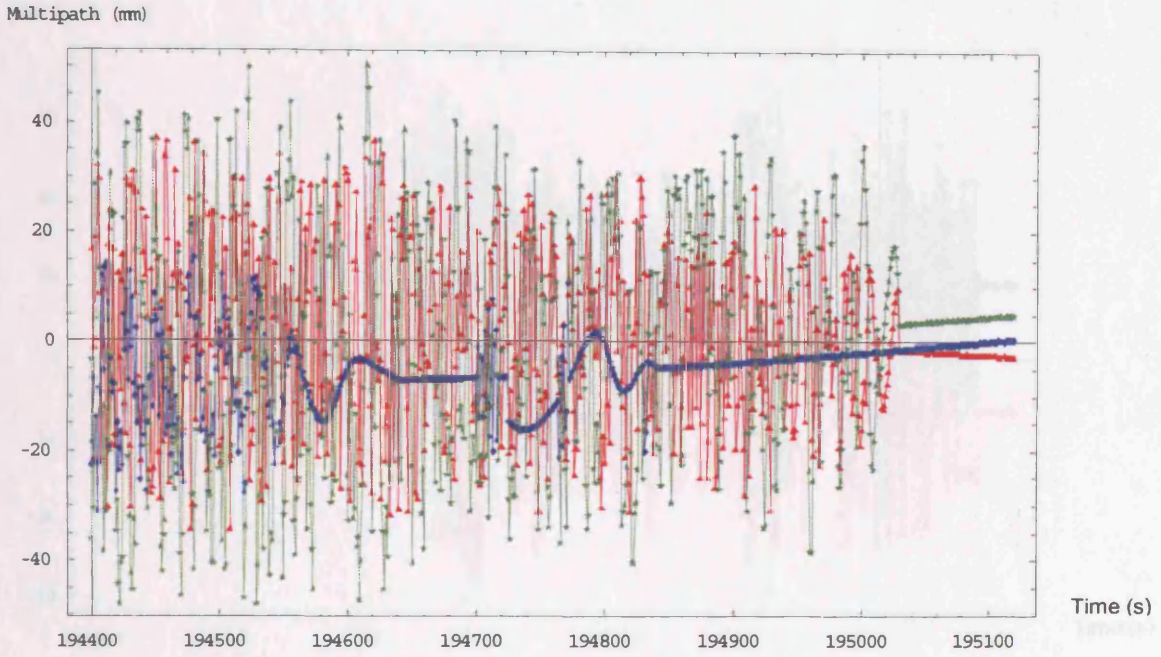

Figure E-15: Simulated GPS three-frequency (red: L1, blue: L2, green: L5) phase multipath error in PRN14 of the K-HK7-600 dataset.

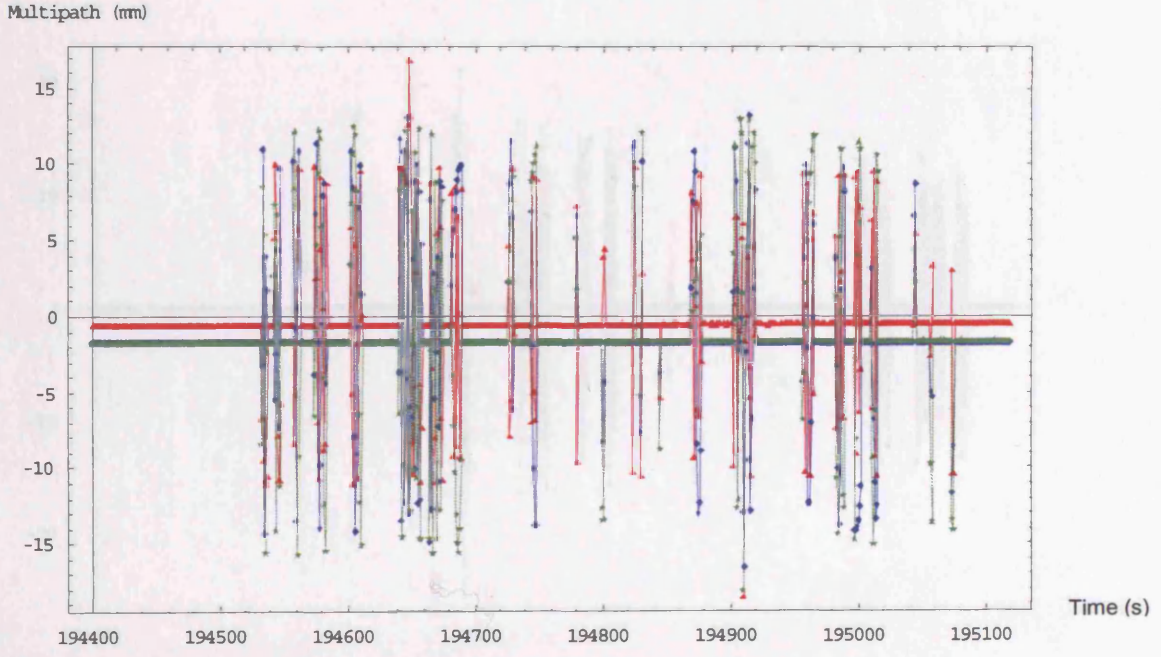

Figure E-16: Simulated GPS three-frequency (red: L1, blue: L2, green: L5) phase multipath error in PRN16 of the K-HK7-600 dataset.

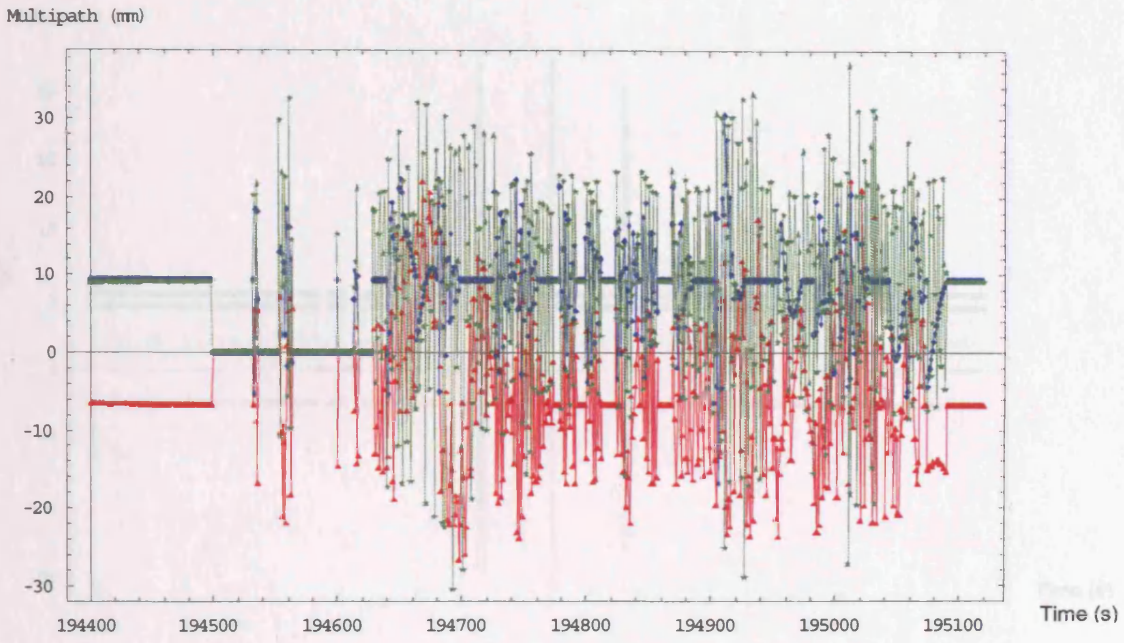

Figure E-17: Simulated GPS three-frequency (red: L1, blue: L2, green: L5) phase multipath error in PRN20 of the K-HK7-600 dataset.

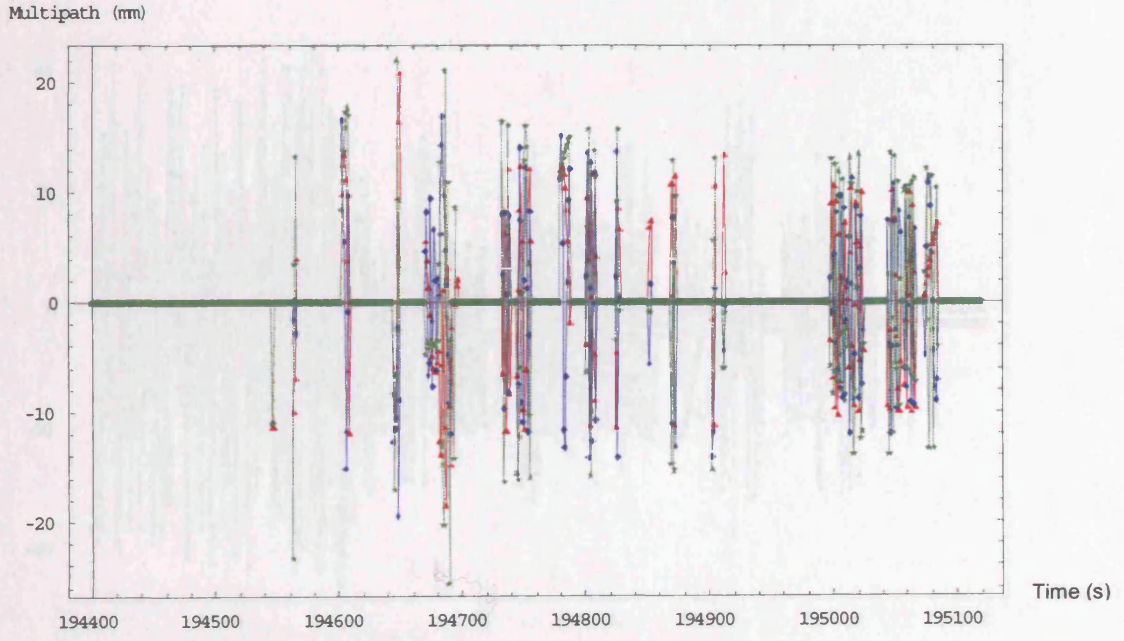

Figure E-18: Simulated GPS three-frequency (red: L1, blue: L2, green: L5) phase multipath error in PRN23 of the K-HK7-600 dataset.

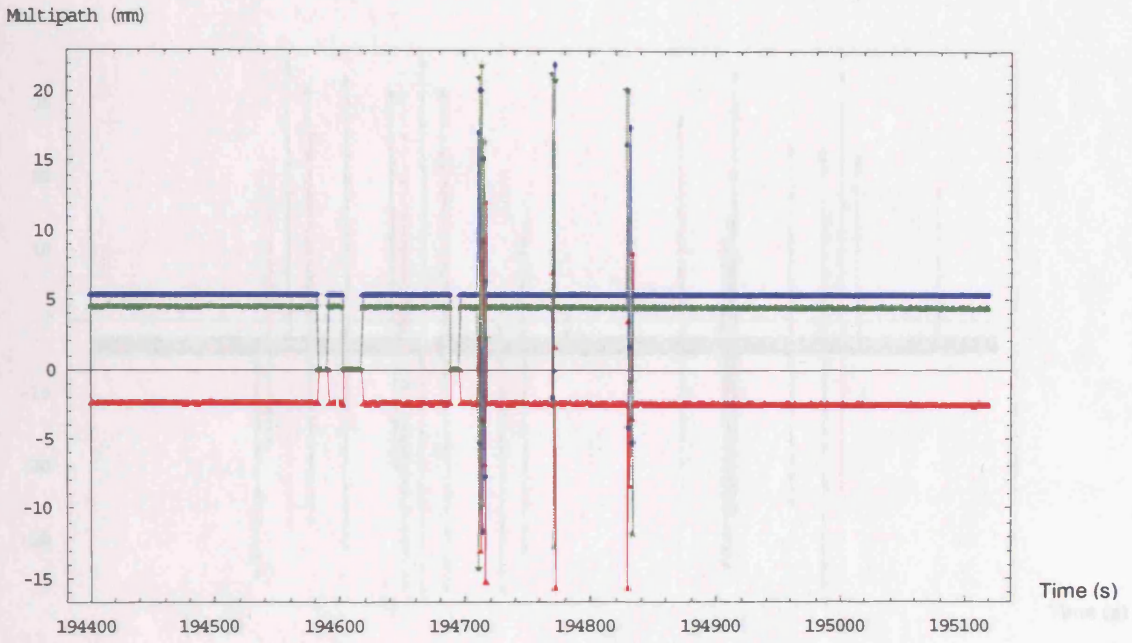

Figure E-19: Simulated GPS three-frequency (red: L1, blue: L2, green: L5) phase multipath error in PRN25 of the K-HK7-600 dataset.

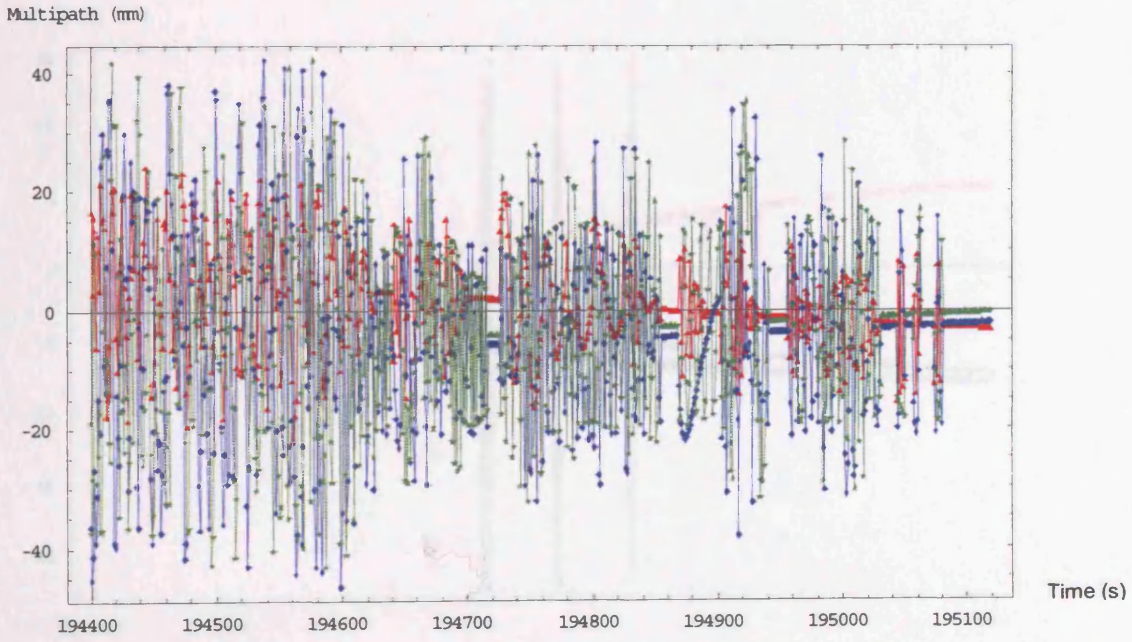

Figure E-20: Simulated Galileo three-frequency (red: L1, blue: E5a, green: E5b) phase multipath error in SV03 of the K-HK7-600 dataset.

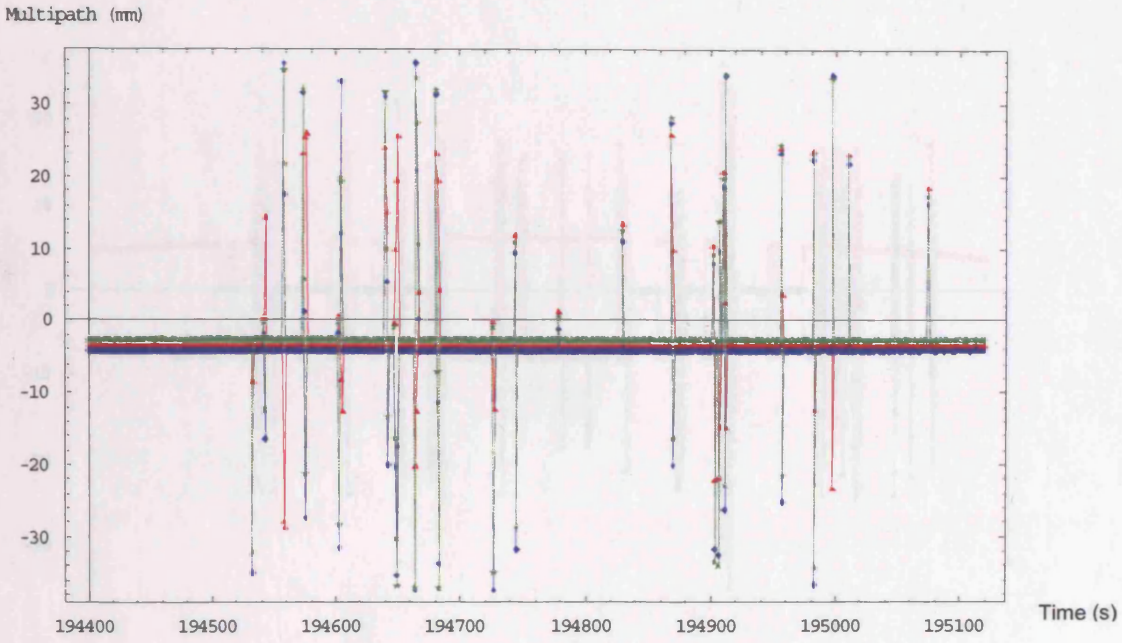

Figure E-21: Simulated Galileo three-frequency (red: L1, blue: E5a, green: E5b) phase multipath error in SV04 of the K-HK7-600 dataset.

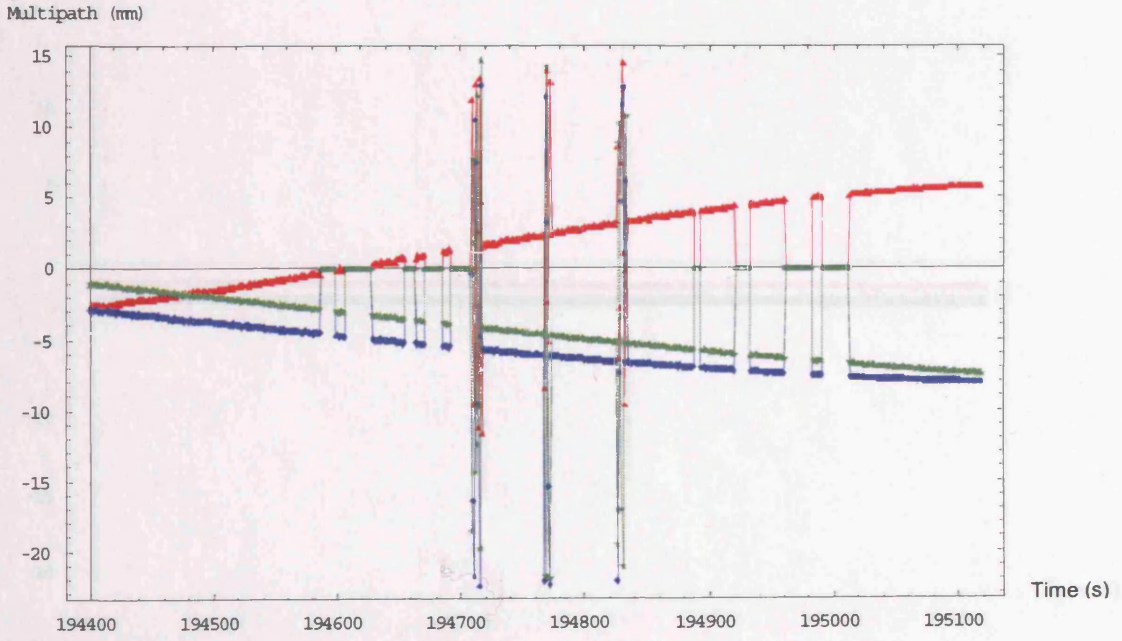

Figure E-22: Simulated Galileo three-frequency (red: L1, blue: E5a, green: E5b) phase multipath error in SV05 of the K-HK7-600 dataset.

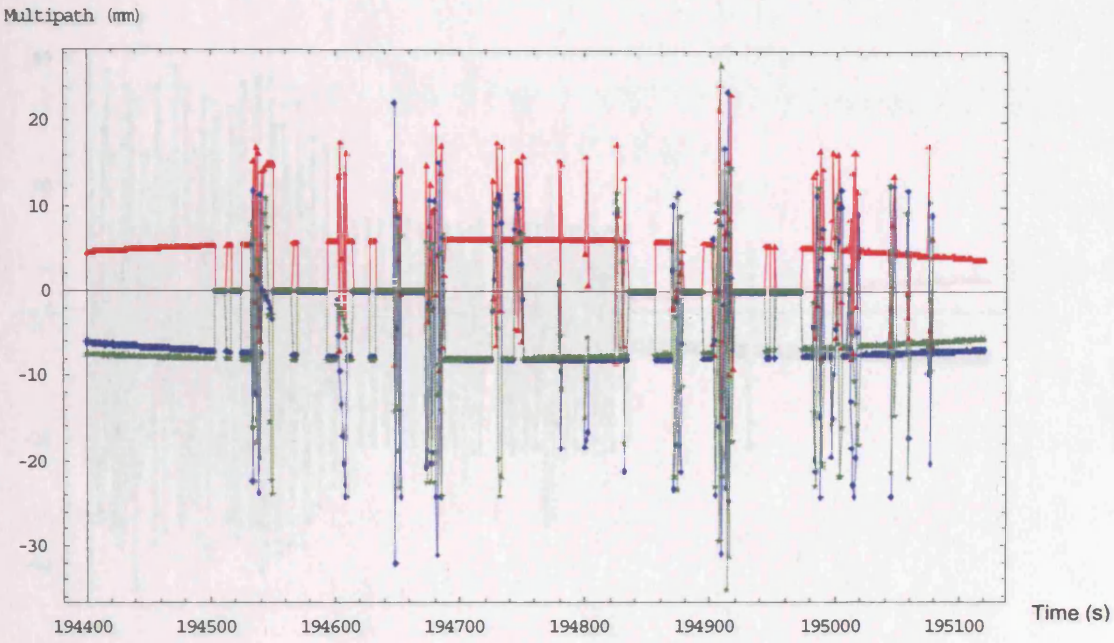

Figure E-23: Simulated Galileo three-frequency (red: L1, blue: E5a, green: E5b) phase multipath error in SV23 of the K-HK7-600 dataset.

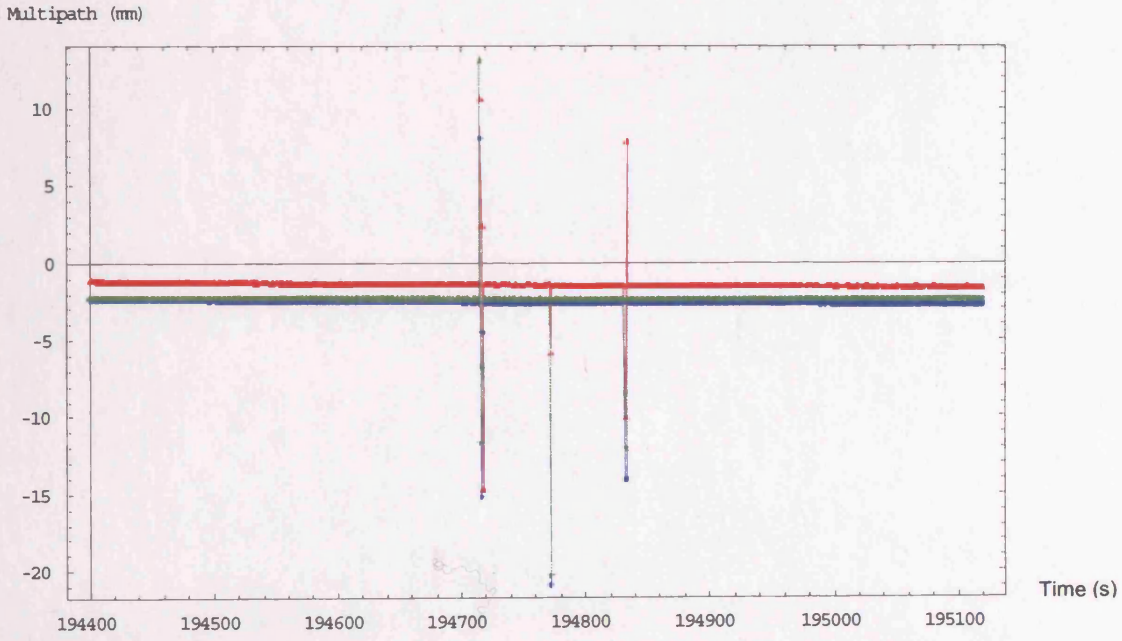

Figure E-24: Simulated Galileo three-frequency (red: L1, blue: E5a, green: E5b) phase multipath error in SV24 of the K-HK7-600 dataset.

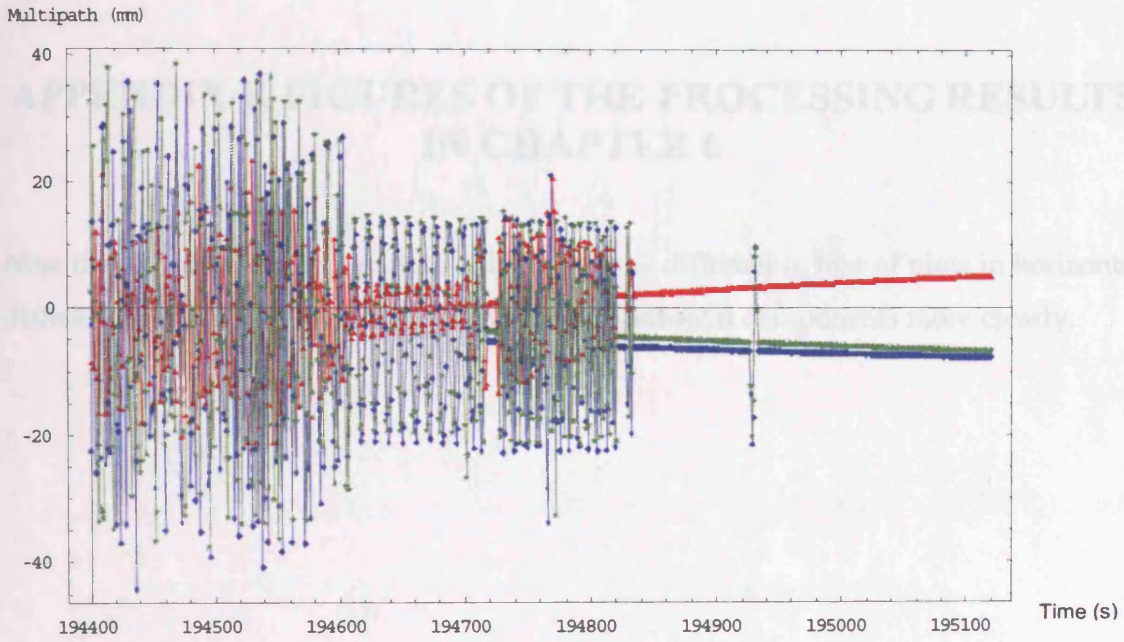

Figure E-25: Simulated Galileo three-frequency (red: L1, blue: E5a, green: E5b) phase multipath error in SV25 of the K-HK7-600 dataset.

APPENDIX F. FIGURES OF THE PROCESSING RESULTS IN CHAPTER 6

Note that the scale of plots in height differences is different to that of plots in horizontal differences in order to show the differences in horizontal components more clearly.

See next page

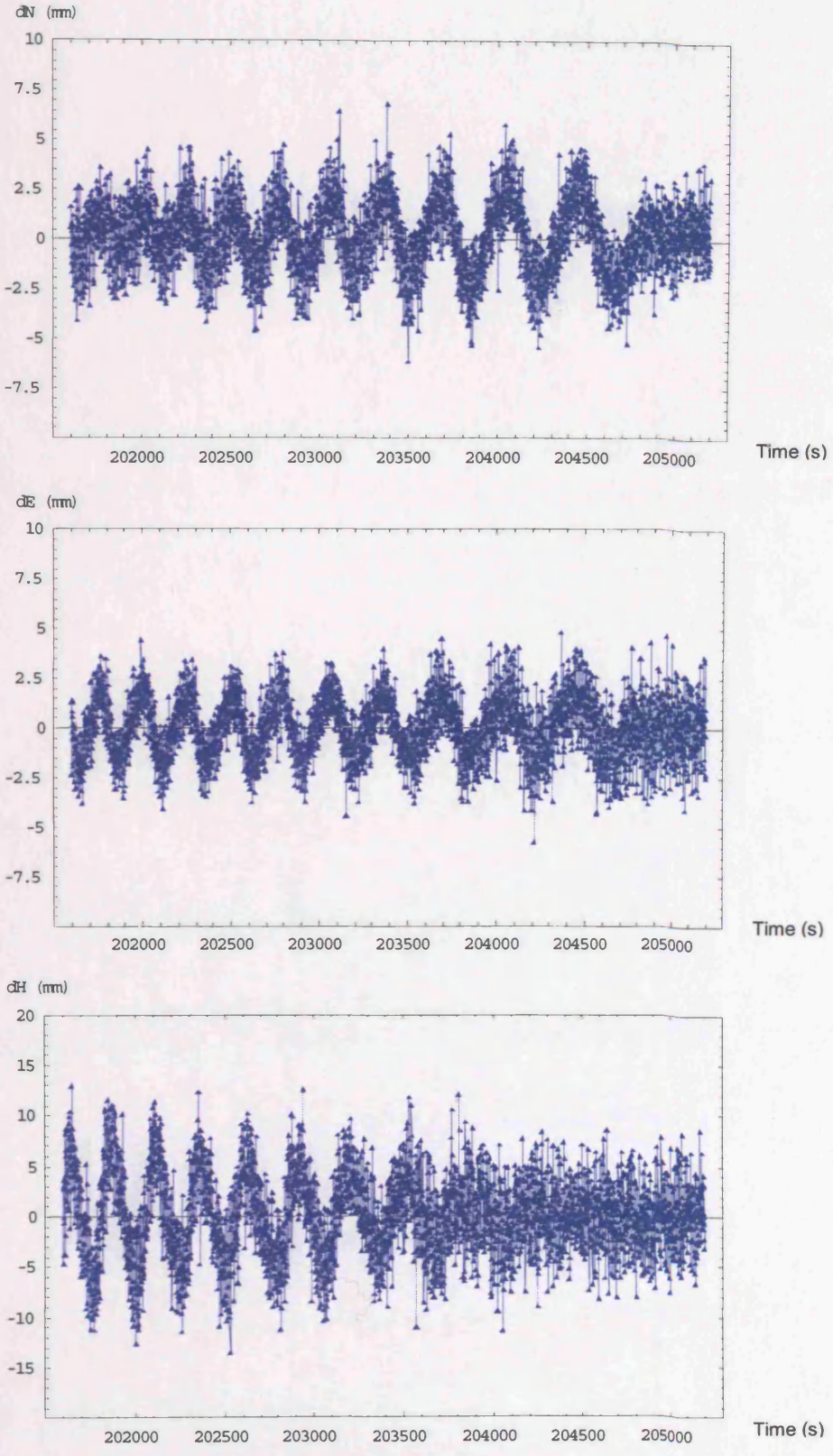

Figure F-1: Positioning error in northing (top), easting (middle), and vertical (bottom) of single-epoch solution using GPS single-frequency data in the LCPC-20 dataset.

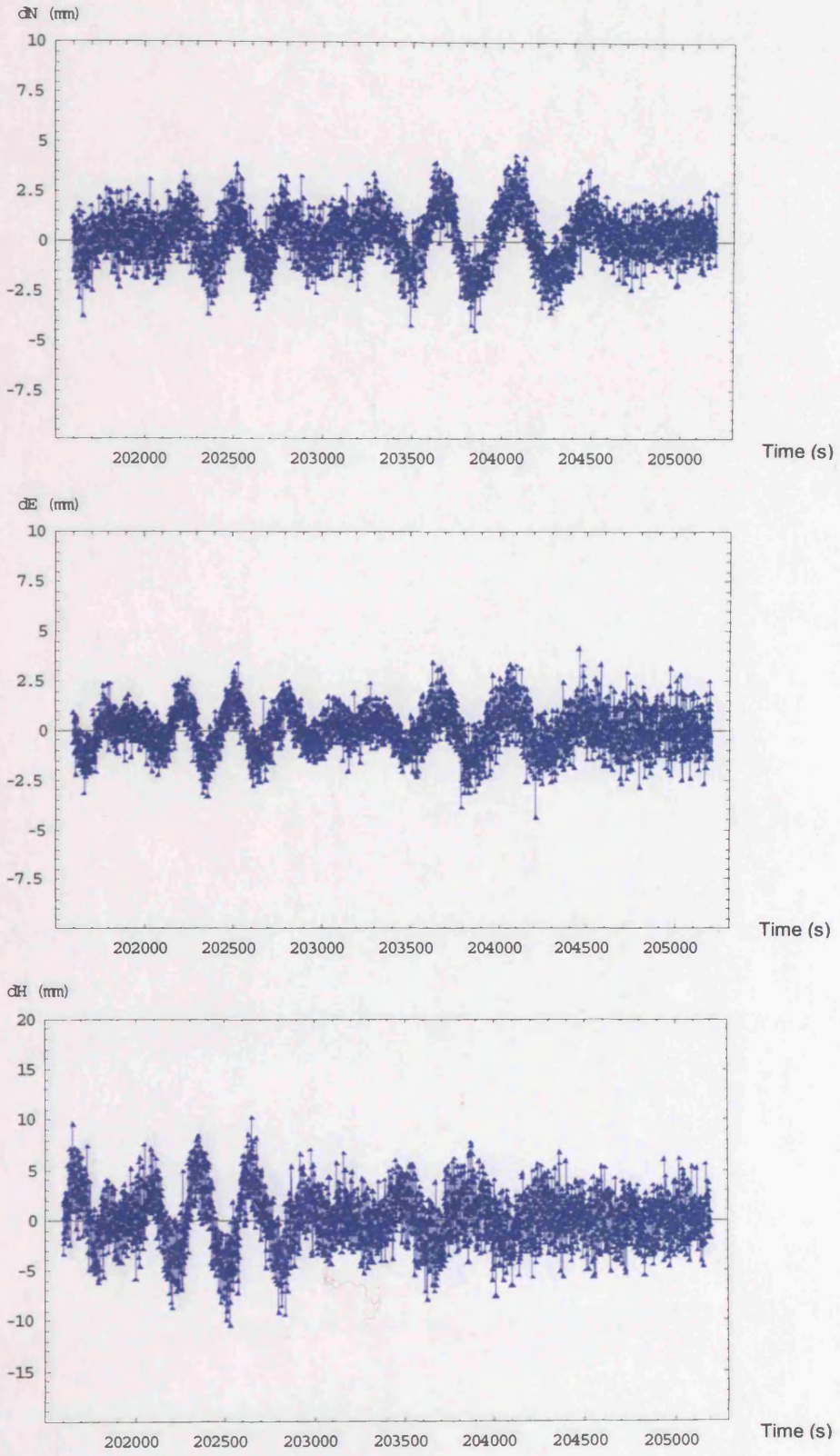

Figure F-2: Positioning error in northing (top), easting (middle), and vertical (bottom) of single-epoch solution using GPS dual-frequency data in the LCPC-20 dataset.

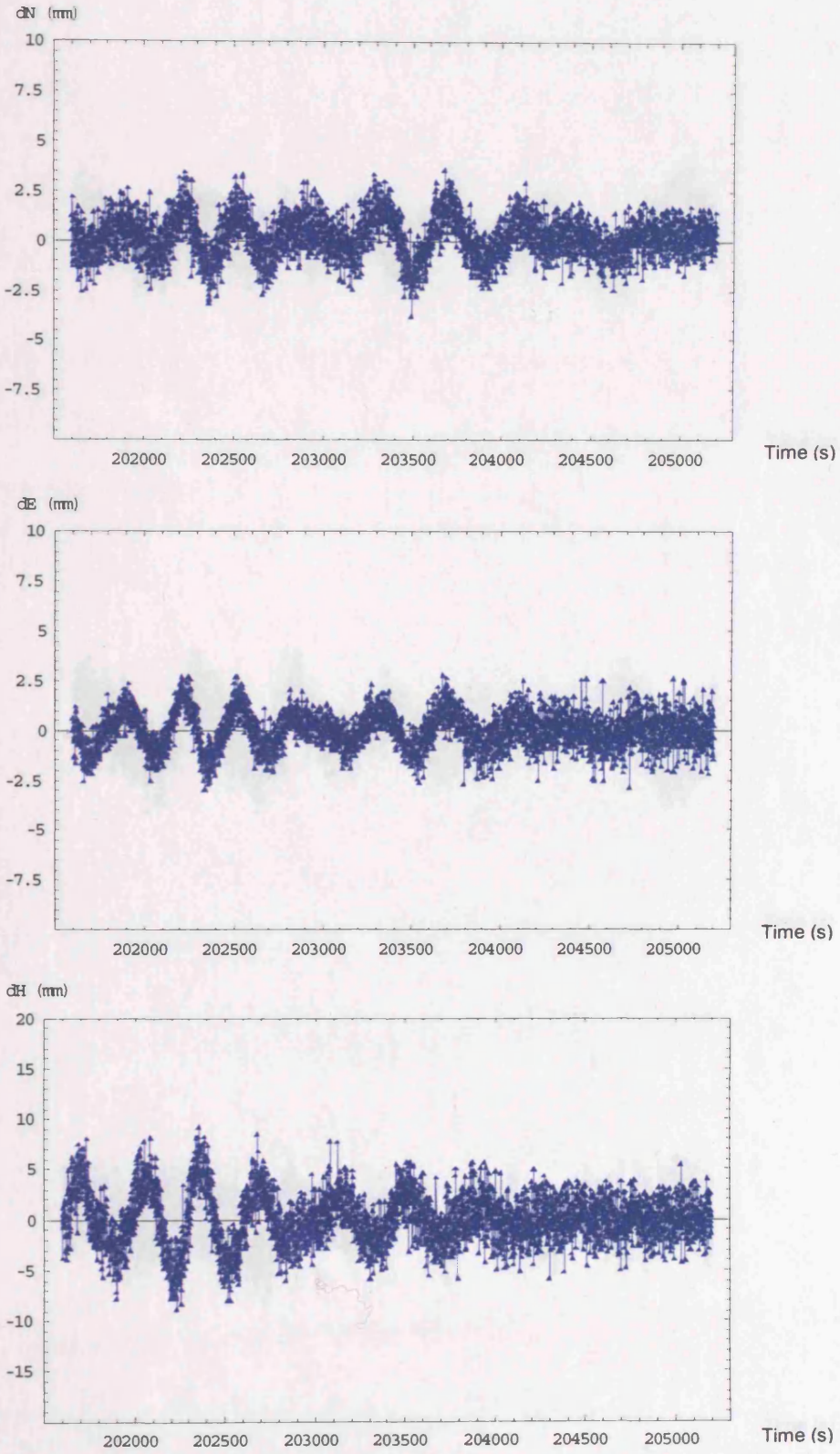

Figure F-3: Positioning error in northing (top), easting (middle), and vertical (bottom) of single-epoch solution using GPS three-frequency data in the LCPC-20 dataset.

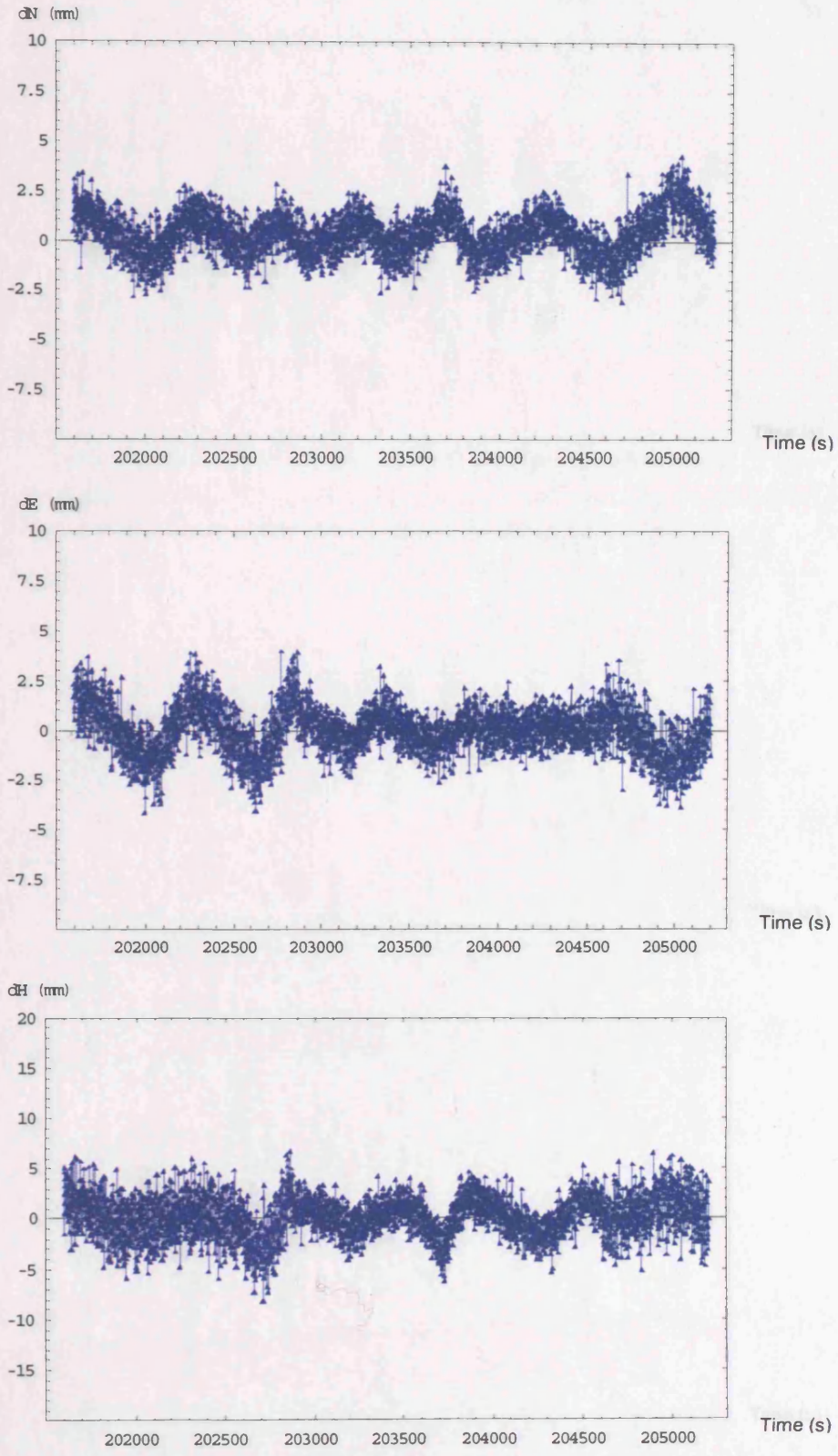

Figure F-4: Positioning error in northing (top), easting (middle), and vertical (bottom) of single-epoch solution using Galileo three-frequency data in the LCPC-20 dataset.

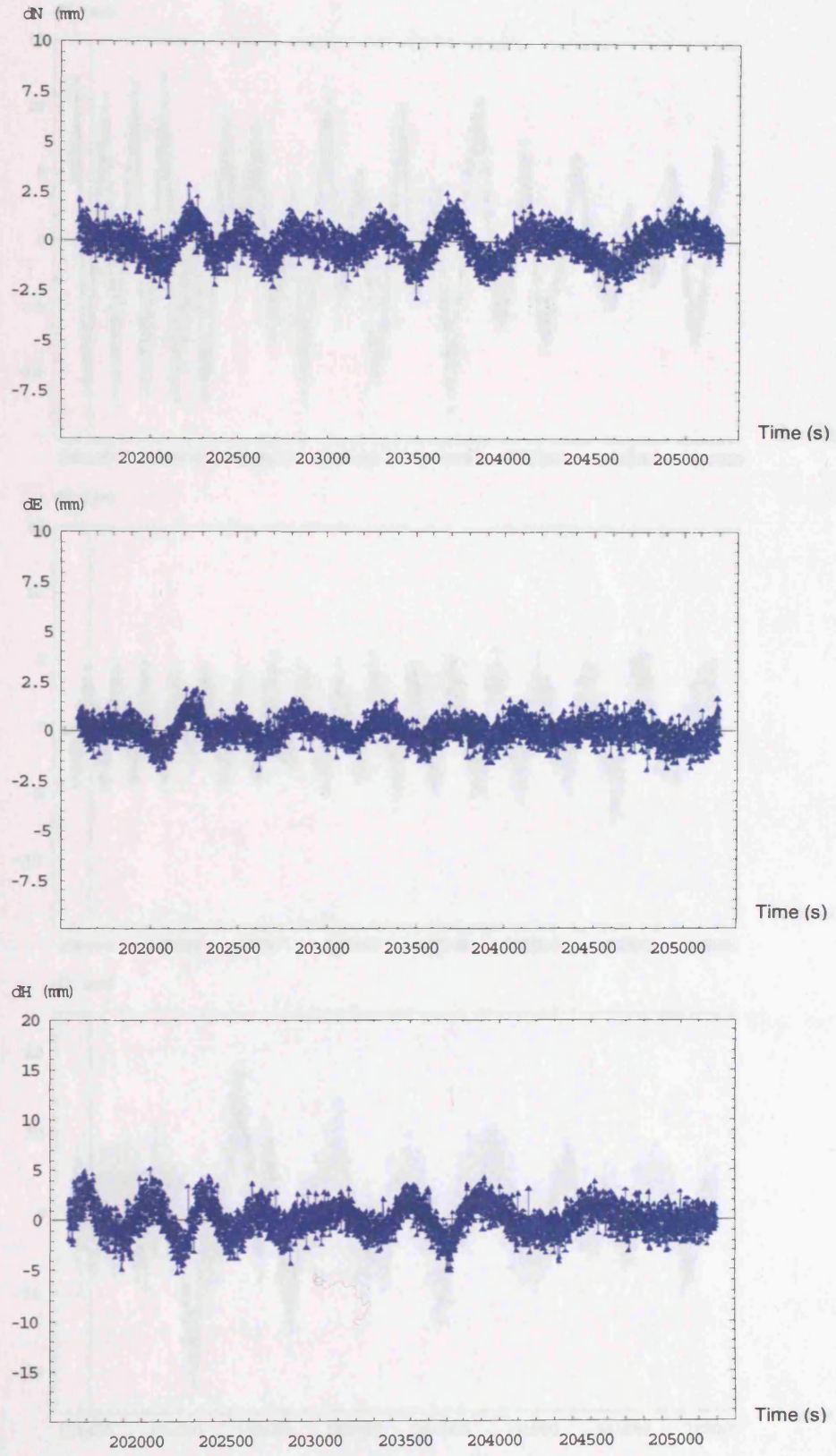

Figure F-5: Positioning error in northing (top), easting (middle), and vertical (bottom) of single-epoch solution using Galileo + GPS multiple-frequency data in the LCPC-20 dataset.

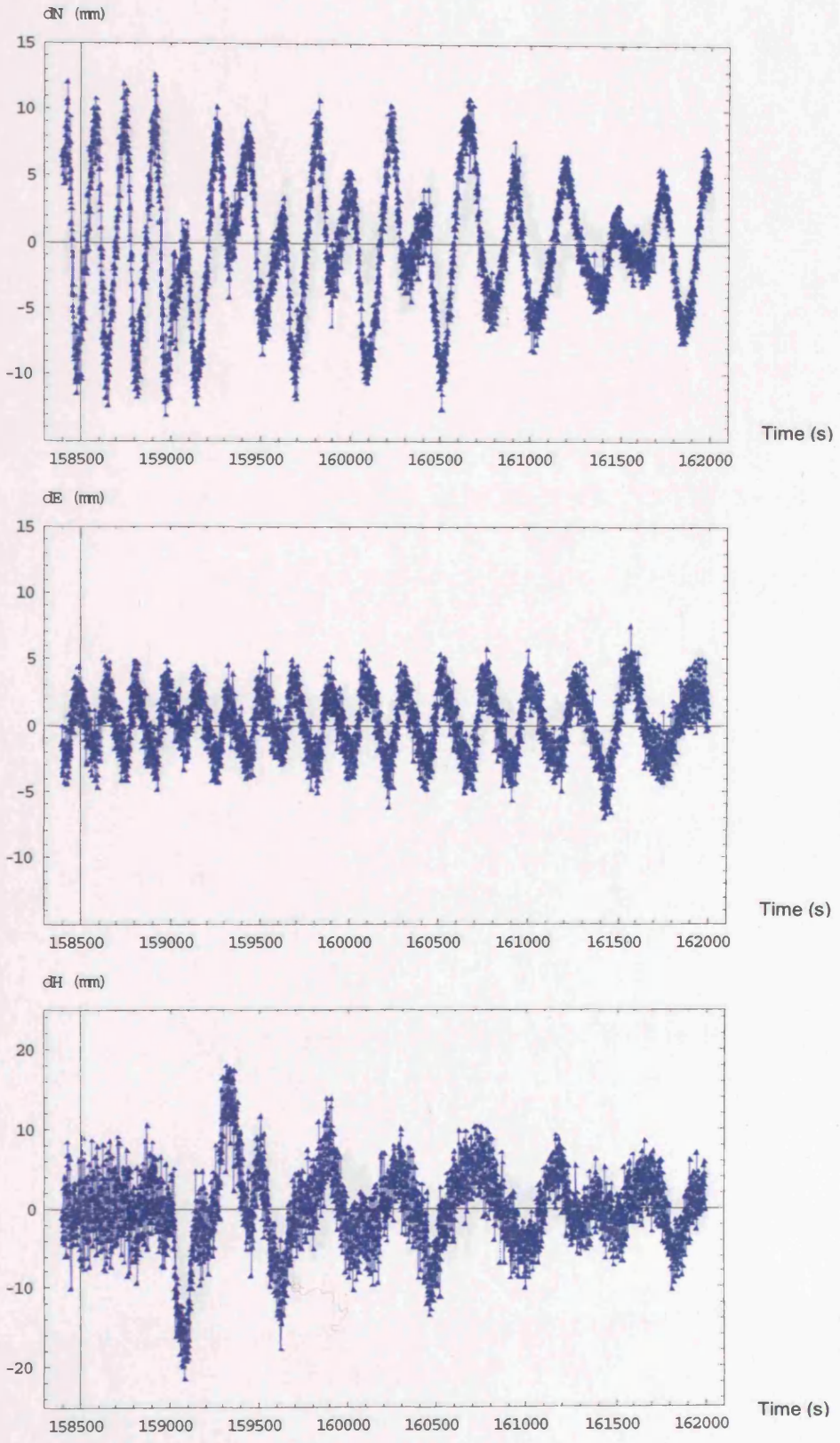

Figure F-6: Positioning error in northing (top), easting (middle), and vertical (bottom) of single-epoch solution using GPS single-frequency data in the LBCH-7 dataset.

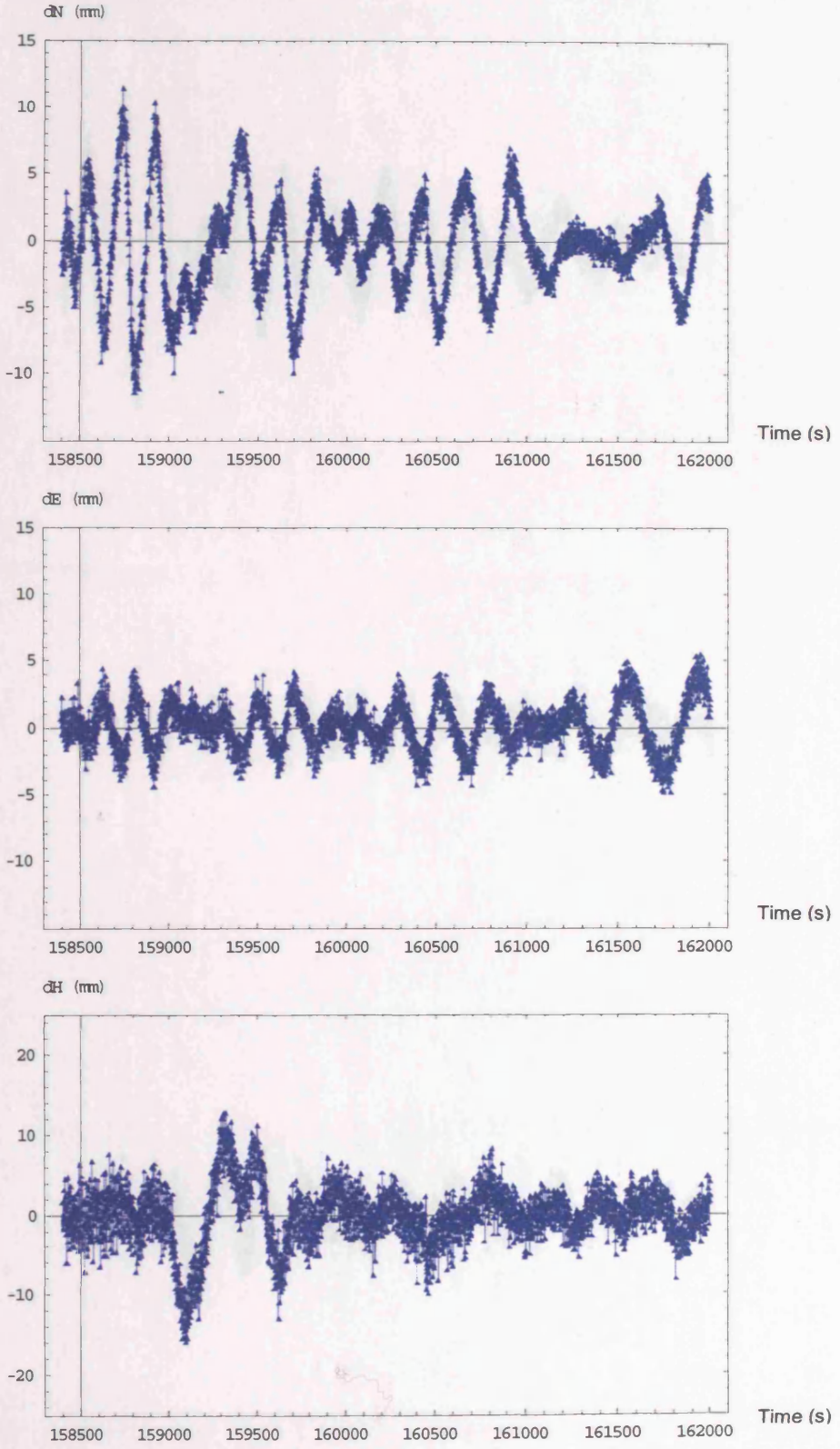

Figure F-7: Positioning error in northing (top), easting (middle), and vertical (bottom) of single-epoch solution using GPS dual-frequency data in the LBCH-7 dataset.

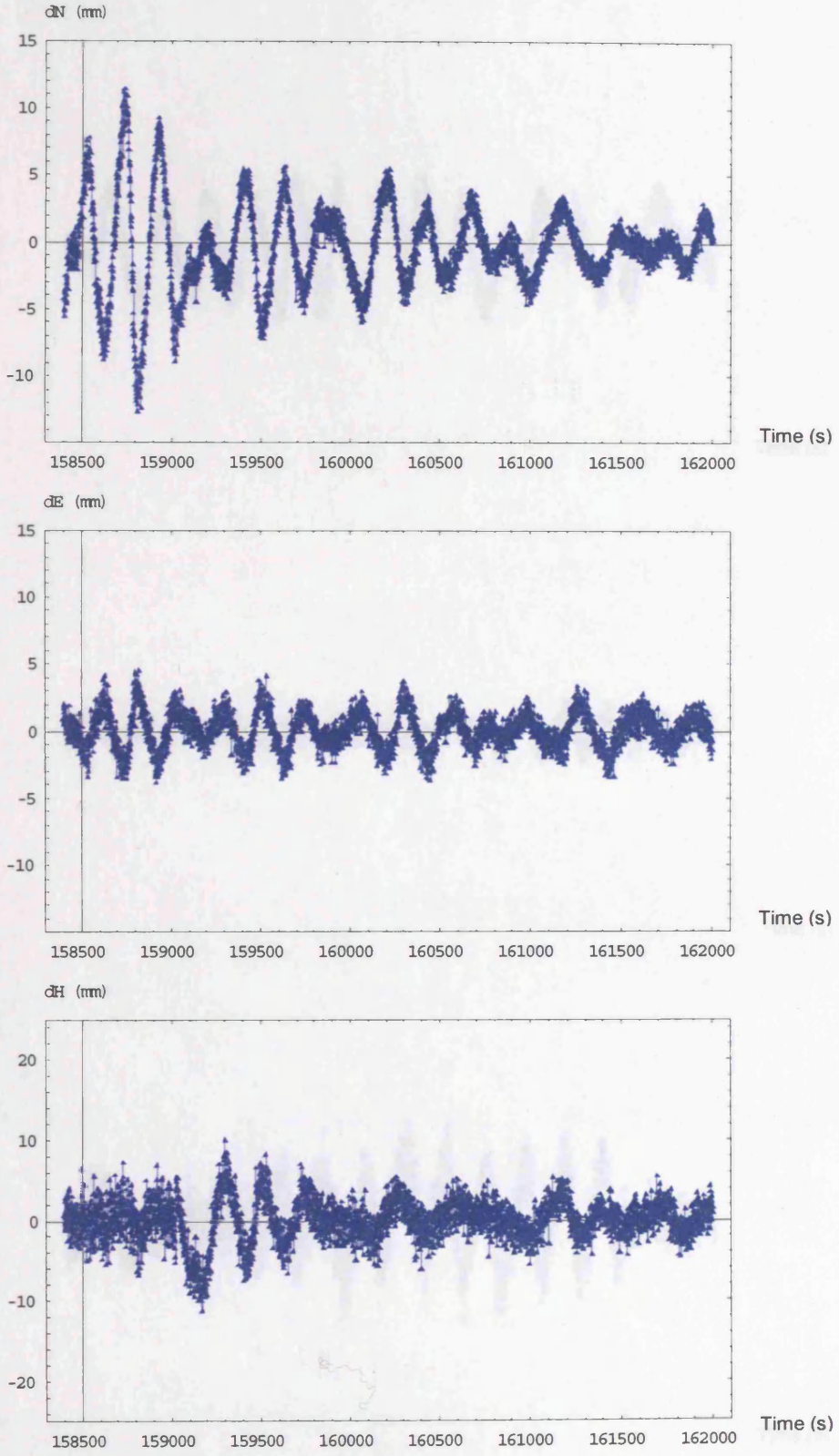

Figure F-8: Positioning error in northing (top), easting (middle), and vertical (bottom) of single-epoch solution using GPS three-frequency data in the LBCH-7 dataset.

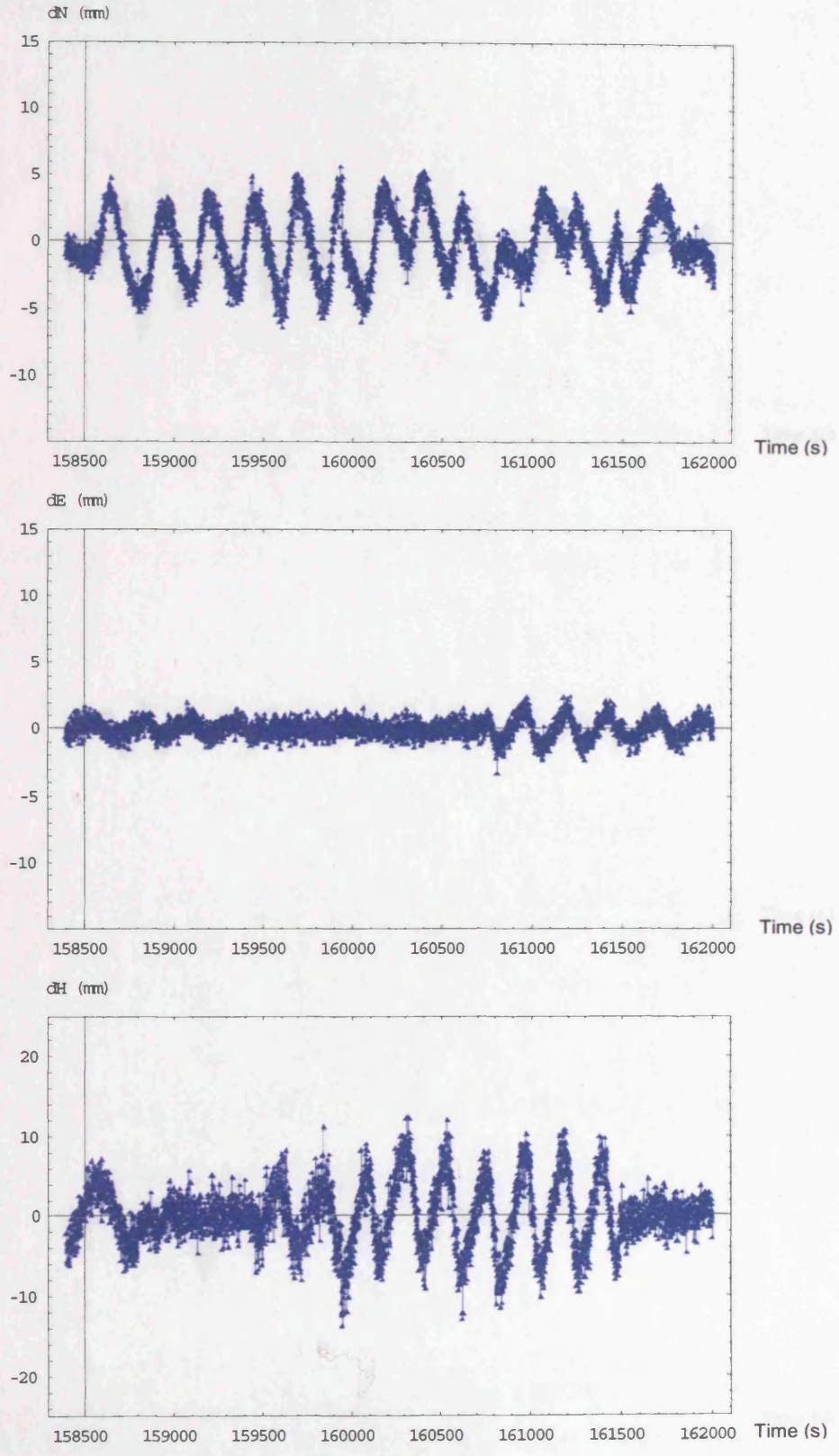

Figure F-9: Positioning error in northing (top), easting (middle), and vertical (bottom) of single-epoch solution using Galileo three-frequency data in the LBCH-7 dataset.

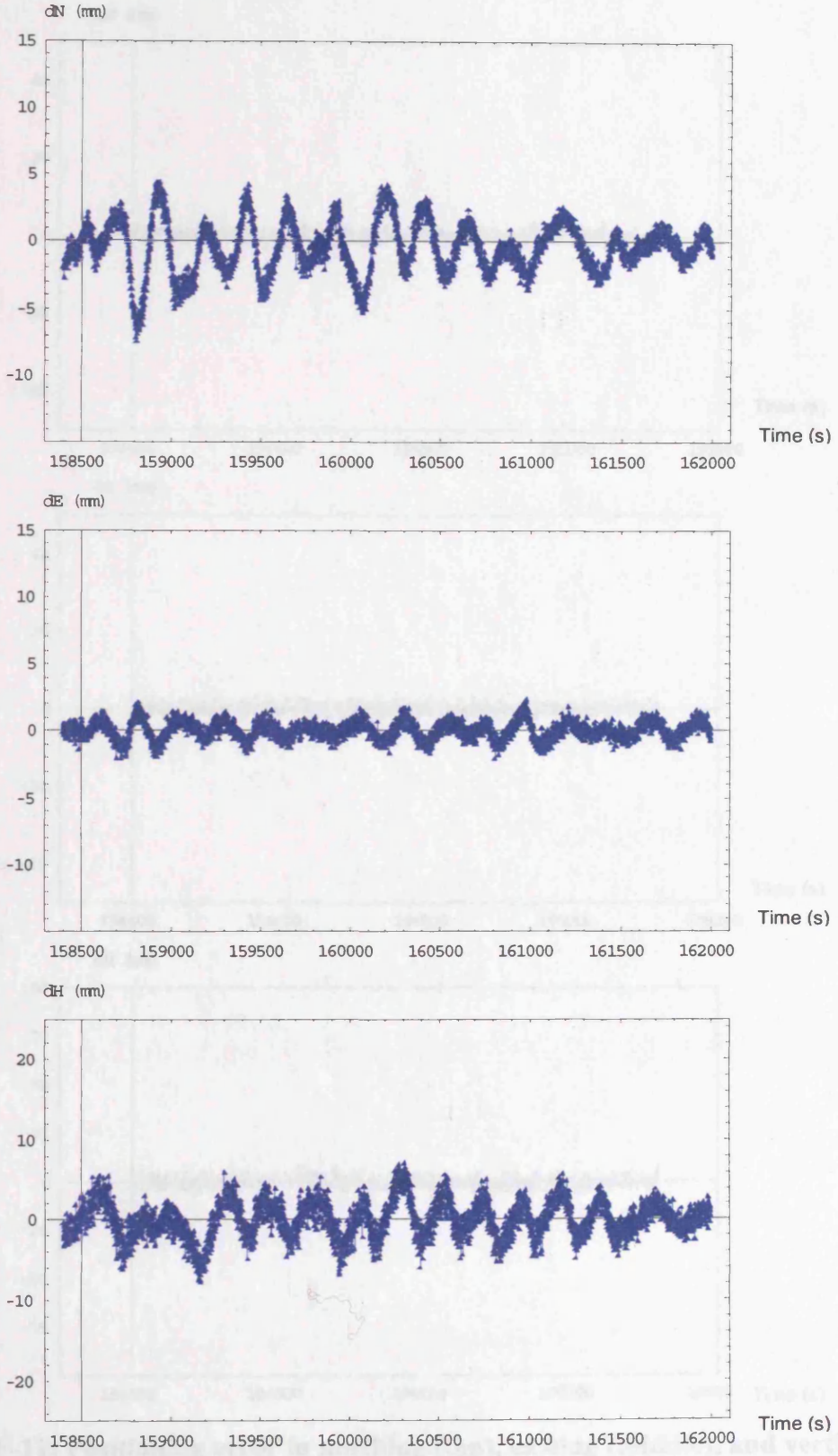

Figure F-10: Positioning error in northing (top), easting (middle), and vertical (bottom) of single-epoch solution using Galileo + GPS multiple-frequency data in the LBCH-7 dataset.

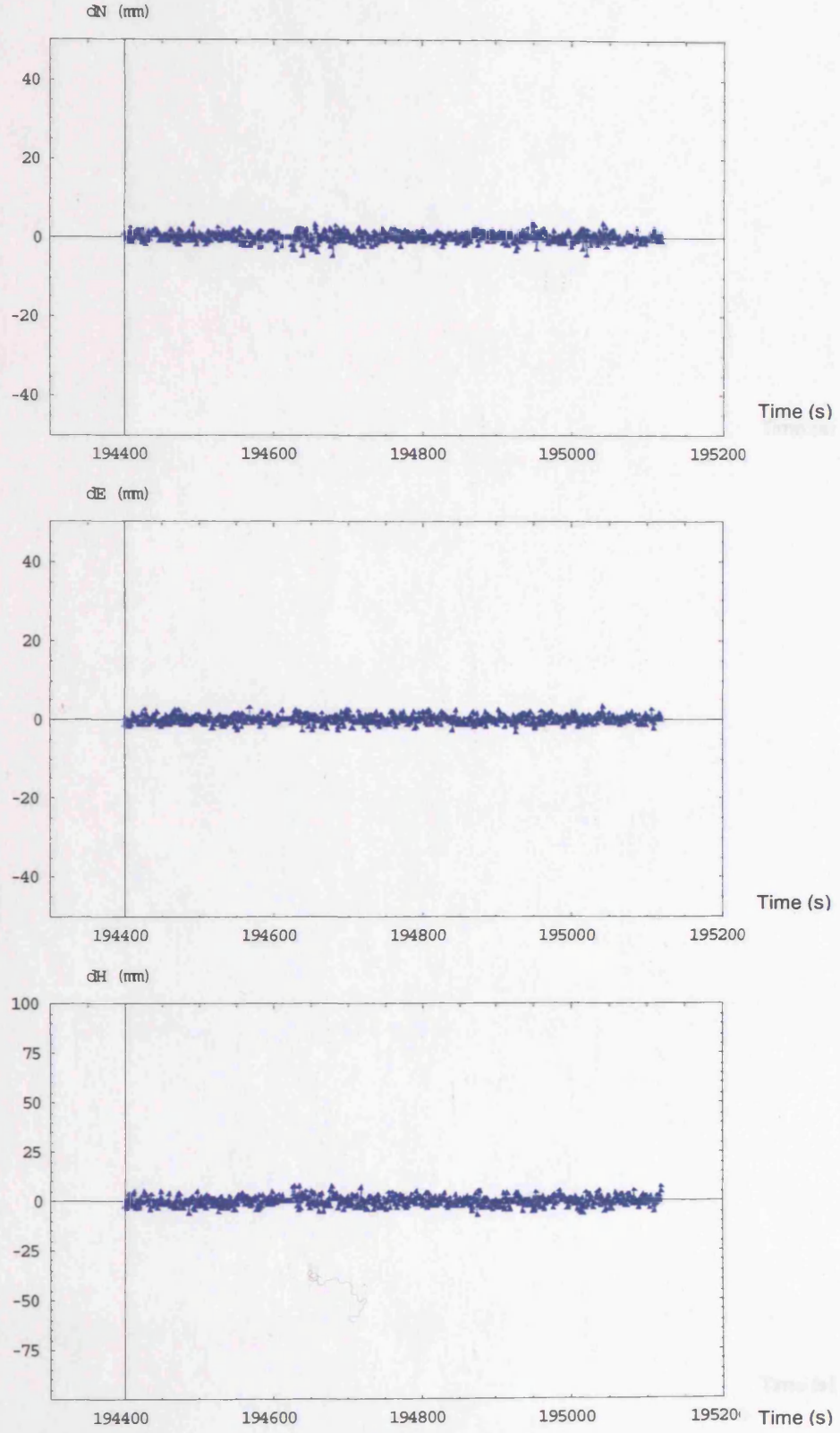

Figure F-11: Positioning error in northing (top), easting (middle), and vertical (bottom) of single-epoch solution using GPS single-frequency data in the K-HK7-600 dataset.

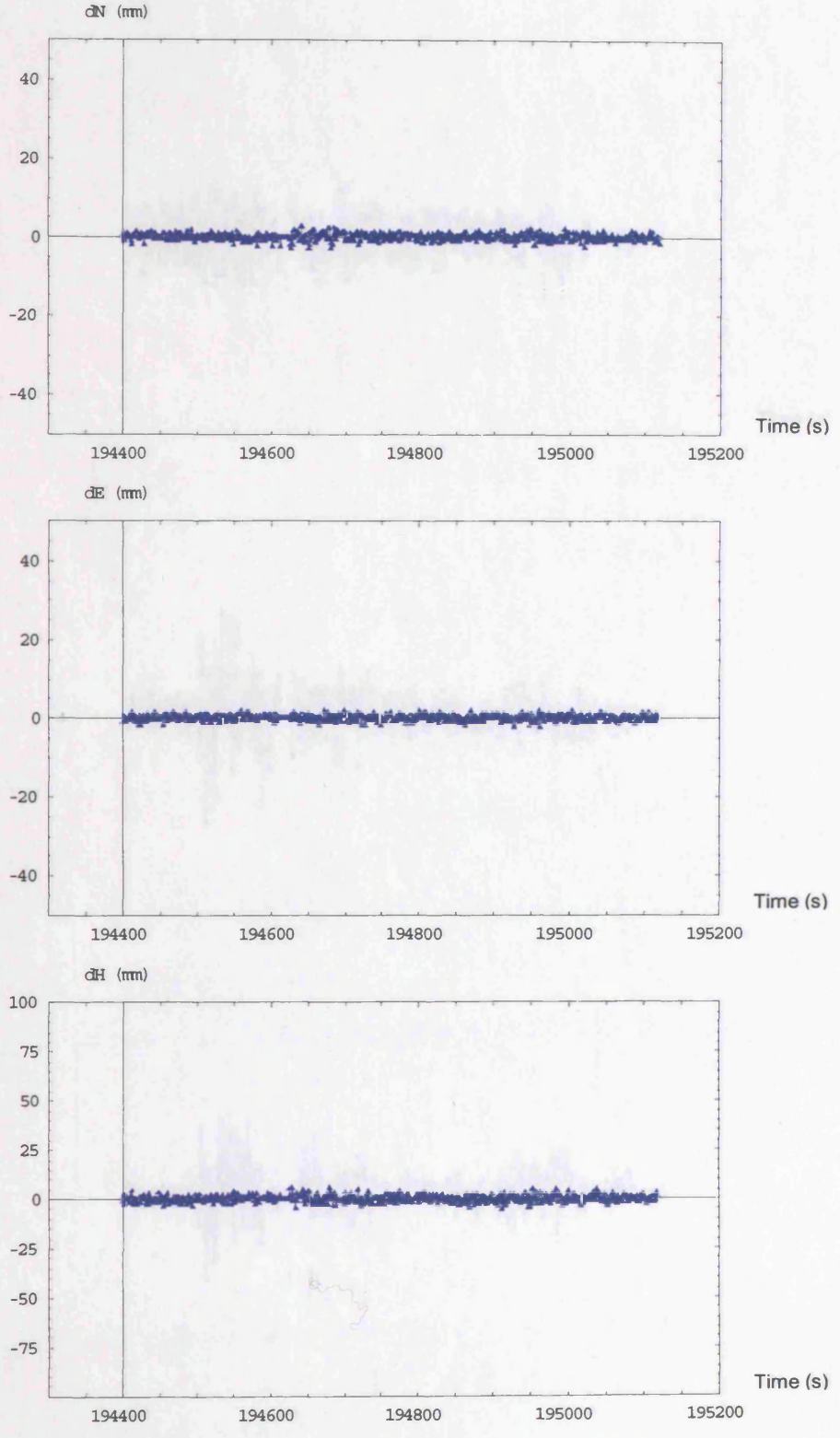

Figure F-12: Positioning error in northing (top), easting (middle), and vertical (bottom) of single-epoch solution using GPS dual-frequency data in the K-HK7-600 dataset.

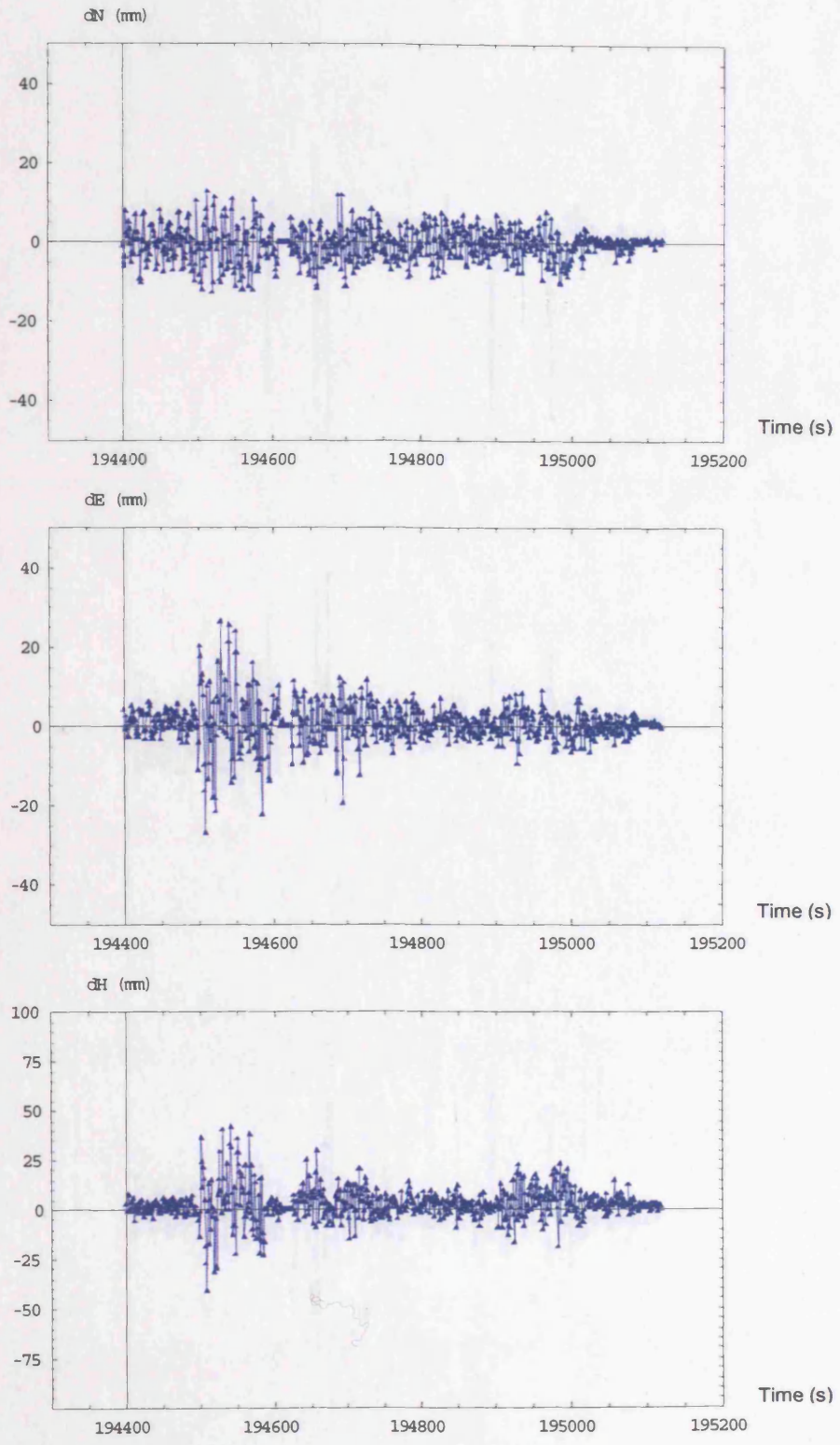

Figure F-13: Fig.15. Positioning error in northing (top), easting (middle), and vertical (bottom) of single-epoch solution using GPS three-frequency data in the K-HK7-600 dataset.

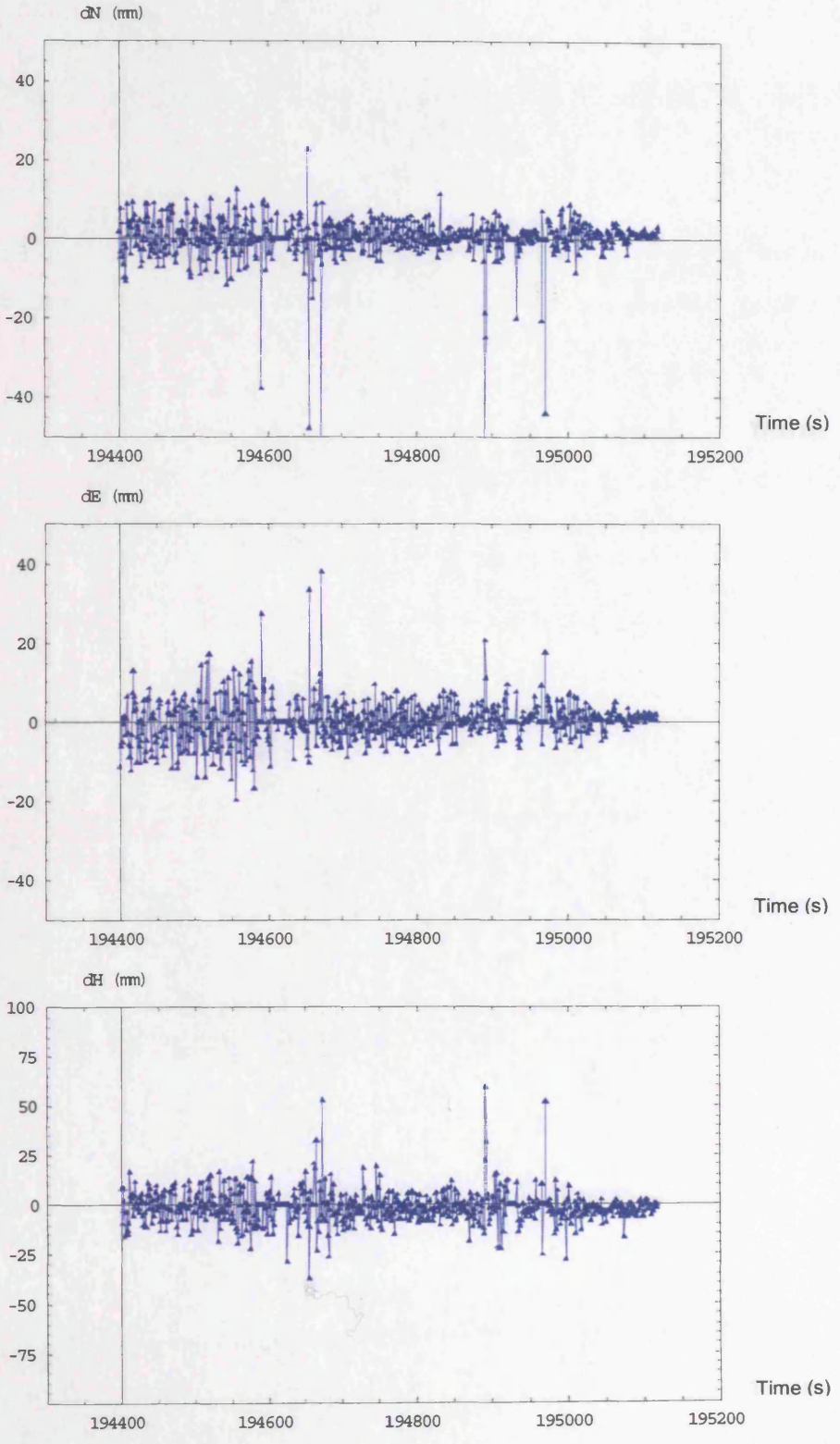

Figure F-14: Positioning error in northing (top), easting (middle), and vertical (bottom) of single-epoch solution using Galileo three-frequency data in the K-HK7-600 dataset.

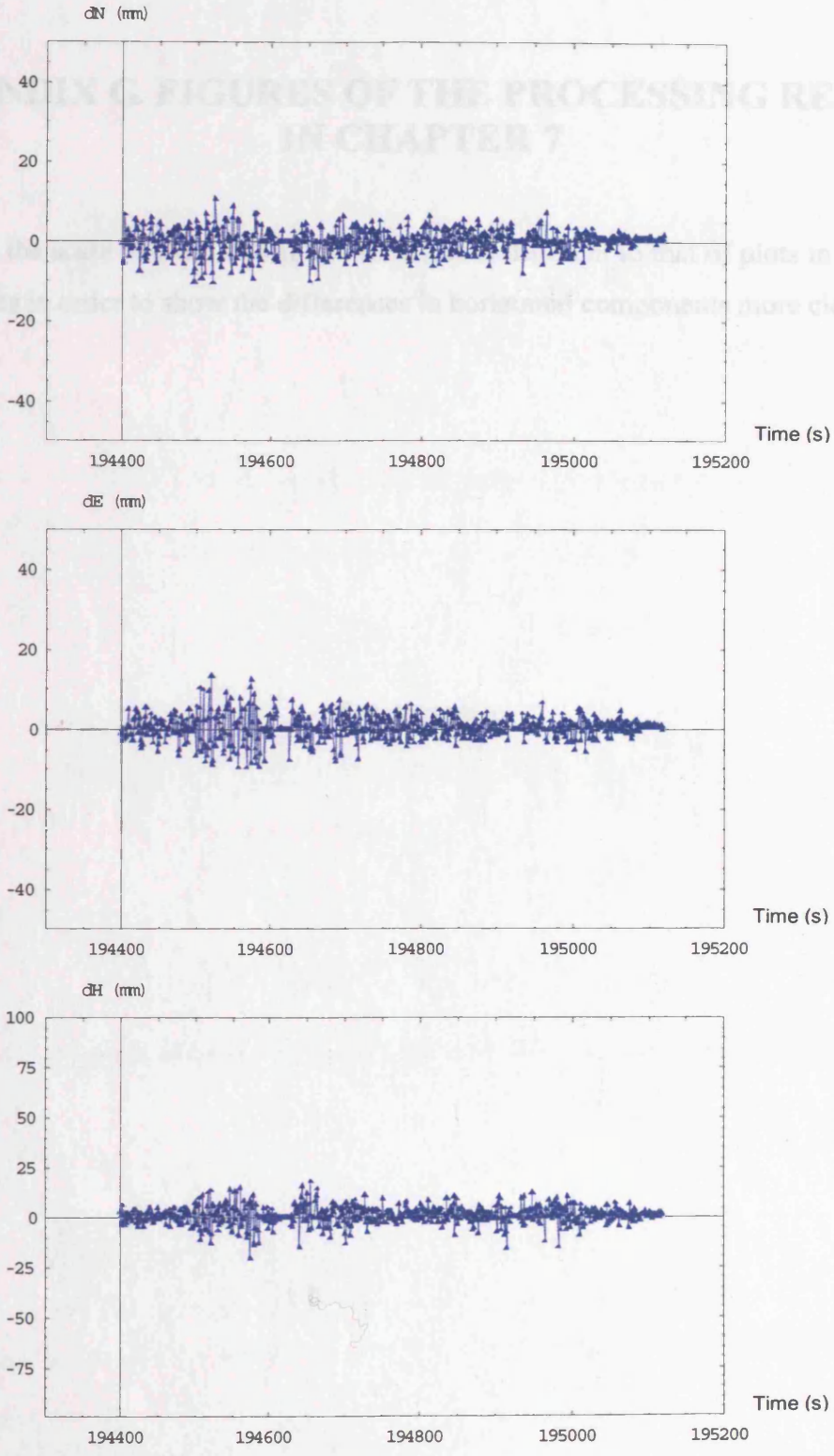

Figure F-15: Positioning error in northing (top), easting (middle), and vertical (bottom) of single-epoch solution using Galileo + GPS multiple-frequency data in the K-HK7-600 dataset.

APPENDIX G. FIGURES OF THE PROCESSING RESULTS IN CHAPTER 7

Note that the scale of plots in height differences is different to that of plots in horizontal differences in order to show the differences in horizontal components more clearly.

See next page

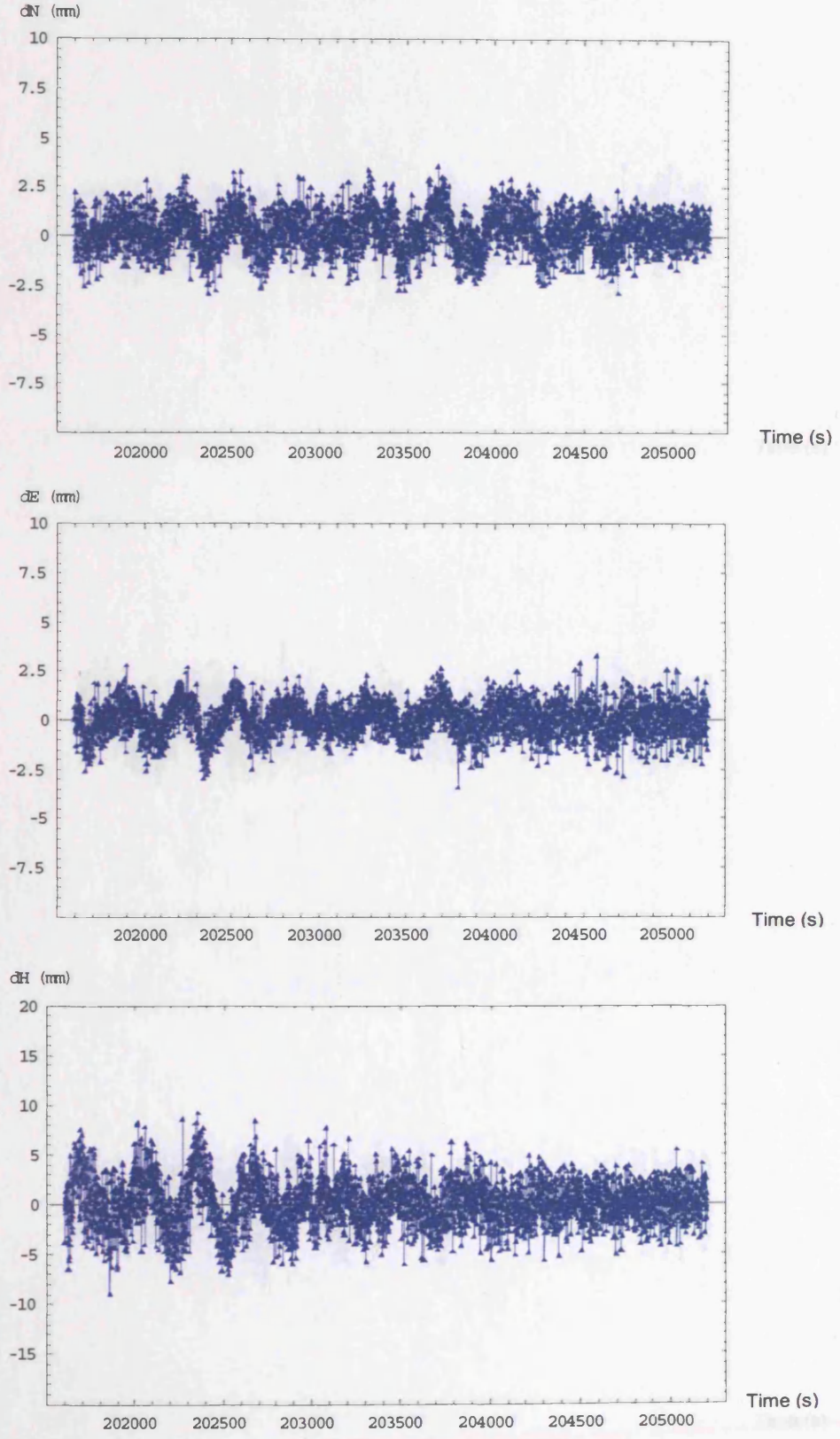

Figure G-1: Positioning error in northing (top), easting (middle), and vertical (bottom) of single-epoch solution with MOD using GPS three-frequency data in the LCPC-20 dataset.

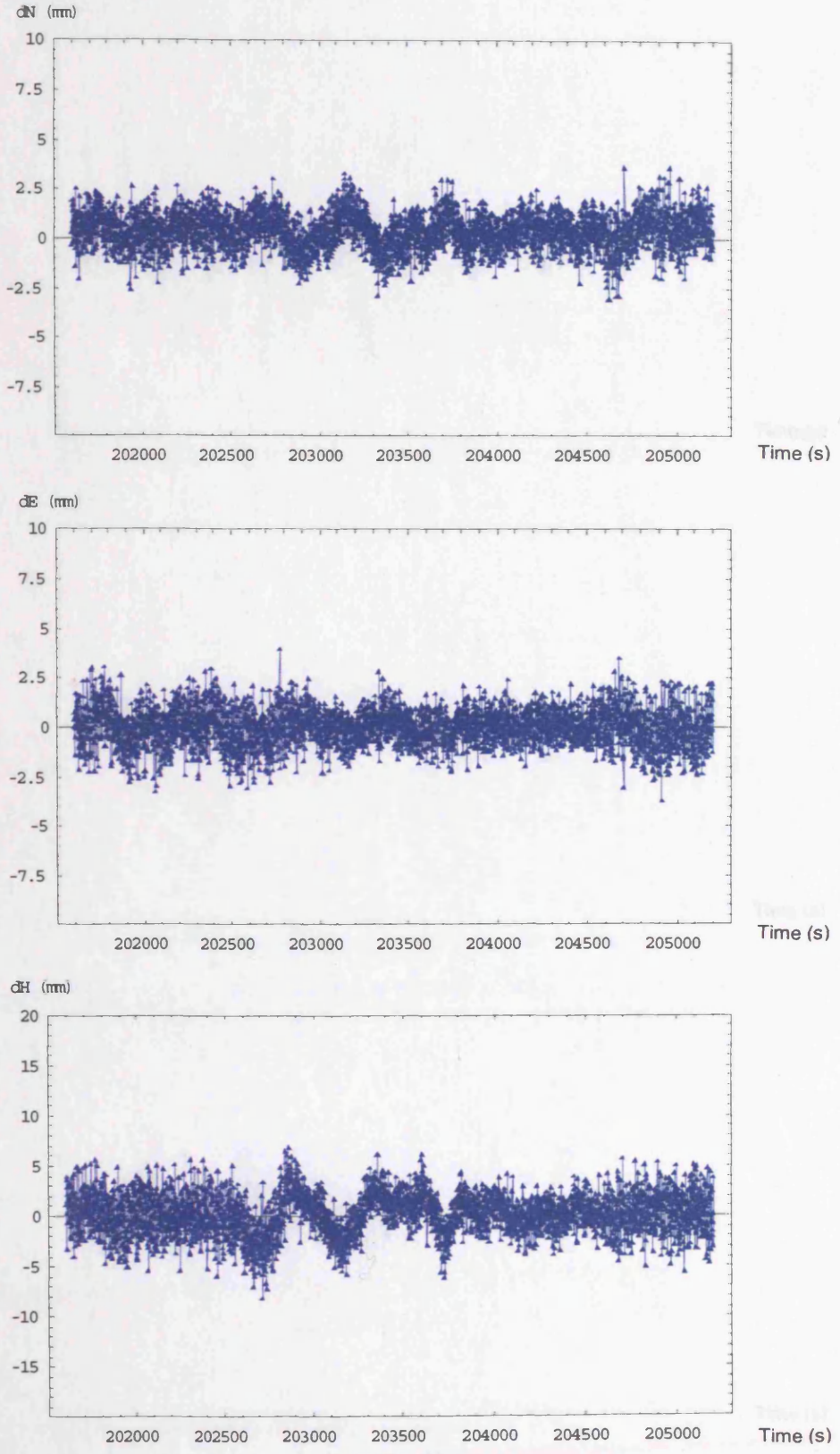

Figure G-2: Positioning error in northing (top), easting (middle), and vertical (bottom) of single-epoch solution with MOD using Galileo three-frequency data in the LCPC-20 dataset.

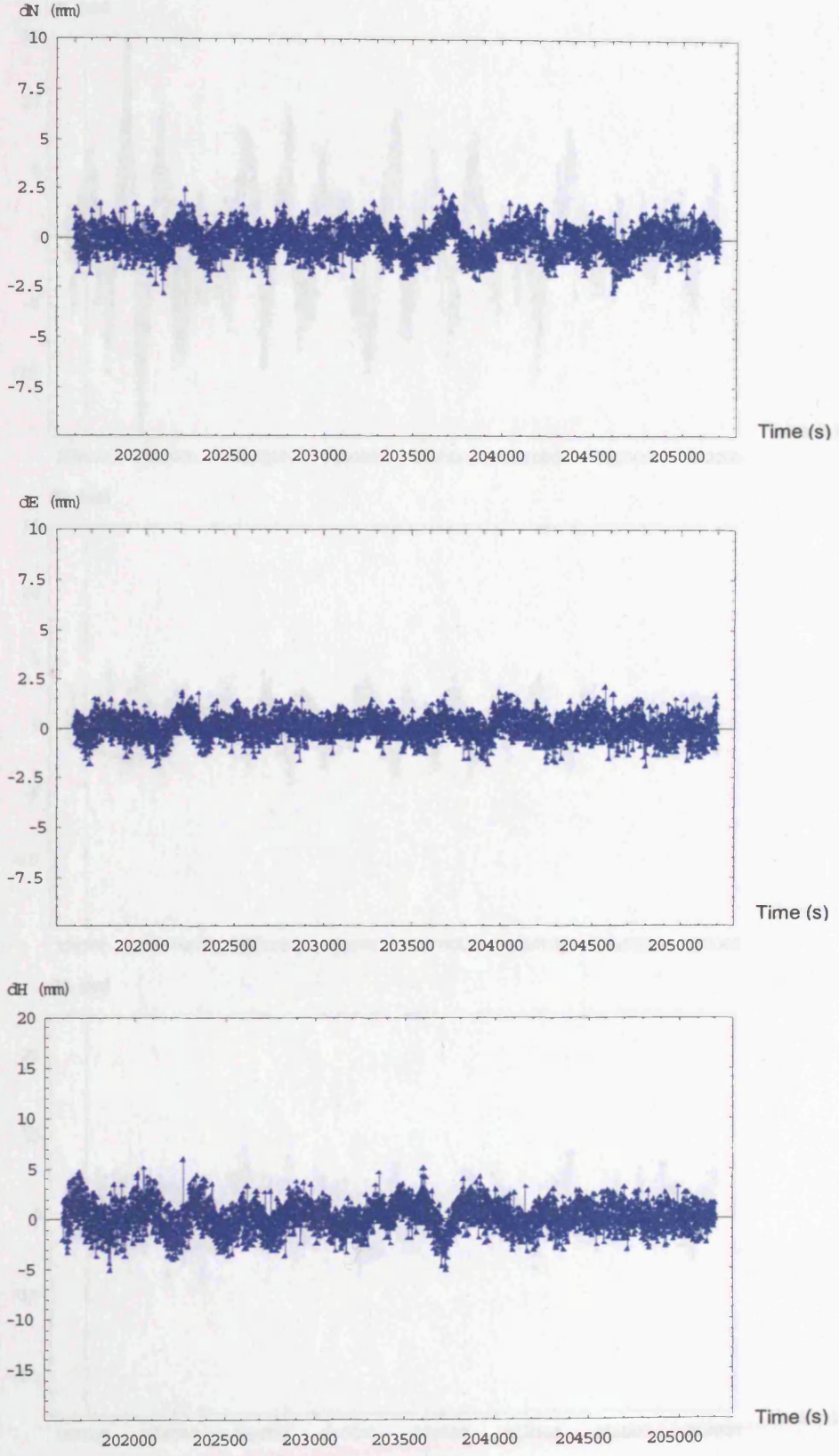

Figure G-3: Positioning error in northing (top), easting (middle), and vertical (bottom) of single-epoch solution with MOD using Galileo + GPS multiple-frequency data in the LCPC-20 dataset.

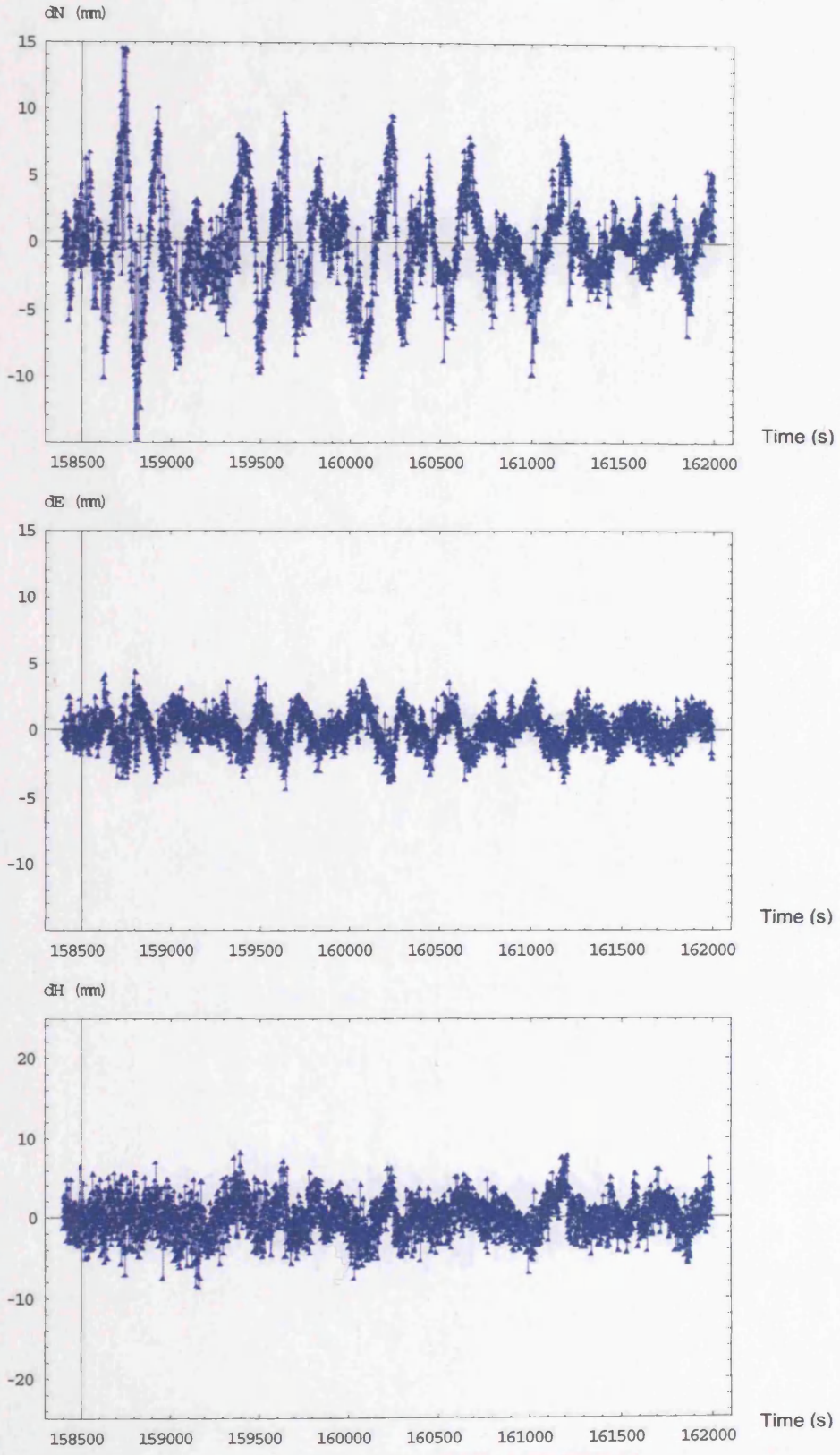

Figure G-4: Positioning error in northing (top), easting (middle), and vertical (bottom) of single-epoch solution with MOD using GPS three-frequency data in the LBCH-7 dataset.

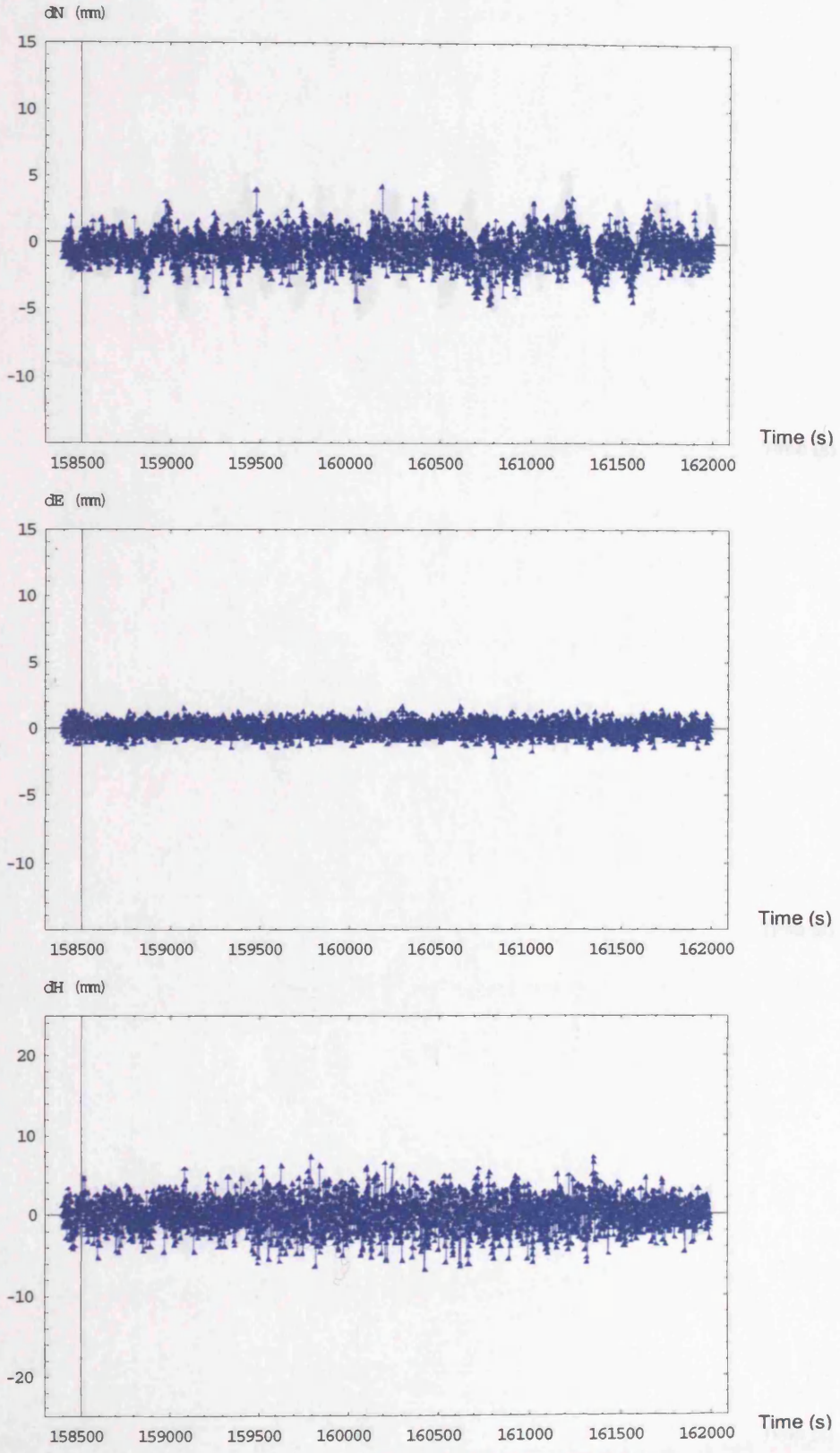

Figure G-5: Positioning error in northing (top), easting (middle), and vertical (bottom) of single-epoch solution with MOD using Galileo three-frequency data in the LBCH-7 dataset.

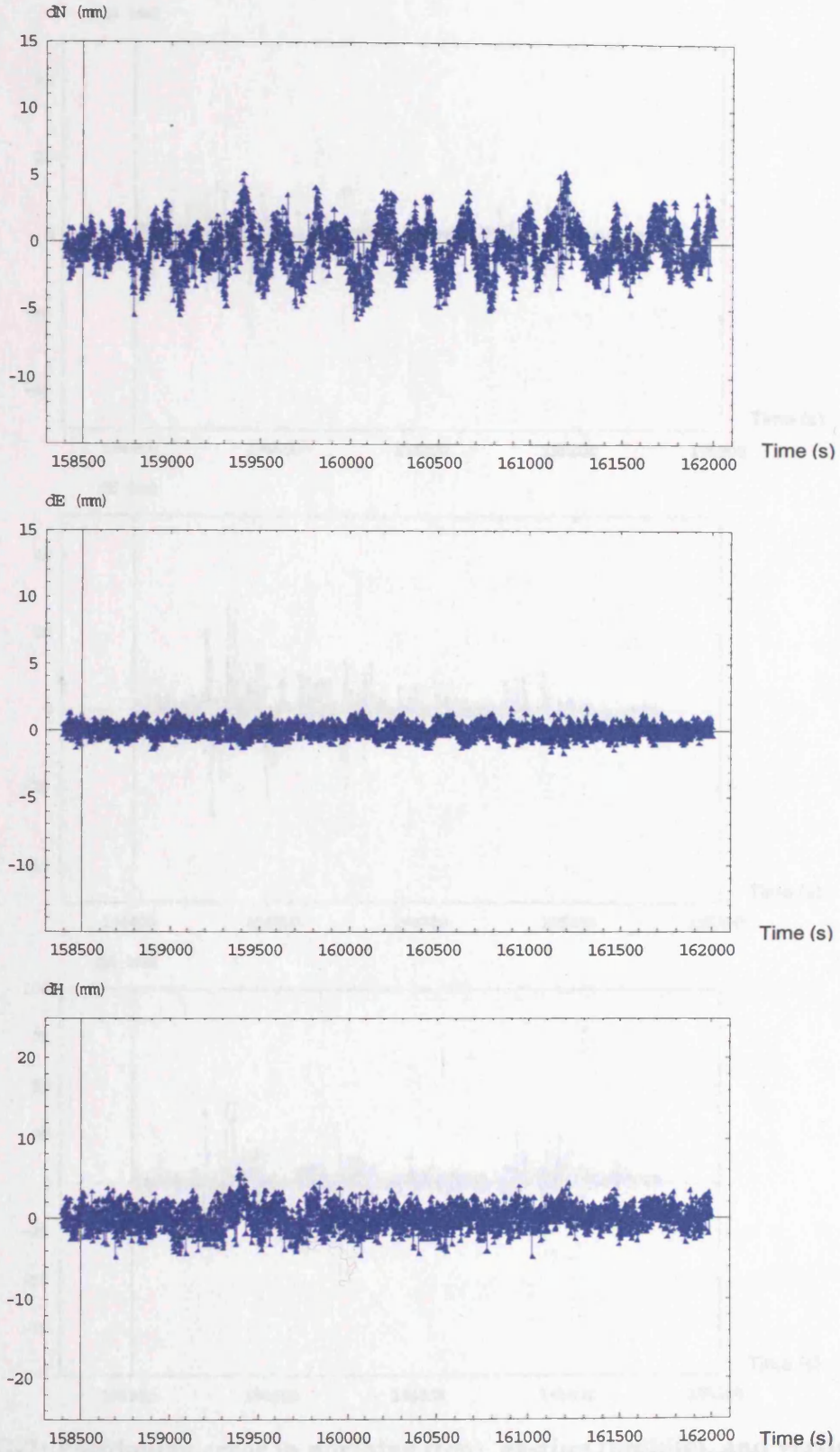

Figure G-6: Positioning error in northing (top), easting (middle), and vertical (bottom) of single-epoch solution with MOD using Galileo + GPS multiple-frequency data in the LBCH-7 dataset.

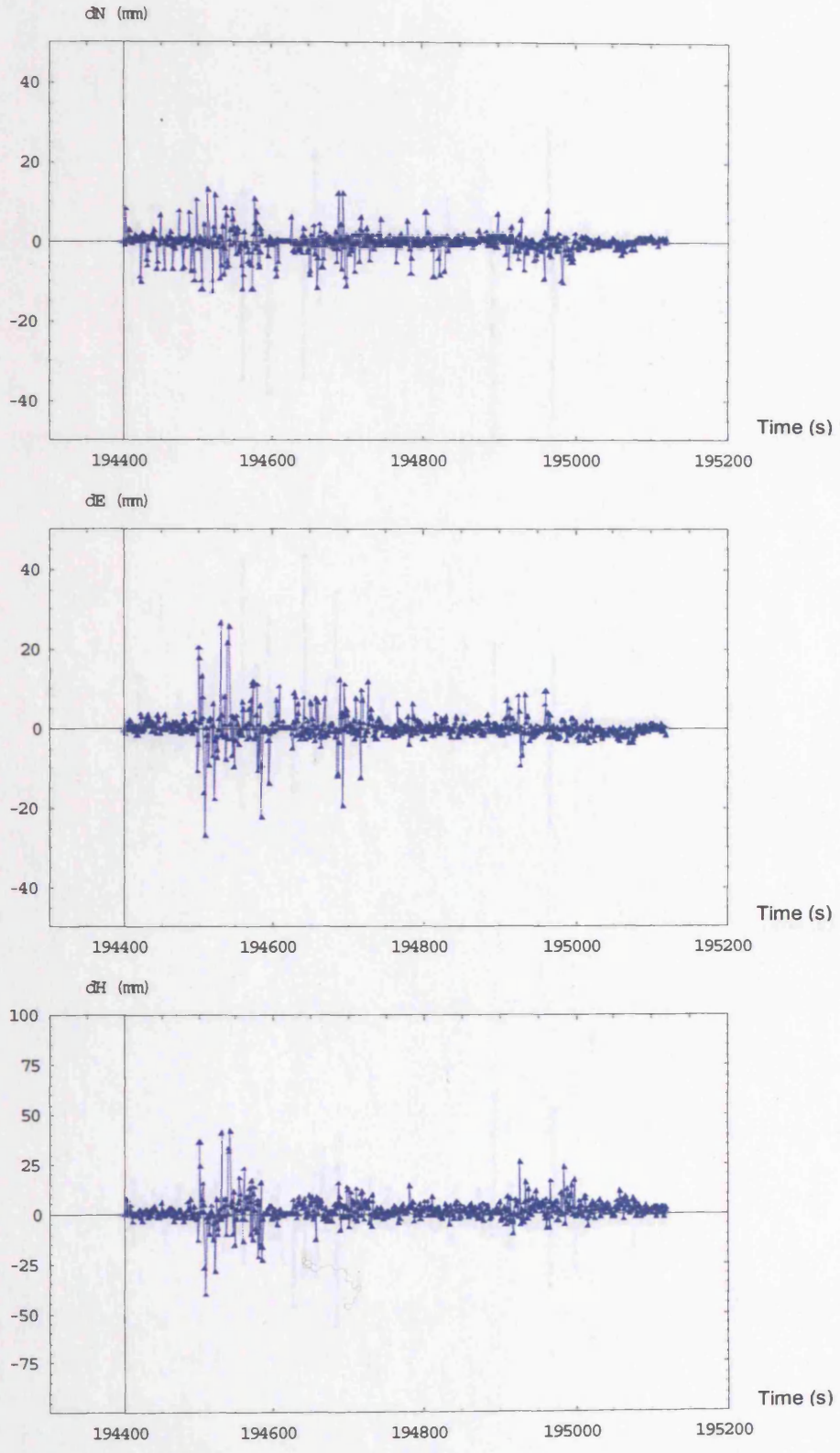

Figure G-7: Positioning error in northing (top), easting (middle), and vertical (bottom) of single-epoch solution with MOD using GPS three-frequency data in the K-HK7-600 dataset.

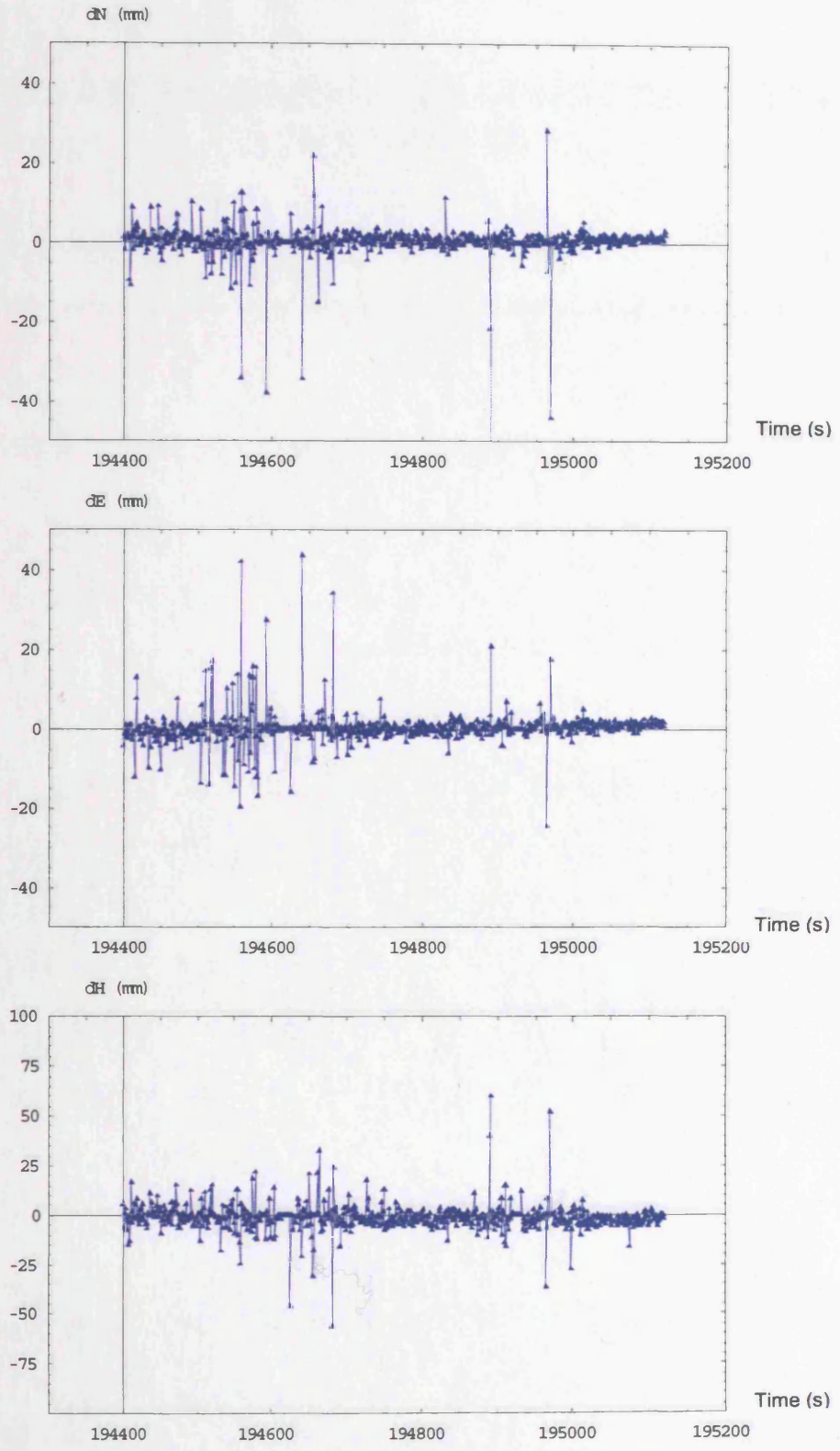

Figure G-8: Positioning error in northing (top), easting (middle), and vertical (bottom) of single-epoch solution with MOD using Galileo three-frequency data in the K-HK7-600 dataset.

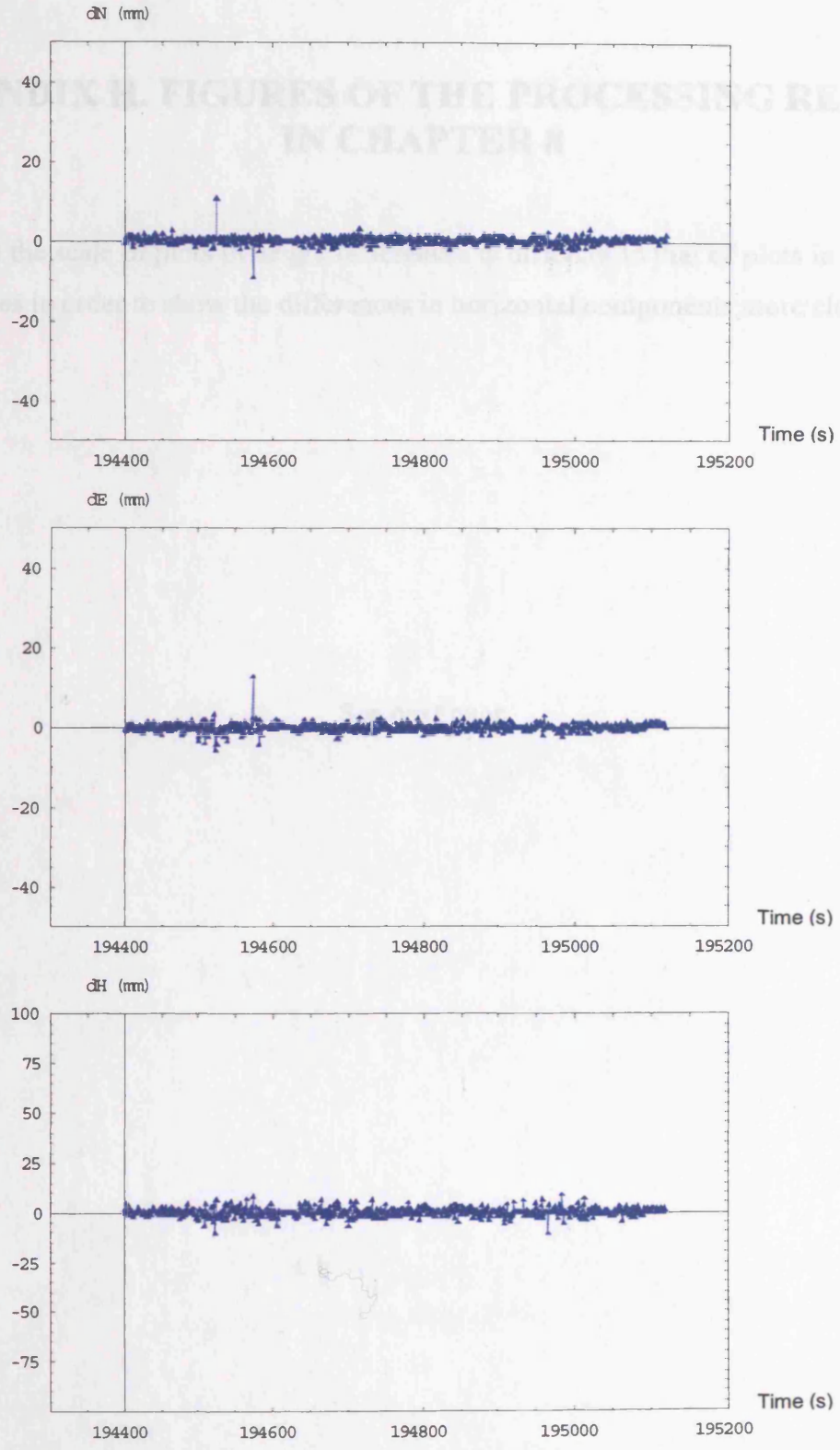

Figure G-9: Positioning error in northing (top), easting (middle), and vertical (bottom) of single-epoch solution with MOD using Galileo + GPS multiple-frequency data in the K-HK7-600 dataset.

APPENDIX H. FIGURES OF THE PROCESSING RESULTS IN CHAPTER 8

Note that the scale of plots in height differences is different to that of plots in horizontal differences in order to show the differences in horizontal components more clearly.

See next page

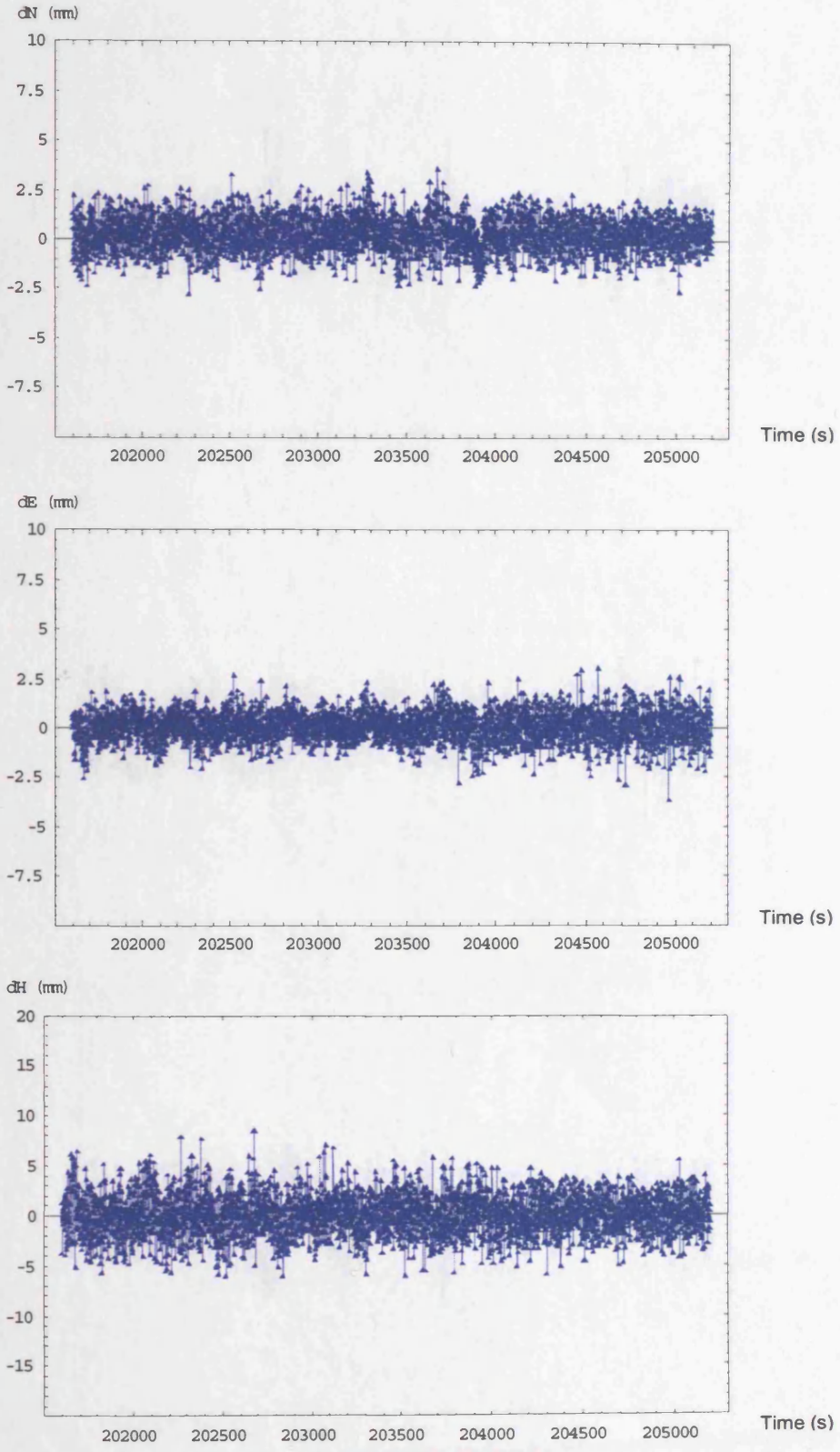

Figure H-1: Positioning error in northing (top), easting (middle), and vertical (bottom) of single-epoch solution with CMOD using GPS three-frequency data in the LCPC-20 dataset.

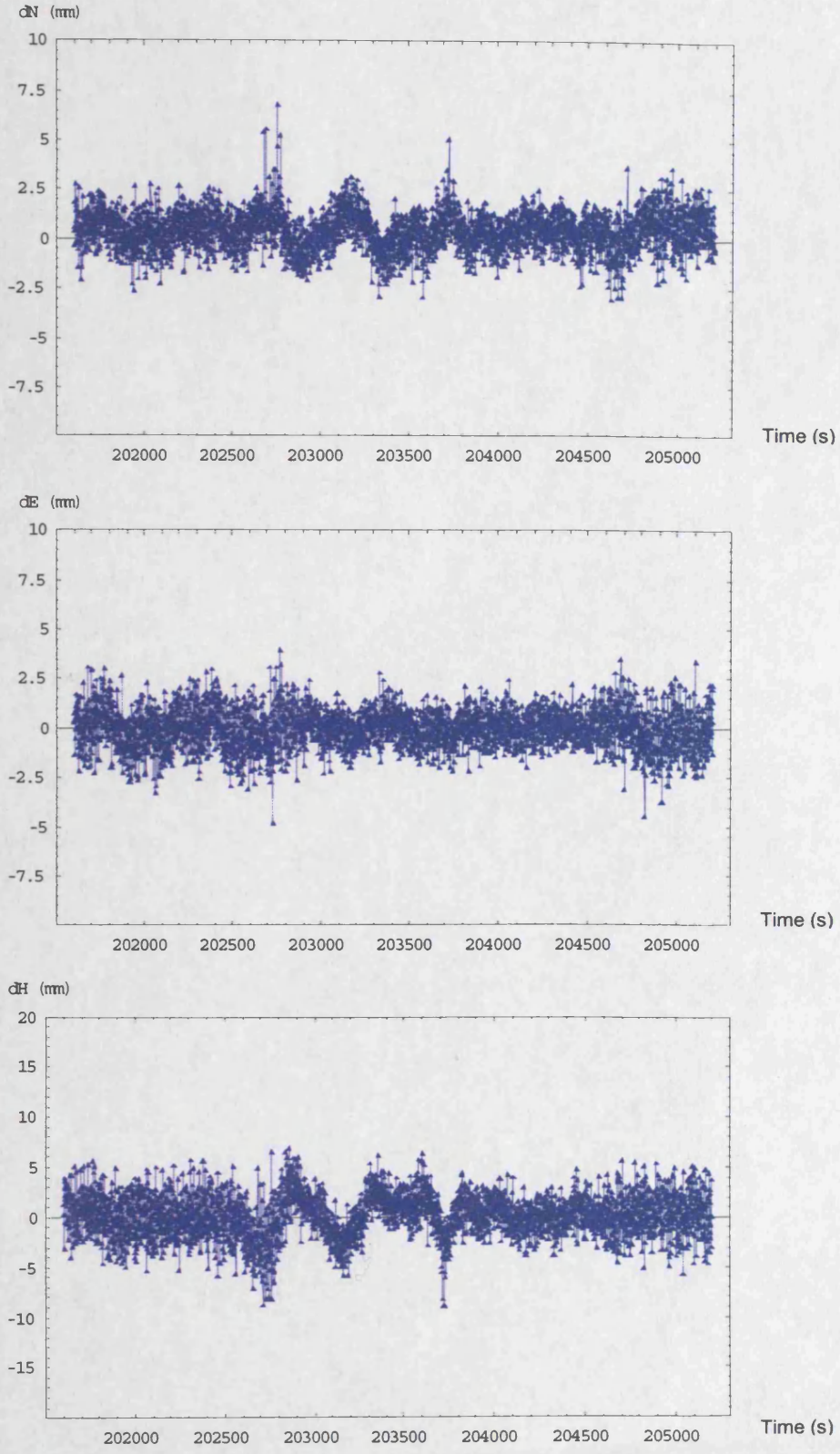

Figure H-2: Positioning error in northing (top), easting (middle), and vertical (bottom) of single-epoch solution with CMOD using Galileo three-frequency data in the LCPC-20 dataset.

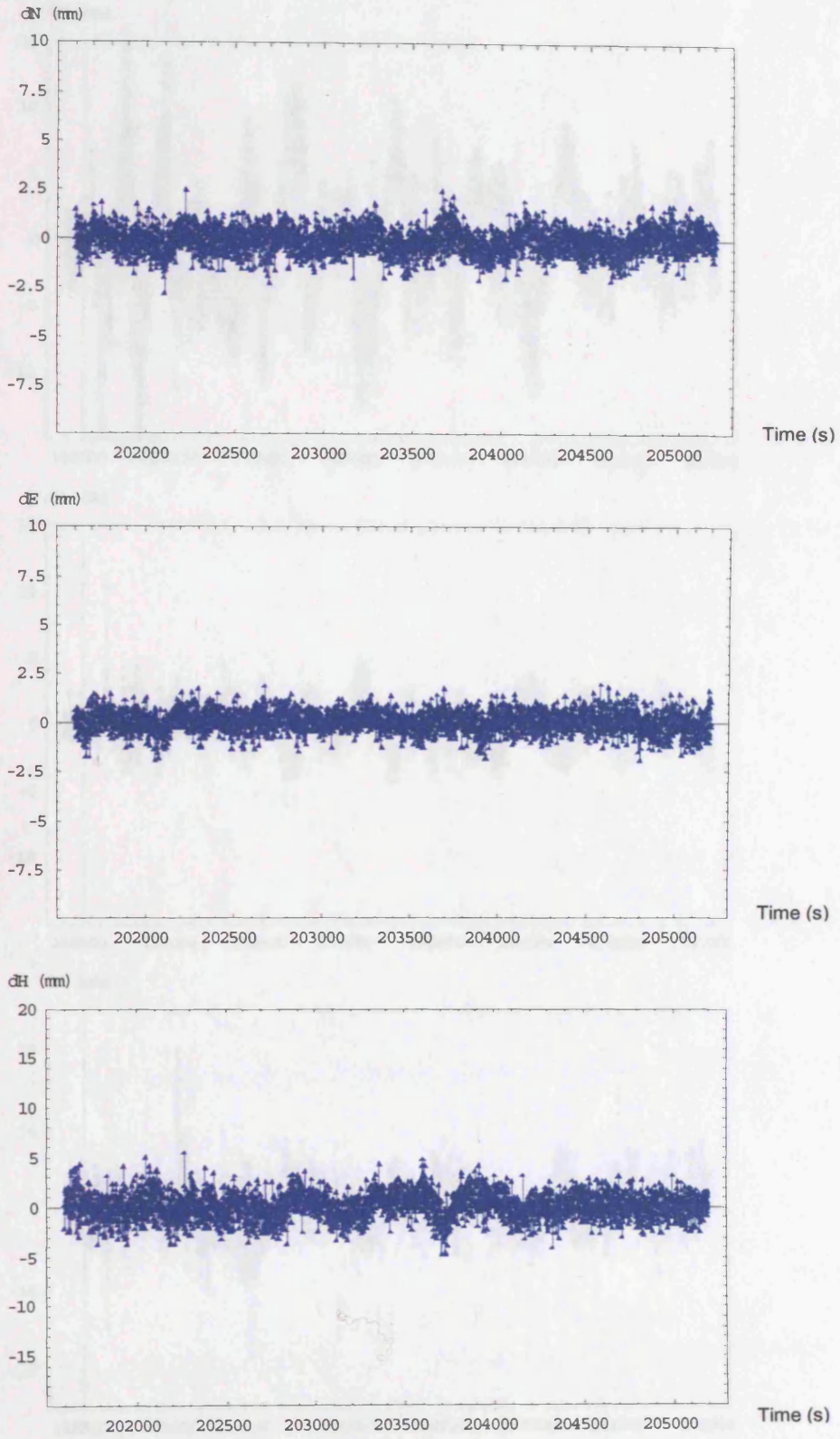

Figure H-3: Positioning error in northing (top), easting (middle), and vertical (bottom) of single-epoch solution with CMOD using GPS + Galileo multiple-frequency data in the LCPC-20 dataset.

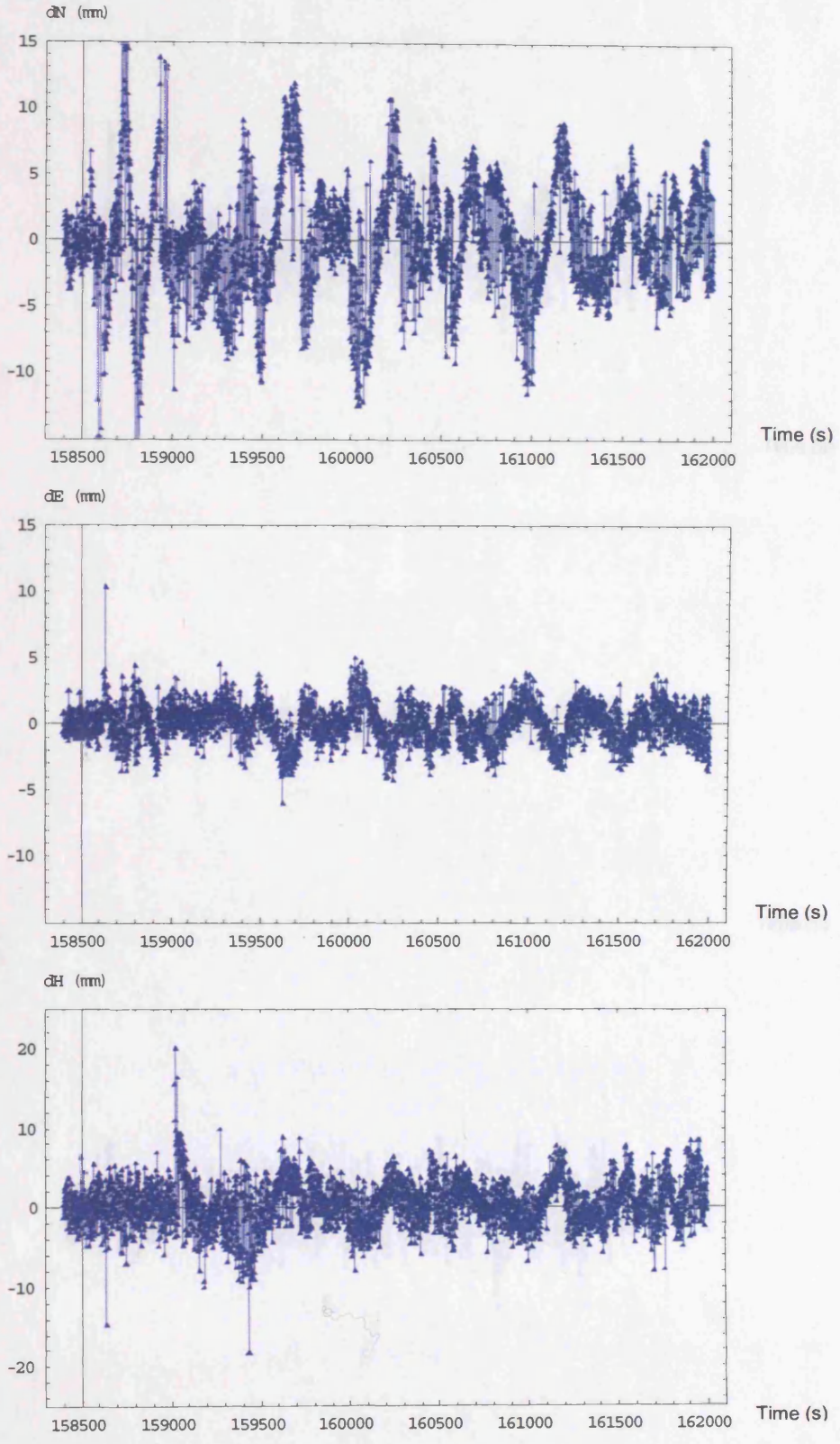

Figure H-4: Positioning error in northing (top), easting (middle), and vertical (bottom) of single-epoch solution with CMOD using GPS three-frequency data in the LBCH-7 dataset.

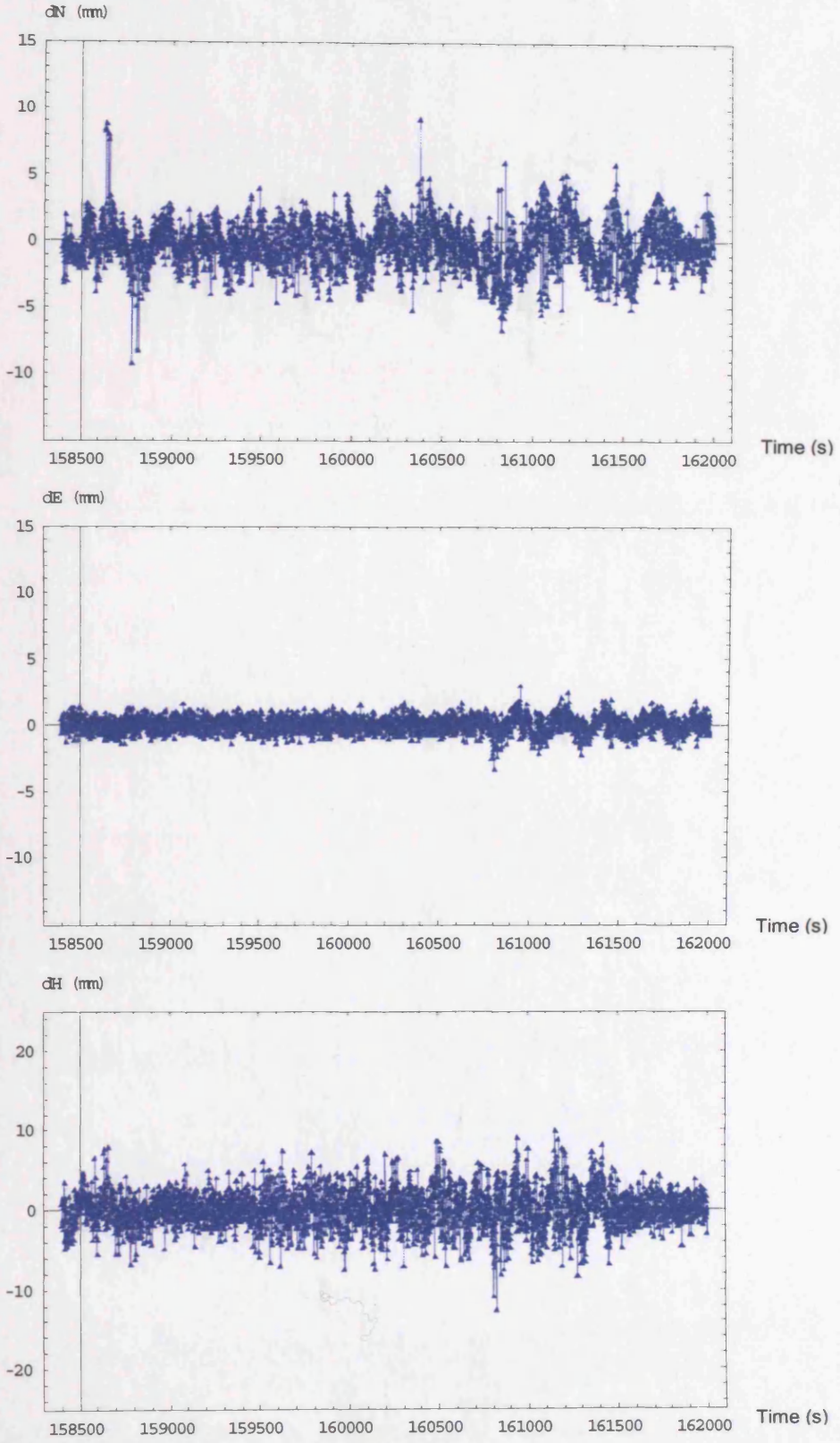

Figure H-5: Positioning error in northing (top), easting (middle), and vertical (bottom) of single-epoch solution with CMOD using Galileo three-frequency data in the LBCH-7 dataset.

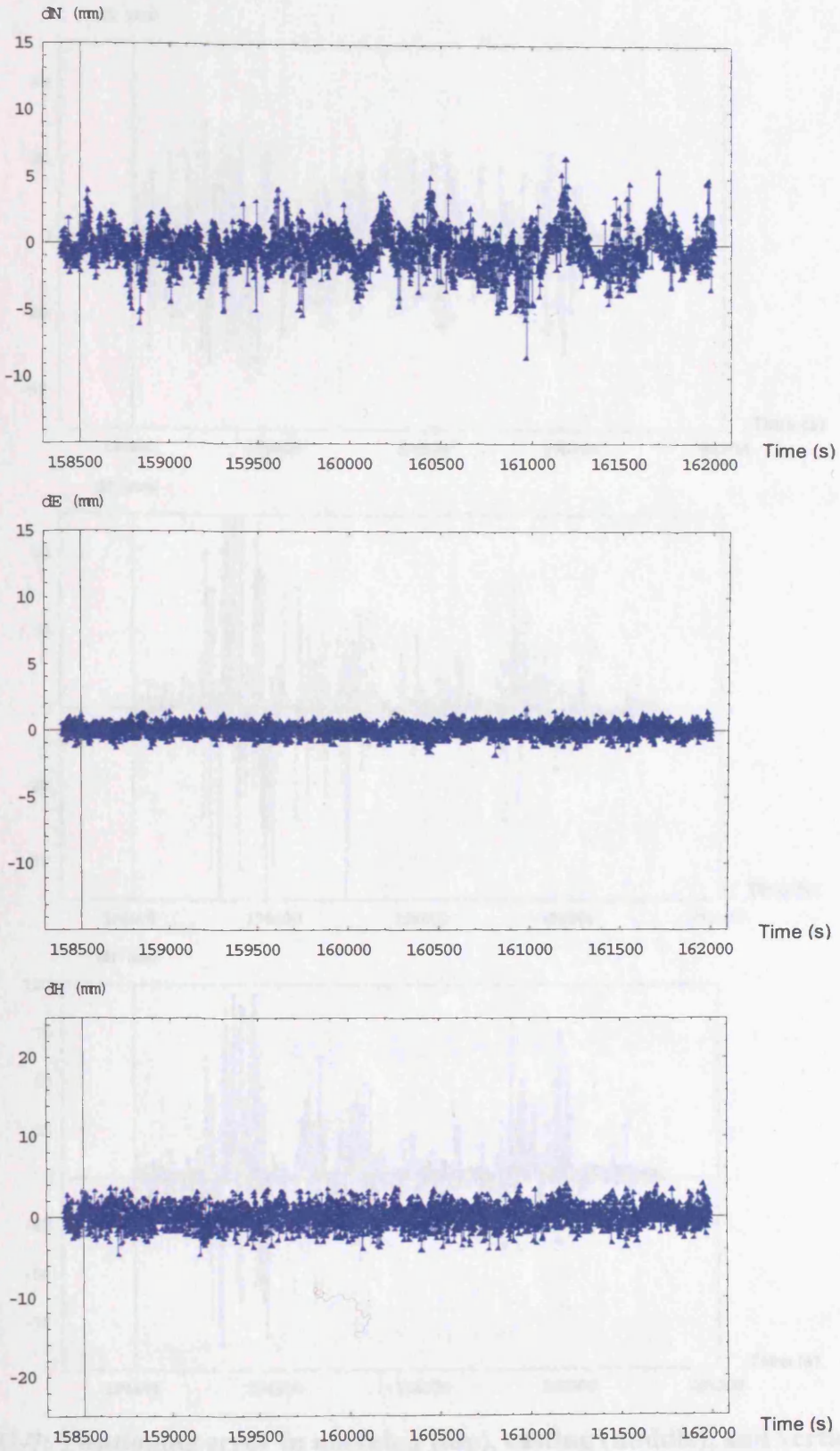

Figure H-6: Positioning error in northing (top), easting (middle), and vertical (bottom) of single-epoch solution with CMOD using GPS + Galileo multiple-frequency data in the LBCH-7 dataset.

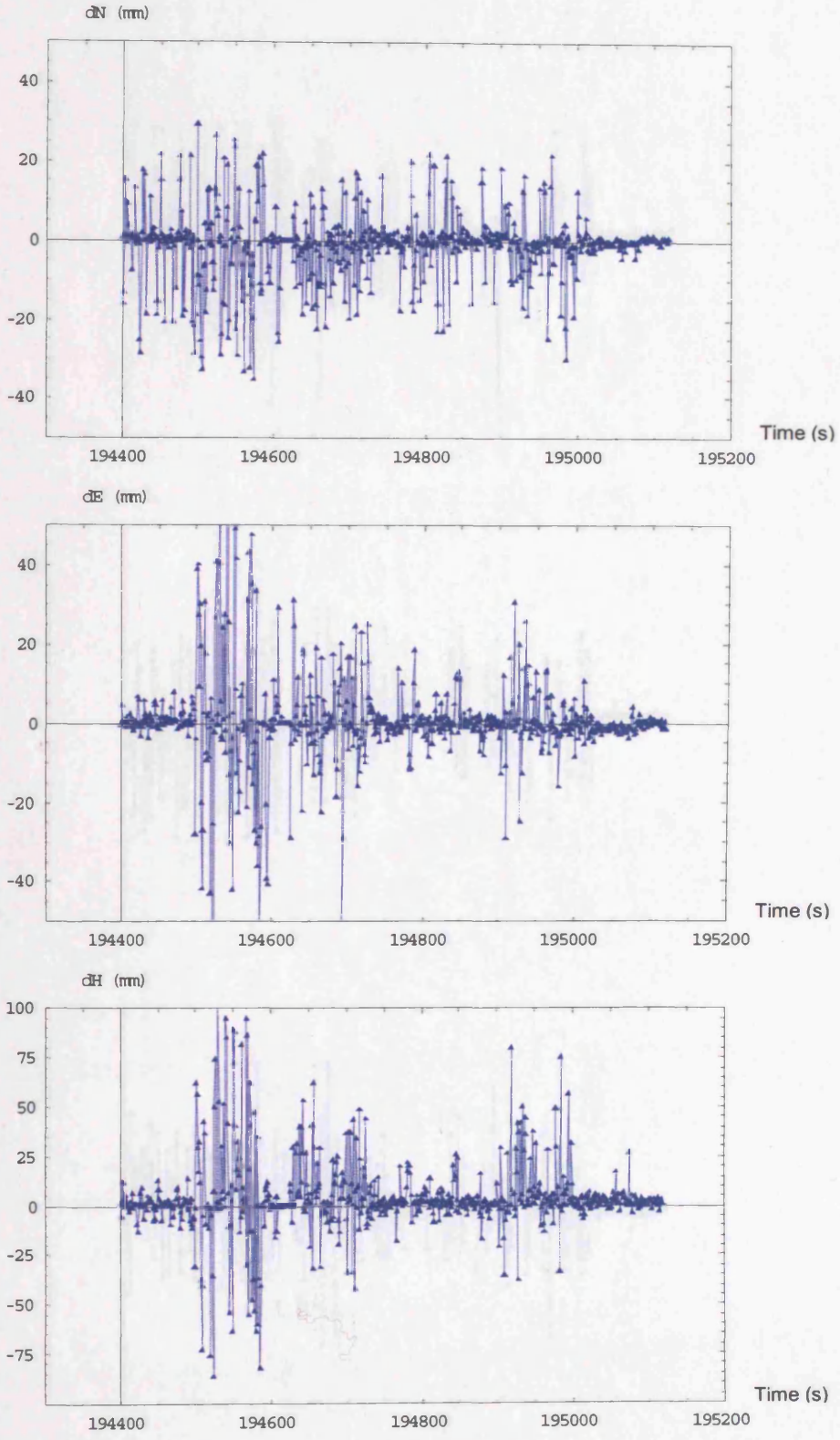

Figure H-7: Positioning error in northing (top), easting (middle), and vertical (bottom) of single-epoch solution with CMOD using GPS three-frequency data in the K-HK7-600 dataset.

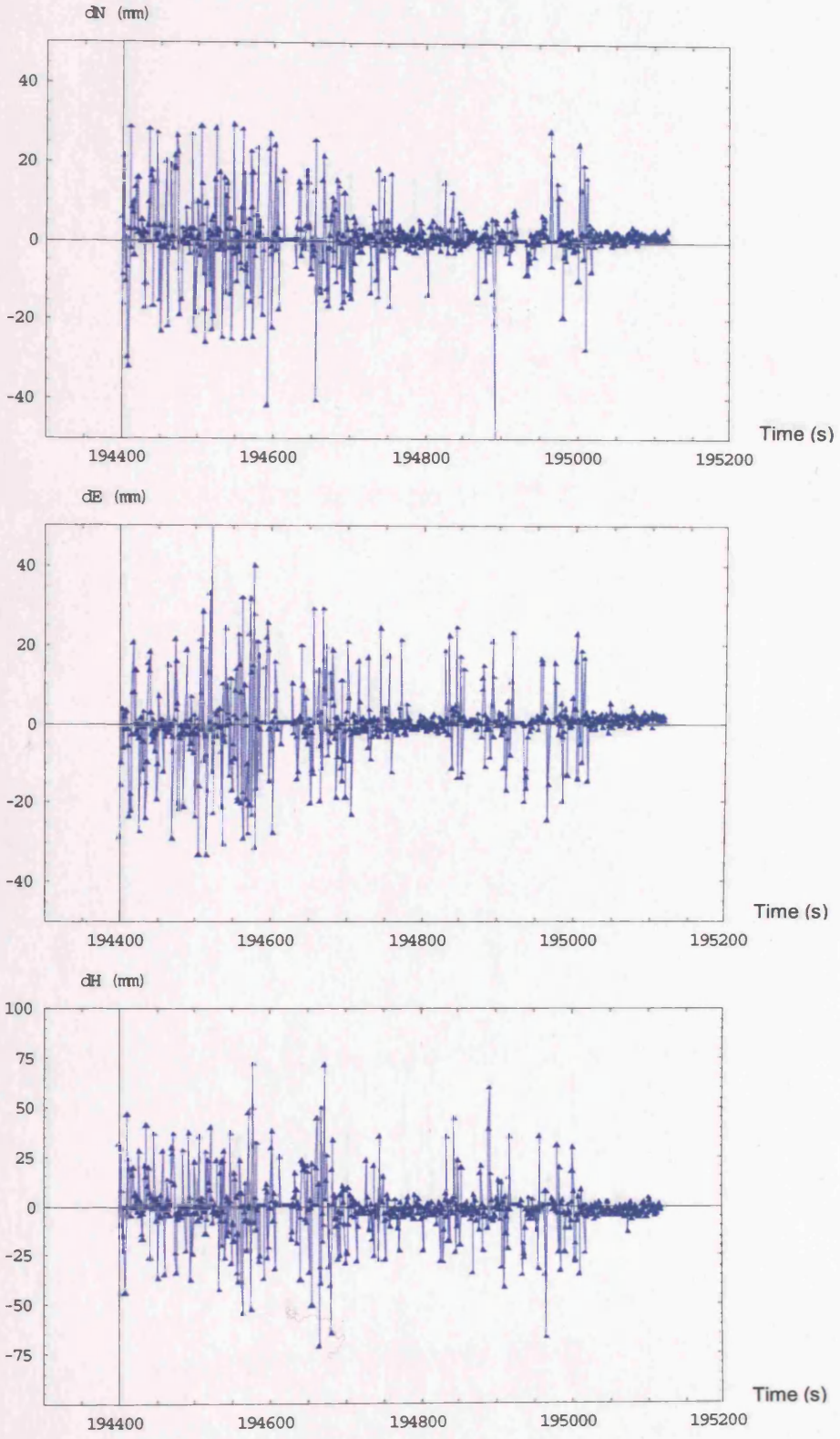

Figure H-8: Positioning error in northing (top), easting (middle), and vertical (bottom) of single-epoch solution with CMOD using Galileo three-frequency data in the K-HK7-600 dataset.

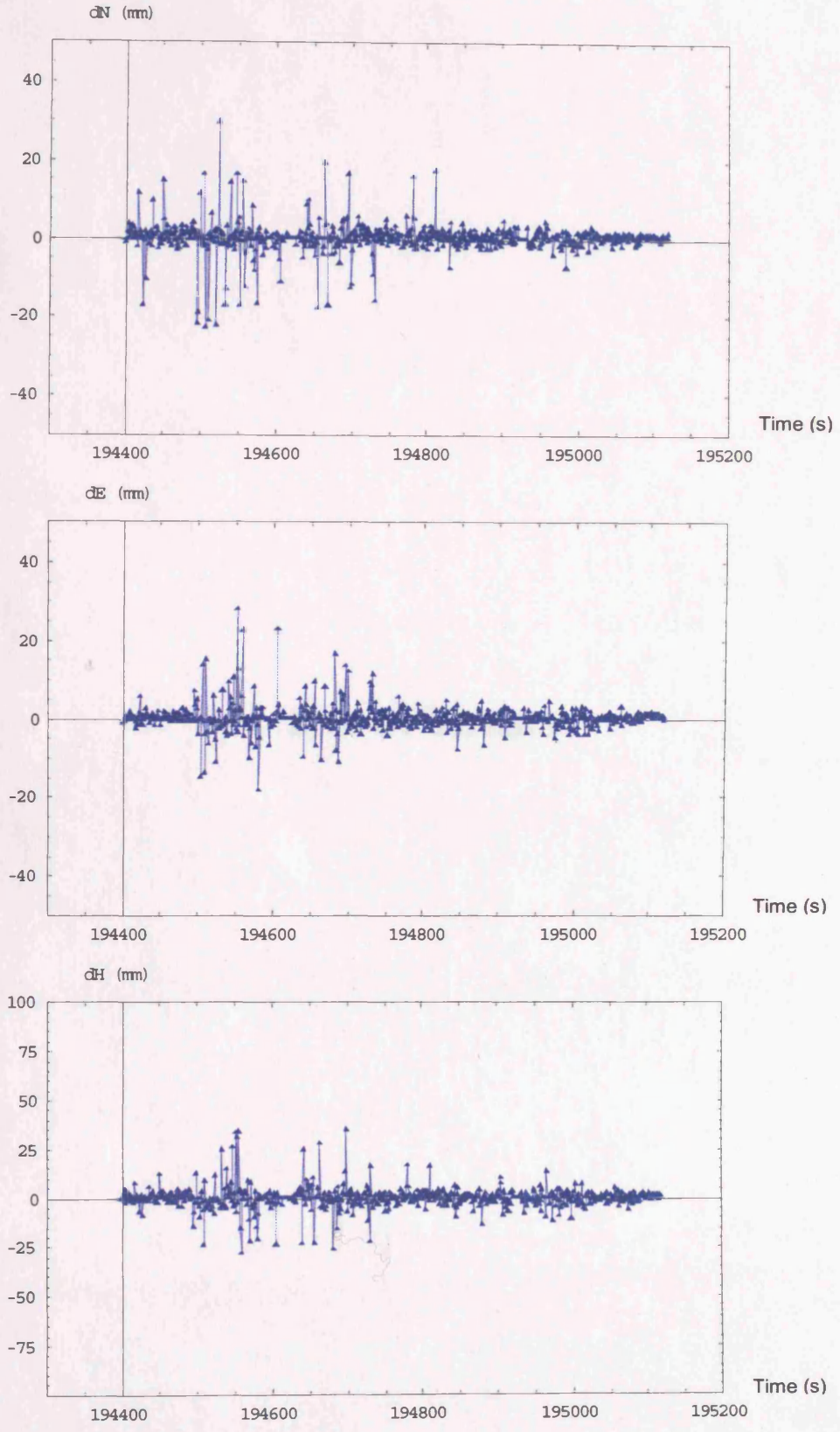

Figure H-9: Positioning error in northing (top), easting (middle), and vertical (bottom) of single-epoch solution with CMOD using GPS + Galileo multiple-frequency data in the K-HK7-600 dataset.

END OF THESIS